TRANSACTIONS
OF THE ASME
Series B

Journal of ENGINEERING FOR INDUSTRY

November 1961

Divisions: AVIATION • MACHINE DESIGN • MANAGEMENT • PROCESS INDUSTRIES MAINTENANCE AND PLANT ENGINEERING • RAILROAD • PRODUCTION ENGINEERING MATERIALS HANDLING • RUBBER AND PLASTICS • PETROLEUM • SAFETY • TEXTILE WOOD INDUSTRIES • **Research Committees:** METAL PROCESSING • FLOW OF BULK MATERIALS • ELEVATORS • MECHANICAL SPRINGS

Published Quarterly by
THE AMERICAN SOCIETY OF MECHANICAL ENGINEERS

TRANSACTIONS OF THE ASME
Series B

Journal of
ENGINEERING FOR INDUSTRY

VOLUME 83 • SERIES B • NUMBER 4
November 1961

CONTENTS

373 **A Tabular Collocation Method for Beam Vibration** (60—WA-76)
R. Chicurel and E. Suppiger

377 **Critical Speeds of Two Bearing Machines With Overhung Weight** (60—WA-39)
R. F. Wojnowski and T. R. Faucett

383 **Balancing Flexible Rotors** (60—WA-13)
A. H. Church and R. Plunkett

390 **Stress and Strain in Spinning Paraboloid Dishes—2** (60—WA-91)
M. J. Cohen

397 **The Flexural Vibrations of Thin Laminated Cylinders** (60—WA-6)
J. C. White

403 **Damping Structural Resonances Using Viscoelastic Shear-Damping Mechanisms, Part I—Design Configurations** (60—WA-73)
J. E. Ruzicka

414 **Damping Structural Resonances Using Viscoelastic Shear-Damping Mechanisms, Part II—Experimental Results** (60—WA-72)
J. E. Ruzicka

425 **Magnetic Properties of Malleable Irons** (60—WA-218)
W. K. Bock and T. D. Hutchinson

434 **Free Oscillations of Edge-Connected Simply Supported Plate Systems** (60—WA-112)
E. E. Ungar

441 **The Yielded Compound Cylinder in Generalized Plane Strain** (60—WA-71)
S. J. Becker

449 **Stresses in a Pipe Bent Into a Circular Arc** (60—WA-157)
N. A. Weil, J. E. Brock, and W. E. Cooper

460 **Deflection of Heat Exchanger Flanged Joints as Affected by Barreling and Warping** (60—WA-70)
W. M. Dudley

467 **Thermal-Stress Analysis of Irregular Shapes** (60—WA-131)
P. P. Bijlaard and R. J. Dohrmann

478 **A Study of Shear-Spinnability of Metals** (60—WA-187)
Serope Kalpakcioglu

485 **A Theory of Shear Spinning of Cones** (60—WA-134)
S. Kobayashi, I. K. Hall, and E. G. Thomsen

496 **An Experimental Investigation of Temperature Distribution at Tool-Flank Surface** (60—WA-87)
B. T. Chao, H. L. Li, and K. J. Trigger

505 **Forces on a Worn Cutting Tool** (60—WA-86)
H. T. McAdams and Paul Rosenthal

513 **Some Controlled Metal-Cutting Studies With Resulfurized Steels** (60—WA-115)
E. G. Thomsen, S. Kobayashi, and M. C. Shaw

523 **On the Mechanics of Wire Drawing** (60—WA-114)
C. T. Yang

531 **Fundamental Machinability Research in Japan** (60—WA-78)
Katsundo Hitomi

(Continued on inside back cover)

EDITORIAL DEPARTMENT

Editor, J. J. JAKLITSCH, JR.
Consulting Editor, LEO BLODGETT
Production, JEAN NORTH
Art Editor, HENRY BALFOUR

OFFICERS OF THE ASME

President, W. H. BRYNE
Secretary, O. B. SCHIER, II
Treasurer, E. J. KATES
Assistant Treasurer, H. J. BAUER

PUBLICATIONS COMMITTEE

Chairman, HENDLEY N. BLACKMON
MARTIN GOLAND
VITO L. SALERNO
F. J. HEINZE
R. E. DERBY
Junior Representatives
J. W. FOLLANSBEE
STEWART H. ROSS

REGIONAL ADVISORY BOARD

Region I, H. M. ROGERS, JR.
Region II, ROBERT E. ABBOTT
Region III, A. F. BOCHENEK
Region IV, FRANCIS C. SMITH
Region V, WM. J. TITZEL
Region VI, C. R. EARLE
Region VII, RALPH L. SCORAH
Region VIII, G. CORRY MCDONALD
Region IX, M. S. UMBENHAUER
Region X, CARL J. ECKHARDT

Published quarterly by The American Society of Mechanical Engineers. Publication office at 20th and Northampton Streets, Easton, Pa. The editorial department is located at the headquarters of the Society, 345 East Forty-Seventh Street, New York 17, N. Y. Cable address, "Mechanover," New York. Price $3.00 a copy, $10.00 annually; to members, $1.50 a copy, $5.00 annually. Add 50 cents for postage to all countries outside the United States and Canada. Changes of address must be received at Society headquarters seven weeks before they are to be effective on the mailing list. Please send old as well as new address. . . . By-Law: The Society shall not be responsible for statements or opinions advanced in papers or . . . printed in its publications (B13, Par. . . . Second-class mail privileges authorized at Easton, Penna. . . . This publication is authorized to be mailed at the special rates of postage prescribed by Section 132.122 . . . © Copyrighted 1961, by The American Society of Mechanical Engineers. Reprints from this publication may be made on condition that full credit be given the TRANSACTIONS of the ASME, Series B—Journal of Engineering for Industry, and the author, and that date of publication be stated.

TRANSACTIONS OF THE ASME
is Indexed by the Engineering Index, Inc.

R. CHICUREL
Associate Professor,
Virginia Polytechnic Institute,
Blacksburg, Va. Assoc. Mem. ASME

E. SUPPIGER
Professor, Princeton
University, Princeton, N. J.

A Tabular Collocation Method for Beam Vibration

This paper presents a procedure, based on the integral equation method, for the calculation of the natural frequencies of lateral vibration of beams with variable cross section. The approximate solution is obtained by collocation [1, 2].[1] *A preliminary step in the analysis is the determination of static deflection curves; this is carried out in a convenient tabular form. An example of a stepped beam is given and the results are compared to those obtained by Myklestad's method* [3].

The Integral Equation

Green's function [4] for a beam (supported so that translation of the beam is not possible) is written as $G(x, s)$ and is the static deflection at x due to a unit lateral load applied at s (see Fig. 1). It follows from Maxwell's reciprocal theorem [5] that

$$G(x, s) = G(s, x) \qquad 0 \leq x, s \leq L$$

For a normal mode of vibration, the deflection y at any section x of a beam may be written as

$$y(x, t) = X(x) \cos pt$$

Using d'Alembert's principle, the load acting on an element of length ds is the inertia force

$$-\frac{A(s)ds\,\gamma(s)}{g}\ddot{y} = \frac{A(s)\gamma(s)}{g} X(s)p^2 \cos pt\, ds$$

and the deflection of the vibrating beam at any section x, due to the inertia forces distributed continuously along the beam from $s = 0$ to $s = L$, may be found by superposing the contributions of the infinitesimal inertia forces:

$$y = X(x) \cos pt = \int_0^L \frac{A(s)\gamma(s)}{g} X(s)p^2 \cos pt\, G(x, s)ds$$

Thus

$$X(x) = p^2 \int_0^L G(x, s) \frac{A(s)\gamma(s)}{g} X(s)ds$$

Let

$$K(x, s) = G(x, s) \frac{A(s)\gamma(s)}{g}, \qquad \lambda = p^2;$$

then

$$X(x) = \lambda \int_0^L K(x, s)X(s)ds \tag{1}$$

Eq. (1) is a homogeneous linear integral equation of the second kind. We seek the solutions X_i corresponding to the λ_i.

Collocation Procedure

The method of collocation may be used to obtain approximations to functions, or to solutions of differential or integral equations. One assumes a function containing the parameters a_1, a_2, a_3, . . . whose values are determined so that the assumed function satisfies the equation for N values ($N = 1, 2, 3, \ldots$) of the independent variables.

For the solution of Eq. (1), the procedure to be followed is:

1 Assume $X(x) = a_1\phi_1(x) + a_2\phi_2(x) + \ldots = \sum_{j=1}^{N} a_j\phi_j(x)$,

wherein the a_j are the parameters and the $\phi_j(x)$ are known functions. The criterion used in the selection of these functions is that the shapes corresponding to the modes being investigated be simulated reasonably well by the assumed form of $X(x)$; experience and common sense are assets in this selection.

2 Select N points along the length of the beam. The values of x for these points are $x_1, x_2, \ldots, x_N$.

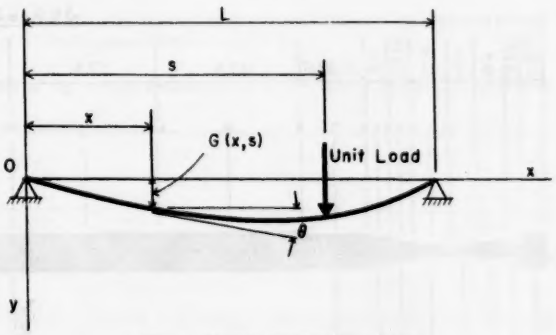

Fig. 1 Green's function for a beam

[1] Numbers in brackets designate References at end of paper.

Contributed by the Machine Design Division and presented at the Winter Annual Meeting, New York, N. Y., November 27–December 2, 1960, of The American Society of Mechanical Engineers. Manuscript received at ASME Headquarters, April 14, 1960. Paper No. 60—WA-76.

Nomenclature

- A = area of cross section of beam
- E = modulus of elasticity in tension or compression
- g = acceleration of gravity
- G = Green's function
- I = moment of inertia of cross section
- L = length of beam
- M = bending moment
- p = circular frequency
- s = distance from left end of beam to location of unit load
- t = time
- x = distance from left end of beam to station at which the deflection is computed
- X = normal function for beam
- y = dynamic deflection
- γ = weight per unit volume
- $\lambda = p^2$
- θ = slope of beam
- $(\dot{}) = \frac{d}{dt}(\ )$

Additional notation is defined where first used.

3 Evaluate each of the functions $K(x_1, s)$, $K(x_2, s)$, . . ., $K(x_N, s)$.

4 Force the assumed function to satisfy Eq. (1) at *each* of the N selected points, i.e.,

$$\sum_{j=1}^{N} a_j \phi_j(x_i) = \lambda \int_0^L K(x_i, s) \sum_{j=1}^{N} a_j \phi_j(s) ds$$

$$i = 1, 2, \ldots, N$$

In any specific case, after the indicated integration is performed, the equations above reduce to a system of linear, homogeneous, algebraic equations of the form

$$\sum_{j=1}^{N} (\lambda k_{ij} - c_{ij}) a_j = 0 \qquad i = 1, 2, \ldots, N \qquad (2)$$

wherein

$$k_{ij} = \int_0^L K(x_i, s) \phi_j(s) ds$$

$$c_{ij} = \phi_j(x_i)$$

5 The unknowns in Eqs. (2) are the a_j (plus the λ) and the nontrivial solution requires the determinant of the coefficients of the a_j to vanish. This condition yields the frequency equation of degree N in λ(i.e., in p^2). Note that it is necessary to select as many points x_i as terms $a_j\phi_j$ in the assumed X function in order to have the same number of Eqs. (2) as unknowns a_j.

To evaluate the various k_{ij} it is necessary to find the various $G(x_i, s)$ since

$$k_{ij} = \int_0^L K(x_i, s) \phi_j(s) ds = \int_0^L G(x_i, s) \frac{A(s)\gamma(s)}{g} \phi_j(s) ds$$

but $G(x_i, s) = G(s, x_i)$ = deflection at s due to unit load at x_i; the boundary conditions are always satisfied by the $G(s, x_i)$.

Tabular Procedure for $G(s, x_i)$

The flexural rigidity EI of the beam is assumed to vary in a series of steps. If the actual variation is continuous, this assumption involves an approximation.

The procedure for determining the functions $G(s, x_i)$ will be described with reference to the beam considered in the example at the end of this paper; the extension to other cases is quite simple. The beam of the example is shown in Fig. 2. The deflections found by the procedure outlined below are those due to bending of the beam only. To these one must add the deflections due to the displacements of the elastic supports.

First, a number of points along the length of the beam are chosen (see Fig. 2) and labeled successively 0, 2, 4, . . ., 24. These should include at least all those at which EI changes, as well as the point at which the unit load is applied. In this case, however, the overhanging portions are ignorable as their rigidity does not influence the deflection for the unit load positions chosen. The mid-points between 0 and 2, 2 and 4, etc., are labeled 1, 3, etc., respectively. All points 0, 1, 2, 3, . . ., 24 are called "stations."

Table 1 (a work sheet) shows, in part, the operations made in the calculation of the deflection curve. Row 13 exhibits the values of the deflection G for a unit load applied at station 12. The technique of filling in the table progressively by rows is as follows:

Row 1 lists the station numbers 0, 1, 2, . . ., 24; the stations at which EI changes are repeated.

Row 2 gives, in the dimensionless form s/L, the distance of each station from the left end of the beam.

Each number in *row 3* is the rigidity, in dimensionless form, of a section of beam adjacent to the station. When a station number is repeated, the rigidity of the section to the left appears first and then that of the section to the right. If the station number is not repeated, then the rigidity indicated is that of the section to the left of the station. The rigidity is made dimensionless by dividing it by that of a reference section (in this case the reference section was chosen as that between stations 0 and 1).

Row 4 gives the ratio of the length h between each station and the preceding one, to the length h_r of the reference section.

In *row 5* are given the bending moments in the dimensionless form $M/PL = M/L$ (since the load $P = 1$).

Row 6 gives the values of M/EI in dimensionless form. These values are obtained by dividing the numbers in row 5 by those in row 3, for each station.

A number in the ith column of *row 7* is obtained by adding the numbers in the $(i - 1)$th and ith columns of row 6. The spaces

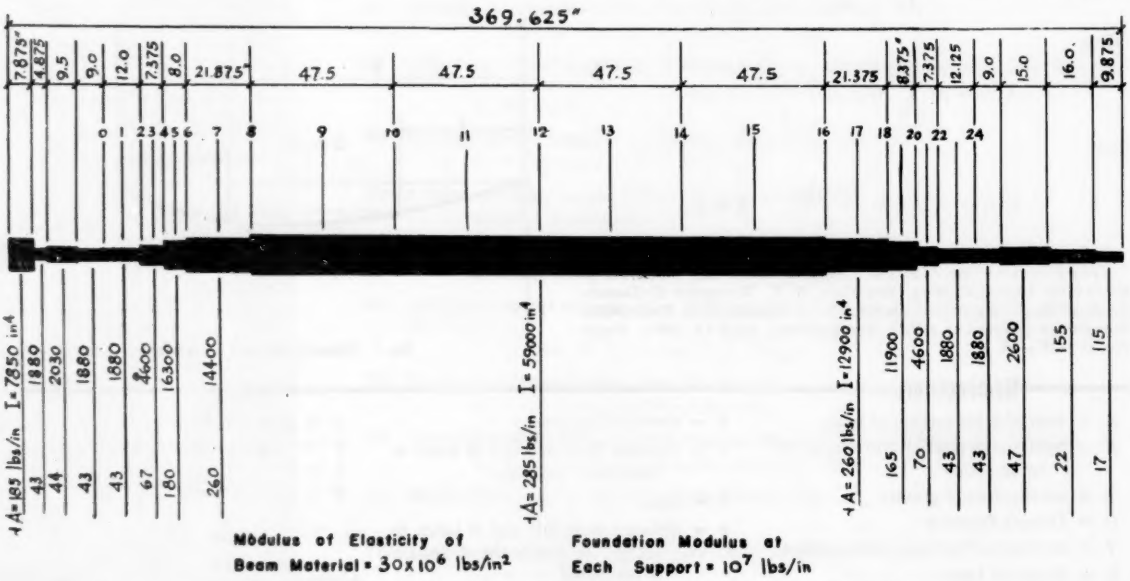

Fig. 2 Stepped beam. Simple supports on elastic foundations at stations 0 and 24.

corresponding to repeated stations remain blank in row 7. The numbers in row 7 are proportional to the *change* in the slope θ between successive stations. In going from row 6 to row 7, one integrates the function M/EI with respect to s by use of the trapezoidal rule. Since M/EI varies linearly with s between any two stations, no approximation occurs here. In symbols, $d\theta/ds = M/EI$ and hence $\Delta\theta = \int_{s_{i-1}}^{s_i} M/EI\, ds$.

The first number in *row 8* is zero and each of the others is obtained by adding to the preceding one in that same row the number immediately above it (i.e., in the same column but in row 7). These values give the changes in the slope θ from station 0 to each of the other stations. For example, the number in row 8 corresponding to station 3 is 0.041882 = 0.03247 + 0.009412.

A number in *row 9* is obtained by multiplying the number immediately above it by 4 for odd stations and by 1 for even stations. This factor of multiplication is denoted by S.

Each number in *row 10* is the sum of three numbers in row 9: the one in the same column and the ones corresponding to the two preceding stations. For example, for station 4, we have 0.243072 = 0.03247 + 0.167528 + 0.043074.

Row 11 results from the multiplication of the numbers in row 10 by the corresponding ones in row 4.

Rows 9, 10, and 11 represent an integration of $(\theta - \theta_0)$, where θ_0 is the slope at station 0, with respect to s by means of Simpson's rule. It will be recalled that, to integrate a function $y(x)$ from x_a to x_b by Simpson's rule using n intervals, the applicable formula is:

$$\int_{x_a}^{x_b} y(x)dx \cong \frac{h}{3}\,[y(x_0) + 4y(x_1) + 2y(x_2) + 4y(x_3) + 2y(x_4) + \ldots + 2y(x_{n-2}) + 4y(x_{n-1}) + y(x_n)]$$

where $h = (x_b - x_a)/n$ and $x_k = x_a + kh$

In this case, $n = 2$; therefore

$$\int_{x_a}^{x_b} y(x)dx \cong \frac{h}{3}\,[y(x_a) + 4(x_a + h) + y(x_b)]$$

Since the slope θ is the derivative of the displacement G, the result of the integration of $(\theta - \theta_0)$ from station $(i - 2)$ to station i is:

$$\int_{s_{i-2}}^{s_i} (\theta - \theta_0)ds = G(s_i) - G(s_{i-2}) - \theta_0(s_i - s_{i-2}) = \Delta G - 2\theta_0 h_i$$

For the stepped beam, the slope equation between any two even numbered stations is second degree in s; thus, the use of Simpson's rule does not involve an approximation.

Row 12 is a summation of the values in row 11, just as row 8 is a summation of the values in row 7.

If $N_i^{(j)}$ represents a number in the ith column of the jth row, then the numbers in *row 13* are found by using the formula:

$$N_i^{(13)} = N_i^{(12)} - N_l^{(12)} \left(\frac{s}{L}\right)_i \quad \text{where } l \text{ refers to last column.}$$

The numbers in row 13 are proportional to the deflections G. Examination of the formula for $N_i^{(13)}$ shows that $N_0^{(13)} = N_l^{(13)} = 0$.

Example[2]

The first two natural frequencies of the beam of Fig. 2 are calculated by assuming a shape given by

$$X(x) = \sum_{j=1}^{3} a_j\phi_j(x) = a_1 + a_2 \sin\frac{\pi x}{L} + a_3 \sin\frac{2\pi x}{L}$$

and using $x_i/L = 0.08455, 0.47481, 0.86507$ as collocation points (i.e., the points at which the governing integral equation is to be satisfied). The first and third collocation points are located at the left and right supports, which are simple supports on elastic foundations. The deflection curve for a unit load at either of these points is a straight line and is easily determined. Only the second collocation point requires a tabular calculation as described; the numbers in Table 1 correspond to this collocation point. As indicated before, since the supports are elastic, a linear deflection is added to the deflections given in Table 1 since the latter are calculated by assuming rigid simple supports.

The integrations required in the determination of the k_{ij} were made by planimeter. Eqs. (2) for this example are:

$$(1 - 6.02m)a_1 + (0.2627 - 4.496m)a_2 + (0.5096 - 2.46m)a_3 = 0$$

$$(1 - 32.60m)a_1 + (0.9968 - 28.46m)a_2 + (0.1583 - 2.66m)a_3 = 0$$

$$(1 - 5.844m)a_1 + (0.4112 - 4.776m)a_2 + (-0.7497 + 1.804m)a_3 = 0$$

[2] Data for this example were obtained through the courtesy of General Electric Co., Schenectady, N. Y.

Table 1 Tabulated calculations (shown in part) of deflection values for beam of Fig. 2 with a unit load at x/L = 0.4748 (station 12) excluding effect of displacement of supports.

ROW	STATION NUMBER								
1	0	1	2	2	3	4	4	5	6
2 s/L	.08455	.10078	.11701	.11701	.12699	.13696	.13696	.14779	.15861
3 EI/EI_r	1	1	1	2.4468	2.4468	2.4468	8.6702	8.6702	8.6702
4 h/h_r		1	1		.61491	.61491		.66728	.66728
5 M/L	0	.00812	.01623	.01623	.02122	.02621	.02621	.03162	.03703
6 $(EI_r/L)M/EI$	0	.00812	.01623	.006633	.008673	.010712	.003023	.003647	.004271
7 $-(2EI_r/h_rL)\cdot\Delta\theta$	0	.00812	.02435		.009412	.011920		.004451	.005284
8 $-(2EI_r/h_rL)\Sigma\Delta\theta$	0	.00812	.03247		.041882	.043074		.047525	.052809
9 $-S(2EI_r/h_rL)\cdot\Sigma\Delta\theta$	0	.032480	.03247		.167528	.043074		.190100	.052809
10 $-(6EI_r/h_rL)\cdot(\Delta G/h - 2\theta_o)$	0		.06495			.243072			.285983
11 $-(6EI_r/h_rL)\cdot(\Delta G - 2\theta_o h)$	0		.06495			.149467			.190831
12 $-(6EI_r/h_rL)\cdot(\Sigma\Delta G - 2\theta_o h)$	0		.06495			.214417			.405248
13 $(6EI_r/h_rL)\cdot G$	0		1.3517			2.0726			2.8268

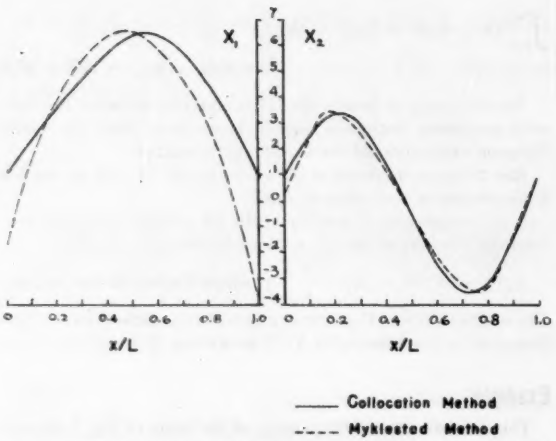

Fig. 3 First and second modal configurations for beam of Fig. 2. Ordinates in arbitrary units.

where $m = \dfrac{p^2 A_r \gamma_r h_r^2 L^2}{6gEI_r}$ (r indicates the reference section)
and the resulting frequency equation is:

$$77.4393m^3 - 105.8728m^2 + 27.5623m - 0.8689 = 0$$

The first and second roots, when converted to values of p, are:

$$p_1 = 150.2 \text{ rad/sec}, \; p_2 = 428 \text{ rad/sec}$$

The modal configurations X_1 and X_2 corresponding to p_1 and p_2, respectively, are found by determining in each case, a set of a_j values from Eqs. (2).

Calculations [6] using Myklestad's method gave values of $p_1 = 148.9$ rad/sec and of $p_2 = 426$ rad/sec. The modal configurations, based on the collocation and Myklestad procedures, are plotted in Fig. 3.

Concluding Remarks

The present method of calculating the natural frequencies of lateral vibration of beams requires that a function with undetermined parameters, approximating the deflection curves for the normal modes, be assumed. In this respect, the method is similar to the well-known Rayleigh-Ritz method. However, in the latter method, it is necessary that the assumed function satisfy the boundary conditions (e.g., zero deflection and slope at a built-in end). In the collocation procedure as applied to the integral equation, it is not essential that the assumed function $X(x)$ satisfy the boundary conditions; these conditions are satisfied by Green's function. In comparing the time required for finding frequencies by the method presented in this paper with other known methods, it may be noted that in actual design applications the static deflection curves for unit loads at the collocation points have a value *per se*. In such cases the time spent in the determination of the static deflections should not be charged entirely to the calculation of the natural frequencies.

References

1 Frazer, Jones, and Skan, "Approximations to Functions and to the Solutions of Differential Equations," Aero. Res. Counc., London Rep. Mem. 1799, March, 1937.

2 Z. Kopal, "Numerical Analysis," John Wiley & Sons, Inc., New York, N. Y., 1956.

3 N. O. Myklestad, "Vibration Analysis," McGraw-Hill Book Company, Inc., New York, N. Y., 1944, p. 184.

4 G. Temple and W. G. Bickley, "Rayleigh's Principle and Its Application to Engineering," Dover Publication, Inc., New York, N. Y., 1956, p. 47.

5 S. Timoshenko and D. H. Young, "Theory of Structures," McGraw-Hill Book Company, Inc., New York, N. Y., 1945, p. 250.

6 E. E. Zwicky, unpublished data, General Electric Co., Schenectady, N. Y., 1956.

REYTON F. WOJNOWSKI
Applied Science Representative, International Business Machines Corporation, Rochester, N. Y.

THOMAS R. FAUCETT[1]
Associate Professor, The University of Rochester, Department of Mechanical Engineering, Rochester, N. Y. Mem. ASME

Critical Speeds of Two Bearing Machines With Overhung Weight

The purpose of this study was to determine the general frequency expression for a rotating shaft with uniformly distributed weight, supported by two bearings, and carrying a concentrated weight at the free end. The bearing spacing and the ratio of the concentrated weight to the total distributed weight have been used as parameters. The data have thus been reduced to dimensionless form so that the results are generally applicable for this type of machine. Frequencies for the first three modes of vibration have been determined and curves plotted for rapid calculation of these frequencies.

Derivation of Frequency Equation

The system investigated in this study is pictured in Fig. 1. The shaft is assumed to be of uniform cross section, with simple supports at two points as indicated, and a concentrated weight at the free end. It will be assumed that the critical speed is suitably approximated by the natural frequency of the system in transverse vibration.

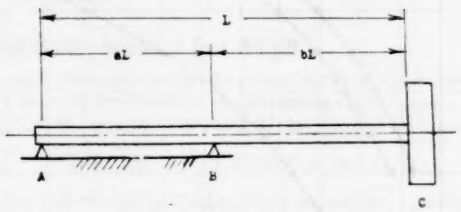

Fig. 1 Vibrating system

In the analysis of the system the following symbols are used:

W_b = total weight of shaft
w = weight of shaft per unit length
W = concentrated end weight
$N = W/W_b$ = ratio of end weight to total shaft weight
L = length of shaft
a = fraction of shaft length between supports
b = fraction of shaft length between support B and the end weight

The equation of motion for a vibrating bar with uniformly distributed weight is

$$\frac{\partial^2}{\partial x^2}\left(EI\frac{\partial^2 y}{\partial x^2}\right) = -\frac{w}{g}\frac{\partial^2 y}{\partial t^2} \tag{1}$$

where y is the transverse deflection, and x is the distance measured along the length of the bar from some arbitrary origin, in this case the left-hand bearing, A. EI is the flexural rigidity of the beam. Under the assumption that the deflection is a harmonic function of time when the bar is vibrating in a normal mode, the equation reduces to

$$\frac{d^4y}{dx^4} - p^4y = 0 \tag{2}$$

where

$$p = \sqrt[4]{\frac{w\omega^2}{gEI}}$$

In this expression ω is the circular frequency of the vibration from which the critical speed can be determined as

$$N_c = 60\omega/2\pi \text{ revolutions per minute.} \tag{3}$$

The critical speed is thus

$$N_c = \frac{60}{2\pi}\sqrt{\frac{(pL)^4gEI}{wL^4}} \tag{3a}$$

The values of (pL) in this expression are the roots of the frequency equation that satisfies equation (2), and the support and end conditions of the shaft.

The solution of equation (2) can be written as

$$y = C_1 \sin px + C_2 \cos px + C_3 \sinh px + C_4 \cosh px. \tag{4}$$

This relation satisfies equation (2) regardless of the values of C_1, C_2, C_3, and C_4 which must be adjusted to meet the support and end conditions. In this case the equation (4) must be applied independently to the portion AB and the overhung section BC. In addition, the shaft must pass over the support B with a smooth and continuous deflection curve. The conditions for AB can be specified as follows:

$$\left.\begin{aligned} &\text{At } x = 0, && y = 0 \text{ and } M = EId^2y/dx^2 = 0 \\ &\text{At } x = aL, && y = 0 \text{ and } (dy/dx)_L = (dy/dx)_R \\ & && (d^2y/dx^2)_L = (d^2y/dx^2)_R \end{aligned}\right\} \tag{5}$$

The subscripts L and R refer to the derivatives to the left and right, respectively, of the bearing support B. For the overhung portion of the shaft the following conditions are required:

$$\left.\begin{aligned} &\text{At } x = aL, && y = 0 \text{ and } (dy/dx)_L = (dy/dx)_R \\ & && (d^2y/dx^2)_L = (d^2y/dx^2)_R \\ &\text{At } x = L, && V_e = -EI\,(d^3y/dx^3)_e = (W/g)y_e\omega^2 \\ & && M_e = -EI\,(d^2y/dx^2)_e = 0, \end{aligned}\right\} \tag{6}$$

where V_e is the end shear force, y_e the end deflection, and M_e the end moment, considered zero if the rotational inertia of the end weight is neglected (this effect is evaluated later).

[1] At present, Professor of Mechanical Engineering, University of Missouri, Rolla, Mo.

Contributed by the Machine Design Division and presented at the Winter Annual Meeting, New York, N. Y., November 27–December 2, 1960, of The American Society of Mechanical Engineers. Manuscript received at ASME Headquarters, January 18, 1960. Paper No. 60—WA-39.

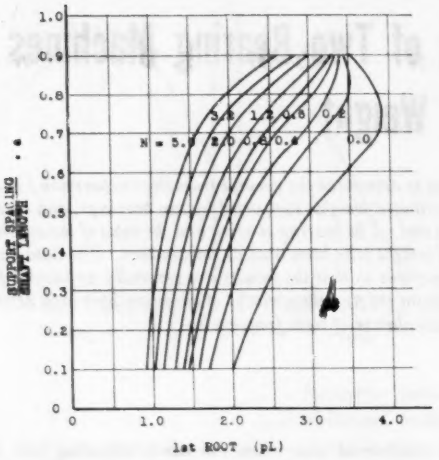

Fig. 2 Roots for determining the lowest critical speed

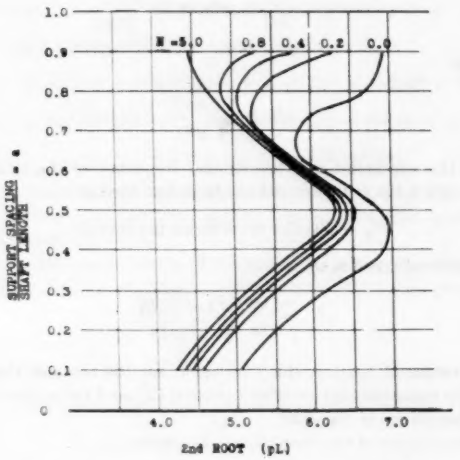

Fig. 3 Roots for determining the second critical speed

Impressing these conditions on equation (4) leads to the following result

$$1 + \cos bpL \cosh bpL + NpL(\cos bpL \sinh bpL - \sin bpL \cosh bpL) + 0.5(\operatorname{ctn} apL - \operatorname{ctnh} apL)(\sin bpL \cosh bpL - \cos bpL \sinh bpL + 2NpL \sin bpL \sinh bpL) = 0 \quad (7)$$

The values of pL that satisfy this equation for a specified N, a, and b determine the critical speeds in accordance with equation (3a). It is not a simple matter to solve for the roots of equation (7), and the values here presented were obtained from an interpolative procedure using a digital computer.

The roots corresponding to the first, second, and third critical speeds for various bearing spacings and ratios of end weight to shaft weight are graphically presented in Figs. 2, 3, and 4, respectively. The maximum weight ratio was taken as 5 ($N = 5$), for above this value no large error is made if the weight of the shaft is neglected. Higher frequencies were not computed because they are generally beyond the speeds of practical interest.

Fig. 5 shows the comparison of the calculated and experimental results for the lowest frequency obtained from a mechanical model. The agreement in this case is excellent. Fig. 6 indicates

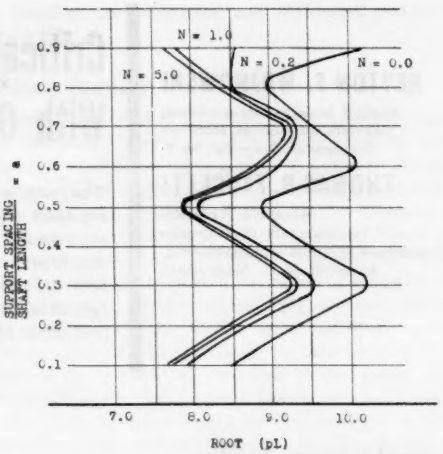

Fig. 4 Roots for determining the third critical speed

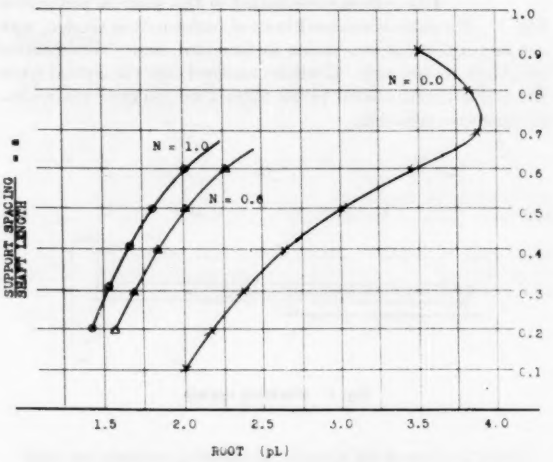

Fig. 5 Comparison of calculated and experimental roots for the fundamental mode

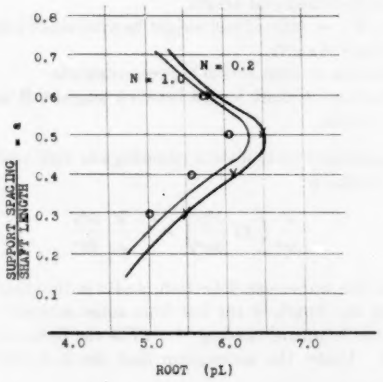

Fig. 6 Comparison of calculated and experimental roots for the second mode

that there is a discrepancy in the second mode frequency that increases as the size of the overhung weight is increased. It is believed that this error is associated with the angular inertia of the

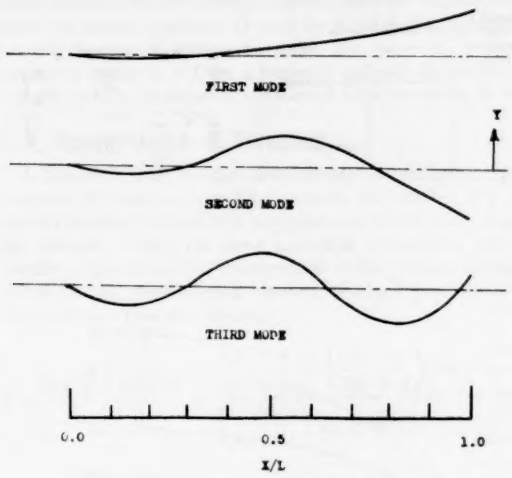

Fig. 7 Normal elastic curves

end weight as it rotates about an axis perpendicular to the center line of the shaft. The third frequency was difficult to excite in the mechanical model, but it is believed that the error induced by the rotary inertia of the end mass would be even more significant in this case.

Effect of Rotary Inertia of End Weight

It is possible to account for the rotary inertia of the end weight if its moment of inertia about the transverse axis is known. This entails that the boundary moment M_e be changed from zero to

$$x = L, \quad M_e = -EI(d^2y/dx^2) = J\omega^2(dy/dx)_e \tag{8}$$

Adopting this change in the boundary conditions, equation (7) becomes

$$\begin{aligned} &1 + \cos bpL \cosh bpL + NpL(\cos bpL \sinh bpL \\ &\quad - \sin bpL \cosh bpL) - P(pL)^3(\sin bpL \cosh bpL \\ &\quad + \cos bpL \sinh bpL) \\ &\quad + PN(pL)^4(1 - \cos bpL \cosh bpL) \\ &\quad + 0.5(\text{ctn } apL - \text{ctnh } apL)[(PN(pL)^4 \\ &\qquad - 1.0)(\cos bpL \sinh bpL)] \\ &\quad = 0 \end{aligned} \tag{9}$$

P is the dimensionless parameter Jg/W_bL^3.

An extensive investigation of this relation has not been made, but it was confirmed that the roots of the new equation would be lower than the previous results. Since the commonly used formulas for computing critical speeds rarely include the rotational effects, the accuracy of the simplified analysis is that generally achieved in design analysis.

The Normal Elastic Curve

The configuration of the system when vibrating in one of the natural modes is largely of academic interest, but on occasion the location of nodal points is desired. These are obtained in the present problem with considerable effort, and a generalized solution has not been obtained.

The elastic curve will obviously have nodal points at the supports, and will also contain $(n - 1)$ additional nodes where n is the modal or frequency number, first, second, or third.

The elastic curve can be obtained for each mode by using the root (pL) corresponding to the frequency in the deflection equation (4) and plotting the normalized transverse displacements.

The deflection curve between the supports subject to the previously stated support conditions is

$$y_1 = C_1 \sin px + C_3 \sinh px \tag{10}$$

The displacement of the overhanging portion is

$$y_2 = D_1 \sin px + D_2 \cos px + D_3 \sinh px + D_4 \cosh px. \tag{11}$$

Applying the continuity conditions at support B, the following relations between constants can be found:

$$C_1 = -D_4/(\sin apL) \tag{12}$$

$$C_3 = D_4/(\sinh apL) \tag{13}$$

$$D_1 = \frac{D_4[\cos bpL + \cosh bpL + \sinh bpL(\text{ctnh } apL - \text{ctn } apL)]}{\sinh bpL + \sin bpL} \tag{14}$$

$$D_2 = -D_4 \tag{15}$$

$$D_3 = \frac{-D_4[\cos bpL + \cosh bpL + \sin bpL(\text{ctn } apL - \text{ctnh } apL)]}{\sinh bpL + \sin bpL} \tag{16}$$

Once these constants have been evaluated in terms of D_4 for the particular frequency and support conditions, they may be placed in the deflection equations (10) and (11), and the elastic curve plotted. For this purpose assign a value to the largest deflection of +1, and the curve thus obtained is at every point proportional to the actual vibratory amplitude.

While it appears that the plotting of the deflection curve is a prodigious task, use of a computer will greatly speed the work, and once programmed it will become a routine calculation.

Illustrative Example

To demonstrate the method of calculation consider a system as in Fig. 1 with a steel shaft 3 inches in diameter and 10 feet long, supporting an end weight of 100 lb. The bearings are spaced 3 feet apart.

Given data:

$$\begin{aligned} a &= 3/10 = 0.3 \\ b &= 0.7 \\ W_b &= (\pi/4)3^2 \times 120 \times 0.283 = 266 \text{ lb} \\ W &= 100 \text{ lb} \\ N &= 100/266 = 0.375 \end{aligned}$$

From Figs. 2, 3, and 4

$$(pL)_1 = 1.80 \qquad (pL)_2 = 5.40 \qquad (pL)_3 = 9.43$$

$$N_{c1} = (60/2\pi)\sqrt{\frac{(1.80)^4 \times 32.2 \times 12 \times 30 \times 10^6 \times 3.97}{266 \times 120^3}}$$

$$\begin{aligned} &= 310 \text{ rpm} \\ N_{c2} &= 2790 \text{ rpm} \\ N_{c3} &= 8460 \text{ rpm} \end{aligned}$$

Data for plotting the normal elastic curves are tabulated below

pL	C_1	C_3	D_1	D_2	D_3	D_4
1.80	$-1.94D_4$	$1.77D_4$	$1.08D_4$	$-D_4$	$-0.73D_4$	$+1D_4$
5.40	$-1.00D_4$	$0.411D_4$	$2.14D_4$	$-D_4$	$-1.02D_4$	$+1D_4$
9.43	$-3.24D_4$	$0.118D_4$	$5.09D_4$	$-D_4$	$-1.0D_4$	$+1D_4$

The deflection curves for the given frequencies are given in Fig. 7.

Conclusions

The results of this study as presented in Figs. 2, 3, and 4 serve as a rapid and accurate means of evaluating the lowest three critical speeds of the machine if the deflections are small and the rotary inertia of the end weight can be neglected.

For larger end masses and for large deflections, the rotary inertia of the end weight must be taken into account as in equation (9), and appreciable error will result if this effect is neglected.

DISCUSSION

John L. Maulbetsch[2]

This interesting paper provides valuable information which is quite laborious to obtain even with an electronic computer.

Some years ago, the writer investigated the case of two bearing shafts without the overhung weight and obtained results similar to those shown in this paper. There are, however, some discrepancies which it would be of interest to clarify.

For the lowest critical speed, Fig. 2, the 0.0 curve is shown as a continuous curve, while the writer obtained a curve consisting of two branches meeting at $pL = 4.4$ and $a = 0.73$, with the branch for values of "a" larger than 0.73 curving in the opposite direction from the curve shown in Fig. 2 and ending at $a = 1.0$ with $pL = 3.14$. The case $a = 1$ corresponds to a bar with hinged ends where the first root is well known and is equal to π. This point is common also for the curves for shafts with overhung weight, and these curves should be aimed in that direction.

In Fig. 3 for the second critical speed, the curves are also shown continuous. The writer found a curve with a somewhat different shape for the case 0.0 with discontinuities (two tangents) at $pL = 7.3$ for $a = 0.47$ and 0.88. From $a = 0.88$ the curve then reaches point $pL = 2\pi$ for $a = 1.0$ which is the second critical speed of a bar with hinged ends.

For the third order, Fig. 4, the points of discontinuity are at $pL = 10.3$ at $a = 0.31$, 0.63, and 0.92 with the curve ending for $a = 1$ at $pL = 3\pi$.

The writer also extended the curves to the solution $a = 0$ which coincide with the solution for a bar with one end built in and one end free.

These results are brought to the attention of the authors since it is believed that the curves for the overhung weight may be shaped somewhat differently, especially in Figs. 3 and 4. In Fig. 3 the curves should converge to a common point at $a = 1$ with $pL = 2\pi$ and Fig. 4 to $pL = 3\pi$.

Philip M. Strong[3]

We have had resonance problems in a machine of the general configuration described in this paper. In solving for the fundamental natural frequency we neglected the shaft weight as compared to the end weight. Using elementary strength of materials to find the stiffness of the system, and setting the fundamental natural frequency $= \omega_n = \sqrt{K/m_0}$

$$\omega_n^2 \left[\frac{m_0(bL)^3}{EI}\right] = 3b$$

where

m_0 = end mass

Putting this relation in terms of p and N as defined in this paper

$$pL = \frac{3}{Nb^3} = \frac{3}{N(1-a)^2}$$

a	$N = 5$	$N = 2$	$N = 0.2$
0.1	0.93	1.26	2.24
0.3	1.05	1.32	2.32
0.5	1.09	1.37	2.44
0.7	1.61	2.02	3.58
0.9	2.79	3.50	6.22

Notice that, at $N = 5$ and $N = 2$, the agreement is quite good (see Fig. 2 of the paper) except for $a = 0.9$, where evidently the shaft weight is much more important in relation to end weight.

We also investigated the rotary inertia effect on the first natural frequency. In our case, the end weight was a fan, and its effect was to raise the natural frequency. The basic mechanism of this stiffening effect is outlined in "Mechanical Vibrations," by Den Hartog, p. 254. We applied this stiffening effect to the overhung weight and shaft system and used elementary strength of materials again to arrive at the natural frequencies given in Fig. 8.

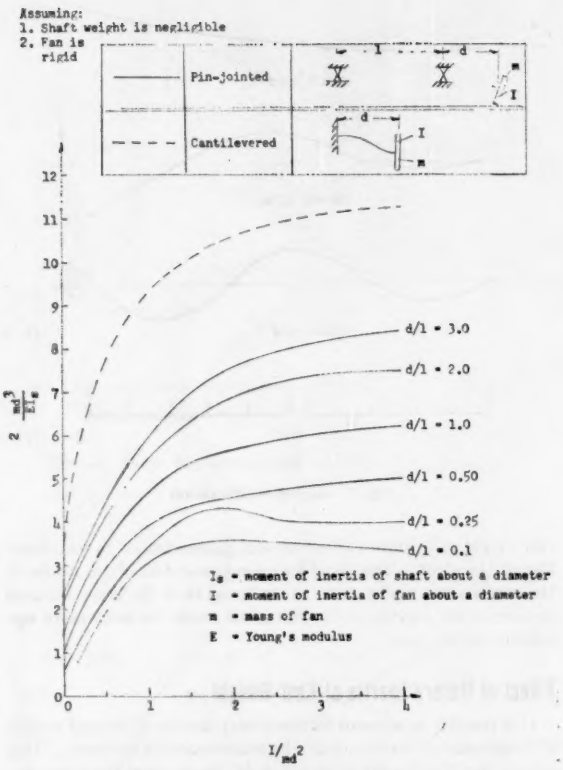

Fig. 8 Natural frequency of fan and overhung shaft

J. P. Vidosic[4]

The system investigated is typical of equivalent systems representative of many engineering situations. Therefore, data obtained and presented should prove of much practical value. Information contained in Figs. 2, 3, and 4 can save considerable labor and time in computing the first three critical speeds. Thus, the curves should be of great interest to engineers finding themselves involved in natural frequency investigations and not having access to computers.

A more extensive analysis of discrepancies in the second and third mode frequencies with size of overhung weight should prove not only interesting but valuable too. It is hoped the authors shall find time to do so. Should the error appear noticeable at larger end loads it might become profitable to provide additional data. If the error is associated with the angular inertia as supposed, "correction" factors or a new set of root curves might be provided.

Since knowledge of nodal point location may at times be of value a generalized solution should be of considerable interest.

---

[2] President, Lerma Engineering Corporation, Northampton, Mass. Mem. ASME.

[3] Development Engineer, Air Impellers, The Torrington Manufacturing Company, Torrington, Conn.

[4] Regents' Professor, Georgia Institute of Technology, Atlanta, Ga. Mem. ASME.

Thus, it should be additionally beneficial were the authors to consider the matter further. It may be possible, for instance, to provide families of curves, in which the $(n - 1)$ nodes are located in terms of x/L for a series of support distances a.

Both authors are to be congratulated for a useful bit of work.

F. R. Wunder[5] and P. R. Trumpler[6]

A Master's thesis by the first discusser submitted to Illinois Institute of Technology in 1954 contains the solution of a more general problem, including as a special case the solution given by the authors. Using the same analytical procedures, but with overhung span constants independent of the corresponding constants for the shaft section between bearings (see Fig. 9) the following equation was obtained:

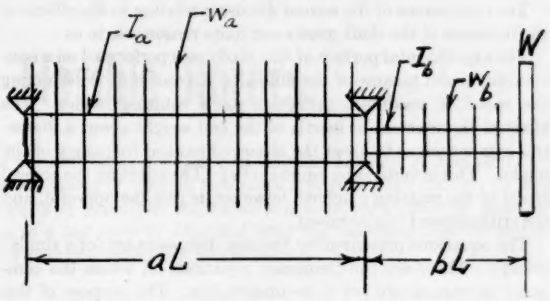

Fig. 9

$$0 = \frac{\text{ctn } Q - \text{ctnh } Q}{2k} + \frac{\dfrac{AD-1}{AD+1} - \left(\dfrac{A-D}{AD+1}\right)\sin R \cosh R + \left(\dfrac{A+D}{AD+1}\right)\cos R \sinh R + \cos R \cosh R}{\left(\dfrac{2A}{AD+1}\right)\sin R \sinh R - \left(\dfrac{2D}{AD+1}\right)\cos R \cosh R + \sin R \cosh R - \cos R \sinh R} \quad (17)$$

where

$$Q = p_a a L$$

$$R = p_b b L$$

$$k = \frac{E_a I_a p_a}{E_b I_b p_b}$$

$$p_a = \sqrt[4]{\frac{w_a \omega^2}{g E_a I_a}} \qquad p_b = \sqrt[4]{\frac{w_b \omega^2}{g E_b I_b}}$$

$$A = \frac{w_b}{g I_D p_b^3} \qquad D = \frac{w_b}{W p_b}$$

The gyroscopic moment exerted by the rotating mass at the end of the overhanging shaft (the effect of which is often of importance in applications) is accounted for by A in the equation. Similarly, D introduces the effect of the magnitude of the concentrated overhung mass. Q and R contribute the influence of the lengths of the two spans.

Eliminating the effect of gyroscopic moment in (17) by making $I_D = 0$, or $A \to \infty$, we obtain

$$0 = \frac{\text{ctn } Q - \text{ctnh } Q}{2k} + \frac{1 - \dfrac{1}{D}(\sin R \cosh R - \cos R \sinh R) + \cos R \cosh R}{\sin R \cosh R - \cos R \sinh R + \dfrac{2}{D}\sin R \sinh R} \quad (18)$$

which checks the authors' equation (7) if the p's, (EI)'s, and w's are the same for both spans.

Some comment should be made concerning the validity of results obtained by this form of analysis in establishing the speed ranges for large vibratory amplitudes in a turbomachine. The authors have not described their test program. Engineers with experience know that calculated "criticals" are often hardly detected, that speed ranges other than those calculated produce large vibratory amplitudes, and that the phenomenon of precession (whirling) is a serious and unpredictable source of difficulty. There is little doubt that the idealized dynamic system model of "indifferent equilibrium" with forward synchronous precession, which is implicit not only in the authors' work but in the usual approaches to the problem, is becoming increasingly limited in its value.

[5] Superintendent of Engineering, Mars Incorporated, Chicago, Ill.

[6] Professor of Mechanical Engineering, University of Pennsylvania, Philadelphia, Pa. Mem. ASME.

Authors' Closure

The authors wish to express their appreciation for the interest and helpful comments of the discussers of our paper.

We are unable to verify the discontinuities and curve shapes indicated by the first discusser. It is difficult to understand why small adjustments in the location of a support in a continuous system should cause the irregularities described. With $N = 0.0$ and $a = 0.73$, the first of the points in question, the lowest value of pL given by equation (7) is 3.92, which agrees precisely with the value read from Fig. 2.

With $N = 0.0$ and $a = 0.73$, the left side of equation (7) contains an infinite discontinuity at $pL = 4.3$, being negative for values less than 4.3 and positive for values greater than 4.3. Similar discontinuities will occur when the product apL is equal to π, 2π, 3π, etc., and the factor $(\sin bpL \cosh bpL - \cos bpL \sinh bpL + 2NpL \sin bpL \sinh bpL)$ is not zero. The sign changes associated with these discontinuities may have caused the corresponding values of pL to be identified as roots of the frequency equation although they do not satisfy that equation. A tabulation of points where this condition exists is as follows:

	a	pL	apL
First Mode (Fig. 2)	0.73	4.3	π
Second Mode (Fig. 3)	0.43	7.3	π
	0.86	7.3	2π
Third Mode (Fig. 4)	0.305	10.3	π
	0.610	10.3	2π
	0.915	10.3	3π

This list agrees well with the points questioned by the first discusser. None of the points listed above satisfies equation (7) or yields data applicable to Figs. 2, 3, and 4.

The observation that for $a = 1$ the curves of Figs. 2, 3, and 4 should terminate at π, 2π, and 3π, respectively, is correct. The roots at $a = 0.9$ and at $a = 0.8$ have been plotted from the computed data, and the curves can be extended to include the $a = 1$ condition. This was not done as the hinged end result is well known.

At $a = 0$ the curves do approach the fixed-free end condition, but this is a questionable interpretation in that the system cannot be simply supported by two coincident supports. Closely spaced supports entail tremendous bearing reactions.

The conclusions of the second discusser relating to the effects of the inclusion of the shaft mass seem quite reasonable to us.

The experimental portion of this study was performed on a nonrotating model because of the difficulty of accurately determining the speed of maximum deflection for a rotating model. The effect of the moment of inertia of the end weight about a diametral axis is such as to lower the observed natural frequency of the model. This is verified by equation (9). The effect on the critical speed of the rotating machine, however, is just the opposite, and the critical speed will be raised.

The equations presented by the last discussers are for a similar system. These are the frequency equations on which the computer operations are yet to be undertaken. The purpose of this paper is to present a problem on which the computer analysis has been completed, and the data reduced to usable form. The computer analysis of the discusser's equation could be carried out by the same method as that used by the authors, but a presentation of the data in a form similar to Figs. 2, 3, and 4 is impossible because of the greater number of variables.

It is true as the discussers point out that several unpredictable factors have been left from the analysis by the authors. However, in situations where the approximations of this study are met, and this is often the case, the data presented yield a rapid estimate of the critical speeds. The results must, of course, be applied with caution using experience and judgment to determine whether or not a more refined and diligent study is required.

One final observation can be made comparing Figs. 2 and 3. It can be seen that the greatest range between first and second critical speeds is obtained if the bearings are separated by a distance of from 0.4 to 0.5 of the length of the shaft.

A. H. CHURCH
Professor of Mechanical Engineering, New York University, New York, N. Y.[1] Mem. ASME

R. PLUNKETT
Consulting Engineer, General Engineering Laboratories, General Electric Company, Schenectady, N. Y.

Balancing Flexible Rotors

A method is presented for computing the size and angular location of the correction weights required in selected planes of rotation to balance a flexible shaft rotating at high speeds. It is based on mobility principles and requires a minimal number of measurements. Its application to a test rotor is described, and this indicates that the method could be developed into a practical operating procedure.

Introduction

ROTORS operating at speeds above the first critical are difficult to balance since the centrifugal action of added correction weights creates deformations of the shaft in addition to those produced by the inherent unbalance.

This paper describes a procedure using mobility principles that can be applied to determine the magnitude and angular position of correction weights to be placed in selected planes of rotation to balance a flexible shaft or rotor.

General Analysis

The deflection y_0 of an undamped beam at any point x along its length due to a static force F_0 acting at a distance ξ from one support, as shown in Fig. 1, may be expressed in terms of the normal modes of vibration of the beam. For a simply supported uniform beam this is a sine series:[2]

$$y_0 = \frac{2F_0L^3}{EI\pi^4} \sum_{i=1}^{i=\infty} \frac{1}{i^4} \sin \frac{i\pi\xi}{L} \sin \frac{i\pi x}{L} \tag{1}$$

where

y_0 = deflection of the shaft at point x, in.
E = modulus of elasticity of the shaft, psi
I = rectangular moment of inertia of shaft, in.^{4}
i = number of the normal mode

and the other symbols have the meaning shown in Fig. 1.

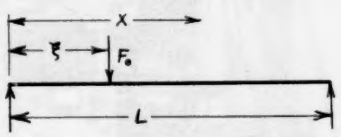

Fig. 1

If a known weight is attached to a rotating shaft the impressed force F_0 is the product of its mass and the distance of its center of gravity from the line of bearing centers times the square of the angular velocity or

$$F_0 = m(r + y_b)\omega^2$$

where

m = mass of the correction weight, lb-sec^2/in.
y_b = shaft deflection at correction mass, in.
r = initial, or static, radius of mass center from bearing center line, in.
ω = rotational speed of shaft, rad/sec

In most practical balancing situations the size of the correction mass is quite small compared with the mass of the shaft, and its radius r is relatively large compared with the shaft deflection y_b, so that

$$F_0 \approx mr\omega^2 = \bar{U}\omega^2 \tag{2}$$

where $\bar{U}$ is the unbalance in lb-sec^2.

When the shaft is rotating at a speed of ω rad/sec in this deflected condition the action of the force F_0 is equivalent to that of a harmonic force $F = F_0 \sin \omega t$ acting at the point ξ on a nonrotating beam so that the deflection equation is given[3] by

$$y_0 = \frac{2gF_0L^3}{A\gamma} \sum_{i=1}^{i=\infty} \frac{\sin\left(\frac{i\pi\xi}{L}\right) \sin\left(\frac{i\pi x}{L}\right)}{i^4\pi^4\lambda^2 - \omega^2L^4} \tag{3}$$

where

A = cross-sectional area of shaft, sq in.
γ = specific weight of shaft material, lb per cu in.
$\lambda^2 = \frac{EIg}{A\gamma}$, or $\frac{\omega_{ni}^2L^4}{i^4\pi^4}$
ω_{ni} = ith normal mode circular frequency, rad/sec

Equation (3) may be expressed in terms of the first natural frequency ω_{n1} and the impressed frequency ω by introducing a speed ratio $\beta = \omega/\omega_{n1}$. For a uniform simply supported beam $\omega_{ni} = i^2\omega_{n1}$, and the denominator following the summation sign can be manipulated as follows:

$$i^4\pi^4\lambda^2 - \omega^2L^4 = \omega_{ni}^2L^4 - \omega^2L^4 = (i^4\omega_{n1}^2 - \omega^2)L^4$$

If we now substitute equation (2) for F_0, divide the numerator and denominator of the portion of equation (3) following the summation sign by $i^4\omega_{n1}^2$, introduce the β-term, and bring the constant L^4-term outside the summation sign, we obtain expression for the response amplitude, y_0:

$$y_0 = \frac{2g\bar{U}}{A\gamma L} \sum_{i=1}^{i=\infty} \frac{(\beta/i^2)^2}{1 - (\beta/i^2)^2} \sin \frac{i\pi\xi}{L} \sin \frac{i\pi x}{L} \tag{4}$$

It may be observed in equation (4) that for given values of x

[1] Work done at the General Engineering Laboratories of the General Electric Company while on a leave of absence from New York University.

[2] S. Timoshenko and D. H. Young, "Vibration Problems in Engineering," third edition, D. Van Nostrand Company, New York, N. Y., 1955, equation (k), p. 348.

Contributed by the Machine Design Division and presented at the Winter Annual Meeting, New York, N. Y., November 27–December 2, 1960, of THE AMERICAN SOCIETY OF MECHANICAL ENGINEERS. Manuscript received at ASME Headquarters, March 24, 1960. Paper No. 60—WA-13.

[3] Ibid., equation (i), p. 348; equation (114), p. 325; and equation (133), p. 332.

and ξ the response amplitude y_0 for any normal mode i is a function of the frequency ratio β only. Hence a template[4] representing this response for any normal mode can be constructed and used if the effective mass function and the natural frequency of the mode are known. The effective mass function for any mode is given by the last two terms on the right side of equation (4), hence is a function of x and ξ. The net response curve for given values of the measuring point located at station x and the excitation point located at station ξ can then be obtained by adding algebraically the responses of the several normal modes.

The usual definition of mobility[5] is that it is the ratio of the maximum velocity response to the maximum value of the impressed force. In this discussion it is desirable to use a mobility defined as the ratio of the response amplitude to the impressed unbalance. This ratio may be written as y_0/mr, where y_0 is the shaft deflection at the measuring point. This has the units of in/lb-sec^2 or (in/sec^2)/lb, so that the response is measured in terms of acceleration per unit force. Thus the mobility function is on an acceleration basis rather than the more usual velocity basis.

The location of the measuring points and the balancing planes must necessarily be a function of the configuration of the rotor and the machine in which it is used. However, it is desirable to locate the measuring points away from normal-mode nodal points at the balancing speeds in order to increase the sensitivity of measurement, and to position the balancing planes so that the correction weights will be most effective for the predominant modes. To illustrate, a balance weight placed at mid-span for a simply-supported rotor would be effective in correcting the unbalance of odd-numbered normal modes, but would have little or no effect for even-numbered normal modes since it would be located at a node.

Response curves can be plotted on a dimensionless basis for a given type of rotor and values of x and ξ by rewriting equation (4) in the form

$$\frac{y_0}{\frac{2g\bar{U}}{A\gamma L}} = \alpha = \sum_{i=1}^{i=\infty} \frac{(\beta/i^2)^2}{1-(\beta/i^2)^2} \sin\frac{i\pi\xi}{L} \sin\frac{i\pi x}{L} \qquad (5)$$

and plotting α against the frequency ratio β.

The left side of this equation may be written in the form

$$\alpha = \frac{A\gamma L}{2}\frac{y_0}{g\bar{U}} = \frac{A\gamma L}{2}\frac{y_0}{U} \qquad (6)$$

where $\bar{U}$ is the unbalance in mass units, and U is expressed in weight units. Thus $U = g\bar{U}$. The numerical factor $A\gamma L/2$ is one half the weight of the rotor or shaft.

Equations (5) and (6) can be used to write a set of equations to relate the response of the rotor to the addition of known balance weights added in selected balance planes. Knowing the response of the actual unbalanced shaft the equations may be solved to determine the magnitude and angular location of the balance weights required to achieve zero deflection at the measuring points.

This procedure is best illustrated by an example, and this is outlined in the next section.

Example

To verify the efficacy of the method, it was applied to a specific case and then the results checked experimentally. This will be described in some detail to make the previous discussion more definite and to outline the experimental techniques of implementing it.

A uniform steel shaft, 1/2 in. in diameter, was mounted on self-aligning ball bearings located 68 in. apart as shown in Fig. 2. The shaft was driven through reduction gears by a direct-current motor to obtain satisfactory speed control.

For the preliminary analysis it was assumed that the bearings acted as simple supports and that the system was undamped. These assumptions proved not to be entirely valid and required some modification of the procedure as outlined in the next section.

The first three natural frequencies of the shaft were calculated to be 500, 2000, and 4500 rpm, and the maximum rotational speed of the shaft was limited by the motor speed to about 2000 rpm. For this maximum rotational speed only the first three normal modes are of importance. This was later verified by the modal-response curves similar to Fig. 3 or 6.

It can be shown (see Appendix) that the number of balance weights and number of measurements required should be the same and equal to the number of influential normal modes. For the example being considered this number is three.

It was decided to measure the shaft deflection at x-values of $0.4L$ and $0.7L$ from the top bearing to avoid nodes in the shaft within the operating range. The balancing planes were located at values of $0.2L$, $0.5L$, and $0.9L$ from the top bearing. These

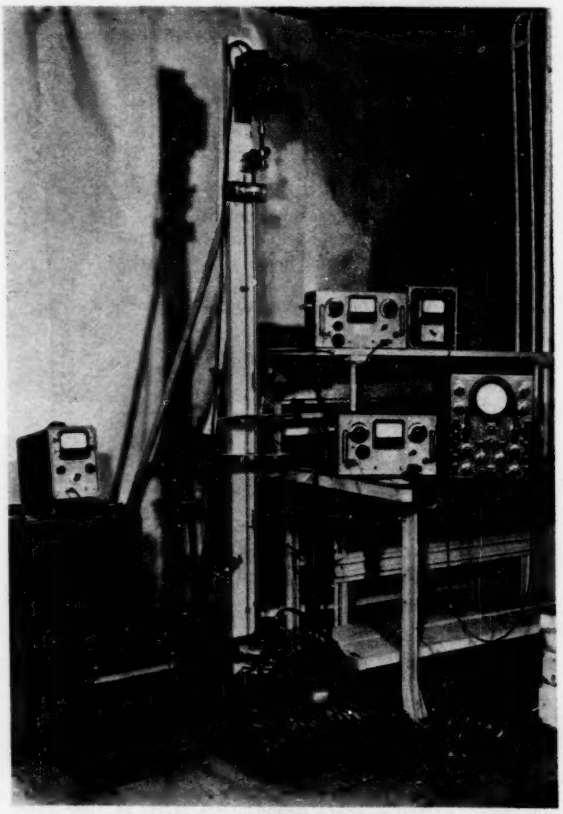

Fig. 2 Apparatus used for rotational balancing

[4] R. Plunkett, "Semi-Graphical Method for Plotting Vibration Response Curves," Proceedings of the Second National Congress of Applied Mechanics, ASME, June, 1954, pp. 121–126.

R. Plunkett, "Experimental Measurement of Mechanical Impedance or Mobility," *Journal of Applied Mechanics*, vol. 21, TRANS. ASME, vol. 76, 1954, pp. 250–256.

[5] "Mechanical Impedance Methods for Mechanical Vibrations," edited by Robert Plunkett, ASME, 1958.

values were chosen so that the $0.5L$ weight would provide correction for the first and third normal modes; the $0.2L$ weight primarily for the second normal mode, and the $0.9L$ weight primarily for the third normal mode.

Substituting these values of x and ξ in equation (5) and using a template based on this equation, the required response curves α as a function of the frequency ratio β for various combinations of x and ξ were drawn. Fig. 3 illustrates the curve for stations at $0.2L$ and $0.4L$, and the others are similar. It should be recalled in connection with these curves that the reciprocity principle holds; i.e., that $\alpha_{0.2L,\,0.4L} = \alpha_{0.4L,\,0.2L}$. In plotting these curves the modal-response curves are shown as short dashes and the combined or resultant response curve is shown as a solid line.

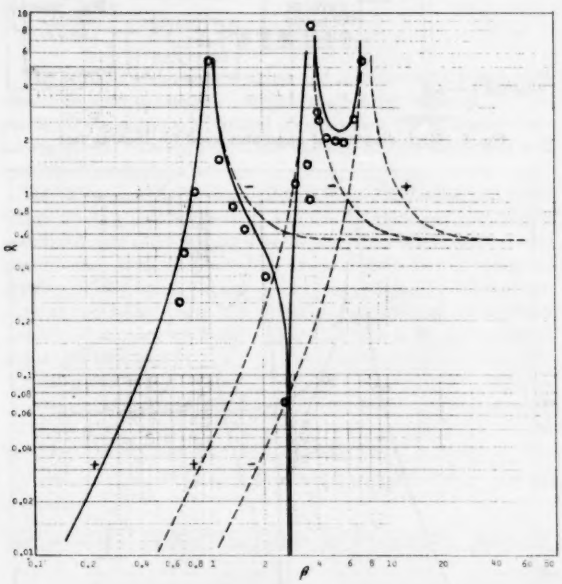

Fig. 3 Initial response curve for points at 0.2L–0.4L

Since three unknown balance weights are involved in the example three simultaneous equations are needed involving suitable combinations of running speeds (or β) and measuring points. If three speed ratios of $\beta = r$, s, and t are used we may write the equations in the form

$$\beta_1 = r: \frac{A\gamma L}{2} y_1 = \alpha_{0.7L,\,0.2L} U_{0.2L} + \alpha_{0.7L,\,0.5L} U_{0.5L} + \alpha_{0.7L,\,0.9L} U_{0.9L}$$

$$\beta_2 = s: \frac{A\gamma L}{2} y_2 = \alpha_{0.4L,\,0.2L} U_{0.2L} + \alpha_{0.4L,\,0.5L} U_{0.5L} + \alpha_{0.4L,\,0.9L} U_{0.9L} \quad (7)$$

$$\beta_3 = t: \frac{A\gamma L}{2} y_3 = \alpha_{0.7L,\,0.2L} U_{0.2L} + \alpha_{0.7L,\,0.5L} U_{0.5L} + \alpha_{0.7L,\,0.9L} U_{0.9L}$$

In setting up these equations, or selecting values of β, it is desirable to have one value in each equation relatively large and the others small. Furthermore, there should be one relatively large value of α for each correction point or U-value.

Equations (7) may be solved simultaneously to give expressions for the intentional unbalances $U_{0.2L}$, $U_{0.5L}$, and $U_{0.9L}$ in terms of the measured amplitudes y_1 at gage $0.7L$ and speed $\beta = r$; y_2 at gage $0.4L$ and speed $\beta = s$; and y_3 at gage $0.7L$ and speed $\beta = t$.

Flexible rotors are apt to have a bent center line so that, if they are rotated slowly, a given point on them will have a runout or eccentricity. When the shaft rotates at the running speed its deflection at the measuring point is a function of both the initial runout and the unbalance.

It is now possible to outline a step-by-step procedure to balance a flexible rotor after the mobility response curves are at hand:

1 Rotate the shaft by hand and measure its distance from a fixed point or a measuring gage to determine the runout in, say, 30-deg steps of rotation. The magnitude and angular position of the runout relative to a timer point on the shaft can be found by plotting the displacements in polar co-ordinate paper and determining the radius and angular location of the center of the resulting circle. Experience showed that harmonic analysis provided a simpler and more exact method.

2 The shaft is then rotated at a selected speed and the measuring signal triggered by a timer on the shaft once per revolution. This gives a sine curve on an oscilloscope whose abscissa represents the angular shaft position relative to the timer, and whose ordinate represents the magnitude of the displacement. Again, the magnitude and phase position (relative to the timer) of the running response may be found by plotting or using harmonic analysis. The vector difference of the "static" and "running" deflections at the measuring station represents the net response due to the inherent unbalance alone and thus eliminates the effect of initial runout. These net responses are designated as y_1, y_2, and y_3 and are used in equations (7) to determine the magnitude and angular position of the necessary correction weights.

3 If the shaft amplitude is small compared to the correction-weight radius the approximate force at the balance weight is equal to $\bar{U}\omega^2 = (W/g)r\omega^2$. It should be noted that the ω^2-term has been incorporated into the numerator of the right side of equation (5). The angular position of the balance weight is placed opposite to the unbalance as determined by the solution of equations (7) so that its force annuls the inherent distributed unbalance in the shaft and makes the deflection amplitude equal to zero at the balancing speed. There will, of course, be deflections at other axial positions along the shaft but their magnitudes will be reduced, particularly at the lower critical frequencies. It is not practical to balance in more than one plane per mode shape due to second-order effects.

Experimental Investigation

To determine the feasibility of the procedure outlined, the shaft mentioned previously was subjected to tests. Fig. 2 shows the apparatus, while Fig. 4 is a block diagram of the apparatus used.

The amplitudes at the measuring points were measured by capacitor gages in which the shaft acted as one "plate" and the other plate was attached to the frame but insulated from it as shown in Figs. 2 and 4.

The electric signal resulting from the change in capacitance was fed to a dual-beam oscilloscope through a Fielden proximity meter as shown in Fig. 4. The oscilloscope was triggered by a timer attached to the shaft. The speed of rotation was determined by a striped cardboard disk attached to the bottom end of the shaft. The light interruptions were picked up by a photocell and measured by a Hewlett-Packard frequency meter.

The test procedure using this apparatus has already been described, so need not be repeated.

Difficulty was encountered in checking the ideal α-values of the response curves (Fig. 3 and others), which were plotted on the basis of an undamped steel beam simply supported at the ends. This discrepancy is due to such factors as the slight overhang at both bearings, slight play in the bearings, damping in the system due to bearing friction, windage of the shaft, and friction in the

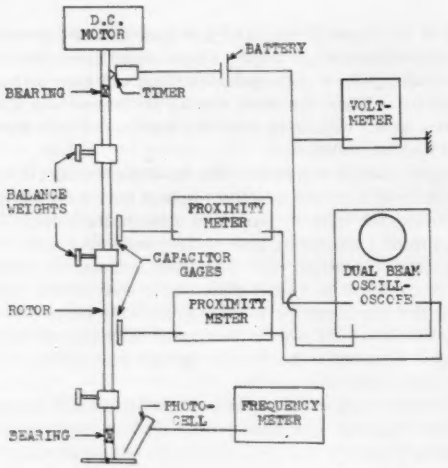

Fig. 4 Block diagram of apparatus used for rotational balancing

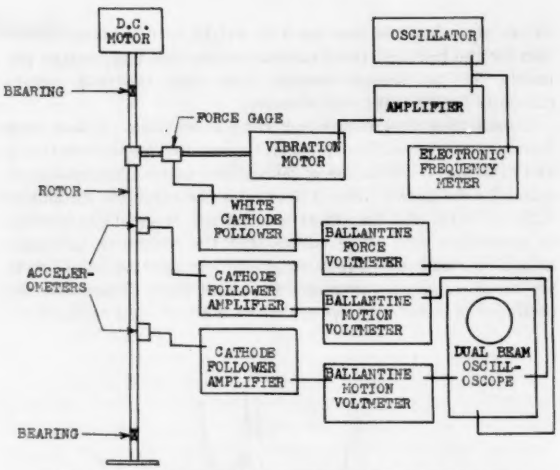

Fig. 5 Block diagram of apparatus used for shaking test

spherical seats of the bearings. These effects were proportionally large compared with the size and weight of the experimental apparatus and so severely affected the results.

To determine the corrections required for the response curves a shaking force was applied to the nonrotating shaft in the balance plane and the response measured at the capacitor gages. This was done by connecting a vibration motor through a force gage to the shaft at a balance weight. The motor was actuated by an oscillator and amplifier as shown by the block diagram in Fig. 5. The impressed force acting on the shaft was measured on a voltmeter. The response at the measuring points was measured by accelerometers attached to the shaft. Both the force and acceleration voltages were fed into a dual-beam oscillograph so that phase angles could be determined. The input frequency was varied through the operating range and the shaft response found at the measuring points.

Three results of this phase of the experimental investigation were found: (*a*) The three lowest natural frequencies of the shaft were found to be 550, 2000, and 4180 cpm (corresponding β-values being 1, 3.64, and 7.6), rather than the ideal values of 500, 2000, and 4500 cpm (corresponding β-values of 1, 4, and 9). (*b*) That the responses were generally about 15 per cent below their ideal values. These responses are the points plotted in Fig. 3. (*c*) The position of the nodal points along the shaft axis were not located at the ideal positions. For the second mode the node was located at $9.49L$ from the top bearing rather than at the midpoint. For the third mode the nodes were located at $0.353L$ and $0.676L$ from the top bearing rather than at the one-third points. This last effect is directly traceable to the overhang of the shaft and looseness in the bearings. When correcting the values of α it was assumed that the deflection curve passed through the actual nodes and remained sinusoidal. The effective mass function is given by the product of the last two terms of equation (4), which are

$$\sin i\pi\xi/L \sin i\pi x/L.$$

The value of these terms is obtained by proportion of the distance of x and ξ from the known nodes. The product of these terms gives the effective mass constant for each mode, which shows on the graph as α when β is infinite.

The revised set of response (α) curves was drawn with the effective masses corrected as outlined previously. One of these corrected curves is given as Fig. 6. These curves were then used for further balancing.

After the shaft was balanced it was run at various speeds between 400 and 1900 rpm and the amplitude measured at both gages. These values are plotted in Fig. 7. The displacement when the shaft was turned by hand (runout) was 17 mils for the upper gage and 21 mils for the lower gage as noted in the figure.

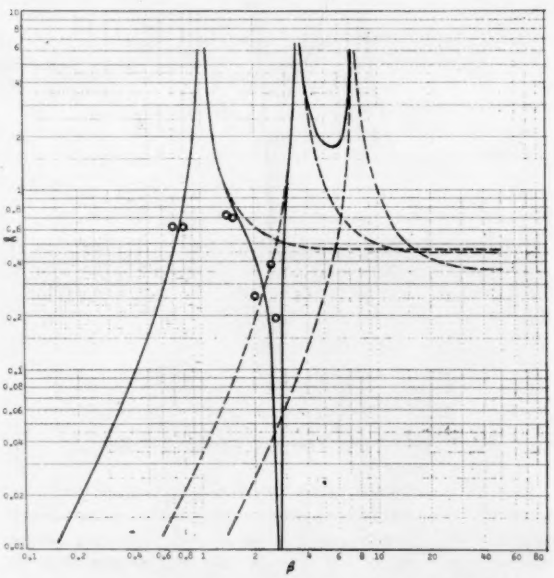

Fig. 6 Corrected response curve for points at 0.2L–0.4L

These curves are plotted against β and it may be observed that the shaft deflection was within 3 or 4 mils of the runout or initial eccentricity between β-values of about 1.5 to 2.5 (running speed from 800 to 1500 rpm) which was considered satisfactory. However, the deflections become excessive at the modal resonant frequencies where $\beta = 1$ and $\beta = 3.64$. If the shaft were to run at a constant specified speed it would, of course, be possible to balance it to obtain zero deflection at that speed.

Following this, the top balance weight was turned 180 deg to introduce intentional unbalance and the variation in response from that of the "balanced" shaft was found at seven points. These responses were calculated in terms of α and are shown as the plotted points in Fig. 6 for the upper gage. A similar curve was found for the lower gage. These points show good agreement with the adjusted curve.

Conclusions

1 This preliminary investigation indicates that the acceleration mobility method could be developed into a practical operating procedure for balancing flexible rotors.

2 The number of correction-weight locations must be equal to or less than the number of measurement points and speeds.

3 It is not feasible to balance a flexible shaft to operate at high rotational speeds unless the balancing is done at or near those speeds. Conversely, it is not necessary to balance a flexible shaft much above its maximum operating speed.

4 The number of balance weights and measurement points that should be used for any flexible-shaft balancing is not optional, but equals the number of critical speeds below the maximum balancing speed.

APPENDIX

The number of balance weights and measurement points that should be used to balance a flexible shaft is not optional, but depends on the number of critical speeds below the maximum balancing speed. The proof of the validity of this statement will now be developed.

Let us assume that a rotor extends from 0 to L with any number of intermediate supports. Assume the mass per unit length is variable and given by $\mu(x)$, while the initial eccentricity $\epsilon(x)$ is the distance from the line of bearing centers to the center of gravity of any cross section. Then we can find the deflection, $y(x)$, at any point x from the initial configuration of the shaft by using the influence coefficient $K(x, \xi)$, which is the deflection at x due to a unit load at ξ:

$$y(x) = \int_0^L P(\xi)K(x, \xi)d\xi \tag{8}$$

where $P(\xi)$ is the load at point ξ and is given by

$$P(\xi) = [\epsilon(\xi) + y(\xi)]\mu(\xi)\omega^2 \tag{a}$$

Therefore

$$y(x) = \omega^2 \int_0^L \epsilon(\xi)K(x, \xi)\mu(\xi)d\xi + \omega^2 \int_0^L y(\xi)K(x, \xi)\mu(\xi)d\xi \tag{9}$$

Equation (9) may be expressed more simply by letting

$$\int \epsilon(\xi)K(x, \xi)\mu(\xi)d\xi = h(x) \tag{10}$$

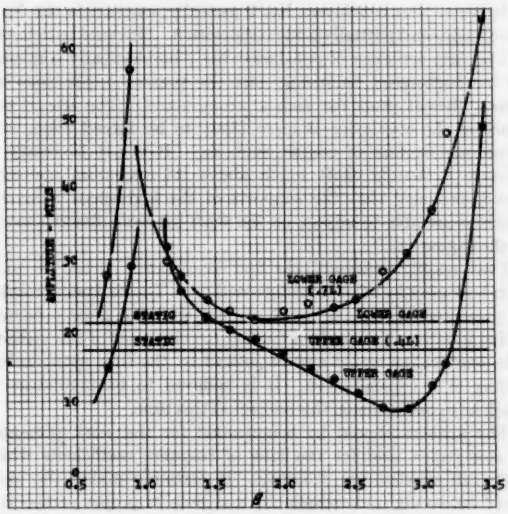

Fig. 7 Amplitude response of balanced shaft as function of β

Thus $h(x)$ is the deflection of the beam from its initial eccentricity due to the inertia forces developed at a unit rotational speed.

$$\text{Let } h(x) = \sum_s \frac{a_s}{\omega_s^2}\phi_s(x) \tag{b}$$

where $\phi_s(x)$ is the mode shape of the sth natural frequency, ω_s, and a_s is a constant whose magnitude is to be determined.

Den Hartog[6] shows that

$$\phi_n(x) = \omega_n^2 \int_0^L \phi_n(\xi)K(x, \xi)\mu(\xi)d\xi \tag{c}$$

and

$$\int_0^L \phi_n(\xi)\phi_s(\xi)\mu(\xi)d\xi = M\delta_{ns} \tag{d}$$

where

$$\delta_{ns} = \begin{matrix} 0 & n \neq s \\ 1 & n = s \end{matrix}$$

If we multiply both sides of equation (b) by $\mu(x)\phi_n(x)dx$ and integrate over the length we get

$$\int_0^L \phi_n(x)h(x)\mu(x)dx = \sum_s \frac{a_s}{\omega_s^2}\int_0^L \phi_s(x)\phi_n(x)\mu(x)dx = M\frac{a_n}{\omega_n^2} \tag{e}$$

or

$$\int_0^L\int_0^L \phi_n(x)\mu(x)\mu(\xi)\epsilon(\xi)K(x, \xi)d\xi dx = \frac{Ma_n}{\omega_n^2} \tag{f}$$

If we reverse the order of integration and integrate x first we simplify equation (f) by making use of equation (c). Then

$$\int_0^L \mu(\xi)\epsilon(\xi)\frac{\phi_n(\xi)}{\omega_n^2}d\xi = \frac{Ma_n}{\omega_n^2}$$

or

$$a_n = \frac{1}{M}\int_0^L \mu(\xi)\epsilon(\xi)\phi_n(\xi)d\xi \tag{g}$$

Now let

$$y(x, \omega) = \sum_n b_n(\omega)\phi_n(x) \tag{11}$$

where b_n is written as $b_n(\omega)$ to indicate it is a function of ω only. If we substitute for y from equation (9), (10), and (b), then

$$\Sigma b_n\phi_n(x) = \omega^2 \sum_n \frac{a_n\phi_n(x)}{\omega_n^2} + \sum_n \omega^2 b_n \int_0^L \mu(\xi)\phi_n(\xi)K(x, \xi)d\xi \tag{12}$$

If both sides of equation (12) are multiplied by $\phi_s(x)\mu(x)dx$ and integrated from 0 to L, by making use of equations (c) and (d)

$$b_n = \frac{\omega^2}{\omega_n^2}a_n + \frac{\omega^2}{\omega_n^2}b_n = \frac{\beta_n^2}{1 - \beta_n^2}a_n \tag{13}$$

If we now add balance weights m_b at a radius r_b and positions x_b, they will exert forces on the shaft of $\omega^2 m_b[r_b + y(x_b)]$ at positions x_b.

[6] J. P. Den Hartog, "Mechanical Vibrations," McGraw-Hill Book Company, Inc., New York, N. Y., 1956, fourth edition, Section 4.8, equations 4.50 and 4.48.

If r_b is considerably larger than $y(x_s)$ for all values of ω then these forces are equal to $\omega^2 m_b r_b$.

If we let

$$c_i = \sum_b m_b r_b \phi_i(x_b) \tag{14}$$

and let $\bar{y}(x)$ be the deflection shape due to both the original unbalance and the added balance weights m_b, then we can write

$$\bar{y}(x) = \sum_i d_i(\omega)\phi_i(x) \tag{15}$$

where

$$d_i = \frac{\beta_i^2}{1 - \beta_i^2}(a_i + c_i) \tag{16}$$

corresponding to b_n in equation (13).

The problem now is to find optimum values for the unbalance $m_b r_b$. The optimum we have chosen is to make $\bar{y}$ zero at several discrete positions and speeds. Let the measured values of y (without balance weights) at these several conditions be $\bar{y}$ where $\bar{y}$ is a vector of k elements. Then, from equations (10) and (12) we may write

$$y = Aa \tag{17}$$

where a is a vector of the a_n, and A is the square matrix of the k elements a_{ij}. Since we wish to solve for a, A must be inverted. Thus there can be no more than k a_n and if there are fewer than k a_n or, if the coefficients of some of the a_n in A are zero, A will be singular. Now the relative values of a_n are given by the relative values of the modes shown dashed in Fig. 3 and similar figures. It is obvious that for all measurements taken at β less than 5, A will be almost singular unless n is 1 or 2; i.e., only the first two modes are excited. From equation (15) it is clear that our condition requires $c_n = -a_n$. Since there are k and only k a_n, there are k and only k $(m_b r_b)$.

Therefore we must measure at exactly as many points as we have balance weights. If we measure more points and have more balance weights than there are excited modes in the unbalanced rotor, the solution will be almost singular and the results are apt to be such as to cause large unbalance in the higher modes. Actually, it is possible to use more than k measurement points, but then the equations must be reduced to k by least squares methods. If some other balance criterion were used, it would be reduced to the form of equation (15) by suitable transformation and the same conclusions would hold. One possible minimal criterion would be

$$\int_0^L y^2(x)dx = \min$$

DISCUSSION

Josef K. Sevcik[7]

The aim of this paper is to demonstrate the feasibility of high-speed balancing of flexible rotors and that it can be achieved with a minimum number of measurements. The analysis and experimental investigation deal with simply supported uniform shaft, but from the Appendix it can be deduced that the same reasoning may be applied to any rotating body with general mass and flexibility distribution along its axis, and confined by any linear boundary conditions.

A very limited amount of experimental data is presented, so that no comparison is possible between unbalanced and balanced shaft. The authors explain more at length the discrepancies encountered in checking the calculated response coefficients α, and the application of a shake test analysis which helped to define these coefficients experimentally. In addition to the response coefficients α, the natural frequencies and flexural modes have also changed. To the factors affecting these changes should be added, that it is the over-all system, shaft and balancing apparatus included, which also contributed to these deviations.

In the actual balancing, where the ratio between the weights of balanced piece and of balancing machine will be higher than in the described laboratory test, the difficulty in calculating the response coefficients will be greater, and the calculation will have to be replaced by the shake test analysis, which will only add to the number of measurements.

The elimination of initial runout at measuring planes is explained very well in the outline of the balancing procedure. It would have been of great interest to show that the effect of bearing clearance can also be accounted for. Since the system damping changes the phase angle of the measured deflections in relation to the unbalance in the vicinity of natural frequency, making the angular location of these readings difficult, it would be interesting to know at what speeds the described shaft was actually balanced.

With reference to equations (7), it should be said that two such sets were apparently written for proper resolution of unbalance components: one in the plane of timer mark, and one in the plane perpendicular to the former.

The balancing conditions were defined in connection with these equations, i.e., zero deflections at the measuring planes and speeds. No wonder then that conclusion No. 4 has been reached, i.e., that "the number of balance weights and measurement points should be equal to the number of critical speeds." But it should not be forgotten that also other balancing conditions, genuinely different, can be set up, such as zero reactions for instance or minimum kinetic energy. The number of balancing equations (7) would then be equal to the number of balancing conditions, and would require an equal number of balancing weights and points of measurement. The minimum number of balancing conditions is given by the number of flexural modes for which the balancing is required, being the last one, eventually, above the maximum operating speed. On the other hand, it should be remembered that the first two modes in balancing precede the bow shaped mode normally considered as the first one of a simply supported shaft. Low-speed balancing takes care of those two modes at which the rotor behaves like a rigid body.

It seems that conclusion No. 2 partially contradicts the No. 4 conclusion, and partially is identical with it. It could be deleted.

The first sentence of conclusion No. 3 emphatically condemns all but high-speed balancing, but the present paper does not offer sufficient proof for such a strong stand. The second sentence of the conclusion is more likely to be agreed upon, with some qualification of course, such as: "It is not necessary to balance a flexible shaft much above its maximum operating speed, provided that the supports of the high-speed balancing machine are able to impose on the shaft the same flexural modes as the engine will."

I can readily agree with the first conclusion. It has yet to be seen how practical the procedure will be. The balancing results, as presented in Figs. 6 and 7, do not show too great accuracy, which indicates the need for further development of the method. The practicality would also be judged by the time spent in balancing of a typical piece. It is believed to be premature to reach any conclusion on this subject at this time.

The authors should be commended for the work presented in this paper, and for the idea of response coefficients which they call acceleration mobility. It certainly makes the high-speed balancing understandable, and puts in proper perspective the various parameters important in this type of balancing.

[7] Specialist, Mechanical Analysis, Applied Mechanics—CDO, Large Jet Engine Department, General Electric, Evendale, Ohio.

It is my opinion that perhaps some references of similar type of work could have been mentioned, such as: "Fundamentals of Systematic Vibration Elimination From Rotors With Elastic Shafts" (Grundlagen einer systematischen Schwingungsentstörung wellenelastischer Rotoren) by Prof. Klaus Federn of Darmstadt, Germany (VDI—Berichte Bd. 24/1957).

Authors' Closure

The authors appreciate comments from one with as much experience as Mr. Sevcik has in the problems of balancing flexible rotors and are looking forward to the publication of his method of distributing balance weights from low-speed measurements.

Most of his comments appear to stem from a misunderstanding of the nature of our experimental apparatus. As mentioned in the body of the paper, it was built for experimental purposes only and was deliberately made to be a very flexible low-speed shaft with stiff ball bearings. Mr. Sevcik is quite correct when he says the rigid body modes must be included in any practical case. Conclusion 4 is incorrectly stated, as he points out, and should refer only to balance weights and not measurement points.

Only actual experience can show whether calculations alone would give sufficiently accurate values for response coefficients and to what extent supplementary measurements would be necessary. One would hope that, as usual, the accuracy of computed results would improve with experience.

The authors thank Mr. Sevcik for mentioning one of Dr. Federn's many important contributions to the over-all problem. This oversight was because his work is in a different direction. More directly pertinent are three papers appearing in vol. 1, no. 1, of the *Journal of Mechanical Engineering Science*, June, 1959. These are: "The Vibration of Rotating Shafts," by Dr. R. E. D. Bishop, pp. 50–65; "The Vibration and Balancing of an Unbalanced Flexible Rotor," by R. E. D. Bishop and G. M. L. Gladwell, pp. 66–77; and "The Receptances of Uniform and Non-Uniform Rotating Shafts," by G. M. L. Gladwell and R. E. D. Bishop, pp. 78–91.

M. J. COHEN
Senior Lecturer, Northampton College of Advanced Technology, London, England

Stress and Strain in Spinning Paraboloid Dishes—2

Solutions for the stress and strain systems in spinning paraboloid dishes, both holed and whole, are presented. They are applicable to all such dishes of aperture small enough to justify the usual approximation for small angles of $\cos\theta \approx 1$, $\sin\theta \approx 0$. *The direct stress* p, *the hoop stress* f, *the shear stress* s, *the bending moments* M_θ *and* M_ϕ, *and the radial displacement* Δ *are obtained as power series in* θ, *the angular distance of any point of the dish at the center of the sphere of curvature at the dish apex. These series in* θ *are expressed in terms of tabulated coefficients which are essentially functions of a single basic dish parameter* $R\alpha^2/h$. *The range for* $R\alpha^2/h$ *covered is* $0 \leq R\alpha^2/h \leq 10$.

Introduction

This note follows on a paper[1] by the author on the same subject. It extends the range of applicability of the method of determining the stresses and strains in a spinning paraboloid dish to values of a key parameter of the dish, $R\alpha^2/h$ larger than $^1/_3$. For such values of $R\alpha^2/h$, the equation of compatibility of strains used in that paper must be modified to take into consideration the contribution of the normal displacement of the dish to the hoop strain. This effect is now incorporated in the general method described previously[1] and values for the coefficients A_r', $r = 1, 3, \ldots\ldots 11$, in the series expansion

$$s = \frac{3+\sigma}{8}\rho\Omega^2R^2\alpha^3\sum_1^\infty A_r'\theta'^r$$

assumed for the shear stress, for a more comprehensive set of values of $R\alpha^2/h$, are tabulated for both the whole and holed dish cases. The method used being identical with that presented in the original basic paper, the detailed analysis is not repeated here, the results, following on a shortened argument, being listed for reference. These include the stresses, bending moments, and normal displacement in the dishes as functions of the angular distance θ', $(\theta' = \theta/\alpha)$ from the dish axis.

[1] M. J. Cohen, "Stress and Strain in Spinning Paraboloid Dishes," TRANS. ASME, Series B, JOURNAL OF ENGINEERING FOR INDUSTRY, vol. 81, 1959, pp. 43–50.

Contributed by the Machine Design Division and presented at the Winter Annual Meeting, New York, N. Y., November 27–December 2, 1960, of THE AMERICAN SOCIETY OF MECHANICAL ENGINEERS. Manuscript received at ASME Headquarters, July 28, 1960. Paper No. 60—WA-91.

Fundamentals

The basic equations linking the stresses, strains, and bending moments are given in the author's previous paper.[1] When $R\alpha^2/h > {}^1/_2$, however, the compatibility equations as used, with appropriate reservations, in that paper, must be modified to account for the contribution of the normal displacement of the dish to the hoop strain. Equation (v) then becomes

$$e_\theta + \frac{d(\theta\Delta)}{d\theta} = \frac{d(\theta e_\phi)}{d\theta} \qquad \text{(v } a\text{)}$$

Equations (vii) and (viii), following on this, become

$$M_\theta = \frac{Eh^3}{12(1-\sigma^2)}\left\{\frac{d^2\Delta}{R^2d\theta^2} + \frac{\sigma}{R\theta}\left(\frac{d\Delta}{Rd\theta} + \theta e_\phi\right)\right\} \qquad \text{(vii } a\text{)}$$

$$M_\phi = \frac{Eh^3}{12(1-\sigma^2)}\left\{\frac{1}{R\theta}\left(\frac{d\Delta}{Rd\theta} + \theta e_\phi\right) + \frac{\sigma}{R^2}\frac{d^2\Delta}{d\theta^2}\right\} \qquad \text{(viii } a\text{)}$$

Equation (v a) affords the relation enabling the successive coefficients of θ^r, i.e., a_r in the expression for s, the shear stress,

$$s = \sum_1^\infty a_r\theta^r \qquad (1)$$

to be determined.

The equations (v a), (vii a), and (viii a) can be expressed more conveniently in terms of a new variable θ', where $\theta' = \theta'/\alpha$ (or θ/α_2 in the case of the holed dish), as

$$e_\theta + \frac{d(\theta'\Delta')}{d\theta} = \frac{d(\theta' e_\phi)}{d\theta'} \qquad (2)$$

Nomenclature

e_θ = radial strain
e_ϕ = tangential strain
E = Young's modulus
f = hoop stress
ϕ = tangential circular measure
θ = radial circular measure
θ' = θ/α for whole dish, or θ/α_2 for holed dish
M_θ = bending moment across faces of a sector element of an elementary hoop normal to radius of hoop
M_ϕ = bending moment across faces of a sector element of an elementary hoop normal to tangent to hoop
h = uniform thickness of dish
O = center of sphere of which paraboloid dish forms approximately a spherical cap
p = radial stress
P = apex of dish
r = radial distance of a point in dish from axis of spin
r_1 = radius of hole
r_2 = radius of outer rim
R = radius of spherical cap
s = shear stress normal to dish and tangential to sides of an element
σ = Poisson's ratio
α = angular semiaperture of whole dish at center O
α_1 = angular semiaperture of inner rim of holed dish
α_2 = angular semiaperture of outer rim of holed dish
Δ = deflection of dish normal to its surface
Δ' = Δ/R

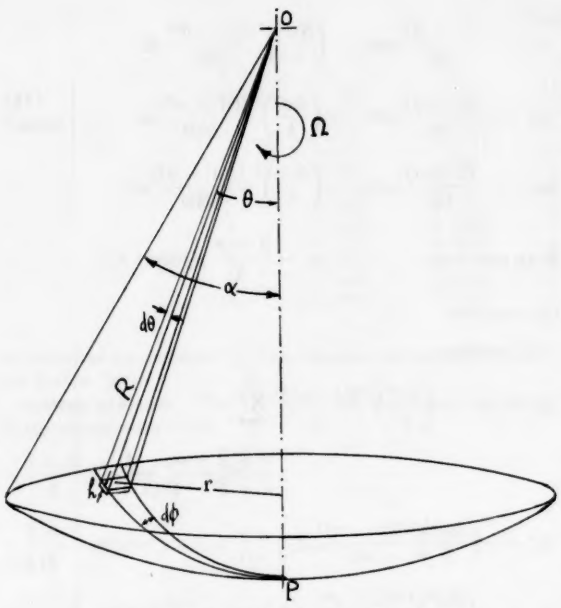

Fig. 1 Type element of a spinning dish (geometry)

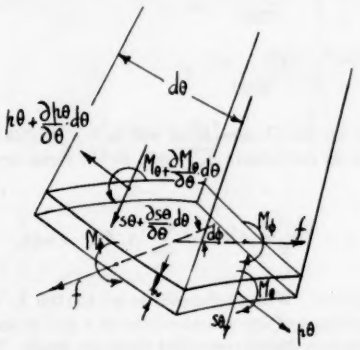

Fig. 2 Type element of a spinning dish (forces and moments)

$$M_\theta = \frac{Eh^3}{12(1-\sigma^2)\left(\frac{R\alpha^2}{h}\right)}\left\{\frac{d^2\Delta'}{d\theta'^2} + \left(\alpha^2\theta' e_\phi + \frac{d\Delta'}{d\theta'}\right)\frac{\sigma}{\theta'}\right\} \tag{3}$$

$$M_\phi = \frac{Eh^3}{12(1-\sigma^2)\left(\frac{R\alpha^2}{h}\right)}\left\{\frac{1}{\theta'}\left(\frac{d\Delta'}{d\theta'} + \alpha^2\theta' e_\phi\right) + \sigma\frac{d\Delta'^2}{d\theta'^2}\right\} \tag{4}$$

where, $\Delta' = \Delta/R$. It can be shown [from an examination of the order of magnitude of the terms in (14) or (14a)] that if the parameter $R\alpha^2/h < 1/2$ the results of the previous paper give an accuracy within 5 per cent of the exact and thus vindicate the assumption of the simplified equation of compatibility of strains adopted in that paper. Since, however, the example chosen at the end of the paper corresponds to $R\alpha^2/h = 6$, those results should not have been used on that particular problem. The same problem will be solved using the extended method presented here to cover a wider range of $R\alpha^2/h$, ($1/2 \leq R\alpha^2/h \leq 10$).

Extension of Method to Values of $R\alpha^2/h > 1/2$

Problem A—The Whole Dish

In order to derive the recurrence relation for the a_r''s, and then the a_r''s themselves, use must be made of (2), the equation of compatibility of strains. Hence the need for obtaining an expression for $d(\theta'\Delta')/d\theta'$ in terms of these coefficients. This can be achieved as follows:

Making use of the shear-bending moment relation (vi) of the previous paper[1] expressed in terms of the new variable θ', i.e.,

$$\frac{d(M_\theta\theta')}{d\theta'} - M_\phi = -s\theta' hR\alpha \tag{5}$$

and substituting for M_θ and M_ϕ from (3) and (4) in (5) yields the differential equation for Δ':

$$\theta'^2\frac{d^3\Delta'}{d\theta'^3} + \theta'\frac{d^2\Delta'}{d\theta'^2} - \frac{d\Delta'}{d\theta'} = \alpha^2\theta' e_\phi - \alpha^2\sigma\theta'\frac{d(\theta' e_\phi)}{d\theta'} - \frac{s\theta'^2 hR\alpha}{D} \tag{6}$$

where $$D = \frac{Eh^3}{12(1-\sigma^2)\left(\frac{R\alpha^2}{h}\right)}$$

If we write $$a_r' = a_r\alpha^{r-1} \quad \text{and} \quad s = \alpha\sum_1^\infty a_r'\theta'^r \tag{7}$$

the expressions for e_θ and e_ϕ become

$$e_\theta = \frac{1}{E}\left\{(1-\sigma)a_1' + (1-2\sigma)a_2'\theta' + \sum_1^\infty\left[(1-\overline{r+2}\sigma)a_{r+2}' - \frac{1+\sigma}{r+3}a_r'\alpha^2\right]\theta'^{r+1} - \sigma\rho\Omega^2R^2\alpha^2\theta'^2\right\} \tag{8}$$

$$e_\phi = \frac{1}{E}\left\{(1-\sigma)a_1' + (2\sigma)a_2'\theta' + \sum_1^\infty\left[(\overline{r+2}-\sigma)a_{r+2}' + \frac{1+\sigma}{r+3}a_r'\alpha^2\right]\theta'^{r+1} + \rho\Omega^2R^2\alpha^2\theta'^2\right\}$$

with $a_2' = 0$ and, more generally, $a_{2m}' = 0$, from considerations of symmetry.

Substituting from (7) and (8) in (6), retaining only significant terms, the right-hand side of (6) becomes essentially

$$\frac{1}{E}\left\{(1-\sigma)^2\alpha^2 a_1'\theta' - \left(\frac{R\alpha^2}{h}\right)^2 12(1-\sigma^2)\sum_1^\infty a_r'\theta'^{r+2}\right\} \tag{9}$$

(6) can now be solved to give

$$\frac{d\Delta'}{d\theta'} = A\theta' + \frac{1}{E}\left\{(1-\sigma)^2\alpha^2 a_1'\left[1 + \frac{1}{2}\log|\theta'|\right]\theta' - \left(\frac{R\alpha^2}{h}\right)^2 12(1-\sigma^2)\sum_1^\infty\frac{a_r'\theta'^{r+2}}{(r+2^2-1)}\right\} \tag{10}$$

The constant A is determined from the consideration that $M_\theta = 0$ at $\theta' = 1$, giving,

$$A = \frac{-\alpha^2 a_1'(1-\sigma)(3-2\sigma)}{2E} + \frac{1}{E}\left(\frac{R\alpha^2}{h}\right)^2 12(1-\sigma)\sum_1^\infty \frac{\overline{r+2}+\sigma}{\overline{r+2^2-1}}\, a_r'$$

and hence,

$$\frac{d\Delta'}{d\theta'} = \frac{-a_1'\alpha^2}{2E}(1-\sigma)^2\left[\frac{3-2\sigma}{1-\sigma} - \log|\theta'|\right]\theta' + \frac{12(1-\sigma^2)}{E}\left(\frac{R\alpha^2}{E}\right)^2 \sum_1^\infty \frac{a_r'}{(r+2^2-1)}\left[\frac{r+2+\sigma}{1+\sigma}\theta' - \theta'^{r+2}\right] \quad (11)$$

(11) reduces to the expression obtained in the previous paper if the first term only in the summation were considered and if the first term on the right-hand side were neglected compared with the subsequent ones. The former assumption is not justified for all values of the parameter $R\alpha^2/h$ whereas the second is certainly justified provided the immediate neighborhood of $\theta' = 0$ is ignored. This region is extremely restricted and for all practical purposes the expression to be derived for $d\Delta'/d\theta'$ holds throughout the dish except at $\theta' \simeq 0$. Equation (11) now reduces to

$$\frac{d\Delta'}{d\theta'} = \frac{12(1-\sigma^2)}{E}\left(\frac{R\alpha^2}{h}\right)^2 \sum_1^\infty \frac{a_r'}{(r+2^2-1)}\left[\frac{r+2+\sigma}{1+\sigma}\theta' - \theta'^{r+2}\right] \quad (11a)$$

From (11a), it follows by integration that

$$\Delta' = \frac{12(1-\sigma^2)}{E}\left(\frac{R\alpha^2}{h}\right)^2 \sum_1^\infty \frac{a_r'}{(r+2^2-1)}\left[\frac{1}{2}\frac{r+2+\sigma}{1+\sigma}\theta'^2 - \frac{\theta'^{r+3}}{r+3}\right] \quad (12)$$

and then,

$$\frac{d(\theta'\Delta')}{d\theta'} = \frac{12(1-\sigma^2)}{E}\left(\frac{R\alpha^2}{h}\right)^2 \sum_1^\infty \frac{a_r'}{(r+2^2-1)}\left[\frac{3}{2}\frac{r+2+\sigma}{1+\sigma}\theta'^2 - \frac{r+4}{r+3}\theta'^{r+3}\right] \quad (13)$$

The Recurrence Relation, $R\alpha^2/h > 1/2$

If the expressions for e_θ and e_ϕ from (8) and that for $d(\theta'\Delta')/d\theta'$ from (13) are substituted in the equation of compatibility of strains (2), i.e., in

$$e_\theta + \frac{d(\theta'\Delta')}{d\theta'} = \frac{d(\theta' e_\phi)}{d\theta'}$$

and the coefficients of θ'^{r+1}, r odd, equated to zero there results:

$$\left.\begin{aligned}
&a_1', \text{ arbitrary,}\\
&a_3' = -\frac{(1+\sigma)}{8}\alpha^2 a_1' - \frac{3+\sigma}{8}\rho\Omega^2R^2\alpha^2 + \frac{9(1-\sigma)}{4}\left(\frac{R\alpha^2}{h}\right)^2 \sum_1^\infty \frac{\overline{r+2}+\sigma}{\overline{r+2^2-1}}\, a_r'\\
&a_5' = -\frac{(1+\sigma)}{24}\alpha^2 a_3' - \left(\frac{R\alpha^2}{h}\right)^2 \frac{5(1-\sigma^2)}{64}\, a_1'\\
&a_7' = -\frac{(1+\sigma)}{48}\alpha^2 a_5' - \left(\frac{R\alpha^2}{h}\right)^2 \frac{7(1-\sigma^2)}{576}\, a_3'\\
&a_9' = -\frac{(1+\sigma)}{80}\alpha^2 a_7' - \left(\frac{R\alpha^2}{h}\right)^2 \frac{9(1-\sigma^2)}{2560}\, a_5'\\
&a_{11}' = -\frac{(1+\sigma)}{120}\alpha^2 a_9' - \left(\frac{R\alpha^2}{h}\right)^2 \frac{11(1-\sigma^2)}{8000}\, a_7'
\end{aligned}\right\} \quad (14)\ (cont.)$$

If we now write $a_r' = \frac{3+\sigma}{8}\rho\Omega^2R^2\alpha^2 A_r'$

(14) becomes:

$$\left.\begin{aligned}
&A_1', \text{ arbitrary,}\\
&A_3' \doteq -1 + \left(\frac{R\alpha^2}{h}\right)^2 \frac{9(1-\sigma^2)}{4}\sum_1^{11} \frac{\overline{r+2}+\sigma}{\overline{r+2^2-1}}\,\frac{A_r'}{(1+\sigma)}\\
&A_5' \doteq -\left(\frac{R\alpha^2}{h}\right)^2 \frac{5(1-\sigma^2)}{64}\, A_1'\\
&A_7 \doteq -\left(\frac{R\alpha^2}{h}\right)^2 \frac{7(1-\sigma^2)}{576}\, A_3'\\
&A_9' \doteq -\left(\frac{R\alpha^2}{h}\right)^2 \frac{9(1-\sigma^2)}{2560}\, A_5'\\
&A_{11}' \doteq -\left(\frac{R\alpha^2}{h}\right)^2 \frac{11(1-\sigma^2)}{8000}\, A_7'
\end{aligned}\right\} \quad (14a)$$

The range for $R\alpha^2/h$ considered will be $0 < R\alpha^2/h \leq 10$, and only the first six coefficients A_r', r odd, in the series expansion for s, i.e.,

$$s = \frac{3+\sigma}{8}\rho\Omega^2R^2\alpha^2 \sum_1^{11} A_r'\theta'^r, \quad r \text{ odd}, \quad (15)$$

will be computed. With s expressed as in (15) the A_r''s are practically independent of the actual values of σ and α (except in so far as α appears in $R\alpha^2/h$) provided these are small. The values of A_1' tabulated correspond to nominal values for σ and α of 0.2 and 20 deg, respectively. The dependence of the stresses and strains themselves on σ and α thus appears in the factor

$$\frac{3+\sigma}{8}\rho\Omega^2R^2\alpha^2 \quad \text{or} \quad \frac{3+\sigma}{8}\rho\Omega^2R^2\alpha^3$$

Determination of A_1'

This will be achieved by satisfying the condition that $s = 0$ when $\theta' = 1$; then, for r odd,

$$\sum_1^{11} A_r' = 0, \quad (16)$$

and hence

$$A_1' = -\sum_3^{11} A_r' \quad (16a)$$

Equations (14a) with A_1' given by (16a) now afford the six equations for the determination of $A_1', A_3', \ldots\ldots A_{11}'$, essentially as functions of $R\alpha^2/h$ only. The values for A_r' have been evaluated and tabulated as functions of the parameter $R\alpha^2/h$ for values of this parameter of $^1/_2$, 1, 2, 3, 4, 5, 6, 7, 8, 9, 10. The values of the coefficients A_r' for $R\alpha^2/h < {}^1/_2$ will be considered

Table 1

$\frac{R\alpha^2}{h}$	A_1'	A_3'	A_5'	A_7'	A_9'	A_{11}'
"Small"	1.012	−1.018	0.006			
1/2	0.935	−0.920	−0.018	0.003		
1	0.785	−0.735	−0.059	0.009		
2	0.461	−0.341	−0.138	0.016	0.002	
3	0.253	−0.098	−0.171	0.010	0.004	
4	0.144	0.024	−0.173	−0.005	0.008	
5	0.0845	0.0756	−0.1585	−0.0220	0.0135	0.0008
6	0.0447	0.1029	−0.1208	−0.0433	0.0141	0.0021
7	0.0242	0.1079	−0.0889	−0.0619	0.0147	0.0042
8	0.0116	0.1017	−0.0555	−0.0758	0.0120	0.0064
9	0.0037	0.0823	−0.0225	−0.0777	0.0061	0.0083
10	−0.0004	0.0707	0.0027	−0.0825	−0.0009	0.0109

as adequately represented by those obtained in a previous paper[1] for $R\alpha^2/h$ "small."

Summary of Results. With the A_r"s now determined we obtain in succession, with r odd,

$$
\left.
\begin{aligned}
s &= \frac{3+\sigma}{8}\rho\Omega^2R^2\alpha^2\sum_1 A_r'\theta'^r \\
p &= \frac{3+\sigma}{8}\rho\Omega^2R^2\alpha^2\left[A_1' + \sum_1\left(A_{r+2}' - \frac{A_r'\alpha^2}{r+3}\right)\theta'^{r+1}\right] \\
&\doteq \frac{3+\sigma}{8}\rho\Omega^2R^2\alpha^2\sum_1 A_r'\theta'^{r-1} \\
f &= \frac{3+\sigma}{8}\rho\Omega^2R^2\alpha^2\left[\frac{8}{3+\sigma}\theta'^2 + A_1' \right. \\
&\qquad \left. + \sum_1\left(\overline{r+2}A'_{r+2} + \frac{A_r'\alpha^2}{r+3}\right)\theta'^{r+1}\right] \\
&\doteq \frac{3+\sigma}{8}\rho\Omega^2R^2\alpha^2\left[\frac{8}{3+\sigma}\theta'^2 + \sum_1 rA_r'\theta'^{r-1}\right]
\end{aligned}
\right\} \quad (17)
$$

$$
M_\theta = \left(\frac{R\alpha^2}{h}\right)\frac{3+\sigma}{8}\rho\Omega^2\alpha^2h^2\sum_1\frac{A_r'(\overline{r+2}+\sigma)}{(\overline{r+2}^2-1)}(1-\theta'^{r+1})
$$

$$
M_\phi = \left(\frac{R\alpha^2}{h}\right)\frac{3+\sigma}{8}\rho\Omega^2R^2\alpha^2h^2\sum_1\frac{A_r'(\overline{r+2}+\sigma)}{(\overline{r+2}^2-1)}\left(1-\frac{1+\overline{r+2}\sigma}{\overline{r+2}+\sigma}\theta'^{r+1}\right)
$$

$$
\Delta' \doteq \left(\frac{R\alpha^2}{h}\right)^2\frac{3+\sigma}{8}\rho\Omega^2R^2\alpha^2\frac{6(1-\sigma)}{E}\theta'^2 \sum_1\frac{A_r'(\overline{r+2}+\sigma)}{(\overline{r+2}^2-1)}\left(1-\frac{2(1+\sigma)}{\overline{r+2}+\sigma}\frac{\theta'^{r+1}}{(r+3)}\right)
$$

Hence if ϵ is a small positive quantity, as $\theta' \to \epsilon$,

$$
M_\theta \to M_\phi \simeq \frac{R\alpha^2}{h}\frac{3+\sigma}{8}\rho\Omega^2R^2\alpha^2h^2\sum_1\frac{A_r'(\overline{r+2}+\sigma)}{(\overline{r+2}^2-1)}
$$

At $\theta' = 0$, however, both M_θ and M_ϕ tend to an infinity of the log 0 kind; since, however, both M_θ and M_ϕ are bending moments per unit length, this behavior is of academic interest only as the lengths involved tend simultaneously to zero, as $\theta' \to 0$; i.e., the products $M_\theta\theta'$ and $M_\phi\theta'$ both tend to zero as $\theta' \to 0$. Also at the dish rim,

$$
\Delta' = \left(\frac{R\alpha^2}{h}\right)^2\frac{3+\sigma}{8}\rho\Omega^2R^2\alpha^2\frac{6(1-\sigma)}{E}\sum_1\frac{A_r'(r+4+\sigma)}{\overline{r+2}^2-1}\frac{r+1}{r+3}
$$

For the problem of the 60-deg paraboloid dish spinning at 6000 rpm worked out by the basic method of the previous paper, it is found that $R\alpha^2/h = 6$, and this value does not fall within the range of applicability of that method. From the results listed in (17), however, and from the values of the A_r"s tabulated, for $R\alpha^2/h = 6$,

$s_{max} = 108$ psi, at $\theta' = 0.76$; $p_{max} = 280$ psi, at $\theta' = 0.62$;
$f_{max} = 7400$ psi, at $\theta' \approx 1$

$M_\theta = M_\phi = 111$ psi, at $\theta' = \epsilon$;

$\Delta'_{\theta'=1} = 0.00079$, i.e., $\Delta_{\theta'=1} \simeq \frac{1}{100}$ in.

Thus it appears that, due to the rather large semiaperture α of the dish, the hoop constraint f is very much increased, inhibiting the development of the radial and shear stresses, and hence also of the bending moments.

Problem B—The Holed Dish, $R\alpha^2/h > 1/2$

The argument to be used in the solution of this problem is similar to that used in the previous sections for a whole dish. But the solution to the differential equation for $d\Delta'/d\theta'$, (6), is now:

$$
\frac{d\Delta'}{d\theta'} = A\theta' + \frac{B}{\theta'} - \frac{1}{E}\left\{\left(\frac{R\alpha_2^2}{h}\right)^2 12(1-\sigma^2)\sum_1\frac{a_r'\theta'^{r+2}}{(\overline{r+2}^2-1)}\right\} \quad (10a)
$$

since B, now, is not necessarily equal to zero.

In (10a) the term involving $\log|\theta'|$ has been ignored as being always of a higher order of small quantities compared with the other terms throughout the θ'-range; i.e., $\alpha_1' \le \theta' \le 1$, $\alpha_1' \neq 0$. The constants A and B in (10a) are determined from the consideration that $M_\theta = 0$ when $\theta' = \alpha_1'$ and $\theta' = 1$. This yields the simultaneous equations in A and B,

$$
(1+\sigma)A - (1-\sigma)B = \frac{1}{E}\left(\frac{R\alpha_2^2}{h}\right)^2 12(1-\sigma^2)\sum_1\frac{\overline{r+2}+\sigma}{\overline{r+2}^2-1}a_r',
$$

$$
(1+\sigma)A - \frac{(1-\sigma)}{\alpha_1'^2}B = \frac{1}{E}\left(\frac{R\alpha_2^2}{h}\right)^2 12(1-\sigma^2)\sum_1\frac{\overline{r+2}+\sigma}{\overline{r+2}^2-1}\alpha_1'^{r+1}a_r'
$$

which solved give:

$$
A = \frac{1}{E}\left(\frac{R\alpha_2^2}{h}\right)^2\frac{12(1-\sigma)}{(1-\alpha_1'^2)}\sum_1\frac{\overline{r+2}+\sigma}{\overline{r+2}^2-1}a_r'(1-\alpha_1'^{r+2}) \quad (18)
$$

Table 2

$R\alpha_2^2/h$	α_1'	A_1'	A_3'	A_5'	A_7'	A_9'	A_{11}'	B_0'
"Small"	0.10	1.034	−1.019	0.006				−0.011
	0.20	1.074	−1.020	0.006				−0.043
	0.30	1.163	−1.021	0.006				−0.096
	0.40	1.297	−1.024	0.006				−0.171
1/2	0.10	0.943	−0.918	−0.018	0.003			−0.009
	0.20	0.966	−0.914	−0.018	0.003			−0.037
	0.30	1.003	−0.906	−0.019	0.003			−0.083
	0.40	1.052	−0.897	−0.020	0.003			−0.147
1	0.10	0.789	−0.731	−0.059	0.008			−0.008
	0.20	0.800	−0.718	−0.060	0.008			−0.031
	0.30	0.817	−0.698	−0.061	0.008			−0.068
	0.40	0.841	−0.671	−0.063	0.008			−0.104
2	0.10	0.460	−0.335	−0.138	0.016	0.002		−0.005
	0.20	0.457	−0.320	−0.137	0.015	0.002		−0.018
	0.30	0.451	−0.294	−0.135	0.013	0.002		−0.038
	0.40	0.445	−0.262	−0.134	0.012	0.002		−0.065
3	0.10	0.252	−0.094	−0.170	0.010	0.006		−0.003
	0.20	0.247	−0.084	−0.167	0.009	0.006		−0.010
	0.30	0.239	−0.068	−0.161	0.007	0.005		−0.021
	0.40	0.230	−0.048	−0.155	0.005	0.005		−0.035
4	0.10	0.143	0.026	−0.171	−0.005	0.010		−0.001
	0.20	0.139	0.030	−0.167	−0.006	0.010		−0.006
	0.30	0.133	0.038	−0.160	−0.007	0.009		−0.013
	0.40	0.125	0.049	−0.150	−0.009	0.008		−0.020
5	0.10	0.0839	0.0761	−0.1572	−0.0222	0.0132	0.0007	−0.0008
	0.20	0.0819	0.0776	−0.1526	−0.0227	0.0129	0.0007	−0.0031
	0.30	0.0783	0.0802	−0.1469	−0.0234	0.0124	0.0008	−0.0064
	0.40	0.0732	0.0840	−0.1373	−0.0245	0.0116	0.0008	−0.0144
6	0.10	0.0443	0.1029	−0.1195	−0.0432	0.0146	0.0020	−0.0006
	0.20	0.0433	0.1029	−0.1169	−0.0432	0.0142	0.0020	−0.0020
	0.30	0.0412	0.1028	−0.1114	−0.0432	0.0136	0.0020	−0.0046
	0.40	0.0378	0.1027	−0.1022	−0.0431	0.0125	0.0020	−0.0088
7	0.10	0.0240	0.1077	−0.0882	−0.0615	0.0146	0.0040	−0.0003
	0.20	0.0235	0.1071	−0.0863	−0.0613	0.0143	0.0039	−0.0011
	0.30	0.0223	0.1058	−0.0819	−0.0604	0.0135	0.0039	−0.0028
	0.40	0.0202	0.1035	−0.0742	−0.0592	0.0123	0.0038	−0.0054
8	0.10	0.0080	0.0922	−0.0384	−0.0688	0.0064	0.0058	−0.0001
	0.20	0.0078	0.0918	−0.0374	−0.0685	0.0063	0.0057	−0.0007
	0.30	0.0075	0.0909	−0.0360	−0.0678	0.0060	0.0057	−0.0016
	0.40	0.0068	0.0890	−0.0326	−0.0664	0.0055	0.0056	−0.0024
9	0.10	0.0037	0.0823	−0.0225	−0.0777	0.0061	0.0083	−0.0000
	0.20	0.0036	0.0817	−0.0219	−0.0772	0.0059	0.0082	−0.0003
	0.30	0.0033	0.0804	−0.0200	−0.0759	0.0054	0.0081	−0.0011
	0.40	0.0027	0.0773	−0.0164	−0.0730	0.0045	0.0078	−0.0019
10	0.10	−0.0004	0.0707	0.0027	−0.0825	−0.0009	0.0109	−0.0000
	0.20	−0.0004	0.0704	0.0027	−0.0823	−0.0009	0.0108	−0.0011
	0.30	−0.0005	0.0693	0.0034	−0.0808	−0.0011	0.0107	−0.0005
	0.40	−0.0008	0.0662	0.0054	−0.0772	−0.0018	0.0102	−0.0015

$$B = \frac{\alpha_1'^2}{E}\left(\frac{R\alpha_2^2}{h}\right)^2 \frac{12(1+\sigma)}{(1-\alpha_1'^2)} \sum_1 \frac{\overline{r+2}+\sigma}{\overline{r+2}^2-1}\, a_r'(1-\alpha_1'^{r+1}) \qquad (18)\ (cont.)$$

Derivation of Recurrence Relation, $R\alpha_2^2/h > 1/2$

This is derived via the equation of compatibility of strains,

$$e_\theta + \frac{d(\theta'\Delta')}{d\theta'} = \frac{d(\theta' e_\phi)}{d\theta'} \qquad (2)$$

From the expressions for e_θ and e_ϕ derived in the previous paper,[1] reduced from considerations of symmetry about $\theta' = 0$, by ignoring the $a_r''s$, for r even, there obtains:

$$e_\theta = \frac{1}{E}\left\{A_1'(1-\sigma) + \frac{B_0'(1+\sigma)}{\alpha_2^2\theta'^2} + \sum_1\left[(1-\overline{r+2}\sigma)A_{r+2}' - \frac{1+\sigma}{r+3}\alpha_2^2 A_r'\right]\theta'^{r+1} - \frac{8\sigma}{3+\sigma}\theta'^2\right\}\frac{3+\sigma}{8}\rho\Omega^2R^2\alpha_2^2 \qquad (8a)$$

$$e_\phi = \frac{1}{E}\left\{A_1'(1-\sigma) - \frac{B_0'(1+\sigma)}{\alpha_2^2\theta'^2} + \sum_1\left[(\overline{r+2}-\sigma)A_{r+2}' + \frac{1+\sigma}{r+3}\alpha_2^2 A_r'\right]\theta'^{r+1} + \frac{8}{3+\sigma}\theta'^2\right\}\frac{3+\sigma}{8}\rho\Omega^2R^2\alpha_2^2 \qquad (8a)\ (cont.)$$

where

$$B_0' = \frac{b_0'}{\frac{3+\sigma}{8}\rho\Omega^2R^2\alpha_2^2},$$

Also from the second of (8a) and from (10a),

$$\frac{(\theta' e_\phi)}{d\theta'} = \frac{1}{E}\left\{A_1'(1-\sigma) + \frac{B_0'(1+\sigma)}{\alpha_2^2\theta'^2} + \sum_1\left[(r+2)(\overline{r+2}-\sigma)A_{r+2}' - \frac{1+\sigma}{r+3}(r+2)\alpha_2^2 A_r'\right]\theta'^{r+1} + \frac{8.3}{3+\sigma}\theta'^2\right\}\frac{3+\sigma}{8}\rho\Omega^2R^2\alpha_2^2 \qquad (19)$$

$$\frac{d(\theta'\Delta')}{d\theta'} = \frac{3}{2}A\theta'^2 + B(1 + \log|\theta'|) - \frac{1}{E}\left(\frac{R\alpha_2^2}{h}\right)^2 12(1-\sigma^2)\sum_1 \frac{(r+4)a_r'\theta'^{r+3}}{(r+3)(\overline{r+2}^2-1)} \quad (19)\ (cont.)$$

$$\doteq \frac{3}{2}A\theta'^2 - \frac{1}{E}\left(\frac{R\alpha_2^2}{h}\right)^2 12(1-\sigma^2)\sum_1 \frac{(r+4)a_r'}{(r+3)(\overline{r+2}^2-1)}\theta'^{r+3}$$

where in the last equality, having regard to the values of A and B given by (18), $B(1 + \log|\theta'|)$ has been neglected compared with $(3/2)A\theta'^2$. This assumption is valid for values of θ' not too close to α_1', and for values of $\alpha_1'^2$ not too large; the upper limit adopted for α_1' is 0.4. On the other hand, for values of θ' close to α_1', the dominant terms in the equation of compatibility of strains yield the identity,

$$A_1'(1-\sigma) + \frac{B_0'(1+\sigma)}{\alpha_2^2\theta'^2} \approx A_1'(1-\sigma) + \frac{B_0'(1+\sigma)}{\alpha_2^2\theta'^2};\ \text{i.e.,}\ e_\theta \approx \frac{d(\theta' e_\phi)}{d\theta'}$$

Thus, neglecting the term $B(1 + \log|\theta'|)$ will not introduce appreciable errors in the analysis provided α_1' is small. If the expressions for

$$e_\theta,\quad \frac{d(\theta' e_\phi)}{d\theta'},\quad \text{and}\quad \frac{d(\theta'\Delta')}{d\theta'}$$

are substituted from (8a) and (19) in the equation of compatibility of strains (2) and the coefficients of θ'^{r+1}, r odd, are equated to zero, there results:

A_1', B_0', arbitrary,

$$A_3' \doteq -1 + \frac{9}{4}(1-\sigma^2)\left(\frac{R\alpha_2^2}{h}\right)^2 \sum_1^{11} \frac{\overline{r+2}+\sigma}{\overline{r+2}^2-1}\,\frac{A_r'}{1+\sigma}\,\frac{(1-\alpha_1'^{r+3})}{(1-\alpha_1'^2)}$$

$$A_5' \doteq -\left(\frac{R\alpha_2^2}{h}\right)^2 \frac{5}{64}(1-\sigma^2)A_1'$$

$$A_7' \doteq -\left(\frac{R\alpha_2^2}{h}\right)^2 \frac{7}{576}(1-\sigma^2)A_3' \qquad (14b)$$

$$A_9' \doteq -\left(\frac{R\alpha_2^2}{h}\right)^2 \frac{9}{2560}(1-\sigma^2)A_5'$$

$$A_{11}' \doteq -\left(\frac{R\alpha_2^2}{h}\right)^2 \frac{11}{8000}(1-\sigma^2)A_7'$$

The range for $R\alpha_2^2/h$ considered is again, $\frac{1}{2} \le R\alpha_2^2/h \le 10$ and only the first six terms in the series for s, i.e.,

$$s = \frac{3+\sigma}{8}\rho\Omega^2R^2\alpha_2^3\sum_1^{11} A_r'\theta'^r \qquad (15a)$$

will be used for purposes of computation.

After the evaluation of A_1', to be described in the next section, the six simultaneous equations for $A_1', \ldots\ldots A_{11}'$ can be solved; this has been done and the values of the A_r's (and of B_0'/α_2^2) as functions of the parameters $R\alpha_2^2/h$ and α_1' have been tabulated in Table 2.

Determination of A_1' and B_0'

A_1' and B_0' are determined from the consideration that $p = 0$ at $\theta' = 1$ and $\theta' = \alpha_1'$. This yields the two simultaneous equations for A_1' and B_0':

$$A_1' + \frac{B_0'}{\alpha_2^2} + \sum_1^9\left[A'_{r+2} - \frac{\alpha_2^2}{r+3}A_r'\right] = 0$$
$$A_1' + \frac{B_0'}{\alpha_2^2\alpha_1'^2} + \sum_1^9\left[A'_{r+2} - \frac{\alpha_2^2}{r+3}A_r'\right]\alpha_1'^{r+1} = 0 \qquad (16b)$$

The last five of (14b) and (16b) form a system of seven equations in the seven unknowns $A_1', \ldots\ldots A_{11}', B_0'$, which have been solved for a range of values of $R\alpha_2^2/h$ and α_1'.

Summary of Results For r odd,

$$s = \frac{3+\sigma}{8}\rho\Omega^2R^2\alpha_2^3\sum_1 A_r'\theta'^r$$

$$p = \frac{3+\sigma}{8}\rho\Omega^2R^2\alpha_2^2\left[\frac{B_0'}{\alpha_2^2\theta'^2} + A_1' + \sum_1\left(A'_{r+2} - \frac{A_r'\alpha_2^2}{r+3}\right)\theta'^{r+1}\right]$$
$$\doteq \frac{3+\sigma}{8}\rho\Omega^2R^2\alpha_2^2\left[\frac{B_0'}{\alpha_2^2\theta'^2} + \sum_1 A_r'\theta'^{r-1}\right]$$

$$f = \frac{3+\sigma}{8}\rho\Omega^2R^2\alpha_2^2\left[\frac{-B_0'}{\alpha_2^2\theta'^2} + \frac{8}{3+\sigma}\theta'^2 + A_1' + \sum_1\left(\overline{r+2}A'_{r+2} + \frac{A_r'\alpha_2^2}{r+3}\right)\theta'^{r+1}\right]$$
$$\doteq \frac{3+\sigma}{8}\rho\Omega^2R^2\alpha_2^2\left[\frac{-B_0'}{\alpha_2^2\theta'^2} + \frac{8}{3+\sigma}\theta'^2 + \sum_1 rA_r'\theta'^{r-1}\right]$$

$$M_\theta = \frac{R\alpha_2^2}{h}\,\frac{3+\sigma}{8}\,\frac{\rho\Omega^2R^2\alpha_2^2}{(1-\alpha_1'^2)}\,h^2 \sum_1 \frac{\overline{r+2}+\sigma}{\overline{r+2}^2-1}A_r'\left[(1-\theta'^{r+1}) + \alpha_1'^2(\theta'^{r+1}-\alpha_1'^{r+1}) - (1-\alpha_1'^{r+1})\frac{\alpha_1'^2}{\theta'^2}\right] \qquad (20)$$

$$M_\phi = \frac{R\alpha_2^2}{h}\,\frac{3+\sigma}{8}\,\frac{\rho\Omega^2R^2\alpha_2^2}{(1-\alpha_1'^2)}\,h^2 \sum_1 \frac{\overline{r+2}+\sigma}{\overline{r+2}^2-1}A_r'\left[\left(1 - \frac{1+\overline{r+2}\,\sigma}{\overline{r+2}+\sigma}\theta'^{r+1}\right) + \alpha_1'^2\left(\frac{1+\overline{r+2}\,\sigma}{\overline{r+2}+\sigma}\theta'^{r+1} - \alpha_1'^{r+1}\right) - (1-\alpha_1'^{r+1})\frac{\alpha_1'^2}{\theta'^2}\right]$$

$$\Delta' = B\log|\theta'| + \frac{1}{E}\left(\frac{R\alpha_2^2}{h}\right)^2 6(1-\sigma)\theta'^2 \sum_1 \frac{\overline{r+2}+\sigma}{\overline{r+2}^2-1}\left[\frac{(1-\alpha_1'^{r+3})}{(1-\alpha_1'^2)} - \frac{2(1+\sigma)}{\overline{r+2}+\sigma}\,\frac{\theta'^{r+1}}{(r+3)}\right]A_r'$$

Conclusions

A basic method, developed elsewhere,[1] of assessing the stresses and strains in spinning paraboloid dishes both holed and whole has been extended to cover a larger range of values of the critical dish parameter $R\alpha^2/h$. It avers that, as this parameter increases, more of the elastic reaction of the spinning dish to the inertia forces generated by the spin appears as hoop stress and strain at the expense of the radial stresses and bending moments. The filament stresses on either side of the neutral surface of an element derived from the local bending-moment system are of course algebraically adducible to the direct radial and hoop stresses. Tables of the A_r' coefficients have been compiled for use in the estimation of these stresses and strains.

Bibliography

I. S. Sokolnikoff, "Mathematical Theory of Elasticity," McGraw-Hill Book Company, Inc., New York, N. Y., 1946.

S. Timoshenko, "Theory of Elastic Stability," McGraw-Hill Book Company, Inc., New York, N. Y., first edition, 1936.

The Flexural Vibrations of Thin Laminated Cylinders

J. C. WHITE

Project Engineer, Large Motor and Generator Department, General Electric Company, Schenectady, N. Y.

A method is developed for calculating the natural frequencies of vibration of a thin right circular cylinder. The vibration pattern may contain any number of peripheral or axial nodes. The cylinder is assumed to consist of a large number of thin laminations of two dissimilar materials, arranged alternately, and with the plane of a lamination normal to the axis of the cylinder. Built-in and simply supported end conditions are considered.

Introduction

THE PROBLEM of the determination of the natural frequencies of vibration of an unsupported isotropic right circular cylindrical shell has been treated extensively in the literature. In two recent papers,[1,2] Arnold and Warburton have presented solutions for isotropic cylinders with built-in and with simply supported ends, together with a considerable amount of supporting experimental evidence.

One anisotropic structure of considerable engineering importance consists of a stack of circular laminations, assembled into a cylinder. The plane of a lamination is normal to the axis of the cylinder. Each lamination has, within itself, isotropic and uniform elastic properties. The laminations consist, however, of two dissimilar materials, arranged alternately in the stack, and bonded together into a solid structure.

The purpose of this paper is to present an analysis of the vibrational characteristics of such a structure. In particular, a method is developed for determining the natural frequencies of a laminated cylinder for any number of axial or peripheral nodes and for either simply supported or built-in end conditions.

The cylinder to be considered will consist of a great many very thin laminations. It will be assumed that the discontinuous structure can be replaced by a continuous structure with uniform, but not isotropic, properties. Both the actual and the equivalent structures are assumed to have linear elastic properties; in any given direction, the moduli are the same in tension and compression. The various constants of the equivalent material are derived in the Appendix, in terms of the properties of the individual laminations. The method of analysis will be that used by Arnold and Warburton.

The Strain Energy

We will consider flexural vibrations of a shell in the form of a right circular cylinder of length l, thickness h, and mean radius a. In general, the thickness will be assumed to be much smaller than any other dimension. An element of this cylinder is illustrated in Fig. 1, with co-ordinate axes and sign conventions indicated. The cylinder is constructed of laminations normal to the x-axis.

The total strain energy in the cylinder may be expressed approximately as:

$$S = \frac{1}{2}\int_0^{2\pi}\int_0^{l}\int_{-\frac{1}{2}h}^{\frac{1}{2}h} [\sigma_x e_x + \sigma_y e_y + \tau_{xy}\gamma_{xy}]a\,dz\,dx\,d\phi \tag{1}$$

In writing this expression for strain energy, we have neglected the

[1] R. N. Arnold and G. B. Warburton, "Flexural Vibrations of the Walls of Thin Cylindrical Shells Having Freely Supported Ends," *Proceedings, Royal Society (London)*, series A, vol. 197, 1959, pp. 238–256.

[2] R. N. Arnold and G. B. Warburton, "The Flexural Vibrations of Thin Cylinders," *Proceedings, I. Mech. E.*, series A, vol. 167, 1953, pp. 62–80.

Contributed by the Machine Design Division and presented at the Winter-Annual Meeting, New York, N. Y., November 27–December 2, 1960, of THE AMERICAN SOCIETY OF MECHANICAL ENGINEERS. Manuscript received at ASME Headquarters, March 24, 1960. Paper No. 60—WA-6.

Nomenclature

The co-ordinate system used is illustrated in Fig. 1.

A, B, C = indeterminate amplitudes of motion of a point on the middle surface in axial, peripheral, and radial directions, respectively
E = Young's modulus
G = shear modulus
S = strain energy stored in shell
T = kinetic energy of shell
a = mean radius of shell
e = direct strain
f = natural frequency
g = gravitational acceleration
h = shell thickness
l = shell length
$m + 1$ = number of axial nodes in vibration pattern
$2n$ = number of peripheral nodes in vibration pattern
p = a wave-length factor for the built-in case
t = time
u, v, w = displacements of a point on the middle surface in the axial, peripheral, and radial directions, respectively
$\beta = h^2/12a^2$
γ = shear strain
Δ = dimensionless frequency factor
δ = a wave-length factor for the simply supported case
$\lambda = 1 - \mu_{xy}\mu_{yx}$
μ = Poisson's ratio
ξ = per-unit thickness of one of the two types of laminations making up the shell
ρ = density of shell
σ = direct stress
τ = shear stress
$\omega = 2\pi f$

Subscripts x, y, and z denote parameters associated with the three co-ordinate directions. Subscripts 1 and 2 denote parameters associated with the two types of laminations making up the shell.

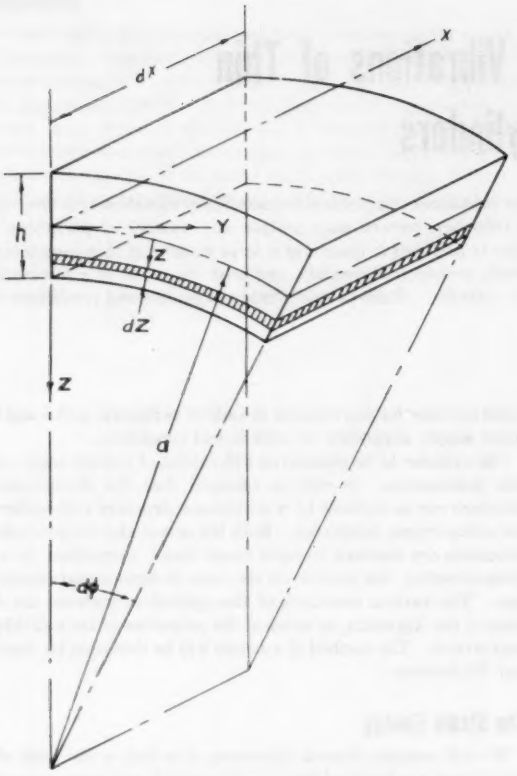

Fig. 1 An element of a thin cylindrical shell

trapezoidal form of the faces of the element normal to the x-axis. We have also neglected the direct stress in the radial direction, σ_z, and the shear strains involving the radial direction, γ_{yz} and γ_{zx}.

In the Appendix, expressions have been derived relating stresses and strains in such a laminated material, under the same assumptions as those made in deriving equation (1). Substituting for the stresses in terms of strains, equation (1) becomes:

$$S = \frac{1}{2\lambda}\int_0^{2\pi}\int_0^{l}\int_{-\frac{1}{2}h}^{\frac{1}{2}h} [E_x e_x^2 + E_y e_y^2 + 2\mu_{yx}E_x e_x e_y + \lambda G_{xy}\gamma_{xy}^2]a\,dz\,dx\,d\phi \quad (2)$$

In establishing relationships between the various strains and displacements, we will make use of the method presented by Love.[3] This assumes a linear variation in strains in the radial direction.

$$e_x = \frac{\partial u}{\partial x} - z\frac{\partial^2 w}{\partial x^2} \quad (3)$$

$$e_y = \frac{1}{a}\left(\frac{\partial v}{\partial \phi} - w\right) - \frac{z}{a^2}\left(\frac{\partial^2 w}{\partial \phi^2} + \frac{\partial v}{\partial \phi}\right) \quad (4)$$

$$\gamma_{xy} = \left(\frac{\partial v}{\partial x} + \frac{1}{a}\frac{\partial u}{\partial \phi}\right) - \frac{2z}{a}\left(\frac{\partial^2 w}{\partial x \partial \phi} + \frac{\partial v}{\partial x}\right) \quad (5)$$

[3] A. E. H. Love, "A Treatise on the Mathematical Theory of Elasticity," fourth edition, 1929, Dover Publications, pp. 529–543.

Natural Frequency With Simply Supported Ends

To evaluate the strain energy stored in the shell, we must establish some form or mode of vibration. With the cylinder simply supported at its ends, we will assume the following expressions for the displacements, which are reasonable and which match the boundary conditions:

$$u = U\cos\frac{m\pi x}{l}\cos n\phi \quad (6)$$

$$v = V\sin\frac{m\pi x}{l}\sin n\phi \quad (7)$$

$$w = W\sin\frac{m\pi x}{l}\cos n\phi \quad (8)$$

in which U, V, and W are functions of time alone. The origin of co-ordinates lies in a plane passing through one end of the cylinder. Substituting in equations (2) to (5), the strain energy becomes:

$$S = \frac{\pi l h}{4a\lambda}\{E_x\delta^2[U^2 + W^2\delta^2\beta] + E_y[(Vn - W)^2 + \beta(Vn - Wn^2)^2] - 2\mu_{yx}E_x\delta[U(Vn - W) + W(Vn - Wn^2)\delta\beta] + \lambda G_{xy}[(V\delta - Un)^2 + 4\beta\delta^2(V - Wn)^2]\} \quad (9)$$

where we have defined:

$$\beta = \frac{h^2}{12\,a^2} \quad (10)$$

$$\delta = \frac{m\pi a}{l} \quad (11)$$

The kinetic energy in the shell at any instant is given by:

$$T = \frac{\rho}{2g}\int_0^{2\pi}\int_0^{l}\int_{-\frac{1}{2}h}^{\frac{1}{2}h}\left[\left(\frac{\partial u}{\partial t}\right)^2 + \left(\frac{\partial v}{\partial t}\right)^2 + \left(\frac{\partial w}{\partial t}\right)^2\right]a\,dz\,dx\,d\phi \quad (12)$$

Substituting and integrating, this becomes:

$$T = \frac{\pi\rho l h a}{4g}[\dot{U}^2 + \dot{V}^2 + \dot{W}^2] \quad (13)$$

where the dot indicates the time derivative.

Next, it will be assumed that U, V, and W represent in-phase sinusoidal motions, with independent and undetermined amplitudes:

$$U = A\cos\omega t \quad (14)$$

$$V = B\cos\omega t \quad (15)$$

$$W = C\cos\omega t \quad (16)$$

Since A, B, and C are independent variables, we may apply Lagrange's equations:

$$\frac{d}{dt}\left(\frac{\partial T}{\partial \dot{U}}\right) - \frac{\partial T}{\partial U} = -\frac{\partial S}{\partial U} \quad (17)$$

and similarly for V and W. This leads to the following set of three linear homogeneous equations:

$$\begin{bmatrix} (\alpha_{11} - \Delta) & \alpha_{12} & \alpha_{13} \\ \alpha_{12} & (\alpha_{22} - \Delta) & \alpha_{23} \\ \alpha_{13} & \alpha_{23} & (\alpha_{33} - \Delta) \end{bmatrix} \begin{bmatrix} A \\ B \\ C \end{bmatrix} = 0 \quad (18)$$

with the coefficients being defined as follows:

$$\alpha_{11} = \frac{E_x}{E_y}\,\delta^2 + \frac{\lambda G_{xy}}{E_y}\,n^2 \quad (19)$$

$$\alpha_{12} = -\delta n\left(\frac{\mu_{yx}E_x}{E_y} + \frac{\lambda G_{xy}}{E_y}\right) \quad (20)$$

$$\alpha_{13} = \frac{\mu_{yx}E_x}{E_y}\,\delta \quad (21)$$

$$\alpha_{22} = n^2(1+\beta) + \frac{\lambda G_{xy}}{E_y}\,\delta^2(1+4\beta) \quad (22)$$

$$\alpha_{23} = -n(1+n^2\beta) - \beta n\delta^2\left(\frac{\mu_{yx}E_x}{E_y} + \frac{4\lambda G_{xy}}{E_y}\right) \quad (23)$$

$$\alpha_{33} = 1 + \beta\left(n^4 + \frac{E_x}{E_y}\,\delta^2\right) + 2\beta\delta^2 n^2\left(\frac{\mu_{yx}E_x}{E_y} + \frac{2\lambda G_{xy}}{E_y}\right) \quad (24)$$

$$\Delta = \frac{\rho\lambda a^2\omega^2}{E_y g} \quad (25)$$

The natural frequency can be determined by expanding the determinant of equation (18), equating it to zero, and solving for Δ. Expansion of the determinant leads to a cubic equation in Δ, which has three real, positive roots. The significance of the three roots is discussed below. From equation (25), the natural frequency corresponding to a particular value of Δ may be obtained from:

$$f = \frac{1}{2\pi}\sqrt{\frac{\Delta E_y g}{\rho\lambda a^2}} \quad (26)$$

Natural Frequency With Built-In Ends

For this condition, we will assume displacements which match the boundary conditions, and the variation in w in the axial direction will be taken to have the same form as that of a fixed beam during flexural vibration. The origin of co-ordinates will be shifted to the plane half way between the ends of the cylinder. For an even number of axial nodes, the displacements of the middle surface will be assumed to be:

$$u = U\left(-\sin\frac{px}{a} + k\sinh\frac{px}{a}\right)\cos n\phi \quad (27)$$

$$v = V\left(\cos\frac{px}{a} + k\cosh\frac{px}{a}\right)\sin n\phi \quad (28)$$

$$w = W\left(\cos\frac{px}{a} + k\cosh\frac{px}{a}\right)\cos n\phi \quad (29)$$

and for an odd number of axial nodes:

$$u = U\left(\cos\frac{px}{a} - k\cosh\frac{px}{a}\right)\cos n\phi \quad (30)$$

$$v = V\left(\sin\frac{px}{a} - k\sinh\frac{px}{a}\right)\sin n\phi \quad (31)$$

$$w = W\left(\sin\frac{px}{a} - k\sinh\frac{px}{a}\right)\cos n\phi \quad (32)$$

in which:

$$k = \frac{\sin\dfrac{pl}{2a}}{\sinh\dfrac{pl}{2a}} \quad (33)$$

and the values of p are given by the roots of the equation:

$$\tan\frac{pl}{2a} - (-1)^m\tanh\frac{pl}{2a} = 0 \quad (34)$$

To a very good approximation:

$$\frac{pl}{\pi a} = \left(m + \frac{1}{2}\right) \quad (35)$$

Substituting either set of assumed displacements in equations (2) to (5), we obtain:

$$\begin{aligned} S = \frac{\pi lh}{4a\lambda}\,\{&E_x\theta_1[U^2p^2 + W^2p^4\beta] \\ &+ E_y\theta_1[(Vn - W)^2 + (Vn - Wn^2)^2\beta] \\ &+ 2\mu_{yx}E_x\theta_2[Up(W - Vn) + W\beta p^2(Wn^2 - Vn)] \\ &+ \lambda G_{xy}\theta_2[(Vp - Un)^2 + 4\beta p^2(V - Wn)^2]\} \end{aligned} \quad (36)$$

where we have defined:

$$\theta_1 = 1 - (-1)^m k^2 \quad (37)$$

$$\theta_2 = 1 + (-1)^m\left[k^2 - \frac{2a}{pl}\sin\frac{pl}{a}\right] \quad (38)$$

The kinetic energy may be evaluated from equation (12):

$$T = \frac{\pi\rho lha}{4g}\,[\theta_2\dot{U}^2 + \theta_1(\dot{V}^2 + \dot{W}^2)] \quad (39)$$

It should be noted that the expressions for strain energy and kinetic energy are identical with those for the simply supported case, except for the presence of θ_1 and θ_2 and the exchange of p for δ.

Applying Lagrange's equations as before, we obtain the following set of three linear homogeneous equations:

$$\begin{bmatrix} (\alpha_{11} - \Delta) & \alpha_{12} & \alpha_{13} \\ \zeta\alpha_{12} & (\alpha_{22} - \Delta) & \alpha_{23} \\ \zeta\alpha_{13} & \alpha_{23} & (\alpha_{33} - \Delta) \end{bmatrix} \begin{bmatrix} A \\ B \\ C \end{bmatrix} = 0 \quad (40)$$

in which Δ is defined as in equation (25), and:

$$\zeta = \frac{\theta_2}{\theta_1} \quad (41)$$

The coefficients are:

$$\alpha_{11} = \frac{E_x p^2}{E_y\zeta} + \frac{\lambda G_{xy}}{E_y}\,n^2 \quad (42)$$

$$\alpha_{12} = -pn\left(\frac{\mu_{yx}E_x}{E_y} + \frac{\lambda G_{xy}}{E_y}\right) \quad (43)$$

$$\alpha_{13} = \frac{\mu_{yx}E_x}{E_y}\,p \quad (44)$$

$$\alpha_{22} = n^2(1+\beta) + \frac{\zeta\lambda G_{xy}}{E_y} p^2(1+4\beta) \tag{45}$$

$$\alpha_{23} = -n(1+n^2\beta) - \zeta\beta np^2\left(\frac{\mu_{yx}E_x}{E_y} + \frac{4\lambda G_{xy}}{E_y}\right) \tag{46}$$

$$\alpha_{33} = 1 + \beta\left(n^4 + \frac{E_x}{E_y}p^4\right) + 2\zeta\beta p^2 n^2\left(\frac{\mu_{yx}E_x}{E_y} + \frac{2\lambda G_{xy}}{E_y}\right) \tag{47}$$

As in the simply supported case, expansion of the determinant of equation (40) leads to a cubic equation in Δ. Once a value of Δ has been obtained, the natural frequency can be determined from equation (26).

Discussion of Results

An arbitrary numerical example was selected to illustrate the nature of the results. The parameters:

$$\frac{\pi a}{l} = 1.0 \qquad \frac{h}{a} = 0.05 \qquad \mu_{yx} = 0.30$$

Calculations were made for various numbers of peripheral and axial nodes and for a constant $E_x/E_y = 0.20$. The results are plotted, for the simply supported case, in Fig. 2. The ordinate is a dimensionless frequency factor $\sqrt{\Delta}$, where Δ is defined in equation (25). This parameter was chosen, rather than the natural frequency f, since it is independent of the density and the numerical magnitudes of the moduli and dimensions.

To illustrate the variation in natural frequency with axial modulus, calculations were also made, using the above parameters and $m = 4$, with variable n and E_x/E_y. The results are plotted in Fig. 3.

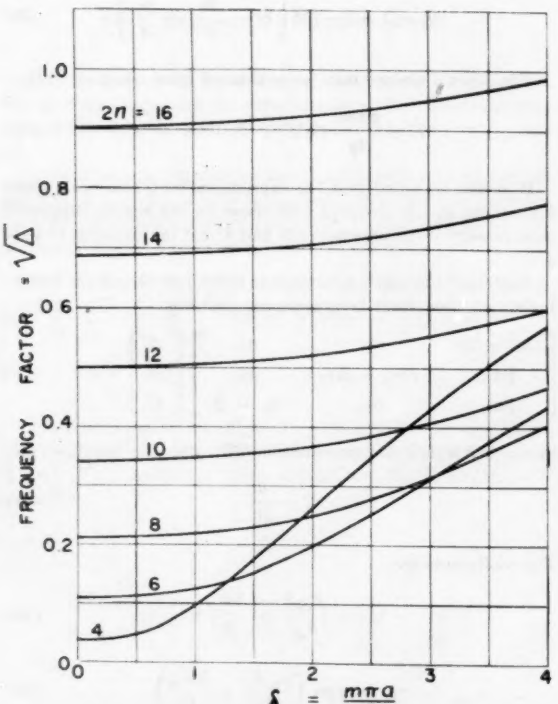

Fig. 2 Natural frequency of a laminated cylindrical shell with simply supported ends, as a function of the number of peripheral and axial nodes in the vibration pattern

The behavior of the natural frequency as a function of the number of peripheral nodes is quite interesting. Figs. 2 and 3 indicate that, for a low number of peripheral nodes, the natural frequency actually decreases as the complexity of the vibrational pattern increases (i.e., as the number of peripheral nodes increases). This phenomenon was noted by Arnold and Warburton and confirmed experimentally by them.

A fairly simple explanation of this behavior may be obtained if we investigate the nature of the strain energy storage in the system. There are two basic forms of elastic energy storage in the system: that associated with bending and that associated with stretching of the middle surface.

Equations (18) and (40) are, of course, indeterminate systems which do not have unique solutions. For a determined value of Δ, however, we can solve them for two parameters in terms of the third. For example, we could determine A/C and B/C. By separating the bending and stretching energy terms in equations (9) or (36), the ratio of stretching to bending energy can be evaluated. Doing this for the foregoing numerical example, and for $m = 4$ and $E_x/E_y = 0.2$, we obtain the values in Table 1, for the

Table 1

Number of peripheral nodes in vibration pattern = $2n$	Ratio of stretching energy to bending energy
4	17.72
6	3.908
8	0.893
10	0.234
12	0.0684
14	0.0254
16	0.0106

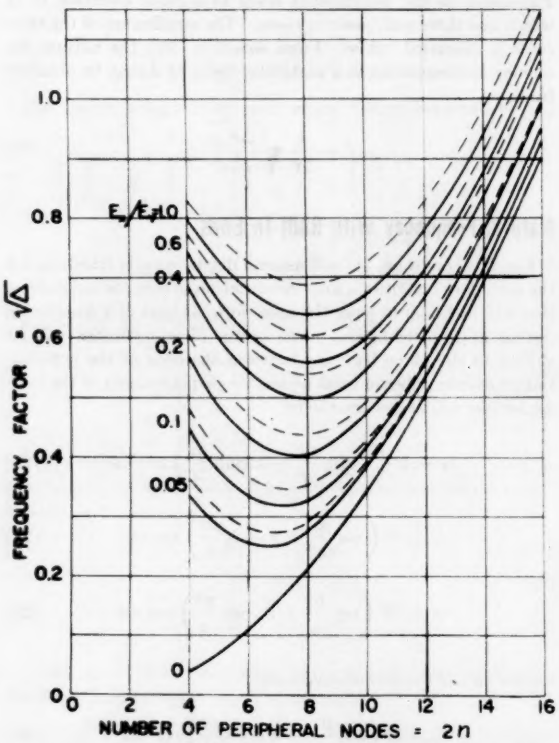

Fig. 3 Natural frequency of a laminated cylindrical shell as a function of the number of peripheral nodes and the ratio of axial to peripheral moduli of elasticity. Solid curves: simply supported ends; dotted curves: built-in ends.

simply supported case. It is quite apparent from the table that, for low numbers of peripheral nodes, the energy associated with stretching of the middle surface predominates. As the number of peripheral nodes increases, bending energy tends to become more important. This explains the increase in natural frequency as n becomes small. The effect is, of course, entirely absent in the case of an unsupported ring or shell.

Investigation of the relative amplitudes of vibration in the three co-ordinate directions (A, B, and C) also yields a physical picture of the significance of the three roots of the cubic equation obtained by expansion of the determinant of equations (18) or (40). If the ratios A/C and B/C are determined for each of the three values of Δ, it is apparent that each of the roots is associated with a predominance of one of the three amplitudes. Over the region where thin shell theory applies:

1 The lowest root is associated primarily with radial motion of points on the middle surface of the shell (i.e., C predominates).

2 The middle root is associated primarily with peripheral motion of points on the middle surface of the shell (i.e., B predominates).

3 The highest root is associated primarily with axial motion of points on the middle surface of the shell (i.e., A predominates).

In no case is any root associated with only one amplitude of motion; all three contribute to the determination of each Δ. This is particularly true for low n, where stretching energy predominates. It is also worth emphasizing that the three values of Δ (i.e., the three roots of the cubic) correspond to only one vibrational mode. In theory, this particular mode of vibration could be excited to resonance at any of the three frequencies determined by the three values of Δ.

It is important to note that, over the region in which thin shell theory applies, only the lowest root is of practical significance. The other two correspond to very much higher frequency and energy levels and are therefore more difficult to excite. Furthermore, in most cases of practical importance, excitation will be provided by a radial force system, which would tend to produce a motion corresponding to the lowest root.

As we would expect, the method presented in this paper reduces identically to that of Arnold and Warburton for $E_x = E_y$ (i.e., an isotropic cylinder). In the other limit, for $E_x = 0$, the expression for the natural frequency reduces to that for an unsupported ring.

APPENDIX

The Equivalent Elastic Constants of a Laminated Material

Consider a structure composed of alternate laminations of two dissimilar materials (identified in the following by subscripts "1" and "2"). The structure is well bonded together, and the laminations of each type are of uniform thickness and of uniform and isotropic properties. The laminations are oriented normal to the x-axis. An elemental cube of the material is illustrated in Fig. 4.

In correspondence with the assumptions made in establishing equation (1), we will neglect the direct stress in the z-direction and the shear strains involving the z-direction. Two conditions will be imposed on the direct stress-strain system:

1 Direct strain in the y-direction must be the same in the two materials.

2 Direct stress in the x-direction must be the same in the two materials.

If a direct stress σ_y is applied in the y-direction, then the strains in the y-direction will be:

$$e_y = \frac{\sigma_1}{E_1} = \frac{\sigma_2}{E_2} \tag{48}$$

The total force on the element must equal the sum of the forces on the two materials:

$$\sigma_y dz\, dx = \xi\sigma_1\, dz\, dx + (1 - \xi)\sigma_2 dz\, dx \tag{49}$$

where ξ is the per-unit thickness of the laminations of type 1. Then:

$$\sigma_y = [\xi E_1 + (1 - \xi)E_2]e_y \tag{50}$$

and the equivalent modulus of the material in the y-direction is:

$$E_y = \xi E_1 + (1 - \xi)E_2 \tag{51}$$

Next, let us apply a direct strain in the x-direction. The total strain in the x-direction will be:

$$e_x = \xi \frac{\sigma_x}{E_1} + (1 - \xi)\frac{\sigma_x}{E_2} \tag{52}$$

$$\sigma_x = \frac{e_x}{\dfrac{\xi}{E_1} + \dfrac{(1 - \xi)}{E_2}} \tag{53}$$

and the equivalent elastic modulus of the material in the x-direction is:

$$E_x = \frac{E_1 E_2}{\xi E_2 + (1 - \xi)E_1} \tag{54}$$

Now, let us consider Poisson's ratio. If we apply direct stresses in both the x and y-directions, the total strain in the x-direction will be:

$$e_x = \xi \frac{\sigma_x}{E_1} + (1 - \xi)\frac{\sigma_x}{E_2} - \xi\mu_1 \frac{\sigma_1}{E_1} - (1 - \xi)\mu_2 \frac{\sigma_2}{E_2} \tag{55}$$

Applying equation (54), this reduces to:

$$e_x = \frac{\sigma_x}{E_x} - [\xi\mu_1 + (1 - \xi)\mu_2]\frac{\sigma_y}{E_y} \tag{56}$$

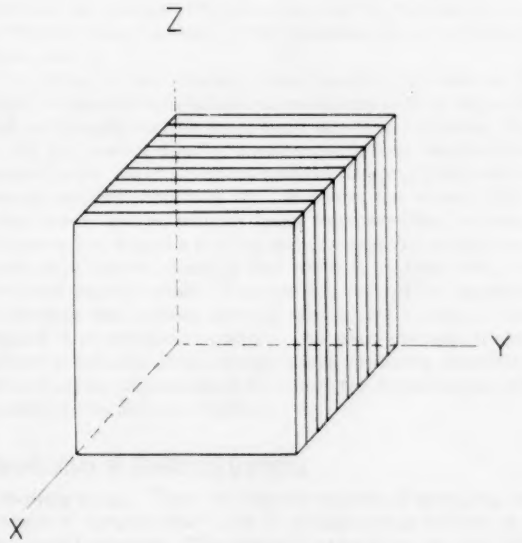

Fig. 4

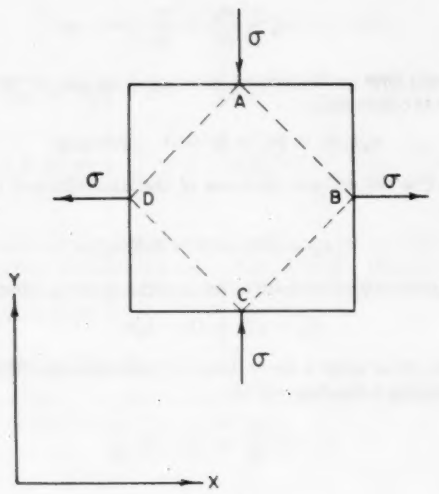

Fig. 5

By analogy with Hooke's law for isotropic materials:

$$\mu_{yz} = \xi\mu_1 + (1 - \xi)\mu_2 \tag{57}$$

Next, consider the total strain in the y-direction. This must be the same in both materials:

$$e_y = \frac{\sigma_1}{E_1} - \mu_1\frac{\sigma_x}{E_1} = \frac{\sigma_2}{E_2} - \mu_2\frac{\sigma_z}{E_2} \tag{58}$$

Introducing equation (49), which still applies, and reducing, we have:

$$e_y = \frac{\sigma_y}{E_y} - \mu_{yz}\left(\frac{E_z}{E_y}\right)\frac{\sigma_z}{E_z} \tag{59}$$

By analogy with Hooke's law for isotropic materials:

$$\mu_{zy} = \mu_{yz}\frac{E_z}{E_y} \tag{60}$$

The shear modulus remains to be evaluated. Consider a cube of the material subjected to a uniform tensile stress σ, over the pair of opposite faces normal to the x-axis, and an equal compressive stress over the pair of faces normal to the y-axis, as illustrated in Fig. 5. If we consider equilibrium of the corner denoted by $\overline{AB}$, we see that the surface $\overline{AB}$ has only a pure shear stress acting on it of magnitude $\tau = \sigma$.

The deformation of the subelement $\overline{ABCD}$ can be evaluated in terms of the stresses and the moduli already evaluated. The shear strain of $\overline{ABCD}$ is, assuming small displacements:

$$\gamma_{xy} = \frac{\tau}{G_{xy}} = \frac{\sigma}{E_x} + \mu_{yz}\frac{\sigma}{E_y} + \frac{\sigma}{E_y} + \mu_{zy}\frac{\sigma}{E_x} \tag{61}$$

Since $\tau = \sigma$, this reduces to:

$$G_{xy} = \frac{E_xE_y}{E_y(1 + \mu_{zy}) + E_x(1 + \mu_{yz})} \tag{62}$$

With the moduli defined, the equations relating stress and strain can be written in the form:

$$\sigma_x = \frac{E_x}{\lambda}(e_x + \mu_{yz}e_y) \tag{63}$$

$$\sigma_y = \frac{E_y}{\lambda}(e_y + \mu_{xy}e_x) \tag{64}$$

$$\tau_{xy} = G_{xy}\gamma_{xy} \tag{65}$$

$$\lambda = 1 - \mu_{yz}\mu_{xy} \tag{66}$$

Damping Structural Resonances Using Viscoelastic Shear-Damping Mechanisms

Part I Design Configurations

JEROME E. RUZICKA
Staff Consultant, Barry Controls, Division of Barry-Wright Corporation, Watertown, Mass. Assoc. Mem. ASME

This paper considers the problem of resonant vibration control in designing structures to function in modern dynamic environments. Methods of specifying structural damping are given and damping properties of engineering materials are reviewed. The disadvantages of some current design practices are outlined and special structural designs which incorporate viscoelastic shear-damping mechanisms are suggested as a method of controlling the resonant flexural vibrations of structures. The general dynamic characteristics and design philosophy of structures and strip dampers (additive damping techniques) that incorporate viscoelastic shear-damping mechanisms are discussed. A description is given of some parameters useful in the design of viscoelastic-damped structures.

Introduction

Resonant-vibration control is an important consideration when designing structures to function in a dynamic environment. The high vibration and noise levels associated with modern high-energy power sources exist over a broad frequency range. The amplification of power-source vibration by structural members creates large dynamic stresses in the structure, with high accelerations transmitted to critical components. Uncontrolled resonant vibrations result in excessive noise, structure fatigue, and component failure.

Until recently, conventional structural designs were acceptable because interest was focused on the dynamic response of the structures at relatively low frequencies. However, current design objectives, which include low noise, light weight, increased reliability, and long life, at higher operating speeds, make many conventional structural designs unacceptable. Approaches that may be used to avoid detrimental resonance conditions include:

1 Rigidization of structural members.
2 Decoupling of resonating systems.
3 Detuning of coupled resonators.
4 Using high fatigue-strength structural materials.
5 Reducing the vibration excitation of the structure.
6 Incorporating high-energy dissipating mechanisms into the structural fabrication.

Excepting the last, these are conventional design approaches that have been used in recent years. In general, they prove inadequate in coping with modern problems of structural resonance because of the complex nature of the dynamic environment.

Designs involving rigidization, decoupling, and detuning are not acceptable in many applications because they add too much weight and, in some cases, involve relatively complicated trial-and-error procedures. Also, increased structural stiffness may react with local mass properties to produce a new resonance that is more damaging than the original.

Decoupling decreases the number of coupled resonators that exist between the environment input and the position of a given component, whereas detuning separates the natural frequencies of the components from the structural natural frequencies and predominant excitation frequencies [1].[1] However, the natural resonances of the structures and components can still be excited because the frequency range of mechanical and acoustic random excitation prevalent in modern dynamic environments is sufficiently broad to encompass many of the natural frequencies of the structures and components.

The approach of using high fatigue-strength structural materials relies on the progress to be made in the area of materials research. The fatigue, damping, and elastic properties of an engineering material as well as the stress distribution in the member must be considered as joint criteria when selecting a material for resonant strength [2, 3, 4]. At the present time, there are not enough high-strength materials available to satisfy general design requirements.

Vibration isolators can reduce the vibration transmitted to the structure and thus subject it to a less severe vibration excitation. However, the structure vibrations may still be increased to unacceptable levels because of the amplifications at structural resonances [5].

In contrast to the foregoing design considerations, the use of heavily damped structural fabrications appears to be an approach that successfully controls broad-band structural vibrations [6]. In the past several decades, considerable interest has been expressed in the use of structural material damping properties to control resonant vibrations [7]. However, the modern high-energy power source, with its broad frequency-band vibration excitation, has created a need for energy dissipation in structural fabrications greatly exceeding that which is available from the structural material itself. Attention has focused on structural fabrications that possess damping mechanisms capable of dissipating large amounts of energy. This paper discusses specific structural damping design configurations employing viscoelastic shear-damping mechanisms that produce the desired energy dissipation during flexural vibrations.

Specification of Structural Damping

Damping Energy. There are various methods of specifying the amount of damping that exists in an engineering material or a structural fabrication. The *specific damping energy D* (in-lb/in^3/

Contributed by the Machine Design Division and presented at the Winter Annual Meeting, New York, N. Y., November 27–December 2, 1960, of The American Society of Mechanical Engineers. Manuscript received at ASME Headquarters, July 11, 1960. Paper No. 60—WA-73.

[1] Numbers in brackets designate References at end of paper.

cycle) of a material represents the area within the stress-strain hysteresis loop for uniform stress conditions. While this basic damping measurement depends on the temperature, stress history, dynamic-stress level, and the material itself, it is not a function of the shape, stress distribution, or volume of the specimen. The *total damping energy* D_0 (in-lb/cycle) of a structural member depends on the shape and size of the member, the method of loading, and the stress distribution as well as the specific damping-energy property of the structural material. The total damping energy can be determined analytically by integrating the specific damping energy over the total effective volume of the structural member contributing to the energy dissipation [8].

Damping Capacity. The *damping capacity* ψ is defined as the ratio of the total damping energy D_0 to the maximum potential energy W_0 (in-lb/cycle) developed during a completely reversed vibration cycle [9]:

$$\psi = \frac{D_0}{W_0} \tag{1}$$

The maximum potential energy W_0 is the total strain energy in the specimen at the maximum induced stress. Because it is defined in terms of the total damping energy D_0, the damping capacity also depends on the properties of the material as well as the shape and stress distribution of the member. The damping-energy definitions discussed are valid for a material or for a structural member subjected to a steady forced vibration.

Quality Factor. The *quality factor* (or figure of merit) Q is defined as 2π times the ratio of the maximum potential energy W_0 to the total damping energy D_0 for a completely reversed vibration cycle [10]:

$$Q = \frac{2\pi W_0}{D_0} \tag{2}$$

This definition is valid only for steady-state vibrations.

Logarithmic Decrement. The *logarithmic decrement* δ specifies the damping in a structural member that is undergoing free vibrations [11]. A diagram showing the decay of vibration of a point on a freely vibrating structure is depicted by Fig. 1. The logarithmic decrement, which is defined in terms of the decay rate of the vibration, is given by

$$\delta = \ln \frac{X_n}{X_{n+1}} = \frac{1}{n} \ln \frac{X_0}{X_n} \tag{3}$$

where X represents the general displacement vibration amplitude of the structural member. After n cycles of free vibration, the displacement amplitude has decreased from X_0 to X_n. The logarithmic decrement is thus determined by the relative decrease of the vibration amplitude over a given number of vibration cycles.

Resonance Curve: Bluntness and Bandwidth. The comparative damping properties of structures are indicated by the steady-state structure vibration response plotted as a function of excitation frequency. A typical vibration-response comparison for a conventional and a heavily damped structure is shown in Fig. 2.

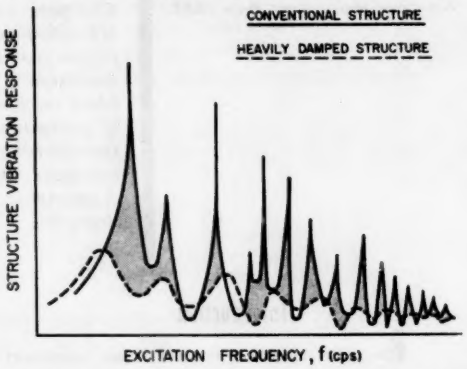

Fig. 2 Typical steady-state structure vibration response of a conventional and a heavily damped structure as a function of excitation frequency

The conventional-structure response is indicative of the type of motion experienced by a structure that relies on the inherent damping of the structural material and the energy dissipation at conventionally fabricated structural joints to control the resonance amplification. The response curve for the heavily damped structure indicates the typical reduction in resonant and near-resonant vibrations that can be obtained by optimized structural damping techniques. The vibration amplification factor (steady-state output-input vibration ratio) of a typical resonant peak is shown in Fig. 3. The *bluntness* b of the resonance curve is defined by [11, 12]

$$b = \frac{\Delta f}{f_n} \sqrt{\frac{\left(\frac{A}{A_r}\right)^2}{1 - \left(\frac{A}{A_r}\right)^2}} \tag{4}$$

where A_r is the resonance amplification factor for a given point on

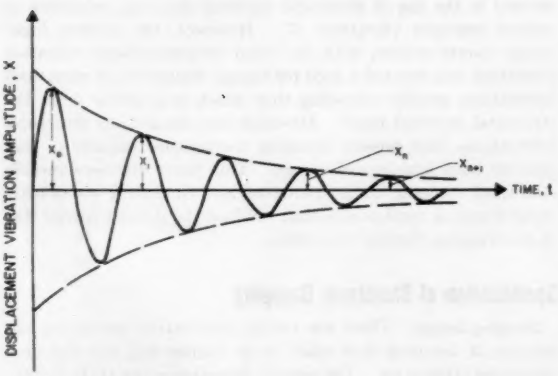

Fig. 1 Free vibration time-decay pattern defines the logarithmic decrement of a damped structure

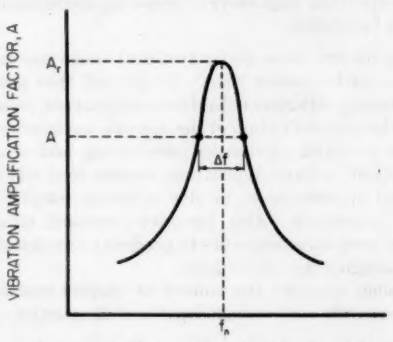

Fig. 3 The bluntness of a structural resonance is defined by the shape of the vibration amplification curve. The resonance amplification factor A_r is the maximum value of vibration amplification.

the structure and A is the vibration amplification factor at the frequencies on either side of the resonant frequency f_n for which the bandwidth is Δf. Because of the difficulty in making accurate measurements of Δf, the bandwidth method of damping specification generally is limited to values of the resonance amplification factor between 5 and 100.

Resonance Amplification Factor. The *resonance amplification factor* A_r is a convenient parameter used to indicate the comparative damping properties of similar structural members subjected to the same vibration excitation. Since the resonant vibration can be measured at arbitrary points on structural members, there is no specific relationship between a general resonance amplification factor and the methods of specifying structural damping previously discussed. However, if the vibration excitation, the geometric configuration, the boundary conditions, and the resonant frequencies of the members being compared are approximately the same, the ratio of resonance amplification factors of the members is inversely proportional to the ratio of respective damping parameters of the members such as the damping capacity and the resonance curve bluntness [13].

Relationships Among Damping Parameters. Theoretically, definite relationships among certain of the parameters used to specify structural damping exist only for a single-degree-of-freedom system with linear damping. For this case, the damping capacity ψ, the quality factor Q, the logarithmic decrement δ, and the resonance curve bluntness b are related as follows [8, 13, 14]:

$$\psi = \frac{2\pi}{Q} = 2\delta = 2\pi b \tag{5}$$

This relationship is approximately valid for nonlinear structural damping if the different measurements are made at the same stress level in the vibrating structural member.

Damping in Engineering Materials

Material Damping. When a structural member is vibrated at its resonant frequency, the amplification of the excitation vibration is limited to some finite value by the internal damping property of the structural material. The internal damping (material damping) is a manifestation of the inelasticity of the structural material; that is, rather than being a single-valued curve, the dynamic stress-strain curve for the material will form a hysteresis loop, the shape of which depends on the damping mechanisms operative. Typical dynamic stress-strain loops for a structural material (metal or nonmetal undergoing tension-compression vibration) and a viscoelastic material (damping material undergoing shear vibration) are shown in Fig. 4. For typical (inelastic) structural materials, the hysteresis loop is generally pointed, whereas it is elliptical for a viscoelastic material. Since many damping mechanisms may be operating concurrently within the structural material, the description of the energy dissipation process is complicated. However, the general phenomenon of material damping may be described as the dissipation of applied potential (strain) energy into heat or surface-damage energy [15].

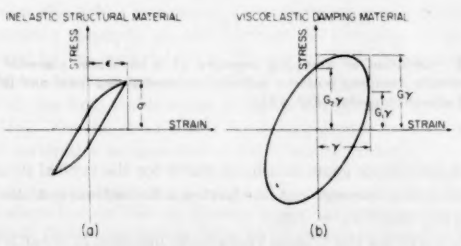

Fig. 4 Typical dynamic stress-strain hysteresis loops for (a) structural material and (b) viscoelastic shear damping material

Viscoelastic Damping Material Properties. A schematic diagram representing the shear-damping mechanism of viscoelastic damping materials is shown in Fig. 5. The system consists of a viscoelastic damping layer of uniform thickness h_V (in.) undergoing a cyclic shear strain γ produced by the applied force P (lb).

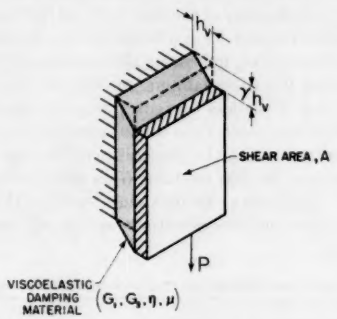

Fig. 5 Schematic diagram of the shear-damping mechanism of viscoelastic damping materials. The damping layer has a shear area A and a uniform thickness h_V. The coefficients G_1, G_2, η, and μ represent the dynamic elastic constants of the viscoelastic damping material.

The damping property of a viscoelastic material undergoing cyclic shear strain is best described by the *complex modulus of rigidity*

$$G = G_1 + jG_2 = G_1(1 + j\eta) \tag{6}$$

where G (lb/in.^{2}) $= \sqrt{G_1^2 + G_2^2}$ is the absolute value of the complex modulus of rigidity, and G_1 (lb/in.^{2}) and G_2 (lb/in.^{2}) are the *storage* (real) and *loss* (imaginary) parts of the complex modulus of rigidity, respectively. The *loss factor* $\eta = G_2/G_1$ is the damping-stiffness ratio for the viscoelastic material and represents the tangent of the phase angle by which the stress vector leads the strain vector during a harmonic vibration cycle.

The storage modulus G_1 is the ratio of that component of induced stress in phase with the strain to the resulting total strain. The loss modulus G_2 is the ratio of that component of induced stress 90 deg out of phase with the strain to the resulting total strain; it is proportional to the area of the elliptical dynamic hysteresis loop. The values of G, G_1, and G_2 may be determined directly from the dynamic stress-strain loop as indicated in Fig. 4(b). Since the loss modulus is the product of the classical dynamic coefficient of viscosity μ (lb-sec/in.^{2}) and the frequency of excitation ω (rad/sec),

$$G_2 = \mu\omega \tag{7}$$

the loss factor η may be written

$$\eta = \frac{\mu\omega}{G_1} \tag{8}$$

If the complex modulus of rigidity is used to describe the dynamic elastic properties of the viscoelastic damping layer shown in Fig. 5, the force P is related to the deflection γh_V as follows

$$P = GA\gamma = (G_1 + jG_2)A\gamma = (1 + j\eta)G_1A\gamma \tag{9}$$

where A (in.^{2}) is the shear area.

The dynamic elastic coefficients G_1, G_2, μ, and η are independent of spatial and time variables. Thus, they may be considered as constants when analyzing structural fabrications em-

ploying shear-damping mechanisms. In general, the dynamic elastic coefficients of viscoelastic materials vary with vibration frequency and temperature. It is required only that their appropriate values for a given frequency and temperature be inserted in the equations. The variation of the shear moduli G, G_1, and G_2 and the loss tangent η with vibration frequency and temperature is shown in Fig. 6 [14, 16]. In the *rubbery region*, for low frequency or high temperature, both the storage modulus G_1 and the loss modulus G_2 are small and little energy dissipation is derived from cyclic shearing of the material. In the *transition region*, for intermediate frequencies and temperatures, the loss modulus G_2 has its maximum value, indicating that maximum energy dissipation is obtained from the damping material in this region. The maximum value of the loss tangent η occurs in the transition region at a lower frequency than the maximum value at which the loss modulus occurs. In the *glassy region*, for high frequency or low temperature, the loss modulus G_2 is small while the storage modulus G_1 approaches its maximum value; the viscoelastic material therefore behaves essentially as a purely elastic material in this region.

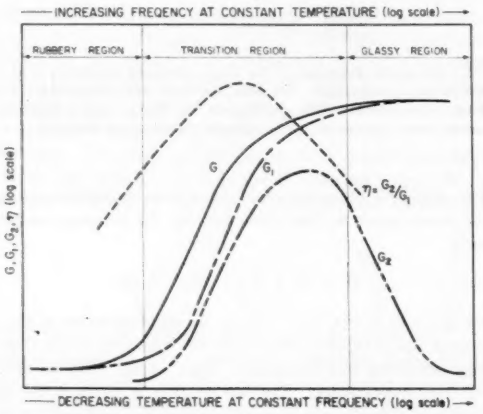

Fig. 6 Variation of the dynamic elastic constants of typical viscoelastic damping materials with temperature and vibration frequency [Ref. 14 and 16]

Specific Damping Energy. The specific damping energy of structural materials depends on the temperature, the stress and vibration history of the material, and the current level of the induced dynamic stress. For a large number of structural materials at a constant temperature and stress history, the specific damping energy D varies as the nth power of the induced stress [17, 18]

$$D \sim \sigma^n \tag{10}$$

where σ (lb/in.^{2}) is the amplitude of uniform induced stress and n is a dimensionless constant. For many conventional structural materials, $n \approx 3$ for low-to-intermediate stress levels and $n \approx 8$ at large stresses. For viscoelastic materials, $n = 2$ at all stress levels below the fatigue limit.

The use of viscoelastic materials as damping media is currently the subject of intensive investigation because large energy dissipation can be realized by proper utilization of this material in structural designs [19, 20, 21, 22]. The damping property of a viscoelastic material in shear is compared with that of typical structural materials in Fig. 7. This diagram gives the specific damping energy D as a function of the ratio of induced stress σ to fatigue strength stress at 2×10^7 vibration cycles σ_e. Data for a large variety of common structural materials fall into a well-established area indicated in Fig. 7 [3, 23]. Certain types of steel, aluminum, magnesium, titanium, and glass-fabric laminate are among the engineering materials represented in this area.

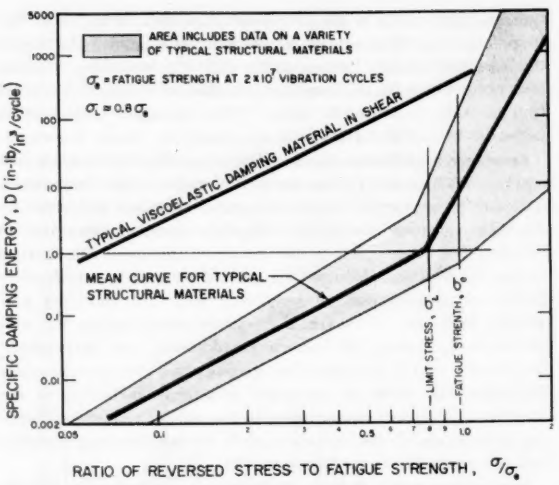
AREA INCLUDES DATA ON A VARIETY OF TYPICAL STRUCTURAL MATERIALS
σe = FATIGUE STRENGTH AT 2x10^7 VIBRATION CYCLES
σL ≈ 0.8 σe
TYPICAL VISCOELASTIC DAMPING MATERIAL IN SHEAR
MEAN CURVE FOR TYPICAL STRUCTURAL MATERIALS
LIMIT STRESS, σL
FATIGUE STRENGTH, σe
SPECIFIC DAMPING ENERGY, D (in-lb/in.³/cycle)
RATIO OF REVERSED STRESS TO FATIGUE STRENGTH, σ/σe

Fig. 7 Comparison of specific damping energy of typical structural and viscoelastic-shear damping materials as a function of the ratio of reversed stress to fatigue strength [Ref. 3 and 22]

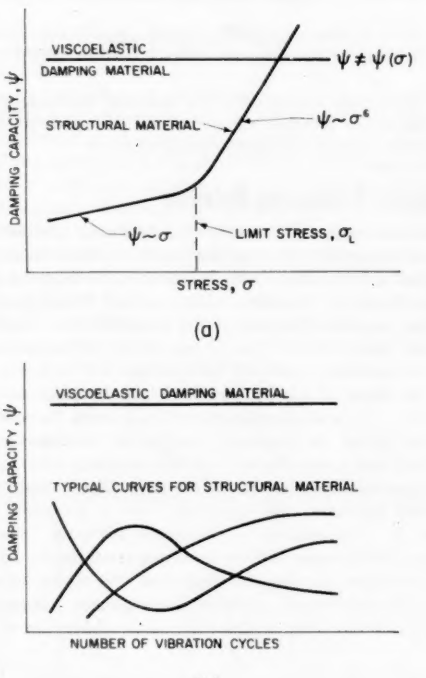

Fig. 8 Variation of damping capacity of a structural material and a viscoelastic damping material with (a) induced stress level and (b) number of vibration cycles [Ref. 15]

The approximate geometric-mean curve for the typical structural materials is a two-segment line having a discontinuity at the limit stress σ_L, where $\sigma_L \approx 0.8\sigma_e$.

The curve for the typical viscoelastic material in shear is based on a permissible shear strain of unity. Actually, this type of material can sustain shear strains considerably greater than unity

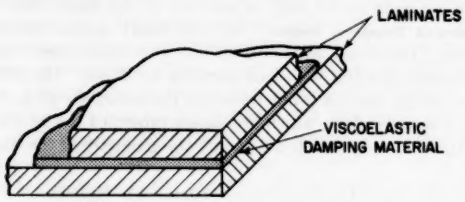

VISCOELASTIC-DAMPED LAMINATED SHEET

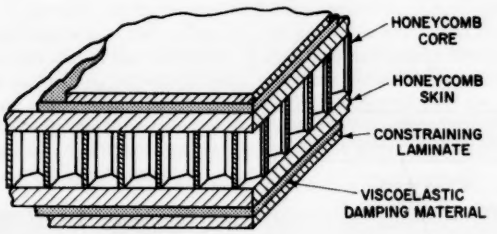

VISCOELASTIC-DAMPED HONEYCOMB SHEET

Fig. 9 Damped structural sheet designs in the form of (a) viscoelastic-damped laminated sheet and (b) viscoelastic-damped honeycomb sheet

for millions of cycles without deterioration [22]. Comparison of the curves shown in Fig. 7 indicates that the specific damping energy of the typical viscoelastic damping material is several hundred times that of the typical structural material for all stress levels considered.[2] Thus, energy dissipation considerably greater than that which is available from common structural materials can be obtained from structural fabrications that properly incorporate viscoelastic damping materials.

Damping Capacity. The damping capacity ψ of a uniformly stressed member or material depends on the induced stress σ in the following manner:

$$\psi \sim \sigma^{n-2} \tag{11}$$

The variation of damping capacity with stress and number of vibration cycles is shown qualitatively by Fig. 8 [15]. Referring to Fig. 8(*a*), when the induced stress is below the limit stress σ_L, the damping capacity of the structural material varies as the first power of stress since $n \approx 3$ in this stress region. For stresses greater than the limit stress, the damping capacity varies as the 6th power of stress since $n \approx 8$. In contrast to this nonlinear damping property of structural materials, a viscoelastic material exhibits a constant value of damping capacity since $n = 2$ for all stress levels.

The effect of vibration history on the damping capacity is shown by Fig. 8(*b*). For common structural materials, the damping capacity depends on the number of vibration cycles experienced by the material [11]. If a structure is being designed for resonant vibrations considering the damping property of the material, the final stable value of the damping capacity must be used [15]. On the other hand, the damping capacity of a viscoelastic material is independent of the vibration history.

[2] There are certain magnetoelastic and plastic-strain damping metal alloys that exhibit significantly higher values of specific damping energy than those materials for which data is included in Fig. 7 [14]. The specific damping energy of typical viscoelastic materials is generally greater than ten times that available from special high damping metal alloys available at the time of this writing.

Structural Damping Design Configurations

The following discussion considers special design configurations that incorporate viscoelastic shear-damping mechanisms in typical members such as structural sheet (panels and plates) and structural shapes (beams). In addition, a discussion of the strip damper, which is a member that is capable of dissipating large amounts of energy when attached to a structure vibrating in flexure, is given. While the designs may be different for the various structural configurations, each relies on the cyclic shear of a viscoelastic damping material for energy dissipation during flexural vibrations.

Damped Structural Sheet. The application of structural damping techniques to the fabrication of structural sheet is particularly appropriate because large-area sheet members, such as panels or plates, are susceptible to noise transmitted through the atmosphere as well as to mechanically transmitted forces and motions.

Two designs of damped structural sheet are shown in Fig. 9. The damped laminated sheet illustrated is composed of two laminates separated by a uniform layer of viscoelastic damping material. The damped honeycomb sheet fabrication consists of a standard honeycomb section (core plus bonded skin members) to which a constrained layer of viscoelastic damping material has been added. The laminates in both of these designs are load

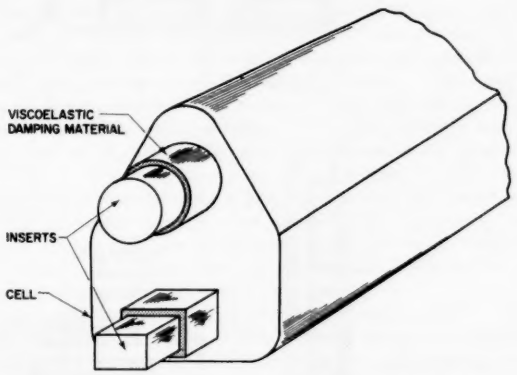

Fig. 10(a) Model illustrating the cell-insert design of damped structural beams

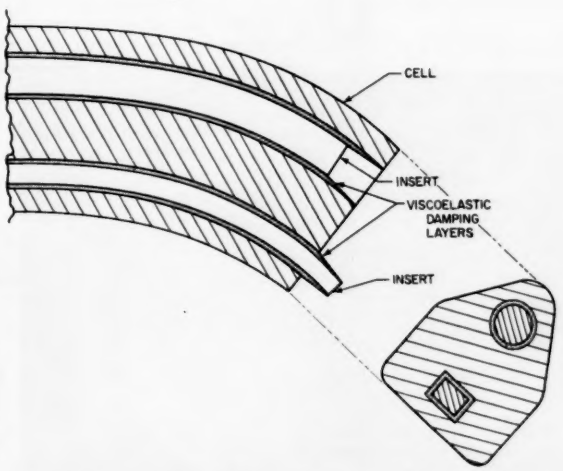

Fig. 10(b) Longitudinal cross-sectional view of cell-insert beam model illustrating shear of the viscoelastic damping layers between the insert and cellular portions of the beam

carrying members. When the damped-sheet designs undergo flexural vibrations, the viscoelastic damping layer is subjected to a cyclic shear strain which dissipates energy.

The energy dissipated by the damped sheet fabrications is a function of the geometry of the design and the physical properties of the viscoelastic damping material. Some particular applications may require using two or more laminates of various thicknesses in the damped laminated sheet, while other applications may derive adequate damping properties with a constrained damping layer added only to one side of the honeycomb sheet.

Damped Structural Beams. The cell-insert design concept[3] of damping structural beams produces a viscoelastic-shear damping mechanism integral with load carrying members. The cell-insert beam design concept is illustrated by the model shown in Fig. 10. The insert members, which are shown projected out of the beam in Fig. 10(*a*) only to indicate clearly the geometry of the construc-

[3] Patent applied for in the name of Jerome E. Ruzicka.

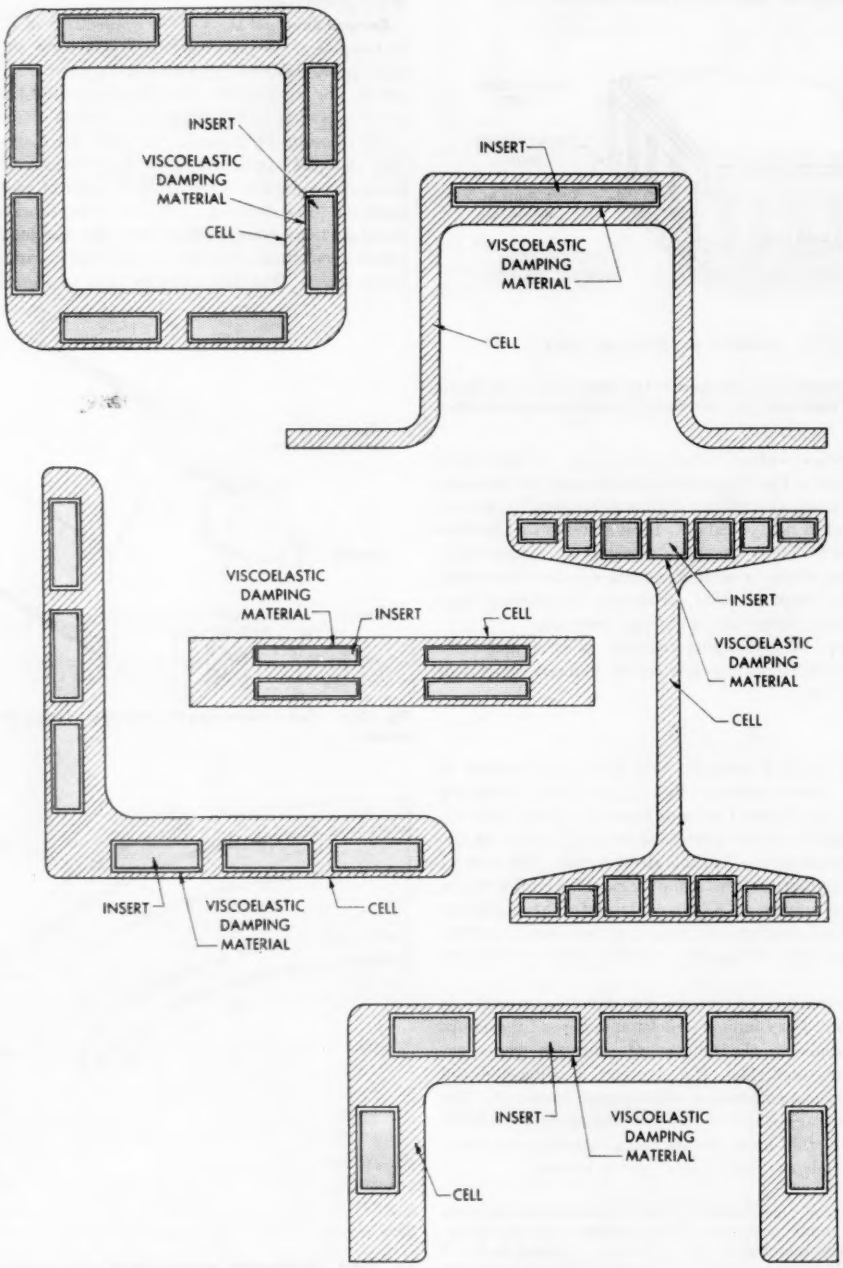

Fig. 11 Cross sections of cell-insert damped beam designs for common structural shapes including tubular, hat, angle, rectangular, channel, and I-sections

tion, are separated from longitudinal hollow cells by a viscoelastic damping material. The hollow cells and the insert may exist for only a portion or the entire length of the beam. The inserts can have any cross-sectional shape; a circular and a square insert are shown in Fig. 10. Flexural vibrations in the plane of the two inserts produce relative motion between the cell walls and the inserts which creates a viscoelastic shear-damping effect in the intervening damping layer. The slippage between the inserts and the cells is illustrated in Fig. 10(*b*) for the downward portion of a vibration cycle. The circular insert has withdrawn into the beam and the square insert has protruded beyond the extent of the cellular body to produce the indicated shear of the viscoelastic damping layer. Both the cell and the inserts are load-carrying members that are made from conventional structural materials.

Application of the cell-insert design concept to typical structural shapes is shown in Fig. 11. In general, a number of inserts are included in the fabrication so that high damping is developed for all bending vibration modes as well as torsional vibrations of the beam. Also, use of a multiplicity of inserts decreases the possibility that a fabrication device, such as a bolt or rivet, will prevent gross shear from developing in the viscoelastic damping layer during vibration.

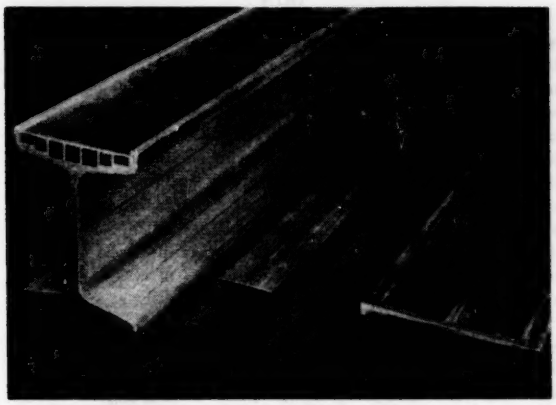

Fig. 12 Prototypes of cell-insert damped I-section, hat-section, and rectangular-section beams

Prototypes of a damped I-beam, hat-section, and rectangular-section are pictured in Fig. 12. The resonant response of the beams is lower when the modulus of elasticity of the inserts is greater than the modulus of elasticity of the cell member. The inserts in the prototypes shown in Fig. 12 are steel and the cell members are aluminum. In general, the cell-insert design concept may be applied to members constructed from any engineering structural material.

The inserts in the damped I-beam are placed only in the flanges since greater shear of the viscoelastic damping layer occurs at positions far removed from the neutral axis of bending. Since the hat-section beam is generally used by attaching the flanges to other parts of a structural assembly, the viscoelastic damping layer is automatically far removed from the neutral axis of bending. In the damped rectangular bar, the inserts are displaced from the neutral axis of bending for vibrations about either of the principal axes of inertia. Accommodations are provided for bolts or other fastening devices at the center and edges of the cross section so that they do not prevent relative slip between the inserts and cell.

The energy dissipated by the cell-insert damped beam is a function of the geometry of the cell-insert design and the physical properties of the cell, inserts, and viscoelastic damping material. The geometry of the cell-insert design is determined, therefore, by considering the requirements and limitations on stiffness, space, weight, and damping properties for a specific application.

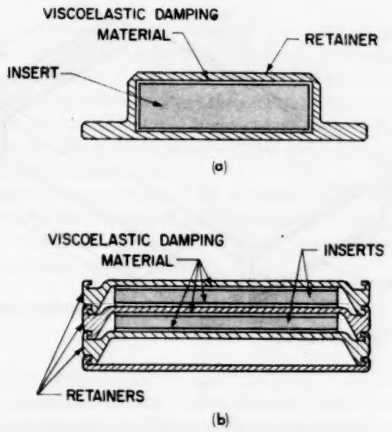

Fig. 13 Strip-damper cross sections of (a) single-insert design and (b) interlocking multi-insert design

Strip Dampers. The resonances of a conventionally fabricated structure may be damped by application of a *strip damper*. Cross sections of two strip damper designs are shown in Fig. 13. The strip dampers illustrated consist of an insert housed by a retainer strip. The insert is separated from the retainer strip walls by a layer of viscoelastic damping material. Additional retainer strips and inserts may be added to the strip damper design shown in Fig. 13(*b*) thus providing a convenient means of varying the amount of damping supplied to a conventionally fabricated structure. The hat-section beam shown in Figs. 11 and 12 may be used as a strip damper. When used as a strip damper, the cell of the hat-section performs the function of the retainer strip. The strip damper generally would be used as a "fix" at the field location of the structure. Therefore, the flexibility provided by the design of Fig. 13(*b*) is convenient.

The strip-damper technique dissipates energy much in the same way as a cell-insert beam. With the strip damper attached to a structure, the insert will slip relative to the retainer strip during flexural vibrations to create a cyclic shear strain in the viscoelastic damping layer. This type of structural damping device should be attached to the vibrating structure so that the viscoelastic damping layers are displaced at great distances from the neutral axis of bending of the structure.

The two types of strip dampers illustrated in Fig. 13 are shown

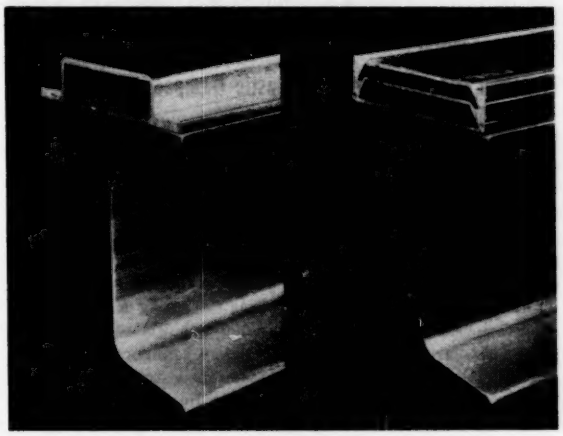

Fig. 14 Strip dampers attached to flange of solid I-beam

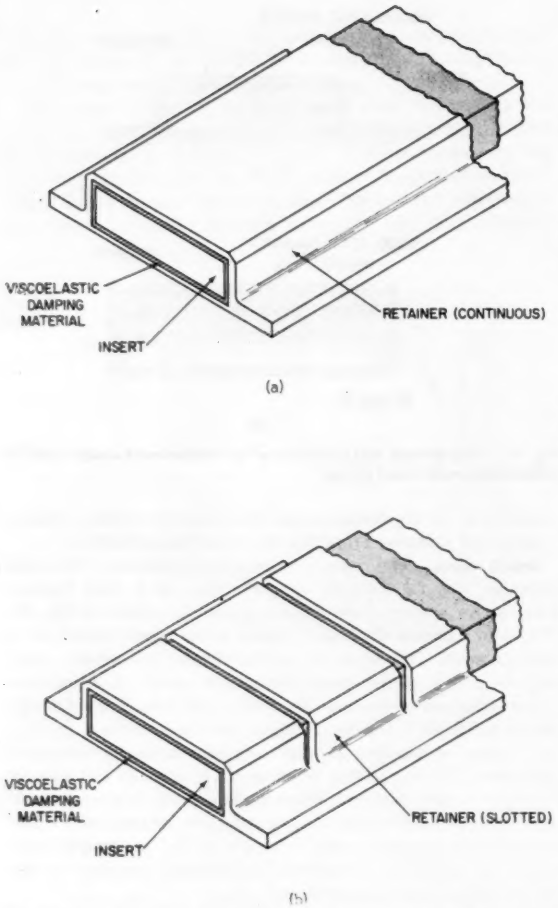

Fig. 15 Strip-damper designs with (a) continuous retainer and (b) slotted retainer

attached to an I-Beam in Fig. 14. The retainer strip is continuous along the length of the strip dampers shown. However, for some applications, better resonance control may be obtained by slotting the retainer strip at positions along its length at the cross-sectional area. A strip damper having a slotted retainer strip is illustrated with one having a continuous retainer strip in Fig. 15. The choice between using a continuous or a slotted retainer strip in a strip-damper design is made according to the requirements of each application problem.

Dynamic Properties of Viscoelastic-Damped Structures

Viscoelastic-Damped Structure Analogy. Certain dynamic properties and design parameters for structures embodying viscoelastic shear-damping mechanisms may be determined by considering the lumped parameter model shown in Fig. 16 [21, 24]. The model consists of a mass m, representing the effective mass of the structure or a concentrated mass on the structure, supported by a spring-dashpot combination representing the dynamic elasticity of the structure. The spring in series with the viscous dashpot is designated as being N times as stiff as the spring K. As will be shown, the stiffness ratio N is a parameter that is useful in evaluating viscoelastic-damped structure design configurations.

The analogy between viscoelastic-damped structures and the model shown in Fig. 16 may be established by varying the dashpot coefficient from zero to infinity while maintaining a constant value of the N-factor. For zero damping, the mass is supported solely by the stiffness K and the resonant frequency is given by

$$f_0 = \frac{1}{2\pi}\sqrt{\frac{K}{m}} \tag{12}$$

Similarly, for infinite damping, the resonant frequency is given by

$$f_\infty = \frac{1}{2\pi}\sqrt{\frac{K+NK}{m}} = \sqrt{N+1}\, f_0 \tag{13}$$

This equation provides a relation between the N-factor and the resonant frequencies for zero and infinite damping as follows:

$$N = \left(\frac{f_\infty}{f_0}\right)^2 - 1 \tag{14}$$

The natural frequency of a structure varies as the square root of its flexural rigidity EI, where E and I represent the modulus of elasticity of the structural material and the cross-sectional moment of inertia, respectively. Therefore, the N-factor for the viscoelastic-damped structural configuration may be written

$$N = \frac{(EI)_\infty}{(EI)_0} - 1 \tag{15}$$

where $(EI)_0$ and $(EI)_\infty$ represent the flexural rigidity of the structure for zero and infinite damping, respectively. The storage modulus G_1 of most practical viscoelastic damping materials is very small compared to the storage modulus E of the structural materials used in the fabrication. Therefore, the flexural rigidity for zero damping $(EI)_0$ may be determined by disregarding the contribution of stiffness by the damping material and summing up the flexural rigidity properties of the individual structural elements of the fabrication. The N-factors for the viscoelastic-damped structural configurations previously discussed are given by Equation (15) in terms of the modulus of elasticity of the structural materials and the geometry of the designs.

Dynamic Properties. Typical vibration amplification curves in the neighborhood of the fundamental resonance of the viscoelastic-damped structure for various degrees of damping are shown in Fig. 17. For zero damping, no energy is dissipated and the resonant frequency f_0 is defined by the flexural rigidity properties of the individual structural elements of the fabrication. For infinite damping, no relative motion is induced into the damping layers and no energy is dissipated; the resonant frequency f_∞ is defined by the flexural rigidity properties of the composite structural section. Thus, for both zero and infinite damping, the resonant amplification of the structure is limited only by the material damping of the structural members.

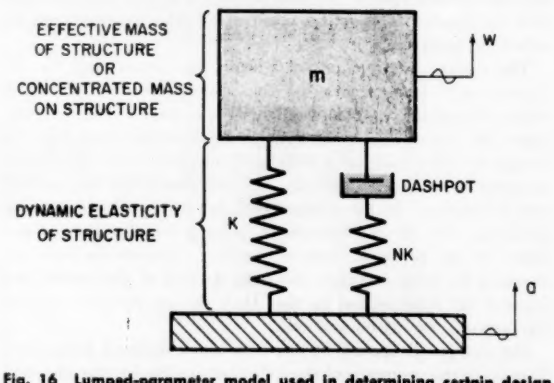

Fig. 16 Lumped-parameter model used in determining certain design parameters and dynamic characteristics of viscoelastic-damped structures [Ref. 21 and 24]

For low and high degrees of damping, the resonant amplification of the structure is reduced below that which exists for zero and infinite damping; the resonant frequencies are approximately equal to the zero and infinitely damped resonant frequencies for these intermediate degrees of damping.

There is an optimum value of damping coefficient for which the resonant amplification of the structure is minimized. For damping other than optimum, the resonance amplification factor A_r is greater than the optimum resonance amplification factor $(A_r)_{op}$. For a given value of the storage modulus G_1 of the viscoelastic damping material, there is an optimum coefficient of viscosity μ_{op} for each damped structure application. The variation of the resonance amplification factor A_r with the N-factor of the structural configuration and the damping material viscosity coefficient μ is illustrated in Fig. 18. Large values of the damping material viscosity coefficient are required to provide optimum damping for structural fabrications having large N-factors. If the damping material possesses a very low viscosity coefficient, the resonance amplification factor is relatively high and is independent of the N-factor for the structural configuration.

A low optimum resonance amplification factor is obtained for damped structural designs having large N-factors; therefore, it is generally desirable to design viscoelastic-damped structural configurations having large N-factors. However, according to Equation (15), the flexural rigidity $(EI)_0$, and therefore the static stiffness and the natural frequency of the structural element, is low for large values of the N-factor. Hence, the N-factor must be kept as small as is necessary to satisfy static stiffness or natural frequency design requirements.

The variation of the ratio of the resonance amplification factor A_r to the optimum resonance amplification factor $(A_r)_{op}$ with the viscosity coefficient ratio μ/μ_{op} is given approximately by the following dimensionless equation:

$$\frac{A_r}{(A_r)_{op}} = \frac{1}{2}\left[\frac{\mu}{\mu_{op}} + \frac{1}{\mu/\mu_{op}}\right] \tag{16}$$

This relation, which is shown graphically by Fig. 19, indicates that the optimum damping coefficient is not a critical one. For example, a resonance amplification factor that is only 25 per cent greater than $(A_r)_{op}$ is obtained when the viscosity coefficient is one half or twice the optimum viscosity coefficient. The noncritical nature of optimum damping provides flexibility in designing viscoelastic-damped structures.

The resonant frequency of the viscoelastic-damped structure having the optimum degree of damping is

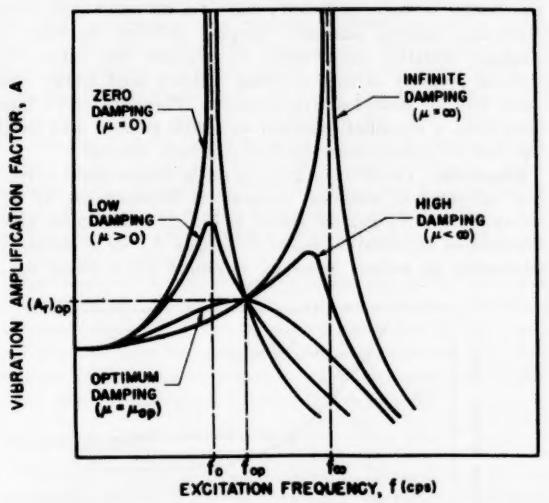

Fig. 17 Typical resonant response of a viscoelastic-damped structure as a function of excitation frequency for various degree of damping [Ref. 21]

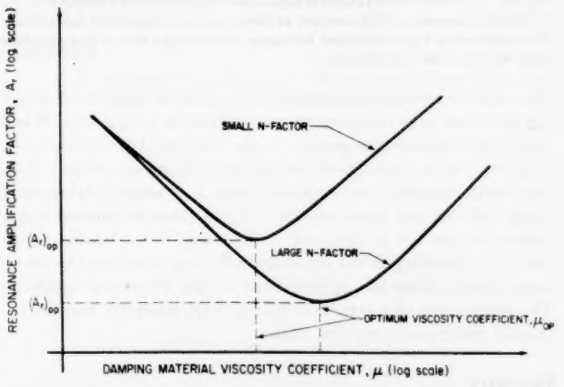

Fig. 18 Variation of resonance amplification factor with damping material viscosity coefficient for specific viscoelastic-damped structure designs having a small and a large N-factor [Ref. 24]

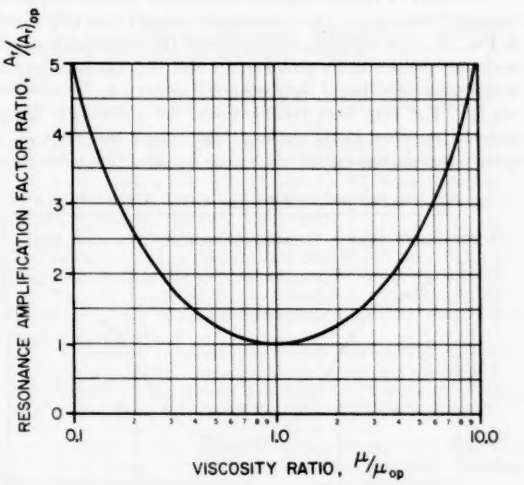

Fig. 19 Approximate variation of resonance amplification factor with the dynamic coefficient of viscosity of the viscoelastic-shear damping material used in a specific viscoelastic-damped structure design

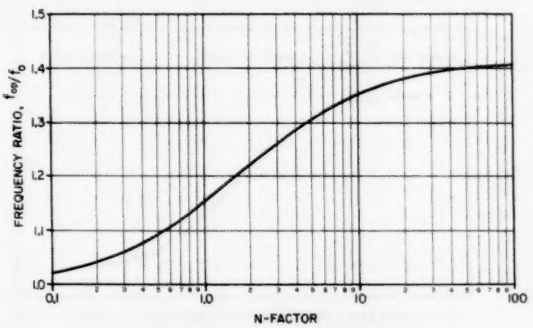

Fig. 20 Variation of resonant frequency of optimum damped structure with the N-factor of the viscoelastic-damped structure design

$$f_{op} = \sqrt{\frac{2(N+1)}{N+2}} f_0 \qquad (17)$$

The frequency ratio f_{op}/f_0 is shown graphically as a function of the N-factor in Fig. 20. For small N-factors, the resonant frequency for optimum damping f_{op} is approximately equal to the resonant frequency for zero damping f_0. The resonant frequency for optimum damping f_{op} asymptotically approaches $\sqrt{2}\ f_0$ for the larger values of the N-factor.

The effects of environmental temperature and fundamental resonant frequency on the resonance amplification factor of the viscoelastic-damped structure is shown in Fig. 21. For very high temperature or low fundamental resonant frequency, the viscoelastic damping material is operating in its *rubbery region* (see Fig. 6), and, since little energy is dissipated (G_2 is small), the resonance amplification factor is large. A similar situation exists for viscoelastic-damped structures that have a very high fundamental resonant frequency or are exposed to a very low environmental temperature; the damping material operates in its *glassy region* and the resonance amplification factor is large. In the *transition region* of the viscoelastic damping material, for intermediate values of environmental temperature or fundamental resonant frequency, the viscoelastic-damped structural fabrication dissipates sufficient energy to provide good resonant vibration control and a low value of the resonance amplification factor is obtained.

The effect of environmental temperature on the fundamental resonant frequency of the viscoelastic-damped structure is shown in Fig. 22. For very low temperatures, the viscoelastic damping material operates in its *glassy region* and the resonant frequency is approximately that of the resonant frequency for infinite damping f_∞. For very high temperatures, the viscoelastic damping material operates in its *rubbery region*, and the resonant frequency is given approximately by the resonant frequency for zero damping f_0. The resonant frequency varies between f_0 and f_∞ for intermediate temperatures at which the viscoelastic damping material operates in its *transition region*. The resonant frequency for the structure having optimum damping f_{op} normally exists at a temperature in the transition region.

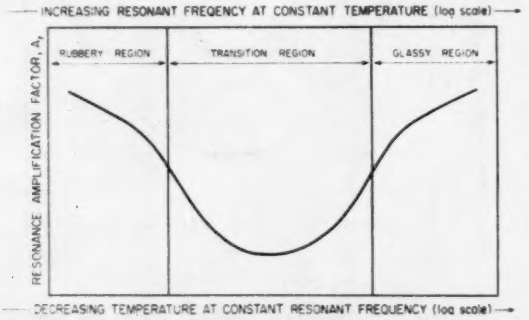
INCREASING RESONANT FREQENCY AT CONSTANT TEMPERATURE (log scale)
RUBBERY REGION
TRANSITION REGION
GLASSY REGION
RESONANCE AMPLIFICATION FACTOR, A_r
DECREASING TEMPERATURE AT CONSTANT RESONANT FREQUENCY (log scale)

Fig. 21 Variation of the resonance amplification factor of a viscoelastic damped structure with environmental temperature and resonant frequency

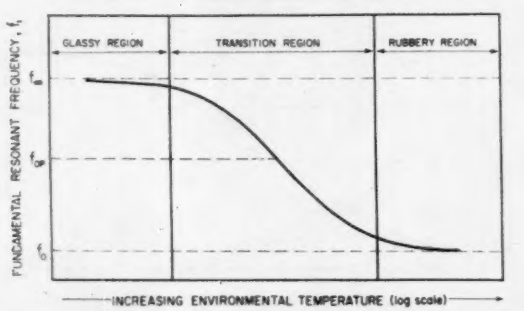

Fig. 22 Variation of fundamental resonant frequency of a viscoelastic-damped structure with environmental temperature

Design Philosophy

Strength and Weight. The static load requirements of a structure can be satisfied by use of conventional design procedures considering weight and space limitations in conjunction with static stiffness requirements. However, the capability of a structure to withstand static load is not enough. Structures operating in a dynamic environment must also be immune to the destructive effects of high peaked dynamic loadings and fatigue that result from transient shock or sustained vibration conditions. This immunity may be accomplished by applying the structural damping techniques discussed in this paper.

When compared on the basis of equal static stiffness, the viscoelastic-damped structural configurations discussed earlier in the paper weigh more than the corresponding conventional solid structural members. However, if attempts are made to control the resonant vibration of a given member by structural rigidization, an overdesign for static loads will result. On the other hand, if the structural member possesses damping sufficient to limit its resonant vibration amplification to relatively low values, the stiffness property of the structural member need satisfy little more than the static load requirements. Therefore, under these conditions, a viscoelastic-damped structural member may weigh less than the conventional rigidized structural member.

Fatigue Life. The effect of damping on the fatigue life of a structure subjected to sustained vibration is demonstrated by reference to the σ-N_f diagram shown in Fig. 23. The curve gives the number of vibration cycles to fatigue N_f for a structural fabrication at various levels of maximum cyclic stress σ_{max}.

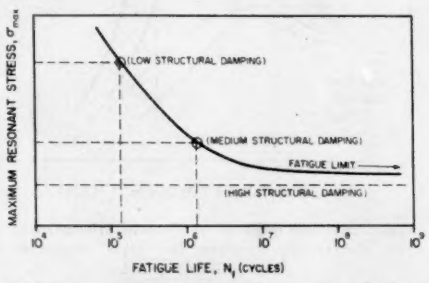

Fig. 23 The maximum resonant stress and the number of vibration cycles to fatigue depend on the amount of damping in a structural fabrication. For sufficiently high structural damping, the fatigue life of the structure may be extended indefinitely.

For a given vibratory excitation, the degree of structural damping determines the resonant stress and thus the fatigue life. When insufficient damping is present in the structural fabrication, the fatigue life is low because of the high induced stress. For medium structural damping, as obtained from a structural fabrication using bolt or rivet fasteners, the induced stress is reduced and a higher fatigue life is obtained. Moreover, it is possible to incorporate damping in the structure sufficient to reduce the maximum stress below the fatigue limit of the structural material. The fatigue life of a structure having high damping may be increased indefinitely on this basis.

Summary

When designing for modern dynamic environments, the stiffness, weight, space, and the *damping property* of the structure

should be considered as joint design criteria. Viscoelastic-damped structure and (additive) strip-damper designs have been developed for the purpose of damping structural vibrations over relatively broad frequency and temperature ranges. Each damped structure design, whether it be a laminated sheet, a cell-insert beam, or a strip damper, requires an optimum amount of damping to minimize the resonant response. However, for many practical purposes, sufficient resonant vibration control may be obtained by use of a damping material having only nearly optimum damping properties.

While the resonant amplification of structural designs employing viscoelastic shear damping mechanisms is essentially independent of the level of vibration excitation, it is a function of environmental temperature and structure resonant frequency.

When compared on the basis of equal static stiffness, the viscoelastic-damped structure weighs more than the corresponding conventionally fabricated structure. However, by proper application of the structural damping techniques, the stiffness property of the structure need only satisfy static load requirements. Therefore, a weight less than that of a rigidized structure may be obtained.

The approximate lumped-parameter analogy discussed gives both qualitative and quantitative information regarding the design and performance of viscoelastic-damped structures. The N-factor for a given structural configuration does not define what degree of resonant vibration control will be obtained; rather, it indicates the relative merits of one design over another assuming optimum damping will be provided in the fabrication. In general, it is desirable to design damped structural configurations having large N-factors. However, realizing that the static stiffness varies inversely as the N-factor, proper consideration should be given to requirements on structural stiffness and natural frequency when choosing the design value of the N-factor for the structural member.

Significant end results derived from the use of the structural damping designs presented herein, such as improved reliability, increased fatigue life, reduction of resonant structural vibrations, and improved high frequency vibration attenuation of vibration isolation systems, will be demonstrated in the second part of this paper devoted mainly to experimental results [25].

Acknowledgments

The author expresses his appreciation to Kenneth Ray, for the preparation of most of the line drawings in the paper; Lewis Colson and Bartlett Hauthaway, for the photographs; and Henry Perley, Adolf Arnold, Clarence Metcalf, Thomas Hynes, Rose-Marie Pollock, and Mary Reilly for their contributions in preparing the manuscript for publication.

References

1 C. T. Morrow, "Techniques for Design to Shock and Vibration Conditions," *Jour. Environmental Engineering*, February, 1959, p. 3.

2 J. Marin and F. B. Stulen, "A New Fatigue Strength-Damping Criterion for the Design of Resonant Members," *Journal of Applied Mechanics*, vol. 12, TRANS. ASME, vol. 67, 1947, p. A-209; discussion 1948, p. 83.

3 E. R. Podnieks and B. J. Lazan, "Effect of Material Damping and Stress Distribution on the Resonant Fatigue Strength of Parts," WADC TN 55-284, August, 1955.

4 J. Marin and M. G. Sharma, "Material Design for Resonant Members," Section 6 of Reference [6], pp. 133–157.

5 J. E. Ruzicka and R. D. Cavanaugh, "Vibration Isolation of Non-Rigid Bodies," Part 9 of "Mechanical Impedance Methods for Mechanical Vibrations" (edited by R. Plunkett), ASME, New York, N. Y., 1958.

6 J. E. Ruzicka (editor) "Structural Damping," ASME, New York, N. Y., 1959.

7 L. J. Demer, "Bibliography of the Material Damping Field," WADC TR 56-180, June, 1956.

8 E. R. Podnieks and B. J. Lazan, "Analytical Methods for Determining Specific Damping Energy Considering Stress Distribution," WADC TR 56-44, June, 1957, ASTIA Document No. AD130777.

9 G. S. Van Heydekampf, "Damping Capacity of Materials," *Proceedings, ASTM*, vol. 31, 1931, part 1, pp. 157–175.

10 G. P. Harnwell, "Principles of Electricity and Electromagnetism," second edition, McGraw-Hill Book Company, Inc., New York, N. Y., 1949, p. 460.

11 A. L. Kimball and D. E. Lovell, "Internal Friction in Solids," *Physical Review*, second series, vol. 30, 1927, pp. 948–959.

12 F. Forster, "Ein Neues Messverfahren Zur Bestimmung des Elastizätsmoduls und Der Dämpfung" (A New Measurement Technique for the Determination of the Modulus of Elasticity and Damping), *Zeitschrift Metallkunde*, vol. 29, 1937, pp. 109–115.

13 R. Plunkett, "Measurement of Damping," Section 5 of Reference [6], pp. 117–131.

14 B. J. Lazan, "Energy Dissipation Mechanisms in Structures, With Particular Reference to Material Damping," Section 1 of Reference [6], pp. 1–34.

15 A. M. Freudenthal, "The Inelastic Behavior of Engineering Materials and Structures," John Wiley & Sons, Inc., New York, N. Y., 1959, Chap. 10.

16 T. Alfrey, Jr., "Mechanical Behavior of High Polymers," Interscience Publishing Company, New York, N. Y., 1948, p. 189.

17 J. M. Robertson and A. J. Yorgiadis, "Internal Friction in Engineering Materials," *Journal of Applied Mechanics*, vol. 13, TRANS. ASME, vol. 68, 1946, pp. A-173–182.

18 B. J. Lazan, "Effect of Damping Constants and Stress Distribution on the Resonance Response of Members," *Journal of Applied Mechanics*, vol. 20, TRANS. ASME, vol. 75, 1953, pp. 201–209.

19 D. Ross, E. E. Unger, E. M. Kerwin, Jr., "Damping of Plate Flexural Vibrations by Means of Viscoelastic Laminae," Section 3 of Reference [6], pp. 49–87.

20 T. J. Mentel, "Vibrational Energy Dissipation at Structural Support Junctions," Section 4 of Reference [6], pp. 89–116.

21 J. E. Ruzicka, "Increased Reliability of Aviation and Missile Electronics by Use of Damped Structures," SAE Paper No. 100 Y, SAE National Aeronautic Meeting, October, 1959.

22 B. J. Lazan, "Material and Structural Damping for Vibration Control," SAE Paper 100 U, SAE National Aeronautic Meeting, October, 1959.

23 B. J. Lazan, "Fatigue Failure Under Resonant Vibration Conditions," WADC TR 54-20, March, 1954.

24 J. E. Ruzicka and R. D. Cavanaugh, "New Method for Vibration Isolation," *Machine Design*, October 16, 1958, pp. 114–121.

25 J. E. Ruzicka, "Damping Structural Resonances Using Viscoelastic Shear-Damping Mechanisms: Part II Experimental Results," published in this issue, pp. 414–424.

Damping Structural Resonances Using Viscoelastic Shear-Damping Mechanisms

Part II Experimental Results

JEROME E. RUZICKA

Staff Consultant, Barry Controls, Division of Barry-Wright Corporation, Watertown, Mass. Assoc. Mem. ASME

This paper describes the experimental dynamic response characteristics of structural design configurations employing viscoelastic shear-damping mechanisms that have been discussed in a previous paper. Experimental results are given for cantilever beams fabricated from viscoelastic-damped sheet and structural shape members; results are also given for cantilever beams damped by use of the strip damper (an additive damping technique). The effects of shock excitation, steady-state vibration excitation, vibration excitation level, structure resonant frequency, and environmental temperature on the damping properties of the structural design configurations are demonstrated. The effects of structural damping on the performance of vibration isolation systems are determined and the significance of employing highly damped structural designs in fabrications intended for use in modern dynamic environments is discussed.

Introduction

In a previous paper, the author discussed the general concept of incorporating a high degree of damping in structural fabrications.[1] Methods of specifying structural damping and the damping properties of engineering materials were reviewed. Specific design configurations were suggested for fabricating structural sheet and beam members that embodied viscoelastic shear-damping mechanisms. The strip damper, an additive damping technique employing viscoelastic shear-damping mechanisms, was also discussed.

This paper describes the results of an experimental study made on the performance of the viscoelastic-damped structure design configurations as applied to cantilever beams. The cantilever beam model is an idealized structural member; it is useful, however, in the elementary study of the vibration transmission characteristics of structures.

Theoretical Response

To establish the typical manner in which mechanical vibration is transmitted through a structure, consider the forced vibration of a cantilever beam as illustrated in Fig. 1. The beam is excited by a prescribed sinusoidal motion at its support. The general solution for the transverse deflections $w(x, t)$ is determined in the Appendix. The transmissibility, or steady-state transfer response function, for the end point of an undamped cantilever beam is given by

$$T(l) = \frac{w(l)}{a_0} = \frac{\cosh\sqrt{\frac{\omega}{\omega_r}} + \cos\sqrt{\frac{\omega}{\omega_r}}}{\cosh\sqrt{\frac{\omega}{\omega_r}}\cos\sqrt{\frac{\omega}{\omega_r}} + 1}$$

where

ω = excitation frequency (rad/sec)

$\omega_r = \sqrt{\frac{EI}{m_B l^3}}$ = reference frequency (rad/sec)

E = modulus of elasticity of beam material (lb/in.^{2})

I = moment of inertia of cross-sectional area (in.^{4})

m_B = mass of beam $\left(\frac{\text{lb-sec}^2}{\text{in.}}\right)$

l = length of beam (in.)

This equation is shown graphically by Fig. 2 for the first five natural modes of vibration. The denominator of the transmissibility expression becomes zero when the excitation frequency coincides with a natural frequency of the beam. When this occurs, the end-point transmissibility of the cantilever beam theoretically becomes infinite. Actually, all structural materials possess some degree of damping and the transmissibility, rather than being infinite, may become very large at beam natural frequencies. The theoretical transmissibility curve illustrated in Fig. 2, which indicates the general type of transfer vibration response characteristics exhibited by structures, may be compared to the experimental response curves that are presented in following sections.

Experimental Study

The transient response characteristics of cantilever beams are determined by use of a free-fall shock machine. The support of

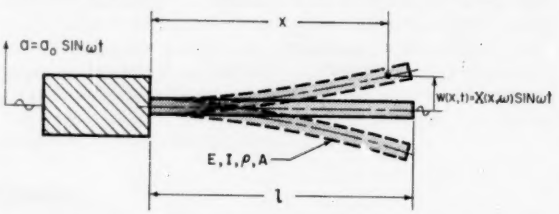

Fig. 1 Schematic diagram of a cantilever beam excited by a prescribed harmonic motion at the support

[1] J. E. Ruzicka, "Damping Structural Resonances Using Viscoelastic Shear-Damping Mechanisms: Part I Design Configurations," published in this issue, pp. 403–413.

Contributed by the Machine Design Division and presented at the Winter Annual Meeting, New York, N. Y., November 27–December 2, 1960, of The American Society of Mechanical Engineers. Manuscript received at ASME Headquarters, July 11, 1960. Paper No. 60—WA-72.

the beam specimen is attached to the shock table, which is released from a specific drop height and allowed to fall freely until it strikes a rubber pad. A half-sine acceleration pulse is imposed on the support of the cantilever beam during the impact period, after which the beam specimen freely vibrates. The beam shock-test configuration is pictured in Fig. 3. Accelerometers measure the transient response at the end point of the cantilever beams.

The steady-state response characteristics of cantilever beams are determined by use of an electrodynamic shaker as pictured in Fig. 4. The electrodynamic shaker imposes a sinusoidal vibration excitation on the beam support. A schematic diagram indicating the steady-state vibration test configuration as well as important system parameters is shown in Fig. 5. When the test beams are very heavy, a double length center-clamped cantilever beam is tested to avoid applying unbalanced moments to the shaker armature. The effects of concentrated mass loadings are determined by attaching weights at the ends of the beams. Depending on the particular test being performed, either optical methods or standard transducers are used to measure the steady-state beam response.

The damping materials used in the beam test specimens include commercially available sealing compounds, adhesive transfer films, and soft-setting adhesives as well as various forms of silicone based compounds.

Transient Response Measurements. The logarithmic decrement δ, which indicates the decay rate of the cantilever beam free-vibrations, as illustrated in Fig. 6, is defined by the relative decrease of the vibration amplitude over a given number of vibration cycles. If the vibration amplitude of free vibration decreases from X_0 to X_n in n number of vibration cycles, the logarithmic decrement δ is given by

$$\delta = \ln \frac{X_n}{X_{n+1}} = \frac{1}{n} \ln \frac{X_0}{X_n}$$

In general, the logarithmic decrement depends on the stress level existing in the structural member that is undergoing the free vibrations.

Steady-State Response Measurements. The steady-state transmissibility, or vibration amplification factor, of the cantilever is defined as the ratio of the motion response amplitude at a specific point on the beam to the amplitude of motion imposed at the support. If the response is measured at the free end of the beam the end-point transmissibility (see Fig. 5) is defined as

$$T(l) = \frac{w(l)}{a_0}$$

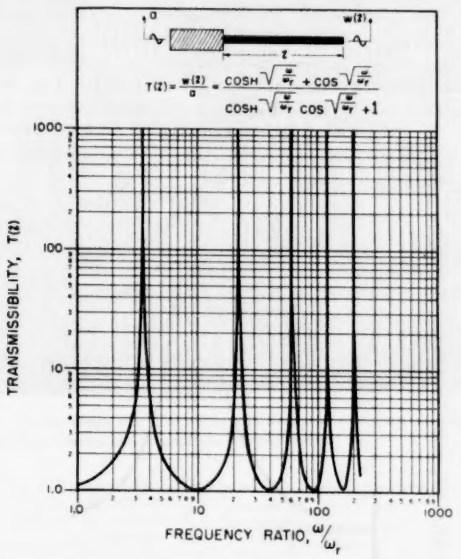

Fig. 2 Theoretical end-point transmissibility of a cantilever beam as a function of the ratio of excitation frequency to reference frequency

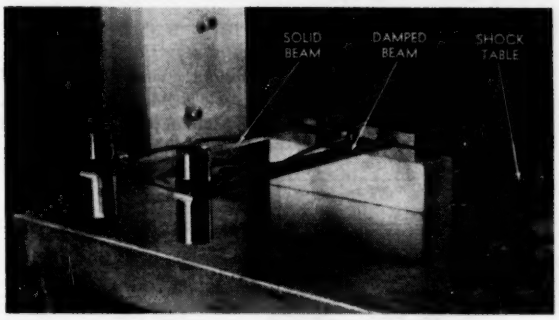

Fig. 3 Beam test configuration for a shock excitation

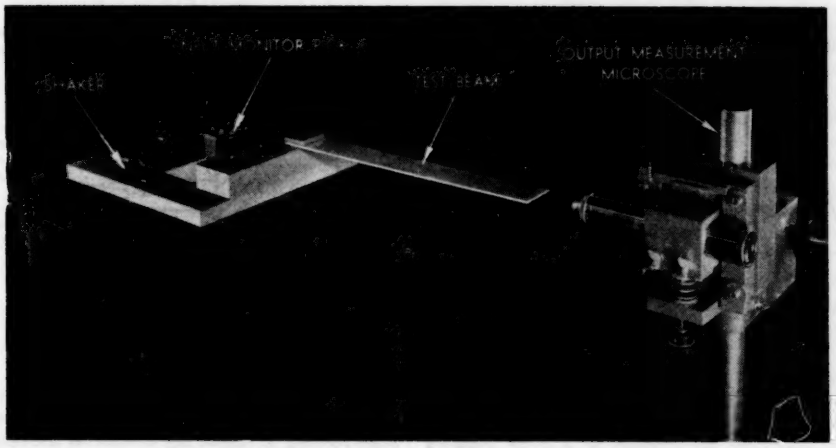

Fig. 4 Beam test configuration for steady-state vibration excitation

and the resonance amplification factor $A_r(l)$ is the (maximum) value of the transmissibility that occurs at a beam resonance:

$$A_r(l) = T(l)_{\max}$$

As illustrated in Fig. 7, for structural vibration measurements, the bandwidth quality factor Q is usually defined as

$$Q = \frac{f_n}{\Delta f}\sqrt{\frac{A_r^2 - A^2}{A^2}}$$

where f_n is the resonant frequency of the beam, A_r is the resonance amplification factor, and A is the vibration amplification factor at frequencies on either side of the resonant frequency for which the bandwidth of the resonance curve is Δf. It is common practice to measure the bandwidth Δf at points on the resonance curve for which the vibration amplification factor A is either $1/2$ or $1/\sqrt{2}$ times the resonance amplification factor A_r. The bandwidth quality factor Q, when the bandwidth is measured at the *half-amplitude points*, is given by

$$Q = \frac{\sqrt{3}\, f_n}{\Delta f} \qquad \left(\frac{A}{A_r} = \frac{1}{2}\right)$$

whereas, for the bandwidth measured at the *half-power points*, the bandwidth quality factor Q is given by

$$Q = \frac{f_n}{\Delta f} \qquad \left(\frac{A}{A_r} = \frac{1}{\sqrt{2}}\right)$$

While the resonance amplification factor A_r is dependent upon the particular measurement point on the beam, the bandwidth quality factor Q is the same for all measurement positions.

Damped Structural Sheet

Test Specimen. A schematic diagram of the viscoelastic-damped laminated test beam is shown in Fig. 8. The damped test beam, which consists of two equal thickness laminates separated by a viscoelastic damping layer of uniform thickness h_V, has a cross section illustrated in Fig. 8(*b*). The slip between the laminates, shown in Fig. 8(*a*) for the extreme displaced positions of the beam during a vibration cycle, creates an energy dissipating cyclic shear action in the viscoelastic damping layer. The N-factor (see Part I: Design Configurations) for this test specimen may be calculated as follows:

$$N = \frac{(EI)_\infty}{(EI)_0} - 1 = \frac{(2h)^3}{2(h)^3} - 1 = 3$$

Thus, $N = 3$ for a two-laminate system having both laminates made from the same structural material when the thicknesses of the two laminates are equal and the viscoelastic damping layer thickness h_V is small compared to the laminate thickness h. Experimental data presented in this section are obtained for test specimens employing viscoelastic damping layers of approximately 0.005 in. uniform thickness.

Shock Response. The transient response of a solid aluminum beam and a viscoelastic-damped aluminum beam resulting from a half-sine (acceleration) shock pulse imposed at the beam support is shown in Fig. 9. The oscilloscope traces indicate acceleration time-decay patterns as measured by accelerometers attached to the free ends of the cantilever beams (see Fig. 3). The vibration traces shown in Fig. 9 may be compared directly since the same vertical (acceleration) and horizontal (time) oscilloscope calibrations are used in recording the vibration response of the solid and damped beams.

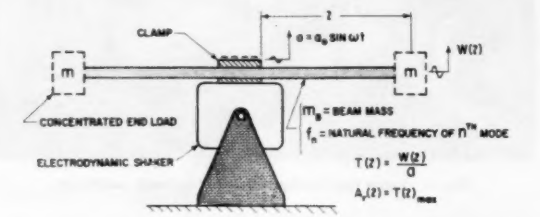

Fig. 5 Schematic diagram of cantilever beam test configuration for steady-state vibration excitation

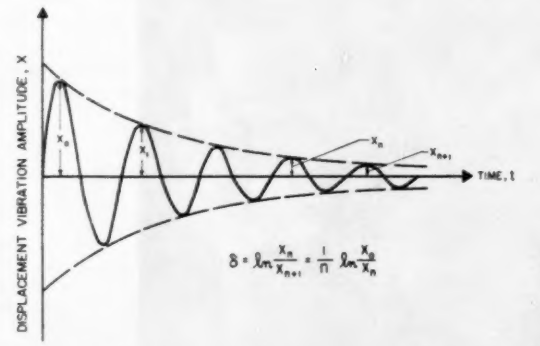

Fig. 6 Logarithmic decrement measurement for a freely vibrating structure

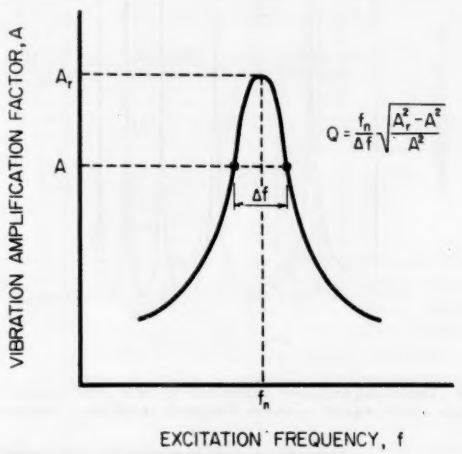

Fig. 7 Resonance amplification factor and bandwidth quality factor measurements for a structure subjected to a steady-state vibration excitation in the neighborhood of resonance

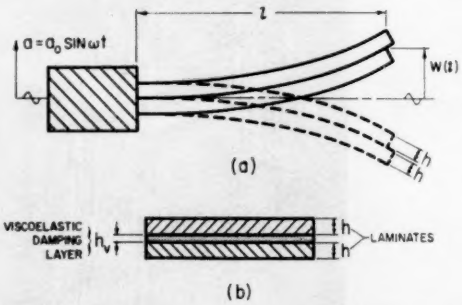

Fig. 8 Schematic diagram of viscoelastic-damped laminated cantilever beam showing (a) relative slip between the laminates and (b) cross section of experimental damped beams

The vibration of the end point of the damped beam decays rapidly as compared to a very slow decay rate for the solid beam. For the traces shown, the logarithmic decrement $\delta = 0.025$ for the solid beam, whereas $\delta = 0.7$ for the damped beam. Therefore, the damped aluminum beam exhibits approximately 30 times as much damping as the solid aluminum beam for the particular dynamic excitation imposed. While structural damping greatly affects the amplitude of the beam vibrations following the shock excitation, it has little effect on the maximum (peak) amplitude of vibration that results from the shock excitation. Therefore, structural damping techniques generally are not useful in reducing the severity of the shock amplification by a structure but are useful in controlling the vibrations that follow the peak structural response.

Frequency Response. The end-point transmissibility $T(l)$ of a conventional-solid and a viscoelastic-damped laminated beam is shown in Fig. 10 as a function of the ratio of excitation frequency f to the fundamental resonant frequency f_1 of the beam. The resonant amplification of the beam vibration is drastically reduced by use of the viscoelastic-damped beam design. For example, the fundamental mode resonance amplification factor for the damped aluminum beam has a value of 10 as compared to a value of 300 for the solid aluminum beam. The reduction of resonant vibration is even greater for the higher natural modes of the beam. The beam excitation is amplified by a factor greater than 100 for the first five modes of the solid aluminum beam. The resonant peaks of the damped aluminum beam decrease at a rate of 4 db/octave, indicating that the higher modes of the beam vibration are heavily damped. The transmissibility curve for the solid aluminum beam agrees well with the theoretical transmissibility curve (Fig. 2) except for the fact that the transmissibility is finite, rather than infinite, at beam natural frequencies.

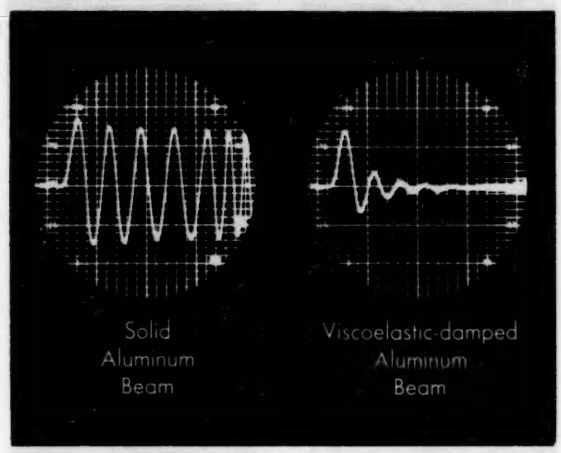

Fig. 9 Oscilloscope traces showing the decay of vibration with time for a solid and a viscoelastic-damped aluminum beam

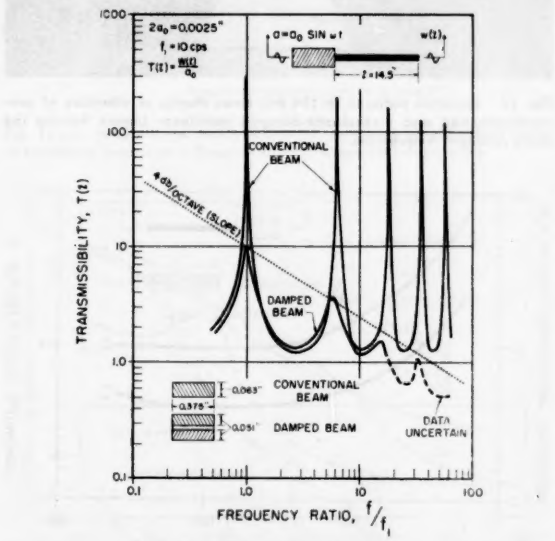

Fig. 10 End-point transmissibility of conventional-solid and viscoelastic-damped laminated cantilever beams as a function of the ratio of the excitation frequency to the fundamental resonant frequencies of the beams

A detailed graph of the end-point transmissibility $T(l)$ of a typical viscoelastic-damped aluminum beam is shown in Fig. 11 as a function of the excitation frequency f. The resonance amplification factor $A_r(l) = 7.8$ and the bandwidth quality factor $Q = 5.3$ for the first mode occurring at $f_1 = 21$ cps. For the second mode occurring at $f_2 = 112$ cps, the resonance amplification factor $A_r(l) = 2.5$ and the bandwidth quality factor $Q = 3.2$. A solid aluminum beam subjected to the same vibration excitation would exhibit a resonance amplification factor of approximately 100 at its fundamental resonant frequency.

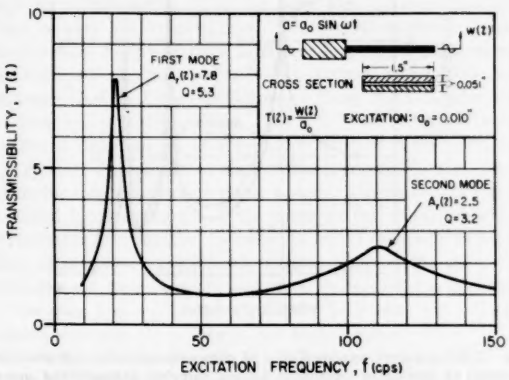

Fig. 11 End-point transmissibility of a viscoelastic-damped cantilever beam showing in detail the first and second mode response

Effect of Concentrated Mass Loading. The effect of adding a concentrated mass to the end of the cantilever beam on the transmissibility is illustrated in Fig. 12. For both the conventional-solid and viscoelastic-damped beams, the weight of the concentrated load is made equal to the weight of the beam by adjusting the beam length. The addition of the concentrated mass effects a reduction in vibration transmission at the higher natural modes of beam vibrations. As in the case of the beams carrying no concentrated mass, the resonant amplification of the beam vibration is drastically reduced by use of the viscoelastic-damped beam design. For example, the fundamental mode resonance amplification factor for the viscoelastic-damped aluminum beam has a value of 10 as compared to a value of 180 for the conventional-solid aluminum beam.

The curves of Fig. 12 are representative of the dynamic response characteristics of mass-spring systems in which the spring element takes the form of a leaf or beam spring. The elastic body resonances of the spring element cause peaks to occur in the frequency response curve. The size and control of these resonant peaks are of considerable importance if the beam is used as a leaf-spring stiffness element in a vibration isolator.

Effect of Vibration Excitation Level. The resonance amplification

factor $A_r(l)$ of the fundamental mode for a conventional-solid and a viscoelastic-damped aluminum beam is shown in Fig. 13 as a function of the fundamental resonant frequency and the level of excitation displacement imposed at the support. Data are included on beams having fundamental resonant frequencies of 20 cps and 100 cps. The resonance amplification factor of the conventional-solid beam varies between 300 and 80 for the range of excitation displacement levels tested. For the same levels of excitation displacement, the viscoelastic-damped beam exhibits nearly constant values of the resonance amplification factor. For example, when the fundamental resonant frequency $f_1 = 20$ cps, $A_r(l) \approx 8$; when $f_1 = 100$ cps, $A_r(l) \approx 5$. The conventional-solid beam transmits from 10 to 60 times more vibration at the fundamental resonance than does the viscoelastic-damped beam. The curves of Fig. 13 indicate the linear damping property that is typical of viscoelastic-damped structures as well as the nonlinear damping characteristics of conventional structural materials.

The vibration patterns exhibited by conventional-solid and viscoelastic-damped laminated cantilever beams having the same resonant frequencies are pictured in Fig. 14 for the first three modes of vibration. Resonant vibrations of the damped beam are visible only for the lower natural modes. However, the large vibration amplification and the vibration modal patterns are very obvious for all modes of the conventional beam.

Effect of Structure Resonant Frequency. The resonance amplification factor $A_r(l)$ and the bandwidth quality factor Q for the viscoelastic-damped aluminum beam are shown as a function of fundamental resonant frequency f_1 in Fig. 15. The curves indi-

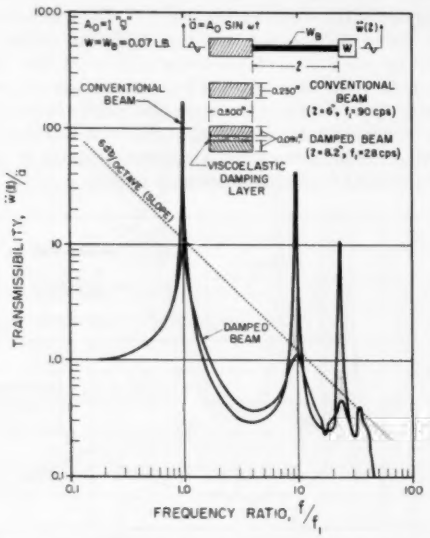

Fig. 12 End-point transmissibility of conventional-solid and viscoelastic-damped laminated cantilever beams carrying concentrated masses at their free ends as a function of the ratio of the excitation frequency to the fundamental resonant frequencies of the beams

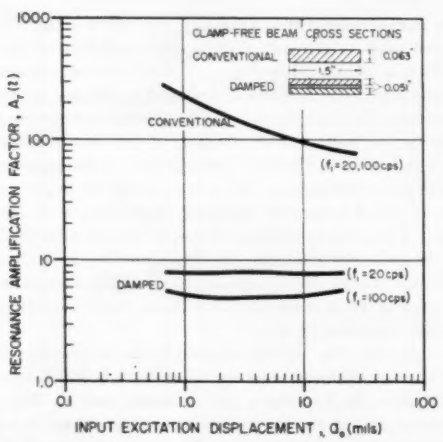

Fig. 13 Fundamental mode end-point resonance amplification factor of conventional-solid and viscoelastic-damped cantilever beams as a function of their fundamental resonant frequencies and the level of excitation displacement

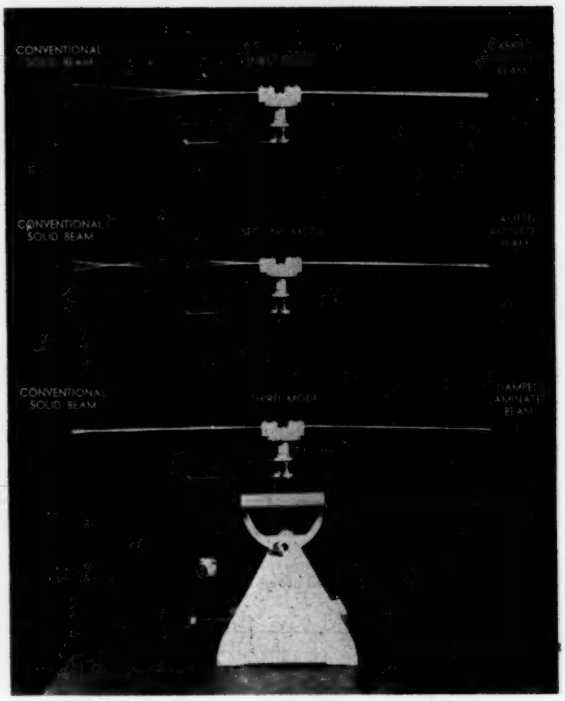

Fig. 14 Vibration patterns for the first three modes of vibration of conventional-solid and viscoelastic-damped cantilever beams having the same resonant frequencies

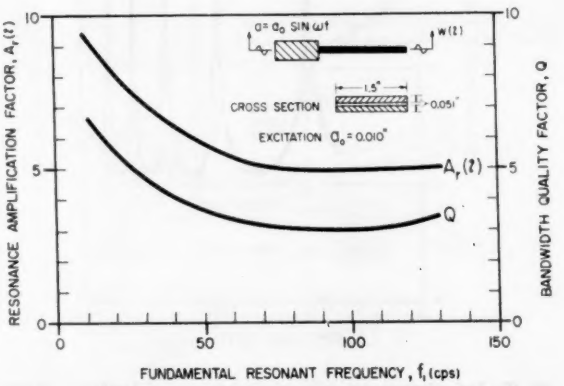

Fig. 15 Fundamental mode end-point resonance amplification factor and bandwidth quality factor of a viscoelastic-damped cantilever beam as a function of the fundamental resonant frequency of the beam

cate the effect of structure resonant frequency on the damping properties of the viscoelastic-damped laminated beam. The fundamental resonant frequency of the beam is varied between 10 cps and 130 cps by changing its length. The resonance amplification factor and the bandwidth quality factor are greater at the lower values of the fundamental resonant frequency. For intermediate values of the fundamental resonant frequency, $A_r(l)$ and Q decrease and approach constant values. Experimental data at the higher resonant frequencies indicate that $A_r(l)$ and Q increase for resonant frequencies greater than those included in Fig. 15. The curves of Fig. 15 demonstrate that resonant beam vibrations are highly damped for values of the fundamental resonant frequency extending over a relatively broad frequency range.

Effect of Environmental Temperature. All the experimental data previously presented apply only at room temperature. The effect of extreme high and low temperatures on the fundamental mode resonance amplification factor $A_r(l)$ and resonant frequency f_1 of conventional-solid and viscoelastic-damped aluminum beams is indicated in Fig. 16. The beam specimens are subjected to temperatures ranging from -100 to $+500$ F in a temperature environmental chamber for a period of four hours, after which the resonance amplification factor and the resonant frequency for the fundamental mode is measured.

The variation of the resonance amplification factor with environmental temperature is shown in Fig. 16(a) for damped aluminum beams employing different viscoelastic damping materials as well as for the solid aluminum beam. The value of the resonance amplification factor for the solid beam, indicated by the solid curve, is nearly independent of the environmental temperature for the temperature range tested. The curves for the damped beams indicate that the value of the resonance amplification factor for viscoelastic-damped structural members may be relatively large at extremely high and low temperatures, as compared with the value at intermediate temperatures. The damped beam specimens (1) and (2), indicated by *dotted* and *dot-dot-dash* curves, respectively, employ adhesive transfer films as the viscoelastic damping material. The damped beam specimens (3) and (4), indicated by *dashed* and *dot-dash* curves, respectively, employed a silicone-based viscoelastic material. The two curves (3) and (4) represent measurements made on damped laminated beams employing similar silicone-based viscoelastic compounds subjected to different cure cycles. The superiority of damped beam (4) for use in a broad range of temperature environments demonstrates the importance of properly curing damped structural configurations employing certain viscoelastic damping materials.

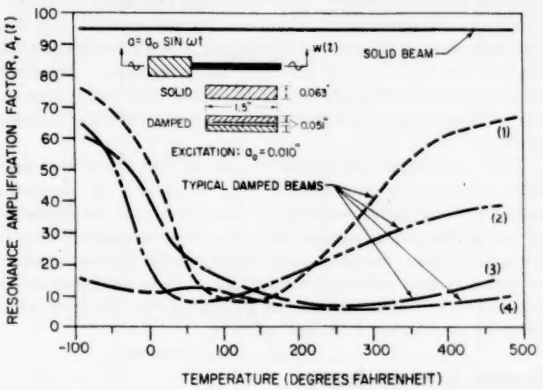

Fig. 16(a) Fundamental mode end-point resonance amplification factor of cantilever beams as a function of environmental temperature

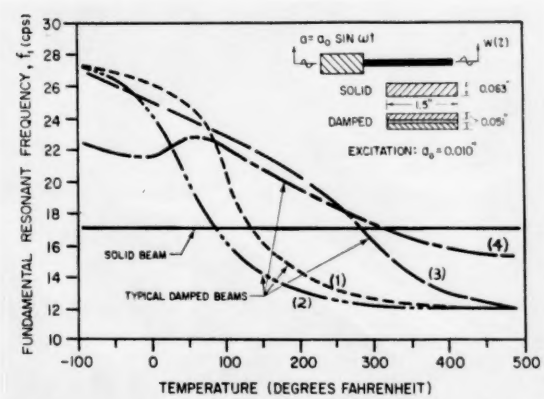

Fig. 16(b) Fundamental resonant frequency of cantilever beams as a function of environmental temperature

The variation of the resonant frequency f_1 with environmental temperature for the solid and damped beams is shown in Fig. 16 (b). The curves indicate the resonant frequency of each beam at the specified temperature for which the resonance amplification factor $A_r(l)$ is given in Fig. 16(a). The resonant frequency of the solid aluminum beam is independent of environmental temperature. For damped beam specimens (1), (2), and (3), the resonant frequency f_1 approaches 12 cps for very high temperatures and 27 cps for very low temperatures. The two resonant frequencies corresponding to the extreme high and low temperature conditions represent the zero and infinitely damped natural frequencies, respectively. (The significance of these characteristic natural frequencies is discussed in Part I of this paper.) Therefore, the damping materials employed in damped beam specimens (1), (2), and (3) operate in their *rubbery*, *transition*, and *glassy* regions for the temperature range tested. The *transition* region (indicated by that portion of the curve in Fig. 16(a) for which the resonance amplification factor is low and of relatively constant value) encompasses a relatively narrow temperature range for damped beam specimens (1) and (2). Damped beam specimen (3) has poor low temperature damping properties but exhibits excellent damping properties at the higher temperatures.

For damped beam specimen (4), a smaller resonant frequency change is experienced over the temperature range tested. At the extreme high and low temperatures, the resonant frequency does not approach the zero and infinitely damped natural frequencies. The conclusion may be drawn that the damping material in damped beam specimen (4) is operating in its *transition* region over the entire temperature range tested. Therefore, as illustrated in Fig. 16(a), the silicone-based material employed in damped beam specimen (4) possesses excellent damping properties over the temperature range of -100 to $+500$ F.

Vibration Isolation Systems. The effect of structural damping on the performance of a vibration isolation system is determined from an idealized experimental model, pictured in Fig. 17, consisting of a nonrigid structure in the form of a free-free beam supported at its center by a simple ring-spring isolator. A sinusoidal vibration excitation is imposed at the rigid support to which the ring-spring is attached. The absolute transmissibility, which is the ratio of the vibration response at the center of the free-free beam to the vibration imposed at the support, is shown in Fig. 18 as a function of the ratio of excitation frequency f to the rigid body natural frequency f_0. Transmissibility curves for the steel beams possessing predominantly material, rivet, or viscoelastic-shear damping mechanisms may be compared with each other and with the transmissibility curve that would exist for a rigid beam. The material damping response is characteristic of a welded fabrication; the rivet damping response is characteristic of a riveted or bolted assembly; and the viscoelastic-shear damp-

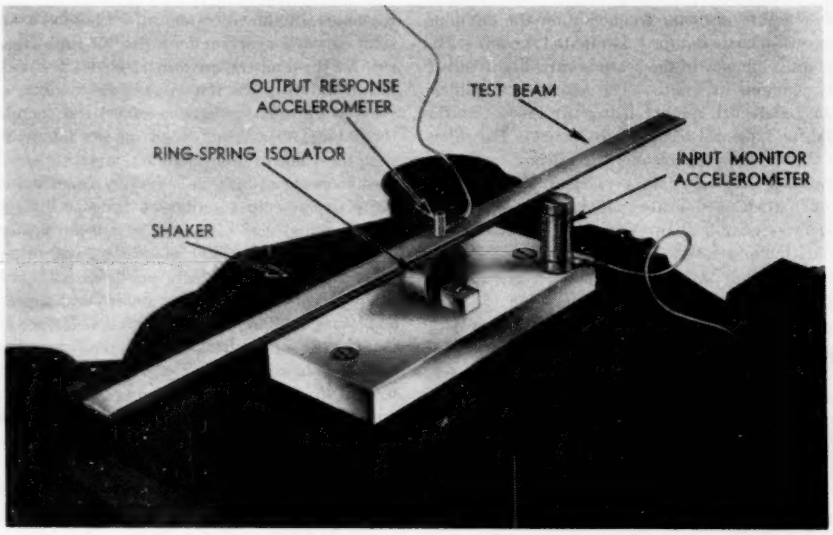

Fig. 17 Beam test configuration used to study the effects of structural damping on the performance of vibration isolation systems

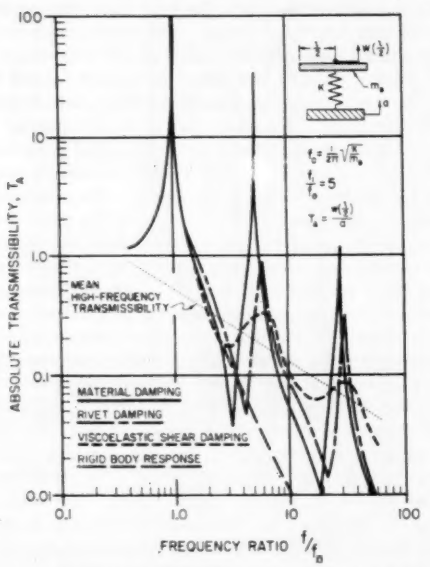

Fig. 18 Absolute transmissibility of the vibration isolation system pictured in Fig. 17 as a function of the ratio of the excitation frequency f to the rigid body natural frequency f_0, where the fundamental free-free beam frequency $f_1 = 5f_0$

ing response is typical of the viscoelastic-damped structural configurations discussed in Part I of this paper.

The curve for material damping represents the response obtained for a solid steel beam; at the fundamental resonant frequency of the beam ($f/f_0 = 5$), the transmissibility is over 800 times that obtained for a rigid beam. The curve for rivet damping represents the response obtained for a riveted laminated steel beam; at the fundamental resonant frequency of the beam, the transmissibility is 30 times that obtained for a rigid beam. The curve for viscoelastic shear-damping represents the response obtained for a viscoelastic-damped laminated steel beam; at the fundamental resonant frequency of the beam, the transmissibility is 10 times that obtained for a rigid beam. While the riveted structure is an improvement over the solid structure, the best control of resonant structural vibration is obtained from the viscoelastic-damped structure design. The mean high frequency transmissibility of all damped beams (indicated by the dotted line in Fig. 18), regardless of the amount of damping, has an attenuation rate that is less than that of the rigid body response. Therefore, structural resonances, whether highly damped or not, reduce the over-all high frequency isolation efficiency of a vibration isolation system.

The variation of transmissibility above and below the mean high frequency transmissibility line, as caused by structural resonances and anti-resonances, is reduced by the incorporation of energy dissipating mechanisms into the structural fabrication. Viscoelastic-shear damping mechanisms provide the best resonant vibration control without disadvantages, such as nonlinear damping and surface fretting, that are associated with the dry-friction damping mechanism of riveted joints.

Damped Structural Beams

Test Specimen. The solid and cell-insert test beams pictured in Fig. 19 are 3-in. high I-sections having a 2.33-in. flange width.

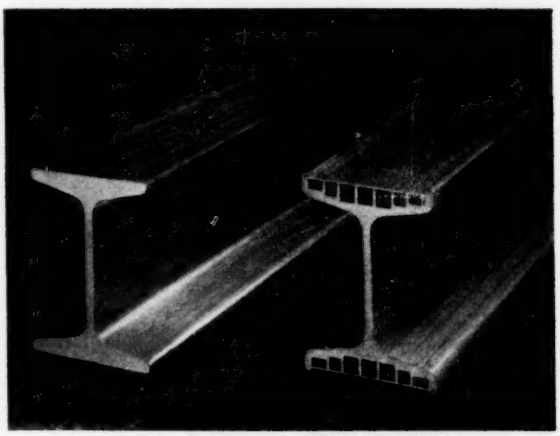

Fig. 19 Cell-insert and solid I-section test beams

The conventional beam (left) is a solid aluminum rolled section. The viscoelastic-damped beam (right) is a cell-insert design configuration having an aluminum cellular housing and steel insert rods. The inserts are embedded longitudinally in the cells and are separated from the cell walls by a layer of viscoelastic damping material approximately 0.010 in. thick. The slip between the inserts and the cell that occurs during flexural vibrations creates an energy dissipating shear action in the intervening viscoelastic damping layer. The determination of the N-factor for this test specimen (see Part I of this paper) involves lengthy numerical calculations not to be included here. Upon performing these calculations, it is determined that $N = 1.9$ for the cell-insert damped beam. The beams are tested as double length center-clamped cantilever beams, as shown in Fig. 5, with a free length of 30 in.

Frequency Response. The end-point transmissibility $T(l)$ of the solid and cell-insert damped I-beams is shown in Fig. 20 as a function of the ratio of excitation frequency f to the fundamental resonant frequency f_1 of the beam. The fundamental resonant frequency f_1 is 132 cps for the solid beam and 96 cps for the cell-insert damped beam. The resonant amplification of the beam vibration is drastically reduced by use of the viscoelastic-damped cell-insert beam design. For example, at the fundamental resonant frequency, amplification of the solid beam vibration is 15 times that of the cell-insert damped beam; at the second mode resonant frequency, the solid beam amplifies the excitation vibration more than 40 times that of the damped beam.

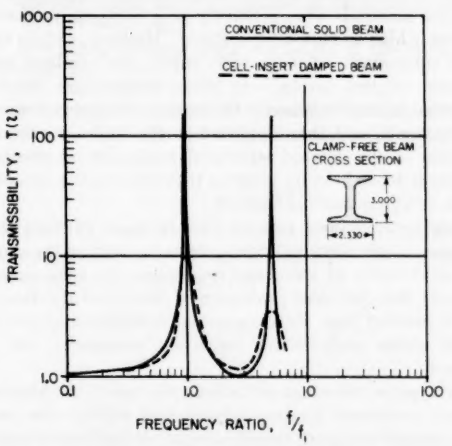

Fig. 20 End-point transmissibility of solid and cell-insert I-section cantilever beams as a function of the ratio of the excitation frequency to the fundamental resonant frequencies of the beams

Effect of Concentrated Mass Loading. The effect of adding a concentrated mass to the end of the cantilever beam on the transmissibility is illustrated in Fig. 21. The fundamental resonant frequency f_1 is 22 cps for the solid beam and 20 cps for the cell-insert damped beam. The solid beam amplifies the excitation vibration 10 times more than the damped beam at the fundamental resonant frequency; at the second mode resonant frequency, the end-point transmissibility of the solid beam is 2.5 times that of the damped beam. The addition of the concentrated mass effects a reduction in vibration transmission at the higher natural modes of beam vibrations.

Effect of Vibration Excitation Level. The resonance amplification factor $A_r(l)$ of the fundamental mode for the solid and cell-insert I-beams is shown in Fig. 22 as a function of the level of excitation displacement imposed at the support. Data are included on beams with and without the concentrated end-weights. The resonance amplification factor of the solid beam varies between

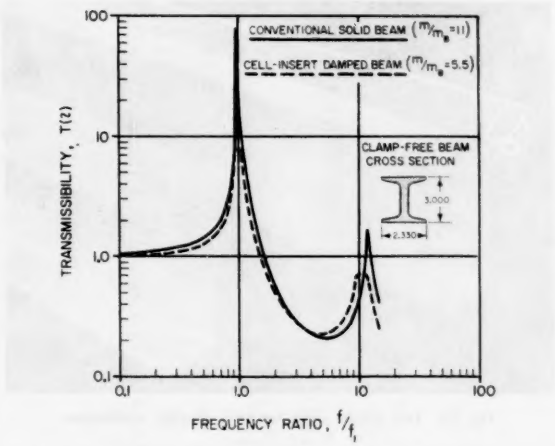

Fig. 21 End-point transmissibility of solid and cell-insert I-section cantilever beams carrying concentrated masses at their free ends as a function of the ratio of the excitation frequency to the fundamental resonant frequencies of the beams

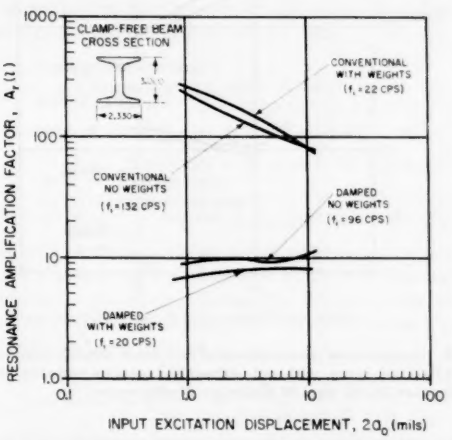

Fig. 22 Fundamental mode end-point resonance amplification factor of solid and cell-insert I-section cantilever beams, with and without end weights, as a function of the level of excitation displacement

300 and 80 for the range of excitation displacement levels tested. The cell-insert damped beam exhibits values of the resonance amplification factor less than 10 that are nearly constant for all levels of vibration excitation tested. The cell-insert damped beam design possesses very linear damping properties in contrast to those of the conventional solid beam.

Strip Dampers

A 3-in. solid aluminum I-beam, with and without strip dampers attached to both flanges, is shown in Fig. 23. The beams are tested as double length center-clamped beams, as shown in Fig. 5, with a free length of 30 in. The strip damper, which employs a continuous aluminum retainer strip and a single steel insert, is attached continuously along the full double length of each flange of the I-beam, i.e., the strip dampers are clamped in the support fixture along with the I-beam.

The resonance amplification factor $A_r(l)$ for the fundamental mode of vibration of I-beams, with and without the strip dampers attached, is shown in Fig. 24 as a function of the excitation displacement of the support. The resonance amplification factor

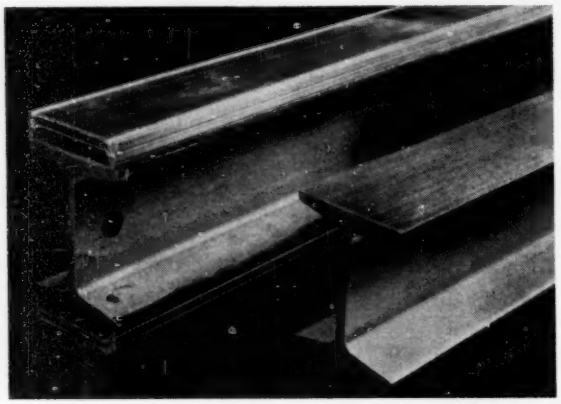

Fig. 23 Test beams used for strip damper evaluation

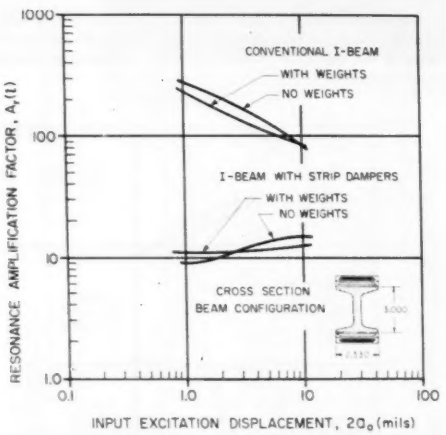

Fig. 24 Fundamental mode end-point resonance amplification factor of a solid I-section beam, with and without end weights and strip dampers, as a function of the level of excitation displacement

for the beam without end weights nearly equals that of the beam with end weights, whether or not the strip dampers are attached. For the I-beam with strip dampers attached, the resonance amplification factor varies between 9 and 15 for the range of excitation displacements tested. In comparison, the resonance amplification factor for the conventional I-beam varies between 300 and 80 for the same range of excitation displacements imposed at the support. Considerable reduction in resonant vibration amplification is afforded by use of the strip dampers; at the lower excitation displacements, the resonant vibration is reduced to $^1/_{30}$ of its original value while, at the higher excitation displacements, the resonant vibration is reduced to $^1/_8$ of its original value.

Summary and Conclusions

Viscoelastic-damped structure and (additive) strip damper design configurations have been developed to damp flexural structural vibrations over broad frequency and temperature ranges. While the experimental data presented herein apply only to cantilever beams fabricated from metal, similar results are obtained for cantilever beams fabricated from plastics and glass-fabric laminate materials.

Each damped structure design, whether it be a laminated sheet or a cell-insert beam, requires an optimum amount of damping to minimize the resonant response. However, sufficient resonant vibration control may be obtained by use of viscoelastic-damped structural configurations possessing only nearly optimum damping properties. In many applications, the reduction of resonant vibrations may mean the difference between a reliable design and one that is not. The damaging high frequency accelerations that normally are transmitted to critical components can be drastically reduced, thus providing increased equipment reliability and decreased component malfunction due to vibration. This is of particular value where a design is considered marginal due to recurring component failures known to be caused by excessive vibration.

Viscoelastic-damped structural configurations do not reduce appreciably the severity of the initial shock amplification produced by a structure. However, the configurations are useful in controlling the vibrations that follow the peak structural response.

The resonance amplification factor and the bandwidth quality factor for a viscoelastic-damped structure are nearly independent of the level of vibration excitation. In addition, excellent vibration control may be obtained from viscoelastic-damped structures having resonant frequencies that extend over a broad frequency range. The higher natural modes of flexural vibrations of a structure are generally exceedingly well damped if the fundamental resonance is highly damped.

The degree to which the resonant structural vibrations are limited by the viscoelastic-damped structural configurations depends on the environmental temperature. Some viscoelastic damping materials have relatively poor damping properties for extremely high and low temperatures. However, certain silicone-based compounds, when properly cured, give excellent resonant vibration control over a very broad temperature range. For structural fabrications used in the severe current-day temperature environments, and those expected in the future, successful application of the damped structural configurations discussed in this paper depends on the progress to be made in the area of viscoelastic damping material research.

Viscoelastic-damped structural fabrications improve the performance of vibration isolation systems by limiting the amplification of vibration at structural resonances. In some cases, it is probable that sufficient protection of the structural fabrication that is isolated from the dynamic environment may not be obtained unless predominant structural resonances are highly damped.

For a given vibration excitation, the use of the viscoelastic-damped structural design configurations reduces the dynamic stress created in a given structural member and thus increases the allowable number of vibration cycles that it can withstand before fatiguing. For sufficiently high structural damping, the fatigue life of the structure may be increased indefinitely. Hence, increased reliability and longer life of the over-all structural system is obtained.

The experimental data presented herein apply only for cantilever beam specimens. The very large amplification of vibration exhibited by the solid beam members generally is not representative of most structural fabrications. It is not uncommon, however, for the excitation vibration to be amplified by a factor of 20 to 50 at the resonant frequencies of conventionally fabricated structures. Therefore, large reductions in resonant vibrations may still be obtained by use of the viscoelastic-damped laminated sheets, as well as by the cell-insert beams and the strip damper, in structural fabrications intended for use in modern dynamic environments.

Acknowledgments

The author sincerely appreciates the help given by many people during the course of the research investigation and the prepara-

tion of the manuscript. In particular, the following acknowledgments are made: Arthur Oster, William Schoen, and Lawrence Corbett, for their help in obtaining much of the experimental data; Sidney Hamel, for his help in designing and producing extruded aluminum sections; Kenneth Ray, for the preparation of the line drawings in the paper; Lewis Colson and Bartlett Hauthaway, for the photographs; and Henry Perley, Adolf Arnold, Clarence Metcalf, Thomas Hynes, RoseMarie Pollock, and Mary Reilly, for their contributions in preparing the manuscript for publication.

APPENDIX

Transfer Response Function of a Cantilever Beam

The differential equation of transverse motion for the flexural vibration of a uniform beam is given by

$$EI\frac{\partial^4 w(x,t)}{\partial x^4} + \rho A\frac{\partial^2 w(x,t)}{\partial t^2} = 0 \tag{1}$$

where

E = modulus of elasticity of the beam material (lb/in.^{2})
I = moment of inertia of cross-sectional area (in.^{4})
ρ = mass density of beam material $\left(\frac{\text{lb-sec}^2}{\text{in.}^4}\right)$
A = cross-sectional area (in.^{2})
w = absolute transverse displacement of the neutral surface of the beam (in.)
x = co-ordinate distance along the length of the beam (in.)
t = time (sec)

Since only harmonic time-dependent boundary conditions will be considered, the solution for the absolute transverse displacement is assumed to be

$$w(x,t) = X(x,\omega)e^{j\omega t} \tag{2}$$

where $X(x,\omega)$ is a function solely of the co-ordinate position x and the excitation frequency ω. Using this assumed solution, the differential equation of motion becomes

$$\frac{d^4X(x,\omega)}{dx^4} - \beta^4 X(x,\omega) = 0 \tag{3}$$

where

$$\beta^4 = \frac{\rho A\omega^2}{EI} \tag{4}$$

The general solution of this equation can be written as

$$X(x,\omega) = C_1\cosh\beta x + C_2\sinh\beta x + C_3\cos\beta x + C_4\sin\beta x \tag{5}$$

where the function $X(x,\omega)$ is subject to the boundary conditions of the beam being considered. The boundary conditions for the cantilever beam shown in Fig. 1 are as follows

$$\left.\begin{aligned} X(0) &= a_0 \qquad \frac{d^2X(l)}{dx^2} = 0 \\ \frac{dX(0)}{dx} &= 0 \qquad \frac{d^3X(l)}{dx^3} = 0 \end{aligned}\right\} \tag{6}$$

If these boundary conditions be imposed on the general solution, the coefficients C_1, C_2, C_3, and C_4 are determined to be

$$\left.\begin{aligned} C_1 &= a_0 - C_3 \\ &= \frac{a_0}{2}\left[\frac{\cosh\beta l\cos\beta l + \sinh\beta l\sin\beta l + 1}{\cosh\beta l\cos\beta l + 1}\right] \\ C_2 &= -C_4 = -\frac{a_0}{2}\left[\frac{\cosh\beta l\sin\beta l + \sinh\beta l\cos\beta l}{\cosh\beta l\cos\beta l + 1}\right] \end{aligned}\right\} \tag{7}$$

which, when substituted in Eq. (5), give the general solution for $X(x,\omega)$ as follows:

$$\left.\begin{aligned} X(x,\omega) = {} & \frac{a_0}{2}\left[\frac{\cosh\beta l\cos\beta l + \sinh\beta l\sin\beta l + 1}{\cosh\beta l\cos\beta l + 1}\right]\cosh\beta x \\ & - \frac{a_0}{2}\left[\frac{\cosh\beta l\sin\beta l + \sinh\beta l\cos\beta l}{\cosh\beta l\cos\beta l + 1}\right]\sinh\beta x \\ & + \frac{a_0}{2}\left[\frac{\cosh\beta l\cos\beta l - \sinh\beta l\sin\beta l + 1}{\cosh\beta l\cos\beta l + 1}\right]\cos\beta x \\ & + \frac{a_0}{2}\left[\frac{\cosh\beta l\sin\beta l + \sinh\beta l\cos\beta l}{\cosh\beta l\cos\beta l + 1}\right]\sin\beta x \end{aligned}\right\} \tag{8}$$

Using trigonometric and hyperbolic expansion formulas, the response function can be made to take the form

$$\begin{aligned} T(x,\omega) = {} & \frac{1}{2(\cosh\beta l\cos\beta l + 1)}\left[\cosh\beta l\cos\beta(l-x)\right. \\ & - \sinh\beta l\sin\beta(l-x) + \cos\beta l\cosh\beta(l-x) \\ & \left. + \sin\beta l\sinh\beta(l-x) + \cosh\beta x + \cos\beta x\right] \end{aligned} \tag{9}$$

where $T(x,\omega) = \dfrac{X(x,\omega)}{a_0}$ represents the general transfer response function solution for a cantilever beam, which is the ratio of the resulting transverse beam displacement function to the displacement imposed at the clamped boundary. For $x = l$, the transfer response function, or transmissibility function, for the free end of the cantilever beam becomes

$$T(l,\omega) = \frac{X(l,\omega)}{a_0} = \frac{\cosh\beta l + \cos\beta l}{\cosh\beta l\cos\beta l + 1} \tag{10}$$

The free-vibration frequency equation for a cantilever beam is

$$\cosh\beta_n l\cos\beta_n l + 1 = 0 \tag{11}$$

which corresponds to the denominator of the transfer response functions (9) and (10) when the excitation frequency ω coincides with a resonant frequency ω_n and, therefore, $\beta = \beta_n$. For this case, the denominator of the transfer response function becomes zero thus causing the response to become either indeterminate or infinite.

By defining a reference frequency ω_r as

$$\omega_r = \sqrt{\frac{EI}{m_B l^3}} \tag{12}$$

where EI/l^3 can be thought of as a reference stiffness and $m_B = \rho Al$ represents the total mass of the beam, the parameter β may be written

$$\beta = \frac{1}{l}\sqrt{\frac{\omega}{\omega_r}} \tag{13}$$

and the end-point cantilever transmissibility defined by Eq (10) becomes

$$T(l, \omega) = \frac{\cosh \sqrt{\frac{\omega}{\omega_r}} + \cos \sqrt{\frac{\omega}{\omega_r}}}{\cosh \sqrt{\frac{\omega}{\omega_r}} \cos \sqrt{\frac{\omega}{\omega_r}} + 1} \tag{14}$$

The frequency ratios for which a resonance occurs are set forth in Table 1 for the first five natural modes of a clamp-free beam. The resonances exhibited in the graphical representation of Eq. (10) shown by Fig. 2 correspond to the frequency ratio values given in Table 1.

Table 1

n	1	2	3	4	5
ω_n/ω_r	3.52	22.03	61.7	120.9	200

DISCUSSION

Edward M. Kerwin, Jr.,[2] and Eric E. Ungar[3]

The author is to be congratulated for his efficient summary of many of the important facts regarding structural damping, for his development of several clever configurations based on his "cell-insert" concept, and for having demonstrated experimentally the advantages to be gained with structures incorporating viscoelastic damping.

The author's insert configurations represent one of the many types of damping arrangements that depend on the shearing motion of viscoelastic materials contained between two elastic members [1, 2].[4] Such damping systems have been called "constrained viscoelastic layer" systems in the literature. Damping tapes [3, 4, 5], "spaced" damping treatments [6, 7], laminated structures [8, 9, 10], "strip" dampers [9], and various other configurations utilize the same principle. It has, in fact, been demonstrated that all of these arrangements can be treated as special cases of the same general analysis [11]. (These results have not yet been published in full, however.) It is of interest to note that the author's analysis of a lumped-parameter analog to the damped structure resulted in a number of conclusions that agree with those obtained from available analyses dealing with flexural waves in composite structures with viscoelastic interlayers [1, 2, 11]. These conclusions are:

(*a*) As one changes the viscosity of the viscoelastic material, everything else remaining unchanged, damping passes through a maximum.

(*b*) The amount of damping attainable increases with the modulus of elasticity and/or the cross-sectional area of the secondary structural members (e.g., cell inserts or tapes).

(*c*) Better damping is obtained with greater separation between the neutral planes of the primary (e.g., basic beam or plate) and secondary (see above) structures.

Conclusions (*b*) and (*c*) are quantified in terms of the author's N-factor, which may be shown to be related to the "geometric" or "structural" parameters defined in previous studies [1, 2, 11].

While the author's experimental work served to illustrate the feasibility and performance level of his damping system, he presented no comparison between his theoretically predicted and experimentally measured results. Such a comparison, and a discussion of the rational design of viscoelastically damped structures, would have been extremely useful. It is true that most of the analytical work to date applies only for the higher modes when taken strictly; nevertheless, the analyses should provide reasonable approximations for all but the lowest mode or two.

Since the author's main interest is in stress reduction, he is naturally primarily concerned with the lowest few modes, and it is for these that analyses tend to be most complicated and previously published results are least accurate. Recent theoretical work [12] has shown that for the lowest modes the interconnections of the various substructures and the boundary conditions are very important, and that the damping observed in a beam may even be extremely sensitive to beam length under certain circumstances. It would be most helpful to all workers in the field of viscoelastic damping if the author would, perhaps in the future, set forth his general conclusions and design procedures, and if he would delineate the effects of various special features that, as he states, influence the design of damped structures or systems.

[2] Senior Consultant, Bolt Beranek and Newman, Inc., Cambridge, Mass.

[3] Senior Engineering Scientist, Bolt Beranek and Newman, Inc., Cambridge, Mass. Assoc. Mem. ASME.

[4] Numbers in brackets designate References at end of this discussion.

References

1 E. M. Kerwin, Jr., "Damping of Flexural Waves by a Constrained Visco-Elastic Layer," *Journal, Acoustical Society of America*, vol. 31-7, 1959, pp. 952–962.

2 D. Ross, E. E. Ungar, and E. M. Kerwin, Jr., "Damping of Plate Flexural Vibrations by Means of Viscoelastic Laminae," "Structural Damping," J. E. Ruzicka, Ed., ASME, New York, N. Y., 1959.

3 E. E. Ungar, "Damping Tapes for Vibration Control," *Product Engineering*, vol. 31, Jan. 25, 1960, pp. 57–62.

4 "Mile of Silver Tape Maker Silence Golden Aboard 880 Jet," *Western Aviation*, vol. 40, September, 1960, pp. 20, 21, 28.

5 E. E. Ungar and D. Ross, "Damping of Flexural Vibrations by Alternate Viscoelastic and Elastic Layers," Proceedings, Fourth Midwestern Conference Solid Mechanics, University of Texas, 1959, pp. 468–487.

6 E. M. Kerwin, Jr., "Ideal Spaced Damping Treatments for Flexural Waves," *Journal of the Acoustical Society of America*, vol. 31, 1959, p. 846(A).

7 E. M. Kerwin, Jr., "Damping of Flexural Waves in Plates by Spaced Damping Treatments Having Spacers of Finite Stiffness," Paper IC3, III International Congress on Acoustics, Stuttgart, Germany, September, 1959 (Proceedings to be published by Elsevier Publishing Company, Amsterdam, Netherlands).

8 "Noise- and Vibration-Damping Material," *Product Engineering*, 14 March 1960, p. 81.

9 "Wide-Band Vibration Damper in Sheets, Hats, Angles," *Machine Design*, vol. 32, 17 March 1960, p. 34.

10 H. Rosen and E. D. Veilleux, "Designing Damping Into Laminated Structures," *Machine Design*, vol. 32, 4 February 1960, pp. 24–26.

11 E. E. Ungar and E. M. Kerwin, Jr., "Damping of Composite Structures by Viscoelastic Interlayers," *Journal of the Acoustical Society of America*, vol. 32, July, 1960, p. 912(A).

12 E. M. Kerwin, Jr., and R. J. McQuillin, "Plate Damping by a Constrained Viscoelastic Layer: Partial Coverage and Boundary Effects," *Journal, Acoustical Society of America*, vol. 32, November, 1960, p. 1513(A).

Author's Closure

The author thanks the discussers for their comments and agrees that it would be desirable to present comparisons between theoretically predicted and experimentally measured results, as well as procedures for designing viscoelastic-damped structures. In limiting the length of the papers, these considerations were excluded and the author confined himself to a general discussion of important design parameters such as strength, weight, structure, N-factor, and fatigue. In addition, general conclusions regarding the use of viscoelastic shear-damping materials in structural fabrications were set forth. The author plans to present specific design data useful to the structural design engineer in future publications.

Magnetic Properties of Malleable Irons

W. K. BOCK
Director of Research, National Malleable and Steel Castings Company, Cleveland, Ohio. Mem. ASME

T. D. HUTCHINSON
Supervisor of Physical Metallurgy, Malleable Research and Development Foundation, Dayton, Ohio

Standard or ferritic malleable iron is satisfactory for use as a cast, soft magnetic material. It is made by heat-treating white iron. In addition to its magnetic properties, it can be readily cast into intricate shapes and is one of the most machinable ferrous metals. By merely changing the heat-treatment, pearlitic or martensitic malleable iron can be produced from the same white iron.

Like all soft, magnetic materials, ferritic malleable iron is mechanically soft. On the other hand, pearlitic malleable and martensitic malleable irons are graphitic steels and exhibit a range of hardness and strength. They have the same availability as ferritic malleable and much of its machinability. Ordinarily, carbon steels are not used for magnetic applications, but because the pearlitic and martensitic malleables have the advantages outlined above, there is some idea that they might be used as a compromise by giving up some magnetic quality to gain mechanical properties. This paper supplies the magnetic properties necessary for such compromise.

Magnetically, pearlitic and martensitic malleables behave like steels if allowance is made for the graphite which is present.

Introduction

THERE IS a definite and growing need for soft, magnetic material in cast form. Dynamo steel was developed to supply this need, but dynamo steel, despite its good magnetic properties, has several drawbacks. It presents problems in the foundry and in the machine shop. Since castings for magnetic application are usually subjected to a considerable amount of machining, machinability is an important factor in the selection of an alloy. In a recent paper by one of the authors [1],[1] it was shown that standard ferritic malleable iron had almost the ideal metallurgy for a soft, magnetic alloy plus the advantages of being a free machining material which is made in considerable tonnage. This paper gave the important magnetic properties of standard malleable iron in some detail.

The data in this paper showed that the permeability of malleable iron was not as high as for a silicon iron and the *B-H* curve and saturation values were lower than for comparable iron. The reason for this is obvious when one considers that part of the cross section of malleable iron is graphite, which does not furnish an easy path for magnetic lines of force. These apparent shortcomings of malleable, it was demonstrated, can be overcome by slight increase in the pole area, or, if the application is one at low magnetizing force, a simple increase in the number of ampere turns can overcome the lower values of malleable iron.

At the same time, it was shown that both hysteresis loss and eddy current loss in malleable iron were low.

It was also pointed out in this paper that malleable and all other soft, magnetic alloys have certain physical and mechanical properties in common. All have low hardness, low or fair strength, and are not particularly good for abrasion or wear resistance. There is no way in which an alloy can be specified to give optimum soft, magnetic properties plus high hardness and strength.

In the malleable industry, white iron is cast and heat-treated to produce standard ferritic malleable iron. By changing the heat-treatment, the white iron is converted to pearlitic or martensitic malleable iron, depending on whether or not a quench is employed. Thus, from a single base alloy, a whole family of alloys is produced covering a wide range of physical and mechanical properties. It is tempting to try to use one of these other malleable irons for magnetic applications.

Unfortunately, the martensitic malleable may contain up to about 0.80 per cent combined (nongraphitic) carbon. The pearlitic malleable usually is lower in combined carbon. As shown by Yensen [2], carbon in steel increases hysteresis loss and electrical resistance and decreases saturation value.

At first glance, it would appear that pearlitic and martensitic malleables should not be considered for magnetic work. Gains in hardness, strength, or wear resistance would be made only at the expense of magnetic properties. There is always the possibility, however, that for a given purpose a compromise might be made. This compromise would involve giving up some of the magnetic properties to gain strength or hardness. The physical and mechanical properties of these materials are known [3], but what is lacking for effective compromise is the knowledge of the magnetic properties of pearlitic and martensitic malleable irons. This paper attempts to supply the necessary information.

Later in the paper, an example will be given to show what magnetic properties can be expected if pearlitic or martensitic malleable is used in magnetic applications. However, in any particular design problem, the compromise is the responsibility of the designer. In this paper we can only furnish the data on which he can base his specification.

Experimental Procedure

The material used in this investigation was cast into plates $10^1/_2$ in. long, $1^1/_4$ in. wide, and $^1/_2$ in. thick. A number of plates were cast from a single ladle of metal. The analysis was:

Carbon	2.59 per cent
Silicon	1.26 per cent
Manganese	0.44 per cent

The castings were given a first-stage anneal[2] in a production furnace after which the risers were removed and heat-treatment was completed in a laboratory furnace. Seven different heat-treatments were employed and these are given in Table 1.

Sample No. 1 was completely graphitized and magnetic data

[1] Numbers in brackets designate References at end of paper.

Contributed by the Machine Design Division and presented at the Winter Annual Meeting, New York, N. Y., November 27–December 2, 1960, of THE AMERICAN SOCIETY OF MECHANICAL ENGINEERS. Manuscript received at ASME Headquarters, June 8, 1960. Paper No. 60—WA-218.

[2] First-stage anneal consists in holding in the austenite region until massive carbides are decomposed to graphite and austenite.

Table 1 Heat-treatment of magnetic samples

Sample	Hours at 1600°	Cool	Tempering Temp	Tempering Time
1	1/2[a]	fur. to 1390° 5°/hr to 1280°		
2	2	Air	1300°	2 hr.
3	2	Air	1250°	2 hr.
4	2	Air	1180°	2 hr.
5	2	Oil	1180°	2 hr.
6	2	Oil	1120°	2 hr.
7	2	Oil	1040°	2 hr.

[a] 1650 deg was used on this sample instead of 1600 deg.

Table 2 Hardness and combined carbon content

Sample	Combined carbon (%)	Hardness (BHN)	Approx. tensile strength (psi)
1	0.05	109	50000
2	0.55	179	75000
3	0.51	197	78000
4	0.57	212	82000
5	0.79	217	89000
6	0.89	229	95000
7	0.76	277	105000

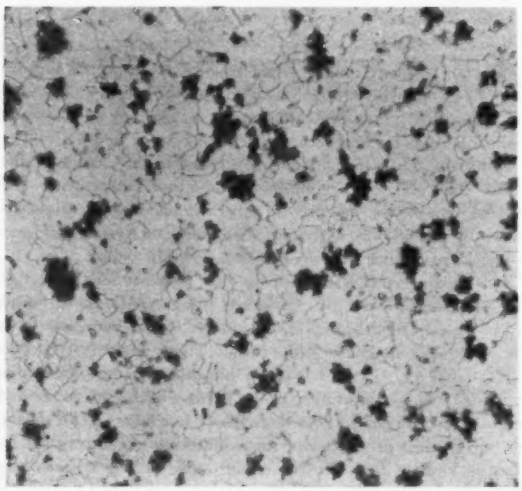

Fig. 1 Microstructure of a ferritic malleable iron; 100X; nital etched

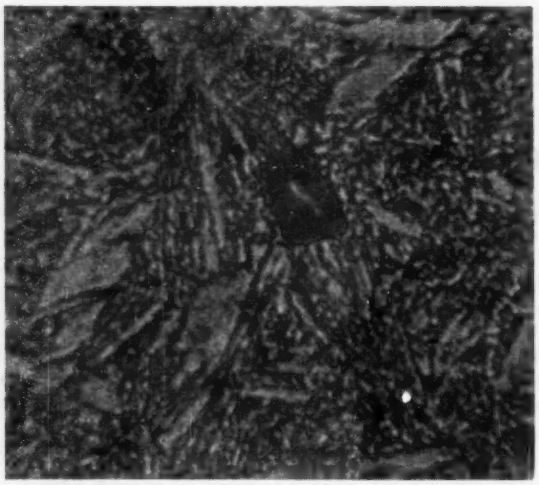

Fig. 2 Microstructure of a pearlitic malleable iron; 2000X; nital etched

from this ferritic malleable sample were checked against the previously published data. Samples 2, 3, and 4 are pearlitic malleable and samples 5, 6, and 7 are martensitic malleable.

Fig. 1 shows the microstructure of the ferritic malleable. Fig. 2 shows a typical microstructure of pearlitic malleable, and Fig. 3 of martensitic malleable.

The latter two figures are taken at rather high magnification to show the details of the structure. It will be noted that what is termed martensitic malleable is more completely described by the term tempered martensite.

After heat-treating, the samples were machined and ground to 0.394 in. × 1.181 in. × 10 in. This removed all scale and any decarburization which might have been present.

All magnetic and electrical measurements were made by the Electrical Testing Laboratories, Inc., of New York. Testing methods employed followed the ASTM procedures. The magnetic properties were determined by the Burrows method.[3]

It was desirable to cover the full range of grades of pearlitic and martensitic malleable irons in this investigation. The heat-treatments in Table 1 were designed to do this. In order to check compliance with this requirement, all samples were Brinelled and the hardnesses are shown in Table 2 along with the approximate tensile strengths estimated from the hardness.

The material considered here is essentially a graphitic steel and since magnetic properties of steel depend on carbon content as well as microstructure, the combined carbon, or nongraphitic carbon of our samples, is included in Table 2.

Results of the Investigation

The first result to be considered is the *B-H* curve for each sample. The data are given in Table 3.

The induction curve for each sample was plotted and the three curves for pearlitic malleable were found to fall within 2000 gauss at the point of greatest deviation. Since there was no systematic shift of these curves, it was decided that they represent a single *B-H* curve for the three pearlitic malleable samples. The three curves for martensitic malleable appear to shift to the right with increased hardness, but since the differences were about the same as in the case of the pearlitic samples, it was accepted that all three martensitic samples had the same *B-H* curve.

[3] Electrical Testing Laboratories, Inc., measured the magnetic properties and electrical resistivity on samples submitted to them. The selection and preparation of samples, interpretation of data, and conclusions reached are the responsibility of the authors.

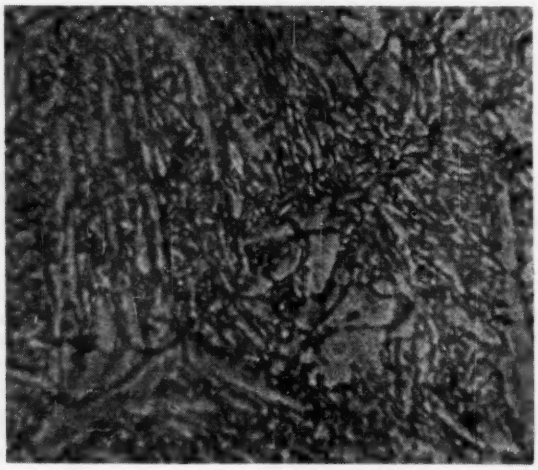

Fig. 3 Microstructure of a martensitic malleable iron; 2000X; nital etched

Table 3 Induction curves

No. 1		No. 2		No. 3		No. 4	
Magnetizing force-H (oersteds)	Induction-B (gausses)	Magnetizing force-H (oersteds)	Induction-B (gausses)	Magnetizing force-H (oersteds)	Induction-B (gausses)	Magnetizing force-H (oersteds)	Induction-B (gausses)
1.1	3420	1.1	330	1.1	245	1.1	245
2.0	4575	2.2	495	2.3	410	2.3	325
3.1	5590	3.1	575	2.9	535	2.9	490
4.9	7050	4.9	1065	5.6	1065	4.9	820
7.5	8380	6.6	1730	6.1	1395	7.0	1480
9.0	9060	9.1	3385	9.1	3380	8.9	2280
12.0	9970	11.9	5220	10.5	5210	12.0	3470
14.9	10640	14.9	6620	17.1	8060	14.7	5360
20.4	11200	19.8	8200	20.2	8850	20.0	6950
29.8	11920	30.0	9920	29.6	10420	29.6	9120
50.0	12670	50.5	11370	50.0	11800	49.5	10870
80.0	13390	80.0	12390	78.0	12490	83.0	12280
120.0	14000	120.0	13180	119.0	13380	118.0	12990
182.0	14800	160.0	13730	158.5	13880	160.0	13680
		199.0	14190	200.0	14170	198.0	14080

No. 5		No. 6		No. 7	
Magnetizing force-H (oersteds)	Induction-B (gausses)	Magnetizing force-H (oersteds)	Induction-B (gausses)	Magnetizing force-H (oersteds)	Induction-B (gausses)
1.1	245	1.2	245	1.1	165
2.3	325	2.3	285	2.2	245
3.0	410	2.9	320	3.0	320
4.9	565	4.8	590	4.9	415
6.9	890	7.2	815	7.0	560
9.0	1430	8.9	1060	8.9	810
12.1	2730	12.0	1800	12.0	1300
14.9	4060	15.0	3120	14.9	1960
20.2	7620	20.3	6350	20.2	4450
29.8	9820	29.9	9520	29.9	8420
49.0	11470	50.0	11520	65.0	11730
79.0	12440	80.5	12390	80.0	12290
120.0	13180	120.0	13280	120.0	13180
158.0	13580	158.5	13740	160.5	13730
202.0	14070	200.0	14170	199.0	14020

Table 4 Hysteresis loop B mag = 10 kilogauss

No. 1		No. 2		No. 3		No. 4	
Magnetizing force-H (oersteds)	Induction-B (gausses)	Magnetizing force-H (oersteds)	Induction-B (gausses)	Magnetizing force-H (oersteds)	Induction-B (gausses)	Magnetizing force-H (oersteds)	Induction-B (gausses)
11.7	10000	30.0	9900	26.5	9900	39.0	10100
8.0	9230	15.0	9120	20.0	9610	14.8	9040
1.0	6000	5.0	8500	5.0	8600	4.8	8070
0.0	5000	0.0	7650	0.0	7650	0.0	7200
−1.0	3670	−5.0	5850	−9.8	0	−11.6	0
−2.3	0	−10.0	0	−10.0	−775	−19.8	−5860
−2.6	−690	−15.0	−5500	−15.0	−5460	−29.6	−8400
−4.0	−3790	−19.0	−7070	−20.0	−7900	−39.0	−10100
−7.0	−7180	−30.0	−9900	−26.5	−9900		
−11.7	−10000						

No. 5		No. 6		No. 7	
Magnetizing force-H (oersteds)	Induction-B (gausses)	Magnetizing force-H (oersteds)	Induction-B (gausses)	Magnetizing force-H (oersteds)	Induction-B (gausses)
30.0	9900	35.0	10220	40.0	10000
18.6	9450	10.3	9440	20.0	9440
5.0	8820	5.0	9150	5.05	8820
0.0	8300	0.0	8750	0.0	8500
−16.3	0	−18.2	0	−19.3	3700
−17.1	−1250	−19.0	−980	−22.1	0
−19.7	−4150	−25.2	−6600	−29.8	−6760
−25.0	−7930	−35.0	−10220	−35.0	−8400
−30.0	−9900			−40.0	−10000

This means that there can be one curve for ferritic malleable, one for pearlitic malleable, and a third for martensitic malleable. These curves are shown in Fig. 4. As might be expected, the ferritic malleable curve lies above the other two. The main difference between the latter is at low magnetizing force. The data for this part of each curve are plotted in Fig. 5, where the magnetizing force is plotted on an arithmetic scale, not a log scale as in Fig. 4, for easier reading at low magnetizing force.

The curves of Figs. 4 and 5 for ferritic malleable agree reasonably well with previously published curves [1]. The reference paper gave the saturation value of malleable as 18 kilogauss. The present curves were not carried beyond a magnetizing force of 200 oersteds, but there is no reason shown to assume that the saturation value of 18 kilogauss is not still acceptable. It would appear from Fig. 4 that the saturation value of pearlitic and martensitic malleable is the same and slightly lower than that of ferritic malleable.

Permeability, the ratio of induction to magnetizing force, was computed and plotted in Fig. 6 as a function of the magnetizing force on log-log paper. The curves will be discussed later, but for the moment the maximum permeabilities are recorded in Table 7.

The data for hysteresis loops are shown in Table 4 and were taken so that the maximum induction was approximately 10 kilogauss.

A separate hysteresis loop was plotted for each sample. The three curves for pearlitic malleable were close together and the three curves for martensitic malleable were similar to each other. Fig. 7 shows a loop for ferritic malleable and a typical hysteresis curve for pearlitic and martensitic malleable. The curves of Fig. 7 show the increase in hysteresis loss, retentivity, and coercive force, which was to be expected due to the increases in combined carbon. While Fig. 7 is satisfactory for displaying the general relation of the size of the hysteresis loops for the three types of malleable, there are systematic differences which make it necessary to study these loops further. Table 5 gives the essential data for each sample tested. The Steinmetz constant is computed from the equation

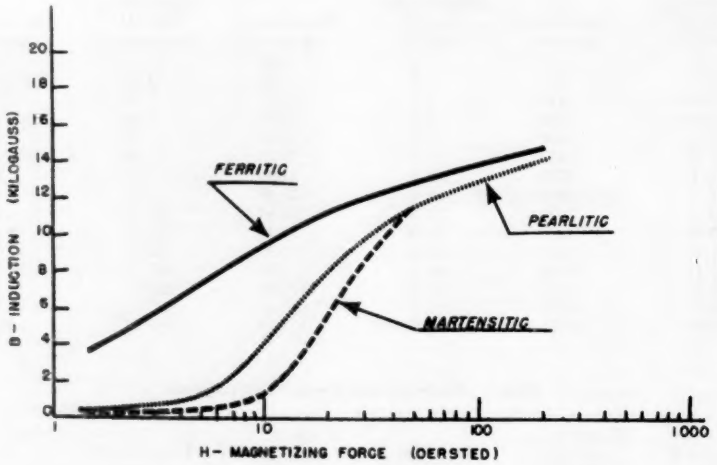

Fig. 4 Induction curves

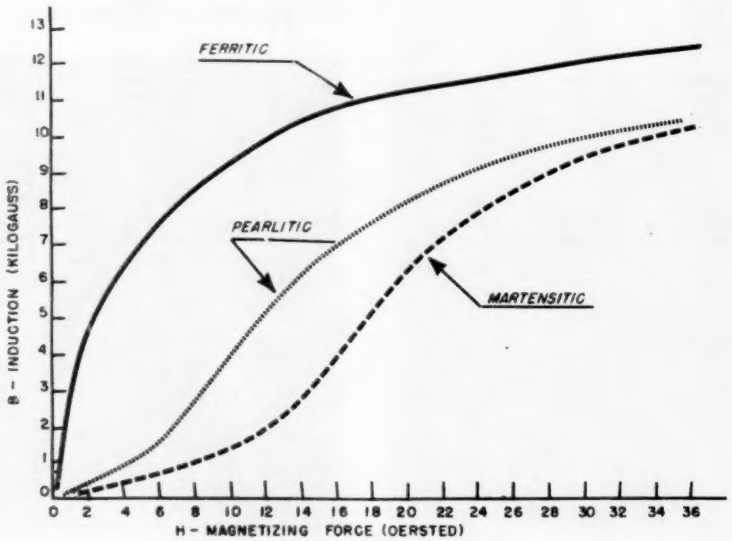

Fig. 5 Induction curves—low magnetizing force

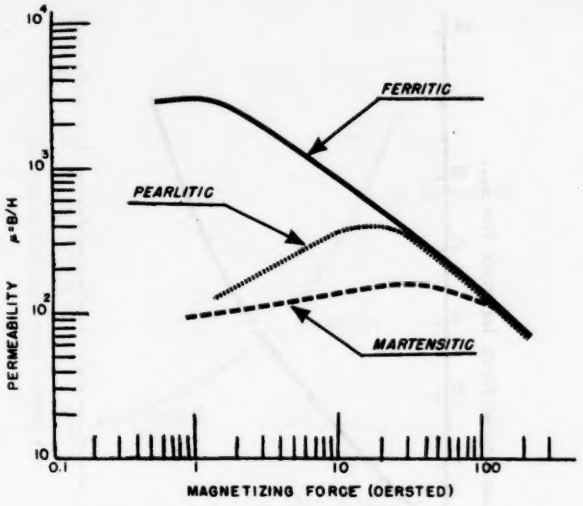

Fig. 6 Permeability

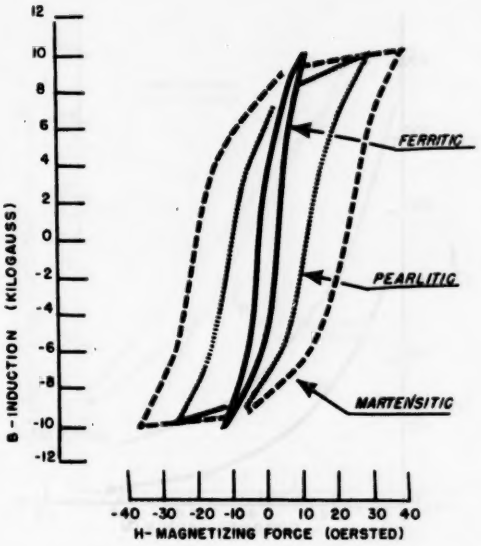

Fig. 7 Hysteresis curves. B = 10000 gausses.

Table 5 Hysteresis data

Sample	Hysteresis loss (ergs/cycle/cm³)	Retentivity (gausses)	Coercive force (oersteds)	Steinmetz constant
1	6400	5000	2.3	0.0025
2	12000	7650	10.0	0.0048
3	11800	7650	9.8	0.0060
4	14500	7200	11.6	0.0057
5	18500	8300	16.3	0.0073
6	21700	8750	18.2	0.0083
7	25500	8500	22.1	0.0102

Table 6 Electrical resistivity

Sample	Type	Resistivity (microhm-in.)	Average
1	Ferritic	14.14	14.14
2	Pearlitic	15.78	
3	Pearlitic	15.74	
4	Pearlitic	16.29	15.94
5	Martensitic	16.24	
6	Martensitic	16.25	
7	Martensitic	16.28	16.26

$$W = hB^{1.6}$$

where h is the constant, W is the hysteresis loss in ergs per cycle per cubic centimeter, and B is the maximum induction in gausses. These data will be discussed further in the next section.

There is one electrical property, resistivity, which is used in magnetic designs. To make the data complete, this property is listed in Table 6. The value of resistivity for ferritic malleable agrees very well with the value published earlier [1].

Discussion

In discussing the results obtained, it is convenient to refer to data in the literature on the magnetic properties of iron and steel. When making such reference, it must be remembered that the magnetic properties of the malleables will not be as high as those of iron or steel. It was pointed out in discussing the properties of malleable iron that only a part of the cross section is magnetically active because of the presence of graphite in the metal. Pearlitic and martensitic malleables are graphitic steels and should behave as steel if due allowance is made for the effect of graphite.

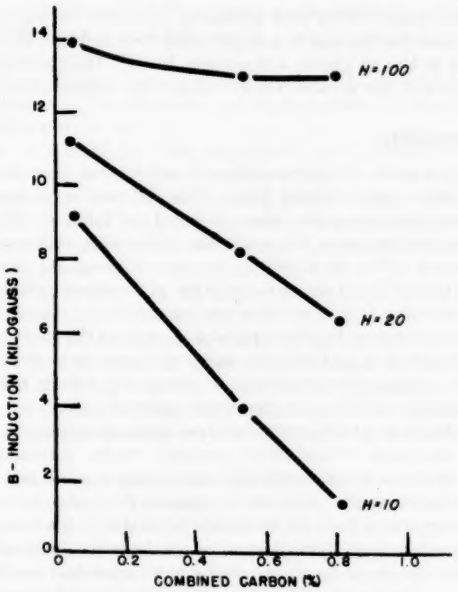

Fig. 8 Effect of combined carbon on induction

B-H Curves

It was observed (Fig. 5) that, at low magnetizing force, the ferritic malleable had a higher induction than the pearlitic malleable, which in turn had a higher induction than the martensitic malleable. This difference between pearlitic and martensitic malleables disappears at a magnetizing force of between 50 and 60 oersteds (Fig. 4). Furthermore, it can be seen that the difference between ferritic and the other two malleables decreases as the magnetizing force increases. From Table 2 it can be seen that the average carbon for ferritic malleable is 0.05 per cent, for pearlitic malleable 0.54 per cent, and for martensitic malleable 0.81 per cent. Using these figures and the values of induction at magnetizing forces of 10, 20, and 100 oersteds, Fig. 8 was prepared.

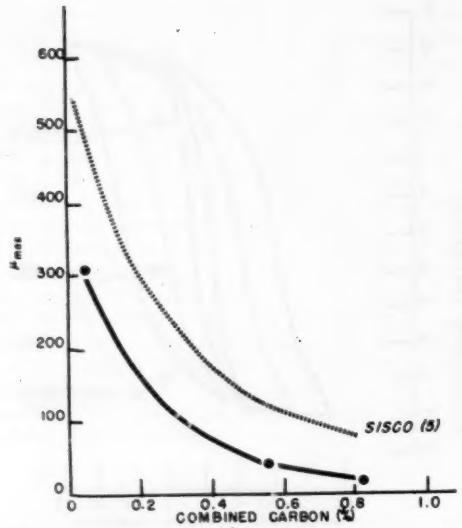

Fig. 9 Maximum permeability as a function of combined carbon

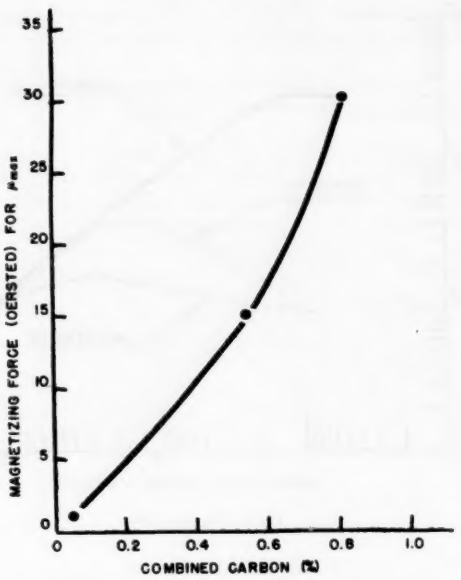

Fig. 10 Effect of combined carbon on magnetizing force for maximum permeability

This graph shows that increasing combined carbon content decreases the response to a magnetizing force and that the carbon effect is less at higher magnetizing forces. Qualitatively, this agrees with the work of Yensen [4] on iron-carbon-silicon alloys.

Permeability

Fig. 6 shows the permeability of each type of malleable as a function of magnetizing force. The differences in maximum permeability are shown and are noted in Table 7. Sisco [5] shows that, for steels, the maximum permeability decreases with increased carbon as shown by the dotted line of Fig. 9. The solid line of Fig. 9 shows the relation of maximum permeability of malleables as a function of combined carbon. The fact that the two curves of Fig. 9 are parallel shows that the effect of combined carbon in malleable is exactly the same as in steel. The lower position of the malleable curve merely reflects the effect of graphite on the ease of passage of magnetic lines.

In Fig. 6 it is to be noted that the magnetizing force at which the maximum permeability occurred varies systematically. Fig. 10 shows this magnetizing force plotted as a function of the combined carbon. Although it appears from this figure that the magnetizing force for maximum permeability is a function of combined carbon, there is some reason to believe that this apparent relation is spurious. Jackson [6] examined steels with carbon contents between 0.10 and 0.34 per cent and showed that all steels, either normalized or annealed, had essentially the same magnetizing force for maximum permeability in a given condition of heat-treatment. The maximum permeability itself varied as a function of carbon. From this work we might argue that the differences in magnetizing force for maximum permeability in Fig. 10 are, therefore, not related to the combined carbon, but are merely reflections of the different microstructures. If this argument is accepted, then we have one more example of where the pearlitic and martensitic malleables are behaving like steel.

Hysteresis Loss

In connection with Table 5, it was noted that the hysteresis curves could not be grouped as the induction curves were. Fig. 7 showed the progressive increase in hysteresis loss from ferritic to pearlitic to martensitic malleable, but in each group it was found that there was a progressive increase in hysteresis properties with increased hardness. For this reason, individual samples must be considered in studying the hysteresis curves.

As a first approximation, it is natural to plot the hysteresis loss against combined carbon (Fig. 11). As might be expected from the knowledge of the effect of carbon in steel, the hysteresis loss of malleable increases with increased combined carbon.

As a means of demonstrating the similarity between steel and the malleables in the behavior of carbon, Fig. 11 is satisfactory but, as was seen in Table 2, the combined carbon does not vary widely for a given type of malleable. Malleables are not made

Table 7 Magnetic properties of malleable irons

	Ferritic	Pearlitic	Martensitic	Dynamo steel
Brinell range		163–241	179–269	
Saturation (gausses)	18000	<18000	<18000	21400
Maximum permeability	3100	430	170	6000
Magnetizing force for μ max (oersteds)	11	15	30.5	
Hysteresis loss $B = 10$ (ergs/cycle/cm^3)	6400	10000–16500	15000–26000	
Retentivity $B = 10$ (gausses)	5000	6500–8500	6900–8800	8500
Coercive force $B = 10$ (oersteds)	2.3	7.5–15	11–22	5.0
Steinmetz constant	0.0025	0.0043–0.0072	0.0059–0.0102	
Electrical resistivity (microhm-in.)	14.14	15.94	16.26	

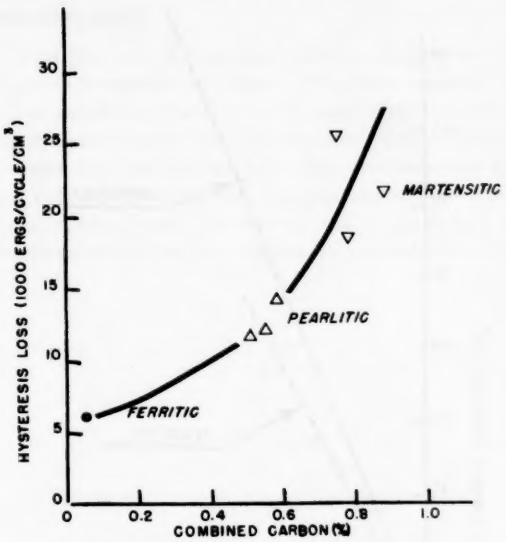

Fig. 11 Hysteresis loss of malleable irons

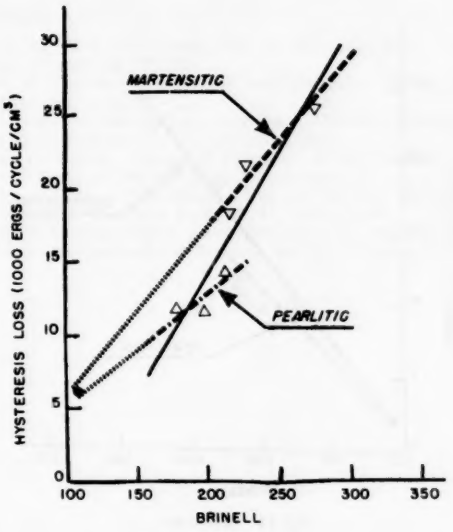

Fig. 12 Hysteresis loss

to a specific combined carbon and so some other relation for hysteresis loss would be of more use to both designer and producer.

From the user's viewpoint, Brinell is important because most of the useful mechanical properties are functions of Brinell and Brinell is often used as an inspection tool by the purchaser. From the producer's viewpoint, Brinell is also important since it is used frequently as a means of control of the process.

In steel, it is a well-known fact that the harder or stronger the steel, the more it behaves as a hard, magnetic alloy. Therefore Brinell is a reasonable gage to be applied to magnetic properties.

Fig. 12 shows the relation of hysteresis loss to Brinell. Disregarding the solid point which represents the ferritic iron, the relation as a first approximation is shown by the solid line. A better fit can be obtained, however, if one curve (the dot-dash line) is used for pearlitic malleable and the other (dashed line) is used for martensitic malleable.

The curves for both malleables were extended to low Brinell to illustrate an interesting point. If either a pearlitic or martensitic malleable were tempered enough, it would become ferritic malleable. If the curve for pearlitic malleable or the one for martensitic malleable in Fig. 12 is extended, the point for ferritic malleable fits well on either curve.

Other Hysteresis Data

Since Brinell is an acceptable test for both producer and purchaser, and since the hysteresis loss was shown to be indicated by Brinell, there is some point in plotting the other hysteresis data against hardness. Fig. 13 shows the coercive force as a function of Brinell. Again, there are preferably two curves, one for martensitic and one for pearlitic and the extensions of these curves fit to the solid dot which represents ferritic malleable.

The same situation obtains in Fig. 14, where the Steinmetz constant is plotted against Brinell.

When retentivity is plotted against Brinell (Fig. 15), one curve can be drawn to fit all the points.

Conclusions

Ferritic or standard malleable iron has an ideal microstructure and composition for a machinable soft, magnetic alloy, since it consists of graphite in an iron matrix which contains practically no combined carbon and does contain 1.0 to 1.5 per cent silicon. Compared to pure iron or silicon iron, malleable has a lower saturation and lower maximum permeability. It has close to the same hysteresis characteristics and higher resistivity; therefore, lower eddy current loss.

There is a need for cast magnetic alloys and only ferritic malleable iron and dynamo steel are available. Dynamo steel is difficult to cast and its machinability is poor. Malleable in all types, on the other hand, is produced at an annual rate of just under a million tons in this country and its castability and machinability are two of its strong points.

Ferritic malleable, like all magnetically soft alloys, is also soft mechanically. There is no help for this.

White iron is the base from which ferritic malleable is made and when the white iron is given different heat-treatment, it is converted to either pearlitic or martensitic malleable. Thus, from a single starting alloy, the malleable foundry produces a family of products which cover a wide range of hardness and strengths.

The pearlitic and martensitic malleables bear the same relation to ferritic malleable that steels do to iron. They are, in fact, graphitic steels.

Although steels, particularly the higher carbon grades, are not generally considered for soft, magnetic work, some designers have been tempted by the inherent advantages of malleables to use the stronger types even though the magnetic properties are not as good as the properties of ferritic malleable. Data on the magnetic properties were determined to make such a compromise possible. The essential magnetic properties and electrical resistivity are given in Table 7. For comparison, magnetic data on dynamo steel are included in the table.

The Brinell ranges shown in Table 7 are those which are generally available in pearlitic and in martensitic malleable irons. The magnetic data in some cases were extrapolated to cover the full Brinell range. The data of Table 7 can be taken to show the magnetic properties and electrical resistivity of ferritic, pearlitic, and martensitic malleables as produced commercially.

In order to show what sacrifice of magnetic properties would be made for a gain in hardness, Table 8 was prepared. This table gives the essential magnetic properties for the condition that the induction must equal 10 kilogauss. The first column headed

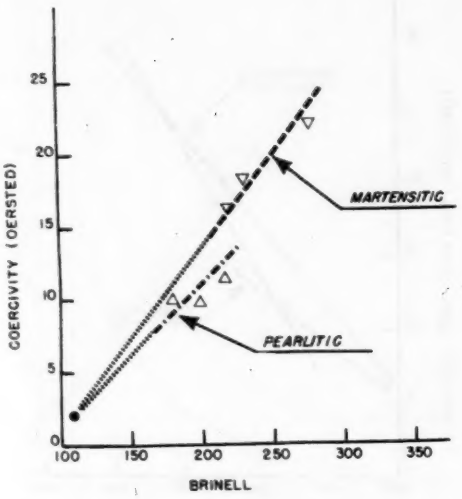

Fig. 13 Coercivity

"Ferritic" shows the properties which would be obtained in a ferritic malleable iron with its low Brinell of 109. The second and third columns together show the properties when the hardness is increased to 212. The second column gives the properties if a pearlitic iron is chosen and the third column gives the properties of a martensitic iron of the same hardness.

It is possible in some cases to obtain a given hardness either in the martensitic malleable or pearlitic malleable. As shown in Table 8, the magnetic properties in such a case are better if a pearlitic malleable is specified.

In malleable, as in steel, the higher strengths and hardnesses can only be attained by quenching. Table 8 shows the magnetic properties which are obtained with a martensitic malleable of hardness of 260. As might be expected from the foregoing discussion, the increased hardness is made only at the sacrifice of certain magnetic properties, notably, hysteresis loss, coercive force, and retentivity.

From this example we can draw certain conclusions; namely, that, if a given hardness can be attained in either the pearlitic or martensitic types, pearlitic malleable is to be preferred and, if either of these types is used, the lowest possible Brinell should be specified.

As might be expected, the pearlitic and martensitic malleables investigated here have behaved like unalloyed steel. The response to magnetizing force and maximum permeability followed exactly the relations in steel of different carbon contents. The magnetizing force for maximum permeability seemed to be influenced by microstructure, as in the case of steels. The data from the hysteresis curves varied according to carbon content as would be expected in steels, but in seeking a more useful parameter for judging the values, it was found that Brinell furnished a good gage of hysteresis loss, coercive force, Steinmetz constant and retentivity. One relation was enough for retentivity, but in the case of the other three, two relations, one for pearlitic malleable and the other for martensitic malleable, were needed. Extrapolation of these latter relations to low hardness values showed that the curves coincided with the data from ferritic malleable.

Finally, it can be concluded that pearlitic malleable and martensitic malleable are essentially graphitic steels and behave as steel in magnetic tests. The difference between one of these malleables and steel of equal carbon content can be due to the presence of graphite.

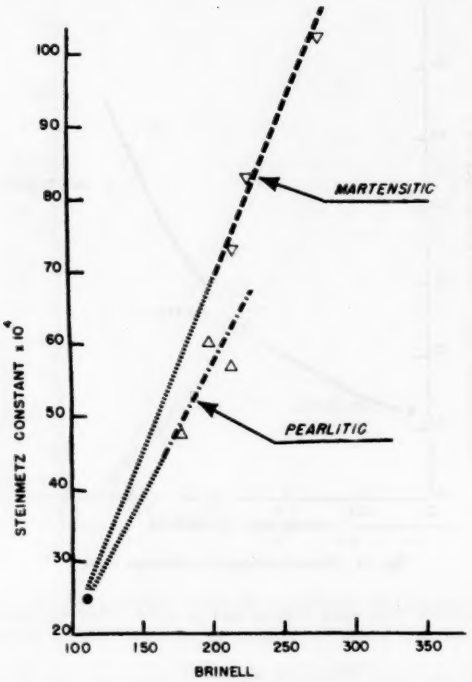

Fig. 14 Steinmetz constant

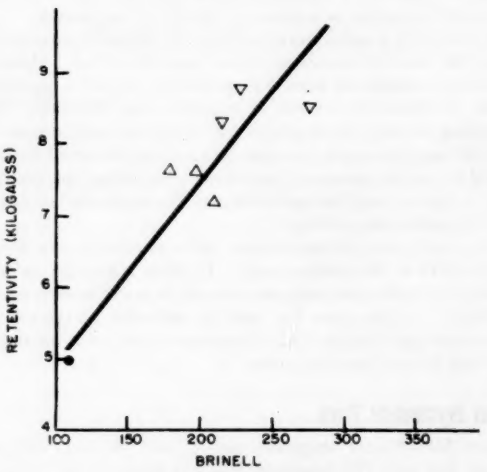

Fig. 15 Retentivity

Table 8 Comparison of malleable irons for 10 kilogauss induction

	Ferritic	Pearlitic	Martensitic	
Brinell	109	212	212	260
Magnetizing force (oersted)	12	30	35	35
Permeability	800	340	160	160
Electrical resistivity (microhm-in.)	14.14	15.94	16.21	16.21
Hysteresis loss (erg/cycle/cm³)	6	14	18.5	24
Coercive force (oersted)	2	12.5	15.5	21
Retentivity (gauss)	5000	7700	7700	9000

Acknowledgments

The authors wish to thank the Malleable Research and Development Foundation of Dayton, Ohio, who sponsored this work as part of their extensive investigation on the properties of these irons, and National Malleable and Steel Castings Company for design of the test castings and production of them, and Electrical Testing Laboratories, Inc., for permitting use of their name in this report. Finally, the authors wish to thank both the Foundation and the National Company for permission to publish.

References

1 W. K. Bock, "Malleable Iron—A Magnetic Alloy," *Trans. AFS*, vol. 67, 1959, pp. 199–206.

2 T. D. Yensen, "Magnetically Soft Materials," Metals Handbook, 1948 edition, pp. 587–595.

3 Modern Pearlitic Malleable Handbook, Malleable Research and Development Foundation, Dayton, Ohio, 1958.

4 T. D. Yensen, "Magnetic Properties of the Ternary Alloys Fe-Si-C," *Trans. AIEE*, vol. 43, 1924, pp. 145–175.

5 Frank T. Sisco, "The Alloys of Iron and Carbon," McGraw-Hill Book Company, Inc., New York, vol. II, 1937, p. 598.

6 W. J. Jackson, "Effect of Heat-Treatment on Magnetic Properties," *Journal of Iron and Steel Institute*, vol. 194, 1960, pp. 29–36.

ERIC E. UNGAR
Senior Engineering Scientist,
Bolt Beranek and Newman, Inc.,
Cambridge, Mass. Assoc. Mem. ASME

Free Oscillations of Edge-Connected Simply Supported Plate Systems

A simple semigraphical method for calculating the natural frequencies of two-plate systems is developed, a two-plate system being one made up of two rectangular plates simply supported at all edges and joined at a common edge. Charts for easy determination of the afore-mentioned natural frequencies are developed. One of these gives, as a by-product, the natural frequencies of rectangular plates (of any dimensions) having one edge clamped, the remaining three simply supported. It is demonstrated that the higher natural frequencies of two-plate systems are very nearly equal to those of the individual component plates. Equations for the mode shapes are also given.

Introduction

Many practical structures, such as submarine or surface vessel hulls and aircraft or missile fuselages, are made up of plates with multiple relatively rigid reinforcements. The various subplates between the stiffeners are not likely to oscillate independently of each other in general, and the interaction of these subplates may be of major importance in determining the responses of the total structure.

The prevalence of multiple beam-reinforced plate construction has caused several investigators to be concerned with the coupled oscillation problem. Rectangular plates which are hinged along two opposite edges and continuous over-rigid supports perpendicular to the hinged edges were treated by Veletsos and Newmark.[1] They developed a numerical procedure for calculating the natural frequencies which is analogous to the well-known method of Holzer for torsional vibrations of shafts. Dill and Pister[2] have presented a detailed analysis of structures that can be considered as composed of a number of rectangular plate elements and have developed a rather elegant procedure for obtaining the equations which govern the natural frequencies of plates like those treated by Veletsos and Newmark. However, the afore-mentioned investigators did not present an over-all view of the trends of the natural frequencies of composite plate structures. The subsequent analysis is intended as a first step toward filling this gap and thus toward providing the "feel for the problem" so necessary to the practical engineer.

The present paper deals essentially with a rectangular plate which is simply supported on all four edges and which rests on an additional simple support placed parallel to and between a pair of edges. Although the frequency-governing equation may be obtained by suitable specialization of the previously cited work of Dill and Pister, the subsequent discussion begins with a derivation of this equation. This inclusion was thought desirable in order to provide the reader with a convenient view of the analysis (the elegance and breadth of the afore-mentioned work may tend to obscure the details to some extent) and to present the results in a form more readily adapted to the subsequent discussion.

[1] A. S. Veletsos and N. M. Newmark, "Natural Frequencies of Continuous Plates," *Journal of Applied Mechanics*, vol. 23, TRANS. ASME, vol. 78, 1956, pp. 97–102.

[2] E. H. Dill and K. S. Pister, "Vibrations of Rectangular Plates and Plate Systems," Proceedings of Third Midwestern Conference on Solid Mechanics, 1957, pp. 123–132.

Contributed by the Machine Design Division and presented at the Winter Annual Meeting, New York, N. Y., November 27–December 2, 1960, of THE AMERICAN SOCIETY OF MECHANICAL ENGINEERS. Manuscript received at ASME Headquarters, July 27, 1960. Paper No. 60—WA-112.

The Frequency Equation

Consider a rectangular plate of dimensions $(a + c) \times b$ simply supported on all four edges, with a co-ordinate system attached to the plate as shown in Fig. 1. If an additional simple support is added along the y-axis, then the motion of the original plate may be analyzed as if it were two plates, provided the proper conditions of juncture at $x = 0$ are taken into account.

It is assumed that the plate deflection η obeys the classical equation of free undamped plate motion,

$$\nabla^4\eta + K^2 \frac{\partial^2\eta}{\partial t^2} = 0, \tag{1}$$

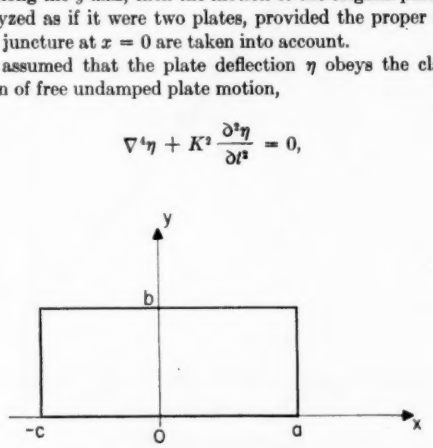

Fig. 1 Plate dimensions and co-ordinates

Nomenclature

a, b, c = plate edge dimensions (see Fig. 1)
A_n, B_n, C_n, D_n = constants
$D = Eh^3/12(1 - \nu^2)$, plate flexural rigidity
E = Young's modulus
$F_n(x), f_n(x), g_n(x)$ = deflection functions (Eqs. 4, 8)
h = plate thickness
$H(\alpha\gamma), h(a\alpha)$ = computation functions (Eqs. 11, 13)
$K = \sqrt{\rho h/D}$
n, m, m' = integers
t = time
x, y = Cartesian co-ordinates
$\alpha_n, \beta_n, \gamma_n$ = mode parameters (Eq. 7)
η = normal deflection of plate mid-plane
ν = Poisson's ratio
ρ = material density
ω = circular frequency

where K is a constant for a given plate[3] and t denotes time. If the plate oscillates at one of its natural frequencies ω, all points on it move in phase and one may employ the usual convention of complex notation to write

$$\eta(x, y, t) = \bar{\eta}(x, y)e^{i\omega t}. \tag{2}$$

The latter permits Eq. (1) to be reduced to

$$\nabla^4\bar{\eta} - \omega^2K^2\bar{\eta} = 0. \tag{3}$$

An arbitrary plate deflection may conveniently be expressed as a Fourier sine series in terms of y in view of the simple supports postulated at $y = 0, b$. Thus, one may set

$$\bar{\eta}(x, y) = \sum_{n=1}^{\infty} f_n(x) \sin (n\pi y/b) \tag{4}$$

and substitute this into Eq. (3) to obtain

$$\sum_{n=1}^{\infty}\left[\frac{d^4f_n}{dx^4} - 2\left(\frac{n\pi}{b}\right)^2\frac{d^2f_n}{dx^2} + \left\{\left(\frac{n\pi}{b}\right)^4 - K^2\omega^2\right\}f_n\right]\sin\frac{n\pi y}{b} = 0. \tag{5}$$

This last equation must hold for all values of y; hence, each of the bracketed terms must vanish individually. This last requirement results in a set of differential equations which the functions f_n must satisfy. The general solution of the nth such differential equation may be expressed as

$$f_n(x) = A_n \exp(\alpha_n x) + B_n \exp(-\alpha_n x) + \begin{cases} \bar{C}_n \exp(\beta_n x) + \bar{D}_n \exp(-\beta_n x), & \beta_n^2 > 0 \\ \bar{C}_n + \bar{D}_n x, & \beta_n^2 = 0 \\ C_n \sin(\gamma_n x) + D_n \cos(\gamma_n x), & \beta_n^2 < 0 \end{cases} \tag{6}$$

where $A_n, B_n, C_n, D_n, \bar{C}_n, \bar{D}_n, \bar{C}_n, \bar{D}_n$, are constants and the coefficients α_n and β_n obey

$$\left.\begin{aligned} \alpha_n^2 &= (n\pi/b)^2 + K\omega \\ \beta_n^2 &= -\gamma_n^2 = (n\pi/b)^2 - K\omega. \end{aligned}\right\} \tag{7}$$

For the double-plate arrangement of Fig. 1 it is convenient to think of the two component plates separately and to write

$$\bar{\eta}(x, y) = \sum_{n=1}^{\infty} F_n(x) \sin (n\pi y/b) \tag{8}$$

$$F_n = \begin{cases} f_n(x), & x > 0 \\ g_n(x), & x < 0 \end{cases}$$

where $g_n(x)$ is of the same form as $f_n(x)$, except that the constants may assume different values in the two regions of the plate. Henceforth, primed constants will be taken to refer to g_n and unprimed constants to f_n.

One may easily verify that the foregoing deflections satisfy identically the conditions of zero deflection and zero moment at $y = 0, b$. The requirements of zero deflection and moment at $x = -c, a$, of continuity of moment and slope at the middle support ($x = 0$), and of zero deflection of that support impose eight conditions on $\bar{\eta}(x, y)$. Since the boundary conditions hold for all values of y, they may be reduced to the following set of requirements on f_n and g_n (where the primes denote differentiation with respect to x):

$$\left.\begin{aligned} f_n(a) = f_n''(a) = g_n(-c) = g_n''(-c) = f_n(0) = g_n(0) = 0, \\ f_n'(0) - g_n'(0) = 0, \quad f_n''(0) - g_n''(0) = 0. \end{aligned}\right\} \tag{9}$$

Substitution of Eq. (6) for f_n and a similar expression (with primed constants) for g_n into Eq. (9) results, for any given β_n, in a set of eight homogeneous linear equations in terms of eight constants. Such a set of equations has nonzero solutions if, and only if, the determinant of the coefficients vanishes. This condition on the determinant leads to the following frequency-determining equations after some algebraic manipulation:

$$h(a\alpha_n) = h(a\beta_n), \quad \beta_n^2 > 0 \tag{10a}$$

$$\frac{1}{2a\alpha_n} + \frac{1}{1 - \exp(2\alpha_n a)} = \frac{\exp(2\alpha_n c)}{\exp(2\alpha_n c) - 1} - \frac{1}{2c\alpha_n}, \quad \beta_n = 0 \tag{10b}$$

$$(a\gamma_n)\sin(a\gamma_n + c\gamma_n) = \sin(a\gamma_n)\sin(c\gamma_n)\cdot h(a\alpha_n), \quad \beta_n^2 < 0. \tag{10c}$$

The function $h(a\xi)$, introduced here for the sake of convenience, is defined by

$$h(a\xi) \equiv \frac{(a\xi)\sinh(a\xi + c\xi)}{\sinh(a\xi)\cdot\sinh(c\xi)}. \tag{11}$$

This function is found to be symmetric, to be positive everywhere, and to increase monotonically with the absolute value of the argument. Consequently, Eq. (10a) can be satisfied only when $\alpha_n = \beta_n$. In view of Eq. (7), this condition corresponds to the trivial case of $\omega = 0$, which is of no interest in the present analysis.

It may also readily be shown that the function of the left-hand side of Eq. (10b) can only assume values between 0 and $^1/_2$ whereas the right-hand side can only take on values between $^1/_2$ and 1, and that the equation can be satisfied only when $\alpha_n = 0$. But from Eq. (7) one finds that $\alpha_n = \beta_n = 0$ implies $\omega = n = 0$, so that satisfaction of Eq. (10b) again occurs only for the trivial case.

Only Eq. (10c), which corresponds to $\beta_n^2 < 0$, need be considered further. Inspection of this equation reveals that it is satisfied by any value of α_n, provided that $\sin(a\gamma_n) = \sin(c\gamma_n) = 0$. If these two sine terms do not vanish, it is convenient to rewrite Eq. (10c) as

$$H(a\gamma_n) = h(a\alpha_n), \tag{12}$$

where $h(a\alpha_n)$ is defined in Eq. (11) and $H(a\gamma_n)$ is defined as

$$H(a\gamma_n) \equiv \frac{(a\gamma_n)\sin(a\gamma_n + c\gamma_n)}{\sin(a\gamma_n)\sin(c\gamma_n)} = (a\gamma_n)[\cot(a\gamma_n) + \cot(c\gamma_n)]. \tag{13}$$

The solutions of Eq. (12) and those of Eq. (10c) with vanishing sine terms are discussed subsequently.

Mode Shapes

In view of the foregoing discussion, for a nonzero natural frequency ω the plate deflection η_n corresponds to $\beta_n^2 < 0$ and may be expressed as

$$\eta_n(x, y) = F_n(x) \sin (n\pi y/b), \tag{14}$$

with F_n as given in Eq. (8), and

$$f_n = A_n \exp(\alpha_n x) + B_n \exp(-\alpha_n x) + C_n \sin(\gamma_n x) + D_n \cos(\gamma_n x), \tag{15}$$

[3] $K^2 = \rho h/D$; where h, D, ρ denote plate thickness, flexural rigidity, and material density, respectively. Also, $D = Eh^3/12(1 - \nu^2)$, where E and ν denote the Young's modulus and Poisson's ratio of the material.

$$g_n = A_n' \exp(\alpha_n x) + B_n' \exp(-\alpha_n x) + C_n' \sin(\gamma_n x) + D_n' \cos(\gamma_n x). \quad (15)\ \textit{cont.}$$

The eight relations of Eqs. (9) reduce to a set of eight homogeneous equations in terms of the eight constants. Since the determinant of the coefficients of these constants vanishes for natural frequencies ω, one may discard any one of the eight equations and solve the remaining seven for the magnitudes of any seven of the constants in terms of the eighth.

One finds that for $\cos(a\gamma_n) \neq 0$,

$$\frac{A_n}{C_n} = \frac{\tan(a\gamma_n)}{1 - \exp(2a\alpha_n)}; \qquad \frac{B_n}{C_n} = -\frac{A_n}{C_n}\exp(2a\alpha_n);$$

$$\frac{D_n}{C_n} = \frac{D_n'}{C_n} = -\tan(a\gamma_n); \quad \frac{A_n'}{C_n} = \tan(a\gamma_n) - \left(\frac{B_n'}{C_n}\right);$$

$$\frac{C_n'}{C_n} = \frac{\dfrac{\gamma_n}{2\alpha_n} + \left[\dfrac{\exp(2a\alpha_n)}{1 - \exp(2a\alpha_n)} + \dfrac{1 - \exp(\alpha_n c)\cos(\gamma_n c)}{1 - \exp(2\alpha_n c)}\right]\tan(a\gamma_n)}{\dfrac{\gamma_n}{2\alpha_n} + \dfrac{\exp(2\alpha_n c)\sin(\gamma_n c)}{1 - \exp(2\alpha_n c)}}; \quad (16)$$

$$\frac{B_n'}{C_n} = \frac{1}{1 - \exp(2\alpha_n c)}\left[\{1 - \exp(\alpha_n c)\cos(\gamma_n c)\}\tan(a\gamma_n) - \exp(\alpha_n c)\cdot\sin(\gamma_n c)\left(\frac{C_n'}{C_n}\right)\right];$$

and for $\cos(a\gamma_n) = 0$,

$$C_n = 0; \quad \frac{B_n}{A_n} = -\exp(2\alpha_n a); \quad \frac{A_n'}{A_n} = 1 - \frac{\gamma_n}{2\alpha_n}\left(\frac{C_n'}{A_n}\right);$$

$$\frac{D_n}{A_n} = \exp(2\alpha_n a) - 1 = -\left(1 + \frac{B_n}{A_n}\right);$$

$$\frac{B_n'}{A_n} = -\left(\frac{D_n}{A_n} + \frac{A_n'}{A_n}\right); \quad (17)$$

$$\frac{C_n'}{A_n} = \frac{[1 - \exp(\alpha_n c)\cos(\gamma_n c)][1 - \exp(2\alpha_n a)] + \exp(2\alpha_n a)[1 - \exp(2\alpha_n c)]}{\exp(\alpha_n c)\sin(\gamma_n c) - \dfrac{\gamma_n}{2\alpha_n}[\exp(2\alpha_n c) - 1]}$$

Oscillations at Natural Frequencies of Subplates. For the special case where $\sin(a\gamma_n) = \sin(c\gamma_n) = 0$ one finds from Eqs. (16) that

$$C_n' = C_n, \quad A_n = B_n = D_n = A_n' = B_n' = D_n' = 0. \quad (18)$$

In view of Eq. (15) this implies that f_n and g_n are pure sinusoids of equal amplitude and wave length.

Vanishing of the two sine terms requires that both $a\gamma_n$ and $c\gamma_n$ be integral multiples of π. That is, if $a\gamma_n = m\pi$, then $c\gamma_n = \left(\frac{c}{a}m\right)\pi$, where $\frac{c}{a}m$ must be an integer as well as m. (This means, of course, that a/c must be expressible as a ratio of integers.) Thus, for integral values of m for which $\frac{c}{a}m$ is also an integer, there exist mode shapes

$$\bar{\eta}_{nm}(x, y) = C_{nm} \sin(m\pi x/a) \sin(n\pi y/b). \quad (19)$$

In view of Eq. (7), the frequencies corresponding to such modes are given by

$$K\omega = \left(\frac{n\pi}{b}\right)^2 + \gamma_n^2 = \left(\frac{m^2}{a^2} + \frac{n^2}{b^2}\right)\pi^2. \quad (20)$$

These frequencies are identical to the natural frequencies that the $a \times b$ component plate would have if the other component plate (dimensions $c \times b$) were missing. This can easily be understood in physical terms. The afore-mentioned mode shape implies that at $x = 0$ the bending moment and deflection vanish at all times and that continuity of slope at $x = 0$ of the two component plates is also always maintained. Thus, one plate is unaffected by the other, and each oscillates as if it were present and simply supported by itself.

It may also be noted that, for $c = 0$, Eq. (10c) reduces to $\sin(a\gamma_n) = 0$ and leads to mode shapes as given by Eq. (19), with no restriction on the integers m. Thus, the present analysis reduces to the well-established results for a single plate if c is set equal to zero.

Determination of Other Natural Frequencies

Since the natural frequencies of a given two-plate system may be found by means of Eq. (7) if the values of the α_n or γ_n are known, the problem of finding the natural frequencies may be reduced to that of finding the α_n and/or γ_n.

As pointed out previously, the values of α_n and γ_n for which free sinusoidal (in time) oscillations are possible must satisfy Eq. (10c). The particular values of α_n and γ_n which result in purely sinusoidal (in space) mode shapes and the corresponding frequencies have already been discussed. The remaining values of α_n and γ_n may then be determined by the simultaneous solution of

$$H(a\gamma_n) = h(a\alpha_n) \quad (21)$$

and

$$(a\alpha_n)^2 = (a\gamma_n)^2 + 2(n\pi a/b)^2. \quad (22)$$

The first of the previous two equations is identical to Eq. (12) and is repeated here only for ease of reference; the functions H and h are defined in Eqs. (13) and (11), respectively. Equation (22) is obtained by elimination of $K\omega$ from Eqs. (7).

Equation (21) is transcendental, and hence must be solved by numerical or graphical means. One convenient way of doing this consists of plotting the functions $H(a\gamma_n)$ and $h(a\alpha_n)$ and then obtaining a cross-plot of values of $a\gamma_n$ and $a\alpha_n$ for which these functions take on equal values. This plot then is a graphic representation of one of the two equations to be solved simultaneously for the two unknown parameters. Obtaining a plot to represent Eq. (22) is a simple matter. The intersections of curves representing Eq. (22) with those of the afore-mentioned cross-plot of $a\gamma_n$ versus $a\alpha_n$ then yield sets of values of these two parameters which satisfy the two equations (21) and (22). The entire calculation procedure is illustrated in the next section

Equation (22) represents a set of parabolas in the $a\gamma_n$-$a\alpha_n$ plane. These parabolas are symmetric about the $a\alpha_n$-axis; different parabolas correspond to different values of (na/b), of course. By elimination of $(n\pi/b)^2$ from Eqs. (7) one finds

$$(a\alpha_n)^2 + (a\gamma_n)^2 = 2Ka^2\omega, \quad (23)$$

which indicates that curves of constant $Ka^2\omega$ in the $a\gamma_n$-$a\alpha_n$ plane are circles with centers at the origin. These circles may be used as a means for reading the natural frequencies directly from the afore-mentioned plots.

Some additional simplification may be obtained by use of the

$(a\gamma_n)^2$ versus $(a\alpha_n)^2$ plane instead of the one based on the first powers of these parameters. In this new plane Eq. (22) represents a family of straight lines of positive unit slope, and Eq. (23) a family of straight lines of negative unit slope. However, the square-variable plot generally results in reduced accuracy for a given size of graph paper.

It should also be noted that the functions $H(a\gamma_n)$ and $h(a\alpha_n)$ depend on the ratio c/a, but are independent of b. The dependence on b is introduced only through Eq. (22); hence, a plot representing Eq. (21) for a given value of c/a may be used to determine the natural frequencies for plates with the given c/a ratio, with all a/b ratios.

Illustration: Symmetric Two-Plate System

In order to clarify the procedures involved and to point out some results, it may be useful to consider the special case of identical subplates in some detail. For this symmetric configuration $a = c$. The corresponding function $H(a\gamma_n)$ as given by Eq. (13) then appears as the solid curves of Fig. 2, and $h(a\alpha_n)$ as defined by Eq. (11) appears as the dotted curve of Fig. 2.

From Fig. 2 one may easily determine those values of $a\gamma_n$ which make $H = h$ for any arbitrarily selected value of $a\alpha_n$. A plot of $a\gamma_n$ corresponding to values of $a\alpha_n$ in this manner represents sets of these two parameters that satisfy Eq. (21). The heavy nearly horizontal curves of Fig. 3 are such a plot.

The dotted curves of Fig. 3 are parabolas representing Eq. (22) for different values of na/b; the circular arcs correspond to Eq. (23) for different values of $Ka^2\omega$. Then, for example for $a/b = 1$, one finds that the $m = n = 1$ mode (for plate deflections symmetric about the middle support) corresponds to the intersection of the $m = 1$ horizontal curve with the $na/b = 1$ parabola. This point is marked by a triangle in Fig. 3. By referring to the circles one finds that for this mode $\sqrt{2K\omega}\ (a/\pi)$ is about 2.12, so that one may readily compute the frequency corresponding to this mode for a plate of given thickness, density, and flexural rigidity.

Fig. 4 is similar to Fig. 3, except that the squares of the parameters $a\gamma$ and $a\alpha$ are used as co-ordinates instead of the first powers of these parameters. In Fig. 4 the parabolas of Fig. 3 appear as lines of positive unit slope, whereas the circles of Fig. 3 appear as lines of negative unit slope. The advantage of Fig. 4 in increased ease of plotting and interpolation and its disadvantage in loss of accuracy over Fig. 3 are apparent.

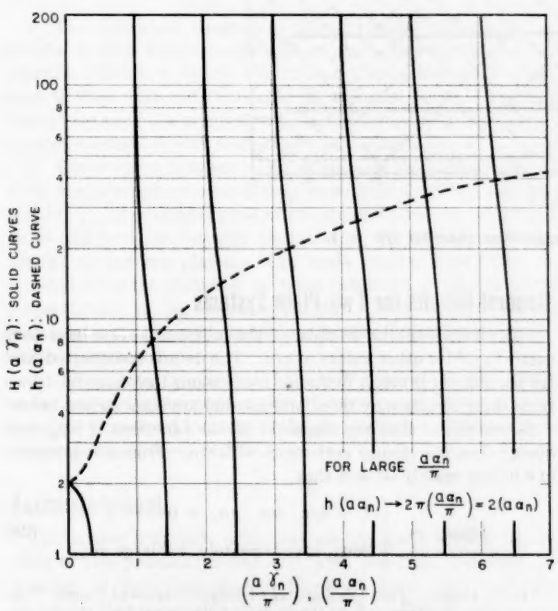

Fig. 2 The functions $H(a\gamma_n)$ and $h(a\alpha_n)$ for $c/a = 1$

All of the afore-mentioned figures were plotted in terms of the variables divided by π in order to make it more obvious that $a\gamma_n/\pi$ approaches integral values m as n increases, and that $a\gamma_n/\pi$ is always greater than m. But $a\gamma_n/\pi = m$, when introduced in Eq. (7), results in the expression (20) for the natural frequency. This expression, as has already been pointed out, corresponds to the natural frequencies of a single simply supported plate with sides a and b. One may thus conclude that the natural frequencies of the two-plate system considered are slightly higher than those of a single plate with all four edges simply supported. The two-plate system frequencies approach those of the single plate more closely for higher mode numbers[4] n and m. This increased "uncoupling" of the two plates with increasing frequency is exactly what one might expect intuitively, since one expects that for shorter wave lengths the boundary effects on a plate are "felt" over a shorter distance.

It is surprising, however, to note how closely the "single-plate frequencies" are approached by the "two-plate frequencies" even at the lower modes. This closeness may be visualized also by means of Fig. 3, where some of the two-plate frequencies for $a/b = 1$ are marked with crosses (i.e., values of $\sqrt{\omega}$ are proportional to lines drawn from the origin to these crosses) and the corresponding single-plate frequencies are similarly indicated by circles nearly below the crosses. Table 1 compares the two-plate natural frequencies determined from Fig. 3 to those for a single plate [Eq. (20)] for the case where $a = b$. From this table it is apparent that the difference in these two values is of the order of 20 per cent only for the 1,1 and 2,1 modes. The difference is 10 per cent or less for $m \geq 5$, $n > 1$, and 5 per cent or less for $n > 2$.

Table 1 Ratios of two-plate to single-plate frequencies[a] for $a = b = c$

n | $m =$	1	2	3	4	5	6
1	1.19	1.06	1.02	1.01	1.00	1.00
2	1.21	1.09	1.05	1.02	1.02	1.01
3	1.14	1.09	1.06	1.03	1.02	1.02
4	1.11	1.09	1.06	1.04	1.03	1.02
5	1.10	1.08	1.06	1.05	1.03	1.02
6	1.08	1.07	1.06	1.05	1.04	1.02

[a] "Two-plate frequencies" are frequencies of free oscillations, symmetric about $x = 0$, of a two-plate system (Fig. 1). Here $a = b$, and the two-plate frequencies are equal to those of a single square plate which is simply supported on three edges and built-in on the fourth. "Single-plate frequencies" are the natural frequencies of a single square plate, simply supported on all four edges.

The mathematically demonstrated fact that the two-plate frequencies are always somewhat higher than those of a single plate also agrees with physical reasoning, since for the mode shapes symmetric about $x = 0$ the action of one plate on the other is to make the $x = 0$ boundary condition "built-in" instead of simply supported, thus increasing the stiffness and hence the natural frequencies of the system.

One must be careful to note that calculations carried out with Figs. 3 and 4 pertain only to those modes which are symmetric about $x = 0$. The anti-symmetric modes do not obey Eq. (21); for these modes the two plates are essentially uncoupled and the frequencies are given by Eq. (20).

In view of the symmetry mentioned in the foregoing discussion, Fig. 3 applies also to a single plate which is simply supported on

[4] Although the absolute error increases with increasing m, the per cent error appears to decrease with m for values of m greater than some critical value which depends on n.

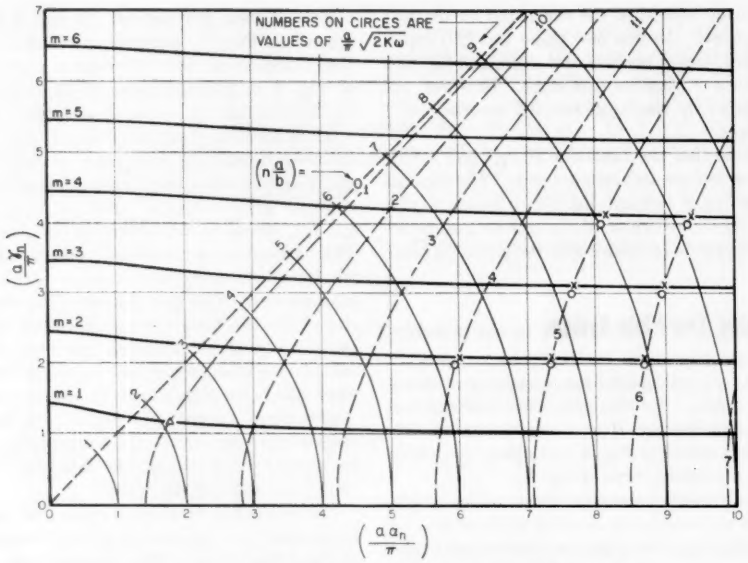

Fig. 3 Two-plate frequency computation chart for $c/a = 1$

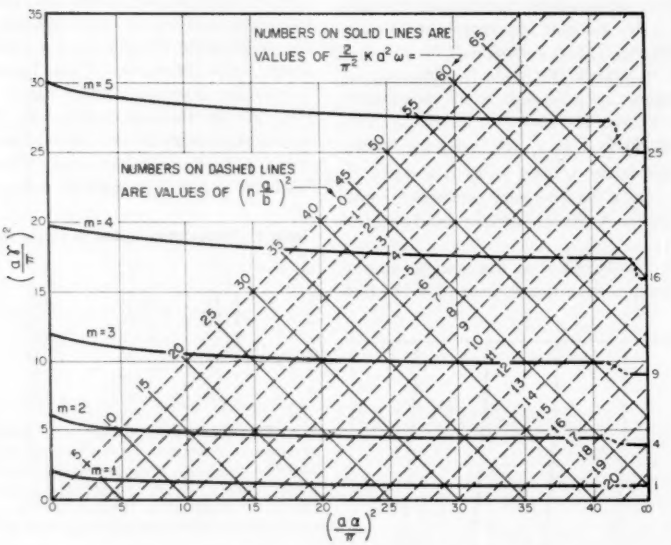

Fig. 4 Alternate frequency computation chart for $c/a = 1$

three of its edges and clamped on the fourth. The charts of Figs. 3 or 4 may thus be used directly to determine the natural frequencies of such a plate for any given geometry.

Calculations for the lowest few modes of a square steel plate and for the first mode of some rectangular plates have been carried out and were found to lead to values which agree substantially with those listed by Macduff and Felgar.[5] The small discrepancies observed undoubtedly are due to the inaccuracies introduced by the semigraphical nature of the present solution; however, the present method does have the advantages of permitting rapid evaluation of many of the natural frequencies and of providing an insight into the over-all trends associated with these frequencies.

General Results for Two-Plate Systems

Calculations similar to those of the previous section have been carried out[6] for other values of c/a. The details are omitted here for the sake of brevity, but some conclusions that may be drawn from these results may be of interest and are summarized below.

It was found that the character of the functions $H(a\gamma_n)$ and $h(a\alpha_n)$ does not change very much with c/a. From the definition of h it may readily be seen that

$$h(a\alpha_n) = \begin{cases} 1 + a/c & \text{for } a\alpha_n = 0 \\ 2a\alpha_n, \text{ approximately, for large } a\alpha_n, \end{cases} \tag{24}$$

[5] J. N. Macduff and R. P. Felgar, "Vibration Design Charts," TRANS. ASME, vol. 79, 1957, p. 1459.

[6] E. E. Ungar, "Free Oscillations of Edge-Connected Simply Supported Plate Systems," Bolt Beranek and Newman, Inc., Report No. 721, January, 1960.

and hence that h is independent of a/c for large values of the argument. Similarly, from the definition of H one finds that this function takes on large positive values only when $a\gamma_n = m\pi^+$ and/or $c\gamma_n = m'\pi^+$, where m and m' are integers. Thus, to large values of $a\alpha_n$ (say, $a\alpha_n > 3\pi$) there correspond the values

$$a\gamma_n = m\pi^+ \quad \text{or} \quad c\gamma_n = m'\pi^+; \quad m, m' = 1, 2, 3, \ldots \tag{25}$$

where the plus superscript is intended to indicate a value slightly greater than that corresponding to the symbol without superscript. For these values Eq. (7) gives the natural frequencies

$$\omega_{mn} = \frac{\pi^2}{K}\left(\frac{m^{+2}}{a^2} + \frac{n^2}{b^2}\right); \quad \omega_{m'n} = \frac{\pi^2}{K}\left(\frac{m'^{+2}}{c^2} + \frac{n^2}{b^2}\right) \tag{26}$$

which are slightly higher than those of single plates of dimensions $a \times b$ and $c \times b$, respectively. One may conclude thus once more that the higher natural frequencies of two-plate systems are nearly equal to, but slightly greater than, those of the two component plates; a fact which again agrees with physical reasoning.

The frequencies corresponding to modes for which $\frac{c}{a}m$ is an integer and which are anti-symmetric about the common support at $x = 0$ are found to be exactly equal to those of a single plate. In view of the nature of the function H, Eq. (26) is found to give a poorer approximation for those m-modes symmetric about $x = 0$ for which cot $(a\gamma)$ and cot $(c\gamma)$ are of the same order of magnitude, i.e., for values of m which are integral multiples of a/c. For modes symmetric about $x = 0$ and corresponding to integral values of cm/a, however, the frequencies are found to be exactly equal to those of a single plate.

Conclusion; Extrapolation for n Plate Systems

Although the previously discussed results were derived only for systems consisting of two plates, physical reasoning lends credence to the extrapolation of the conclusions to multiple plate systems. Some of these conclusions may have been considered "intuitively obvious," but it should be reassuring that these statements are validated mathematically at least to some extent. The general conclusions may be summarized as follows:

1 The individual component plates become effectively uncoupled at their higher modes. These plates then oscillate at frequencies which are slightly higher than those which they would have if they were not connected to adjacent plates. The difference between the coupled and uncoupled natural frequencies generally decreases with increasing mode number.

2 The coupling between adjacent plates is most significant for those modes which are most nearly symmetric about the common support (in the neighborhood of the support) and for which the mode numbers are integral multiples of the ratio of the edge lengths of the two plates. [The mode numbers are those associated with the variation of plate deflection in the direction perpendicular to the common support. The edges to whose length ratio was referred are those extending perpendicular to the common support.]

3 The natural frequencies of the system are identical to those of any one of the component plates for those modes for which all supports correspond to nodes of the whole system considered as a single edge-supported plate.

Acknowledgment

The author gratefully acknowledges the many helpful discussions of this problem he had with Drs. Ira Dyer and Peter A. Franken of Bolt Beranek and Newman, Inc. The work presented in this paper was sponsored by the Office of Naval Research, Acoustics Branch, under ONR Contract NOnr 2322(00).

DISCUSSION

Raymond N. House, Jr.[7]

Many complex structures, e.g., missile or aircraft fuselages, have such peculiar vibration characteristics that their analyses in most instances are extremely difficult. One primary reason for this is that each component of such a structure has its own vibration characteristic which affects the vibration characteristics of every other component of the structure through "cross-coupling." These effects must be analyzed in order to obtain a clear understanding of the over-all problem.

In his paper, the author is to be congratulated for presenting a method for the determination of the natural frequencies of edge-connected rectangular plate systems which make up such structures. The natural frequencies are evaluated for a two-plate subsystem which is composed of two rectangular plates simply supported on the outside edges and joined along a common edge. A semigraphical procedure is employed for the actual determination of the natural frequencies. It is indicated how the results of the method can be extrapolated to n plate systems.

As an illustration, calculations for a symmetric two-plate system are carried out in some detail. From these calculations it is concluded that the natural frequencies of the particular two-plate system considered are slightly higher than those of a single simply supported plate on all four edges. It is shown that this is even more closely approached for the higher modes and, thus, the two plates tend to "uncouple." The computation charts given by Figs. 3 and 4 of the paper apply only to symmetric modes; hence, it is concluded that they may be used to calculate the natural frequency of a single plate simply supported on three edges and clamped on the fourth.

In underwater systems, e.g., submarine or surface vessel hulls, where the natural frequencies of the various subplates are calculated by the present method, considerable error may be introduced if the effect of the viscous resistance of the water is neglected. This is even more important in so called high Q structures, i.e., structures in which material hysteresis and/or structural damping itself is so small that it safely may be neglected in frequency response calculations. Among the first to consider problems of this nature were Rayleigh[8] and Lamb.[9] For applications of this sort the so-called radiation or acoustic impedance of the mechanical system in its operating medium must be analytically evaluated or obtained by an experimental procedure. Very briefly, if we consider this impedance as a mechanical impedance, which is related to the acoustical impedance, it can be resolved into two components. The first is a reactive component corresponding to an additional mass loading which is due to the reaction of the medium on the vibrating system. This additional mass must be added to the mass of the vibrating plates. The second is a resistive component which can be considered to correspond to viscous damping. In most systems the former or reactive component contributes more to the lowering of the undamped natural frequencies. In fact, if the variables are just right, the undamped natural frequency could be lowered to half its value. The problem of obtaining an "exact" solution for the radiation impedance is indeed very complex; even good approximations are extremely difficult. Of course, it is to be emphasized that this in no way whatsoever detracts from the fine results presented by the author in his paper since it is a separate problem and should be treated as such. The writer suggests that the solution could be extended to cover media of large acoustic impedance at a future date if such solutions are

[7] Senior Research Engineer, American Bosch Arma Corp., Garden City, N. Y. Assoc. Mem. ASME.

[8] Lord Rayleigh, "The Theory of Sound," vol. II, Dover Publications, New York, N. Y., 1945, pp. 162–169.

[9] H. Lamb, *Proceedings, Royal Society*, vol. 98, 1921, p. 205.

warranted. In applications to aircraft and missile structures the above effect is, for all practical purposes, negligible in determining the resonant frequencies. The radiation impedance effects of the gaseous medium should only be considered in cases of high "Q" structures where the amplitudes, associated with the frequency response characteristics, become significant in the determination of the over-all integrity of the structure.

In conclusion, a noteworthy contribution has been given to the solution of problems involving vibrating plate systems. If further investigations are being considered it is hoped that these will include extensions of the present method to other configurations, operating media, and boundary conditions.

Author's Closure

Dr. House's comments are very much appreciated. His remark that the detail results of the paper under discussion apply only to plates vibrating in a medium of low acoustic impedance is certainly a valid one. However, one may expect the qualitative general conclusions of the paper to be applicable also to plate systems immersed in high impedance media. Since damping is known to affect essentially only the resonant response amplitudes and to produce only minor effects on natural frequencies and mode shapes, neglect of damping and of the resistive impedance components in the analysis can introduce only minor errors. As Dr. House points out, the prime effect of the reactive impedance component is a possibly considerable lowering of the natural frequencies. This component should have little influence on the plate-to-plate coupling phenomena, however, except for a lowering of the frequencies at which they are encountered.

It should be noted that some of the conclusions of the paper can be deduced qualitatively from Rayleigh's[8] remark that nodal lines on plates may be considered as equivalent to simple supports. A plate with any boundary conditions oscillating in one of its higher modes thus behaves virtually like a slightly smaller plate on simple supports. The results of the present paper show that this concept produces fairly good approximations even for the lower modes of two-plate systems.

S. J. BECKER
Senior Engineer, Westinghouse Electric Corporation, Bettis Atomic Power Laboratory,[1] Pittsburgh, Pa.

The Yielded Compound Cylinder in Generalized Plane Strain

The theory of a previous paper [1],[2] which was designed for plane strain of a compound cylinder, is extended to generalized plane strain, where the axial strain is a constant nonzero value for every radius and depends only on the external and internal pressures and any extraneous axial load. The method is limited to incompressible elastic material and is found to be completely solvable only if an elastic zone exists in each component. The assumed Tresca yield condition is verified in the process of obtaining the complete solution.

Introduction

In [1], solutions for the partially plastic compound cylinder were obtained for the case of plane strain. However, this appeared to be a singular case and the method also suffered from the inability to check the validity of the assumed maximum shear yield condition. The statement had been made in [1] that the yield condition was valid for plane strain, but this statement was based on assuming a Hencky type of stress-strain law for the plastic state. In working out the theory of generalized plane strain for the cylinder, it was soon found that the Hencky relationship was unsatisfactory, leaving the previously mentioned statement without a foundation.

In order that the axial loads for the elastic and plastic zones be ascertainable, it is found necessary to relate the axial stresses on each side of the elastic-plastic boundary. This relationship is not required for equilibrium. For simplicity and aesthetic reasons, it is chosen to be continuity across the elastic-plastic boundary. This choice, however, necessitates the assumption of incompressibility for the elastic state along with the plastic state.

A Prandtl-Reuss stress-strain relationship [2] is selected for the plastic state, and is proven to be highly successful for the cylinder in combination with axial stress continuity across the elastic-plastic boundary, incompressibility and the assumed yield condition. The validity of the yield condition for plane strain is re-established and the identity of plane strain with a closed ended simple incompressible cylinder is found. Most important, a solution for generalized plane strain of the compound vessel is obtainable.

[1] Operated for the U. S. Atomic Energy Commission by Westinghouse Electric Corporation.

[2] Numbers in brackets designate References at end of paper.

Contributed by the Refining-Gas Products, Petrochemical Committee, Petroleum Division and presented at the Winter Annual Meeting, New York, N. Y., November 27–December 2, 1960, of THE AMERICAN SOCIETY OF MECHANICAL ENGINEERS. Manuscript received at ASME Headquarters, July 14, 1960. Paper No. 60—WA-71.

A Simple Incompressible Cylinder in Generalized Plane Strain

Consider a cylinder with outside boundaries of radii j and k and intermediate elastic-plastic boundary ρ such that $j < \rho < k$. The condition of generalized plane strain can be symbolized by $\epsilon_z = \epsilon_z(Z, p_j, p_k)$ so that, for given pressures and axial load, ϵ_z is constant. For an incompressible material, the equation of incompressibility, $\epsilon_t + \epsilon_r + \epsilon_z = 0$ under generalized plane strain, leads to the deflection equation:

$$u = \frac{A}{r} - \frac{1}{2} r\epsilon_z \tag{1}$$

where $A = A(p_j, p_k)$ and Eq. (1) has been shown to be consistent with linear, isotropic elasticity [1].

It is supposed that ϵ_z itself is not known, but that Z is readily found. Thus, to obtain ϵ_z, it becomes necessary to introduce a stress-strain relationship for the plastic region.

For the case of generalized plane strain, where the principal directions of stress and strain are invariant (Appendix 1), a suitable stress-strain relationship is that of L. Prandtl and E.

Nomenclature

$a, b, c, d, \ldots,$ i, j, k, l = a sequence of boundary radii of mating cylinders; a, the smallest and l, the largest

τ_{ij} = shear yield stress taken as 57.7 per cent of the tensile yield, in cylinder with inner radius i and outer radius j

$\tau_{r\theta}, \tau_{z\theta}, \tau_{rz}$ = shear stresses acting in the co-ordinate direction designated by the first subscript on the co-ordinate surface perpendicular to the second subscript. By an elementary proof based on moment equilibrium, the subscripts are commutative; i.e., $\tau_{r\theta} = \tau_{\theta r}$, etc.

$\gamma_{r\theta}, \gamma_{z\theta}, \gamma_{rz}$ = shear strains between co-ordinate surfaces perpendicular to the directions designated by the subscripts

r, θ, z = designate radial, girth, and axial directions, respectively

$\sigma_r, \sigma_t, \sigma_z$ = radial, tangential, and axial normal stresses, respectively, in a cylinder, positive if tension

$\epsilon_r, \epsilon_t, \epsilon_z$ = normal strains in the radial, tangential, and axial directions, respectively

E, E_{ij} = Young's modulus, used with subscripts when referring to related cylinder.

$E_3(x) = \int_1^\infty \frac{e^{-xu}}{u^3} du$, tabulated in [6]

$-Ei(-x)$ = the exponential integral of x

ρ_{ij} = elastic-plastic boundary radius in cylinder with inner radius i and outer radius j

δ_j = diametral interference at radius j

(Continued on next page)

Reuss [2] which, for the incompressible plastic zone, can be written as

$$\left.\begin{aligned}\frac{d\epsilon_r}{dr} &= \frac{1}{E}\frac{d}{dr}\left[\sigma_r - \frac{1}{2}(\sigma_t + \sigma_z)\right] + S_r\frac{d\lambda}{dr}\\ \frac{d\epsilon_t}{dr} &= \frac{1}{E}\frac{d}{dr}\left[\sigma_t - \frac{1}{2}(\sigma_z + \sigma_r)\right] + S_t\frac{d\lambda}{dr}\\ \frac{d\epsilon_z}{dr} &= \frac{1}{E}\frac{d}{dr}\left[\sigma_z - \frac{1}{2}(\sigma_r + \sigma_t)\right] + S_z\frac{d\lambda}{dr}\end{aligned}\right\} \quad (2)$$

where $S_r = \sigma_r - {}^1/_3\sigma$, $S_t = \sigma_t - {}^1/_3\sigma$, $S_z = \sigma_z - {}^1/_3\sigma$, $\sigma = \sigma_r + \sigma_t + \sigma_z$ and it is assumed, from physical considerations, that, for a fixed ρ, all quantities are, at most, functions of r.

The Tresca or maximum shear yield condition becomes

$$\sigma_t - \sigma_r = S_t - S_r = 2\tau_{jk} \qquad = 2\tau \text{ briefly} \quad (3)$$

is the maximum principal stress difference.

For generalized plane strain $d\epsilon_z/dr = 0$. Hence, the last of Eqs. (2) becomes:

$$S_z\frac{d\lambda}{dr} = -\frac{1}{E}\cdot\frac{d}{dr}\left[\sigma_z - \frac{1}{2}(\sigma_r + \sigma_t)\right] \quad (4)$$

Since $\epsilon_t = u/r$ and $\epsilon_r = du/dr$, Eq. (1) and the first two of Eqs. (2) result in:

$$\frac{2A}{r^2} = \frac{1}{E}\cdot\frac{d}{dr}\left[\sigma_r - \frac{1}{2}(\sigma_t + \sigma_z)\right] + S_r\frac{d\lambda}{dr}$$

and

$$-\frac{2A}{r^2} = \frac{1}{E}\cdot\frac{d}{dr}\left[\sigma_t - \frac{1}{2}(\sigma_r + \sigma_z)\right] + S_t\frac{d\lambda}{dr}$$

Subtracting these last two, and using Eq. (3), the result becomes:

$$\frac{4A}{r^2} = -2\tau\frac{d\lambda}{dr}$$

Hence, $A = -\dfrac{\tau}{2}\dfrac{d\lambda}{dr}r^2$ is independent of r, from which it follows that $\dfrac{d\lambda}{dr} = -\dfrac{C}{r^2}$, $C = C(p_j, p_k)$ for the plastic zone. Thus Eq. (4) becomes:

$$\left[\frac{2}{3}\sigma_z - \frac{1}{3}(\sigma_r + \sigma_t)\right]\cdot\frac{C}{r^2} = \frac{1}{E}\frac{d}{dr}\left[\sigma_z - \frac{1}{2}(\sigma_r + \sigma_t)\right] \quad (5)$$

This integrates immediately to:

$$\sigma_z - {}^1/_2(\sigma_r + \sigma_t) = Be^{-{}^1/_2\cdot\frac{CE}{r^2}}$$

σ_r and σ_t are determined solely by equilibrium and the yield condition ([1],[3] [3], also Appendix 1). Thus $\sigma_r + \sigma_t = 2\tau\left(1 + 2\ln\dfrac{r}{j}\right) - 2p_j$

Hence,

$$\left.\begin{aligned}\sigma_z &= Be^{-{}^1/_2\frac{CE}{r^2}} + {}^1/_2(\sigma_t + \sigma_r)\\ \text{or}\\ \sigma_z &= Be^{-{}^1/_2\frac{CE}{r^2}} + \tau\left(1 + 2\ln\frac{r}{j}\right) - p_j\end{aligned}\right\} \quad (6)$$

At the elastic-plastic boundary, σ_r is continuous and, from Eq. (3), so is σ_t. Since there is no reason why an exception should be made of σ_z (it hardly would be expected that σ_z should suddenly change as an increasing ρ passed through the radius at which σ_z is felt), σ_z is also assumed to be continuous.

For the elastic zone, Hooke's law for the incompressible cylinder becomes

$$\left.\begin{aligned}\epsilon_t &= \frac{u}{r} = \frac{1}{E}\left[\sigma_t - \frac{1}{2}(\sigma_r + \sigma_z)\right]\\ \epsilon_r &= \frac{du}{dr} = \frac{1}{E}\left[\sigma_r - \frac{1}{2}(\sigma_z + \sigma_t)\right]\\ \epsilon_z &= \frac{dw}{dz} = \frac{1}{E}\left[\sigma_z - \frac{1}{2}(\sigma_t + \sigma_r)\right]\end{aligned}\right\} \quad (7)$$

Putting these into Eq. (1), at $r = \rho$:

either

$$\frac{A}{\rho^2} - \frac{1}{2}\epsilon_z = \frac{1}{E}\left[\sigma_t - \frac{1}{2}(\sigma_r + \sigma_z)\right]$$

[3] Equations used in this paper that are from references are listed in Appendix 3.

Nomenclature

p_j = radial pressure at radius j

$p_{\rho_{ij}}$ = radial pressure $(-\sigma_r)$ at radius ρ_{ij}

u = radial deflection, positive outward, from datum at unassembled state of compound vessel

w = axial deflection

r = variable radius

u_{j+} = u at radius j in cylinder jk

u_{j-} = u at radius j in cylinder ij

λ = a parameter of the Prandtl-Reuss equations

σ = sum of normal stresses of a designated point

$S_r = \sigma_r - {}^1/_3\sigma$. Similarly $S_t = \sigma_t - {}^1/_3\sigma$, $S_z = \sigma_z - {}^1/_3\sigma$

A, A_{jk} = constants of integration for radial deflection equation, used with subscripts when referring to related cylinder

$C = -r^3 d\lambda/dr$, independent of r

B, B_{jk} = constants of integration of the Prandtl-Reuss equations, used with subscripts when refering to related cylinder

Z = total axial load

Z_{ij} = axial load taken by cylinder ij

$\eta_{\rho_{jk}} = 2\int_j^\rho re^{-\left(\frac{\rho}{r}\right)^2}dr$ where $\rho = \rho_{jk}$, a special function evaluated in terms of $-Ei(-x)$ or $E_2(x)$

C_{ij}, K_{ij} = constants relating the axial load in cylinders ij to those of the other component cylinders, functions of the boundary pressures

ζ_{jk} = a function similar to $\eta_{\rho_{jk}}$ which appears to be useful in the fully plastic cylinder jk

$\ln x$ denotes natural logarithm (to the base e) of x

or

$$-\frac{A}{\rho^2}-\frac{1}{2}\epsilon_z=\frac{1}{E}\left[\sigma_r-\frac{1}{2}(\sigma_t+\sigma_z)\right]$$

In either case:

$$A=\frac{3}{4}\cdot\frac{\rho^2}{E}(\sigma_t-\sigma_r)$$

which, since the yield condition holds at ρ, becomes:

$$A=\frac{3}{2}\cdot\frac{\tau\rho^2}{E} \tag{8}$$

and therefore

$$C=\frac{3}{E}\rho^2 \tag{9}$$

Note that, if elastic incompressibility had not been assumed as well as plastic incompressibility, then A would not be independent of r. For this reason incompressibility is selected for the elastic zone.

Further, if Eq. (6) is inserted in the last of Eqs. (7) for $r=\rho$, then $Be^{-1/2\frac{CE}{\rho^2}}=E\epsilon_z$ which, with Eq. (9), becomes:

$$B=eE\epsilon_z \tag{10}$$

In addition, since $E\epsilon_z$ is constant for given boundary conditions, using the last of Eqs. (7), this can be written in terms of the stresses in the elastic zone. In Appendix 1 of [4] it is shown that σ_z and $\sigma_t+\sigma_r$ are constant in the elastic zone. Then writing $\sigma_t+\sigma_r=\sigma_t-\sigma_r+2\sigma_r=2(\tau-p_\rho)$ for $r=\rho$ and therefore for $\rho\leqq r\leqq k$, Eq. (6) becomes

$$(\sigma_z)_{\text{plastic}}=[(\sigma_z)_{\text{elastic}}+p_\rho-\tau]e^{-\left(\frac{\rho}{r}\right)^2+1}+\tau\left(1+2\ln\frac{r}{j}\right)-p_j \tag{6a}$$

Finally, $(\sigma_z)_{\text{elastic}}$ can be determined from Eq. (6a), using the condition that $2\pi\int_j^k\sigma_z r\cdot dr=Z$, where $(\sigma_z)_{\text{plastic}}$ holds for $j\leqq r\leqq\rho$ and $(\sigma_z)_{\text{elastic}}$ holds for $\rho\leqq r\leqq k$.

Let $\frac{1}{2}\eta_{\rho_{jk}}=\int_j^\rho re^{-\left(\frac{\rho}{r}\right)^2}dr$, an integral whose value is readily found, as indicated in Appendix 2. Then:

$$Z=2\pi\left\{[(\sigma_z)_{\text{elastic}}+p_\rho-\tau]e\cdot\frac{\eta_{\rho_{jk}}}{2}+\tau\rho^2\ln\frac{\rho}{j}-p_j\left(\frac{\rho^2-j^2}{2}\right)+(\sigma_z)_{\text{elastic}}\cdot\left(\frac{k^2-\rho^2}{2}\right)\right\}$$

and therefore:

$$(\sigma_z)_{\text{elastic}}=\frac{\frac{Z}{\pi}+p_j(\rho^2-j^2)+(\tau-p_\rho)e\eta_{\rho_{jk}}-2\tau\rho^2\ln\frac{\rho}{j}}{e\eta_{\rho_{jk}}+k^2-\rho^2} \tag{11}$$

and

$$E\epsilon_z=(\sigma_z)_{\text{elastic}}-(\tau-p_\rho) \tag{12}$$

It is interesting to observe that for a closed ended simple incompressible cylinder, loaded only by internal and external pressures, $\epsilon_z\equiv 0$, which can be found by substituting Eq. (11) in Eq. (12).

Thus for the simple incompressible cylinder in partially plastic generalized plane strain, the following situations exist, depending on the boundary conditions:

(a) Boundary conditions given in terms of load. In this case the radial and tangential stresses are unaffected by the axial load. A complete solution is obtainable.

(b) Boundary conditions in terms of deflection or strain. The assumption of incompressibility implies that only two boundary conditions of three possible boundaries, $r=j$, $r=k$, and $z=z_0$ can be independently selected. Once this is done, ρ is fixed through Eqs. (1) and (8) and hence, by using Eqs. (1), (2), and (4) of [1],[3] so are the principal stresses to within an arbitrary p_j or p_k.

(c) Loads on radial boundaries, strain on axial boundary. Same as (a).

(d) Radial deflections at radial boundaries, load on axial boundary. These are sufficient to completely define a solution as follows:

1 Eq. (1) then defines A and ϵ_z
2 Eq. (8) then defines ρ.
3 Eq. (3) of [1] defines p_j-p_ρ
4 Eq. (11) produces a linear relationship between p_j, p_ρ, and $(\sigma_z)_{\text{elastic}}$
5 Eq. (12) produces a third linear relationship between $(\sigma_z)_{\text{elastic}}$ and p_ρ.

These last three steps thus give three simple linear equations for $(\sigma_z)_{\text{elastic}}$, p_j, and p_ρ. When these are found then the stresses and deflections at every point are readily obtained.

The validity of Eq. (3) is readily checked. From the expressions for σ_r and σ_t given by Eqs. (1) of [1], and Eq. (9), Eq. (10), and the second of Eqs. (6) of this paper, the following are easily obtained:

$$|\sigma_t-\sigma_z|=\left|\tau-E\epsilon_z e^{1-\left(\frac{\rho_{jk}}{r}\right)^2}\right| \tag{3a}$$

$$|\sigma_r-\sigma_z|=\left|\tau+E\epsilon_z e^{1-\left(\frac{\rho_{jk}}{r}\right)^2}\right| \tag{3b}$$

Thus the assumed yield condition is valid if

$$\tau\geqq|E\epsilon_z|e^{1-\left(\frac{\rho_{jk}}{r}\right)^2}$$

for all pertinent r; that is, if

$$\tau\geqq|E\epsilon_z| \tag{3c}$$

The Partially Plastic Compound Cylinder in Generalized Plane Strain

The presence of differences of axial stress between concentric shrunk cylinders in the elastic state which may come from the manufacturing process or from the loading may represent a violation of the conditions of generalized plane strain for the assembly and, therefore, this violation presumably continues into the plastic state. However, for the purposes of the restricted nature of the analysis, the violations, where they occur, will be assumed to have negligible effects on the condition of generalized plane strain.

If any one of a series of concentric cylinders is assumed to be partially plastic with a plastic yield radius ρ_{ij}, then this is sufficient to determine the yield radii, if they exist, of all the cylinders, as follows;

From Eqs. (1) and (8), for the partially plastic cylinder:

$$u_{j-}=\frac{3}{2}\cdot\frac{\tau_{ij}\rho_{ij}^2}{jE_{ij}}-\frac{1}{2}j\epsilon_z$$

and

$$u_{i+} = \frac{3}{2} \cdot \frac{\tau_{ij}\rho_{ij}^2}{iE_{ij}} - \frac{1}{2}\, i\epsilon_z$$

However

$$u_{j+} = \frac{A_{jk}}{j} - \frac{1}{2}\, j\epsilon_z = u_{i-} + \frac{1}{2}\,\delta_j$$

and

$$u_{i-} = \frac{A_{ki}}{i} - \frac{1}{2}\, i\epsilon_z = u_{i+} - \frac{1}{2}\,\delta_i$$

Thus

$$\left.\begin{aligned} A_{jk} &= \frac{3}{2} \cdot \frac{\tau_{ij}}{E_{ij}}\,\rho_{ij}^2 + \frac{1}{2}\, j\delta_j \\ \text{and} \qquad & \\ A_{ki} &= \frac{3}{2} \cdot \frac{\tau_{ij}}{E_{ij}}\,\rho_{ij}^2 - \frac{1}{2}\, i\delta_i \end{aligned}\right\} \qquad (13a)$$

If the deflection equation, Eq. (1), is used again, in the form:

$$u_{k-} = \frac{A_{jk}}{k} - \frac{1}{2}\, k\epsilon_z$$

and

$$u_{k+} = \frac{A_{ki}}{h} - \frac{1}{2}\, h\epsilon_z$$

with

$$u_{k+} = \frac{A_{kl}}{k} - \frac{1}{2}\, k\epsilon_z = u_{k-} + \frac{1}{2}\,\delta_k$$

and

$$u_{h-} = \frac{A_{gh}}{h} - \frac{1}{2}\, h\epsilon_z = u_{h+} - \frac{1}{2}\,\delta_h$$

from which:

$$\left.\begin{aligned} A_{kl} &= A_{jk} + \frac{k\delta_k}{2} \\ \text{and} \qquad & \\ A_{gh} &= A_{ki} - \frac{h\delta_h}{2} \end{aligned}\right\} \qquad (13b)$$

In this manner all of the A_{ij} can be found. The A_{ij} are solely a result of incompressibility and therefore are otherwise independent, except for the first chosen partially plastic cylinder, of the condition of the material of the component cylinder.

Then from Eq. (8), for any cylinder fg, ρ_{fg} can be determined, if it exists. Thus:

$$\rho_{fg} = \sqrt{\frac{2}{3} \cdot \frac{E_{fg}A_{fg}}{\tau_{fg}}}, \qquad f \leqq \rho_{fg} \leqq g \qquad (14)$$

If $\rho_{fg} < f$ then cylinder fg is all elastic and the computed value of ρ_{fg} is false. If $\rho_{fg} > g$ then cylinder fg is fully plastic and the computed value of ρ_{fg} is false.

Assume then, that a particular assembly for a selected value of elastic-plastic boundary in some component is such that all the components, analyzed as above, are either partially or fully plastic. In that case the complete solution can be obtained, provided that Eq. (3) is not violated. Eq. (3), however, and provided that there are no fully plastic components, is easily checked in the process of obtaining the complete solution.

With all the ρ_{ij} obtained as above, or set equal to j where Eq. (14) would otherwise show $\rho_{ij} > j$, all of the boundary pressures can be obtained, starting from a boundary at known pressure; for example, zero at the outside boundary, according to the following scheme [1]:

$$p_{\rho_{kl}} = \tau_{kl}\left[1 - \left(\frac{\rho_{kl}}{l}\right)^2\right] \qquad \text{if } p_l = 0$$

$$p_k = 2\tau_{kl} \ln \frac{\rho_{kl}}{k} + p_{\rho_{kl}}$$

$$p_{\rho_{jk}} = \tau_{jk}\left[1 - \left(\frac{\rho_{jk}}{k}\right)^2\right] + p_k$$

$$p_j = 2\tau_{jk} \ln \frac{\rho_{jk}}{j} + p_{\rho_{jk}}$$

. . . . . .

. . . . . .

Finally p_a.

For the completely elastic component, Eq. (17) of [4] and the subsequent discussion, by comparison with Eq. (1) of this paper, for incompressible elastic cylinder fg:

$$A_{fg} = \frac{1.5}{E_{fg}} \cdot \frac{f^2g^2}{g^2 - f^2}\,(p_f - p_g)$$

(It is to be noted that, in the statement in [4] following Eq. (17), the quantity $\nu r\epsilon_z$ was erroneously substituted for the correct value $-\nu r\epsilon_z$. In the latter text, however, the oversight was trivial.)

Hence, for the elastic cylinder:

$$p_f - p_g = \frac{E_{fg}A_{fg}}{1.5}\left(\frac{1}{f^2} - \frac{1}{g^2}\right) \qquad (15)$$

With Eq. (15) to supplement the above scheme for analysis of boundary pressures, all the boundary pressures may be obtained, no matter whether the component be elastic, partially plastic, or fully plastic, provided that the yield condition is valid.

For the partially plastic cylinder jk, Eqs. (11) and (12) can be condensed to:

$$E_{jk}\epsilon_z = \frac{\dfrac{Z_{jk}}{\pi} + p_j(\rho_{jk}^2 - j^2) - (\tau_{jk} - p_{\rho_{jk}}) \cdot (k^2 - \rho_{jk}^2) - 2\tau_{jk}\rho_{jk}^2 \ln \dfrac{\rho_{jk}}{j}}{e\eta_{\rho_{jk}} + k^2 - \rho_{jk}^2} \qquad (16)$$

For the completely elastic cylinder fg, from Hooke's law (last of Eqs. (7)) and Lamé's equation (Eq. (14) of [4]):

$$E_{fg}\epsilon_z = \frac{\dfrac{Z_{fg}}{\pi} + p_g g^2 - p_f f^2}{g^2 - f^2} \qquad (17)$$

Since ϵ_z is assumed to be constant, then, for an assembly of elastic and partially plastic components, equating all of the ϵ_z in Eqs. (16) and (17) results in a group of linear equations for the axial loads in the form:

$$K_{ab}Z_{ab} + C_{ab} = K_{bc}Z_{bc} + C_{bc} = \ldots = K_{kl}Z_{kl} + C_{kl} \qquad (18)$$

The total axial load, determined from the load now known is

$$Z = Z_{ab} + Z_{bc} + Z_{cd} + \ldots + Z_{kl} \qquad (19)$$

Eqs. (18) can be used to express each of the Z_{ij} in terms of any selected Z_{fg}. This can be used in Eq. (19) to find any, hence each, of the Z_{ij} in terms of the known load Z. With the values of all of the Z_{ij} now known, it is a straight-forward computation to find all of the σ_z and all of the radial deflections as follows:

1 Find $E\epsilon_z$ for each component through Eq. (16) or Eq. (17). ϵ_z is the same for all components.

2 Test the validity of the yield condition by means of inequality (3c).

$$3 \quad (\sigma_z)_{j\rho_{jk}} = E_{jk}\epsilon_z e^{1-\left(\frac{\rho_{jk}}{r}\right)^3} + \tau_{jk}\left(1 + 2\ln\frac{r}{j}\right) - p_j \quad (20)$$

for the plastic zone in component jk and constant in the elastic zone of jk, determined by setting $r = \rho_{jk}$ in Eq. (20).

$$4 \quad u = \frac{A_{jk}}{r} - \frac{1}{2}r\epsilon_z \quad \text{for any } r \text{ in cylinder } jk.$$

From Eq. (16):

$$\lim_{\rho_{jk}\to k}(E_{jk}\epsilon_z) = \frac{\frac{Z_{jk}}{\pi} + p_j(k^2 - j^2) - 2\tau_{jk}k^2\ln\frac{k}{j}}{e\eta_{jk}} \quad (21)$$

For these values of loading, cylinder jk is fully plastic. For any larger values Eq. (16) fails because it is based on the presence of an elastic zone in the component. It becomes impossible, within the framework of the present theory, to check the validity of the yield condition in the fully yielded component because the axial load cannot be determined exactly. However, if the validity of the yield condition for the assemblage of components is assumed, a good deal of useful information can still be obtained.

Suppose that the first fully yielded component is component fg. Then from Eq. (8), A_{fg} can be chosen such that $A_{fg} > 1.5\tau_{fg}g^2/E_{fg}$. In that case all of the remaining A_{ij} can be determined by means of equations of the form of Eq. (13) and, from Eq. (14), all of the ρ_{ij} where they exist. Alternatively, ρ can be chosen for another component known to be partially plastic and the previous analytic procedure can be applied to determining all of the A_{ij} and the existing ρ_{ij}. In either case the boundary pressures can then be calculated in the usual fashion.

To complete the analysis it is necessary to return to the Prandtl-Reuss equations, Eqs. (2), for the fully yielded components. From these, the assumption of generalized plane strain and the yield condition, Eq. (3), it has been shown previously that $A = -(\tau/2)(d\lambda/dr)r^3$ and $d\lambda/dr = -C/r^3$ hence, $C = 2A/\tau$. With the equilibrium equations, Eq. (6) is obtained, now in the form:

$$\sigma_z = Be^{-\frac{2}{3}\cdot\frac{AE}{\tau r^3}} + \tau\left(1 + 2\ln\frac{r}{j}\right) - p_j$$

Thus for the fully plastic component jk:

$$Z_{jk} = \frac{4\pi}{3}\cdot\frac{A_{jk}E_{jk}}{\tau_{jk}}B_{jk}\zeta_{jk} + 2\pi\left[\tau_{jk}k^2\ln\frac{k}{j} - \frac{p_j}{2}(k^2 - j^2)\right] \quad (22)$$

where $\zeta_{jk} = \int_{j\alpha}^{k\alpha}\xi e^{-\frac{1}{\xi^3}}d\xi$, $\alpha = \sqrt{\frac{3}{2}\cdot\frac{\tau_{jk}}{A_{jk}E_{jk}}}$

which can be evaluated in a manner similar to the parameter $\eta_{\rho_{jk}}$ as in Appendix 2.

For the elastic and partially plastic components, Eqs. (18) are valid as before and, of course, Eq. (19) holds for the entire system. Thus the assembly is determinate up to the values of the axial forces within the fully yielded components; that is, from Eq. (22), within a set of constants B_{jk} equal in number to the number of suitable fully yielded components.

Example

A three-tube container is designed such that each component yields simultaneously under an internal pressure of 100,000 psi for the assembly under operating conditions of 850 F. The shear yields taken at 57.7 per cent of the tensile yields are:

Inner tube	75,600 psi $= \tau_{ab}$
Middle tube	56,600 psi $= \tau_{bc}$
Outer tube	49,500 psi $= \tau_{cd}$

The modulus of elasticity is 24×10^6 psi, and the dimensions are:

$2a = 11^1/_4$ in.

$2b = 17$ in.

$2c = 26$ in.

$2d = 37$ in.

The interferences to give this result at operating conditions are taken as those of the second example of [1] for the purpose of comparison. The values are $\delta_b = 0.02475$ and $\delta_c = 0.04125$ in.

The plastic growth, for suitable stages of the outermost elastic-plastic boundary, is to be calculated for an incompressible cylinder in generalized plane strain, first as an open-ended vessel and second as a closed-ended vessel.

In Table 1; the results obtained by the use of equations of the form of Eqs. (8), (13b), and (14) of this paper and Eqs. (2) and (4) of [1] have been tabulated to a suitable degree of accuracy for values of the yield radius in the outermost cylinder which were used in [1], together with results corresponding to a marginal fully yielded inner cylinder. These are easily and directly obtained by the methods here outlined. Very small differences from the values of the second example of [1] are a result of arithmetic operations; they are not true differences.

Table 2 shows values obtained for the special function $\eta_{\rho_{jk}}$,

Table 1 Deflection integration constants, elastic-plastic boundaries, and boundary pressures

ρ_{cd}, in.	A_{cd}, sq. in.	A_{bc}, sq. in.	A_{ab}, sq. in.	ρ_{bc}, in.	ρ_{ab}, in.	$p_{\rho_{cd}}$, psi	p_c, psi	$p_{\rho_{bc}}$, psi	p_b psi	$p_{\rho_{ab}}$, psi	p_a, psi
13	0.5228	0.2547	0.1495	8.5	5.625	25,100	25,100	57,500	57,500	100,000	100,000
14	0.6064	0.33825	0.2331	9.7785	7.023	21,150	28,500	53,100	68,900	92,900	126,500
15	0.6961	0.4280	0.3228	10.999	8.265	17,000	31,100	47,200	76,400	80,500	138,700
15.1991	0.7147	0.4466	0.3414	11.236	8.500	16,100	31,560	45,900	77,500	77,500	139,900
16	0.7920	0.5239	0.4187	12.169	8.5	12,500	33,000	40,000	80,700	80,700	143,000
17	0.8941	0.6260	0.5213	13	8.5	7,700	34,300	34,300	82,400	82,400	144,800
18	1.0024	0.73425	0.6296	13	8.5	2,600	34,860	34,860	82,950	82,950	145,375
$18^1/_2$	1.0588	0.7907	0.6861	13	8.5	0	34,900	34,900	83,030	83,030	145,450

Table 2 Special functions and axial load relationships

ρ_{cd}, in.	$\eta_{\rho_{cd}}$, sq in.	$\eta_{\rho_{bc}}$, sq in.	$\eta_{\rho_{ab}}$, sq in.	EC_{cd}, psi	EC_{bc}, psi	EC_{ab}, psi	$1/EK_{cd}$, sq in.	$1/EK_{bc}$, sq in.	$1/EK_{ab}$, sq in.
13	0	0	0	−24,440	+ 860	24,350	544.3	303.9	127.58
14	9.216	7.456	5.190	−28,110	−1,765	26,410	538.2	294.2	116.34
15	17.813	13.795	9.178	−31,750	−3,020	39,140	520.5	268.7	90.74
15.1991	19.461	14.963	9.905	−32,500	−3,160	43,490	515.7	262.1	84.58

	$Z_{bc} = \alpha_1 Z_{ab} + \beta_1$		$Z_{cd} = \alpha_2 Z_{ab} + \beta_2$		$Z = \alpha Z_{ab} + \beta$	
ρ_{cd}, in.	α_1	β_1, millions of lb	α_2	β_2, millions of lb	α	β, millions of lb
13	2.382	7.140	4.266	26.558	7.649	33.699
14	2.529	8.290	4.626	29.339	8.154	37.628
15	2.961	11.328	5.736	36.896	9.697	48.225
15.1991	3.099	12.225	6.096	39.181	10.195	51.406

Table 3 Closed ended cylinder—axial loads, axial strain, axial stresses, and radial deflections

ρ_{cd}, in.	Z, millions of lb	Z_{ab}, millions of lb	Z_{bc}, millions of lb	Z_{cd}, millions of lb	$E\epsilon_z$, psi
13	9.935	−3.107	−0.261	13.304	0
14	12.572	−3.073	+0.519	15.126	0
15	13.786	−3.552	+0.8125	16.525	0
15.1991	13.905	−3.678	+0.827	16.756	0

ρ_{cd}, in.	$(\sigma_z)_{d\ \text{to}\ \rho_{cd}}$, psi	$(\sigma_z)_{c+}$, psi	$(\sigma_z)_{c-\ \text{to}\ \rho_{bc}}$, psi	$(\sigma_z)_{b+}$, psi	$(\sigma_z)_{b-\ \text{to}\ \rho_{ab}}$, psi	$(\sigma_z)_a$, psi
13	24,440	24,440	−860	−860	−24,350	−24,350
14	28,350	21,010	3,540	−12,330	−17,320	−50,880
15	32,540	18,380	9,390	−19,780	−4,900	−63,090
15.1991	33,410	17,940	10,720	−20,870	−1,870	−64,290

ρ_{cd}, in.	$u_d = \frac{A_{cd}}{d}$, in.	$u_{c+} = \frac{A_{cd}}{c}$, in.	$u_{c-} = \frac{A_{bc}}{c}$, in.	$u_{b+} = \frac{A_{bc}}{b}$, in.	$u_{b-} = \frac{A_{ab}}{b}$, in.	$u_a = \frac{A_{ab}}{a}$, in.
13	0.0283	0.0402	0.0196	0.0300	0.0176	0.0266
14	0.0328	0.0466	0.0260	0.0398	0.0274	0.0414
15	0.0376	0.0536	0.0329	0.0504	0.0380	0.0574
15.1991	0.0386	0.0550	0.0344	0.0525	0.0402	0.0607

using [6] and the relationships between the axial loads in the component parts obtained by using Eqs. (18) and (19) in the range for which Eq. (16) holds. In this connection it is to be noted that advantage was taken in the calculation of the uniform value of E for all components.

In Table 3, the value of the total axial load for a closed ended assembly corresponding to the internal pressures of Table 1, in the range for which Eq. (16) holds, is shown. From these and the relationships shown in Table 2, the axial loads are calculated for each component, as are the values of $E\epsilon_z$ using Eq. (16). An unanticipated result was that ϵ_z is identically zero for calculations using seven or eight decimal places. This appears to be generally valid for the closed ended compound cylinder of the type analyzed in this paper, just as it is for the simple cylinder. Thus the results for the incompressible closed ended cylinder are identical to that of the incompressible cylinder of [1]. The axial stresses are easily computed by Eq. (6) using Eq. (10) and, of course, the yield condition is always valid by the first form of Eq. (6). The radial deflections are also shown.

Table 4 shows the values of the axial load of each component of an open ended cylinder computed from the relationships of Table 2 with zero total axial load and the corresponding axial strains, using Eq. (16), again over its proven valid range. The yield condition proves to be adequately satisfied. From the nature of Eqs. (1), (8), (12), and (20) and from the fact that the axial strain for the corresponding closed ended cylinder is zero, the calculation for axial stresses and deflections for the open ended cylinder become corrections upon the corresponding small values for the closed ended cylinder. Hence, the deflections verify the assumption of small deflection theory. For the data presented, the extreme values of axial stress in the plastic zones are readily shown to lie on the radial boundaries of the zones.

Conclusions and Remarks

The system for generalized plane strain of the compound cylinder that is presented in this paper is a natural extension of the theory of [1] for plane strain. The original system is augmented by the Prandtl-Reuss stress-strain relationships for the plastic state, which is supplemented by assuming that the axial stress is continuous across the elastic-plastic boundary, necessitating the assumption that the elastic zone is incompressible as well as the plastic zone. Thus, as the original plane strain system is extended, it is also more limited, in the sense of incompressibility of the elastic material.

This system is amenable to complete solution only as long as each cylindrical component contains an elastic zone. Otherwise it is solvable to within a set of constants equal in number to the

Table 4 Open ended cylinder, Z = 0—axial loads, axial strain, axial stresses, and radial deflections

ρ_{cd}, in.	Z_{ab}, millions of lb	Z_{bc}, millions of lb	Z_{cd}, millions of lb	$E\epsilon_z$, psi	$-\frac{1}{2}d\cdot\epsilon_z$, in.	$-\frac{1}{2}c\cdot\epsilon_z$, in.	$-\frac{1}{2}b\cdot\epsilon_z$, in.	$-\frac{1}{2}a\cdot\epsilon_z$, in.
13	−4.406	−3.356	7.762	−10,180	0.0039	0.0028	0.0018	0.0012
14	−4.614	−3.380	7.994	−13,250	0.0051	0.0036	0.0024	0.0016
15	−4.973	−3.397	8.370	−15,670	0.0060	0.0042	0.0028	0.0018
15.1991	−5.042	−3.399	8.441	−16,125	0.0062	0.0044	0.0029	0.0019

ρ_{cd}, in.	$(\sigma_z)_{d\text{ to }\rho_{cd}}$, psi	$(\sigma_z)_{c+}$, psi	$(\sigma_z)_{c-\text{ to }\rho_{bc}}$, psi	$(\sigma_z)_{b+}$, psi	$(\sigma_z)_{b-\text{ to }\rho_{ab}}$, psi	$(\sigma_z)_a$, psi
13	14,260	14,260	−11,040	−11,040	−34,530	−34,530
14	15,100	9,715	−9,720	−21,920	−30,570	−58,460
15	16,870	7,130	−6,280	−27,770	−20,570	−68,010
15.1991	17,290	6,770	−5,410	−28,500	−17,990	−68,760

ρ_{cd}, in.	$u_d = \frac{A_{cd}}{d}-\frac{1}{2}d\cdot\epsilon_z$, in.	$u_{c+} = \frac{A_{cd}}{c}-\frac{1}{2}c\epsilon_z$, in.	$u_{c-} = \frac{A_{bc}}{c}-\frac{1}{2}c\epsilon_z$, in.	$u_{b+} = \frac{A_{bc}}{b}-\frac{1}{2}b\epsilon_z$, in.	$u_{b-} = \frac{A_{ab}}{b}-\frac{1}{2}b\epsilon_z$, in.	$u_a = \frac{A_{ab}}{a}-\frac{1}{2}a\epsilon_z$, in.
13	0.0322	0.0430	0.0224	0.0318	0.0194	0.0278
14	0.0379	0.0502	0.0296	0.0421	0.0298	0.0430
15	0.0437	0.0578	0.0372	0.0531	0.0407	0.0592
15.1991	0.0448	0.0594	0.0387	0.0554	0.0430	0.0626

number of fully yielded components. Whether complete or not, it presents an alternative method to that of [1] for the incompressible case, to obtain elastic-plastic boundaries and radial stresses or pressures without the calculation of deflections.

When the complete solution can be obtained, validation of the yield condition is made in the process of obtaining the solution.

It should be remarked that the arithmetic of the method is quite suitable for slide rule calculations using suitable arithmetic techniques,[4] supplemented by tables of the required special functions.

The examples presented cover a range of partial plasticity which represents 88 per cent of the pressure change between initial and full yielding of the assembly, or 96 per cent of the pressure for full yielding of the assembly.

References

1 S. J. Becker, "An Analysis of the Yielded Compound Cylinder," Trans. ASME, Series B, Journal of Engineering for Industry, vol. 83, 1961, pp. 43–49.

2 R. Hill, "The Mathematical Theory of Plasticity," Clarendon Press, Oxford, England, 1950, p. 40, Eq. (33) or p. 111.

3 S. Timoshenko, "Strength of Materials, Part II," third edition, D. Van Nostrand Company, Inc., New York, N. Y., 1956, Art 70, pp. 386–392, Eqs. (d), (e), (f).

4 S. J. Becker and L. Mollick, "The Theory of the Ideal Design of a Compound Vessel," Trans. ASME, Series B, Journal of Engineering for Industry, vol. 82, 1960, pp. 136–142.

5 S. Timoshenko and J. N. Goodier, "Theory of Elasticity," second edition, McGraw-Hill Book Company, Inc., New York, N. Y., 1951, Eqs. 177, p. 343.

6 "Tables of Functions and Zeros of Functions," National Bureau of Standards, Applied Mathematics Series, 37, Superintendent of Documents, U. S. Government Printing Office, Washington, D. C., November 10, 1954, pp. 57–111.

[4] Examples: Use $\ln\left(1+\frac{b-a}{a}\right)$ for $\ln\frac{b}{a}$ if $a<b<2a$.

Use $(b-a)\cdot(b+a)$ for b^2-a^2.

Use $\frac{b-a}{b}\cdot\frac{b+a}{b}$ for $1-\frac{a^2}{b^2}$ if $0.7\,b<a<b$.

Use $1+\frac{\rho-j}{j}\cdot\frac{\rho+j}{j}$ for $\frac{\rho^2}{j^2}$ if $j<\rho<1.5j$.

APPENDIX 1

Invariance of Principal Directions Under Generalized Plane Strain With Radial Symmetry

The invariance of the principal strain directions is obvious as it is based solely on geometric arguments. Symmetry requires shear strains $\gamma_{z\theta}$ and $\gamma_{r\theta}$ to be identically zero, while γ_{rz} shear strains are zero because of the assumption that plane cross-sections remain plane and congruent under generalized plane strain.

The invariance of the principal stress directions can be demonstrated readily also. Shear stresses $\tau_{r\theta}$ and $\tau_{z\theta}$ must be identically zero from symmetry arguments. Furthermore, the generalized plane strain condition implies the assumption that the condition at each cross section is the same as at every other parallel cross section. Hence $\partial\sigma_z/\partial z = 0$. Thus from equilibrium considerations alone [5]:

$$\frac{\partial\tau_{rz}}{\partial r}+\frac{\tau_{rz}}{r}=0$$

which has the general solution

$$\tau_{rz}=\frac{f(z)}{r}$$

Since at one radial boundary surface, $r \neq 0$, of some component cylinder, $\tau_{rz}=0$, it follows that $f(z)$ must be zero for that component cylinder. Thus $\tau_{rz}\equiv 0$ for that component and, by repeating the argument at the subsequent boundary surfaces, of all component cylinders.

Furthermore, the other force equilibrium equation then takes the form of [3], as has been used in this paper.

Thus the principal directions (those without shear) remain identified with the cylindrical co-ordinate directions for generalized plane strain. Since this is based solely on geometric and

equilibrium considerations, it is fundamental property of the system, irrespective of any material properties or condition.

APPENDIX 2

For the evaluation of $\eta_{\rho_{jk}} = 2\int_j^\rho re^{-\left(\frac{\rho}{r}\right)^2} dr$, where $\rho = \rho_{jk}$, there exist the following forms:

Form 1:

$$\eta_{\rho_{jk}} = 2\int_j^\rho re^{-\left(\frac{\rho}{r}\right)^2} dr = 2\rho^2\int_{j/\rho}^1 \frac{r}{\rho}e^{-\left(\frac{\rho}{r}\right)^2} d\left(\frac{r}{\rho}\right)$$

$$= \rho^2\int_1^{\left(\frac{\rho}{j}\right)^2} \frac{e^{-s}}{s^2} ds$$

$$= \rho^2\left[e^{-1} - e^{-\left(\frac{\rho}{j}\right)^2}\cdot\left(\frac{j}{\rho}\right)^2 - \int_1^{\left(\frac{\rho}{j}\right)^2} \frac{e^{-s}}{s} ds\right]$$

$$= \frac{\rho^2}{e} - \frac{j^2}{e^{(\rho/j)^2}} - \rho^2 Ei\left(-\frac{\rho^2}{j^2}\right) - 0.219384\rho^2$$

The function, exponential integral, $-Ei(-x) = \int_x^\infty \frac{e^{-v}}{v} dv$, can be found in several common references. However, a preferable form is:

Form 2:

$$\eta_{\rho_{jk}} = \rho^2\int_1^{\left(\frac{\rho}{j}\right)^2} \frac{e^{-s}}{s^2} ds$$

$$= \rho^2\left[\int_1^\infty \frac{e^{-s}}{s^2} ds - \int_{v=1}^\infty \frac{e^{-\left(\frac{\rho}{j}\right)^2 v}}{\left(\frac{\rho}{j}\right)^4 v^2} d\left(\frac{\rho^2}{j^2} v\right)\right]$$

$$= \rho_{jk}^2 E_2(1) - j^2 E_2\left(\frac{\rho_{jk}^2}{j^2}\right)$$

where the function $E_n(x)$ is defined and tabulated in [6] and, in this form, has quite desirable arithmetical properties.

APPENDIX 3

List of Equations From References That Are Used in This Paper

From Ref. [1], ASME Paper 60—SA-13.

Eqs. (1) $\sigma_r = -2\tau_{ij}\ln\frac{j}{r} - p_j$ in cylinder ij

$\sigma_t = \sigma_r + 2\tau_{ij}$

Eq. (2) $p_{\rho_{fg}} = \tau_{fg}\left[1 - \left(\frac{\rho_{fg}}{g}\right)^2\right] + p_g$ in cylinder fg

Eq. (3) $\sigma_r = -2\tau_{fg}\ln\frac{\rho_{fg}}{r} - p_{\rho_{fg}}$ in cylinder fg

Eq. (4) $p_f = 2\tau_{fg}\ln\frac{\rho_{fg}}{f} + \tau_{fg}\left[1 - \left(\frac{\rho_{fg}}{g}\right)^2\right] + p_g$ in cylinder fg

From Ref. [3], S. Timoshenko, "Strength of Materials, Part II."

Eq. (d) $\frac{\sigma_t - \sigma_r}{2} = \tau_{y.p.}$

Eq. (e) $\sigma_t - \sigma_r - r\frac{d\sigma_r}{dr} = 0$

Eq. (f) $\frac{d\sigma_r}{dr} = \frac{2\tau_{y.p.}}{r}$

From Ref. [4], S. J. Becker and L. Mollick, "The Theory of the Ideal Design of a Compound Vessel."

Eqs. (14)
$$\left\{\begin{aligned}\sigma_r &= \frac{p_a a^2 - p_b b^2}{b^2 - a^2} - \left(\frac{p_a - p_b}{r^2}\right)\frac{a^2 b^2}{b^2 - a^2}\\ \sigma_t &= \frac{p_a a^2 - p_b b^2}{b^2 - a^2} + \left(\frac{p_a - p_b}{r^2}\right)\frac{a^2 b^2}{b^2 - a^2}\end{aligned}\right\}$$

(Lamé's Equations)

Eq. (17) $u = \frac{(1+\nu)(1-2\nu)}{E}\cdot\left(\frac{p_a a^2 - p_b b^2}{b^2 - a^2}\right)r + \frac{1+\nu}{E}\cdot\left(\frac{p_a - p_b}{r}\right)\frac{a^2 b^2}{b^2 - a^2}$ for plane strain

(ν = Poisson's ratio)

From Ref. [5], S. Timoshenko and J. N. Goodier, "Theory of Elasticity."

Eqs. (177)
$$\left\{\begin{aligned}\frac{\partial\sigma_r}{\partial r} + \frac{\partial\tau_{rz}}{\partial z} + \frac{\sigma_r - \sigma_t}{r} &= 0\\ \frac{\partial\tau_{rz}}{\partial r} + \frac{\partial\sigma_z}{\partial z} + \frac{\tau_{rz}}{r} &= 0\end{aligned}\right\}$$

N. A. WEIL
Director of Mechanics Research,
Armour Research Foundation,
Chicago, Ill. Mem. ASME

J. E. BROCK
Professor of Mechanical Engineering,
U. S. Naval Postgraduate School,
Monterey, Calif. Mem. ASME

W. E. COOPER
Manager—S5G Structural Evaluation,
General Electric Company,
Knoll Atomic Power Laboratory,
Schenectady, N. Y. Mem. ASME

Stresses in a Pipe Bent Into a Circular Arc

The stress distribution in circular bends formed from straight pipe and subjected to internal pressure is presented. The analysis determines first the thickness distribution after forming, followed by an examination of the validity of membrane solutions for a complete torus. The predicted thickness distribution is in excellent agreement with experimental results as well as with three previous empirical formulations. The analysis shows that stresses in curved bends will always exceed the governing hoop stress in a comparable straight pipe, the deviation becoming greater with increased corrosion allowance. The authors recommend that, for purposes of acceptance by the ASA B31 Code, an excess stress level of the order of 5 per cent be allowed to develop in pipe bends. The resulting bend radius to pipe diameter limitations are listed in Table 3 and shown in Fig. 5. The last section of the paper deals with the major assumptions made in the derivation, and finds all of them to be acceptable for purposes of this analysis.

Introduction

THE Mechanical Design Committee (MDC) of the American Standards Association has been considering the problem of stresses in curved pipes subjected to internal pressure. The questions appear to fall into three categories: (*a*) The prediction of changes in wall thickness which accompany the fabrication of pipe bends from straight pipe, (*b*) the determination of stress distribution in pipe bends having a known wall-thickness variation, and (*c*) practical considerations relating to corrosion and the tolerable increase in stress above a nominal level. In spite of the importance of these questions, little information exists on this subject in the literature. This note is intended to place on public record what the authors believe to be some significant theoretical aspects of these questions, and to solicit comments from other engineers for consideration and use by the MDC. In preparing this note the authors, who are members of the MDC, are acting with the permission of the MDC, although their views do not necessarily represent those of the Committee as a whole.

Changes in Wall Thickness Resulting From Bending Straight Pipe

Analysis. When a straight circular cylinder of uniform wall thickness (a straight pipe) is bent such that its axis assumes the shape of a circular arc (pipe bend), the resulting wall thickness will no longer be uniform. In the ensuing derivation aimed at determining this thickness distribution, ϵ will be used to denote natural or logarithmic strains, as opposed to e for engineering strains. Making the customary assumption for volume constancy during plastic flow [1],[1] it follows that

$$\epsilon_\theta + \epsilon_r + \epsilon_\phi = 0 \tag{1}$$

where θ, r, and ϕ refer to the circumferential, radial, and meridional directions, respectively. Of these, the circumferential direction is along the lengthwise run of the pipe.

Referring to Fig. 1, consider a pipe bend already having a center-line radius ρ, which is bent to an even sharper radius. Denoting the arc $\widehat{AB}$ by l, we have

$$l = \rho\theta$$

so that

$$dl = \rho d\theta + \theta d\rho \tag{2}$$

If it can be assumed that the center line of the pipe suffers no change in length during the bending operation, then

$$dl = 0$$

and

$$d\theta = -\theta d\rho/\rho \tag{3}$$

The incremental circumferential strain is given by $\widehat{DE}/\widehat{CD}$, so that

$$d\epsilon_\theta = \frac{y\,d\theta}{(\rho + y)\theta}$$

Substitution of equation (3) reduces the foregoing expression to

$$d\epsilon_\theta = -\frac{y d\rho}{\rho(\rho + y)} = \frac{d\rho}{\rho + y} - \frac{d\rho}{\rho} \tag{4}$$

which, upon integration and observance of the boundary condition that $\epsilon_\theta = 0$ at $\rho = \infty$, leads to

$$\epsilon_\theta = \ln\left(1 + \frac{y}{\rho}\right) \tag{5}$$

It is seen from Fig. 2 that $y = r \sin \phi$; therefore, if the pipe is bent to a final center-line radius of R, equation (5) modifies to

$$\epsilon_\theta = \ln\left(1 + \frac{r}{R}\sin\phi\right) = \ln(1 + k \sin\phi) \tag{6}$$

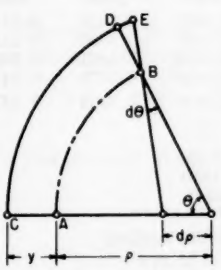

Fig. 1 Assumed deformation pattern

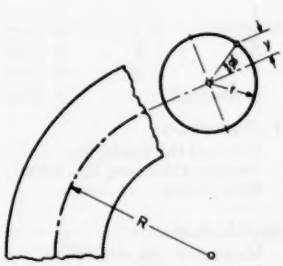

Fig. 2 Co-ordinate system for pipe bends

[1] Numbers in brackets designate References at end of paper.

Contributed by the Petroleum Division and presented at the Winter Annual Meeting, New York, N. Y., November 27–December 2, 1960, of THE AMERICAN SOCIETY OF MECHANICAL ENGINEERS. Manuscript received at ASME Headquarters, August 1, 1960. Paper No. 60—WA-157.

where the notation $k = r/R$ has been introduced.

This result could have been obtained also by noting that the conventional circumferential strain is

$$e_\theta = \frac{(R + r \sin \phi)\theta - R\theta}{R\theta} = k \sin \phi$$

If this expression is now substituted into the general relationship between conventional and logarithmic strains,

$$\epsilon_\theta = \ln(1 + e_\theta)$$

the result would be identical with equation (6).

The foregoing derivation assumes that y stays constant (meaning that the section remains circular) during the bending operation. With good bending technique this condition is very nearly met in practice. Moreover, the procedure followed here would retain its validity for the case where the cross section was allowed to ovalize.

Assuming further that no meridional natural strain develops,

$$\epsilon_\phi = 0 \tag{7}$$

and a combination of equations (1), (6), and (7) leads to

$$\epsilon_r = -\ln(1 + k \sin \phi) \tag{8}$$

But, from the definition of logarithmic strain,

$$\epsilon_r = \ln(t/t_0) \tag{9}$$

where t_0 is the original (predeformation) thickness. Equating equations (8) and (9) then yields

$$\frac{t}{t_0} = \frac{1}{1 + k \sin \phi} \tag{10}$$

This equation indicates a thickening of the wall at the intrados and a thinning at the extrados. The thinning at the extrados is of greatest practical importance; at this point $\phi = 90$ deg so that equation (10) simplifies to

$$t/t_0 = (1 + k)^{-1} \tag{11}$$

Experimental Results. As it happens, equation (11) is precisely the same as the formula given in 1956 by the Engineering and Standards Committee of the Pipe Fabrication Institute [2]. The PFI formula was presented without derivation as

$$\frac{T_b}{T_m} = \frac{\frac{2\pi}{4}\left(R + \frac{D}{2} - \frac{T_m}{2}\right)}{\frac{2\pi}{4} R} \tag{12}$$

where T_m is the thickness after bending, T_b the thickness before bending, R the bend center-line radius, and D the outside diameter of the pipe. The PFI Committee then simplified the formula by omitting the term $(-T_m/2)$ which led to the result derived before

$$t/t_0 = R/(R + 0.5D) = (1 + k)^{-1} \tag{11}$$

The relationship of $y = r \sin \phi$ would appear to limit the validity of the previous derivation to cases where the pipe is "thin walled." However, the PFI report discusses measurements performed on 43 bends of "heavy-wall" pipe in which the bend radius was five times the nominal diameter. Of these cases, 53 per cent showed less thinning while 47 per cent gave thinning greater than or equal to the amount predicted by equation (11). By the inclusion of a small safety factor the equation was then changed to

$$t/t_0 = R/1.015(R + r) = [1.015(1 + k)]^{-1} \tag{13}$$

which modified the percentages to 79 and 21 per cent, respectively. Equation (11) also appears in a publication of the Pines Engineering Company [3]. The authors have not been able to obtain any information concerning the background of the PFI or the Pines formula, but it is assumed that they were obtained empirically.

A similar expression, leading to very nearly the same results in the range of greatest practical interest was given by the Seamless Steel Tube Institute [4]. It is

$$t/t_0 = (R + r)/(R + 2r) = (1 + k)/(1 + 2k) \tag{14}$$

Efforts to learn the background of this formula have also proved to be fruitless.

Further confirmation of the adequacy of theoretical predictions is given in Table 1, drawn from results presented in [5]. This reference describes a set of careful thickness measurements made on large-diameter (nominal 36-in. OD) thin-walled (nominal thickness 0.344 in.) gas transmission piping bent to a small arc having a very generous radius ($R = 64$ ft).

Thickness measurements, using Vidigage and Audigage methods, were made at 14 points spaced 6 in. apart each on the extrados and intrados of the pipe both before and after bending (a total of 56 readings). Only the average of each set of 14 measurements is shown in Table 1 for the four pipe bends examined.

As Table 1 shows, the pipe had some out-of-roundness before bending which became more pronounced after completion of the bending operation. Nonetheless, the amount of initial out-of-roundness was small enough to be ignored, permitting equation (11) to be used in the calculations.

Table 1 Thickness changes in small-angle bends. Measured values by reference [5]; calculated results by equation (11).

		Thickness of bend, in.						Per cent change in thickness during bending			
		Extrados			Intrados			Extrados		Intrados	
Bend no.	Subtended angle, deg	Initial meas	Postbending Calc	Postbending Meas	Initial meas	Postbending Calc	Postbending Meas	Predicted	Actual	Predicted	Actual
1	2.5	0.3480	0.3402	0.3420	0.3419	0.3500	0.3509	−2.26	−1.73	2.37	2.64
2	6.5	0.3567	0.3487	0.3505	0.3514	0.3596	0.3549	−2.26	−1.74	2.37	1.00
3	3.5	0.3530	0.3450	0.3461	0.3486	0.3569	0.3557	−2.26	−1.96	2.37	2.04
4	2.5	0.3539	0.3459	0.3478	0.3470	0.3552	0.3509	−2.26	−1.73	2.37	1.13
Average		0.3529	0.3449	0.3466	0.3472	0.3554	0.3531	−2.26	−1.79	2.37	1.70

Pipe geometry:

Nominal thickness, in.	= 0.344
Average thickness, in. (initial)	= 0.350
Bend radius	= 64 ft = 768 in.

Outside diameters:	Before bending	After bending
Major axis $(2a + t)$, in.	35.978	36.339
Minor axis $(2b + t)$, in.	35.606	35.481
Average (D_0) in.	35.792	35.910
Nominal, in.	36.0	

As Table 1 shows, the agreement of predicted values with actual measurements is generally good, although measured values are somewhat lower than calculated results (7 out of 8 cases). This is probably traceable to the very small subtended angle of the bends, which permitted a magnification of end effects, most importantly plastic deformations transferred from the bend into the end tangents, which always act to lower the effective changes in wall thickness for the as-bent condition. For larger subtended angles these influences should become insignificant.

Stress Analysis for Bends of Circular Section

No Corrosion Allowance. After the bending operation involving large plastic strains has been carried out, sufficient accuracy is attained in the subsequent pressure stress analysis by reverting to engineering strains in the treatment of the problem.

In the design of ductile piping subject to internal pressure one is primarily concerned with either gross distortion or rupture of the piping should the wall be too thin. Since such behavior depends primarily upon the "average" stress distribution throughout the thickness, we will first consider the "membrane" stress solution to the problem, and then obtain confirmation of the adequacy of this approach by another technique.

The membrane forces per unit length, N_ϕ and N_θ, for the torus which remains circular follow directly from the expressions given by Timoshenko [6] which, using the notation of the present work, can be given as

$$N_\phi = \frac{2R + y}{2(R + y)}\, pr$$
$$N_\theta = pr/2 \tag{15}$$

Since these results are independent of thickness, they remain valid for the meridionally variable thickness condition treated here. Noting that $y = r \sin \phi$, and using the notation $k = r/R$, the membrane stresses can be expressed as

$$\sigma_\phi = \frac{N_\phi}{t} = \frac{2 + k \sin \phi}{2(1 + k \sin \phi)}\, \frac{pr}{t}$$
$$\sigma_\theta = \frac{N_\theta}{t} = \frac{pr}{2t} \tag{16}$$

Equations (16) are identical with the "Lorenz formulas" [7], developed for a complete circular torus of uniform thickness. For the thickness variation considered here, substitution of equation (10) into (16) results in

$$\sigma_\phi = \left(1 + \frac{k}{2} \sin \phi\right) \frac{pr}{t_0}$$
$$\sigma_\theta = (1 + k \sin \phi)\, \frac{pr}{2t_0} \tag{17}$$

An examination of equations (17) reveals that the meridional stress σ_ϕ is always the larger numerically. The absolute maximum membrane stress will be its value at the extrados (the outside of the bend) as given by

$$\left.\frac{\sigma_\phi}{\sigma_0}\right|_{\max} = 1 + \frac{k}{2} \tag{18}$$

where $\sigma_0 = pr/t_0$ represents the nominal hoop stress in the undeformed pipe. The absolute minimum stress occurs at the intrados, with a value of

$$\left.\frac{\sigma_\phi}{\sigma_0}\right|_{\min} = 1 - \frac{k}{2} \tag{19}$$

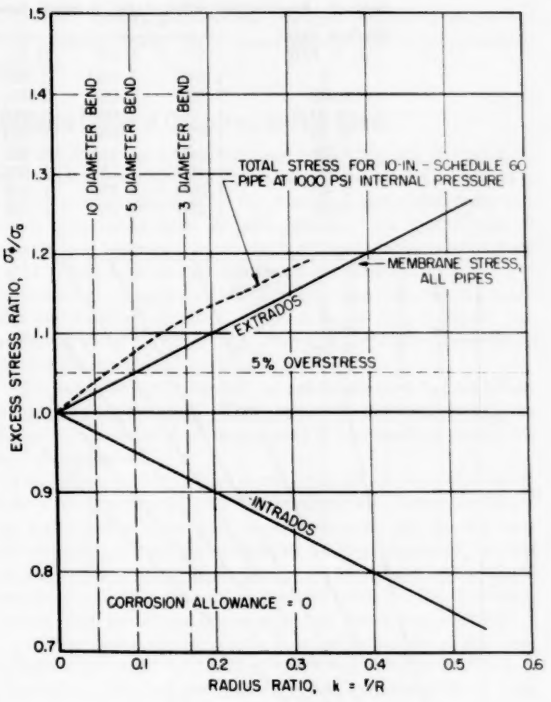

Fig. 3 Extreme stress ratios in formed bends

Equations (18) and (19) are plotted in Fig. 3.

Analysis With Corrosion Allowance. Assume now that the entire pipe-wall thickness is not available for load-carrying purposes; instead, a given portion of it must be reserved for corrosion allowance. If conditions are such that internal corrosion may result in the eventual removal of a certain amount C (in.) of the wall thickness, the fundamental approach of the previous analysis can be retained with the following modifications. Paying attention to the meridional stress only, since it governs design, and making use of equation (10), equation (16) would then be replaced by

$$\sigma_\phi = \frac{2 + k \sin \phi}{2(1 + k \sin \phi)}\, \frac{rp}{t - C} = \left(1 + \frac{k}{2} \sin \phi\right) \frac{rp}{t_0 - C(1 + k \sin \phi)} \tag{20}$$

or, at $\phi = 90$ deg, where the maximum occurs

$$\sigma_\phi = \left(1 + \frac{k}{2}\right) \frac{rp}{t_0 - C(1 + k)} \tag{21}$$

The reference stress, i.e., the hoop stress in the undeformed straight pipe, will now be given by

$$\sigma_0 = \frac{rp}{t_0 - C}$$

so that equation (21) can be rewritten as

$$\frac{\sigma_\phi}{\sigma_0} = \frac{1 + \dfrac{k}{2}}{1 - k\dfrac{C/t_0}{1 - \dfrac{C}{t_0}}} \tag{22}$$

Table 2 Excess stress ratios, σ_ϕ/σ_0, in bends formed from straight pipe, with various corrosion allowance

Radius ratio, $k = r/R$	Corrosion-allowance ratio, C/t_0							
	0	0.05	0.10	0.15	0.20	0.30	0.40	0.50
0	1.000	1.000	1.000	1.000	1.000	1.000	1.000	1.000
0.05	1.025	1.028	1.031	1.034	1.038	1.047	1.060	1.079
0.10	1.050	1.056	1.062	1.069	1.077	1.097	1.125	1.167
0.15	1.075	1.084	1.093	1.104	1.117	1.149	1.194	1.265
0.20	1.100	1.111	1.125	1.140	1.158	1.203	1.269	1.375
0.30	1.150	1.169	1.190	1.214	1.243	1.320	1.438	1.643
0.40	1.200	1.226	1.256	1.291	1.333	1.448	1.636	2.000
0.50	1.250	1.284	1.324	1.371	1.429	1.591	1.875	2.500

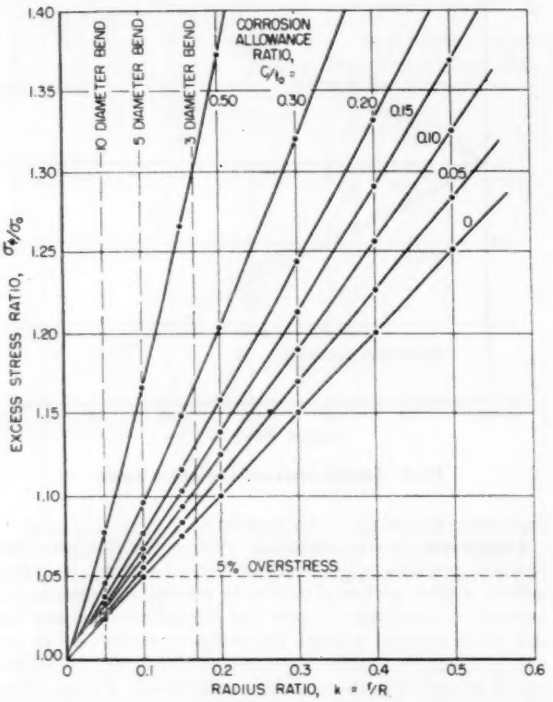

Fig. 4 Overstress in bends at various corrosion allowances

The ratio C/t_0 represents the percentage of the initial pipe-wall thickness t_0 reserved for corrosion allowance. Obviously, $0 \leq C/t_0 \leq 1$ and, when $C/t_0 = 0$, equation (22) reduces to equation (18).

The "excess stress ratio" σ_ϕ/σ_0 is presented in Table 2 and Fig. 4 for values of C/t_0 equal to 0, 0.05, 0.10, 0.15, 0.2, 0.3, and 0.5. As this figure shows, the excess stress becomes the higher the greater the ratio of corrosion to initial wall thickness.

Adequacy of Membrane Solution

In the interest of assessing the reliability of the membrane solution, Mirabal [8] obtained the solution to a specific problem through the use of E. Reissner's thin elastic-shell equations. The results of this calculation, which included a consideration for the bending-stress component, are also plotted in Fig. 3. It was found that the membrane stress is a maximum at the extrados and varies with the ratio of the pipe radius to the bend radius k, exactly as predicted by equation (18). In addition, it is shown that the sum of the bending stress and the membrane stress is only 3 per cent higher than is the membrane stress alone. These results are considered to be sufficient proof of the ability of equation (18) to predict the significant stress in a thin-walled bent pipe which remains circular in cross section.

The specific numerical problem considered by Mirabal was that of a nominal 10-in. Sch. 60 pipe, bent to various radii and subjected to an internal pressure of 1000 psi. The problem was solved on a digital computer, using the approach of sectioning the torus at the horizontal center line (a plane of symmetry) and integrating the shell equations over the upper half. The program treats the shell as an initial value problem starting at the outer edge and integrating to the inner edge, making use of the fact that the horizontal shear force, rotation, and axial deflection are all zero at both edges. This type of approach allows the computer to continuously check the accuracy during integration and automatically increase or decrease the integration interval to maintain uniform accuracy through the solution with a minimum of computer time. The values of the variables at no more than six points need be stored at any one time and the required accuracy is supplied as input data. In this case, both membrane and total stress were held accurate to within one per cent.

Ovalization of Section During Bending

In this section we will examine the effect on the membrane hoop stress of permitting the originally circular section of radius r to flatten slightly by imperfect restraints during the bending operation. We assume that the section deforms without change of perimeter into an ellipse of eccentricity $e \ll 1$ and semi-axes a and b, the former being the semi-major axis parallel to that of the torus. It can be shown that

$$\left.\begin{aligned} a &= r + c \\ b &= r - c \\ c &= 4re^2 \end{aligned}\right\} \tag{23}$$

Let β be the angle subtended at the center of the original circular section by the arc between the extrados point (most distant from the center of the bend), and a general point, $P(x, y)$. The initial position of P on the circle is defined the co-ordinates

$$\left.\begin{aligned} x_0 &= r \sin \beta \\ y_0 &= r \cos \beta \end{aligned}\right\} \tag{24}$$

Because of flattening, this point is transposed to the position P' on the ellipse whose co-ordinates, to the first order in the small quantity c, will be given by

$$\left.\begin{aligned} x_1 &= x_0 + c(x_0/r)^3 \\ y_1 &= y_0 - c(y_0/r)^3 \end{aligned}\right\} \tag{25}$$

For an elliptical section, the unit membrane forces given by equations (15), will modify to

$$\left.\begin{aligned} N_\phi' &= \frac{2R + y}{2(R + y)} \frac{[a^4y^2 + b^4x^2]^{1/2}}{a^2} p \\ N_\theta' &= \frac{p}{2[a^4y^2 + b^4x^2]^{1/2}} [2y(a^2 - b^2)(y + R) + b^4] \end{aligned}\right\} \tag{15a}$$

The membrane-stress-flow ratio

$$\gamma = N_\phi'(P')/N_\phi(P) \tag{26}$$

for corresponding points P and P' may be shown to be (to the first order in c)

$$\gamma = 1 - \frac{cM}{r} \tag{27}$$

where

$$M = 1 + 2\sin^2\beta - Q\cos^2\beta;\ k = r/R$$
$$Q = q/(2+q)(1+q);\ q = k\cos\beta;$$

For $k < 1$, $M > 0$, which shows that the membrane hoop-stress flow at any point of the section is *reduced* by slight ovalization.

In addition to its effect upon the membrane meridional force, ovalization will also affect the degree of thinning or upsetting entering into the hoop-membrane stress equation $\sigma_\phi = N_\phi/t$. It may be shown that equation (4) is valid even though y does not remain constant during the bending operation. However, the proper relationship between y and ρ, required to integrate equation (4), is not known under conditions of ovalization. (It may be noted that there is no single "correct" relationship. For example, if a well-packed sand-filled pipe were to lose its sand filling part way through the bending operation, ovalization would be small up to this stage and relatively much greater during the remainder of the operation.) Nonetheless, one can invoke the mean-value theorem according to which

$$t' = \frac{t_0}{1 + \bar{y}/R} \tag{28}$$

where $\bar{y}$ lies between the initial and final values of y. Thus

$$\delta = \sigma_\phi'/\sigma_\phi = \gamma t/t' = \gamma\left(\frac{1+\bar{y}/R}{1+y/R}\right) \tag{29}$$

and

$$\left(y - \frac{cy^3}{r^3}\right) \leq \bar{y} \leq y$$

For $y \geq 0$, it is clear that $\delta \leq \gamma < 1$.
For $y < 0$,

$$\delta < \gamma\left(\frac{R + y - cy^3/r^3}{R+y}\right) = \gamma^* \tag{30}$$

and it may be shown that the product on the right may be written as

$$\gamma^* = 1 - \frac{cM^*}{r} \tag{31}$$

where

$$M^* = 1 + 2\sin^2\beta - Q^*\cos^2\beta$$
$$Q^* = (3+q)q/(2+q)(1+q)$$

Over the entire range $0 < k < 1$, we have $Q^* < 2/3$, so that $M^* > 0$ for all points on the section. Thus, for all points on the section of a bend for which $k < 1$, slight ovalization *reduces* the membrane hoop stress.

Circumferential membrane stresses σ_θ are much smaller than meridional stresses σ_ϕ and therefore will not be considered further. It is true that there are meridional bending stresses superimposed upon the stresses σ_ϕ discussed in the foregoing analysis. However, we will not treat these bending stresses further, since (*a*) such bending stresses also exist in the bent pipe with circular cross section, as was shown in the preceding section; (*b*) "slight" ovalization would only induce moderate bending stresses; (*c*) the general effect of bending stresses resulting from ovalization is to reduce out-of-roundness; (*d*) experience indicates that these bending stresses are not important with usual engineering materials possessing sufficient ductility; and (*e*) a bending-stress theory for ovalized pipe bends is not presently available.

Allowable Limits of Overstress in Pipe Bends

As the foregoing derivation shows, the thinning occurring at the extrados, when forming a straight pipe into a circular arc, is in some measure mitigated by the resulting membrane-stress distribution in bends under internal pressure; for a pipe bend of uniform wall thickness maximum meridional membrane stresses would be found on the inside of the bend. This mitigating effect, unfortunately, is not enough to overcome the thinning associated with the forming operation. Therefore, as Fig. 3 shows, the maximum stress in bends will always exceed the reference hoop stress in the corresponding straight pipe.

This being so, it is useless to argue whether an overstress should be permitted at all. The question should rather be: Given this condition, what shall be assumed to represent an acceptable level of overstress?

The Code position on this question has always been that safety factors are incorporated into the formulation of allowable stresses, the magnitude of these safety factors varying with the degree of understanding of material properties, loading conditions, and the accuracy of analytical techniques. An overstress is frequently permitted, provided that the stress field is tensile, the material is ductile, and the stress distribution can be determined with a reasonable degree of accuracy. As an example, the AISC Code permits a general 5 per cent overstress to develop under these conditions, with a 15 per cent allowance permitted for the case of built-up sections having rivets in the tensile flange (Section 26(*a*) of AISC Specification).

The case at hand satisfies a condition for which a Code would normally permit an overstress to be tolerated. The stress system is tensile, the material ductile, and the analysis presented here is felt to be sufficiently refined to predict actual stresses within close tolerances. It is the authors' view, therefore, that an overstress of approximately 5 per cent should be readily permitted in pipe bends subjected to internal pressures.

The overstress advocated here is backed up by still another consideration; namely, the decades of successful operating experience with pipe bends. As Fig. 4 shows, a "short-radius bend" (bend radius equal to 5 pipe diameters) carries an inherent stress intensification of 5 per cent overstress, in the absence of corrosion allowance. With corrosion allowance, the overstress is more. Despite this, there is no known case of failure on record ascribable to a direct overstressing of a pipe bend in the meridional direction under static-pressure loading, even though short-radius bends are used as a matter of routine in the construction of piping configurations.

Fig. 5 shows the relationship which holds between bend sharpness (as expressed by k or R/D) and corrosion allowance ratio C/t_0, at various values of overstress. This information is given numerically in Table 3.

Validity of Assumptions

Apart from the assumptions common to the theories of elasticity and plasticity, the foregoing analysis entails five major assumptions:

1 The center line (axis) of the pipe remains unchanged in length during the bending operation. This assumption is utilized in equation (3).

2 The pipe cross section remains circular after bending; use of this assumption was made in equation (6).

3 No meridional strain develops during forming, as embodied in equation (7).

Table 3 Limiting radius ratios, $R/D = 1/2k$, for various values of overstress and corrosion-allowance ratios

Per cent overstress, $100(\sigma_\phi/\sigma_0 - 1)$	Corrosion-allowance ratio, C/t_0							
	0	0.05	0.10	0.15	0.20	0.30	0.40	0.50
1	25.0	27.7	30.6	33.9	37.6	46.6	58.7	75.5
2	12.5	13.8	15.3	17.0	18.9	23.4	29.5	38.0
3	8.33	9.24	10.2	11.4	12.6	15.7	19.8	25.5
4	6.25	6.93	7.69	8.54	9.50	11.8	14.9	19.2
5	5.00	5.55	6.17	6.85	7.62	9.50	12.0	15.5
6	4.17	4.63	5.15	5.73	6.38	7.95	10.1	13.0
7	3.57	3.97	4.42	4.92	5.48	6.85	8.67	11.2
8	3.12	3.48	3.88	4.32	4.81	6.02	7.62	9.88
9	2.78	3.10	3.45	3.85	4.29	5.37	6.81	8.83
10	2.50	2.79	3.11	3.47	3.88	4.86	6.17	8.00
12	2.08	2.33	2.60	2.91	3.25	4.08	5.19	6.75
15	1.67	1.87	2.09	2.34	2.62	3.31	4.42	5.50
20	1.25	1.41	1.58	1.78	2.00	2.54	3.25	4.25
30	0.833	0.947	1.07	1.22	1.38	1.76	2.28	3.00
40	0.625	0.717	0.819	0.934	1.06	1.38	1.79	2.38
50	0.500	0.579	0.667	0.765	0.875	1.14	1.50	2.00

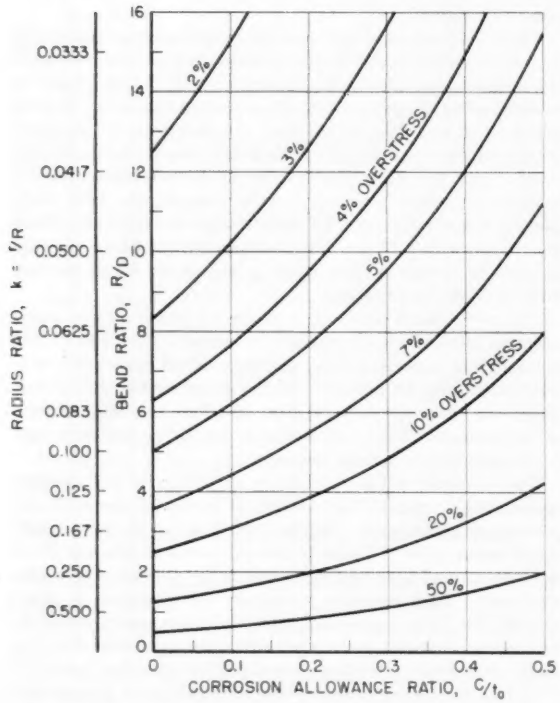

Fig. 5 Limiting bend ratios for various percentages of overstress in formed bends

4 Pressure stresses in the curved pipe are adequately represented by the Lorenz formula for a complete torus, as given by equations (16).

5 End effects (the condition of dealing with a finite torus at specified boundary conditions) can be ignored.

With careful bending operation, as is the practice in all better quality pipe-fabricating shops, assumptions 1 and 2 are closely satisfied. Assumption 4 was dealt with in detail in an earlier section, where it was shown that the Lorenz approximations represented an acceptable and workable condition for the case at hand. This leaves only assumptions 3 and 5 to be considered, which will now be subjected to closer scrutiny.

Assumption 3, which postulates that $\epsilon_\phi = 0$, can be satisfied in practice only "on the average" through the thickness. Since the validity of this assumption would tend to have a direct effect on the resulting thickness distribution, the best measure of its correctness should be sought in experimentally determined values of post-forming thicknesses. In this light, it is considered significant that the same formula resulting from the assumption of $\epsilon_\phi = 0$ has been published twice previously, presumably as empirical formulations based upon observed behavior, and agrees very closely with still another formulation, equation (14), in the significant range of $R \geq 5D$. When one considers, in addition, the excellent experimental substantiation given to equation (11) by the PFI measurements, as well as the results of [5] assembled in Table 1, assumption 3 is seen to be completely acceptable for the analysis developed here.

Assumption 5 is known to be violated in practice, since the bend is a finite rather than a complete torus. The correct boundary conditions placed upon this finite torus would be those that restore compatibility and equilibrate forces between the ends of the bend and the adjoining straight pipe. The reason that these end effects can be ignored stems from two main considerations: By Saint Venant's principle the disturbances introduced at the pipe end will die out within a short distance (say a distance of one pipe diameter), and the end conditions so induced tend to ameliorate stress conditions as compared to a complete torus [9]. The maximum stresses in pipes incorporating curved bends, as well as bursting if the configuration were taken to failure, have always occurred at the middle of the curved portion. Therefore, assumption 5 can be accepted as being representative of governing conditions, provided the arc of the bend is sufficiently large, having a subtended angle of say more than 30 deg. This view is further confirmed by the experimental results referred to before, which show that for a torus with a small subtended angle [5] the thickness changes are less than would be expected, whereas for a pipe bend with a large subtended angle (90 deg or above) the post-bending thickness distribution [2] is substantially as predicted by the theory presented here.

Summary and Conclusions

This paper presents the first rational attempt known to the authors to define the stress distribution in curved pipes formed from straight runs and subjected to internal pressure. The analysis is developed in three steps: (*a*) The thickness distribution resulting from bending a straight pipe into a circular arc is determined; (*b*) the validity of membrane solutions applicable to a complete torus is examined; and (*c*) these results are applied to predict the stress distribution in formed bends in the presence or absence of corrosion.

The analytical prediction for pipe-wall thinning is identical with two previously published formulations and is in close agree-

ment with a third one, all three of which, for lack of any further substantiation, are assumed to be empirical formulations of observed behavior. Most important, the results of the analysis are excellently confirmed by wall-thinning measurements carried out on a large number of pipe bends [2, 5].

As the subsequent analysis shows, the simple membrane solution no longer applies when the wall thickness of the finite torus is not uniform. The deviation is, however, so small (see Fig. 3), that the membrane solution can be accepted as being valid for all practical purposes. This is particularly a tenable position if one considers that the bending-stress component is self-equilibrating and tends to vanish as the pipe is stressed beyond its yield point.

It is also shown that ovalization, whether present initially in the straight pipe or permitted to develop during bending, reduces both the post-forming thickness changes and the governing stresses as represented by the meridional membrane stress due to internal pressure. Although ovalization concomitantly induces meridional bending stresses, the practical significance of the latter is inconsequential. On balance, therefore, ovalization is regarded as being conducive of conditions less severe than those pertinent to carefully fabricated bends having a circular post-forming section.

The analyses so developed allow a formulation of stresses in curved pipes having a varying wall thickness. As shown in Fig. 4, maximum stresses in a pipe bend always exceed the governing hoop stress in a comparable straight pipe. In the presence of corrosion, the excess stress ratio becomes even higher.

In the light of this, the question becomes not whether an excess stress should be tolerated but rather how much excess stress should be regarded as being permissible. The authors advocate an overstress of approximately 5 per cent as compared to the governing hoop stress in comparable straight pipe, for acceptance by the Mechanical Design Committee and subsequently the Executive Committee of the ASA B31 Code. This view is based upon similar positions adopted by the AISC Code for cases (such as this one) where the stress field is tensile, the material ductile, and the governing stresses can be predicted closely. Further substantiation to this view is afforded by the long and satisfactory service experience with pipe bends, many of which (in fact all of the "short radius" bends) have unknowingly operated at stress levels exceeding the assumed design values by 5 per cent or more. The limiting radii to which a pipe of a given diameter may be bent is shown in Table 2, as functions of the corrosion-allowance ratio and per cent allowable overstress. This information is also reproduced graphically in Fig. 5.

The last section of the paper delineates the major assumptions made in the analysis and finds all of them to be acceptable.

Acknowledgments

The authors wish to acknowledge gratefully the valuable suggestions and encouragement extended them by Mr. W. S. Martyn, Chairman, and Messrs. L. L. Ross and M. J. Paul, Members of the MDC of the ASA B31 Code.

References

1 O. Hoffman and G. Sachs, "Introduction to the Theory of Plasticity for Engineers," McGraw-Hill Book Company, Inc., New York, N. Y., 1953, p. 32.

2 Pipe Fabrication Institute Report of Engineering and Standards Committee, "Investigation to Determine Thinning in Hot Bends of Heavy Wall Pipe of Carbon and Ferritic Alloy Steel," February 8, 1956, not available publicly.

3 Catalog materials, Pines Engineering Company, Inc., 601 Walnut Street, Aurora, Ill.

4 "Bending Seamless Steel Tubing," copyright, 1945, by the Seamless Steel Tubing Institute. This Institute became inactive in January, 1949.

5 E. Steffens and A. G. Barkow, "Study of Variations in Wall Thickness and Diameter Caused by Field Bending," Report No. NG-59-1 of the Natural Gas Pipeline Company of America, January 16, 1959, not available publicly.

6 S. Timoshenko, "Theory of Plates and Shells," McGraw-Hill Book Company, Inc., New York, N. Y., 1940, pp. 365–366.

7 H. Lorenz, "Theorie der Röhrenfedermanometer," *Zeitschrift, VDI*, vol. 54, 1910, pp. 1865–1867.

8 J. A. Mirabal, private communication, 1959.

9 T. E. Pardue and I. Vigness, "Properties of Thin-Walled Curved Tubes of Short-Bend Radius," TRANS. ASME, vol. 73, 1951, pp. 77–84.

DISCUSSION

Karl A. Gardner[2]

It should in no way detract from the authors' valuable paper, nor from the credit due them for it, to point out that a portion of their work has been anticipated by others and has, indeed, been published. Their equation (18) appears (in required thickness ratio form) in Paragraphs R-& C-2.31 of the Standards of Tubular Exchanger Manufacturers' Association Fourth Edition, 1959, of which the writer was Editor. It had also appeared prior to that in the Standards of Feedwater Heater Manufacturers' Association, Second Edition, 1958. To the best of the writer's knowledge, it was originally due to Mr. O. W. Heimberger, Vice President-Engineering (retired), The Griscom-Russell Co., *circa* 1936. The derivation was based on the assumption that the product of length times thickness of any originally axial tube wall element must retain its original value during the bending process, i.e., that the volume remains constant and there is no metal displacement circumferentially of the tube; this result, identical with the authors' equation (11), was then used in the Lorenz equation. Some thought was given by TEMA before publication to the incorporation of a limiting k value below which it would be unnecessary to be concerned about a slight degree of overstress. It was concluded, however, that this would amount to usurping a prerogative of the ASME Code Committees, so this further concurrence with the authors' thinking was not published.

The authors' investigations into the effects of corrosion, ovalization, and adequacy of the membrane solution are particularly valuable since they remove much of the obscuring haze which tends to envelop the main subject whenever it comes under discussion.

During the TEMA Technical Committee's deliberations on the advisability of carrying over FHMA's U-bend thickness formula into their own Standards, many facts and several theories were brought to light which have a bearing on the authors' reasoning and conclusions. Briefly, some of these were:

1 The assumption of zero meridional strain is not necessarily valid and, if this be the case, thinning of the outer fibers and stress intensification will be considerably less than predicted by equations (11) and (18). This was brought out by Messrs. John Soehrens and Milton Nehls, Staff Consultants, C. F. Braun & Co. and, it must be admitted, did violence to the writer's preconceived notions on tube bending.

2 Actual bend thinning data on approximately 60 samples of 180-deg tube bends with $0.5 > k > 0.09$ were compiled as shown in Fig. 6, which is reproduced from data in the writer's files made available through TEMA. Some tended to confirm the assumption of no meridional strain, but others seemed to indicate a meridional strain approximately equal to the radial strain.

3 Burst tests on 180-deg nonferrous tube bends were reported in which all failures but one (out of four) occurred in the *straight* portion of the tube, not in the bend.

Although he has no full blown theory to support it, it is the

[2] Vice President-Engineering, Yuba Consolidated Industries, Inc., San Francisco, Calif. Mem. ASME.

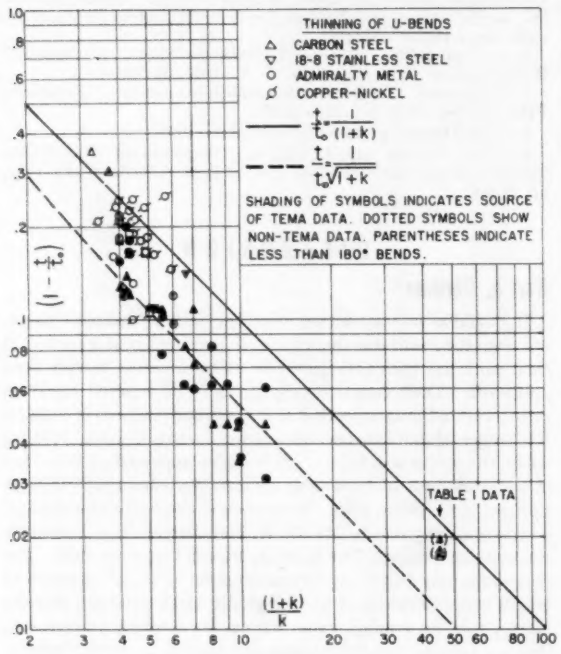

Fig. 6

writer's personal opinion that a major contributing cause for the wide variety of radial strains in Fig. 6 was the presence or absence of an internal mandrel during the forming operation. Unfortunately, the antiquity of the test data was such that no direct confirmation of this hypothesis is possible. Nevertheless, it is apparent from Fig. 6 that those bends in which it is unlikely that a mandrel would be used, i.e., those of small k, tend to cluster about the line for an assumed meridional flow, whereas the others group in such ways as to suggest not merely gross experimental scatter but rather an overlap of two bands of data, one approximating $\epsilon_\phi = 0$, the other, $\epsilon_\phi = \epsilon_r$. It is possible too that the ratio of wall thickness to tube radius and total arc of bend enter into the discrepancies; practically all of the data in Fig. 6, except the authors', are for t_0/r between 0.1 and 0.2, whereas the values from Table 1 are for $t_0/r = 0.0198$.

The writer does not concur in the authors' belief that the PFI equation (12) represents an empirical correlation of observed data. It was in all likelihood derived in the same way as mentioned in the first paragraph of this discussion; if so, it merely confirms that the same basic assumptions (volume constancy, no meridional strain, etc.) produce the same results however manipulated. The point here is, of course, the danger of unwittingly taking the same equation as confirmation of itself. For many years the writer also was of the opinion that data of the nature given in Table 1 of the paper *did* constitute reasonable evidence that the assumption of $\epsilon_\phi = 0$ was valid, never having given thought to alternative assumptions. As mentioned in the foregoing however, Mr. J. Soehrens, in a personal communication, indicated the consequences of the assumption that $\epsilon_\phi = \epsilon_r$, namely, that

$$\frac{t}{t_0} = (1 + k)^{-1/2} \simeq \left(1 + \frac{k}{2}\right)^{-1}$$

On this basis, shown as the lower line in Fig. 6, the predicted per cent change in thickness of the outermost wall would be -1.14 instead of -2.26. Referred to the test data as a base, the assumption that $\epsilon_\phi = 0$ leads to a predicted value that is 26 per cent high, whereas the assumption that $\epsilon_\phi = \epsilon_r$ gives a value 36 per cent low; referred to the theoretical predictions, these values become $+21$ and -57 per cent. In either case the writer would not characterize the agreement as "excellent," particularly in view of the many other data tending to indicate that factors other than k alone must be involved.

As far as the burst failures in the straight portions of hairpin bends are concerned, they may be attributable to the strain-hardening of the thinned section as compared to the thicker, but unworked, metal in the straights. For this reason it seems unwise to place too much reliance on "successful operating experience," at least in the case of metal susceptible to cold work.

Regardless of the personal views of the two preceding paragraphs, or of those of others on the committee, it was the final considered opinion of the TEMA Technical Committee that its formula should be adequate to cover *all U-bends conservatively*, since many manufacturers purchase them ready-made and have no control over the forming process. In effect it was felt that equation (11), while not very accurate, had the virtues of simplicity [when used in conjunction with equation (16)] and of safety.

Although the writer refers in the foregoing to actions and deliberations of the TEMA Technical Committee, of which he was Chairman at the time this subject was under consideration (1958), the present discussion should be construed only as his own views and recollection of events, prompted by desire to have FHMA's and TEMA's contributions more widely known.

E. F. Gerwin[3] and R. H. Caughey[4]

The trend in the power industry during the last decade to higher pressures and temperatures has made the subject of stresses in bends increasingly important to piping designers. The demand has been that the wall thickness after bending must not be less than the minimum calculated for straight pipe. Since most high pressure steam lines are large diameter, heavy wall (2, 3, or 4 inches) material and are purchased to minimum wall requirements, it is often necessary to purchase heavier walls to fulfill this requirement when the pipe is to be bent. This naturally results in added costs for the initial pipe material.

The attention given by the authors to this problem is therefore very appropriate, since it could represent a major step toward the establishment of Code rules for the acceptability of pipe bends.

The authors make reference to the PFI Engineering Standards Committee report on this same subject, to the effect that the formulas shown therein were developed empirically. This was not wholly the case. Equation (12) cited in the authors report (as the PFI formula) was based on theoretical assumptions similar to those used by the authors in this instance.

Concurrent with the theoretical developments, PFI member companies conducted a series of measurements on production hot bent pipe. The analysis of these data and comparison made with the theoretical formula proved that a correction factor was necessary. What dependent variables were involved in the correction factor were not further explored. Accordingly, only the correction factor was developed empirically.

It is believed that an explanation of the variations involved particularly in hot bends would be found in the effects of:

1 Wall thickness variations in the product to be bent: Varying thickness along the arc to be bent would produce varying degrees of plastic deformation during bending, with the most severe at the thinnest section. Each type of pipe product has its

[3] Power Piping Division, The M. W. Kellogg Company, Williamsport, Pa. Mem. ASME.

[4] Power Piping Division, The M. W. Kellogg Company.

won peculiarities. For example, a study of rotary-pierced pipe will reveal a wall thickness variation pattern which generally follows a spiral along the pipe lengths.

2 Metal temperature variations both in the pipe and attendant to cooling during the bending procedure: These again could produce nonuniform and perhaps highly localized deformation for a given bending stress.

3 Application of the bending forces: One of the main assumptions in the theory is that the length of the center line is not altered during bending. As pointed out by the authors, a careful bending operation as practiced by the better quality shops will usually not alter the length appreciably. There is no way to assure that this will be the case at all times and in all shops, however.

The discussers are not in a position to comment on the 5 per cent overstress recommended by the authors. However, we question whether it is their intention to include piping which operates in the creep range.

Needless to say any allowance which would even partially eliminate the need for the selection of special sizes of pipe for bending would be more than welcome. Naturally it would be necessary to have this allowance adopted by the Code bodies, preferably in terms of wall thickness after bending. This would establish a clean-cut rejection limit, and would of course force the individual fabricator to compensate for the variables mentioned in the foregoing.

W. L. Harding[5]

The authors have treated an interesting topic and have performed a useful service in highlighting the expressions for membrane forces in a bend. Their efforts to apply a simple mathematical analysis to the prediction of wall thickness variations in bends is understandably less successful. The plastic flow of metal in a bend does not necessarily follow the assumptions they have used. As a consequence, their equations predict thicknesses which may differ substantially from results of actual practice. Since their comments on stress rest on these calculated thicknesses, many of the authors' conclusions are likewise open to question.

It is not surprising that their elementary formula for wall thickness variation is not adequate. The plastic flow of metal in a pipe or tube bend is strongly influenced by many variables in the technique of bending. Type and fit of dies (if used); selection of pull versus push bending; temperature and temperature distribution during bending; use of filler material; and other factors affect the result. These factors interact in a complex manner which does not conform to the simplifying assumptions which the authors used in their analysis.

It is suggested the authors could make a valuable contribution by extending their stress analysis to establish what minimum values of wall thickness in the various regions of a bend are required to assure the equivalent safety and expected life as in the corresponding straight pipe. This theoretical development should then be verified by an adequate test program. Design, fabrication, and inspection would then aim at assuring that actual wall thickness in a specific application equals or exceeds these defined minimums. This is considered a sounder approach than the acceptance of some hypothetical "overstress" predicated on a calculated under-thickness which may or may not exist.

Specific comment on details of the paper are as follows:

1 Table 1 shows the authors' predicated thinning was 25 per cent more than actually occurred, and their predicted thickening on the inside of the bend was almost 40 per cent greater than the measured average. Opinions may differ on whether this is "good" agreement.

2 The report cited for "heavy-wall" pipe covers bends of only a single value of radius ratio, and the authors list only the averages for thinning on the outside. It would be of interest to know whether thickness changes on the inside and the sides of the bend also support the authors' theory.

3 The limited experimental evidence of (1) and (2) supports the upper line of Fig. 3 only up to a radius ratio of $k = 0.1$. The range from $k = 0.1$ to $k = 0.5$ has no experimental backing, but this is just the range of "tighter" bends in which the special bending techniques are more widely used to control wall thickness. (It would also appear the lines for 10, 5, and 3 in. *diameter* bend on this Fig. 3 should be relabeled as 100, 50, and 30 in. *radius*, respectively, if they refer to the 10-in. pipe.)

4 The authors' hypothesis that bursting would occur in the middle of the curved portion is contrary to the experience of the writer's company. Of many bends carried to bursting either in short-time room temperature tests or in extended-period rupture tests at elevated temperature, practically all have failed in the adjoining length of straight tube. It has been necessary to reduce the straight length about to zero to force the rupture to occur in the bend. It is our understanding that other fabricators have had similar experience in tests of bends.

J. J. Murphy[6] and D. B. Rossheim[7]

The lack of guidance of the Code rules as to the minimum acceptable thickness of pipe after bending has, at times, caused considerable difficulty in establishing the acceptability of a given bend. Consequently, the detailed attention given to this problem by the authors is very welcome and commended.

The analysis presented in the paper to predict wall thinning as a result of bending, as stated, results in a relation identical to that presented in the PFI report (paper reference [2]). The authors state they have not been able to obtain information on the background of the PFI formula and assume it was obtained empirically in a different manner. The discussers are not acquainted with the original development of the PFI formula but the formula merely equates the volume of the outer fiber before and after bending (over a 90-deg arc which is immaterial). It inherently involves assumptions 1, 2, and 3 of Section VII of the subject paper and is not empirical; it arrives at the end result more directly and, therefore, constitutes a check on the mathematics but nothing more.

Assumption 3 of Section VII is questionable. If it were assumed that the meridional and thickness strains are equal, equation (11) would be changed to

$$t/t_0 = (1 + k)^{-0.5}$$

Table 1 results are between the two results and favor the authors assumption somewhat; the PFI data apparently supports assumption 3 more adequately. The choice of formula thus rests heavily on agreement with actual results.

The discussers would like to ask whether the test results cited were plotted and statistically analyzed. If so, the detailed results would be of interest. The PFI test results are cited as showing greater thinning than Equation (11) in 47 per cent of the cases and greater than Equation (13) in 21 per cent of the cases. The extent of the difference is not stated. For accurate evaluation of tests it is desirable to know the thickness and distribution both axially and circumferentially and the out-of-roundness before and after bending.

[5] Research & Product Development, Combustion Engineering, Inc., Windsor, Conn. Mem. ASME.

[6] Section Engineer, Mechanical Engineering Division, The M. W. Kellogg Company, New York, N. Y. Mem. ASME.

[7] Assistant to Vice President, Charge of Engineering, The M. W. Kellogg Company. Fellow ASME.

With regard to assumption 1, there will be a slight shift in the neutral axis even if the pipe remains circular due to thinning at the outside and thickening at the inside of the end. The discussers have investigated the effect of this in changing equation (11) and find it is negligibly small although the correction is in the direction of the PFI modification (Equation 13).

Proceeding from the thinning analysis, the paper proceeds to apply the general membrane stress formulas to evaluate stresses and arrives at a recommendation for about 5 per cent allowable overstress.

The discussers question the reasoning presented in Section VI as to whether an overstress should be permitted and what its level may be. The stress being considered is an average membrane stress and exists over a long length and will produce general yielding if it exceeds the yield strength unless the load can shift to a lower stressed zone. The inner fibers can sustain greater load but it is not obvious how the bend shape could change to shift some load to the inside. There is no question that bends are in service which involve the indicated degree of overstress. This may be an indication that with present safety factors the straight pipe runs could be operated at a higher pressure if the same maximum membrane stress were to be maintained in other portions. It is desirable that the Code Committee more broadly examine the question so as to be in a position to make consistent recommendation as the Code advances toward evaluation of more refined design approaches than those inherent in the present rules.

It also seems to the discussers that bending stresses are dismissed too lightly. Again, looking toward future improvements in design evaluation, these bending stresses must be considered as to their fatigue potential. The bending stress component due to out-of-roundness does tend to vanish as the pipe is stressed beyond its yield point; the bending strain caused by the radial inward and outward components of the axial pressure load is not relieved and is cyclic with each pressure load application.

Is it the conclusion of the authors from their examination of test results and correlation with the analytical prediction that the Code can establish acceptable bend radii once a decision as to permissible overstress is reached on the basis of the analytical results (Table 2), without requiring a wall thickness check after bending? The discussers assume this is the intended suggestion. It is a simple matter to set down the formula for the required minimum thickness at the inside and outside of a bent pipe with the desired control; would not this be the better way to handle it?

Is it the intent of the authors to include short radius weldells? The ASA standard and the Code now requires that these meet only a bursting strength criterion. The Code Committee should first establish basic principles as to allowable stress criteria for all types of stresses for their own guidance. This must include consideration of accuracy of stress evaluation and the probable influence of fabrication and material variables and flaws.

Authors' Closure

The authors are gratified at the detailed and valuable comments concerning the subject presented in the paper, since such discussion is obviously of assistance in arriving at a proper evaluation of the effect of the thinning accompanying the fabrication of pipe bends upon ultimate integrity of a piping system. Contributions of this nature are clearly necessary in order to establish sound Code requirements governing bend thinning.

Several of the discussers point out that the authors should not adduce the PFI formula (Equations 12 and 13) in support of Formula (11) of the paper. The basis for the PFI formula was not known to the authors when this paper was being written; it is now clear that its origin is essentially as described by Mr. Gardner. However, even though the same formula as the authors' was obtained earlier by PFI (and others) and thus one derivation cannot be cited in support of another, the authors' derivation permits, it is believed, a more detailed scrutiny of the assumptions involved and their influence upon the result. Equation (14) of the paper is clearly not the same as the other formulas; it is either based upon different assumptions or represents an empirical relation. Accordingly, it may be adduced in support of the other formulas—a rather weak support, it is true, since the promulgating organization no longer exists, and it has not been possible to learn the background of the formula.

Mr. Gardner's discussion of the background of previous work done by TEMA in establishing Equation (13) of the text is most welcome; also, his remarks on the effect of nonvanishing meridional strain lend substantial support to the author's recommendations. As he points out, supported by the discussion presented by Messrs. Murphy and Rossheim, the occurrence of a nonvanishing meridional strain would have the effect of mitigating the longitudinal (circumferential) strain in causing wall thickness variations. Thus, two of the most important aspects omitted in the derivation presented in the text, namely, the nonzero nature of the meridional strain and ovalization, will both act to reduce wall thickness changes below those predicted by Equation (10). The more conservative analysis of the authors has not assumed such a favorable situation.

While the authors agree with Mr. Gardner's comments regarding the effect of strain-hardening, they did not intend the term "successful operating experience" to refer only to actual resistance against bursting in the bend. All Codes are ultimately intended to assist and promote ultimately a "successful operating experience." Therefore, regardless of mathematical manipulations or postulates for material behavior, it is essential to use the accumulation of successful past operating experience in support of a suggested revision of design practices.

The comments of Messrs. Gerwin and Caughy, regarding the possible sources of variations, are of interest and form a welcome addition to the paper. One source of variation not mentioned by them is the variable loss due to oxidation and scaling. Even in good shops, these effects may become rather substantial. Their influence was present in the case of the actual bends measured by PFI, which leads to the practical conclusion that their contribution is probably not sufficient to invalidate the conclusions of this paper.

With regard to the possibility of incorporating rules on after-bending thickness in the Codes, the B31 Committee also has Advisory Committees on Inspection and Testing and on Fabrication, Assembly, and Erection. The opinion of these groups will certainly be solicited in whatever Code rules may evolve on this matter.

Messrs. Gerwin and Caughy question whether it would be advisable to permit the 5 per cent overstress for piping which operates within the creep range. The authors are of the opinion that the case at hand satisfies conditions for which a Code would normally permit an overstress to be tolerated. Nonetheless, more detailed investigation of this point certainly seems warranted.

The authors were not unaware of the considerations cited by Mr. Harding as influencing the amount of thinning nor of the desirability of verification by an adequate test program. They could not agree more fully that this is "a sounder approach than the acceptance of some hypothetical 'overstress' predicated on a calculated under-thickness which may or may not exist." It happens that the primary responsibility of each of the authors is such as to preclude him from authorizing the undertaking of such a program. The authors also note, with interest, that Mr. Harding's company is in a position to undertake a program of this nature—the results of which would be of interest and benefit to the entire vessel and piping industry.

The first of Mr. Harding's numbered remarks requires no com-

ment, and we certainly agree with his comment No. 2. On comment No. 3, while tight bends may be of importance in the fabrication of heat exchanger tubes and thus of great interest to Mr. Harding, they are not of particular significance in piping systems proper. The labels in Fig. 3, to which Mr. Harding refers, are indeed incorrect in the preprint, but will be corrected in the final printing of the paper. Lastly, Mr. Harding is incorrect in stating in his comment No. 4 that the authors have hypothesized that bursting would occur in the middle of the curved portion. Instead, the authors have confined attention to elastic stress distribution. The phenomenon of bursting outside the bend is rather well known.[8] For complex geometries applying a factor of safety with regard to burst pressure is not equivalent to designing for a specified maximum (equivalent) stress. The state of the art is not such that the Codes can be consistent in this regard. Some portions of the Codes, particularly those portions which relate to the acceptance for Code construction of "pressure parts" such as welding fittings under the ASA B16.9, in effect are based upon resistance to static burst. Others, including the majority of portions of all applicable Codes, specify limiting design stresses which shall not be exceeded by a calculated "equivalent" stress. In some Codes, the "equivalent" stress is that given by the Rankine theory (maximum normal stress); in others it is based on the Guest theory (maximum shearing stress). Furthermore, the treatment of stresses developed under combined bending and torsion in piping systems is based upon the von Mises octahedral shear stress criterion.

The fact remains that the ultimate analysis of piping systems and vessels having a complex geometry and made of materials which are both ductile and strain-hardening is beyond present capabilities. Accordingly, the authors meticulously confined attention to the evaluation of the purely elastic membrane stress distribution in curved pipes under internal pressure loading.

The question posed by Messrs. Murphy and Rossheim in regard to point 3 of the section dealing with the Validity of Assumptions has already been treated by the authors when commenting on Mr. Gardner's discussion. In regard to the question on statistical analysis for the PFI data, such was not carried out because of the insufficient amount of information available. A satisfactory statistical analysis for the mean value and standard deviation (assuming a normal distribution) requires a minimum of five replicates; however, eight to ten replicates are considered to be the desirable number for representative statistical studies. Such a number of replicates were not available in the PFI data which encompassed a number of different pipe sizes and schedules. Likewise, the PFI data contained no detailed measurements of circumferential thickness variation and out-of-roundness before and after bending.

It must be admitted that the stress for pipe bends calculated here is a membrane stress which will cause plastic flow if its level exceeds the yield stress. However, at the stress levels recommended here, such is unlikely to happen in view of the fact that Code allowable stresses in straight runs cannot exceed 62.5 per cent of the offset yield value, and considering that the membrane stress solution for pipe bends is rather accurate.

The authors agree with Messrs. Murphy and Rossheim regarding the importance of bending stresses under fatigue conditions. This phenomenon, if it arises, should be dealt with on a basis similar to the f-factors already incorporated into the ASA B31.1 Piping Code, following a detailed analysis for bending stresses in pressurized pipe bends.[9]

The discussers are correct in stating that the best way of handling the question of allowable overstress is to establish limiting bend radii for the use of pipe bends, based upon the normal thickness tolerance of fabricated pipe. This had not only been the intention of the authors, but was the reason underlying the preparation of Fig. 5 of the text.

[8] c.f. N. A. Weil, "Bursting Pressures and Safety Factor in Thin-Walled Vessels," *Journal of the Franklin Institute*, February, 1958.

[9] A partial treatment of the elastic solution for this problem is presented in R. A. Clark, T. I. Gilroy, and E. Reissner, "Stresses and Deformations in Toroidal Shells of Elliptical Cross Sections," *Journal of Applied Mechanics*, vol. 19, TRANS. ASME, vol. 74, 1952, p. 37.

Deflection of Heat Exchanger Flanged Joints as Affected by Barreling and Warping

W. M. DUDLEY
Senior Consulting Engineer, Research and Development Department, Standard Oil Company (Indiana), Whiting, Ind. Mem. ASME

The conventional formulas for bolted-flange design, given in the ASME Unfired Pressure Vessel Code, provide for stresses due to initial bolt tightening and the axial force of internal pressure. Additional forces tending to loosen a joint are created by unequal radial expansion or barreling of the flange and shell, due to temperature differences or pressure, and by unequally warped flanges. Formulas have been developed for the extra bolt loads required to overcome these effects and applied to a heat-exchanger joint in a catalytic reforming unit. The margin of safety against leakage is increased by using soft gaskets that can re-expand after being compressed, and by retightening bolts after operating temperatures and pressures are reached. Joints designed to resist initial bolting and hydrostatic forces only are likely to leak because of barreling effects or warped flanges.

Introduction

THE rational design of flanged joints, as set forth in the ASME Unfired Pressure Vessel Code [1],[1] is based on the 1937 paper by Waters, Rossheim, Wesstrom, and Williams [2]. A flange with tapered hub is analyzed as a thin disk attached to a cylinder of tapering wall thickness. With both parts subject to bending distortions from initial bolt-tightening and the axial force of internal pressure, the stresses and strains are calculated and the results given by curves.

The WRWW solution does not cover the so-called "barreling effect" in which, because of either internal pressure or temperature differences, the shell or pipe tends to expand radially more than the flange. An extension to cover these effects could be made, with only moderate mathematical complexity. However, typical flanges on heat exchangers do not resemble a thin disk; in fact the radial width is frequently less than the thickness. For such shapes, results that are at least as accurate can be obtained by assuming that, under loading, the flange cross-section moves and turns as a unit but does not change its shape. This approach, besides being simpler, also allows for radial deflection of the entire flange, whereas the conventional procedure does not.

[1] Numbers in brackets designate References at end of paper.

Contributed by the Refining-Gas Products, Petrochemical Committee, Petroleum Division, and presented at the Winter Annual Meeting, New York, N. Y., November 27-December 2, 1960, of THE AMERICAN SOCIETY OF MECHANICAL ENGINEERS. Manuscript received at ASME Headquarters, July 14, 1960. Paper No. 60—WA-70.

All of the above loadings are symmetrical around the central axis of the shell. However, experience shows that the originally plane contact surfaces of the flanges tend to become warped in service. Hence, formulas for the bolt forces required to overcome unsymmetrical warping have also been developed. Finally, the effectiveness of three common types of gasket has been studied.

Deformations Due to Symmetrical Loads

Fig. 1 is a cross-sectional view of a typical flange and shell. ASME nomenclature has been used wherever possible. Bending will cause a moment M_0 and shear Q_0 at the junction of hub and shell. Other forces acting on the flange and hub are the bolt force F_B, the gasket force F_G, and the forces F_T, F_D, and F_R exerted by internal pressure P. All of these forces are taken per circumferential inch at the shell radius r_0. The first step in analysis is to locate the centroid C of the cross-sectional area of flange and hub, and find the moment of inertia I_y about a radial axis through C.

Pressure is usually assumed to act out to the centerline of the gasket. If the piece of flange and hub in Fig. 1 is taken as a free body, with unit circumferential dimension at radius r_0, the three forces due to internal pressure P are:

$$F_D = \frac{B^2P}{8r_0} \tag{1}$$

$$F_R = \frac{PBx}{2r_0} \tag{2}$$

Nomenclature

a = thermal-expansion coefficient
A_b = total cross-sectional area of bolts at root of thread
A_F = cross-sectional area of flange and hub (Fig. 1)
A_G = face area of gasket
B = inside diameter of flange
C = bolt circle diameter
C_s = torsional-spring constant of bolts and gasket (22)
C_F = torsional-spring constant of flange and hub (18)
D = plate constant $= Eg_0^3/12(1 - \mu^2)$
E = modulus of elasticity
F_B = bolt force
F_G = gasket force
F_D, F_T, F_R = forces due to pressure
} See Fig. 1. All forces are per linear inch at radius r_0
G = diameter at location of gasket load reaction
g_0 = thickness at small end of hub
h_G = radial distance from gasket reaction to bolt circle $= (C - G)/2$
I = $g_0^3/12(1 - \mu^2) = g_0^3/10.92$ for steel
I_y = moment of inertia of area A_F about radial axis through C
k_B, k_G = spring constants of bolts and gasket (Fig. 2)
L = effective length of bolt per flange
M_F, M_0, M_P, M_T = moments acting on flange; see (6), (14), (24), (37)

(Continued on next page)

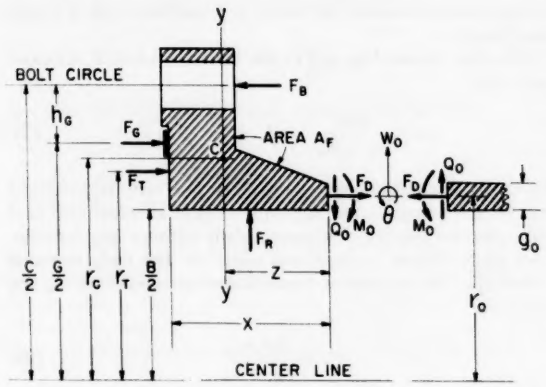

Fig. 1 Cross section of a typical flange, showing forces and moments

$$F_T = \frac{P(G^2 - B^2)}{8r_0} \tag{3}$$

The resultant F_T will act at a radius of

$$r_T = \frac{G^2 + GB + B^2}{3(G + B)} \tag{4}$$

Because the assembly is statically indeterminate, the gasket force can be found only by considering deflections, starting with the initial bolt load and superposing the effects of the other loads.

Effect of Initial Bolt Tightening. If the total thread-root area of the bolts is A_b and the average bolt stress is S_b, then

$$F_B = \frac{S_b A_b}{2\pi r_0} \tag{5}$$

Tests [3] have shown that, when bolts are tightened by mechanics in the field, the bolt stress attained is approximately $45{,}000/\sqrt{d}$, where d is the nominal bolt diameter. This value should be used for S_b unless the bolt stress is controlled to some other value than by torque wrenches or micrometers.

If the bolts are pulled up with no internal pressure, bolt force F_B equals gasket force F_G, and together they form a couple M_F acting counterclockwise on the flange and hub in Fig. 1:

$$M_F = F_B h_G = \frac{S_b A_b h_G}{2\pi r_0} \tag{6}$$

From the elementary solutions for twisting of a ring and bending of a cylindrical shell [4, 5], radial deflections and rotations at the junction of hub and shell are found. For the flange and hub, they are:

$$\theta = (M_F - M_0 - Q_0 z)\frac{r_0 r_c}{EI_y} \tag{7}$$

$$w_0 = (M_F - M_0 - Q_0 z)\frac{r_0 r_c z}{EI_y} - \frac{Q_0 r_0 r_c}{EA_F} \tag{8}$$

where A_F = area of flange and hub cross-section. For the shell

$$\theta = \frac{1}{2\beta^3 D}(2\beta M_0 - Q_0) \tag{9}$$

$$w_0 = \frac{1}{2\beta^3 D}(-\beta M_0 + Q_0) \tag{10}$$

$$\text{in which } \beta = \frac{\sqrt[4]{3(1-\mu^2)}}{\sqrt{r_0 g_0}} = \frac{1.285}{\sqrt{r_0 g_0}} \quad \text{for steel} \tag{11}$$

and

$$D = \frac{E g_0^3}{12(1-\mu^2)} = \frac{E g_0^3}{10.92} = EI \tag{12}$$

The hub moment M_0, shear Q_0, and flange rotation θ can be found in terms of M_F by solving (7) to (10) simultaneously. For brevity, let

$$X = \left(\frac{z}{\beta} + \frac{r_0 r_c z I}{I_y}\right)\left(\frac{1}{2\beta^3 z} + \frac{r_0 r_c I}{z A_F} + \frac{r_0 r_c z I}{I_y}\right) - \left(\frac{1}{2\beta^2} - \frac{r_0 r_c z I}{I_y}\right)^2 \tag{13}$$

If θ_B is the flange rotation (in radians) due to bolting up, then

$$M_0 = \frac{r_0 r_c z I}{X I_y}\left(\frac{r_0 r_c I}{z A_F} + \frac{1}{2\beta^3 z} + \frac{1}{2\beta^2}\right) M_F \tag{14}$$

$$Q_0 = \frac{r_0 r_c I}{X I_y}\left(\frac{1}{2\beta^2} + \frac{z}{\beta}\right) M_F \tag{15}$$

$$\theta_B = \frac{r_0 r_c z}{EX\beta I_y}\left(\frac{r_0 r_c I}{z A_F} + \frac{1}{4\beta^3 z}\right) M_F \tag{16}$$

If A_G is the total face area of the gasket, the initial gasket stress will be:

$$S_G = S_b A_b / A_G \tag{17}$$

When the flange and hub are attached to the shell, the torsional spring rate C_F of the flange can be expressed from (16) as:

$$C_F = \frac{M_F}{\theta_B} = \frac{EX}{\frac{r_0 r_c z}{\beta I_y}\left(\frac{r_0 r_c I}{z A_F} + \frac{1}{4\beta^3 z}\right)} \tag{18}$$

When the bolts are tightened and the flange rotates, the lines of action of the bolt and gasket forces will tend to shift closer together and reduce the effective arm of the couple M_F. Hence, the use of the full distance h_G in computing M_F will give safe results. Test data are available on flange rotations obtained when known bolt forces were applied [6].

Nomenclature

m = number of complete waves in circumference of a warped flange
P = maximum internal pressure
Q_0 = radial shearing force at small end of hub
r_c, r_t, r_0, r_T = radial distances (Figs. 1 and 2)
S_b, S_G = stresses in bolts and gasket
T = thickness of compressed gasket
v = axial displacement of a point of warped shell
w_0 = outward radial displacement at small end of hub
X = a constant (13)
x, y = co-ordinates on shell (Fig. 3)
x_P = axial displacement at Z (23)
z = axial distance from C to small end of hub
α = constant $= m/r_0$
β = shell constant (11)
ΔT = temperature difference between flange and shell
δ_G = change in thickness of gasket (26)
δ_T = thermal expansion (30)
θ = angle of rotation of flange, radians
σ, τ = normal and shear stresses (Fig. 3)
μ = Poisson's ratio; 0.3 for steel

Effect of Hydrostatic Forces. The forces F_D, F_R, and F_T will cause a further counterclockwise (loosening) rotation and an axial movement of the flange and hub. Because the bolts and the gasket are elastic, these movements will change the stresses in them. Thus, they can be considered as a pair of unequal springs attached to the free body as in Fig. 2.

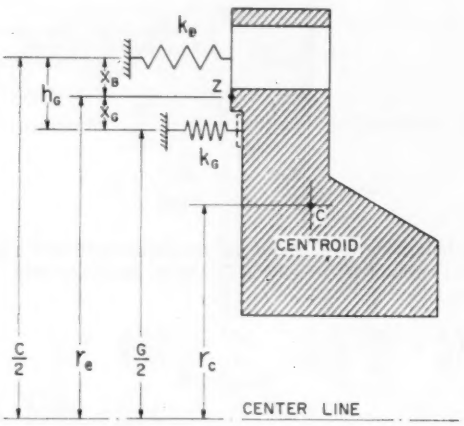

Fig. 2 Elasticity of bolts and gasket replaced by equivalent springs

If the total face area of the gasket is A_G, its thickness is T, and its modulus of elasticity is E_G, the equivalent spring rate k_G for the gasket is:

$$k_G = \frac{A_G E_G}{2\pi r_0 T} \text{ lb/inch per linear inch} \qquad (19)$$

In assigning values to A_G, E_G, and T in a numerical case, there are three pitfalls to be avoided:

(*a*) In a simple joint with two flanges and one gasket, one half of the gasket thickness may be assigned to each flange; but, where a tube sheet is being clamped between two flanges with a gasket on each side, there is one gasket per flange.

(*b*) For filled gaskets, local deformation of the flange surfaces can probably be neglected; but, for solid iron gaskets of commonly used thicknesses, the local surface compression of the flange face may be several times that of the gasket itself.

(*c*) If the gasket contains a soft filler material, such as asbestos, its thickness will be reduced when load is applied, and the stiffness will be correspondingly greater.

To avoid all of these uncertainties, the most reliable procedure is to make a loading (and unloading) versus deformation test of a representative gasket in a testing machine, using compression plates of material and thickness similar to the flanges. The value of $A_G E_G/T$ to be used in (19) is then simply the slope of the load-deflection curve at the working point.

The spring rate for the bolts in Fig. 2 is:

$$k_B = \frac{A_b E_b}{2\pi r_0 L} \text{ lb/inch per linear inch} \qquad (20)$$

where L is the portion of the total bolt length associated with the flange. The ends of L are located as follows: First, photoelastic tests [7] indicate that, when a bolt is loaded axially by a nut, the equivalent length of fully stressed bolt extends one half bolt diameter beyond the base of the nut. Second, for a simple two-flange joint, the midpoint of the bolt will not move, so half the bolt can be assigned to each flange. For a tube-sheet joint with different pressures on shell and tube sides, and flanges of approximately equal stiffness, the total effective bolt length should be apportioned between the flanges in proportion to their respective pressures.

After the values of k_B and k_G are known, a point Z is located such that

$$x_G = \frac{k_B h_G}{k_B + k_G} \quad \text{and} \quad x_B = \frac{k_G h_G}{k_B + k_G} \qquad (21)$$

This point has the property that, if the free body is restrained only by the springs k_B and k_G, application of an axial force at Z will cause the free body to move axially without any rotation. Also, application of a couple will cause the free body to rotate around Z. The equivalent torsional-spring constant of k_B and k_B is:

$$C_e = \frac{k_B k_G h_G^2}{k_B + k_G} \qquad (22)$$

By using Figs. 1 and 2, the flange movements caused by the pressure P can be computed. First, the flange will move axially by an amount

$$x_P = \frac{F_T + F_D}{k_B + k_G} \qquad (23)$$

The moment exerted by pressure is:

$$M_P = F_T(r_e - r_T) + F_D(r_e - r_0) + F_R\left(z - \frac{x}{2}\right) \qquad (24)$$

and the flange will rotate through an angle

$$\theta_P = \frac{M_P}{C_e + C_F} \qquad (25)$$

The gasket will expand by an amount

$$\delta_G = x_P + \theta_P x_G \qquad (26)$$

and the reduction in gasket stress due to the application of internal pressure is:

$$\Delta S_G = \frac{E_G \delta_G}{T} \qquad (27)$$

The change in the length of the bolt is:

$$\delta L_B = x_P - \theta_P x_B \qquad (28)$$

which may be either positive or negative. The change in bolt stress is:

$$\Delta S_B = \frac{E_B(\delta L_B)}{L} \qquad (29)$$

with due regard to sign. Published test data confirm that application of internal pressure sometimes reduces the bolt load [6].

Analysis of Barreling Effects. External insulation is usually provided on the shells of heat exchangers. However, experience shows it is better to leave the flanges uncovered, to reduce distortion and leakage due to creep of bolts and flanges, and to permit retightening of bolts. If the flange is colder than the shell by an amount ΔT, and if the expansion coefficient is a, the shell will tend to move out radially from the flange by an amount

$$\delta_T = a r_0 \Delta T \qquad (30)$$

The outward expansion of the shell due to internal pressure is:

$$w_0 = \frac{P r_0^2}{2 E g_0}(2 - \mu) = \frac{0.85\, P r_0^2}{E g_0} \text{ if } \mu = 0.3 \qquad (31)$$

The corresponding expansion of the flange is:

$$w_F = \frac{F_r r_0 r_c}{A_F E} \tag{32}$$

so the outward shift of the shell relative to the flange is:

$$\delta_P = w_0 - w_F \tag{33}$$

and the total differential movement to be counteracted by elastic action of the shell and flange is:

$$\delta_0 = \delta_T + \delta_P = \alpha r_0 \Delta T + w_0 - w_F \tag{34}$$

A moment M_0 and shear Q_0 will be set up, opposite to the directions shown in Fig. 1, to overcome δ_0. Equating values of θ from (7) and (9), with $M_F = 0$, provides one relation beween M_0 and Q_0. Another is provided by using (8), 10), and (34) in

$$w_{\text{Flange}} - w_{\text{Shell}} = \delta_0 \tag{35}$$

Using X as in (13) gives

$$\theta = \frac{r_0 r_c I \delta_0}{X I_y}\left(\frac{1}{2\beta^2} + \frac{z}{\beta}\right) \tag{36}$$

This gives the angle by which the flange would rotate because of barreling effects, if it were not attached to the other flange. The same rotation could be caused by applying an external moment M_T to the flange, where $M_T = C_F\theta$. Using (18) and (36) gives

$$M_T = \frac{E\delta_0\left(\frac{1}{2\beta} + z\right)}{\frac{r_0 r_c}{A_F} + \frac{1}{4\beta^3 I}} \tag{37}$$

Since the flange is in contact with the gasket and bolts, the actual rotation of the flange due to barreling effects will be:

$$\theta_T = \frac{M_T}{C_F + C_s} \tag{38}$$

The changes in gasket and bolt stresses can be obtained from (26) through (29) with $\theta_p = \theta_T$ and $x_p = 0$, since no new axial force is being applied.

Total Hub and Flange Stresses From Symmetrical Loads. The total rotation of the flange, including the effects of initial bolting, pressure, and barreling from (16), (25), and (38) is:

$$\theta_S = \theta_B + \theta_P + \theta_T \tag{39}$$

The maximum circumferential tensile stress will be at the small end of the hub and is:

$$S_1 = \frac{Ew_0}{r_0} \tag{40}$$

There is a circumferential compressive stress in the flange faces of

$$S_2 = \frac{E(x\theta_s - w_0)}{r_0} \tag{41}$$

At the small end of the hub, there are combined bending and direct stresses in the axial direction. The total bending moment M_H is found from (14), (18), and (39):

$$M_H = \frac{\frac{r_0 r_c I}{A_F} + \frac{1}{2\beta^3} + \frac{z}{2\beta^2}}{\frac{r_0 r_c I}{A_F} + \frac{1}{4\beta^3}} \beta E I \theta_s \tag{42}$$

The maximum axial stresses at the small end of the hub are:

$$S_{3,4} = \frac{B^2 P}{8 r_0 g_0} \pm \frac{6 M_H}{g_0^2} \tag{43}$$

In practical cases these stresses, particularly S_3 and S_4, are likely to approach or exceed the yield strength of the material at the working temperature if a realistic value is used for the bolt stress. This condition is normal; large flanges usually cannot be made tight unless the bending stresses at the hub are well above commonly allowed values of primary stress in other parts of pressure vessels [8]. Unfortunately, such a situation may be unstable. Some redistribution of the high bending stresses will occur if the maximum is beyond yield. Also, with the passage of time at operating temperatures, the stresses in bolts, gaskets, and flanges will be reduced by creep. Thus, even if a joint is tight when first placed in service, leaks can develop later.

This is an area in which the present codes require further development. Experience indicates that allowing secondary (bending) stresses in pressure vessels to go substantially higher than primary stresses is usually safe, but not always. Thus, bending stresses should not be handled either by ignoring them entirely, or, as in the case of flanges, by pretending that the bolt stresses are lower than they really are. A successful solution will probably require consideration of the plastic and creep properties of the materials.

Experimental Verification of Formula. Rossheim, Gebhardt, and Oliver [6] published some test data on typical heat-exchanger flanges. Flange rotations and bolt and hub stresses were measured with different combinations of initial bolt tension and internal pressure. Table 1 compares measured and calculated flange rotations. In flange C1, the length of the tapered portion of the hub was 1.26 times its greatest thickness; for C2, the ratio was 2.25. The increased flexibility due to greater hub length of C2 accounts for the measured flange rotations being greater than calculated, since the analysis assumed zero bending deformation in the hub and flange. Measured stresses in the hub area were usually about half of the calculated values.

Table 1 Calculated versus measured flange rotations for flanges C1 and C2 of Reference [6]

Flange	Load Condition	Rotation, Minutes	
		Calculated	Measured
C1	20,000 psi Initial Bolt Stress	6.6	5.4
C1	150 psi Internal Pressure	0.8	1.0
C2	20,000 psi Initial Bolt Stress	4.9	7.3
C2	150 psi Internal Pressure	1.0	1.5

Neither the WRWW nor the present analysis takes account of two effects that must be of some importance in the narrow, thick flanges typical of heat exchangers: deformations due to shearing stresses, and increased flexibility due to removal of material in bolt holes. These, together with flange and hub bending, probably account for the differences in Table 1.

Deformations Due to Unsymmetrical Loads

Warped End of Shell. Fig. 3 shows a cylindrical shell in which the end plane, where a flange would be attached, is wavy instead of flat. If there are m complete waves in the circumference, the profile of the end is given by

$$y = y_0 \sin \frac{mx}{r_0} \tag{44}$$

For the case shown, m is 2; and, when the end of the shell is set against a flat surface, the greatest separation is $2y_0$.

If the shell is fairly long, the stresses necessary to make the ends fit a plane surface can be computed by elasticity theory [9]. The stress function $\phi(x, y)$ must satisfy the equation

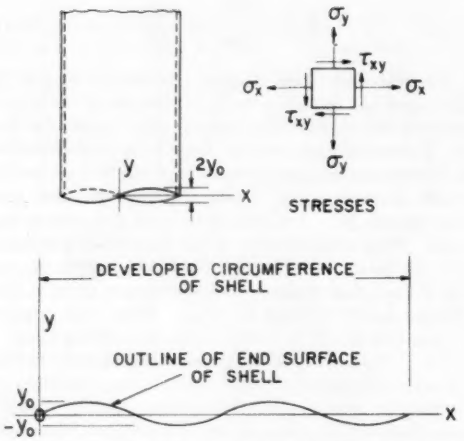

Fig. 3 Out-of-plane distortion of end of shell

$$\frac{\partial^4\phi}{\partial x^4} + \frac{2\partial^4\phi}{\partial x^2\partial y^2} + \frac{\partial^4\phi}{\partial y^4} = 0 \tag{45}$$

Assuming an equation of the form $\phi = F(y) \sin \alpha x$, the variables x and y can be separated and $F(y)$ is found to be:

$$F(y) = C_1e^{\alpha y} + C_2e^{-\alpha y} + C_3\alpha ye^{\alpha y} - C_4\alpha ye^{-\alpha y} \tag{46}$$

where $C_1 \ldots C_4$ are constants of integration. The stresses are found from ϕ by the relations:

$$\sigma_x = \frac{\partial^2\phi}{\partial y^2} \qquad \sigma_y = \frac{\partial^2\phi}{\partial x^2} \qquad \tau_{xy} = \frac{-\partial^2\phi}{\partial x\partial y} \tag{47}$$

Suitable boundary conditions to flatten the loaded end are:

$$\sigma_y = \sigma_0 \sin \alpha x, \qquad \tau_{xy} = 0 \tag{48}$$

Since the loading applied to the end has a zero resultant, the stresses should decrease with distance from the end; hence, C_1 and C_3 must be zero. On solving for C_2 and C_4 using (48), the stresses at any point are found to be:

$$\sigma_x = \sigma_0e^{-\alpha y}(1 - \alpha y) \sin \alpha x \tag{49}$$

$$\sigma_y = \sigma_0e^{-\alpha y}(1 + \alpha y) \sin \alpha x \tag{50}$$

$$\tau_{xy} = \sigma_0\alpha ye^{-\alpha y} \cos \alpha x \tag{51}$$

From these stresses, the strains can be found by Hooke's Law. The axial strain at any point is:

$$\epsilon_y = \frac{\partial v}{\partial y} = \frac{1}{E}(\sigma_y - \mu\sigma_z) \tag{52}$$

where v is the axial displacement. Upon using (49) and (50) and assuming that v is zero when y is large, the end displacement v_0 is:

$$v_0 = \int_0^\infty \epsilon_y dy = \frac{\sigma_0 \sin \alpha x}{E} \times \int_0^\infty [(1 - u)e^{-\alpha y} + (1 + u)\alpha ye^{-\alpha y}]\, dy$$

Letting $\alpha = \dfrac{m}{r_0}$ and integrating gives

$$v_0 = \frac{2\sigma_0 r_0}{Em} \sin \frac{mx}{r_0} \tag{53}$$

From (53) and (44), the maximum end stress σ_0 required to eliminato waviness of amplitude y_0 on the end of the shell (with m complete waves around the circumference) is

$$\sigma_0 = \frac{Emy_0}{2r_0} \tag{54}$$

Warped Flange. If the flange attached to the shell of Fig. 3 is also warped circumferentially according to (44), the amount of loading required to flatten it is readily found. The basic differential equation for bending of beams is $EI\, d^4y/dx^4 = w$, where y is deflection, x is distance along the beam, and w is the loading (a function of x) that is producing the deflection [10]. From (44), with the moment of inertia of the flange I_y as above, the loading required to straighten the flange is:

$$w = \frac{m^4y_0EI_y}{r_0^4} \sin \frac{mx}{r_0} \text{ lb/inch} \tag{55}$$

From (54) and (55), the maximum extra bolt stress required in the worst-situated bolts because of flange and shell warping is:

$$S_w = \frac{\pi Emy_0}{A_B}\left(g_0 + \frac{2m^3r_cI_y}{r_0^4}\right) \tag{56}$$

Comparison of Gasket Types

One purpose of the present study was to calculate the performance of leak-prone heat exchangers, using three different gasket designs. Dimensions of a typical unit in catalytic-reforming service are shown in Fig. 4. Values of bolt stress, gasket stress, and flange rotation, computed under various loading conditions, are shown in Table 2. The three gasket types are:

(*a*) Solid soft-iron gaskets $^1/_8$ in. thick. The channel gasket has a diametral strip $^3/_8$ in. wide to seal the edge of the divider plate.

(*b*) Iron-jacketed asbestos gaskets of the same dimensions. The asbestos sheet was assumed to have a modulus of elasticity of 480,000 psi after compression [11].

(*c*) 600-psi series spiral-wound gaskets. From catalog data, an average modulus of elasticity of 78,700 psi was found. The flange modulus of elasticity was taken as 27×10^6 psi, and thermal expansion, 8.54×10^{-6} per degree F. The bolts were assumed to be tightened initially to the Petrie stress: 38,400 psi for $1^3/_8$-in. bolts.

Discussion and Conclusions

Table 3 shows the stresses at hub and flange for the same exchanger, when all three loads are acting. Maximum axial stresses at the hub are well beyond yield, irrespective of the gasket used.

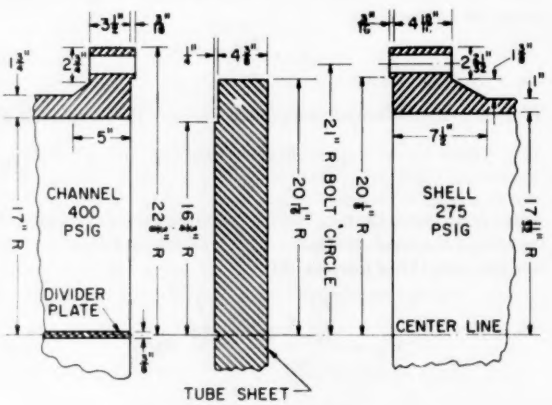

Fig. 4 Heat exchanger tube-sheet joint

Table 2 Study of exchanger (Fig. 4) with various loads and gaskets

	Load Condition (1) Bolts Pulled Up	(2) Pressures: 400 psi Channel 275 psi Shell	(3) Shell and Channel 200° F Hotter than Flanges
1/8-inch Solid Soft-Iron Gaskets, 40-3/16" O.D., 1/2-inch wide			
Bolt Stress, psi	38,400	36,800	23,600
Gasket Stress:			
Shell Side	28,600	21,900	12,600
Channel Side	23,100	15,900	7,600
Total Flange Rotation, minutes:			
Shell Flange	3.3	4.5	12.7
Channel Flange	3.2	4.7	17.8
1/16-inch Asbestos Sheet with Iron Jacket, 40-3/16" O.D., 1/2-inch wide			
Bolt Stress, psi	38,400	39,200	25,000
Gasket Stress;			
Shell Side	28,600	23,900	17,000
Channel Side	23,100	17,200	10,400
Total Flange Rotation, minutes:			
Shell Flange	3.3	4.5	13.1
Channel Flange	3.2	4.9	18.2
1/8-inch Spiral-Wound Gaskets, 40-3/16" O.D., 38-3/4" I.D.			
Bolt Stress, psi	38,400	44,200	36,000
Gasket Stress:			
Shell Side	20,200	19,000	17,400
Channel Side	17,300	15,600	13,300
Total Flange Rotation, minutes:			
Shell Flange	3.6	5.4	14.5
Channel Flange	3.5	5.7	19.6

Since this is a bending stress, yielding will stop after small deformations. Examination of the flange faces after a run showed permanent rotations of 12 to 15 minutes of angle; comparison with angles in Table 2 shows that most of the originally elastic deformation became permanent by creep.

It might be thought that all of the cases in Table 2 are safe against leakage, because the gasket stresses greatly exceed the internal pressure. However, the possible effect of warped flanges must be considered. After a run, a flatness check of the flange surfaces shown in Fig. 4 gave the following results:

Position	Out-of-plane distance
12 o'clock	+0.020 in.
3 and 9 o'clock	0
6 o'clock	+0.020 in.

From (44) with $m = 2$ and $y_0 = 0.010$ in., and (54), the extra hub stress required to straighten the shell is 16,300 psi, and (56) indicates a maximum excess bolt stress of 51,200 psi required to bring the flange in contact with a truly flat surface. As this exceeds the available bolt stress in all cases, any unequal warping of mating surfaces is evidently a serious problem.

Table 2 shows that, with the two harder gaskets, a substantial reduction of gasket stresses occurs when operating temperatures and pressures are applied. This loosening can be overcome by retightening the bolts after the joint is placed in service.

A soft, plastic gasket provides greater initial accommodation for uneven or warped surfaces. However, unless the deflection is recoverable, the gasket may loosen when the load changes. Comparison of the spiral-wound with the harder gaskets shows that, the greater the amount of recoverable deflection or springback in the gasket, the less the gasket and bolt stresses will change as the loads vary, and the easier it is to maintain a tight joint.

To summarize, it is not always sufficient to design a joint for initial bolt load and hydrostatic forces only, as now provided in the Code. Consideration should be given to barreling effects, particularly temperature differences. The use of more resilient gaskets is helpful in counteracting both barreling and warping.

Table 3 Maximum flange and hub stresses, psi (loading 3, Table 2)

	1/8-inch Solid Soft-Iron Gaskets	Iron-Jacketed Asbestos Gaskets	600-psi Series Spiral-Wound Gaskets
Circumferential Stress S_1 at Hub:			
Shell Flange	25,500	26,300	29,000
Channel Flange	22,900	23,400	25,200
Circumferential Stress S_2 at Flange Face:			
Shell Flange	-16,500	-17,100	-18,800
Channel Flange	-16,200	-16,600	-17,800
Axial Stress S_3 at Hub			
Shell Flange	75,000	77,400	85,000
Channel Flange	85,800	87,700	94,000

In some cases, retightening of the bolts at service conditions may be necessary.

References

1 ASME Boiler and Pressure Vessel Code Section VIII, "Rules for Construction of Unfired Pressure Vessels," New York, 1959. See Appendix II.

2 E. O. Waters, D. B. Rossheim, D. B. Wesstrom, and F. S. G. Williams, "Formulas for Stresses in Bolted Flanged Connections," TRANS. ASME, vol. 59, 1937, pp. 161–169.

3 E. C. Petrie, "The Ring Joint, Its Relative Merit and Application," *Heating, Piping and Air Conditioning*, vol. 9, April, 1937, pp. 213–220.

4 S. Timoshenko, "Strength of Materials," D. Van Nostrand Company, Inc., New York, N. Y., 1941, Part II, Art. 34.

5 S. Timoshenko, "Theory of Plates and Shells," McGraw-Hill Book Company, Inc., New York, N. Y., 1940, p. 393.

6 D. B. Rossheim, E. H. Gebhardt, and H. G. Oliver, "Tests of Heat Exchanger Flanges," TRANS. ASME, vol. 60, 1938, pp. 305–314.

7 M. Hetenyi, "A Photoelastic Study of Bolt and Nut Fastenings," *Journal of Applied Mechanics*, vol. 10, TRANS. ASME, vol. 65, 1943, pp. A-93–100.

8 D. B. Wesstrom and S. E. Bergh, "Effect of Internal Pressure on Stresses and Strains in Bolted Flanged Connections," TRANS. ASME, vol. 73, 1951, pp. 553–568.

9 S. Timoshenko and J. N. Goodier, "Theory of Elasticity," McGraw-Hill Book Company, Inc., New York, N. Y., 1951, Art. 23.

10 Reference [4], Part I, p. 137.

11 I. Roberts, "Gaskets and Bolted Joints," TRANS. ASME, vol. 72, 1950, pp. 169–179.

DISCUSSION

D. B. Rossheim[2] and C. A. Honigsberg[3]

A re-examination of bolted gasketed vessel joints, with respect to service-imposed variables on the one hand and more accurate evaluation of structural behavior on the other hand, is long overdue. The author deserves the appreciation of the many mechanical engineers concerned with pressure equipment for the subject paper's contributions in this direction and for this timely awakening of interest in flange design, concurrent with a broad rationalization of pressure equipment for balanced requirements as to materials, design, fabrication, and inspection for improved safety and economics.

The author directs attention to current ASME Unfired Pressure Vessel Code omission of a consideration of pressure stresses, and inadequate appraisal of bending stresses as a result of unrealistic bolt load assumptions. The development which led to the current Code rules and to Reference [2] included an evaluation of direct and discontinuity pressure effects, but these effects were not made a part of the rules or reference paper, due to the Code approach of generous safety factors and consideration only of stress which leads to fracture (i.e., not fatigue), with overbolting and flange distortion considered problems of tightness rather than structural failure. The higher level of allowable hub stress

[2] The M. W. Kellogg Company, New York, N. Y. Fellow ASME.

[3] The M. W. Kellogg Company, New York, N. Y. Mem. ASME.

($1\frac{1}{2} S_A$) permitted so long as the average of the flange and hub stress did not exceed the allowable, was predicated on the assumption that redistribution would occur with gross yielding only with both flange and hub fully stressed.

The author properly points out that for heat exchangers the flange width as compared to flange thickness is such that behavior under bolt loading is better defined by a bar than a flat plate. A possible exception would be the increaser flange on the bonnet end, which is usually required to clear the floating head assembly. Extension of this assumption to the hub is, however, questionable on butt-welded flanges, and would tend to neglect the intersection stresses between the hub and the flange proper, which are often more critical than those at the intersection of the hub and shell. This also applies to the discontinuity stresses caused by temperature distribution.

The weakening effect of bolt holes is, as pointed out, more serious for flanges of narrow width, although resisted in some degree by the stiffening effect of the nuts, and probable shift of the bolt reaction inward with flange rotation. The author presents an interesting evaluation of stresses due to out-of-plane distortion. Such distortion is usually the result of temperature gradients, and can be minimized by weather shields (not insulation), if the maintenance forces can be persuaded to reinstall this protection properly after turn-arounds. Such distorted flanges must be pulled essentially flat to attain a tight joint, and attendant high stresses in the flange and bolts will relax with time, unless re-established by a reappearance of nonsymmetrical temperature.

The author's statement—"experience indicates that allowing secondary (bending) stresses in pressure vessels to go substantially higher than primary stresses is usually safe, but not always," and following remarks, with respect to realistic awareness of all stresses and loads in their proper magnitude, is well taken. As pointed out, plastic behavior and creep-rupture properties must be considered (in addition to short time yielding); equally important are the low cycle fatigue properties which correspond to the attendant higher strain ranges.

It is hoped that the attention of the WRC-Pressure Vessel Research Committee and ASME Boiler and Pressure Vessel Committee will soon be directed to the development of automatic computer programs for all significant pressure equipment structural problems, among them a versatile program for bolted flanged joints by which all loadings (bolts, pressure, thermal effects, etc.) are simultaneously considered. A complete solution will then be available more quickly, and with no greater cost than present crude approximations.

E. O. Waters[4]

It is gratifying to note that flange design continues as an active topic of interest, after a quarter-century of discussion. Possibly a reason for this is the fact that the problem is a many-faceted one, with almost too many variables to be included in a study undertaken by any one individual or group. For example, the Williams-Wesstrom-Waters-Rossheim investigation first came to light as a privately circulated brochure in which the primary aim was to cover a wide range of geometries. Stresses were related to a final operating bolt load and gasket pressure, without regard to the manner in which they might vary during the transition from initial bolt-up to final operating conditions. Barreling of the hub due to internal pressure was recognized in a worked-out illustrative problem, but nothing was done about thermal stresses, weakening effect of bolt holes, shear stress deformation, or other refinements too numerous to mention.

The first outcome of this was the presentation of the ASME paper [2] which shortly thereafter became the basis of a rather drastic revision of Boiler and Pressure Vessel Committee rules that have remained essentially intact up to the present time. In so doing, much thought was given to condensation and simplification, with the inevitable result that concessions had to be made to precise accuracy and coverage of all possible conditions. From one standpoint, the resulting rigidity and narrowness of design procedure may be a legitimate source of complaint. On the other hand, such a treatment gives an opportunity for forward-looking workers in the field to study aspects of the problem that have not yet been covered and are of particular interest to them, as individuals. Examples of this are the various references cited by the author. Mention should also be made of some recent experimental work by Donald and Salomon, published by The Institution of Mechanical Engineers, in which special attention is given to the reduction of bolt load during application of internal pressure.

The present paper gives special emphasis to this phenomenon, noting that the change in bolt load may be either an increase or decrease, and to the effect of internal pressure and temperature differentials on barreling, but at the same time making the simplifying assumption that the flange and hub sections rotate without deformation. This may be substantially true for narrow flanges and short hubs, but it is questionable whether the designer can safely make this assumption when the junction between hub and shell is as far removed from the flange as is often the case with bolted connections of commonly used proportions. In other words, the hub is only partially effective in reinforcing the flange, and any portion of it that extends beyond $1.4\sqrt{r_0 g_0}$ (author's Fig. 1) in the axial direction has negligible effect.

The author's treatment of warped flanges is an interesting application of two-dimensional theory to an essentially three-dimensional problem, and as such its suitability in this instance is perhaps debatable. Since the bolt force and gasket reaction are not directly in line with the shell, it would seem that any attempt to pull the flange face into flatness, by additional tightening of some of the bolts, will accomplish a variation in the angle θ from point to point around the flange and hub, rather than a procrustean stretching of the shell wall. As a result of this combined bending and twisting, a flat *bolt circle* could probably be attained in the example cited by the author, without going to the excessive increment of 51,200 psi bolt stress.

Author's Closure

The author is grateful to Messrs. Rossheim, Honigsberg, and Waters for their careful and detailed reviews. Their experiences shed more light on several aspects of the flange design problem.

As noted by the first discussers, the development of computer programs is the best way to analyze the behavior of flanged pressure vessels under a variety of loads, within reasonable limits of time and cost. When such programs are available, it will also be possible to determine the range of applicability of various approximations, such as the rigid-cross-section assumption used in the paper. Although this shortcut is quite accurate on stubby heat exchanger flanges with short hubs, it will overestimate the rigidity of thin flanges or long hubs, as the discussers point out.

Although the warped-flange analysis somewhat overestimates the bolt stress required for flattening, it is useful in deciding which, or how many, of several fire-damaged flanges must be re-machined. However, Professor Waters is undoubtedly correct in stating that, when twisting due to three-dimensional loads is considered, warped flanges are more flexible than the simple beam formula (Eq. 55) suggests. Although some extension of presently available theory would be required, it seems likely that even this problem can eventually be analyzed on large computers.

[4] Professor, Department of Mechanical Engineering, Yale University, New Haven, Conn. Mem. ASME.

P. P. BIJLAARD
Consultant and Professor of Mechanics, Cornell University, Ithaca, N. Y.

R. J. DOHRMANN
Analytical Engineer, Research Center, The Babcock & Wilcox Company, Alliance, Ohio. Assoc. Mem. ASME

Thermal-Stress Analysis of Irregular Shapes

A method has been developed for determining the thermal stresses resulting from an axially symmetric temperature distribution in an irregularly shaped cylindrical vessel. It permits the calculation of the principal stresses, rotations, and displacements for all points within the cross section and on the boundary of the geometry being considered. Finite-difference techniques are used to solve the governing fourth-order differential equation that must be satisfied. The method was applied to geometries and temperature distributions for which classical analytical solutions are available, and the agreement was very good. An example is given for which the "isostress" and isothermal lines are plotted for an irregular geometry with varying temperature gradients in the radial and longitudinal directions.

Introduction

Since both longitudinal and radial temperature gradients can exist in pressure vessels and associated equipment, it is evident that any method of solution must be capable of handling both types of these temperature gradients singly or in combination. In addition, it must be able to handle geometries of irregular cross section.

In view of the foregoing, a method was developed and applied to a complicated geometry by dividing the geometry into individual free bodies. The thermal stresses then were determined for each section independently. Fig. 1 illustrates the method used. Since in reality the cross-hatched areas are actually one continuous geometry, they again must be rejoined, making certain to satisfy continuity of slope and deflection at the junctures shown by the dots. The stresses introduced by the force system required to rejoin the sections then are merely added to the already calculated thermal stresses.

This method can be used in conjunction with classical analytical methods where the structure consists of a combination of regularly and irregularly shaped geometries as is commonly the case. It may also be used to determine thermal stress for the length of a geometry in which the axial heat flow is present.

Contributed by the Petroleum Division and presented at the Winter Annual Meeting, New York, N. Y., November 27–December 2, 1960, of The American Society of Mechanical Engineers. Manuscript received at ASME Headquarters, August 4, 1960. Paper No. 60—WA-131.

Derivation of Theoretical Thermal-Stress Analysis Method

The thermal-stress analysis of an entire vessel can be broken down into component parts similar to that which is done when calculating stresses from pressure and other loadings. For the purposes of this paper, only one part of the entire vessel will be treated and discussed in detail. This type of treatment will not detract from the general applicability in any way because, to solve the entire structure, one merely must repeat the analysis for each component of the vessel and then combine them, making certain that equilibrium and continuity of slope and deflection are satisfied.

For this paper an irregular flange of a vessel will be considered in which the temperature varies both in the radial and axial directions, Figs. 1 and 2. The principle of superposition will be used, and the analysis will be divided into three cases.

Case 1. Here it is assumed that the necessary forces are applied that will cause full restraint of the expansion, so that

$$\epsilon_x = \epsilon_r = \epsilon_\varphi = 0 \tag{1}$$

where x and r are the directions indicated in Fig. 3, and φ is the tangential direction. The body forces and surface tractions required to cause full restraint are determined in Appendix 1. Since the thermal strains are equal in all directions, the required stresses are also equal. They are

$$\sigma_{x_1} = \sigma_{r_1} = \sigma_{\varphi_1} = p = -\frac{\alpha TE}{1 - 2\nu} \tag{2}$$

Nomenclature

A = area of cross section, sq in.
E = modulus of elasticity, psi
F = total resulting tangential force, lb
I_{RR} = moment of inertia about centroidal axis on meridional cross section, in.^{4}
$I_{\varphi\varphi}$ = moment of inertia of a section with 1/100 radian arc length, in.^{4}
$M_{\bar{t}}$ = total resulting tangential moment, in-lb
M_x = longitudinal bending moment, in-lb per 1/100 radian
R = body force per unit volume in radial direction, lb/in.^{3}
T = temperature at any point, deg F
T_i = temperature at inside radius, deg F
T_m = maximum temperature, deg F
X = body force per unit volume in longitudinal direction, lb/in.^{3}
a = distance from an external point along normal to boundary, in.
b = distance along normal from boundary to a non-nodal point, in.
h = nodal spacing in longitudinal direction or height of ring, in.
k = nodal spacing in radial direction, in.
m = number of nodal points in any single horizontal numbering system, dimensionless
p = $-\alpha ET/(1 - 2\nu)$, or h/k
r = radius to any point measured normal to the longitudinal axis, in.
r' = radial distance from centroidal axis to any point in a section at constant height (x = constant), in.
r_x = distance from longitudinal axis to centroid of horizontal strip, in.
t = thickness of ring, in.
v = radial displacement, in.
x = longitudinal co-ordinate, in.
x' = measurement of extrapolation distance, in.
z = distance from centroid to nodal point, in.
σ_x = stress in the longitudinal direction, psi
σ_r = stress in the radial direction, psi
σ_φ = stress in the tangential direction, psi

(Continued on next page)

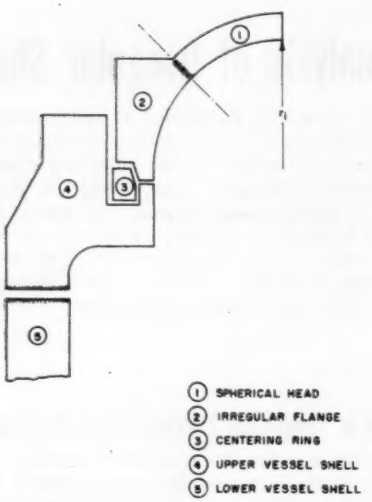

Fig. 1 Component breakdown of an integral vessel

The subscript numbers refer to the stresses in Case 1. Tensile stresses are considered as positive.

From Appendix 1, in order to satisfy full restraint, the required body forces R and X per unit volume in the r and x-directions are

$$R = \frac{\alpha E}{1 - 2\nu} \frac{\partial T}{\partial r} \tag{3}$$

$$X = \frac{\alpha E}{1 - 2\nu} \frac{\partial T}{\partial x} \tag{4}$$

To satisfy the boundary conditions, normal stresses along the boundaries must be equal to p from equation (2). Hence surface pressures of

$$-\sigma_n = \frac{\alpha E T}{1 - 2\nu} \tag{5}$$

must be applied to the boundaries. These stresses and body forces are those associated with a condition of full restraint.

Case 2. Through further superposition, the loading and stress conditions of Case 2 are developed. These loading conditions can be reduced to those for which a known classical solution is available.

Since actually the body forces R and X from equations (3) and (4) and the surface pressures $-\sigma_n$ from equation (5) are not really there, the opposites of these forces and pressures must be applied. This requires that the stress $\sigma_n = \alpha TE/(1 - 2\nu)$ be applied on all free surfaces of the cross section (hence, not to the φ-surface) and body forces be applied per unit volume for internal points of

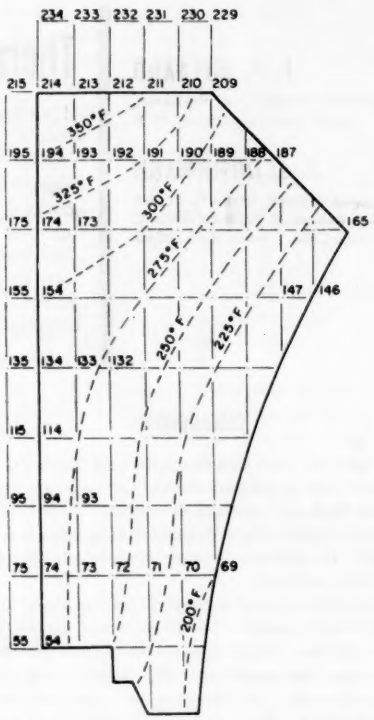

Fig. 2 Temperature distribution for an irregular flange

$$R = -\frac{\alpha E}{1 - 2\nu} \frac{\partial T}{\partial r} \tag{6}$$

$$X = -\frac{\alpha E}{1 - 2\nu} \frac{\partial T}{\partial x} \tag{7}$$

It is also assumed that in Case 2 the tangential strain ϵ_φ remains equal to zero, so that the body can neither move radially nor tilt. These assumptions will later be considered in Case 3. Fig. 4 shows the state of stress of the system for Case 2.

The stresses for this case, except for small radial stresses that can be taken into account later, will be essentially the same as those associated with the case of plain strain occurring in a long prismatic body, when the temperature varies over the cross section, but does not vary along lines parallel to the axis of the prism. These stresses can be calculated by the classical formulas given as follows:[1]

[1] S. Timoshenko and J. N. Goodier, "Theory of Elasticity," McGraw-Hill Book Company, Inc., New York, N. Y., second edition, 1951, p. 424.

Nomenclature

σ_n = stress normal to a surface, psi
τ_{xr} = shear stress, psi
ϕ = stress function
$\bar{\theta}$ = $\sigma_x + \sigma_r + \sigma_\varphi$, psi
ϕ_t = stress function of an external point
ϕ_t' = stress function for an internal non-nodal point
ϵ_x = strain in longitudinal direction, in/in.
ϵ_r = strain in radial direction, in/in.
ϵ_φ = strain in tangential direction, in/in.
ν = Poisson's ratio, dimensionless
α = coefficient of linear expansion, in/in-deg F
θ = rotation of a point, radians

Subscripts

n = normal direction to boundary or subscript for general point
t = tangential direction to boundary
x = longitudinal direction
r = radial direction
φ = tangential direction
$\bar{t}$ = tangential direction of moment
t' = internal non-nodal point
RR = centroidal axis of meridional section
$\varphi\varphi$ = centroidal axis of horizontal section

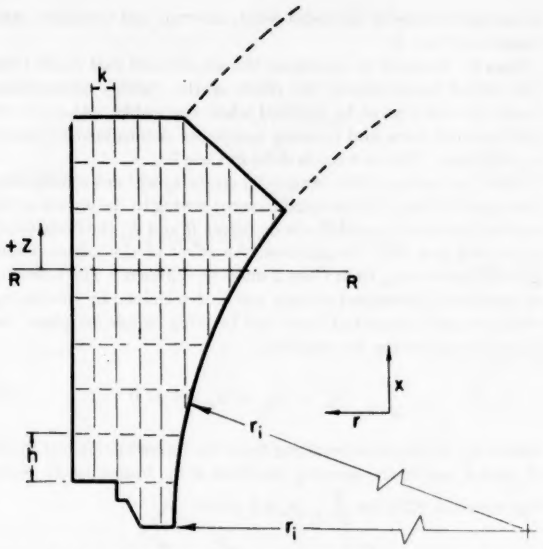

Fig. 3 Grid and geometry notation for an irregular flange

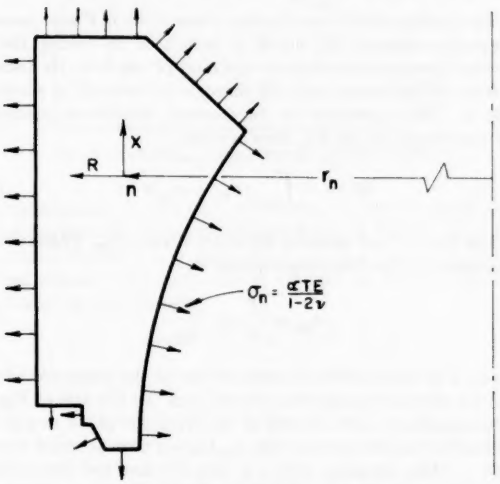

Fig. 4 State of stress for consideration of Case 2

$$\sigma_{z_2} = \frac{\partial^2 \phi}{\partial r^2} + \frac{E\alpha T}{1-2\nu} \tag{8}$$

$$\sigma_{r_2} = \frac{\partial^2 \phi}{\partial x^2} + \frac{E\alpha T}{1-2\nu} \tag{9}$$

$$\tau_{xr_2} = -\frac{\partial^2 \phi}{\partial r \partial x} \tag{10}$$

where ϕ must satisfy the differential equation

$$\frac{\partial^4 \phi}{\partial x^4} + 2\frac{\partial^4 \phi}{\partial x^2 \partial r^2} + \frac{\partial^4 \phi}{\partial r^4} + \frac{\alpha E}{1-\nu}\left(\frac{\partial^2 T}{\partial x^2} + \frac{\partial^2 T}{\partial r^2}\right) = 0 \tag{11}$$

These four equations are obtained[1] by substituting r for y. The tangential stress required to keep ϵ_φ zero is

$$\sigma_{\varphi_2} = \nu(\sigma_{z_2} + \sigma_{r_2}) \tag{12}$$

Equation (11) is solved by expanding it in terms of finite differences and solving the resulting equations for all points simultaneously. From Fig. 3, the grid spacing is taken as h in the x-direction and k in the r-direction. Letting the following relationship be true for h and k:

$$h = pk \tag{13}$$

the expansion of equation (11) in terms of finite difference expressions[2] results in

$$\begin{aligned}
&\frac{1}{p^4k^4}(\phi_{n-2m} - 4\phi_{n-m} + 6\phi_n - 4\phi_{n+m} + \phi_{n+2m}) \\
&+ \frac{2}{p^2k^4}[4\phi_n - 2(\phi_{n-1} + \phi_{n+1} + \phi_{n-m} + \phi_{n+m}) \\
&+ \phi_{n-m-1} + \phi_{n-m+1} + \phi_{n+m+1} + \phi_{n+m-1}] \\
&+ \frac{1}{k^4}(\phi_{n-2} - 4\phi_{n-1} + 6\phi_n - 4\phi_{n+1} + \phi_{n+2}) \\
&+ \frac{\alpha E}{1-\nu}\left[\frac{1}{p^2k^2}(T_{n-m} - 2T_n + T_{n+m})\right. \\
&\left. + \frac{1}{k^2}(T_{n-1} - 2T_n + T_{n+1})\right] = 0
\end{aligned} \tag{14}$$

where m is the number of nodal points in any single horizontal numbering system.

Similarly, the expressions for the σ_{z_2}, σ_{r_2}, σ_{φ_2}, and τ_{zr_2}, would be

$$(\sigma_{z_2})_n = \frac{1}{k^2}(\phi_{n-1} - 2\phi_n + \phi_{n+1}) + \frac{E\alpha T_n}{1-2\nu} \tag{15}$$

$$(\sigma_{r_2})_n = \frac{1}{p^2k^2}(\phi_{n-m} - 2\phi_n + \phi_{n+m}) + \frac{E\alpha T_n}{1-2\nu} \tag{16}$$

$$(\sigma_{\varphi_2})_n = \nu(\sigma_{z_2} + \sigma_{r_2})_n \tag{17}$$

$$(\tau_{zr_2})_n = -\frac{1}{4pk^2}(\phi_{n+m+1} + \phi_{n-m-1} - \phi_{n+m-1} - \phi_{n-m+1}) \tag{18}$$

Equation (14) must be written for all points that are internal points, that is, for all points that do not help form the boundary. Points 192, 188, 147, and 132 in Fig. 2 would, therefore, be considered as internal points. On the other hand, points 154, 174, 69, and 165 would be considered boundary points.

Boundary conditions require that

$$\begin{aligned}
\sigma_n &= \frac{E\alpha T}{1-2\nu} \\
\tau_{nt} &= 0
\end{aligned} \tag{19}$$

where n and t refer to the normal and tangential directions. Therefore, for all boundary points ϕ must be zero and $\partial\phi/\partial n = 0$ to satisfy equations (19) (Appendix 2).

By inspection of equation (14), it will be seen that, to adequately express this equation near boundary points, additional points in a region outside of the geometry under consideration must be used. This requires the use of *reflective points* whose value is extrapolated from internal points. This extrapolation can be accomplished by visualizing the values of ϕ for all points, internal and external, as forming a generated surface. Because ϕ and $\partial\phi/\partial n$ must equal zero at the boundaries, it is reasonable to assume a simple second-degree-curve type of distribution for reflective points outside the boundaries. Assuming that along the

[2] M. G. Salvadori and M. L. Baron, "Numerical Methods in Engineering," Prentice-Hall, Inc., New York, N. Y., 1952, p. 69.

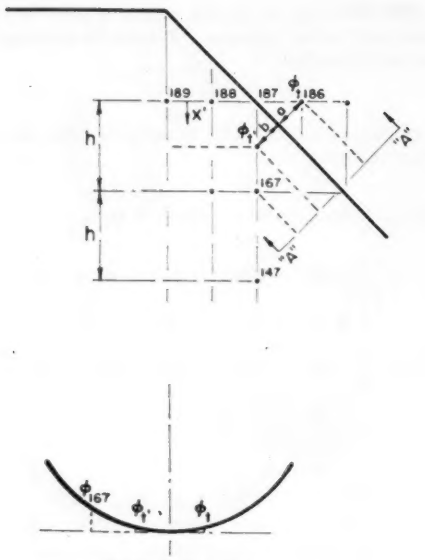

Fig. 5 External reflective point

boundary and at the intersection of a plane normal to the boundary, the ϕ-surface varies parabolically, Fig. 5, the necessary external reflective points can be expressed as

$$\phi_i = \left(\frac{a}{b}\right)^2 \phi_{i'} \tag{20}$$

where i' is a point within the cross section and a and b are the distances measured along the same normal from the external reflective point to the boundary and from the boundary to the internal point, respectively. For the value of the temperature T_i of an external reflective point i, use the temperature in the body on the normal where $b = a$.

It is desirable for the best accuracy to keep a as nearly as possible equal to b in equation (20).

The value of $\phi_{i'}$ can be expressed for the example in Fig. 5 as

$$\phi_{i'} = \frac{(x' - h)(x' - 2h)}{2h^2}\phi_{187} - \frac{x'(x' - 2h)}{h^2}\phi_{167} + \frac{x'(x' - h)}{2h^2}\phi_{147} \tag{21}$$

It will be readily noted that, if $x' = 0$, then $\phi_{i'} = \phi_{187}$ which is as it should be.

Using the foregoing procedure for expressing the external reflective points, all of the required terms in equation (14), whether internal or boundary, can be expressed adequately. For various points, such as ϕ_{233}, ϕ_{230}, ϕ_{175}, ϕ_{95}, Fig. 2, the expressions given in equations (20) and (21) reduce to a simple form. The value of ϕ_{233} can be obtained directly by setting it equal to ϕ_{193}. In a similar manner, the value of ϕ_{230} would be equal to ϕ_{190}, ϕ_{175} to ϕ_{170}, and ϕ_{95} to ϕ_{80}. Similar reasoning can be used for points that may be determined by direct reflection.

By applying equation (14) to all internal points and solving simultaneously, a value of ϕ for all points will be obtained. By substituting the proper values of ϕ into equations (15), (16), (17), and (18), the respective values of σ_{x_2}, σ_{r_2}, σ_{φ_2}, and τ_{xr_2} can be determined. This permits the calculation of all of the principal stresses for all nodal point, internal and boundary, and completes Case 2.

Case 3. In order to determine the net stresses that result from the actual temperature, the effect of the various assumptions made in Case 2 must be nullified when applicable. Also, the resulting axial force and bending couple are determined to satisfy equilibrium. This is what is done in Case 3.

Since the value of the tangential strain ϵ_φ will not remain zero (assumed in Case 2 to be equal to zero), owing to the action of the surface tractions σ_n and the body forces R and X, the body tends to extend and tilt. In addition, the effect of the assumed tangential stresses σ_{φ_2} from Case 2 must be nullified. The influence of these body forces and stresses can be determined by calculating the necessary tangential force and bending couple to place the body in equilibrium by requiring:

$$\int_{(A)} (\sigma_{\varphi_1} + \sigma_{\varphi_2} + \sigma_{\varphi_3}) dA = 0 \tag{22}$$

where σ_{φ_3} is the stress resulting from the forces introduced by R, X, and σ_n and from canceling the effect of σ_{φ_2} from Case 2. Solving equation (22) for $\int_{(A)} \sigma_{\varphi_3} dA$ yields

$$F = -\int_{(A)} (\sigma_{\varphi_1} + \sigma_{\varphi_2}) dA = \int_{(A)} \sigma_{\varphi_3} dA \tag{23}$$

The resultant force distribution whose total is F also causes a tangential moment M_I, which is calculated by taking the individual force on each element and multiplying it by its distance z, from the horizontal axis RR through the centroid as shown in Fig. 3. The expression for the moment, considered positive if causing tension at the top, then becomes

$$M_I = -\int_{(A)} (\sigma_{\varphi_1} + \sigma_{\varphi_2}) z \, dA \tag{24}$$

The force F and moment M_I cause stresses σ_{φ_3}, which can be calculated by the following expression:

$$\sigma_{\varphi_3} = \frac{F}{A} + \frac{M_I z}{I_{RR}} \tag{25}$$

where A is the meridional cross section of the shape considered and z is measured positively upward from the RR-axis of Fig. 3. Intentionally, to take account of the expansion of the ring in the radial direction, in equation (25) σ_{φ_3} has not been assumed to vary with r. This variation with r is true if v does not vary with r, in which case $\epsilon_\varphi = v/r$ so that $\sigma_\varphi = Ev/r$. However, due to the thermal expansion, v is about proportional to r, say $v = v_1 r$, so that $\epsilon_\varphi = v_1 r/r = v_1$, and $\sigma_{\varphi_3} = Ev_1$, independent of r. The first four examples given under "Comparison With Theoretical Results" show that this leads to the correct results.

However, for the more complicated cases of force distribution, the restraining forces supplied by the σ_{φ_3} stresses may not have exactly the same distribution in the x-direction as the deflecting forces caused by the $(\sigma_{\varphi_1} + \sigma_{\varphi_2})$ stresses, Fig. 6. This implies that the moments generated in cross sections x = constant by the restraining forces do not fully cancel the moments generated by the deflecting forces. However, equilibrium of forces is satisfied from equation (23). To allow for this and place the body in complete equilibrium, a bending moment M_x in a section where x is constant can be calculated, Fig. 7. The stresses resulting from this bending moment introduce longitudinal bending stresses that are calculated by the equation

$$\sigma_{x_3} = \frac{M_x r'}{I_{\varphi\varphi}} \tag{26}$$

where $I_{\varphi\varphi}$ is the moment of inertia of a section and x is constant

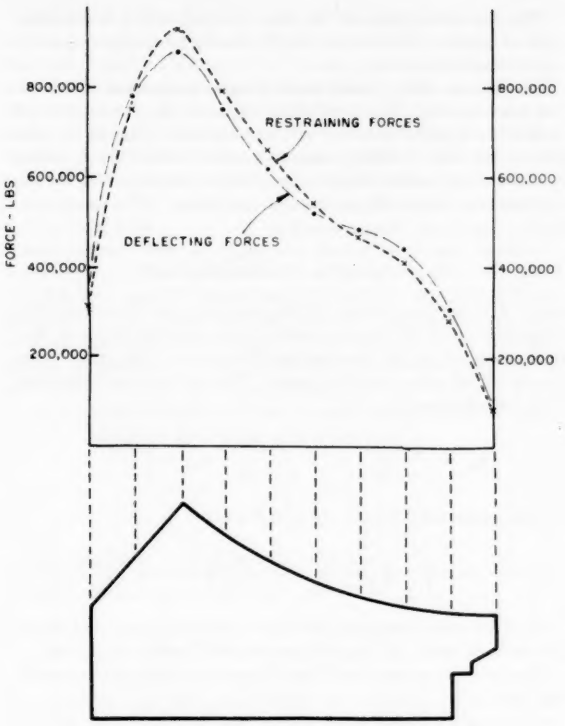

Fig. 6 Deflecting and restraining force distribution

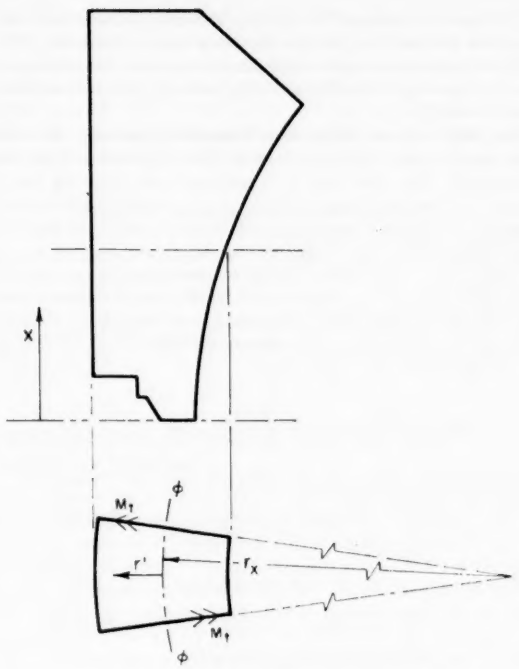

Fig. 7 Longitudinal bending-moment orientation

for, for example, a sector of 1/100 radian arc length and is taken about the centroid of that section, as shown on Fig. 7. σ_{x_3} causes additional stresses $\sigma_{\varphi_3} = \nu\sigma_{x_3}$.

Final Stresses. The final stresses can now be determined from the following expressions:

$$\begin{aligned} \sigma_x &= \sigma_{x_1} + \sigma_{x_2} + \sigma_{x_3} \\ \sigma_r &= \sigma_{r_1} + \sigma_{r_2} \\ \sigma_\varphi &= \sigma_{\varphi_1} + \sigma_{\varphi_2} + \sigma_{\varphi_3} \\ \tau_{xr} &= \tau_{xr_2} \end{aligned} \tag{27}$$

Apparently, the stresses σ_r caused by the curvature of the σ_φ stress trajectories are not taken into account in this way, but can be easily computed from the stresses σ_φ. However, these stresses σ_r will generally not be essential, since they are zero at the inner and outer boundaries, where σ_φ is highest.

Displacement. Since in Case 1 the values of ϵ_x, ϵ_r, and ϵ_φ are all equal to zero, no displacement results. Also in Case 2, the value of ϵ_φ was held to zero so that no radial displacement could result; however, longitudinal displacement u does result.

The radial displacement from Case 3 is determined directly from equation (25) and is expressed as

$$v = \frac{Fr}{AE} + \frac{M_I rz}{I_{RR}E} \tag{28}$$

where r is the radius measured normal to the longitudinal axis of the vessel and A is the area of the meridional cross section of the body.

The total longitudinal strain is given by

$$\epsilon_x = \frac{(\sigma_{x_2} + \sigma_{x_3})}{E} - \frac{\nu}{E}(\sigma_{r_2} + \sigma_{\varphi_2} + \sigma_{\varphi_3}) \tag{29}$$

or, formulated in another way,

$$\epsilon_x = \alpha T + \frac{\sigma_x}{E} - \frac{\nu}{E}(\sigma_r + \sigma_\varphi) \tag{29a}$$

Rotation. Similarly, no rotation is produced by Cases 1 and 2; therefore, only Case 3 need be considered. From equation (28), the rotation can easily be determined by taking the derivative of v with respect to z. If this is done, the following equation results:

$$\theta = \frac{dv}{dz} = \frac{M_I r}{I_{RR}E} \tag{30}$$

This then completes the theoretical derivation of this thermal-stress method. It will be recalled that this method permits the solution of the thermal stresses in irregular cylindrical geometries with temperature gradients varying in both the radial and longitudinal directions. In addition, the displacements in both the radial and longitudinal directions along with rotation can be determined on a point-by-point basis throughout the cross section of the geometry. Next a comparison of the theoretical results for known temperature distributions will be considered.

Comparison With Theoretical Results

Ring With a Constant Temperature. For the case of a ring of height h and thickness t, with a constant temperature, the solution by the method proposed in this paper is very elementary and too trivial for a detailed explanation. The general results, however, will be summarized. The stresses from Case 1 are $\sigma_{x_1} = \sigma_{r_1} = \sigma_{\varphi_1} = -E\alpha T/(1 - 2\nu)$. The stresses from Case 2 are equal to the second right-hand terms of equations (8) and (9) and the tangential stress is given by equation (12). Because of the uniform temperature, there is no rotation and only the first part of equation (25) need be considered. From Equation (23) the value of F can be determined readily to be equal $E\alpha Tth$. Know-

ing all parts of equation (27) the final principal stresses can be determined identically equal to zero, which is as it should be. The radial displacements and longitudinal strains can be determined directly from equations (28) and (29), to be equal to αTr and αT, respectively.

Ring With a Linear Longitudinal Temperature Gradient. *Stresses.* The case of a ring with a linear longitudinal gradient will next be considered. For this case, it is assumed that the ring has a thickness t, height h, and a temperature distribution varying from zero at the base to a maximum temperature T_m at the top. The stresses from Case 1 can be expressed as $\sigma_{x_1} = \sigma_{r_1} = \sigma_{\varphi_1} = -E\alpha T/(1 - 2\nu)$ where T is the temperature at any point expressed in terms of T_m. As was true for the case of constant temperature, here again all of the ϕ-values are zero, since T varies linearly in all directions. The stresses introduced by Case 2 then can be expressed as

$$\sigma_{x_2} = \frac{E\alpha T}{1 - 2\nu}, \quad \sigma_{r_2} = \frac{E\alpha T}{1 - 2\nu}, \quad \sigma_{\varphi_2} = \frac{2\nu E\alpha T}{1 - 2\nu}$$

For Case 3, by using equation (23), the value of F becomes

$$F = -\int_{(A)} \left(\frac{-E\alpha T}{1 - 2\nu} + \frac{2\nu E\alpha T}{1 - 2\nu}\right) dA = \frac{E\alpha T_m th}{2}$$

The value of M_I can be calculated from equation (24)

$$M_I = -\int_{(A)} \left(\frac{-E\alpha T}{1 - 2\nu} + \frac{2\nu E\alpha T}{1 - 2\nu}\right) z\, dA = \frac{E\alpha T_m h^2 t}{12}$$

The stresses caused by F and M_I can then be calculated from equation (25)

$$\sigma_{\varphi_3} = \frac{1}{2}\,\frac{E\alpha T_m th}{th} + \frac{E\alpha T_m h^2 tz}{\frac{12th^3}{12}} = E\alpha T$$

The final principal stresses as calculated from equation (27) would be

$$\sigma_z = 0$$

$$\sigma_r = 0$$

$$\sigma_\varphi = \frac{-E\alpha T}{1 - 2\nu} + \frac{2\nu E\alpha T}{1 - 2\nu} + E\alpha T = 0$$

Thus, it is evident that a linear longitudinal gradient yields no thermal stress in any direction.

Radial Displacement. The radial displacements are calculated from equation (28):

$$v = \frac{1}{2}\,\frac{E\alpha T_m thr}{thE} + \frac{E\alpha T_m h^2 trz}{\frac{12th^3E}{12}} = \alpha Tr$$

Longitudinal Strain. Using equation (29), the longitudinal strain is calculated as

$$\epsilon_z = \frac{\alpha T}{1 - 2\nu} - \frac{\nu}{E}\left(\frac{E\alpha T}{1 - 2\nu} + \frac{2\nu E\alpha T}{1 - 2\nu} + E\alpha T\right) = \alpha T$$

which same result follows directly from equation (29*a*).

For a linear gradient in the longitudinal direction this is in agreement with theory.

Rotation. The rotation is determined from equation (30):

$$\theta = \frac{E\alpha T_m h^2 tr}{\frac{12th^3E}{12}} = \frac{\alpha r T_m}{h}$$

This illustrates that, for the case of a ring with a linear longitudinal gradient, the stresses, displacements, and rotations are in agreement with theory.

Short Cylinder With a Linear Radial Temperature Gradient. *Stresses.* For a further comparison with classical examples, a short cylinder with a linear radial gradient will be considered. Again, for simplicity, the short cylinder is assumed to have a thickness t, height h, and a linear radial temperature gradient varying from zero at the inside radius to T_m at the outside radius. The stresses resulting from Case 1 are expressed as

$$\sigma_{x_1} = \sigma_{r_1} = \sigma_{\varphi_1} = -E\alpha T/(1 - 2\nu),$$

where T is the temperature of the point and can be expressed in terms of T_m. It will be seen readily from equation (14) that, due to the linearity of the temperature distribution, the stress function ϕ for all points must be zero. The stresses resulting from Case 2 then reduce to

$$\sigma_{x_2} = \frac{E\alpha T}{1 - 2\nu}, \quad \sigma_{r_2} = \frac{E\alpha T}{1 - 2\nu}, \quad \sigma_{\varphi_2} = \frac{2\nu E\alpha T}{1 - 2\nu}$$

Using equation (23), the value of F will be

$$F = -\int_{(A)} \left(\frac{-E\alpha T}{1 - 2\nu} + \frac{2\nu E\alpha T}{1 - 2\nu}\right) dA = \frac{E\alpha T_m ht}{2}$$

Since the radial force distribution is balanced above and below the centroid axis, the resulting moment M_I must equal zero.

The value of stresses from Case 3 then is determined from equation (25)

$$\sigma_{\varphi_3} = \frac{1}{2}\,\frac{E\alpha T_m ht}{ht} = \frac{E\alpha T_m}{2}$$

When all components of stress from Cases 1, 2, and 3 are known, the final principal stresses can be determined from equation (27):

$$\sigma_z = 0$$

$$\sigma_r = 0$$

$$\sigma_\varphi = \frac{-E\alpha T}{1 - 2\nu} + \frac{2\nu E\alpha T}{1 - 2\nu} + \frac{E\alpha T_m}{2}$$

$$= -E\alpha T + \frac{E\alpha T_m}{2}$$

A check of the stress distribution at the inside and outside radius shows that the stress values are $\sigma_\varphi = E\alpha T_m/2$ and $\sigma_\varphi = -E\alpha T_m/2$, respectively.

Radial Displacement. The radial displacement is determined from equation (28)

$$v = \frac{1}{2}\,\frac{E\alpha T_m htr}{Eth} = \frac{\alpha T_m r}{2}$$

Longitudinal Strain. By using equation (29), the longitudinal strain at a point can be determined:

$$\epsilon_z = \frac{\alpha T}{1 - 2\nu} - \frac{\nu}{E}\left(\frac{E\alpha T}{1 - 2\nu} + \frac{2\nu E\alpha T}{1 - 2\nu} + \frac{E\alpha T_m}{2}\right)$$

$$= (1 + \nu)\alpha T - \frac{\nu\alpha T_m}{2}$$

The same result is obtained from equation (29*a*).

Rotation. Since $M_I = 0$, the rotation at all points must be zero. This is further evidenced by the fact that temperature distribution is symmetrical about the centroid axis.

The values of the stresses, rotations, and displacements have been completely determined. The value of the tangential stress can be checked by comparing the stresses in a circular disk with a hole at the center and a temperature distribution symmetrical about the center of the disk. This comparison can be made easily by determining the appropriate constants of integration for the governing general equation for the disk.[3] The results of this comparison are given in Table 1 and the agreement with the present method is excellent. The comparison was made for a r_o/r_i ratio of 1.105.

Short Cylinder With a Logarithmic Radial Temperature Gradient. For a case of a nonlinear temperature distribution, the temperature gradient generally associated with steady heat flow will be discussed. The tangential stresses, as determined by the method discussed in this paper, will be compared with the tangential stresses in a circular disk with a circular hole at the center of the disk as was done previously.

For the case of a short cylinder of height h, and thickness t, and with a temperature distribution of the form

$$T = \frac{T_i}{\log_e \frac{r_o}{r_i}} \log_e \frac{r_o}{r}$$

the solution by the method proposed in this paper can be obtained readily. The stresses from Case 1 are

$$\sigma_{x_1} = \sigma_{r_1} = \sigma_{\varphi_1} = -\frac{E\alpha T}{1 - 2\nu}$$

Since for the case being considered the net axial stress must be equal to zero, it can be seen readily from equation (8) that the value of ϕ must be everywhere equal to zero. The resulting stresses from Case 2 can then be calculated directly from equations (8) and (9) and are equal to the right-hand terms of the equations, while the tangential stress is given by equation (12). The value of the tangential force F is found from equation (23) to be

$$F = -\int_{(A)} (\sigma_{\varphi_1} + \sigma_{\varphi_2}) dA = \frac{E\alpha T_i h}{\log \frac{r_o}{r_i}} [(r_o - r_i) - r_i \log r_o/r_i]$$

Since there is no rotation for this case the value of the stress for Case 3 is found from equation (25):

$$\sigma_{\varphi_3} = \frac{E\alpha T_i}{\log \frac{r_o}{r_i}} \left[1 - \frac{r_i}{r_o - r_i} \log \frac{r_o}{r_i}\right]$$

Knowing all components of the stresses from Cases 1, 2, and 3, the final principal stresses can be determined from equation (27):

$$\sigma_x = 0$$

$$\sigma_r = 0$$

$$\sigma_\varphi = \frac{E\alpha T_i}{\log \frac{r_o}{r_i}} \left[1 - \frac{r_i}{r_o - r_i} \log \frac{r_o}{r_i}\right] - E\alpha T$$

Writing the tangential stress in a more general way, it can be reduced to

$$\sigma_\varphi = \frac{E\alpha \int_{(A)} T\, dA}{A} - E\alpha T = E\alpha T_{avg} - E\alpha T$$

where T_{avg} is the average temperature of the cross section.

[3] Timoshenko and Goodier, op. cit., p. 407.

The foregoing tangential stresses were compared to those of a circular disk with a circular hole at the center of the disk and the results were excellent and are shown in Table 1. A ratio of the outside radius to the inside radius of 1.333 was used in the preceding example. It is felt that even closer agreement of the method discussed in this paper would result for outside-radius to inside-radius ratios nearer to unity.

Table 1 Comparison of tangential stresses

Temperature distribution	Theoretical, psi	Present method, psi
Linear radial gradient		
Inside radius	10675	10500
Outside radius	−10325	−10500
Logarithmic radial gradient		
Inside radius	−9870	−9410
Outside radius	8200	8660

Irregularly Shaped Flange With Radial and Axial Temperature Gradients

As a final example, the thermal stresses resulting from the temperature distribution shown in Fig. 2 will be discussed. It is readily apparent that this geometry and temperature distribution are markedly different from any considered thus far. Since this geometry is treated as a free body, it is free from any external force, and axial symmetry of geometry and temperature are assumed.

For given values of temperature at nodal points, Fig. 2, and suitable values of elastic constants, the thermal stresses can be determined by using the method described in this paper. Fig. 8 shows the resulting tangential thermal-stress distribution.

It is interesting to note that the hottest point on the flange is in compression and the coldest point in tension. This is logical and is in agreement with accepted theory. It is also interesting

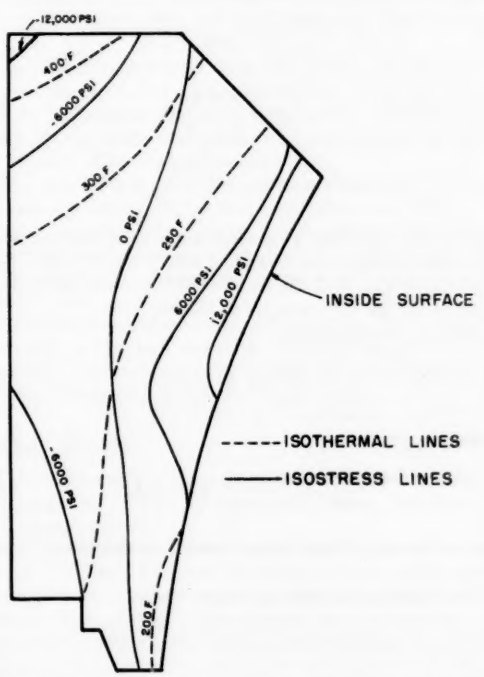

Fig. 8 Tangential stress and temperature distribution for an irregular flange

to note that the "isostress" lines and the isothermal lines tend to intersect at the same angle. Perhaps there is some significance to this fact.

Summary

The method that has been described in this paper provides a means of calculating the thermal stresses, displacements, and rotations resulting from an arbitrary temperature distribution. This method can be applied to irregular shapes of bodies of revolution with an axial symmetric temperature distribution but with the temperature varying in the radial and longitudinal directions. It is felt that now, for the first time, we have a method that is readily usable and workable.

Information resulting from the application of this analysis makes it possible to establish optimum heating and cooling rates and also supplies the necessary stress information to perform a thermal-fatigue analysis.

Presently an effort is being made to permit consideration of geometry flexibility which modification will be especially useful when the geometry is that of a finite or long cylinder. Also an exact but more laborious method was developed.

APPENDIX 1

Derivation of Equations for Case 1 and 2

Case 1. In order to impose the required condition of $\epsilon_z = \epsilon_r = \epsilon_\varphi = 0$, certain surface tractions and body forces must be superimposed. From Timoshenko and Goodier[4]

$$e = \frac{1}{E}(1 - 2\nu)\bar{\theta} + 3\alpha T \tag{31}$$

$$e = \epsilon_z + \epsilon_r + \epsilon_\varphi \tag{32}$$

$$\bar{\theta} = \sigma_z + \sigma_r + \sigma_\varphi \tag{33}$$

Since $\epsilon_z = \epsilon_r = \epsilon_\varphi = 0$, from equation (31)

$$0 = \frac{1}{E}(1 - 2\nu)\bar{\theta} + 3\alpha T$$

$$\bar{\theta} = -\frac{3\alpha TE}{1 - 2\nu} \tag{34}$$

$$\sigma_{z_1} = \sigma_{r_1} = \sigma_{\varphi_1} = \frac{-\alpha TE}{1 - 2\nu} = p$$

To cause the foregoing stress condition to exist, the body forces and surface tractions required must satisfy equilibrium. Since $\tau_{zr_1} = \tau_{r\varphi_1} = \tau_{\varphi z_1} = 0$, the equilibrium equations in the longitudinal and radial directions are as follows:

z-direction (longitudinal)

$$\frac{\partial \sigma_z}{\partial x} + X = 0 \tag{35}$$

r-direction (radial)

$$\frac{\partial \sigma_r}{\partial r} + \frac{\sigma_r - \sigma_\varphi}{r} + R = 0 \tag{36}$$

The values of the body forces X and R are determined by substituting the value of the stresses from equation (34) into the equilibrium equations (35) and (36).

x-direction

$$\frac{-\alpha E}{1 - 2\nu}\frac{\partial T}{\partial x} + X = 0$$

$$X = \frac{\alpha E}{1 - 2\nu}\frac{\partial T}{\partial x} \tag{37}$$

r-direction

$$\frac{-\alpha E}{1 - 2\nu}\frac{\partial T}{\partial r} + R = 0$$

$$R = \frac{\alpha E}{1 - 2\nu}\frac{\partial T}{\partial r} \tag{38}$$

Equations (37) and (38) then represent the required body forces per unit volume.

From equation (34) on the free boundaries normal stresses of $\sigma_n = p = -E\alpha T/(1 - 2\nu)$ are required.

APPENDIX 2

Boundary Conditions for Case 2

Case 2. For this case the boundary conditions are

$$\sigma_n = \frac{E\alpha T}{1 - 2\nu} \tag{39}$$

$$\tau_{nt} = 0 \tag{40}$$

By using equations (8), (9), and (10) of the paper, the values of equations (39) and (40) for the edge become

$$\sigma_n = \frac{\partial^2 \phi}{\partial t^2} + \frac{E\alpha T}{1 - 2\nu} \tag{41}$$

$$\tau_{nt} = \frac{-\partial^2 \phi}{\partial n\, \partial t} \tag{42}$$

For the edge then to satisfy equations (39) and (40), the following relations must exist:

$$\frac{\partial^2 \phi}{\partial t^2} = 0 \tag{43}$$

$$\frac{-\partial^2 \phi}{\partial t\, \partial n} = 0 \tag{44}$$

Integrating equations (43) and (44) gives

$$\frac{\partial \phi}{\partial t} = A \tag{45}$$

$$\phi = At + B$$

$$\frac{\partial \phi}{\partial n} = C \tag{46}$$

where A, B, and C are constants along the boundary (t-axis). They can be chosen arbitrarily. Assuming them to be zero on the edges

$$\phi = 0 \quad \text{and} \quad \frac{\partial \phi}{\partial n} = 0 \tag{47}$$

[4] Timoshenko and Goodier, op. cit., p. 421.

DISCUSSION

D. B. Rossheim[5] and C. A. Honigsberg[6]

The authors have provided a useful method for the thermal stress evaluation of irregular cross-section surfaces of revolution under axially symmetric temperature distribution, which effectively illustrates the complexities confronting pressure vessel engineers in dealing with the stresses introduced by nonuniform heat flow. With innumerable combinations of vessel geometry and transient or steady-state nonuniform thermal gradients, presolved equations and graphs are of limited applicability, even for axially symmetric temperature distribution and geometry. Calculations to establish temperature profiles and attendant thermal stresses are laborious if performed manually, but are rapidly and economically executed by automatic programmed computers, where applicable programs are available.

There is a critical need for a broad co-operative effort in support of a comprehensive development to establish generalized equations for temperature profiles and attendant thermal stress, leading to a broad collection of unitized programs which may be selected and assembled to suit the individual problem. It is hoped that the WRC-PVRC-Design Division, or another professional organization, will soon undertake this project, which deserves the support of the AEC, armed services, National Research Foundation, and industry and professional organizations.

D. B. Wesstrom[7]

It is interesting to note, in Table 1, that if the absolute values of stress at the inside and outside radii are averaged, the average for the theoretical results agrees with the average by the authors' method, for both the linear and logarithmic radial gradient cases. The discrepancies in the stress values may be due to the fact that the authors' method does not appear to take account of the variation in stress resulting from the thick-walled cylinder theory.

This suggests a possible method of making an approximate correction to the solution for an irregular shape. Considering a transverse slice (i.e., normal to the longitudinal axis) of incremental thickness as constituting a short cylinder, the stresses by the theoretical formula and the authors' method can be calculated as in Table 1, and their ratios then used as correction factors at the appropriate radii. The procedure is feasible only to the extent that the variation of temperature with radius can be likened to some mathematical curve, such as a linear or logarithmic gradient.

In considering this matter further, it is not apparent in the two examples for a short cylinder, why σ_r should be zero throughout the thickness of the cylinder. It would seem that a tensile tangential stress at the inside and a compressive one at the outside would require a tensile radial stress varying in some manner over the thickness of the cylinder, as is found to be the case in deriving the theoretical formulas.

Even so, the authors' formulas for σ_ϕ for the two cases seem reasonable, and in both instances show that $\sigma_\phi = E\alpha\,(T_{avg} - T)$. However, the theoretical solution for the case of a long cylinder shows that σ_ϕ is equal to this value divided by $(1 - \nu)$, and also that σ_x has the same value as σ_ϕ at the inside and outside surfaces. It is not readily apparent whether the authors' approach could be modified to include the case of the long cylinder, and if it were possible to do so, whether the result would verify the theoretical formula.

This poses the question as to whether the solution for an irregular shape is essentially one based on the assumption of a short cylinder ($\sigma_x = 0$) or whether it properly reflects the fact that the shape is very long or of some intermediate length, as the case may be. It is the writer's conclusion that the length effect is, in fact, taken into account by Equation (26).

In spite of the discrepancies noted, it is evident that the authors have contributed an excellent method of providing an order-of-magnitude estimate of the thermal stresses in a body of irregular shape, which possibly can be refined to yield more accurate results. The need for refinement, however, is open to question, since the end results also depend on the accuracy with which the temperature distribution has been evaluated. This, of course, is outside the intended scope of the paper.

A. B. Atchley and J. P. Houstrup[8]

The author's paper has been reviewed with considerable interest. Since thermal stresses are often a major factor in the design of pressure vessels, a practical and reliable technique for generally evaluating such stresses is sorely needed. The work of the authors toward this goal is a timely contribution.

As is indicated in the closing summary, this method of determining thermal stresses does not consider geometry flexibility. Unfortunately, the authors do not emphasize the seriousness of this limitation.

In Case 3, stresses, displacements, and rotations are determined on the basis that meridional cross sections do not distort. This assumption is generally held valid only for a certain class of bodies of revolution, namely, rings. Ideally, the ring is thin. The dimensions of its cross section are small compared with the radius.

An analogy is made in Case 2 which further restricts the application. It is assumed that the body of revolution with zero tangential strain may be replaced by a long prismatic body with zero axial strain. Zero tangential strain in a body of revolution precludes radial deformation. For the long prismatic body plane longitudinal strain does not limit transverse displacements to zero.

Thus the long prismatic body will experience transverse displacements dependent on the dimensions of the cross section and the temperature gradients, but since the axial strain is not influenced by these displacements, no account can be made for the tendency of the shell to bend locally.

The tangential stresses for Case 2 are therefore in error depending on the severity of the temperature distribution. The results shown in Table 1 reflect this tendency. Had the case chosen for comparison been that of a finite cylinder with a linear radial gradient, the calculated results would have shown significant error.

Displacements and rotations obtained from Case 3 should be used with caution in a statically indeterminate analysis. Since these deformations inherently assume no local bending, they may result in unduly conservative stress values.

Authors' Closure

The authors wish to thank the discussers for their constructive commentaries. They fully agree with Messrs. Rossheim's and Honigsberg's remarks.

Mr. Wesstrom's discussion leaves some questions to be answered. In Table 1 indeed the average (or sum) of the absolute values of the tangential stresses at inside and outside radii is the same for both methods. The discrepancies in the stress values are not due to the variation of stress from thick wall cylinder

[5] Assistant to Vice President, Charge of Engineering, The M. W. Kellogg Company, New York, N. Y. Fellow ASME.

[6] Design Engineer, The M. W. Kellogg Company, New York, N. Y. Mem. ASME.

[7] Mechanical Engineer, E. I. du Pont de Nemours & Company, Wilmington, Del. Mem. ASME.

[8] Applied Mechanics Section, Product Engineering Department, Combustion Engineering, Inc., Chattanooga, Tenn.

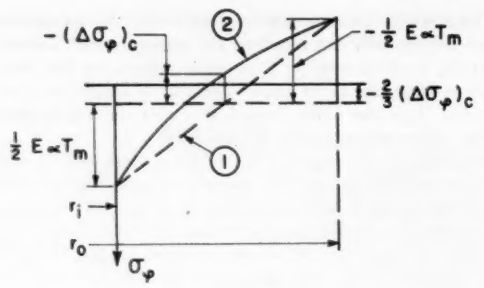

Fig. 9

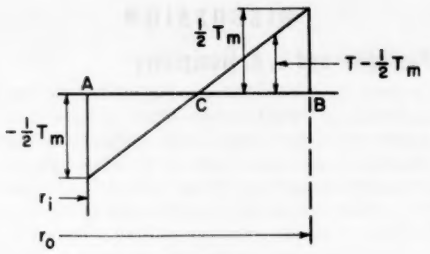

Fig. 10

theory, which neglects the radial expansion due to temperature and thus does not apply here. The reason for the discrepancies can best be explained by showing the way the calculation can be corrected to make it exact, as will be done for the case of a short ring with a linear radial temperature gradient. This then also deals with Mr. Wesstrom's suggestion of an approximate correction.

As pointed out below eq. (25), the authors intentionally assumed σ_{φ_1} to be independent of r. This will be correct if T does not vary in the radial direction, so that for a ring with constant temperature or linear longitudinal temperature gradient exact results were obtained. With a linear radial temperature gradient, however, this condition is not satisfied and therefore here discrepancies will occur. The stress

$$\sigma_\varphi = -E\alpha T + {}^1/_2 E\alpha T_m \tag{48}$$

computed in the paper is shown in Fig. 9 by the dashed lines, the horizontal dashed line being the reference line. As may be easily computed from reference [3] the exact extreme stresses are

$$\left.\begin{aligned}(\sigma_\varphi)_{r=r_i} &= {}^1/_2 E\alpha T_m \frac{2r_o + r_i}{r_o + r_i}\\ (\sigma_\varphi)_{r=r_o} &= -{}^1/_2 E\alpha T_m \frac{r_o + 2r_i}{r_o + r_i}\end{aligned}\right\} \tag{49}$$

These same stresses can also be found from a simple intuitive correction of eq. (48), which, although not taking all influences into account, leads to correct results. As will be explained in a subsequent paper in which the flexibility of the shape will be considered, the same method can be extended for correcting the stresses in an irregularly shaped flange, if judged necessary. Eq. (48) would be correct if everywhere $T = {}^1/_2 T_m$. Then indeed the radial displacement

$$v = {}^1/_2 \alpha T_m r \tag{50}$$

as computed under "Radial Displacement" in the paper, would occur everywhere. Hence, one may find a more correct stress distribution by taking into account the additional displacements arising from the difference between T and ${}^1/_2 T_m$, which is shown in Fig. 10. This excess temperature, which averages zero over the thickness, will not change the distance between the extreme points A and B in Fig. 10. If in these points v would remain given by eq. (50), point C would move over an additional distance

$$\Delta v = -{}^1/_4 \alpha T_m \frac{r_o - r_i}{2} = -{}^1/_8 \alpha T_m (r_o - r_i) \tag{51}$$

Considering intermediate points, since v will vary as the integral curve to the excess temperature, it would vary parabolically, being zero at A and B and given by eq. (51) in C. The excess stresses in C would be

$$(\Delta\sigma_\varphi)_C = E\frac{\Delta v}{r} = -\frac{E\alpha T_m (r_o - r_i)/8}{(r_o + r_i)/2} = -{}^1/_4 E\alpha T_m \frac{r_o - r_i}{r_o + r_i} \tag{52}$$

The extra stresses $\Delta\sigma_\varphi$ would vary as shown in Fig. 9 as the distance between the original dashed line 1 and the solid line 2. However, these extra stresses σ_φ would disturb the equilibrium of ring elements in the radial direction, that would be pushed outward, so that additional stresses σ_φ will be added to equilibrate the distribution between lines 1 and 2. Assuming the latter distribution to be parabolic, equilibrium is obtained by adding constant stresses with an equal and opposite resultant or $\Delta\sigma_\varphi = -{}^2/_3 (\Delta\sigma_\varphi)_C$, as obtained by moving the dashed reference line upward over that distance. The corrected stresses σ_φ are then given by the curve 2 with the solid horizontal axis as reference line, yielding

$$\left.\begin{aligned}(\sigma_\varphi)_{r=r_i} &= \left({}^1/_2 + {}^1/_6 \frac{r_o - r_i}{r_o + r_i}\right) E\alpha T_m\\ &= {}^1/_2 E\alpha T_m \frac{2r_o + r_i}{r_o + r_i}\\ (\sigma_\varphi)_{r=r_o} &= \left(-{}^1/_2 + {}^1/_6 \frac{r_o - r_i}{r_o + r_i}\right) E\alpha T_m\\ &= -{}^1/_2 E\alpha T_m \frac{r_o + 2r_i}{r_o + r_i}\end{aligned}\right\} \tag{53}$$

Comparison with eq. (49) shows that these corrected stresses are exact. Eq. (53) also shows that the difference between the extreme stresses σ_φ, or, as Mr. Wesstrom expresses it, the average of their absolute values, is not changed by the correction and thus is equal for the stresses from the proposed method to that from the exact stresses.

Mr. Wesstrom wonders why σ_r is found to be zero for the short cylinders. However, as mentioned under the caption "Final Stresses," below eq. (27), σ_r is not zero and can be calculated from the stresses σ_φ if one wants to, although this will be generally not essential. Considering the equilibrium in the radial direction of an element embracing an angle $d\varphi$, it follows that

$$\sigma_r = -\frac{1}{r}\int_r^{r_o} \sigma_\varphi dr \tag{54}$$

For the case of the short cylinder with linear radial temperature gradient this becomes

$$\sigma_r = E\alpha T_m \frac{(r - r_i)(r_o - r)}{2(r_o - r_i)r} \tag{55}$$

so that at $r = {}^1/_2(r_o + r_i)$

$$\sigma_r = {}^1/_4 E\alpha T_m \frac{r_o - r_i}{r_o + r_i} \tag{56}$$

It may be noted that this is just the opposite of $\Delta\sigma_\varphi$ from eq. (52).

As to Mr. Wesstrom's next remarks it was stated at the end of the summary that the case of a finite or long cylinder would be considered next. It will be dealt with in another paper. In the present one the shapes are considered to be short. For a long cylinder σ_φ will indeed be divided by $(1 - \nu)$ due to the condition that the curvature in the longitudinal direction must be zero. Eq. (26) computes the stresses due to longitudinal bending moments, but still considers the shape to be short.

The authors agree with Mr. Wesstrom that in many cases there will be no need for refining the original method. However, an extension to long shapes is necessary and will be published shortly.

Finally, it may be explained why in the flange in Fig. 8 the isostress lines and isothermal lines intersect at equal angles. If no rotation would occur in Case 3 a stress of about $\sigma_{\varphi_3} = E\alpha T_{avg}$ would be superimposed, so that σ_φ would be about zero where T would be equal to T_{avg}. Also, isostress lines for this combination would about coincide with isothermal lines. The relative rotation of these lines is due to the rotation in Case 3. For the flange in Fig. 8, due to the rather high temperature in the upper left corner, causing high compressive stresses $\sigma_{\varphi_1} + \sigma_{\varphi_2}$, a counter-clockwise couple will be applied to the flange in Case 3, which will cause extra stresses σ_{φ_3} that vary linearly in the longitudinal direction. Superposition of these stresses will cause all isostress lines, that originally coincided with isothermal lines, to rotate counter-clockwise over equal angles with respect to their original position, that is, with respect to the isothermal lines.

As to Messrs. Atchley and Houstrup's remarks on not considering geometry flexibility, it was already mentioned in the summary of the paper and in our answer to Mr. Wesstrom that finite and long cylinders will be considered in another paper, which is now ready for publication, and that the present paper is meant for relatively short shapes. Also, it was mentioned in the paper that an exact but more laborious method was developed. Therefore, in the examples of the linear and logarithmic radial temperature gradients, the theoretical solutions for short cylinders were used for comparison. It is well known that neglect of geometry flexibility is allowable for short cylinders and that inaccuracies will increase if one surpasses the limiting value for a short cylinder or a short beam on elastic foundation which can be assumed[9] as $\lambda l = \pi/4$.

However, the inaccuracies in the present method remain rather insignificant if one does not exceed the limiting value too far. The theoretical stresses for a cylinder with a linear radial temperature gradient and with $\lambda l = \pi/4$, can be found from those of a long cylinder[10] by removing the axial stresses, σ_x, and adding the resulting stresses to those in the long cylinder. For the case considered in the paper, with a temperature varying from zero at the inside to 100 deg F at the outside radius, this results in tangential stresses at the inside radius of 11,215 psi in the middle and 9826 psi at the ends of the cylinder, to be compared with stresses of 10,500 psi from Table 1 according to the present method. At the outside radius the theoretical tangential stresses are -9885 psi in the middle and $-11{,}174$ psi at the ends of the cylinder, against $-10{,}500$ psi from the present method. Hence, the maximum difference from all causes, including neglect of flexibility, is only ± 6 per cent.

From the discussion of Case 2, it appears that Messrs. Atchley and Houstrup have not understood this point. The tangential strain was kept equal to zero only to prohibit radial movement and tilting of the ring as a whole. These movements then are taken care of in Case 3. But radial strains in the cross section itself are not meant to be prevented, and they are indeed free to occur in the case of plain strain in the long prismatic body. The influence of these radial strains on the distribution of the tangential stresses is taken into account in Case 3 by assuming their distribution according to Equation (25), as justified in the paper. As was further explained in the answer to Mr. Wesstrom, the essential approximation in Equation (25), except for neglect of geometry flexibility, as dealt with above, is the assumption of a constant temperature in the radial direction, which causes the small discrepancies shown in Table 1, that can, if so desired, be corrected (Fig. 9). Hence, although in case of mechanical loading Equation (25) applies for thin rings and cross-sectional dimensions that are small as compared with the radius, its use in the present case for larger cross sections is fully warranted.

The last remarks of these discussers must be due to a lack of familiarity with the theory of shells. If one assumes a cylindrical shell or a beam on elastic foundation to be short, as was done in the paper, one does not assume that it does not deflect or bend, but one assumes, for good reason, that its deflection does not affect the reactions from the elastic foundation, created, in the case of a shell, by the hoop stresses. Hence, one assumes that these reactions are the same as when the longitudinal strips of the shell would remain straight.

For example, the actual deflections and end rotations of the short cylinder with radial temperature gradient can be computed from the difference between the longitudinal strains at the inside and outside radii, which, from the equation for these strains given in the paper, are $-{}^1/_2\,\nu\alpha T_m$ and $(1 + {}^1/_2\,\nu)\alpha T_m$, respectively. Also, for longitudinal moments $M_x = M_0$ acting at the ends of the cylinder, the assumption of a short cylinder, with length l, entails zero restrains from the elastic foundation (hoop stresses), so that the end rotations are

$$\theta = \frac{M_0 l}{2D} \tag{57}$$

where D is the flexural rigidity of the cylinder wall. The exact end rotations are[9]

$$\theta = \frac{4M_0\lambda^3}{k}\,\frac{\cosh \lambda l - \cos \lambda l}{\sinh \lambda l + \sin \lambda l} \tag{58}$$

But for $\lambda l = \pi/4$, at the transition between a short and a finite cylinder, the difference in rotation between Equations (57) and (58) is about ${}^1/_2$ per cent. Therefore, by considering the cylinder as short, the end rotations are not zero, as implied by the discussers, but larger than the theoretical ones, although by ${}^1/_2$ per cent only.

The authors may close in thanking again all discussers for their interest in the paper.

[9] Hetenyi, "Beams on Elastic Foundation," University of Michigan Press, 1958.

[10] Timoshenko and Goodier, op. cit., p. 412.

A Study of Shear-Spinnability of Metals

SEROPE KALPAKCIOGLU
Research Supervisor, The Cincinnati Milling Machine Company, Cincinnati, Ohio

The deformation zone in shear-spinning is idealized for a two-dimensional process and maximum permissible thickness reduction without fracture is predicted in terms of the stress system in this zone. The effect of deviation from the sine law on the maximum reduction before fracture is shown analytically to be due to the influence of distortions of the unspun flange on the state of stress under the roller. The results of analytical work are compared with experimental data and good agreement has been obtained. The phenomenon of back extrusion in shear-spinning is shown to be the result of a compressive stress in the spun section parallel to the mandrel side and is greatly influenced by mandrel angle and deviation from the sine law.

Introduction

THE PROBLEM of fracture during forming operations is an important subject in the metalworking industry. In any operation it is desirable to predict beforehand whether a given workpiece of given dimensions and properties will withstand the strains and stresses imposed upon it without fracturing. Many attempts have been made to establish formability tests to predict the behavior of materials in various forming operations. However, due to the great variety of shapes and many variables involved, all these tests have certain limitations. A comprehensive treatment of this problem in sheet metalworking is given by Sachs [1].[1] In the relatively new process of shear-spinning the desirability of predicting whether a material of given properties would undergo a certain reduction in thickness without fracturing became obvious since there had been considerable waste in development work by trial-and-error methods. The only spinnability test known to this author is the one described by Kegg [2], the principle of which is shown in Fig. 1.

The setup consists of a half-ellipsoid mandrel 8 in. diam and an included cone angle α which varies from 180 deg at the beginning of the spinning operation to 0 deg at the end. Thus, when a flat blank is shear-spun on this mandrel according to the sine law,

$$t_c = t \cdot \sin \alpha/2 \qquad (1)$$

the thickness of the spun part will vary gradually from its maximum, i.e., original value, to zero. Naturally, all materials will fracture somewhere between these two limits. Spinnability is defined as the maximum per cent reduction in thickness a material undergoes before fracture. Thus,

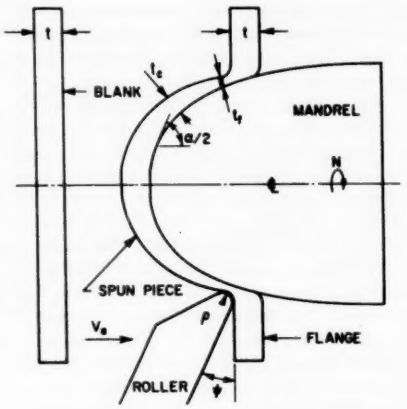

Fig. 1 Sketch of setup for spinnability test

$$\text{Spinning reduction} = \frac{t - t_f}{t} \cdot 100 \qquad (2)$$

The details of the test are given in reference [2]. Various materials were tested in this manner, Table 1, and the value from equation (2) for each material was compared to the mechanical properties of the material. It was observed that the best and most consistent correlation obtained was with the tensile reduction of area of the material. This relationship is shown in Fig. 2. Thus, by knowing the tensile reduction of a material, its maximum spinning reduction may be predicted.

The present paper deals with an analytical study of the problem to explain the experimental results obtained in these spinnability tests, including also the problem of back extrusion in shear-spinning.

[1] Numbers in brackets designate References at end of paper.

Contributed by the Metal Processing Research Activity of the Production Engineering Division and presented at the Winter Annual Meeting, New York, N. Y., November 27–December 2, 1960, of THE AMERICAN SOCIETY OF MECHANICAL ENGINEERS. Manuscript received at ASME Headquarters, July 26, 1960. Paper No. 60—WA-187.

Nomenclature

a = inner radius of flange, in.
b = outer radius of flange, in.
k = ratio: b/a
N = mandrel rpm
t = blank thickness, in.
t_c = finished cone thickness, in.
t_f = thickness at fracture, in.
u_a = radial expansion of flange bore due to over-reduction, in.
V_a = axial velocity of roller, in/min
$\alpha/2$ = mandrel half angle, deg
ψ = angle between planes of roller and flange, deg
ρ = roller corner radius, in.
μ = coefficient of friction between workpiece and mandrel
γ = shear strain
γ_s = shear strain in spinning
$\bar{\epsilon}$ = true strain at fracture in tension test
ϵ_θ = tangential strain at flange bore
Δ = deviation from sine thickness (1 = 100 per cent deviation)
τ_0 = shear yield stress of material, lb/in.^{2}
σ_0 = tensile yield stress of material, lb/in.^{2}
σ_n = normal stress on shear plane, lb/in.^{2}
σ_r = normal stress on shear plane due to Δ, lb/in.^{2}
σ_c = stress in spun cone section, lb/in.^{2}
σ_m = stress on mandrel face, lb/in.^{2}

Table 1 Material properties versus spinnability test results

Material	BHN	Tensile, per cent R	True strain, $\bar{\epsilon}$	Spinning, per cent R	Minimum $\alpha/2$, deg-min	γ_s
1100-0	20	83.7	1.83	85	8-30	6.7
15-7 PH steel	143	50	0.69	82	10-24	5.4
1100 H-14	35	66.5	1.10	80	11-30	4.9
Copper, annealed	38	68.1	1.14	80	11-30	4.9
6061-0	33	62.9	1.0	80	11-30	4.9
304 stainless steel	133	71	1.24	78	12-24	4.5
17-7 stainless steel	143	38	0.48	78	12-24	4.5
6061-T4	58	42.2	0.55	76	13-30	4.2
1020	89	71.3	1.25	75	14-30	3.9
Copper, cold rolled	81	56.4	0.83	73	15-40	3.6
4130	130	62.3	0.97	71	16-50	3.3
6061-T6	93	39.5	0.50	71	16-50	3.3
2024-0	58	30.3	0.36	70	17-30	3.2
Lapelloy "C"	262	29.5	0.35	62	20-50	2.6
2024-T3	107	22	0.25	57	23-20	2.3
2024-T36	124	17.3	0.19	14	59-00	0.6
C iron, gray	114	0	0	0	90-00	0

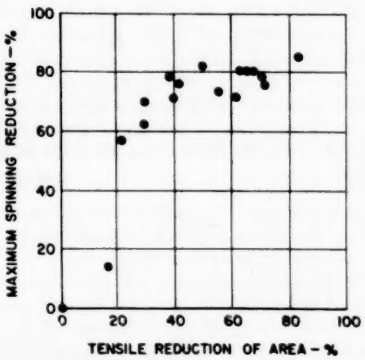

Fig. 2 Relationship between maximum spinning reduction and tensile reduction of area of material spun

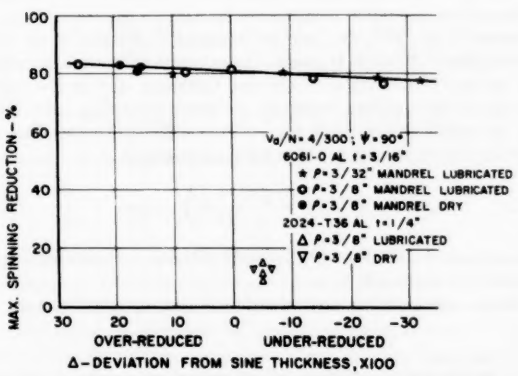
MAX. SPINNING REDUCTION - %
Va/N = 4/300; ψ = 90°
6061-0 AL t = 3/16"
ρ = 3/32" MANDREL LUBRICATED
ρ = 3/8" MANDREL LUBRICATED
ρ = 3/8" MANDREL DRY
2024-T36 AL t = 1/4"
ρ = 3/8" LUBRICATED
ρ = 3/8" DRY
OVER-REDUCED
UNDER-REDUCED
Δ - DEVIATION FROM SINE THICKNESS, X100

Fig. 3 Effect of ρ, μ, and deviation from sine-law thickness on spinnability for two materials

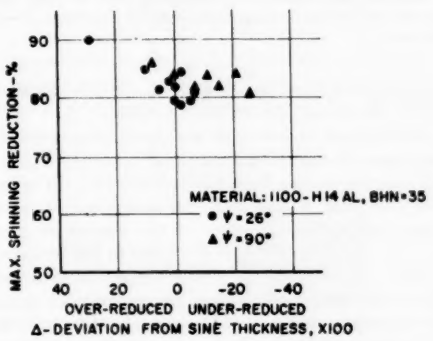

Fig. 4 Effect of ψ on spinnability

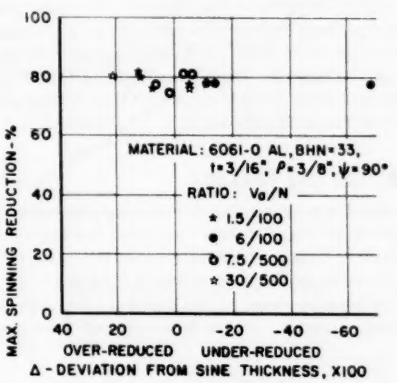

Fig. 5 Effect of V_a/N on spinnability

Experimental Observations

The results reported by Kegg were based on tests conducted with the following variables: $t = 1/4$ in., $V_a = 3 - 20$ in/min, $\rho = 1/4$ in., $N = 200 - 500$ rpm, $\psi = 26$ deg.

No change in spinnability was observed by variations in V_a and N. It was also observed that spinnability increased as the part was over-reduced and decreased when under-reduced, the terminology for deviation from sine-law spinning being

Sine reduction: $t_c = t \cdot \sin \alpha/2$

Over-reduction: $t_c < t \cdot \sin \alpha/2$ (3)

Under-reduction: $t_c > t \cdot \sin \alpha/2$ (4)

For the purposes of the present study it was decided first to obtain quantitative data on the influence on spinnability of ρ, ψ, V_a, N, and also the lubricant between workpiece and mandrel. Tests were conducted with three alloys of aluminum with no coolant and one roller. The experimental results obtained are shown in Figs. 3 to 5. The conclusion to be drawn from these

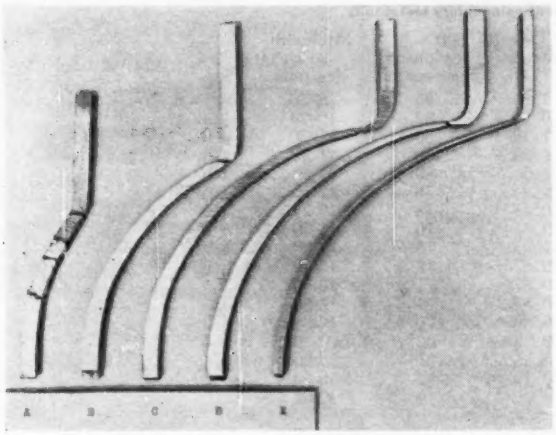

Fig. 6 Fractured specimens from spinnability test: A—gray cast iron, B—2024-T36 aluminum, C—copper, D—6061-0 aluminum, E—17-7 PH stainless steel

tests is that none of these variables appears to have any significant influence on the spinnability of these materials.

The next step was to take cross sections of some of the ellipsoid spun parts and to observe the nature of fracture. Fig. 6 shows five such samples ranging from brittle to ductile. It is observed that both cast iron, A, and 2024-T36 aluminum, B, have fractured essentially in the direction of the motion of concentric cylinders sliding over each other as shown in the idealized case, Fig. 7, and as discussed in the author's paper on shear-spinning [3], while at the same time fulfilling the requirement of equation (1). In contrast to this type of fracture, the three materials (C, D, and E) to the right in Fig. 6 have fractured in a manner which could be described as tensile failure behind the roller after the completion of reduction. A close look at the broken ends of the fracture region shows that the elements are quite similar to a tensile test specimen and that the angle between the mandrel side, i.e., direction of tensile force on the spun section and the plane of fracture, is of about the same magnitude as that in a uniaxial tensile test specimen, and are all greater than 45 deg as measured on numerous fractured spun parts.

Deviation From Sine Thickness

As described in reference [3], the spinning process may be idealized as shown in Fig. 7, where concentric cylinders are sheared over each other axially, forming a cone, the axial thickness of which is the same as the original blank thickness. If, however, the roller is brought closer to the mandrel such that the part is over-reduced, equation (3), the following will take place: The spun section, i.e., the cone, will have a volume which is less than that dictated by the geometry of the process. Ignoring elastic recoveries, the problem will be analyzed as shown in Fig. 8. The solid outline on the mandrel represents sine-law spinning while the dotted outline is the over-reduced case. It is seen that, in order to keep the plastically deformed volume of the cone constant, the original shear plane (sine law) which was at a distance a from the center line of the mandrel will now be at a distance $a + u_a$. The relationship between a, u_a, and deviation from sine thickness is obtained as follows: Equating the two cone volumes, one has

$$\pi a^2 t = \pi(a + u_a)^2 t' \tag{5}$$

where the prime designates the over-reduced cone.

Deviation from sine thickness is defined as

$$\Delta = \frac{t_c - t_c'}{t_c} = \frac{t - t'}{t} = 1 - \frac{t'}{t} \tag{6}$$

Thus

$$\Delta = 1 - \left(\frac{a}{a + u_a}\right)^2 \tag{7}$$

$$= \frac{2au_a + u_a^2}{a^2 + 2au_a + u_a^2}$$

For small values of u , one has $a \gg u_a$, hence the foregoing equation reduces to

$$\Delta = \frac{2u_a}{a} \tag{8}$$

or

$$\frac{u_a}{a} = \frac{\Delta}{2} = \epsilon_\theta \tag{9}$$

The value of u_a is thus determined.

Neglecting the change of length of the shear plane due to over-reduction, one sees that the flange which is now a disk with b as its outer radius has its inner radius expanded from a to $(a + u_a)$. This will induce radial compressive stresses on the inner circumference of the disk, i.e., normal compressive stresses σ_r on the shear plane. While it is possible to calculate this stress in terms of the per cent deviation from sine thickness, due to the complexity of the problem, especially for strain-hardening materials, no derivation will be made here. It is sufficient to note that if the bore flows plastically the stress relationship is

$$\sigma_r = \tau_0 \left(\frac{k^2 - 1}{k^2}\right) \tag{10}$$

as derived by Hill [4] with Tresca's criterion. Hence for large values of k one has $\sigma_r = \tau_0$.

Some comments are now in order concerning the influence of

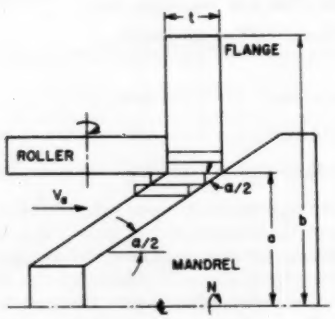

Fig. 7 Idealized shear-spinning process

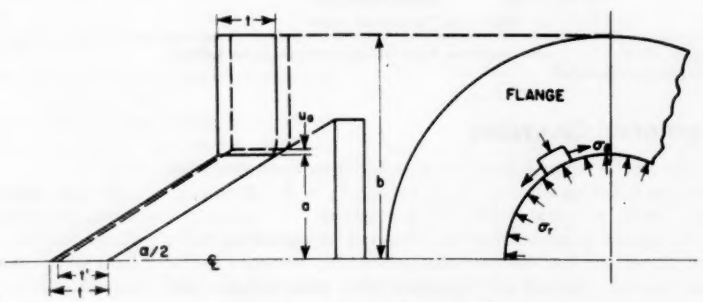

Fig. 8 Over-reduction in shear-spinning

such a deviation from sine thickness and the existence of radial compressive stresses, on the inner circumference of the flange, on the spinning operation as observed experimentally.

The existence of such stresses at the bore will mean expansion of the inner diameter of the flange. However, considering the fact that, in the majority of spinning operations the ratio of blank diameter ($2b$) to blank thickness t is quite large, it can be stated that under such radial stresses at its bore, the flange will be somewhat unstable and will have the tendency to either bend forward, i.e., to the right in Fig. 7, or backward. In practice it is observed that up to a thickness of about $^1/_2$ in. the flange remains essentially straight when the part is spun to the sine thickness, whereas if it is over-reduced, the flange starts bending, the direction of this bend depending on the roller geometry and also on the magnitude of the roller corner radius ρ. The roles, if any, of feed and mandrel rpm on this bending are not clearly established yet. In the case where the part is under-reduced, the flange always bends forward; the analogy here for excessive cases of under-reduction being similar to a deep-drawing operation with no blank holder, with the roller acting as the draw ring and the spinning mandrel as the male die. In such a drawing operation, the flange would start lifting itself as the drawing progressed and if the part is thin enough it would eventually wrinkle. In shear-spinning, if a thin blank is spun with severe under-reduction, the same type of wrinkling is observed.

The Stress System

The stresses in the plastic zone in shear-spinning will now be analyzed on a two-dimensional scale as shown in Fig. 9 (compare Fig. 6 and 9). Ideally, horizontal elements parallel to ab and cd are sheared over each other, conforming to the roller geometry, and the process is completed at the intersection of line cd and except for elasticity considerations, neglected in this study, no further deformation takes place below cd. The roller has a contact surface from a to c and follows the mandrel at a constant setting of $ce = t \cdot \sin \alpha/2$. Assuming the stresses on the shear plane cd as a normal stress σ_n and a shear stress τ_0 and balancing the forces along the mandrel side one obtains

$$\sigma_c \sin \alpha/2 = \tau_0 \cos \alpha/2 - \sigma_n \sin \alpha/2 - \mu\tau_0 \sin \alpha/2 - \mu\sigma_n \cos \alpha/2$$

Hence

$$\sigma_c = \tau_0 (\cot \alpha/2 - \mu) - \sigma_n (1 + \mu \cot \alpha/2) \qquad (11)$$

Equation (11) becomes dimensionless in the form of

$$\frac{\sigma_c}{\tau_0} = (\cot \alpha/2 - \mu) - \frac{\sigma_n}{\tau_0} (1 + \mu \cot \alpha/2) \qquad (12)$$

The plot of this equation is given in Fig. 10 with μ and σ_n/τ_0 as parameters. Of great importance here is the stress σ_c which gives an indication as to how small the mandrel angle $\alpha/2$ can become before σ_c increases sufficiently to cause fracture of the spun section in tension. It is to be noted that, for the same $\alpha/2$, the larger the values of μ and σ_n, the lower the stress σ_c is, assuming of course that τ_0 is independent of σ_n which is commonly accepted in plasticity. It is important to remember that in reality σ_n is not a constant and that it will be a function of $\alpha/2$ and, quite possibly, of ρ and t. At $\alpha/2 = 90$ deg, $\sigma_n = 0$, Fig. 9, but as $\alpha/2$ decreases σ_n will acquire increasingly higher values. Hence the actual σ_c/τ_0 curves in Fig. 10 will probably start at zero at $\alpha/2 = 90$ deg, acquire a negative value (compressive) and then a positive value (tensile) as $\alpha/2$ decreases and approaches zero.

Equation (12) predicts the maximum reduction in spinning, that is, the minimum mandrel angle $\alpha/2$ a material will spin from a flat blank before fracture. The relationship between this angle and reduction is

$$\text{Spinning reduction} = \frac{t - t_c}{t} = 1 - \sin \alpha/2 \qquad (13)$$

It is first necessary to estimate the magnitude of σ_n. In the case of orthogonal metal cutting this normal stress on the shear plane is calculated from experimental data. It has been observed that, depending on cutting conditions, this ratio may be as high as 2. In shear-spinning this ratio is virtually impossible to calculate because of the complex geometry of the system. The influence of different values of σ_n/τ_0 on σ_c is shown in Fig. 10. The existence of high normal stresses on the shear plane may be visualized not only from Fig. 9, but also from the observation that the material has undergone considerably higher shear strain than expected from ordinary mechanical tests. This is observed from Fig. 11 which is a plot of the maximum shear strain in spinning versus the shear strain in tension test using the relationships

$$\gamma_s = \cot \alpha/2 \qquad (14)$$

and from the distortion-energy theory

$$\gamma = \sqrt{3}\,\epsilon \qquad (15)$$

It is thus reasonable to assume that there are considerable compressive stresses on the shear plane since the beneficial role of such stresses on a shear plane in increasing the shear strain to frac-

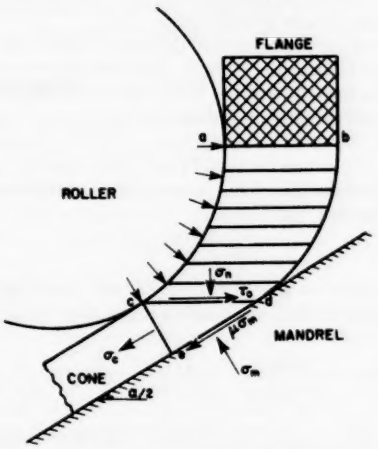

Fig. 9 Zone of deformation in shear-spinning (compare with Fig. 6)

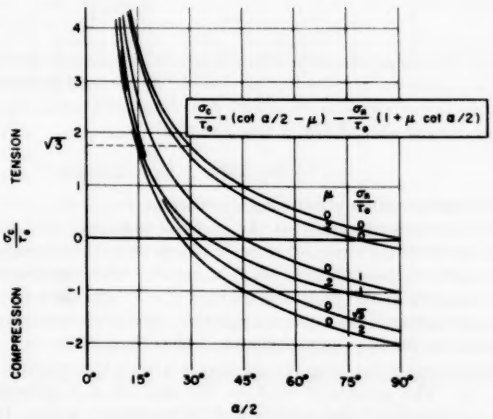

Fig. 10 Relationship of stresses as a function of mandrel angle

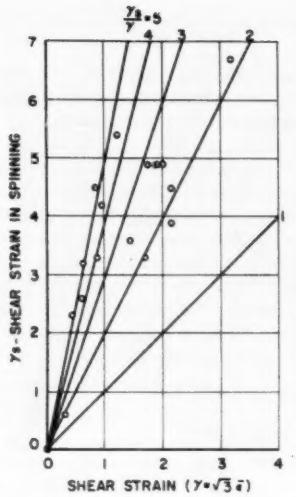

Fig. 11 Relationship between shear strains in spinning and tension test (Table 1)

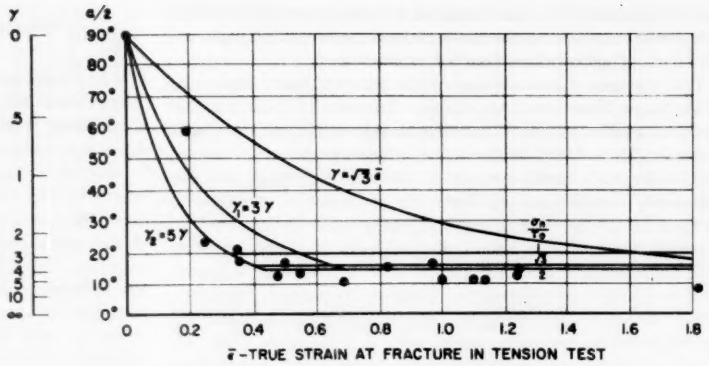

Fig. 13 Correlation between theory and experiment in spinnability

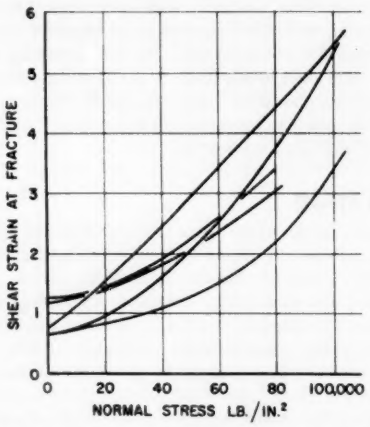

Fig. 12 Effect of normal stress on shear strain at fracture in torsion for various steels (from Bridgman data)

ture is well known [5] (see also Fig. 12). A similar observation has also been made in metal cutting.

Failure of a part being spun in the manner of fracture as shown in specimens C, D, and E in Fig. 6, is predicted from equation (12) by assuming that the stress σ_c behind the roller (Fig. 9) is similar to a simple tensile stress and that when

$$\sigma_c = \sigma_0 \tag{16}$$

failure will take place. Thus, according to the distortion-energy theory, if one lets

$$\sigma_0 = \sqrt{3}\,\tau_0 \tag{17}$$

it is seen that when $\mu = 0$ and for different values of σ_n/τ_0, the minimum mandrel half angle $\alpha/2$ that one may be able to spin is

$$\alpha/2 = \cot^{-1}\left(\frac{\sigma_c}{\tau_0} + \frac{\sigma_n}{\tau_0}\right) \tag{18}$$

Hence

σ_n/τ_0	σ_c/τ_0	$\alpha/2$, deg	Thickness reduction, per cent
1	$\sqrt{3}$	20	66
$\sqrt{3}$	$\sqrt{3}$	16	73
2	$\sqrt{3}$	15	74

The foregoing reductions compare with 63 per cent in frictionless wire-drawing or extruding of rods and 58 per cent in drawing or extruding of strips as obtained by Hoffman and Sachs [6]. If the maximum-shear-stress theory is used where

$$\sigma_0 = 2\tau_0 \tag{19}$$

the foregoing results will be slightly different.

This analysis assumes that the material was capable of withstanding the shear strain on its shear planes without fracturing in the manner of specimens A and B in Fig. 6. While the tension-type fracture in the foregoing analysis is not influenced by the material properties as seen from equation (18), in the brittle-type fracture the ductility of the material will be important.

A synthesis of the foregoing arguments is made and presented in Fig. 13. The agreement between the analysis just presented and experimental results appears to be reasonably good. It is observed that the horizontal theoretical lines in the plot are somewhat higher than the experimental points. Part of this could be due to the fact that, even though care was taken to measure t_f correctly (Fig. 1), necking has already taken place when failure occurs; thus the measured values of t_f are quite possibly less than the actual ones. This is reasonable to expect since in fractured ductile tensile-test specimens it is observed that the specimens have gotten considerably thinner even an inch or so from the fractured end. Therefore, if the values of t_f were corrected it would mean that the parts withstood less reduction in spinning and hence fractured at higher values of $\alpha/2$ and should be plotted in Fig. 13 accordingly.

It is also interesting to observe that:

1 A transition appears to take place at a strain of about $\bar{\epsilon} = 0.5$ which corresponds to a tensile reduction in area of around 40 per cent.

2 Above a strain of 0.5, further increase in ductility does not influence the maximum reduction appreciably.

3 Below this strain the maximum spinning reduction will depend on the ductility of the material.

4 The best agreement with experimental data is obtained when $\sigma_c/\tau_0 = \sigma_n/\tau_0 = \sigma_0/\tau_0 = 2$ where $\alpha/2$ becomes 14 deg (not shown in Fig. 13).

Before concluding this discussion, it is important to remember the difference between the behavior of an ideal material and actual materials. In the ideal case, when the stress reaches a certain value, the material yields and keeps elongating under the

same load, whereas in actual strain-hardening materials the stress has to keep increasing if further elongation past the yield point is desired. This has to take place until necking starts, after which the system is in a state of instability and eventually fracture takes place.

In the present study only the ideal case has been analyzed. If the problems of strain-hardening and necking had been included the analysis would have become more complex. However, it is reasonable to expect that the final result may not be influenced much in view of the fact that, in the actual case, while the effective value of τ in the shear plane cd in Fig. 9 will be greater than τ_0 (depending on $\alpha/2$ and the strain-hardening coefficient) the normal stress σ_e required to cause failure of the spun section by necking will be greater than σ_0 for the same reason. If the increases in these stresses are proportionate then their net influence in the foregoing stress analysis may well be rather small. The reasonable agreement between theory for an ideal material and experimental results with ordinary strain-hardening materials in Fig. 13 appears to support this hypothesis.

Effect of Over-Reduction

The influence of over-reduction on such a stress system can now easily be seen from Fig. 10. When an additional normal stress of σ_r due to over-reduction is exerted on the shear plane, the value of σ_n in Fig. 10 will become $\sigma_n + \sigma_r$. Assuming failure to take place when σ_e/τ_0 = constant, then the influence of increasing σ_n to $\sigma_n + \sigma_r$ will mean that this constant is reached at a lower mandrel half angle $\alpha/2$, hence an increase in maximum spinning reduction, as clearly observed in Figs. 3 to 5. The reverse apparently takes place when a material is under-reduced making σ_r a tensile stress and hence decreasing the maximum reduction. Fig. 10 also indicates that at high values of $\alpha/2$ the stress σ_e is actually compressive while at low $\alpha/2$ it is tensile, and that even with high values of σ_n, including compressive σ_r due to over-reduction, σ_e is tension at low values of $\alpha/2$, but becomes compressive as $\alpha/2$ increases. (This argument does not of course hold true at $\alpha/2$ = 90 deg.) In connection with this observation a test was made where two flat blanks of low-carbon sheet steel were spun on two mandrels, $\alpha/2$ = 21 deg and 45 deg, both over-reduced the same amount, 20 per cent on their sine thickness, respectively, keeping all other conditions the same. The result is shown in Fig. 14. The one on $\alpha/2$ = 21 deg spun well with no back extrusion while the other back-extruded severely, a direct indication of the high compressive stress σ_e. This type of over-reduction is actually practiced in industry to manufacture cones of small included angle since, as seen from Fig. 14, if the tailstock on the $\alpha/2$ = 45 deg mandrel had been taken away, the spun cone section would move toward the left as spinning progressed, resulting in a cone the included angle of which would of course be less than 90 deg. Similar tests have been made with different materials and mandrels with the same consistent result. Similar cases are also observed in practice, the conclusion being that the tendency to back-extrude, because of over-reducing a part being spun, increases as the mandrel angle increases. The foregoing phenomenon is also put to practice in the manufacture of curvilinear shapes by varying the amount of per cent over-reduction on the parts.

Conclusions

1 The roller corner radius, roller swivel, roller velocity, and mandrel rpm do not appear to influence the shear-spinnability of metals.

2 For a given material variation from sine-law thickness appears to be the major factor influencing spinnability.

3 A transition takes place in the type of fracture of spun parts such that for metals with a true fracture strain of 0.5 or greater in a tension test, there is a maximum spinning reduction and that further increase in the ductility of the original material does not increase this maximum reduction appreciably.

4 For metals having a true fracture strain below 0.5, their spinnability depends on their ductility.

5 It has been shown both experimentally and analytically that the minimum angle to which a metal may be shear-spun from a flat blank is about $\alpha/2$ = 15 deg.

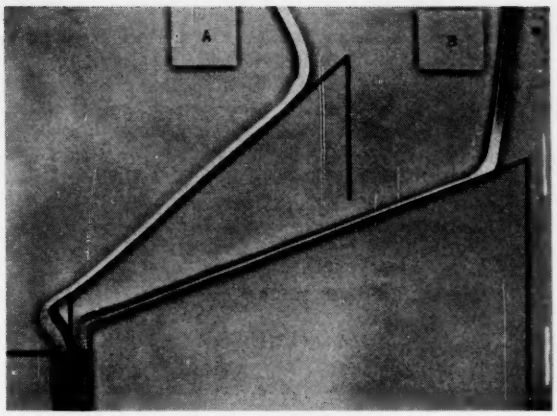

Fig. 14 Influence of over-reduction on back extrusion as a function of mandrel angle. A: $\alpha/2$ = 45 deg, B: $\alpha/2$ = 21 deg.

Acknowledgments

For their interest and comments concerning this work the author wishes to express his sincere thanks to Dr. M. Eugene Merchant, Director of Physical Research, and to Mr. Richard L. Kegg, Senior Research Engineer. The assistance of Messrs. Carl W. Kaesemeyer and Edwin W. Lederle in the experimental phase of this work is deeply appreciated.

References

1 G. Sachs, "Principles and Methods of Sheet-Metal Fabricating," Reinhold Publishing Corporation, New York, N. Y., 1951, chapters 1, 2, 4.

2 R. L. Kegg, "A New Test Method for Determination of Spinnability of Metals," TRANS. ASME, Series B, JOURNAL OF ENGINEERING FOR INDUSTRY, vol. 83, 1961, pp. 119–124.

3 Serope Kalpakcioglu, "On the Mechanics of Shear Spinning," TRANS. ASME, Series B, JOURNAL OF ENGINEERING FOR INDUSTRY, vol. 83, 1961, pp. 125–130.

4 R. Hill, "Plasticity," Oxford University Press, London, England, 1950, p. 109.

5 P. W. Bridgman, "Large Plastic Flow and Fracture," McGraw-Hill Book Company, Inc., New York, N. Y., 1952.

6 O. Hoffman and G. Sachs, "Introduction to the Theory of Plasticity for Engineers," McGraw-Hill Book Company, Inc., New York, N. Y., 1953, pp. 167–173.

DISCUSSION

E. G. Thomsen[2] and S. Kobayashi[3]

The author is to be congratulated for another excellent paper on shear spinning. Analyses like the present one are bound to increase our understanding of the mechanics of such complicated processes as shear spinning and there is no doubt that these technological advances will be of immeasurable aid to industry.

The author in his comparison of shear spinning fracture data with tensile fracture data in Fig. 2 re-emphasizes the known fact

[2] Professor of Metal Processing, University of California, Berkeley, Calif. Mem. ASME.

[3] Lecturer in Industrial Engineering, University of California, Berkeley, Calif.

that forming processes carried out under compressive loading generally result in larger strains before fracture ensues. The additional benefits obtainable with compressive forces are also illustrated in Figs. 3, 4, and 5, but the effects are less spectacular. It should be remarked that the effective strains achieved in shear spinning are in reality much larger than those calculable from equation (14) of the text which the author correctly classifies as the ideal case. This was shown by Kobayashi, Hall, and Thomsen[4] recently and consequently the true ratio of fracture strain in shear spinning to that in tension actually would be much greater than indicated by the ideal case.

The author mentions that a complete analysis should include necking, but that the analysis would become very complex. This admittedly is true and the condition for necking, which in reality is the criterion for fracture in tension, apparently cannot be included at present because of the complex state of stress under the roller. An analysis of necking, however, eventually must be made, since a theoretical analysis would show that necking will not take place under pure shearing and compression loading and consequently the condition leading to fracture in shear spinning under the absence of over or under-straining may throw light on the criterion for fracture of ductile metals when necking is absent. Thus, shear spinning may become an important property test just as metal cutting now has assumed such a role.

In spite of the fact, however, that necking cannot be determined precisely, it is possible to explain, at least qualitatively, the larger strains which may be achieved where over-reduction occurs. A theoretical analysis of necking for a thin-walled tube under biaxial stresses would show that necking will occur, when

$$\bar{\epsilon} = \frac{2}{3} m \sqrt{\alpha^2 - \alpha + 1}$$

where m is the slope of a true stress–true strain curve on log-log co-ordinates, $\alpha = \sigma_z/\sigma_\theta$, and σ_θ is an assumed tensile hoop stress in the cylinder. Assuming further that the cone of a ductile metal near the fracture condition in shear spinning approaches the shape of that of a cylinder, then for an assumed state of stress $\sigma_z/\sigma_\theta = -1/2$ (over-reduction) and $\sigma_z/\sigma_\theta = +1/2$ (under-reduction) the maximum strains at necking would be 0.87 m and 0.57 m, respectively. Consequently, necking for over-reduction results in larger strains at necking which agrees with the observations reported by the author.

In addition, two minor points should be made to clarify the paper: the strain ϵ_θ of equation (9) should be written as a logarithmic strain, since it is a finite strain; the analysis illustrated by Fig. 9 is that of over-reducing or else the direction of the force $\mu\sigma_m$ would be in the opposite direction; a statement to this effect would clarify the analysis.

Author's Closure

The comments of Drs. Thomsen and Kobayashi are greatly appreciated. The analysis for necking presented by the writers in this fine discussion is interesting, particularly in view of the fact that it agrees with the observations made by the author.

The following clarification is made concerning the direction of the friction force in Fig. 9. In an actual case of shear spinning the spun cone section is not infinitely rigid. This means that every time the roller comes to the position shown in Fig. 9 the component of the roller force parallel to the cone side will stretch the spun section thus moving the region *cde* up the mandrel. Hence the friction force should be in the direction shown in the figure, since it is at this stage that the stress system presented in Fig. 9 is of importance to the analysis.

[4] S. Kobayashi, I. K. Hall, and E. G. Thomsen, "A Theory of Shear Spinning of Cones," published in this issue, pp. 485–495.

S. KOBAYASHI[2]
I. K. HALL[3]
E. G. THOMSEN[4]

A Theory of Shear Spinning of Cones[1]

The theoretical deformation mechanism of shear spinning of cones was re-evaluated. It was found that the predicted tangential or power spinning forces for commercially pure aluminum and lead for several spinning conditions agreed well with the experimental data. In addition, the normal force and axial force components were also evaluated and fair agreement between theory and experiment was achieved.

Introduction

A BLANK can be transformed into a cone by the shear spinning process. In this process all elements at certain radii from the axis of rotation remain in their respective positions during deformation. The principal deformation process is assumed to be one of simple shear and hence the name shear spinning is derived from such assumption.

The spinning process, because of its commercial importance, has been the subject of investigation by a number of researchers, namely, Sachs [1],[5] Paulton and Colding [2], Reichel [3], Siebel and Dröge [4] and recent attempts to obtain analytical solutions were made by Colding [5] and Avitzur and Yang [6].

In the present study the mechanics of the deformation process in shear spinning was re-examined and a theoretical solution to the problem is proposed. Experiments were also performed in order to test the validity of the solution. In the theoretical analysis the simple case of shear spinning of cones was considered and the tangential force component on the roller as well as the axial and radial force components were obtained in explicit form.

Mechanics of Shear Spinning of Cones

Deformation Mode. The deformation mechanism of shear spinning of cones is shown schematically in Fig. 1. The process is characterized by the fact that the radial position of an element in the blank remains the same during deformation. This demands that the initial disk thickness t_0 and the final thickness of the cone t_f for the half cone angle α_0 be related by the equation

$$t_f = t_0 \sin \alpha_0. \tag{1}$$

Kalpakcioglu [6, 7] observed by the method of plugged-hole-

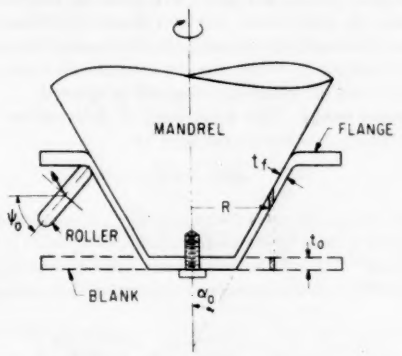

Fig. 1 Schematic diagram of shear spinning process

[1] This paper is based on the PhD dissertation of S. Kobayashi, University of California, Berkeley, Calif., 1960.
[2] Lecturer in Industrial Engineering, University of California, Berkeley, Calif.
[3] Engineer, Pratt and Whitney Aircraft Company, Hartford, Conn.
[4] Professor of Metal Processing, University of California, Berkeley, Calif. Mem. ASME
[5] Numbers in brackets designate References at end of paper.

Contributed by the Metal Processing Research Activity, Production Engineering Division, and presented at the Winter Annual Meeting, New York, N. Y., November 27–December 2, 1960, of THE AMERICAN SOCIETY OF MECHANICAL ENGINEERS Manuscript received at ASME Headquarters, June 21, 1960. Paper No. 60—WA-134.

Nomenclature

A_t, A_R, A_Z = projected areas of the contact surface between roller and cone in the tangential, radial, and axial directions, respectively, in.^{2}
F_t = tangential force component, lb
F_P, F_Q = force components in parallel and perpendicular directions to the roller axis, respectively, lb
F_R, F_Z = force components in the radial and axial directions, respectively, lb
N = speed of rotation of the mandrel, rpm
R_i, R_o, R_n = cone radii, in.
R, θ, Z = cylindrical co-ordinates
x, y, z = rectangular co-ordinates
d_0 = roller diameter, in.
f = feed, ipr
m = fraction
n_0 = number of passes of the element across the deformation zone during its deformation
r_0 = corner radius of roller, in.
ρ, ρ_n = radii of curvature, in.
h = distance of a point from the neutral surface in the thickness direction, in.
t_0, t_f = initial and final thicknesses, respectively, in.
w = specific deformation energy, in-lb/in.^{3}
p = normal stress on the contact surface between roller and cone, psi
$\bar{\sigma}$ = effective stress, psi
$\bar{\sigma}_m$ = mean effective stress, psi
$\Delta\bar{\epsilon}_n$ = increment of effective strain for one pass of an element across the deformation zone
$\Delta\epsilon_{tt}$ = increment of normal strain due to bending
$\int d\bar{\epsilon}$ = total effective strain
α_0 = one half the cone angle, deg
ψ_0 = roller position angle, deg
θ_0, $\bar{\theta}_0$ = angle for deformation zone and its average value, respectively, radian
θ_0', $\bar{\theta}_0'$ = angle functionally related to θ_0 and $\bar{\theta}_0$, respectively, radian
ν_1, ν_2 = ratios of strains

technique and by a grid-line-technique, that the original disk is twisted about the axis of its mandrel during the deformation process. This distortion is not uniform in the thickness direction, hence, the result is a twisting of all radial cross-sectional planes. The distortion is shown schematically in Fig. 2 and it may be observed that twisting of the disk occurs in the direction of rotation.

The deforming of each element in the blank to its deformed state in the cone may be described as follows: The element AB of Fig. 3 undergoes only minor deformation until it reaches the position given by A_1B_1 where the element appears to contact the roller. The principal straining of the element then takes place and it ends at the position A_2B_2. Each element is strained plastically during the transformation from A_1B_1 to A_2B_2 in a stepwise manner.

Inspection of Fig. 3 reveals the fact that there appears to be straining in the R-plane (plane normal to the R-direction) as well as redundant straining of an element as it passes along PQ. This redundant straining may be assumed to be the result of a combination of shearing in two directions on the θ-plane, or of bending and unbending about the R-direction. In either case the results would show that the radial cross-sectional plane remains radial. Since this is not the case (as was already shown in Fig. 2), it seems more likely that this redundant deformation may be due to simultaneous straining by shearing on the θ-plane and by bending, followed by additional unbending, about the R-direction. Such combined effects may explain the distortion θ_t of a cross-sectional plane shown in Fig. 2. It is probable that bending not only about the R-direction, but also about the θ-direction, may cause the rotation θ_R by reducing the thickness of the element.

In the analysis to follow the deformation mechanism will be idealized in that all minor straining will be ignored.

Deformation Energy. The total work of deformation in an infinitesimal time interval is expressed by

$$dW = w\,dv, \tag{2}$$

where w is the specific work (work of deformation per unit volume) and dv is the volume of the metal which was strained in the same time interval. The external work input is closely approximated by $F_t dl$ where F_t is an instantaneous tangential force component on the roller and dl is the distance of contact between roller and cone during an infinitesimal time interval dt. Equating the external work input to the work of deformation given by equation (2) (assuming no losses) permits the following energy balance,

$$F_t dl = w\,dv = dv \int \bar{\sigma}\,d\bar{\epsilon}, \tag{3}$$

where $\bar{\sigma}$ and $d\bar{\epsilon}$ are effective stress and infinitesimal effective strain, respectively. Equation (3) can also be written as

$$F_t = t_0 f \sin \alpha_0 w = t_0 f \sin \alpha_0 \int \bar{\sigma}\,d\bar{\epsilon}, \tag{4}$$

since $dv = t_0 f \sin \alpha_0\, dl$, where t_0 is the initial blank thickness, f is the feed, and α_0 is one half the cone angle.

In order to obtain the tangential force F_t the first problem, which presents itself in equation (4), is the evaluation of the specific deformation energy w. The evaluation of w involves two problems: The determination of the total effective strain at any point within the metal over which the stress-strain curve can be integrated, and the establishment of the stress-strain curve for a given material under the deformation mode encountered in this process. Consequently, the mechanism of straining will be discussed in some detail in the following section.

Finite Strains. Assuming that the strains are discontinuous at point P of Fig. 3, where both shearing and bending are assumed to take place instantaneously, then the state of strain may be approximated by simultaneous superposition of bending and shearing. Therefore, with reference to a cylindrical co-ordinate system $O_1(R, \theta, Z)$ in Fig. 3, whose origin O_1 travels with the roller in the Z-direction and rotates with the mandrel, two nonzero shear strains are found at point P. These are

$$\Delta\gamma_{RZ} = \Delta\left(\frac{\partial u_Z}{\partial R}\right), \qquad \Delta\gamma_{\theta Z} = \frac{1}{R}\,\Delta\left(\frac{\partial u_Z}{\partial \theta}\right), \tag{5}$$

where Δ is the symbol for the integrants of the infinitesimal strains during one pass of the element under the roller.

The bending strain $\Delta\epsilon_\alpha$ shown in Fig. 3, can be approximated by

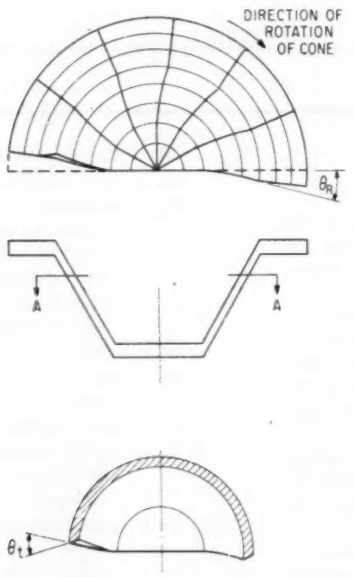

Fig. 2 Diagram showing distortions of cone

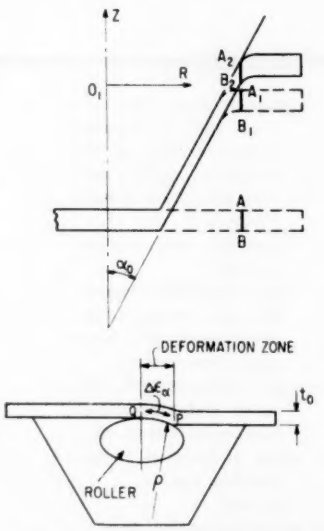

Fig. 3 Deformation in shear spinning

$$\Delta\epsilon_\alpha \simeq \frac{h}{\rho}, \tag{6}$$

where ρ is the radius of curvature of the curve PQ and h is the distance of a point in the thickness-direction from the neutral surface. Since it may be assumed that $\Delta\epsilon_\alpha \simeq \Delta\epsilon_\theta$, therefore, by virtue of the fact that $\Delta\epsilon_r = 0$, the state of strain at point P due to bending is given by

$$\Delta\epsilon_\theta = -\Delta\epsilon_Z = \frac{h}{\rho}. \tag{7}$$

If equations (5) and (7) are superimposed, the state of strain at point P is obtained. After experiencing such strains at P, the element is now subjected to unbending at Q, which results in a strain of the same magnitude as that due to bending given by equation (7). Thus $\Delta\bar{\epsilon}_n$, the total effective strain of an element during one pass of the element across the deformation zone, is given by

$$\begin{aligned}\Delta\bar{\epsilon}_n &= (\Delta\bar{\epsilon})_{\text{at } P} + (\Delta\bar{\epsilon})_{\text{at } Q} \\ &= \frac{2}{\sqrt{3}}\left[\frac{1}{2}\int_{\text{at } P} d\gamma_{RZ}\sqrt{1+\nu_1^2+\nu_2^2} + |\Delta\epsilon_\theta|\right],\end{aligned} \tag{8}$$

where $\nu_1 = |d\epsilon_\theta| \Big/ \frac{d\gamma_{RZ}}{2}$ and $\nu_2 = d\gamma_{\theta Z}/d\gamma_{RZ}$. Assuming ν_1 and ν_2 remain constant during integration at P, then equation (8) can be written as

$$\Delta\bar{\epsilon}_n = \frac{\Delta\gamma_{RZ}}{\sqrt{3}}\left[\nu_1 + \sqrt{1+\nu_1^2+\nu_2^2}\right], \tag{9}$$

where $\nu_1 = |\Delta\epsilon_\theta| \Big/ \frac{\Delta\gamma_{RZ}}{2}$ and $\nu_2 = \Delta\gamma_{\theta Z}/\Delta\gamma_{RZ}$.

The total effective strain of an element $\int d\bar{\epsilon}$, therefore, can be obtained as

$$\int d\bar{\epsilon} = \sum_1^{n_0} \Delta\bar{\epsilon}_n, \tag{10}$$

where n_0 (an integer) is the number of passes of the element under the roller during its major straining and is given by

$$n_0 \simeq \frac{r_0}{f}\cot\alpha_0, \tag{11}$$

where r_0 is the corner radius of the roller.

Total Effective Strain. In order to introduce the property of the material into the plasticity relationships it is necessary to evaluate the effective strains. Let the element ($R = R_n$) be fixed in an original disk assuming that the deformation of the element begins at $R_n = R_o$ and ends at $R_n = R_i$ as is shown in Fig. 4(a). During any one pass when $R_i < R_n < R_o$, it is assumed that the element comes into the deformation zone at P_n and completes one step of the deformation at Q_n in Fig. 4(b). In the previous section the deformation was assumed to be sudden and discontinuous at P. The actual deformation of the element, however, may or may not undergo such sharp changes in shape at P depending on the material and the operating conditions. Thus the deformation mode of the element during any particular pass may be given by P_nQ_n or $P_n'Q_n'Q_n$ where Q_n' is the point of inflection of the curve.

The average value of the strain $|\Delta\epsilon_\theta|$ of equation (7) in the thickness direction is given by

$$|\Delta\epsilon_t| = \frac{t_0}{4\rho_n}, \tag{12}$$

assuming that the neutral surface coincides with the central surface in Fig. 4(c). Moreover, the strain $\Delta\gamma_{\theta Z}$ of equation (5) can be written as

$$\Delta\gamma_{\theta Z} = \frac{1}{R_n}\,\Delta\left(\frac{\partial u_Z}{\partial\theta}\right) = \tan\delta', \tag{13}$$

where δ' is the angle between the tangent to the curve $P_n'Q_n'Q_n$ and the horizontal line at Q_n'.

From the geometry of Fig. 4(c), it is seen that

$$\begin{aligned}\rho_n &\simeq \frac{(R_n\theta_0')^2}{2mz_n'} \simeq \frac{(R_n\theta_0)^2}{2z_n'}, \\ \tan\delta' &\simeq \frac{2mz_n'}{R_n\theta_0'} \simeq \frac{2\sqrt{m}\,z_n'}{R_n\theta_0}.\end{aligned} \tag{14}$$

Equations (14) are obtained by approximating the curve P_nQ_n as an arc of a circle whose radius is ρ_n with its center on the z'-axis, and by neglecting the term $(mz_n')^2$ as compared with $(R_n\theta_0')^2$.

Substitution of equations (14) into equations (12) and (13) yields

$$\begin{aligned}|\Delta\epsilon_\theta| &= \frac{t_0/2}{(R_n\theta_0)^2}\cdot z_n', \\ \Delta\gamma_{\theta Z} &= \frac{2\sqrt{m}}{R_n\theta_0}\cdot z_n'.\end{aligned} \tag{15}$$

If it is assumed further that ν_1 and ν_2 of equation (9) not only re-

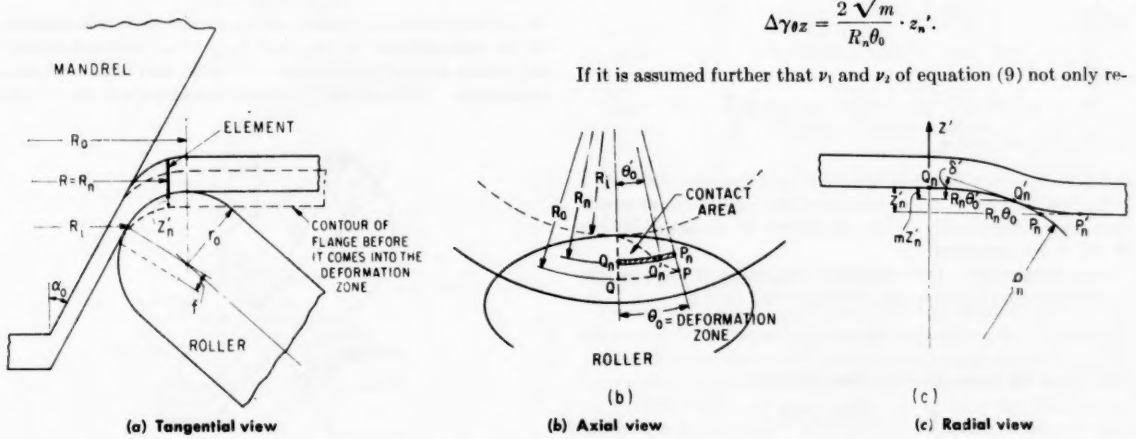

Fig. 4 Straining of an element

main constant during each revolution but also are identical during successive revolutions, then

$$\nu_1 = \frac{|\Delta\epsilon_\theta|}{\Delta\gamma_{RZ}/2} = \frac{\sum_1^{n_0} |\Delta\epsilon_\theta|}{\sum_1^{n_0} \frac{\Delta\gamma_{RZ}}{2}},$$
$$\nu_2 = \frac{\Delta\gamma_{\theta Z}}{\Delta\gamma_{RZ}} = \frac{\sum_1^{n_0} \Delta\gamma_{\theta Z}}{\sum_1^{n_0} \Delta\gamma_{RZ}}. \quad (16)$$

Noting that

$$\sum_1^{n_0} z_n' = r_0 \left(\frac{1}{\sin\alpha_0} - 1\right),$$
$$\sum_1^{n_0} \Delta\gamma_{RZ} = \cot\alpha_0, \quad (17)$$

and combining equations (9), (10), (15), and (16), the total effective strain $\int d\bar{\epsilon}$ becomes

$$\int d\bar{\epsilon} = \sum_1^{n_0} \Delta\bar{\epsilon}_n = \frac{\cot\alpha_0}{\sqrt{3}} [\nu_1 + \sqrt{1 + \nu_1^2 + \nu_2^2}], \quad (18)$$

where

$$\nu_1 = \frac{t_0}{(R_n\bar{\theta}_0)^2} \cdot r_0 \left(\frac{1 - \sin\alpha_0}{\cos\alpha_0}\right),$$
$$\nu_2 = \frac{2\sqrt{m}}{R_n\bar{\theta}_0} \cdot r_0 \left(\frac{1 - \sin\alpha_0}{\cos\alpha_0}\right).$$

$\bar{\theta}_0$ of equation (18) is an average value of θ_0 in the interval between $R_n = R_o$ and $R_n = R_i$ and is taken at the value of θ_0 for $R_n = \frac{R_o + R_i}{2} = R_o - \frac{r_0 \cos\alpha_0}{2}$. The average value of the angle for the deformation zone $\bar{\theta}_0$ is given by

$$\bar{\theta}_0 = \cos^{-1}\left[\frac{\frac{b^2}{a^2} - \sqrt{1 + \left(\frac{b}{R_o}\right)^2\left(\frac{b^2}{a^2} - 1\right)}}{\frac{b^2}{a^2} - 1}\right] \quad (19)$$

where

$$a = \sqrt{r_0^2 - r_1^2},$$
$$b^2 = d_0\left\{\sqrt{r_0^2 - (r_1\cos\psi_0)^2} - r_1\sin\psi_0\right\} + r_0^2 - r_1^2,$$
$$r_1 = r_0 - f\cos\alpha_0,$$

and r_0 is the corner radius of the roller, d_0 is the roller diameter, f is the feed, and α_0, ψ_0 are one half the cone angle and roller position angle, respectively. The derivation of equation (19) is shown in the Appendix.

Force Components. The tangential component of force on the roller from equation (4) may be written in the form of

$$F_t = t_0 f \sin\alpha_0\, \bar{\sigma}_m \int d\bar{\epsilon}, \quad (20)$$

where $\bar{\sigma}_m$ is the mean effective stress defined by

$$\bar{\sigma}_m = \int \bar{\sigma} d\bar{\epsilon} / \int d\bar{\epsilon}, \quad (21)$$

and the total effective strain $\int d\bar{\epsilon}$ is given by equation (18). Thus the tangential force component can be calculated for a given operating condition when the stress-strain curve for the material is known.

It is evident from equation (20) that the evaluation of F_t for a given material requires knowledge of the stress-strain curve at the shear spinning deformation rates. These strain rates can be estimated from the equation,

$$\dot{\bar{\epsilon}}_{avg} = \frac{\frac{\int d\bar{\epsilon}}{n_0}}{\Delta t} = \frac{\frac{\int d\bar{\epsilon}}{n_0}}{\frac{\bar{\theta}_0}{2\pi N}}. \quad (22)$$

The strain rates in the present investigation were of the order of 10 to 10^2 in/in. per sec and, consequently, are high, but not as high as those found in metal cutting. It is believed, nevertheless, that the static stress-strain curves may be used without much error for work-hardening materials in estimating $\bar{\sigma}_m$ of equation (21). For nonwork-hardening materials, on the other hand, the stress-strain curves are very much dependent on strain-rates and the static-strain curve cannot be used for estimating $\bar{\sigma}_m$.

The two force components F_R and F_Z, too, are important from the point of view of machine design in spinning. These components are shown in the force diagram of Fig. 5. The force on the roller can be resolved into the radial and axial directions of the mandrel. The two components F_R and F_Z may be expressed as functions of F_P and F_Q which may be measured together with the tangential force component F_t by a three-component dynamometer, where F_P and F_Q are taken in the parallel and normal directions, respectively, relative to the roller axis. The two force components F_R and F_Z are given by

$$F_R = F_Q\cos\psi_0 - F_P\sin\psi_0,$$
$$F_Z = F_Q\sin\psi_0 + F_P\cos\psi_0. \quad (23)$$

If it is assumed that a normal stress p acting on the contact surface between the roller and cone is uniformly distributed, then

$$F_t = p \cdot A_t, \quad F_R = p \cdot A_R, \quad F_Z = p \cdot A_Z, \quad (24)$$

or

$$F_R = F_t\frac{A_R}{A_t},$$
$$F_Z = F_t\frac{A_Z}{A_t}. \quad (25)$$

The effect of frictional stresses on the contact surface in equation (25) is neglected and A_t, A_R, and A_Z are the projected areas of the contact surface in the tangential, radial, and axial directions, respectively. This system of stresses is analogous to those in the

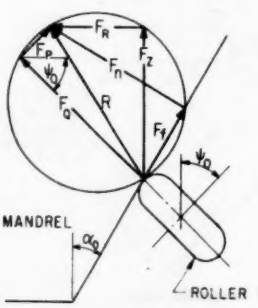

Fig. 5 Force system

problem of plowing of a slider over a softer metal in sliding friction [8].

Thus, when the ratios of projected areas of the contact surfaces are known, the two force components F_R and F_Z can be obtained by means of equation (25) when the tangential component has been determined from equation (20).

Contact Area Between Roller and Cone. It is possible from geometry alone to obtain the ideal contour of the contact surface between roller and cone by either graphical or numerical means. The ideal contour in this case is the exact intersection of the roller with the cone assuming zero predeformation. However, an element in the actual metal tends to deform before it contacts the roller as is depicted in Fig. 4(*b*), and the actual deformation mode cannot be formulated precisely. Consequently, the actual contact surface differs from the ideal and it is doubtful that the additional rigor required to evaluate the ideal contact surface is worth the resulting complexity and labor. Accordingly, only approximate evaluations of the projected contact areas will be made for the two force components of equation (25).

The projected contact areas in the tangential, radial, and axial directions are shown in the schematic diagram of Fig. 6. The contours given by the solid curves are approximate actual contours for $m = 1$ and $m < 1$, respectively, while the contours shown by dashed lines are those when the deformation of an element is assumed to occur only under the roller (i.e., ideal contact surface). It is seen, in Fig. 6, that the projected contact areas in the three co-ordinate directions may be approximated by

$$A_t \simeq \frac{1}{2} r_0 m f \cos^2 \alpha_0,$$

$$A_R \simeq \frac{1}{2} r_0 \sqrt{m}\, R_o \bar{\theta}_0 \left[1 - \sin \alpha_0 + \frac{f \cos \alpha_0}{2 r_0} \right], \qquad (26)$$

$$A_Z \simeq \frac{1}{2} r_0 \cos \alpha_0 \sqrt{m}\, R_n \bar{\theta}_0.$$

Substitution of equations (26) into equations (25) yields

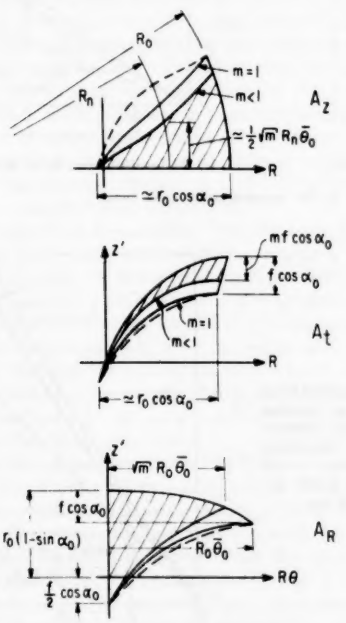

Fig. 6 Projected contact areas

$$F_R \simeq F_t \frac{R_o \bar{\theta}_0}{f \cos \alpha_0} \cdot \frac{1}{\sqrt{m}} \left[\left(\frac{1 - \sin \alpha_0}{\cos \alpha_0} \right) + \frac{f}{2 r_0} \right],$$

$$F_Z \simeq F_t \frac{R_n \bar{\theta}_0}{f \cos \alpha_0} \frac{1}{\sqrt{m}}. \qquad (27)$$

Experimental Procedure

In order to test the validity of the foregoing theory, spinning tests were conducted on commercially pure aluminum (1100-0) and commercially pure lead. In addition some metal-cutting test data were obtained for the same metals, in order to furnish flow stresses at extremely high strain rates [9].

The experimental work was carried out on a modified lathe and on a Universal milling machine. The roller forces were measured with a three-component dynamometer and were recorded autographically on a Sanborn Tape.

It is necessary to obtain the instantaneous cone radius corresponding to each force reading, since the force components as well as the cone radius change during a single spinning test. This could be achieved by marking the Sanborn recording tape simultaneously with the blank. After the blank was spun into a cone, its radii at the marked positions were determined, and the final thickness was checked according to equation (1). The test conditions employed in the spinning tests are given in Table 1 and the metal-cutting test conditions in Table 2.

Table 1 Test conditions in shear spinning of cones

Material	Roller size, in. d_0	r_0	Thickness, in.	Feed, ipr, f	α_0, deg	ψ_0, deg	Speed, rpm
Commercially pure lead	1.0	0.25	0.100 0.150 0.200	0.035, 0.060	30	50	105
	2.0	0.25	0.100 0.150 0.200	0.035, 0.060	30	50	105
	3.0	0.25	0.100 0.150 0.200	0.035, 0.060	30	50	105
Commercially pure aluminum 1100-0	3.0	0.25	0.080 0.100 0.120	0.037	45	45	116

Table 2 Cutting test conditions

	Orthogonal cutting: Lubricant—air			
Material	Rake angle, deg	Feed, ipr	Speed, rpm	Tool material
Commercially pure lead	15	0.00275–0.00981	210, 550	H.S.S. 18-4-1
Commercially pure aluminum, 1100-0	15, 30	0.00199–0.00735	2000	Sintered carbide K5H

Results and Discussion

Stress-Strain Curves. It was pointed out in the foregoing that the tangential force component given by equation (20), can be predicted when the static stress-strain curve for a given work-hardening material is known. The assumption was that the strain rates in spinning would be low enough not to alter the stress-strain properties significantly. For nonwork-hardening materials such as lead, on the other hand, the static stress-strain properties can

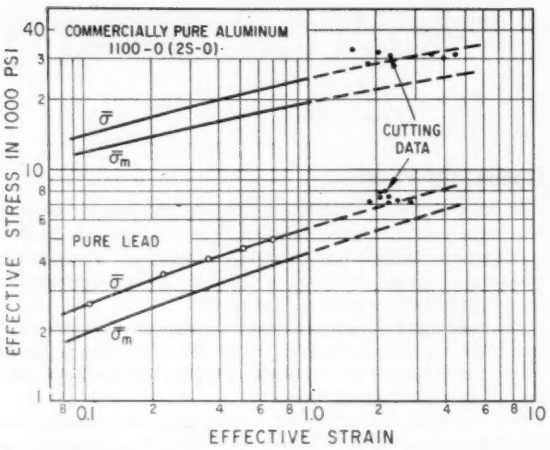

Fig. 7 Effective stress-effective strain curves for commercially pure aluminum and pure lead

However, if the time interval is sufficiently short, then the stress-strain curve obtained by a continuous deformation process may be applicable in the discontinuous deformation process, as that in spinning, although the material may tend to recrystallize between each deformation step. The time interval in the deformation steps of the present investigation was of the order of one half second or less and was assumed to be too short to alter the stress-strain properties significantly. Hence, in the analysis of shear spinning, the dynamic stress-strain relationship for lead, given in Fig. 7, and the static stress-strain curve for aluminum with added cutting test data, also shown in this figure, were assumed to be applicable.

Tangential Force Component. The tangential experimental force components are plotted in Figs. 8 and 9 as functions of $t_0 f \sin \alpha_0$ where t_0 is the initial disk thickness, f is the feed, and α_0 is one half the cone angle. The two solid curves in the same figures are theoretical solutions given by equation (20) for two values of m, while the dashed lines are the solutions obtained by the simple shear theory which neglects the redundant work (i.e., $\nu_1 = \nu_2 = 0$) in equation (18). This tangential component of force F_t for the simple shear theory is given by

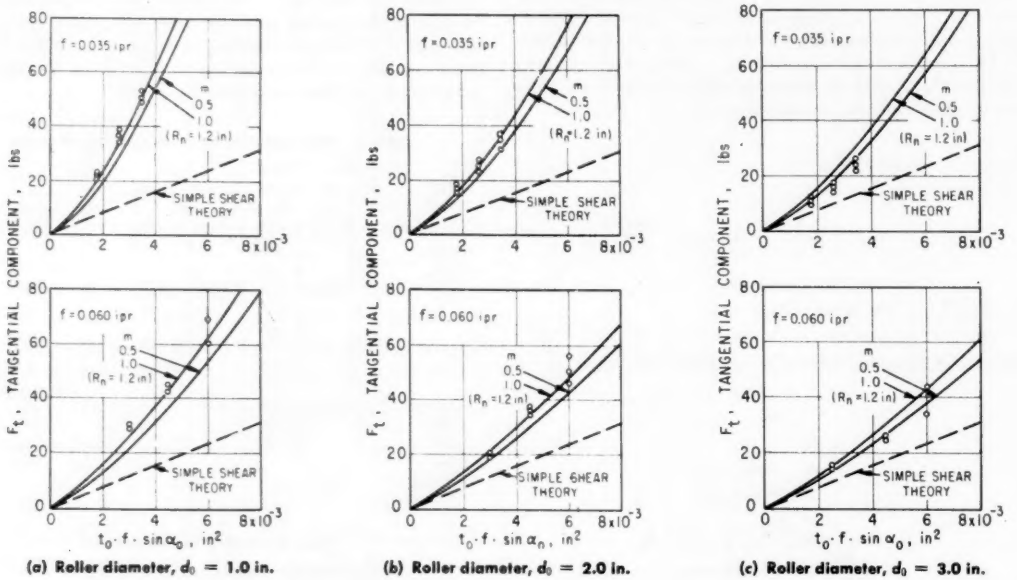

(a) Roller diameter, d_0 = 1.0 in. **(b) Roller diameter, d_0 = 2.0 in.** **(c) Roller diameter, d_0 = 3.0 in.**

Fig. 8 Tangential force component as function of $t_0 f \sin \alpha_0$ for commercially pure lead

no longer be used and the stress-strain relationships at strain-rates of the order of 10 to 10^2 in/in. per sec must be applied. It was fortunate, therefore, that the literature revealed [10] compression test data of pure lead at high rates of strain from which the stress-strain curve shown in Fig. 7 could be constructed. In this figure, the open circles were taken from the literature and the solid circles are the data points from the metal-cutting tests. It is seen that lead, which at room temperature and slow speeds essentially does not work-harden, behaves like a work-hardening material at high rates of strain. It must be remarked that the stress-strain relationship given in Fig. 7 is that applicable to a material which is being deformed continuously at high rates of strain. In spinning, however, the deformation of an element is not continuous. Consequently, if the time interval between the deformation processes of an element is sufficiently long for the material to recover or recrystallize, then only the first small portion of the stress-strain curve may be repeated for each deformation process, independent of the total effective strain achieved.

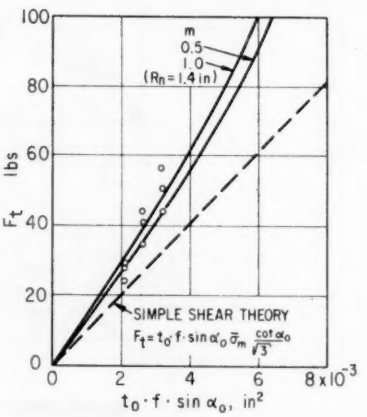

Fig. 9 Tangential force component as function of $t_0 f \sin \alpha_0$ for commercially pure aluminum; roller diameter = 3.0 in., feed = 0.037 ipr, and α_0 = 45 deg

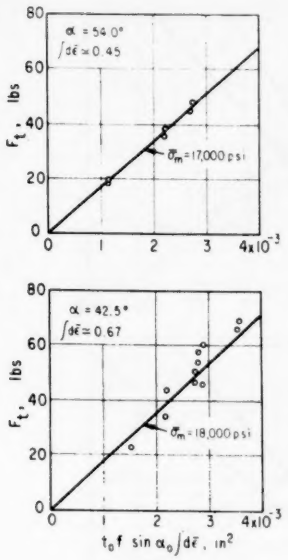

Fig. 10(a)

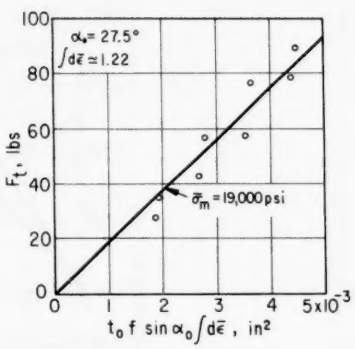

Fig. 10(b)

Fig. 10 Tangential force component as function of $t_0 f \sin \alpha_0 \int d\bar{\epsilon}$ for commercially pure aluminum data from literature [6]; roller diameter ≅ 9 in., feed = 0.04 — 0.10 ipr

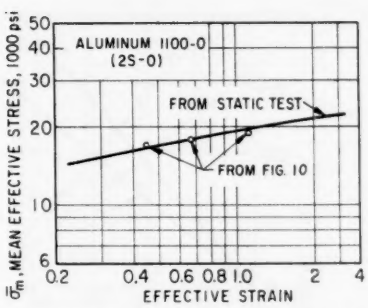

Fig. 11 Comparison of spinning data points [6] with property tests of commercially pure aluminum

$$F_t = t_0 f \sin \alpha_0 \cdot \bar{\sigma}_m \frac{\cot \alpha_0}{\sqrt{3}} \tag{28}$$

It is seen that for lead equation (20) for $m = 1$ is in good agreement with the experimental results for rollers of 1 in. and 2 in. diameter, while it appears that $m = 0.5$ for a 3-in. diameter roller. For aluminum under somewhat different conditions, shown in Fig. 9, the value of m seems to be close to unity for a 3-in. diameter roller. It appears, therefore, that the value of m depends on the spinning conditions and takes on a value of 0.5 for rollers larger than approximately 3 in. in diameter.

In order to confirm the validity of equation (20), data obtained from the literature [6] were examined and are shown in Fig. 10. The tangential force components are plotted against $t_0 f \sin \alpha_0 \int d\bar{\epsilon}$ so that the slopes of the lines yield the mean effective stresses in accordance with equation (20). The total effective strain can be calculated by equation (18) with the value of $m = 0.5$, because of the fact that the roller diameters were approximately 9 in. The mean effective stresses thus obtained are compared in Fig. 11 with the stress-strain curve of Fig. 7. Figs. 8 to 11, inclusive, demonstrate that equation (20) may be used for a satisfactory prediction of the tangential force component.

Axial and Radial Force Components. The two force components F_R and F_Z are plotted as functions of the tangential force component F_t in Figs. 12 to 15, inclusive. The theoretical curves from equations (27) are shown for two values of m in these figures. It is gratifying to note from Figs. 12 and 13 that equation (27) for the axial force component is in good agreement with the experimental data, although the evaluation of the projected areas is only a rough first approximation. It is observed again that the value of m changes with spinning conditions and tends to decrease as the roller diameter increases.

The radial force component F_R, on the other hand, shows more scatter than F_Z. Consequently, the validity of equation (27) for the radial component is not as conclusive as it is for the axial component. It is suggested here that the scatter of the radial force component may be due in part to the fact that the actual deformation mode is not the one assumed in Fig. 4. The flange may overlap the roller and may result in an increase in the projected areas in the axial and tangential directions but not necessarily in the radial direction. Moreover, the stress acting on the overlapped portion would have an opposite component in the radial direction. Thus, because of the foregoing effects, the actual radial force component may deviate from the theoretical values given by equation (27).

Conclusions

In the study of the mechanics of shear spinning of cones, the following conclusions have been reached.

1 The mean flow stress of commercially pure aluminum in shear spinning can be approximated by that obtained from a static stress-strain curve. For commercially pure lead the mean flow stress is that corresponding to the higher strain rates of the order of 10 to 10^2 in/in. per sec obtained from dynamic compression tests under the conditions of the present investigation.

2 The theoretical expression for the tangential force component given by equation (20), based on the assumption that the redundant work is due to shearing and bending followed by unbending, is in good agreement with the experiments.

3 The axial and radial force components can be estimated approximately by equations (27) which indicated in fact that the ratios of the three force components are nearly equal to the ratios of the respective projected contact areas in the three directions.

Acknowledgments

The authors wish to thank The National Science Foundation for the support by its grant G 6298 without which this investigation would have been difficult to perform. They also wish to thank the University of California for making available laboratory space and equipment. They feel particularly indebted to Mr. Petersen for constructing the three-component dynamometer and for his constant interest in the investigation. They finally wish to thank Mr. Kot for preparing all figures and Miss Phillips for typing the manuscript.

References

1 G. Sachs, "Experimental Analysis of Shear Forming Manufacturing Methods," Reports by the Institute of Industrial Research, Syracuse University, 1954.

2 R. A. Paulton and B. N. Colding, "Two New Industrial Processes for Plastic Deformation of Metals," Proceedings, Conference on Technology of Engineering Manufacture, The Institution of Mechanical Engineers, London, England, March, 1958, pp. 54–62.

3 H. Reichel, "Über das Walzdrücken Kegelförmiger Werkstücke aus Aluminum," *Fertigungstechnik*, vol. 8, no. 5, 1958, pp. 181–184; vol. 8, no. 6, 1958, pp. 252–260.

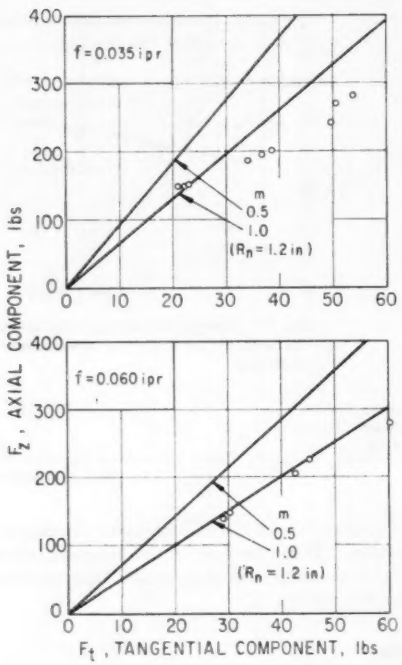

(a) Roller diameter, d_0 = 1.0 in.

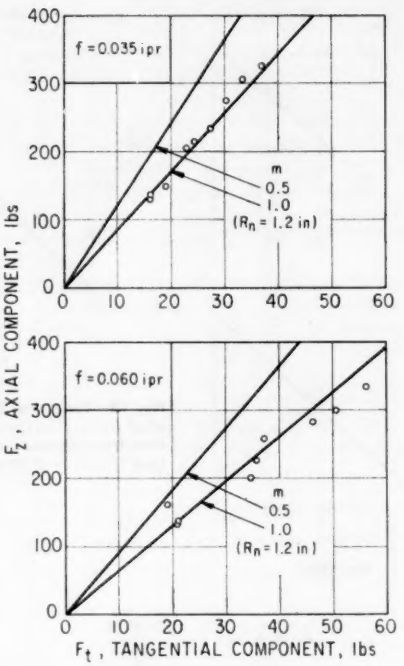

Fig. 12(b) Roller diameter, d_0 = 2.0 in.

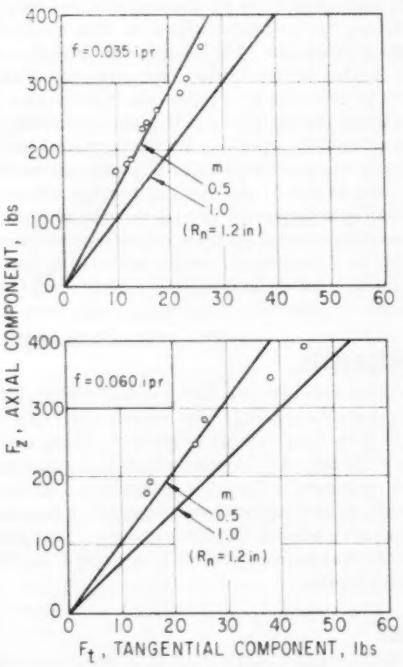

(c) Roller diameter, d_0 = 3.0 in.

Fig. 12 Axial force component as function of tangential force component for commercially pure lead

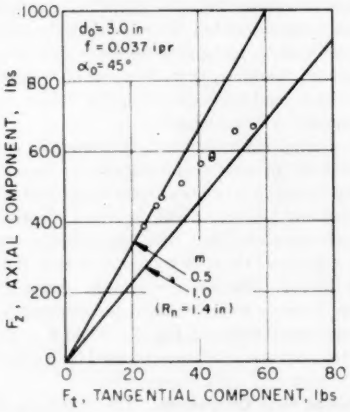

Fig. 13 Axial force component as function of tangential force component for commercially pure aluminum

4 E. Siebel and K. H. Dröge, "Kräfte und Materialfluss beim Drücken," *Werkstattstechnik und Maschinenbau*, vol. 45, no. 1, 1955, pp. 6–9.

5 B. N. Colding, "Shear Spinning," ASME Paper No. 59—Prod-2, May, 1959.

6 B. Avitzur and C. T. Yang, "Analysis of Power Spinning of Cones," TRANS. ASME, Series B, JOURNAL OF ENGINEERING FOR INDUSTRY, vol. 82, 1960, pp. 231–245.

7 S. Kalpakcioglu, "On the Mechanics of Shear Spinning," TRANS. ASME, Series B, JOURNAL OF ENGINEERING FOR INDUSTRY, vol. 83, 1961, pp. 125–130.

8 F. P. Bowden and D. Tabor, "The Friction and Lubrication of Solids," Oxford University Press, London, England, 1954.

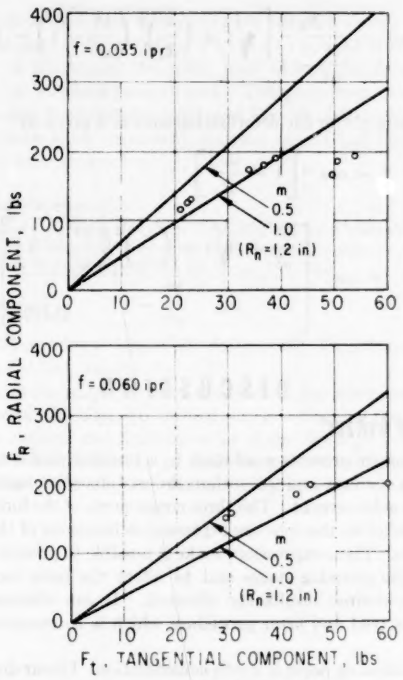

(a) Roller diameter, d_0 = 1.0 in.

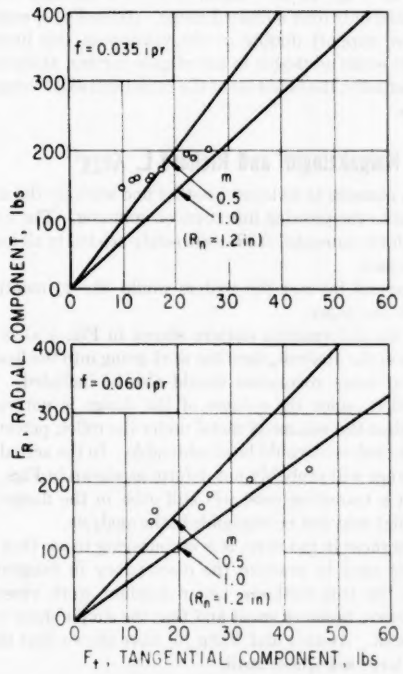

(c) Roller diameter, d_0 = 3.0 in.

Fig. 14 Radial force component as function of tangential force component for commercially pure lead

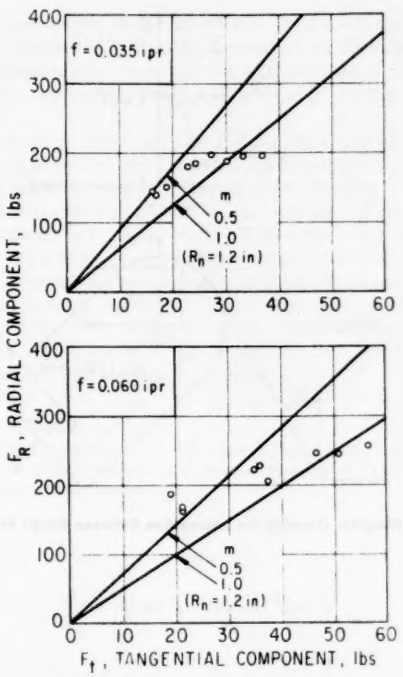

Fig. 14(b) Roller diameter, d_0 = 2.0 in.

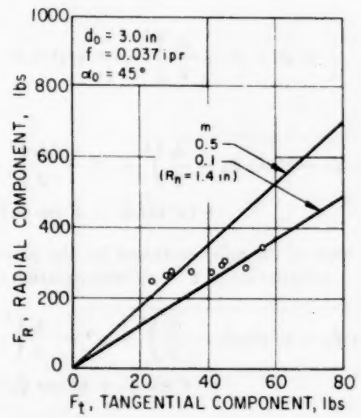

Fig. 15 Radial force component as function of tangential force component for commercially pure aluminum

9 S. Kobayashi and E. G. Thomsen, "Some Observations on the Shearing Process in Metal Cutting," TRANS. ASME, Series B, JOURNAL OF ENGINEERING FOR INDUSTRY, vol. 81, 1959, pp. 251–262.

10 N. Loizou and R. B. Sims, "The Yield Stress of Pure Lead in Compression," *Journal of the Mechanics and Physics of Solids*, vol. 1, 1953, pp. 234–243.

APPENDIX

Angle for Deformation Zone

Referring to Fig. 16, the following relationships are obtained:

Transformation: $0(x, y, z) \rightarrow 0'(x', y', z')$

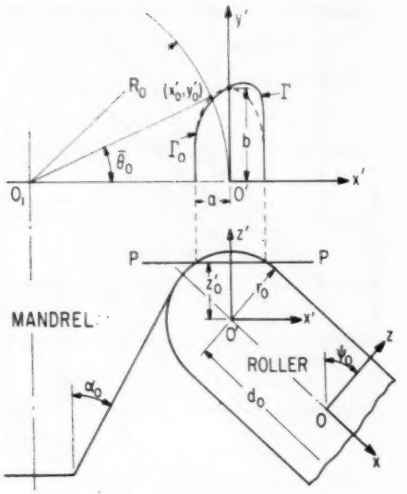

Fig. 16 Diagram showing the intersection between flange of blank and roller

$$\left.\begin{aligned} x &= x' \cos \psi_0 - z' \sin \psi_0 - \frac{d_0}{2} \\ y &= y' \\ z &= x' \sin \psi_0 + z' \cos \psi_0 \end{aligned}\right\} \quad (29)$$

Torus:

$$\left[\sqrt{x^2 + y^2} - \frac{d_0}{2}\right]^2 - r_0^2 + z^2 = 0 \quad (30)$$

or

$$\left\{\sqrt{\left(x' \cos \psi_0 - z' \sin \psi_0 - \frac{d_0}{2}\right)^2 + y'^2} - \frac{d_0}{2}\right\}^2 - r_0^2 + (x' \sin \psi_0 + z' \cos \psi_0)^2 = 0 \quad (31)$$

Curve Γ = trace of the roller sectioned by the plane *PP*. By substitution of $z' = z_0'$ into equation (31),

$$\left\{\sqrt{\left(x' \cos \psi_0 - z_0' \sin \psi_0 - \frac{d_0}{2}\right)^2 + y'^2} - \frac{d_0}{2}\right\}^2 - r_0^2 + (x' \sin \psi_0 + z_0' \cos \psi_0)^2 = 0 \quad (32)$$

Lengths a and b: Substituting $y' = 0$, $z_0' = r_1$ and $x' = 0$, $z_0' = r_1$ into equation (32), where $r_1 = r_0 - f \cos \alpha_0$, we get

$$a = \sqrt{r_0^2 - r_1^2} \quad (33)$$

and

$$b^2 = d_0[\sqrt{r_0^2 - (r_1 \cos \psi_0)^2} - r_1 \sin \psi_0] + r_0^2 - r_1^2 \quad (34)$$

respectively.

Angle for Deformation Zone $\bar{\theta}_0$: With an approximation of the curve Γ_0 (a portion of the curve Γ of interest) by an ellipse as shown in Fig. 16, we have

$$\left.\begin{aligned} \left(\frac{x_0'}{a}\right)^2 + \left(\frac{y_0'}{b}\right)^2 &= 1 \\ x_0'^2 + y_0'^2 &= 2R_o |x_0'| \end{aligned}\right\} \quad (35)$$

which yield

$$|x_0'| = \frac{R_0}{\frac{b^2}{a^2} - 1}\left[\sqrt{1 + \left(\frac{q}{R_o}\right)^2\left(\frac{b^2}{a^2} - 1\right)} - 1\right]. \quad (36)$$

Thus the angle for the deformation zone $\bar{\theta}_0$ is given by

$$\bar{\theta}_0 = \cos^{-1}\left[1 - \frac{|x_0'|}{R_o}\right] = \cos^{-1}\left[\frac{\frac{b^2}{a^2} - \sqrt{1 + \left(\frac{b}{R_o}\right)^2\left(\frac{b^2}{a^2} - 1\right)}}{\frac{b^2}{a^2} - 1}\right]. \quad (37)$$

DISCUSSION

Betzalel Avitzur[6]

This paper presents a solution to a pressing problem in shear spinning of cones, and the authors deserve sincere congratulations for their achievement. The three components of the force exerted by the roller on the cone are expressed as functions of the process variables. These expressions make it possible to predict the force during the planning stages and to affect the basic variables so that the desired results are obtained. It can eliminate much from the trial and error procedure which is so common in this process.

The following point is worth consideration: Linear dependence of the radial, axial, and tangential components of the force on each other is predicted in the solution. The experimental data plotted in Figs. 12–15 suggest that this linearity can be approximated only over a limited range. Reichel's [3] experimental data, too, support doubts in the validity of this linearity. It therefore seems advisable to investigate further, analytically and experimentally, the behavior of the radial and axial components of the force.

Serope Kalpakcioglu[7] and Richard L. Kegg[8]

It is a pleasure to welcome another fine work by the authors to be added to the growing literature on spinning. The writers feel that such fundamental studies are sorely needed in all metalworking processes.

For general interest the writers would like to mention a few points in the paper.

a If the deformation pattern shown in Fig. 4(*a*) is taken as the basis of the analysis, then the work going into the flange deformation at every revolution should also be included. It would appear that, since the volume of the flange is normally much greater than the volume of metal under the roller, percentagewise this neglected work could be considerable. In the actual case, the whole flange will probably not deform as shown in Figs. 4(*a*) and 4(*c*), but a transition zone will still exist in the flange near the roller which may not be negligible in the analysis.

b For those in industry, it is encouraging to see that for roller diameters used in practice the discrepancy in tangential force between the two methods, i.e., redundant work versus simple shear theory, becomes small and that the simple shear method is quite useful. Avitzur and Yang [6] have shown that this is also true for large workpiece radii.

---

[6] Systems and Devices Section, Applied Science Department, Scientific Laboratory, Ford Motor Company, Dearborn, Mich. Assoc. Mem. ASME.

[7] Research Supervisor, The Cincinnati Milling Machine Company, Cincinnati, Ohio.

[8] Senior Research Engineer, The Cincinnati Milling Machine Company, Cincinnati, Ohio. Assoc. Mem. ASME.

c In connection with the correlation between theory and experimental data of F_R and F_Z, we have also noticed that for certain sets of conditions the roller may indent the flange thus changing the idealized contact area. This phenomenon is shown clearly in Fig. 6 of Reference [7] and Fig. 10 of Reference [11]. In such cases close agreement between actual and theoretical forces may not be expected.

Additional Reference

11 Richard L. Kegg, "A New Test Method for Determination of Spinnability of Metals," TRANS. ASME, Series B, JOURNAL OF ENGINEERING FOR INDUSTRY, vol. 83, 1961, pp. 119–124.

Authors' Closure

The authors wish to thank Dr. Avitzur, Mr. Kalpakcioglu, and Mr. Kegg for their comments.

Linear relationships between the three force components are derived assuming that the normal stress acting on the contact surface is uniform and that the ratios of the three projected contact areas remain the same as those based on the idealized contact surface. The authors, therefore, agree with Dr. Avitzur's comment with respect to the linearity of the three force components. It appears [12] that the discrepancy of linearity of the force components may be mainly due to the change of the ratios of the projected contact areas, which depends on the forming conditions.

It is correct, as stated by Mr. Kalpakcioglu and Mr. Kegg, that the redundant deformation is not solely limited to the metal under the roller but extends to a part of the flange. The work dissipated in the flange, however, would be small (except at large feeds) compared to the total work. This is due to the fact that the radius of curvature ρ_R (authors' notation) in the flange is very large because of the indentation of the roller, as was already pointed out in their discussion. This indentation, on the other hand, may affect the evaluation of the radial and axial force components, which results in the discrepancy from the linear relationships of the three force components.

Additional Reference

12 S. Kobayashi and E. G. Thomsen, "Theory of Spin Forging," submitted for presentation at 1961 Annual Meeting of CIRP (Group F) in Prague, Czechoslovakia.

An Experimental Investigation of Temperature Distribution at Tool-Flank Surface[1]

B. T. CHAO
Professor of Mechanical Engineering, University of Illinois, Urbana, Ill.

H. L. LI
Research Engineer, E. I. du Pont de Nemours & Co., Wilmington, Del.

K. J. TRIGGER
Professor of Mechanical Engineering, University of Illinois, Urbana, Ill. Mem. ASME

The measurement of temperature distribution at the flank surface of a cutting tool is characterized by the extremely small extent of the surface over which the temperature field is explored. This paper describes a technique which makes use of a moving lead-sulfide, photoconductive, infrared radiation detector. The surface in question is quickly scanned by the detector's view field. For the level of temperature encountered, data are reproducible and the method may be used to determine temperature distribution over sliding contacts in general. From the measured flank surface temperatures, tool-chip interface temperature distribution was deduced using geometrical, electric analog. The technique also has the general application in finding steady temperatures at locations which are not accessible for direct measurement. The computed tool-chip-interface temperature profile agrees well with known crater-wear patterns. Tool-face frictional force calculated from thermal considerations compares favorably with independent dynamometer measurement.

Introduction

THE direct determination of temperature distribution on the flank of a cutting tool poses a unique problem of exploring the local surface temperatures of a very hard material, like sintered carbide, over an extremely limited area available for observation or measurement. The physical dimensions with which one is concerned are but a few hundredths of an inch.

In contrast to the dearth of information on the temperatures at the flank surface, the temperature at the sliding contact between the tool and the chip has long been the subject of many investigators. This is primarily due to the important role which local temperatures play in influencing the rate of wear of cutting tools.

Shore [1],[2] Gottwein [2], and Herbert [3] were among the pioneers in employing the "tool-work" thermocouple technique. The reported temperatures were some kind of average values. Exploration of the tool-chip-interface temperature and/or its distribution has also been attempted by embedding tiny thermocouples in small holes drilled in tools. Such studies have been made by Schwartz and Flagle [4], Axer [5], Kusters [6], Danielian [7], Rall and Giedt [8], and recently Cook [9]. All measurements, however, were subjected to the limitation that data could not be obtained close enough to the surface where the local temperatures are desired, and, therefore, large errors may be introduced [10].

Other techniques involving the use of thermosensitive paints have been applied by Schallbroch and Lang [11], Pahlitzsch and Helmerdig [12], Bickel and Widmer [13], and others. Results obtained were not considered to be accurate.

A different approach to the measurement of sliding-contact temperatures involves the use of a photoconductive cell. Parker and Marshall [14], in 1948, investigated the temperatures of railway brake shoes. Bowden and Thomas [15] reported results of measurements on temperatures developed at the points of rubbing contact between a steel rod and a glass disk by capturing the infrared radiation transmitted through the transparent disk. Recently, Reichenbach [16] attempted to measure the shear-plane temperature in a metal chip and the clearance-face temperature of a cutting tool using photoconductive cells. Several fundamental difficulties were described in the paper but no solution was offered.

Many investigators have also attempted to evaluate tool temperatures analytically. Chao and Trigger [17, 18] developed methods by which the distribution of temperature both at the tool-work and tool-chip interface might be predicted. The method has since been extended to two-dimensional tools of any arbitrary included angle [19]. In order to make the analysis of the rather complex problem reasonably simple, several assumptions were introduced. One of these which has been the subject of scrutiny is that of *uniform* frictional energy dissipation at the tool-chip interface. Information on the subject has been completely lacking, however. This paper describes a first attempt to evaluate such distribution from measured local flank temperatures. A portion of the material reported herein is condensed from a technical report [20] submitted to the Office of Ordnance Research, U. S. Army.

Measurement of Temperature Distribution at Tool Flank Using Infrared Radiation Detector

The use of an infrared detector in the direct determination of temperature distribution over sliding contacts in general, and that at the tool flank in particular, has been studied in the Metal Cutting Laboratory of the University of Illinois. Before discussing the experimental arrangement in detail, it seems desirable to review some of the underlying principles and limitations of lead-sulfide photoconduotive cells in such applications.

Lead-Sulfide (PbS) Photoconductive Cells. As distinctly different from ordinary thermal detectors, such as thermocouples, the photoconductive cell is one type of quantum detector.

The general characteristics of PbS cells may be enumerated as follows:

(*a*) *Physical Size.* Usually small and has rugged construction.

(*b*) *Spectral Response.* Peak response occurs in the infrared region with wave length ranging from 1 to 2 microns. A typical response curve of a commercial cell is shown in Fig. 1.

(*c*) *Sensitivity.* The electrical resistance of PbS cells decreases with increasing radiant flux falling on its sensitized surface. Hence, if a constant d-c voltage is applied to the cell with a re-

[1] This work evolved from a project sponsored by the Office of Ordnance Research, U. S. Army, under contract No. DA-11-022-ORD-1980.

[2] Numbers in brackets designate References at end of paper

Contributed by the Metal Processing Research Activity of the Production Engineering Division and presented at the Winter Annual Meeting, New York, N. Y., November 27–December 2, 1960, of THE AMERICAN SOCIETY OF MECHANICAL ENGINEERS. Manuscript received at ASME Headquarters, July 25, 1960. Paper No. 60—WA-87.

sistance in series, any decrease in the cell resistance will be reflected in the change of potential difference across the fixed resistor. This output signal is usually referred to as the voltage sensitivity. For a given incident radiant flux, the signal varies approximately linearly with the applied d-c potential. The maximum voltage which may be applied to a PbS cell is limited by the thermal noise generated as a consequence of heating. It differs widely among commercial cells. For instance, the maximum circuit potential recommended for one type of "Mullard"[3] cell is 250 volts, but it is limited to 90 volts for "Cetron"[4] cells. The voltage sensitivity of PbS cells also varies considerably. Manufacturers' data sheets indicated voltage sensitivity ranging from 10^{-4} to 10^{-2} v/(μwatt)(cm^2).

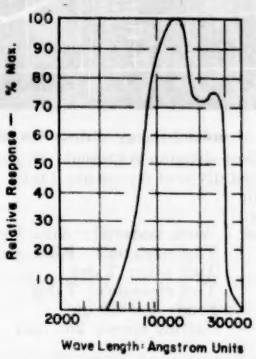

Fig. 1 Spectral response of a commercial lead-sulfide, infrared radiation detector

(*d*) *Dynamic Response and Time Constant.* The time constant of photoconductive cells is much longer than that of the nearly inertialess photoemissive cells. Due to difficulty of control during processing there is considerable variation in the time constant of commercially available cells, the values ranging from 5 to 300 μ sec.[5] The estimated time constant required for the experimental conditions in this investigation was about 100 μsec or less. Details of the procedure used to determine the time constants of the cells have been described elsewhere [20].

Description of the Experimental Arrangement. Orthogonal cutting was performed on a heavy-duty lathe using a tubular workpiece, 9-in. OD and $^{13}/_{16}$-in. wall thickness. An axial slot, $1^1/_2$ in. wide and approximately 3 in. long, was provided in the wall to accommodate the photoconductive-cell assembly. The radiant energy emitted at the tool flank was "seen" by the cell through $^3/_{32}$-in-diam holes drilled axially in the tube wall. Fig. 2 shows the workpiece with the cell assembly in place. The general experimental arrangement is shown schematically in Fig. 3(*a*). The signal produced in the rotating cell is brought out by a brush and slip-ring assembly. Minimum noise by far was obtained using copper rings and phosphor-bronze brushes. Occasional lubrication by kerosene was sufficient.

The important geometric configuration between the tool flank and the sensitized surface of the cell is shown in Fig. 3(*b*). Since in the present investigations the local temperature is of interest, a small slit width is desirable. A wider slit width would admit more energy to the cell resulting in a larger signal. Hence the width selected represents a compromise between these two opposing factors. More recently, the two slits have been replaced by a hypodermic needle 0.005-in. ID and about $^3/_4$ in. long, which

[3] Type 618V, supplied by Mullard Overseas Ltd., London, England.

[4] Type CE-E702-A3, supplied by the Continental Electric Company, Geneva, Ill.

[5] Private communication from Practical Electronics Manufacturing Company, Chicago, Ill.

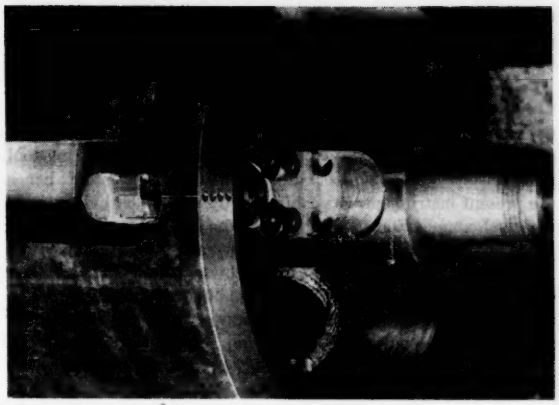

Fig. 2 Tubular workpiece, showing the driving mandrel and cell assembly as an integral unit

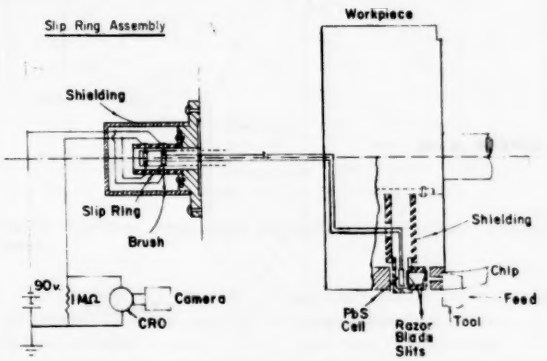

Fig. 3(a) Schematic drawing of experimental arrangement

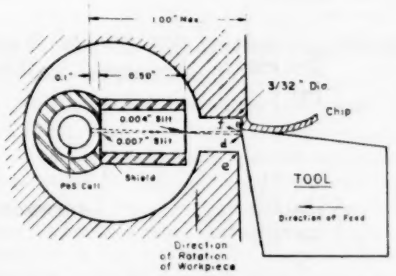

Fig. 3(b) Configuration in radiation measurement

serves the same purpose and simplifies the setup. Either arrangement also serves the useful function of preventing entry into the cell of stray radiation emanating from the walls of the hole.

Referring to Fig. 3(*b*), as the flank surface of the tool is scanned by the effective view field, $\overline{fd}$, of the PbS cell, the output signal as displayed on the cathode-ray oscilloscope (CRO) gives complete information for the temperature distribution at tool-flank surface.

In this figure, it is seen that, immediately after the leading edge of the hole e uncovers the tool tip o, the flank surface would momentarily be exposed to a cold surrounding before it could be seen and scanned by the cell. In order to ascertain the possible drop in temperature due to this unavoidable time delay, tests were conducted for several lengths of $\overline{de}$ under otherwise identical conditions. No noticeable difference in the CRO trace was ob-

served. It was thus concluded that, under the cutting conditions selected for the present investigation, such time delay was of no consequence.

Calibration. Radiation pyrometers are commonly calibrated by using experimental black bodies at known temperatures. When used for nonblack surfaces, the emissivity must be known. Information on the emissivity of cemented-carbide cutting-tool materials at elevated temperatures is virtually nonexistent; hence the present instrument was calibrated by using a carbide strip of identical composition to that used in the cutting tool. The $^3/_{16}$-in-square strip was resistance-heated by a d-c welding machine. Three No. 28 gage chromel-alumel thermocouples were brazed along the length of the carbide strip as illustrated in Fig. 4. The temperature of the end surface is obtained by extrapolating the thermocouple readings. Calibration was done directly on the lathe with the end surface of the carbide strip duplicating the position of the tool flank at which the CRO traces were taken.

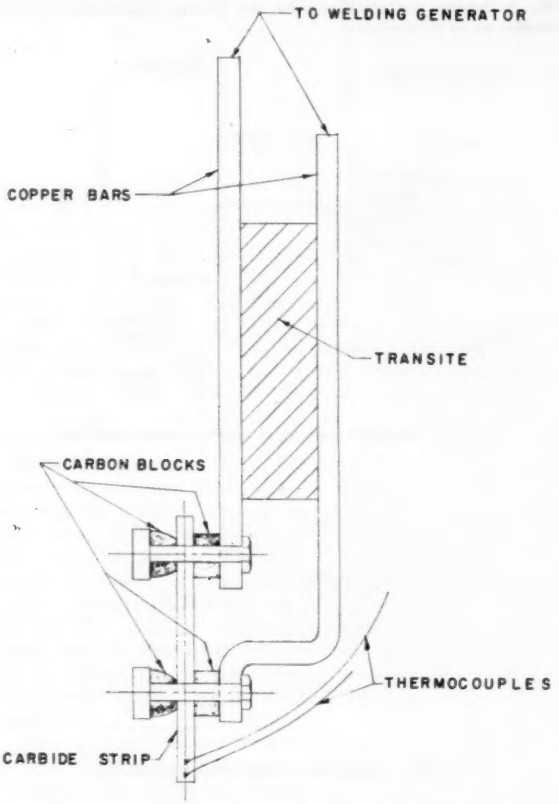

Fig. 4 Electrically heated carbide strip used in calibration

Experimental Results and Their Interpretation. *Sample Photographs of CRO Trace.* Fig. 5 illustrates one of the many CRO traces photographed in this investigation. It corresponds to the steady-state distribution of radiant energy along the tool flank at a cutting speed of 260 fpm and feed of 0.0066 ipr. Other cutting conditions are as indicated.

The bright spot at the lower left corner represents the rest position of the electron beam and may be regarded as the origin of the axes. The internal trigger level of the CRO was suitably adjusted so that when the incoming signal exceeded a certain preset value (1.4 cm in Fig. 5) the main sweep actuates automatically. The minimum trigger setting is dictated by the noise level and it should be set slightly higher than the strongest noise pulse that would be encountered during the test run. It is therefore essential in the present experimentation to suppress the noise as far as possible.

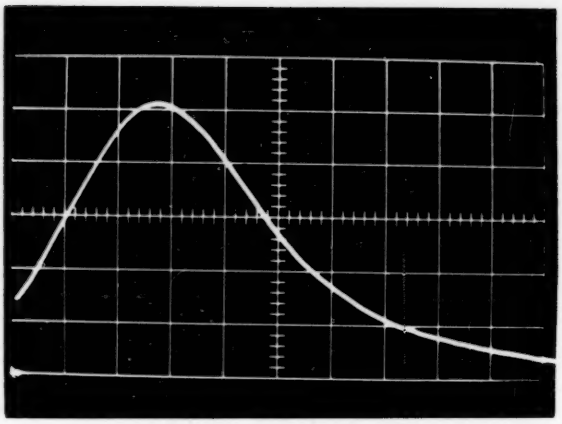

Fig. 5 CRO trace of radiant-energy distribution along flank surface
X-axis: One smallest division represents 40 μs
Y-axis: One smallest division represents 2 mv
Front slit: 0.002 in.
Rear slit: 0.004 in.
Cutting conditions: Work material: AISI 1018 steel
Tool material: K3H carbide
Tool rake: 7 deg
Tool clearance: 7 deg
Feed: 0.0066 ipr
Cutting speed: 260 fpm

Procedure for Obtaining True Radiant-Energy Distribution From the CRO Trace—Approximate Correction for Finite View Field. Referring to Fig. 3(*b*), $\overline{fd}$ represents the extent of the view field of the PbS cell on the flank surface. For theoretically true local temperature measurement, one needs a width of infinitesimal dimension. Under such conditions, however, the very limited radiant energy that the cell could intercept would actually render it useless. An approximate correction procedure was thus adopted to deduce the true energy distribution from the CRO trace obtained with small but still finite-beam width.

As the workpiece rotated, the tool edge *o* would first be sighted by the cell and, at that instant, the leading corner *d* of the view field coincided with *o*. Thereafter, the view field would continue to increase till the trailing corners *f* and *o* were in coincidence. Preceding this position, the signal displayed on the oscilloscope did not represent the actual distribution. In Fig. 6 the distribu-

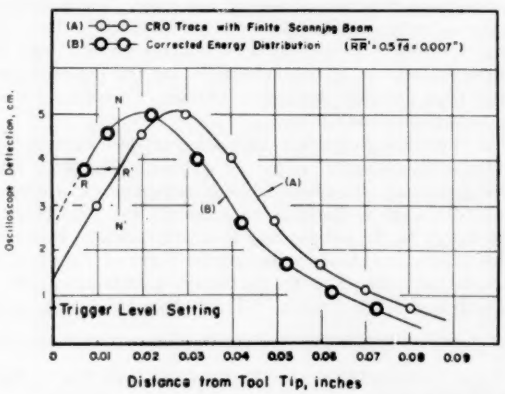
(A) CRO Trace with Finite Scanning Beam
(B) Corrected Energy Distribution
Oscilloscope Deflection, cm.
Trigger Level Setting
Distance from Tool Tip, inches

Fig. 6 Measured and corrected radiant-energy distribution along tool flank

tion labeled A was reproduced directly from the CRO trace without modification. The vertical line NN' gave the location of the corner d at the instant when the trailing corner f coincided with tool edge o. Clearly, the center line of the view field was at a distance $\frac{1}{2}\overline{fd}$ to the left of NN'. The ordinate of R' on the curve would correspond to the average radiant energy emitted at the flank surface over the distance fd from the tool edge o. Hence R' would more correctly represent the local radiant energy at the location $\frac{1}{2}\overline{fd}$ distant from o. The corrected distribution labeled B, Fig. 6, was obtained by displacing the curve A to the left by this amount.

The foregoing analysis was made under the assumption that the electronic beam was instantaneously triggered when the cell saw the edge o. In reality, some time delay was bound to exist. This delay would only shift the origin of the corrected distribution curve toward the left by a small amount and it would not, in any way, influence the shape of the distribution curve.

Results of Measured Flank Temperature Distribution. With the calibrated relation between the radiant energy and temperature available, it is readily possible to determine the distribution of flank-surface temperature from the corrected energy-distribution curve. Fig. 7 shows the results obtained for machining AISI 1018 steel at a cutting speed of 260 fpm and at several feeds. The dotted portion of the curve indicates regions of uncertainty where the energy distribution could not be truthfully evaluated owing to the influence of a continuously changing view field as explained earlier.

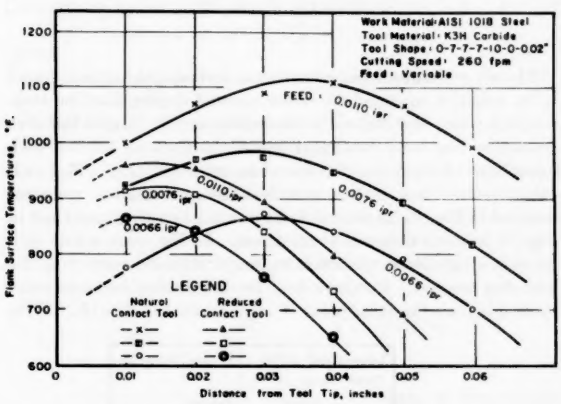

Fig. 7 Tool-flank temperature distribution—constant speed, variable feed

As expected, increasing feed results in an increase of tool-flank temperatures. There is also a gradual shift of the maximum away from the tool edge. Included in the same figure are results obtained with reduced-contact tools under otherwise identical cutting conditions. The natural contact length ranged from 0.025 to 0.032 in., the latter being for the heaviest feed used. Previous tests revealed that, as the tool-chip contact was artificially reduced, the measured *average* interface temperature exhibits a minimum [21], which occurs when the restricted length is approximately $\frac{1}{3}$ of the natural contact length. A fixed length of 0.012 in. was used in the present investigation for reduced-contact tools.

While the reduced-contact tools exhibit lower flank temperatures, the maximum of the temperature curve shifts toward the cutting edge. With cemented-carbide tools in the temperature range involved, such shift will be of little importance in the development of flank wear. On the other hand, if the tool were operating in the temperature-sensitive region, the occurrence of a temperature peak at the proximity of the cutting edge may hasten tool failure. It is pertinent, however, that the data reported herein were obtained from freshly ground tools. Development of wear will undoubtedly alter both the shape and magnitude of the flank temperatures. Research has been under way to investigate such influences.

The effect of cutting speed on local flank temperatures is shown in Fig. 8 for AISI 52100 steel. It is seen that an increase in speed raises the peak temperature and shifts the maximum away from the cutting edge.

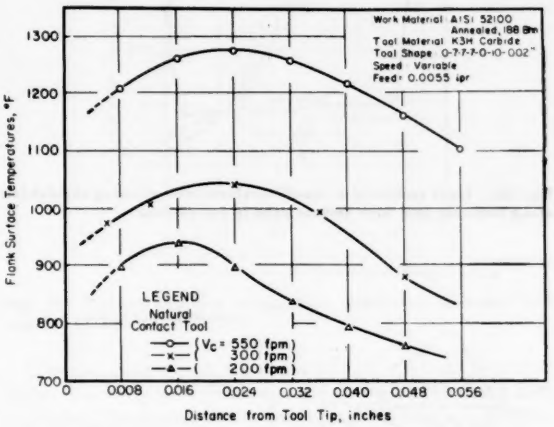

Fig. 8 Tool-flank temperature distribution—constant feed, variable speed

The shape of the flank temperature distribution and the peak temperature as determined by the present technique are believed to be reasonably accurate. They have been demonstrated to be reproducible. However, the location of the peak relative to the sharp tool edge is less reliable and is dictated by the noise level of the system.

Calculation of Local Tool-Chip Interface Temperatures From Measured Flank Temperature

A cross section of the tool used in the present investigation is represented in Fig. 9(a). The length $\overline{OA}$ depicts the extent of tool-chip contact. It may represent a natural contact length on a conventional tool or an artificially constricted length on a controlled contact tool. For purpose of computations $\overline{OA}$ is subdivided into n-segments and the distribution of temperature may be approximated by the block diagram shown in Fig. 9(b). The local temperature at subdivision i is θ_i, where i extends from 1 to n. The remaining tool surfaces are insulated except at the remote region near corner C where the temperature is zero, corresponding to that portion of the tool at ambient temperature, which, for convenience, is taken as the datum. The flank surface of a sharp tool may be regarded as insulated since the heat loss there is small compared to the extremely high heat flux at the tool-chip interface. For a worn tool only that part of the flank which remains intact may be considered insulated. This idealization simplifies the computation.

From the uniqueness theorem in mathematics, it is known that with a prescribed temperature distribution over the boundary $\overline{OA}$ and over the corner region C there is one, and only one, steady temperature distribution in the tool, including that along the insulated boundary. Conversely, if one determines the temperature distribution of a finite length of the insulated boundary, such as that at the flank, the temperature distribution over the tool-chip contact may be found.

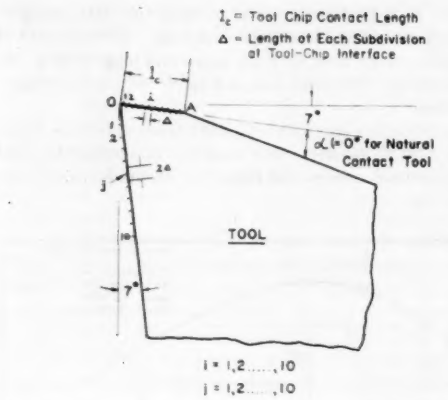

Fig. 9(a) Cross section of a two-dimensional tool, showing subdivision along tool-chip and flank surface used in calculations

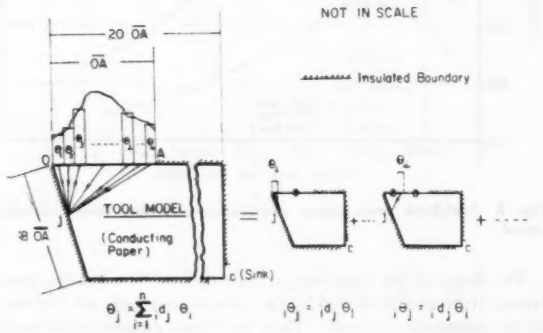

Fig. 9(b) Determination of dimensionless correlation parameter ${}_id_j$ using electric-field plotter

In Fig. 9(*b*) let ${}_i\theta_j$ be the temperature at any arbitrary location j on the tool flank due to a hypothetical temperature distribution of zero degrees everywhere over the tool-chip contact, except at the subdivision i where the temperature is θ_i. In equation form, the relationship between θ_i and ${}_i\theta_j$ is as follows:

$$ {}_i\theta_j = {}_id_j\theta_i \qquad (1) $$

in which the dimensionless correlation parameter ${}_id_j$ may be conveniently determined by using the electric analog plotter. Clearly, it depends on the geometry of the tool and conditions at the rest of the boundary.

Since the problem is a linear one, application of the principle of superposition yields an expression for the resultant temperature at j due to a stepwise temperature distribution over $\overline{OA}$ as:

$$ \theta_j = \sum_{i=1}^{n} {}_id_j\theta_i \qquad (j = 1, 2, \ldots n) \qquad (2) $$

This method of superposition is illustrated in Fig. 9(*b*).

The various temperatures θ_j were obtained from the measured distribution at the tool flank as described in the preceding section. When these were substituted into equation (2), one obtains n simultaneous, linear, algebraic equations with n unknown θ_i's. The subdivision width at the tool flank is selected to be twice that at the tool-chip interface, partly for convenience and partly from the consideration of the extent of the measured flank temperatures.

For the tool geometry and boundary conditions shown in Figs. 9(*a*) and (*b*), the dimensionless distance parameters ${}_id_j$'s have been measured and are listed in Table 1. The major source of error in determining the ${}_id_j$'s is due to the anisotropic nature of the "Teledeltos" conducting paper used in the electrical measurement. This may be identified readily by summing up all the ${}_id_j$'s in any horizontal row and comparing the result with that obtained from a single measurement in which the entire surface $\overline{OA}$ is subjected to a uniform potential identical to that used in each individual measurement. A discrepancy of 2 per cent is oftentimes observed.

Table 1 Dimensionless correlation parameters and measured local tool-flank surface temperatures

	Dimensionless Correlation Parameter, ${}_id_j$, Location Along Tool-Chip Interface										Local Flank Surface Temp. θ_{fj}, °F*
j \ i	1	2	3	4	5	6	7	8	9	10	
1	.179	.191	.141	.115	.081	.068	.053	.049	.047	.079	750
2	.103	.127	.111	.109	.094	.085	.073	.071	.071	.125	765
3	.077	.090	.090	.095	.089	.087	.080	.083	.082	.159	775
4	.064	.081	.077	.081	.083	.083	.081	.087	.096	.183	780
5	.056	.072	.068	.076	.076	.079	.079	.089	.100	.197	785
6	.051	.066	.063	.070	.072	.076	.077	.088	.101	.205	790
7	.048	.061	.059	.066	.068	.073	.075	.087	.102	.211	790
8	.045	.058	.056	.063	.065	.071	.073	.086	.102	.213	790
9	.043	.056	.054	.061	.063	.069	.072	.085	.101	.211	785
10	.042	.053	.052	.060	.062	.067	.071	.084	.100	.211	775

*Room Temperature, θ_0 = 75°F, is used as the datum.

The set of simultaneous equations so formulated has been found to be sensitive to round-off errors injected during machine computation; i.e., the system is "ill-conditioned." A new iterative procedure has been developed by the authors for solving such equations. Details may be found in reference [22]. The tool-chip-interface temperature distributions so evaluated are summarized in Fig. 10 for several feeds at a fixed cutting speed and in Fig. 11 for several speeds at fixed feed. In Fig. 10 it is seen that there is a significant reduction in temperature by restricting the tool-chip contact. Furthermore, the distribution becomes more favorable from the standpoint of improvement in tool life. With

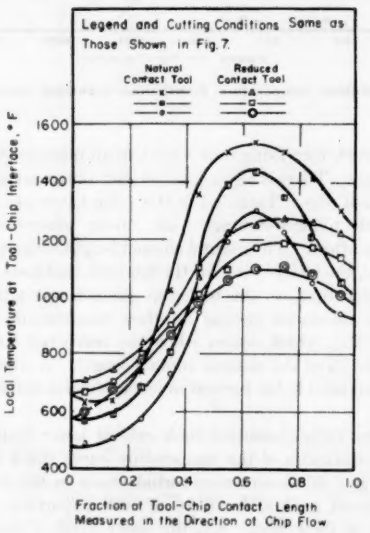

Fig. 10 Tool-chip-interface temperature distribution—constant speed variable feed

the natural contact tools, the peak in the temperature curve occurs at about 65 per cent of the contact length measured from the cutting edge. It increases to about 75 per cent for the reduced-contact tools. The reduction in the peak temperature is some 200 to 250 deg F for controlled-contact tools, while in the immediate vicinity of the cutting edge, there is a slight increase when compared to natural-contact tools with all other conditions fixed. This suggests that the wear on a reduced contact tool would be relatively more uniform than that of a conventional tool. Experimental evidence is needed to verify this prediction.

Fig. 11 shows the marked rise in interface temperature and a shift of the peak toward the trailing edge as speed increases. It is interesting to note that the extrapolated values of temperature at the cutting edge closely approach the shear-zone temperature.

Distribution of Frictional Energy Dissipation Over Tool-Chip Contact

Heat Flux Entering Tool. When the tool-chip-interface temperature distribution is evaluated, the local heat flux entering the tool may be determined conveniently by a method suggested by Bonneville [23]. In this method, one measures the current flowing into the model tool as shown in Fig. 9(*b*) at locations 1 to n due to a fixed voltage applied at an arbitrary location i while the rest of the interface and the remote corner region C are grounded. From the analogy between heat and current flow in purely dissipative circuits, one has

$$q_{t\cdot m} = K \sum_{i=1}^{n} {}_{i}f_{m}\,\theta_{i} \qquad (3)$$

where

$q_{t\cdot m}$ = local heat flux entering tool at location m, Btu/min-sq in.

θ_i = local interface temperature at location i, deg F, measured above room temperature, θ_0

${}_{i}f_{m}$ = so-called influence coefficient; it is current flowing into model at location m due to a unit potential applied at location i as explained above, milliamp/volt

K = conversion constant; it is ratio of electrical resistance of model to thermal resistance of tool. For reduced-contact tool, K equals

$$8.31 \frac{\text{Btu}}{(\text{min})(\text{in.}^2)(\text{deg F})} \Big/ \frac{\text{milliampere}}{\text{volt}}$$

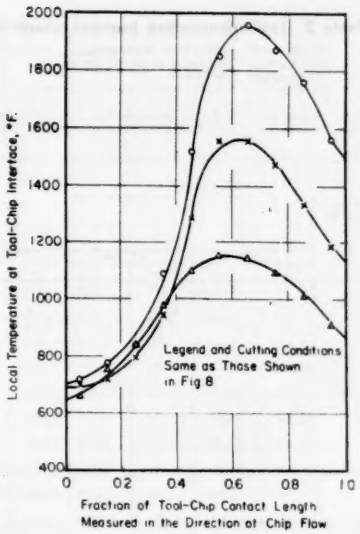

Fig. 11 Tool-chip-interface temperature distribution—constant feed, variable speed

It varies slightly with the contact length for natural-contact tools. The local heat flux entering the tool as calculated from equation (3) is shown in the (*a*) columns of Tables 2 and 3, for the cutting conditions indicated.

Heat Flux Entering Chip. Computational procedure for the local heat flux entering the chip from the known distribution of interface temperatures can be found in the literature [17, 18]. The set of final working equations is

$$\sum_{m=1}^{n} q_{c.m}({}_{m}I_{i}) = \frac{c_c \rho \pi v_f}{2} (\theta_i - \Delta\tilde{\theta}_s) \qquad (4)$$

$$i = 1, 2 \ldots n$$

where

$q_{c.m}$ = local heat flux entering chip at location m, Btu/(min) (sq in.)

${}_{m}I_{i}$ = dimensionless parameter defined by equation (2) in reference [18]

Table 2 Tool-chip-interface heat-flux distribution

Constant Cutting Speed: 260 fpm, Feed: Variable
Work Material: AISI 1018 Steel
Tool Material: K3H Carbide
Tool Shape: 0-7-7-10-0-0-0.200", (Reduced Contact Tool, has 0.012 in. contact length).

Column (a): Heat Flux entering Tool, Btu/(min)(in.^{2})
Column (b): Heat Flux entering Chip, Btu/(min)(in.^{2})

Interface Location i	CONVENTIONAL TOOL						REDUCED CONTACT TOOL					
	Feed = 0.0066 ipr		Feed = 0.0076 ipr		Feed = 0.011" ipr		Feed = 0.0076 ipr		Feed = 0.0076 ipr		Feed = 0.0110 ipr.	
	(a)	(b)	(a)	(b)	(a)	(b)	(a)	(b)	(a)	(b)	(a)	(b)
1	410	420	680	2100	840	3,170	75	7,300	1,900	19,200	1,600	23,200
2	380	180	450	580	610	790	680	2,030	900	2,600	1,240	5,200
3	1290	2100	1220	3110	1600	3,900	2620	7,010	2,300	9,150	2,150	12,100
4	1370	4080	2060	5600	2240	8,400	3550	7,200	2,500	9,030	2,960	15,600
5	4780	6780	5380	8260	6180	11,800	5400	10,300	4,560	14,200	5,160	20,200
6	7160	8400	9260	11400	10300	16,600	5500	8,900	5,400	15,900	6,880	21,600
7	6780	7440	8550	7620	9150	8,800	5750	8,100	4,900	14,200	5,720	20,100
8	7100	3420	7080	3010	8900	5,100	6560	6,600	5,960	13,300	6,100	16,500
9	5300	90	6230	1090	8800	1,390	5060	3,980	8,600	12,200	6,620	13,200
10	2500	60	2800	770	6900	590	2100	250	4,900	7,300	5,100	10,100

Table 3 Tool-chip-interface heat-flux distribution

Constant Feed: 0.0055 ipr. Cutting Speed: Variable
Work Material: Annealed AISI 52100, 188 Bhn.
Tool Material: K3H Carbide
Tool Shape: 0-7-7-7-10-0-0.0300", Conventional Tool

Column (a): Heat Flux Entering Tool, Btu/(min)(in^2)
Column (b): Heat Flux Entering Chip, Btu/(min)(in^2)

Interface Location i	CONVENTIONAL TOOL					
	550 fpm.		300 fpm.		200 fpm.	
	(a)	(b)	(a)	(b)	(a)	(b)
1	380	4,640	800	1,700	580	1,190
2	920	3,940	400	550	2,360	2,730
3	3,010	4,920	800	1,270	2,600	3,250
4	3,700	15,400	920	8,070	2,300	8,960
5	8,770	27,200	12,700	17,600	5,800	9,010
6	11,500	28,800	10,200	15,200	7,560	9,480
7	10,400	21,800	7,400	8,850	6,400	6,580
8	10,100	12,200	9,660	8,240	7,800	4,900
9	9,700	6,200	6,100	1,000	3,010	170
10	3,600	400	2,900	910	1,500	90

$c_w\rho$ = volumetric heat capacity of chip material, Btu/(cu in.) (deg F)
v_f = chip-flow velocity, ipm
θ_i = local interface temperature at location i, deg F, above room temperature, θ_0
$\Delta\bar{\theta}_s$ = average bulk-temperature rise above θ_0 of chip as it leaves shear zone, deg F

The local heat flux entering the chip, calculated from equation (4) is listed in the (*b*) columns of Tables 2 and 3.

The heat flux, evaluated by equations (3) and (4), at locations near the cutting edge is sensitive to errors in the influence coefficient (due to the close proximity of points on the flank and rake surfaces near the cutting edge). Hence the heat flux at such locations should be construed as the trend rather than a true value. This is not the case at positions farther removed from the cutting edge.

The algebraic sum of the two heat fluxes as just computed gives the total heat-flux distribution at the tool-chip sliding interface. It is illustrated in Figs. 12(*a*) and (*b*) for the respective conditions shown. According to the results of this investigation the distribution is quite nonuniform indeed. Comparatively speaking, the natural-contact tools exhibit a more nonuniform distribution. On the other hand, the reduced-contact tools display a high local heat flux in the vicinity of the cutting edge, followed by a sharp drop at locations away from the edge.

If it is assumed that all of the mechanical work at the interface is available as sensible heat and that the chip sliding velocity is uniform, i.e., local fluctuations due to stick-slip phenomena are neglected, the distribution of the frictional sliding stress will have the same shape as that of the total heat flux. Calculations reveal local stresses in excess of the dynamic shear stress, which is most unlikely and suggests local stick-slip conditions. Further study is necessary to confirm the present results from thermal energy considerations.

The total frictional force acting on the top surface of the tool can be obtained by integration. Table 4 compares the results of this computation with direct dynamometer readings.

It is seen that the two are in close agreement except for the one case in which the heaviest feed was used in conjunction with the natural-contact tool.

The reduction in tool-chip frictional force using a reduced-contact tool is substantial. For instance, at a feed of 0.0066 ipr, the reduction is about 40 per cent, Table 4. At larger feeds, the reduction is even higher; e.g., 54 per cent at a feed of 0.011 ipr. Similar findings have been reported earlier by the authors [21].

Conclusions

1 This paper describes the use of infrared radiation detectors for the measurement of tool-flank temperatures. A method is developed by which the tool-chip-interface temperature distribution can be calculated from measured flank temperatures. The technique has general application in the determination of temperatures at surfaces which are inaccessible.

2 The measured tool-flank temperature distribution is nonuniform, the peak occurring some distance from the cutting edge.

3 The tool-chip-interface temperature distribution, calculated

Table 4 Comparison of tool frictional force obtained from thermal considerations and from direct dynamometer measurement

(A) Work material: AISI 1018 Steel; Tool material: K3H Carbide; Tool shape: 0-7-7-7-10-0-0.02 in.; Cutting speed: 260 fpm; Feed: Variable			Tool surface frictional force, lb: Computed from interface heat flux	Tool surface frictional force, lb: Measured from tool-force dynamometer
Controlled-contact tool; contact length, 0.012 in.	Feed, ipr	0.0066	88	87
		0.0076	102	110
		0.0110	121	129
Conventional tool; natural-contact length, 0.025–0.032 in.	Feed, ipr	0.0066	144	151
		0.0076	181	180
		0.0110	280	261

(B) Work material: AISI 52100 Steel, annealed, 188 Bhn; Tool material: K3H Carbide; Conventional Tool Shape: 0-7-7-7-0-10-0.02 in.; Cutting Speed: Variable; Feed: 0.0055 ipr		Tool surface frictional force, lb: Computed from interface heat flux	Tool surface frictional force, lb: Measured from tool-force dynamometer
Cutting speed, fpm	200	156	160
	300	141	134
	550	127	120

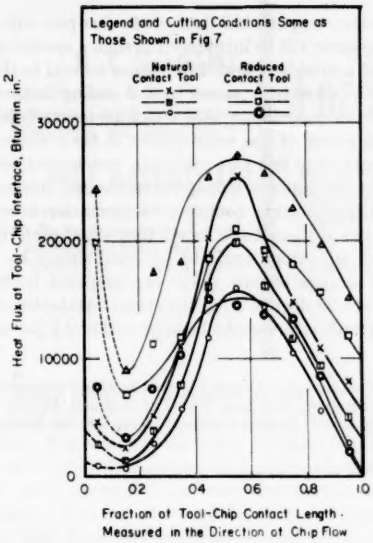

Fig. 12(a) Total heat-flux distribution at tool-chip interface—constant speed, variable feed

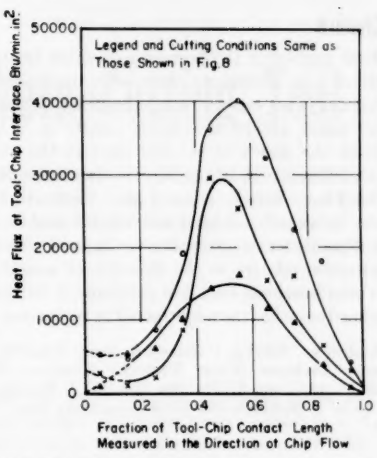

Fig. 12(b) Total heat-flux distribution at tool-chip interface—constant feed, variable speed

by the method presented, is likewise nonuniform and in agreement with known crater wear patterns.

4 The frictional force on the tool-rake surface deduced from thermal-energy considerations agrees closely with direct dynamometer measurements.

5 The frictional force, calculated and measured, is 40 to 50 per cent lower with reduced-contact tools when compared to conventional tools with all other conditions unchanged.

Acknowledgments

The authors express their appreciation to the Office of Ordnance Research, U. S. Army, for support of the program; to Kennametal Inc., Latrobe, Pa., for the carbide tools; and to The Timken Roller Bearing Co., Canton, Ohio, for the 52100 tubing used in the investigation.

References

1 H. Shore, "Thermoelectric Measurement of Cutting Tool Temperatures," *Journal of Washington Academy of Science*, vol. 15, 1925, pp. 85–88.

2 K. Gottwein, "Die Messung der Schneidentemperatur beim Abdrehen von Flusseisen," *Maschinenbau*, 1925, pp. 1129–1135.

3 E. G. Herbert, "The Measurement of Cutting Temperatures," *Proceedings of The Institution of Mechanical Engineers*, vol. 1, 1926, pp. 289–329.

4 H. A. Schwartz and W. W. Flagle, "Significance of Tool Temperatures," *Proceedings, ASTM*, vol. 23, 1923, pp. 27–39.

5 H. Axer, "Temperaturfeld und electro-chemischer Verschleiss am Drehmeissel," 6 Aachen Werkzeugmaschinen Kolloquim, Verlag W. Girardet, Essen, Germany, 1953, pp. 23–26.

6 K. J. Kusters, "Das Temperaturfeld in Drehmeissel," Verlag W. Girardet, Essen, Germany, 1954, pp. 67–71.

7 H. M. Danielian, "Heat and Tool Wear in Metal Cutting," Moscow, Mashgis, 1954.

8 D. L. Rall and W. H. Giedt, "Heat Transfer to, and Temperature Distribution in, a Metal Cutting Tool," TRANS. ASME, vol. 78, 1956, pp. 1507–1605.

9 N. H. Cook, "Cutting Tool Temperatures," ASTE Paper No. 21, 1957.

10 F. P. Bowden, "The Physics of Rubbing Surfaces," *Journal of the Royal Society NSW*, vol. 78, 1944, pp. 187–195.

11 H. Schallbroch and M. Lang, "Messung der Schnittemperatur mittels Temperaturanzeigender Farbanstriche," *Zeitschrift des Vereines Deutscher Ingenieure*, vol. 87, 1943, pp. 15–19.

12 G. Pahlitzsch and H. Helmerdig, "Das Temperaturfeld am Drehmeissel waermetechnische betrachtet," *Zeitschrift des Vereines Deutscher Ingenieure*, vol. 87, 1943, pp. 564–571, 691–698.

13 E. Bickel and W. Widmer, "Die Temperaturen an der Werkzeugschneide," Industrielle Organization, Zurich, Switzerland, 1954.

14 R. C. Parker and P. R. Marshall, "The Measurement of the Temperature of Sliding Surfaces With Particular Reference to Railway Brake Blocks," *Proceedings of The Institution of Mechanical Engineers*, vol. 158, 1948, pp. 209–229.

15 F. P. Bowden and P. H. Thomas, "The Surface Temperature of Sliding Solids," *Proceedings of The Royal Society of London*, series A, vol. 223, 1954, pp. 29–40.

16 G. S. Reichenbach, "Experimental Measurement of Metal-Cutting Temperature Distributions," TRANS. ASME, vol. 80, 1958, pp. 525–546.

17 B. T. Chao and K. J. Trigger, "Temperature Distribution at the Tool-Chip Interface in Metal Cutting," TRANS. ASME, vol. 77, 1955, pp. 1107–1121.

18 B. T. Chao and K. J. Trigger, "Temperature Distribution at Tool-Chip and Tool-Work Interface in Metal Cutting," TRANS. ASME, vol. 80, 1958, pp. 311–320.

19 B. T. Chao, H. L. Li, and K. J. Trigger, "The Influence of Tool Geometry on Interface Temperature," ME Technical Report, ORD-1980-4, University of Illinois, April, 1957.

20 B. T. Chao, H. L. Li, and K. J. Trigger, "Experimental Determination of Temperature Distribution at Tool Flank and Evaluation of Frictional Energy Distribution Over Tool-Chip Contact," ME Technical Report, ORD-1980-5, University of Illinois, March, 1958.

21 B. T. Chao and K. J. Trigger, "Controlled Contact Cutting Tools," TRANS. ASME, Series B, JOURNAL OF ENGINEERING FOR INDUSTRY, vol. 81, 1959, pp. 139–151.

22 B. T. Chao, H. L. Li, and K. J. Trigger, "On the Solution of Ill-Conditioned, Algebraic, Linear, Simultaneous Equations by Machine Computation," ME Technical Report, ORD-1980-7, University of Illinois, June, 1959.

23 J. M. Bonneville, "The Method of Indirect Analog and Its Application in Complex Two Dimensional Heat Transfer Problems," ScD thesis, Massachusetts Institute of Technology, January, 1955.

DISCUSSION

Mrs. F. F. Buckland[6]

The usefulness of "Teledeltos" conducting paper in making flux plots is widely recognized. It is perfectly satisfactory for the commercial use for which it is designed. However, its anisotropy, i.e., difference in conductivity between the rolling direction and the transverse direction, may amount to 10 per cent or more, and result in skewing the flux plot.

The authors state that a discrepancy of 2 per cent is oftentimes observed. This seems rather small in comparison with the large variation noted in the foregoing. How did the authors get around the difficulty?

[6] Heat Transfer Applications Engineer, Mechanical Engineering Laboratory, General Electric Company, Schenectady, N. Y. Mem. ASME.

Authors' Closure

The authors appreciate the pertinent question brought up by Mrs. Buckland. In literature,[7] errors due to anisotropy have been discussed. The current manufacturing process of the "Teledeltos" paper almost invariably results in a higher resistivity across the width of the roll than in the longitudinal direction. A difference of 10 per cent is oftentimes observed as Mrs. Buckland has correctly pointed out. However, the extent to which the measured potential distribution and current flow are in error depends on the geometric configuration of the object and its orientation relative to the direction of anisotropy. For instance, in uni-directional heat flow problems, if the lines of heat flow are confined to either the longitudinal or transverse directions of the roll, the equipotential lines or the flux plot will not be distorted. No error will be introduced in such a special case. More generally, if a solid is bounded by planes normal to the principal axes of the conductivity tensor and if scaling factors are introduced into the co-ordinate axes which are inversely proportional to the square root of the conductivity in their respective directions, distortions in flux plot can again be removed, assuming, of course, that the paper is homogeneous though anisotropic. For irregular-shaped objects, complete compensation is not possible. However, the authors have found that significant reduction of error due to anisotropy could be achieved simply by taking the arithmetic average of two plots—one prepared from paper rotated through 90 degrees from the other. Maheshwari[8] reported that anisotropic errors could be kept within 2.5 per cent by this technique.

[7] R. V. Andrews, "Solving Conduction Heat Transfer Problems With Electric Analogue Shape Factors," *Chemical Engineering Progress*, vol. 51, 1955, pp. 67–73. See also, W. J. Karplus, "Analog Simulation," Ch. 5 McGraw-Hill Book Company, Inc., New York, N. Y., 1958.

[8] B. L. Maheshwari, "Direct Electric Analog Techniques and Their Accuracy in Solving One and Two Dimensional, Steady Heat Conduction Problems," master's thesis, University of Illinois, 1957.

H. T. McADAMS
Principal Physicist, Applied Physics Department, Cornell Aeronautical Laboratory, Inc., Buffalo, N. Y.

PAUL ROSENTHAL
Head, Mechanical Engineering Section, Applied Physics Department, Cornell Aeronautical Laboratory, Inc., Buffalo, N. Y. Mem. ASME

Forces on a Worn Cutting Tool

The forces on a single-point cutting tool under conditions of progressive flank wear are analyzed under the assumptions of constant rake, friction, and shear angle. Relations between wear land area and stock removal rate are derived for the case of constant feed force. For the case of constant depth of cut, the relation between wear land area and feed force is developed.

SINCE the classical work of Taylor [1],[1] tool wear has been recognized as a fundamental factor in the economics of metal cutting. For example, the curve relating tool life and cutting speed is of basic importance in establishing the optimum schedule of tool replacement for either maximum production or minimum cost. This fact has been particularly emphasized by Gilbert [2], who developed practical criteria for optimum tool life in terms of feed, cutting speed, machinability of the work material, type of tool, and other pertinent parameters in the cutting process.

A cutting tool exhibits at least two types of wear: crater wear and flank wear. Because of its predominant importance in most applications, flank wear is a widely used criterion for evaluating tool life, an arbitrary length of the wear land—e.g., 0.030 inch—being used to establish the useful tool life.

More recently, interest in accelerated measurement of tool life has been evidenced, and the advantages of continuously assessing tool wear during the cutting operation has been noted. For example, Mennell and Jeffery [3] investigated the feasibility of using, as a tool-life criterion, the percentage increase in feed force on the cutting tool. Merchant [4] enumerated, among factors known to be to some extent indicative of tool wear, power, temperature at the tool-workpiece interface, noise, surface finish, dimensional change of the workpiece, vibration, and feed force, and suggested that by sensing one or more of these quantities one might use the data in a closed-loop system continuously to optimize the cutting operation.

Although extensive practical experience and a number of experimental studies, such as that of Kobayashi and Thomsen [5], indicate that flank wear is strongly related to the increase in force on the tool, many of the theoretical implications of such a relation have not been explicitly enunciated. In the following development, the conventional model of the metal-cutting process, as envisioned by Merchant [6] for an ideally sharp tool, is extended to a tool exhibiting flank wear.

Force Analysis

In the conventional analysis of the forces on a cutting tool a continuous chip is assumed, and variation of rake angle as the result of crater wear on the tool face or a built-up edge on the tool tip is ignored. In spite of these idealizations, which may depart rather significantly from actual practice, the classical model of the cutting process has provided considerable understanding of the metal-cutting mechanism. In this paper the usual assumptions are retained, and to these are added certain assumptions regarding the tool wear process. As in the case of the nonwearing tool, certain of these assumptions will not always be fulfilled, but it is believed that a mathematical analysis of even a highly idealized model of the cutting operation can shed much light on the implications of tool wear in metal cutting.

[1] Numbers in brackets designate References at end of paper.

Contributed by the Metal Processing Research Activity, Production Engineering Division, and presented at the Winter Annual Meeting, New York, N. Y., November 27–December 2, 1960, of THE AMERICAN SOCIETY OF MECHANICAL ENGINEERS. Manuscript received at ASME Headquarters, July 26, 1960. Paper No. 60—WA-86.

Nomenclature

a_c = chip cross-sectional area before development of wear land
a_{cc} = chip cross-sectional area after development of wear land
a_L = area of wear land
a_r = real contact area of wear land
a_S = area of shear plane before development of wear land
a_{SS} = area of shear plane after development of wear land
d_o = original depth of cut
d = depth of cut after development of wear land
F_H = total horizontal force
F_{HS} = horizontal force on shear plane; cutting force
F_{HW} = horizontal force on wear land; rubbing force
F_S = original shear force on shear plane
F_{SS} = shear force on shear plane after development of wear land
F_V = total vertical force; feed force
F_{VS} = vertical force on shear plane
F_{VW} = vertical force on wear land
k = a constant; welded fraction of real contact area
k_1, k_2, k_3, k_4 = constants
m = a constant
$P(T)$ = unit pressure at time T
$P(\infty)$ = unit pressure when cutting has ceased
R, R' = resultant force
S = shear stress
T = time
v = relative speed between work and tool
V = volume of stock removed
$\dot{V}_0$ = original time rate of stock removal
$\dot{V}$ = time rate of stock removal at time T
w = chip width
α = rake angle
β_1, β_2 = friction angle
ϕ = shear angle
τ = mean shear stress on the wear land
σ = mean normal stress on the wear land
μ = coefficient of friction
τ^* = shear stress required to rupture welds
σ^* = normal stress on the real contact area

The cutting configuration considered is as shown in Fig. 1. Orthogonal cutting in a planing-type cutting operation is assumed, the tool initially making a line contact with the new work surface, as shown in Fig. 1(*a*), and removing a chip having a rectangular cross section. Further, it is assumed that, as the tool wears, a wear land develops on the tool flank, as shown in Fig. 1(*b*), so that the worn tool makes an area contact with the new work surface. It is assumed that in all cases the tool mounting is ideally rigid, so that deflections resulting from the applied forces do not need to be taken into account.

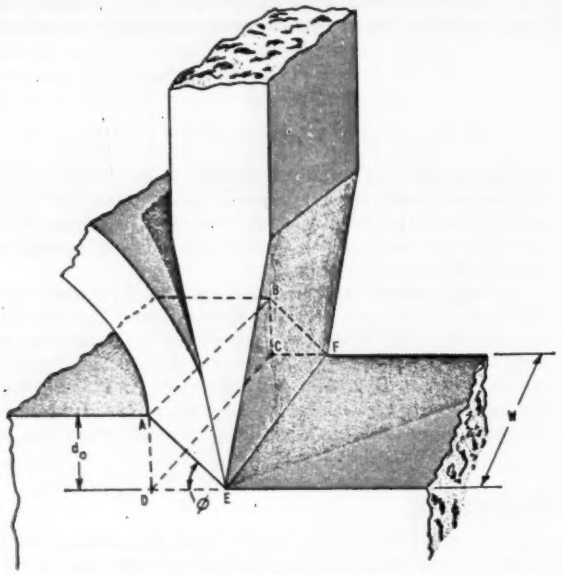

a_c = AREA OF RECTANGLE *ABCD*
a_S = AREA OF RECTANGLE *ABFE*

Fig. 1(a) Orthogonal cutting with a sharp tool

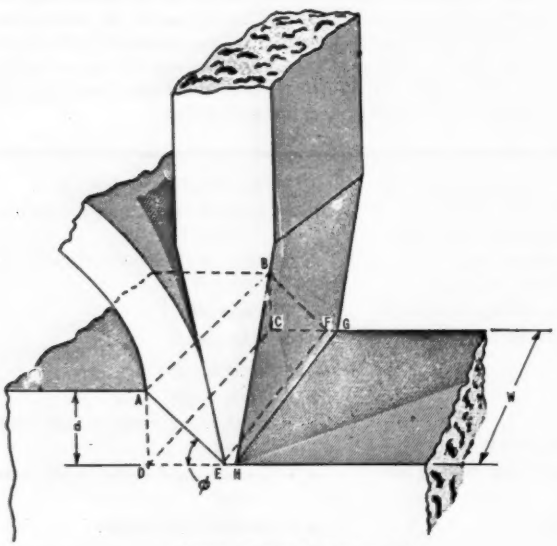

a_{cc} = AREA OF RECTANGLE *ABCD*
a_{SS} = AREA OF RECTANGLE *ABFE*
a_L = AREA OF RECTANGLE *EFGH*

Fig. 1(b) Orthogonal cutting with a dull tool

As analyzed by Merchant, the forces acting on a cutting tool are as shown in Fig. 2(*a*). The chip is held in equilibrium by the action of two equal and opposite resultant forces R and R'. The forces are assumed to be collinear and it is assumed that the chip is of continuous type without built-up edge. The tool is ideally sharp, in that it presents a line contact with the new work surface. The vertical force F_V is the same as the feed force, and the horizontal force F_H on the shear plane is the same as the cutting force.

Such a picture of the cutting process, except possibly during the early life of the tool, is unrealistic because of the tendency of the tool to dull with time. As shown in Fig. 2(*b*), a more realistic diagram for a worn tool is one in which the feed force acting on the tool is shared between the shear plane and the wear land:

$$F_V = F_{VS} + F_{VW} \tag{1}$$

Feed force = Vertical force on shear plane + Vertical force on wear land

Therefore,

$$F_{VS} = F_V - F_{VW}, \tag{2}$$

and, for a worn tool, the vertical force F_{VS} on the shear plane is less than the applied feed force F_V.

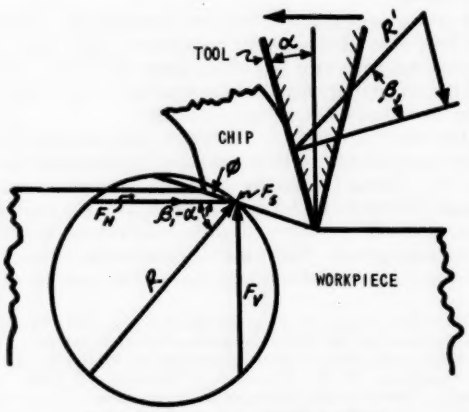

Fig. 2(a) Forces on a nonwearing tool

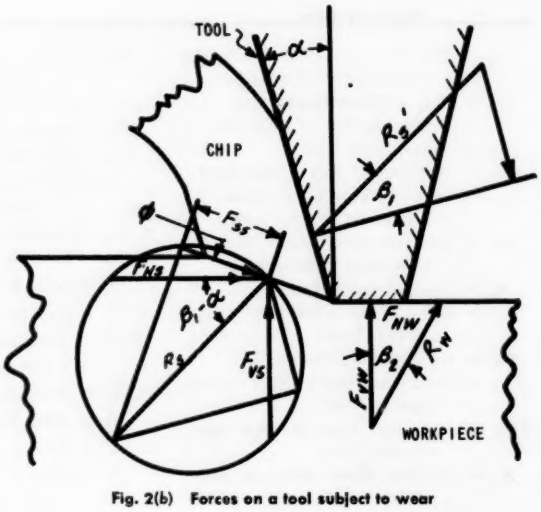

Fig. 2(b) Forces on a tool subject to wear

In Fig. 2(*b*), F_{HS} is the familiar cutting force. Almost collinear with F_{HS} is F_{HW}, the rubbing force between wear land and the new work surface. The moment due to lack of alignment between the two forces is neglected, since the dimensions of the workpiece can be considered large relative to the distance between the shear plane and wear land. The sum of the cutting and rubbing forces is not a constant, if it is assumed that the tool is driven by an electric motor. In an induction motor the speed is essentially constant over a considerable power range. The power is proportional to the torque, the cutting force can assume the value required to cut the chip, and the rubbing force can change according to the friction conditions existing between the tool and the workpiece.

If F_{VS} decreases as a result of an increase in F_{VW}, F_{HS} decreases also. Fig. 3 shows the relation between F_{VS} and F_{HS} for the original condition (*a*) before a wear land had developed and for a worn tool (*b*) in which it is assumed that F_{VS} and F_{HS} decrease proportionally. The angle $\beta_1 - \alpha$ is the difference between the friction angle β_1 between chip and tool face and the rake angle α.

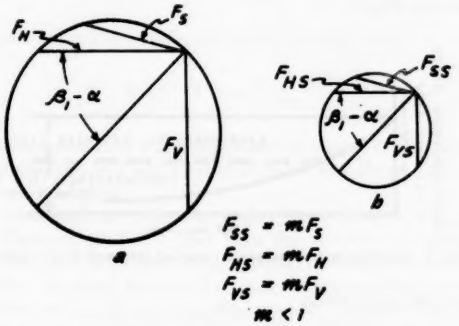

Fig. 3 Effect of tool wear on cutting forces

For the conditions assumed, α, β_1, and ϕ are constant. Therefore,

$$\frac{F_{VS}}{F_V} = \frac{F_{HS}}{F_H} = \frac{F_{SS}}{F_S} = m \tag{3}$$

as shown in Fig. 2. By definition, the shear stress S, considered constant, is

$$S = \frac{F_{SS}}{a_{SS}} = \frac{mF_S}{a_{SS}} = \frac{F_S}{a_S}, \tag{4}$$

where

a_S = original area of the shear plane before development of a wear land

and

a_{SS} = area of the shear plane after development of the wear land

Therefore, $a_{SS} = ma_S$.

As is evident from Fig. 1, the original cross-sectional area of the chip a_c is related to the original area of the shear plane by

$$a_c = a_S \sin \phi.$$

The cross-sectional area of the chip a_{cc} after the development of the wear land is given by

$$a_{cc} = a_{SS} \sin \phi = ma_S \sin \phi. \tag{5}$$

Therefore,

$$\frac{a_{cc}}{a_c} = m. \tag{6}$$

Since the chip width W is assumed constant,

$$\frac{a_{cc}}{a_c} = \frac{Wd}{Wd_o} = m, \tag{7}$$

where d_o is the original depth of cut and d is the depth of cut after development of the wear land. Then,

$$\frac{d}{d_o} = m = \frac{F_{VS}}{F_V}. \tag{8}$$

Equation (8) suggests two possibilities of interest in metal cutting and particularly in grinding. In general, either F_{VS} or F_V can vary with time.

If F_V is held constant, as in billet grinding or snagging, the equation becomes

$$\frac{d(T)}{d_o} = m(T) = \frac{F_{VS}(T)}{F_V} \tag{9}$$

or

$$d(T) = \frac{F_{VS}(T)}{F_V} d_o. \tag{10}$$

Thus, depth of cut is proportional to the vertical force $F_{VS}(T)$ effective on the shear plane. The depth of cut will tend to decrease monotonically with time because of the increase in flank wear.

In cutting at a constant depth of cut, on the other hand, the depth of cut remains substantially constant and so must the effective vertical force on the shear plane. Because of the increasing area of the flank wear land, however, F_V will increase with time, so that the equation becomes

$$\frac{d}{d_o(T)} = m(T) = \frac{F_{VS}}{F_V(T)} \tag{11}$$

$$F_V(T) = \frac{d_o(T)}{d} F_{VS}. \tag{12}$$

Here $d_o(T)$ is a fictitious depth of cut which would have been realized if the feed force $F_V(T)$ required at time T to maintain the fixed depth of cut d had been applied when the tool was ideally sharp.

Constant Feed Force

Let us consider first the case of constant applied feed force. To determine how F_{VS}, the vertical force on the shear plane, varies with time, it is necessary to know F_{VW}, the normal force on the wear land. F_{VW} is determined by the friction between the wear land and the new work surface, on which there is no experimental information. This friction process, however, has certain similarities to that involved in the friction between the chip and the tool face. The same materials are involved, sliding velocities are of the same order of magnitude, and in both cases the tool rubs against a nascent surface.

According to Shaw and Finnie [7], the coefficient of friction between chip and tool is given by

$$\mu = \frac{\text{Friction force}}{\text{Normal force}} = \frac{\tau^* k a_r}{\sigma^* a_r} = k \frac{\tau^*}{\sigma^*} \tag{13}$$

where

a_r = the real contact area
k = the welded fraction of the real contact area
τ^* = the shear stress required to rupture the welds
σ^* = the normal stress on the real contact area

According to the afore-mentioned investigators, μ is variable in metal cutting, and its values are higher than the values obtained

in the ordinary sliding process. The real contact area increases with the normal force.

In (13), the friction force is defined in terms of the welded real contact area ka_r and the stress τ^* required to rupture the welds. Therefore,

$$F_{HW} = k\tau^* a_r \tag{14}$$

In terms of the mean shear stress τ on the wear land, the friction force F_{HW} is given by

$$F_{HW} = \tau a_L \tag{15}$$

From (14) and (15),

$$k\tau^* a_r = \tau a_L \tag{16}$$

or

$$\tau = k\tau^* \frac{a_r}{a_L} \tag{17}$$

where a_r/a_L is the ratio of the real to the apparent area of contact between tool flank and new work surface. If τ^*, k, and a_r/a_L are assumed constant, τ is constant, and the friction force F_{HW} is proportional to the area of the wear land.

Since

$$F_{HW} = F_{VW} \tan \beta_2, \tag{18}$$

one can write

$$\tau a_L = F_{VW} \tan \beta_2 \tag{19}$$

or

$$F_{VW} = \frac{\tau a_L}{\tan \beta_2}. \tag{20}$$

Since

$$F_{VS} = F_V - F_{VW},$$

then

$$F_{VS} = F_V - \frac{\tau a_L}{\tan \beta_2}. \tag{21}$$

Then, since

$$d(T) = \frac{F_{VS}(T)}{F_V} d_0, \tag{22}$$

one can write

$$d(T) = d_0 \left[1 - \frac{\tau a_L(T)}{F_V \tan \beta_2} \right] \tag{23}$$

where $a_L(T)$ is a function of time and F_V is fixed. Therefore, if the cutting tool moves with a velocity v relative to the workpiece, the volume cutting rate $\dot{V} = dV/dT$ is related to the total wear land area by

$$\dot{V} = vwd(T) = vwd_0 \left[1 - \frac{\tau a_L(T)}{F_V \tan \beta_2} \right] \tag{24}$$

or, in terms of lumped constants,

$$\dot{V} = k_1 - k_2 a_L(T) \tag{25}$$

or

$$a_L(T) = k_3 - k_4 \dot{V}(T). \tag{26}$$

As $T \to \infty$, $\dot{V} \to 0$, and $a_L(T) \to k_3$; therefore, k_3 can be interpreted as the final area $a_L(\infty)$ of the wear land when cutting ceases. At $T = 0$, it may be assumed that no wear has taken place. Therefore,

$$k_3 - k_4 \dot{V}_0 = 0, \tag{27}$$

or

$$k_4 = \frac{k_3}{\dot{V}_0} = \frac{a_L(\infty)}{\dot{V}_0}. \tag{28}$$

Thus,

$$k_4 = \frac{\text{Final wear land area}}{\text{Initial stock removal rate}}.$$

Substitution in (26) then gives

$$a_L(T) = a_L(\infty) - \frac{a_L(\infty)}{\dot{V}_0} \dot{V} \tag{29}$$

or,

$$\frac{a_L(T)}{a_L(\infty)} = 1 - \frac{\dot{V}}{\dot{V}_0}. \tag{30}$$

Therefore,

$$\frac{\text{Wear land area at time } T}{\text{Final wear land area}} = 1 - \frac{\text{Stock removal rate at time } T}{\text{Initial stock removal rate}}.$$

Thus, stock removal rate and wear land area as functions of time may be nondimensionalized. The nondimensionalized stock removal rate curve and the nondimensionalized wear land area curves are complementary or are reflection images of each other, as shown in Fig. 4.

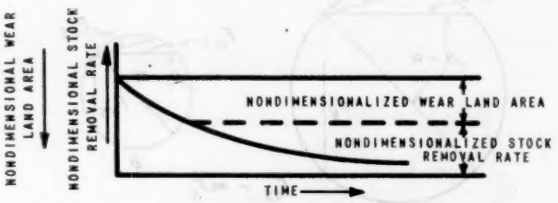

Fig. 4 Relation between stock removal rate and flank wear

From (30) one obtains

$$a_L(T) = \frac{\dot{V}_0 - \dot{V}}{\dot{V}_0} a_L(\infty). \tag{31}$$

Because the feed force F_V is constant, a corresponding relation between stock removal rates and unit pressures can be derived. Dividing both sides of equation (31) into F_V one obtains

$$\frac{F_V}{a_L(T)} = \frac{\dot{V}_0}{\dot{V}_0 - \dot{V}} \frac{F_V}{a_L(\infty)} \tag{32}$$

or

$$P(T) = \frac{\dot{V}_0}{\dot{V}_0 - \dot{V}} P(\infty) \tag{33}$$

where $P(T)$ is the unit pressure at time T, and $P(\infty)$ is the unit pressure when cutting has ceased. When solved for $\dot{V}$, expression (33) becomes

$$\dot{V} = \dot{V}_0 - \frac{P(\infty)}{P(T)} \dot{V}_0 \tag{34}$$

or, in nondimensionalized form,

$$\frac{\dot{V}}{\dot{V}_0} = 1 - \frac{P(\infty)}{P(T)} = \frac{P(T) - P(\infty)}{P(T)}. \tag{35}$$

Thus, it is implied that a minimum unit pressure $P(\infty)$ is required for cutting to occur, and that the cutting rate at any time T is determined largely by the extent to which the unit pressure at that time exceeds this minimum or critical unit pressure. This requirement implies that the tool must be sufficiently hard so that it will not yield under this pressure; otherwise, cutting could not occur.

Qualitative confirmation of equation (34) is afforded by data presented by Kobayashi and Thomsen [5], relating vertical and horizontal forces to feed. Straight-line relations were ob-

tained with nonzero intercepts which depended on the flank clearance angle.

Constant Feed or Depth of Cut

Let us now consider the case of fixed-feed cutting. Since the depth of cut is constant, the effective vertical force F_{VS} on the shear plane must remain constant. Since the rubbing force will change with time, however, so will the vertical force F_{VW} on the wear land. Therefore because of the relation

$$F_V = F_{VS} + F_{VW},$$

the total feed force F_V required to maintain constant depth of cut must vary with time according to the relation

$$F_V(T) = F_{VS} + F_{VW}(T). \tag{36}$$

By the previous argument,

$$F_{VW} = \frac{\tau a_L}{\tan \beta_2}.$$

For constant friction angle, therefore, one can write

$$F_V(T) = F_{VS} + \frac{\tau a_L(\tau)}{\tan \beta_2} \tag{37}$$

if it is assumed that τ is independent of time. Under these assumptions, the feed force would increase as a linear function of the wear land area.

In tests made on tools with controlled wear lands, Kobayashi and Thomsen [5] found that both the vertical and horizontal forces on the tool tend to be substantially linearly related to the length of the flank wear land, except under conditions described by Shaw, et al. [8] as being catastrophic. Catastrophic failure comes about as a result of the softening of the workpiece and possibly of the tool material. In reality, it is likely that τ in equation (37) will be time-dependent. With increasing flank wear, the friction contribution to the energy involved will increase. Since this energy appears largely as heat at the tool-workpiece interface, the workpiece and eventually the tool may tend to soften. This softening, in turn, will affect both k, the welded fraction of the real contact area, and τ^*, the shear stress required to rupture the welds.

Summary and Conclusions

The conventional analysis of forces on an ideally sharp cutting tool has been extended to a tool exhibiting flank wear. If constant tool rake angle, friction angle, and shear angle are assumed, then it can be concluded that tool depth of cut is proportional to that part of the feed force acting on the shear plane. If one assumes that the friction process is adequately described by Shaw and Finnie [7], then at constant applied feed force the depth of cut is a linear function of the area of the flank wear land. Similarly, at a fixed depth of cut, the feed force increases as a linear function of the area of the wear land, provided the shear stress required to rupture the friction welds remains constant and that the welded fraction of the real contact area does not change.

The analysis indicates that a certain minimum critical normal pressure is required for cutting to occur; otherwise the tool will not penetrate the workpiece.

Acknowledgment

The research leading to the results reported in this paper was supported by the Coated Abrasives Division of The Carborundum Company, Niagara Falls, N. Y.

References

1 F. W. Taylor, "On the Art of Cutting Metals," TRANS. ASME, vol. 28, 1907, pp. 31–35.

2 W. W. Gilbert, "Economics of Machining," *Machining Theory and Practice*, American Society for Metals, Cleveland, Ohio, 1950, pp. 465–485.

3 R. F. Mennell and E. A. Jeffery, "Evaluation of Several Lathe Tool-Life Testing Techniques," Paper No. 216, American Society of Tool Engineers.

4 Proceedings of the Exploratory Clinic on New Instrumentation Requirements for Metalcutting, Foundation for Instrumentation Education and Research, Inc., New York, N. Y., September, 1958, pp. 108–112.

5 S. Kobayashi and E. G. Thomsen, "The Role of Friction in Metal Cutting," TRANS. ASME, Series B, JOURNAL OF ENGINEERING FOR INDUSTRY, vol. 82, 1960, pp. 324–332.

6 M. E. Merchant, "Basic Mechanics of the Metal-Cutting Process," *Journal of Applied Mechanics*, vol. 11, TRANS. ASME, vol. 66, 1944, pp. A-168–175

7 M. C. Shaw and I. Finnie, "The Friction Process in Metal Cutting," TRANS. ASME, vol. 78, 1956, pp. 1649–1657.

8 M. C. Shaw, P. A. Smith, N. H. Cook, and E. G. Loewen, "Leaded Steel and the Real Area of Contact in Metal Cutting," TRANS. ASME, vol. 77, 1955, pp. 115–125.

DISCUSSION

Katsundo Hitomi[2]

The authors are to be complimented on their analysis of forces on a worn cutting tool.

In their analysis, they derived equations for two cases—one constant feed forces and the other constant feed or depth of cut. The writer would like to suggest an alternate and more general analysis.

Fig. 5 shows the variation of depth of cut as flank wear occurs with an orthogonal cutting tool with rake angle α and clearance angle γ.

(1) is the initial condition with a sharp tool and depth of cut of t_{10}.

(2) is the condition after some amount of flank wear, l_2, has occurred which reduced the depth of cut by an amount equal to h_2.

[2] Department of Industrial Engineering, Pennsylvania State University, University Park, Pa.

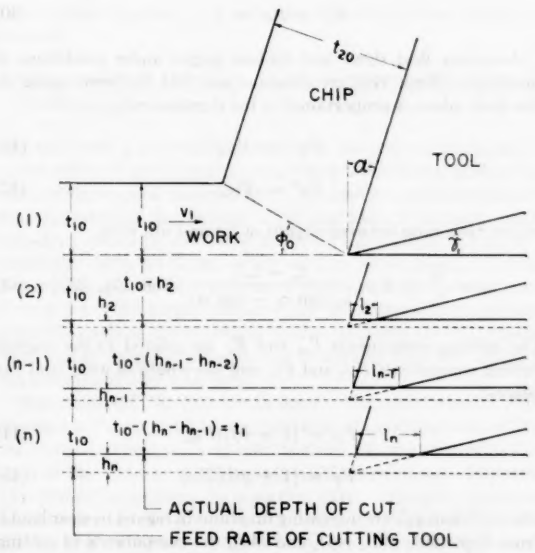

Fig. 5 Variation of depth of cut due to flank wear of cutting tool

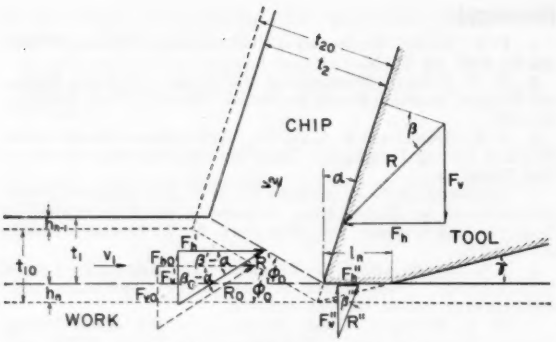

Fig. 6 Analysis of cutting forces acting on a worn tool

The resulting depth of cut equals $t_{10} - h_2$.

In general, if $(n-1)$ and (n) are the $(n-1)$th and nth cuts, the tool has a flank wear land of l_{n-1} and l_n, depth of cut is reduced by h_{n-1} and h_n, respectively, and the nth depth of cut is:

$$t_1 = t_{10} - (h_n - h_{n-1}) = t_{10} - \frac{l_n - l_{n-1}}{\cot\gamma - \tan\alpha}. \quad (38)$$

Fig. 6 shows the forces acting on the cutting tool under initial and nth cutting conditions. Initially, the tool is sharp and no force acts on the flank of the tool. The horizontal and vertical components of force are F_{H0} and F_{V0}, producing the resultant force R_0. In nth cutting condition, the cutting force R (horizontal component F_H and vertical component F_V) is divided into two parts:

(1) Force acting on the shear plane R' (horizontal component F_H' and vertical component F_V') and;

(2) Force acting on the wear land R'' (horizontal component F_H'' and vertical component F_V'').

Since the vector sum of both forces R' and R'' is equal to the resultant force R,

$$F_H' + F_H'' = F_H, \quad (39)$$

$$F_V' + F_V'' = F_V. \quad (40)$$

Assuming that shear and friction angles under conditions of progressive flank wear are constant and that the force acting on the shear plane is proportional to the depth of cut,

$$F_H' = rF_{H0}, \quad (41)$$

$$F_V' = rF_{V0}, \quad (42)$$

where r is a ratio between depths of 1st and nth cuts.

$$r = \frac{t_1}{t_{10}} = 1 - \frac{l_n - l_{n-1}}{t_{10}(\cot\gamma - \tan\alpha)} \quad \text{[from Eq. (38)]} \quad (43)$$

The cutting components F_H and F_V are related to the original cutting components F_{H0} and F_{V0} and the length of wear land l as follows:

$$F_H = [1 + f(l)]F_{H0}, \quad (44)$$

$$F_V = [1 + g(l)]F_{V0}, \quad (45)$$

where $f(l)$ and $g(l)$ are increasing functions in regard to wear land l. From Eqs. (39), (40), (44), and (45), the components of cutting force acting on the wear land, F_H'' and F_V'' are related to the original cutting components F_{H0} and F_{V0} and the length of wear land l.

$$F_H'' = [1 + f(l) - r]F_{H0} \quad (46)$$

$$F_V'' = [1 + g(l) - r]F_{V0} \quad (47)$$

According to Shaw and Finnie, as the authors cited in Eq. (13) in their paper,

$$\tan\beta'' = \frac{F_H''}{F_V''} = \frac{k\tau''}{\sigma''}, \quad (48)$$

where

β'' = friction angle on wear land
k = welded fraction of the real contact area
τ'' = shear stress required to rupture the welds
σ'' = normal stress

and

$$F_V'' = l\sigma'' \quad (49)$$

for unit width of cut.

From Eqs. (48) and (49),

$$F_V'' = \frac{lk\tau''}{\tan\beta''}. \quad (50)$$

Then, from Eqs. (40) and (50),

$$F_V' = F_V - \frac{lk\tau''}{\tan\beta''}. \quad (51)$$

Hence, from Eqs. (42), (43), (45) to (48), and (51),

$$t_1 = t_{10}\left[\frac{F_V}{F_{V0}} - \frac{lk\tau''}{F_{V0}\tan\beta''}\right]$$

$$= t_{10}\left[1 + g(l) - \frac{lk\tau''}{F_{V0}\tan\beta''}\right]$$

$$= t_{10}\left[1 + g(l) - \frac{lk\tau''}{F_{V0}}\,\frac{1 + g(l) - r}{1 + f(l) - r}\right]. \quad (52)$$

The volume cutting rate w expressed in relation to cutting speed v_1 and depth of cut t_1 is

$$w = v_1 t_1$$

$$= v_1 t_{10}\left[1 + g(l) - \frac{lk\tau''}{F_{V0}\tan\beta''}\right]$$

$$= v_1 t_{10}\left[1 + g(l) - \frac{lk\tau''}{F_{V0}}\,\frac{1 + g(l) - r}{1 + f(l) - r}\right]. \quad (53)$$

This is a general equation.

In a particular case, if the components of cutting force expressed in Eqs. (44) and (45) increase linearly with wear land,

$$f(l) = ml \quad (54)$$

and

$$g(l) = nl, \quad (55)$$

where m and n are positive constants. Also, assuming $r = 1$, Eqs. (52) and (53) yield

$$t_1 = t_{10}\left[1 - \left(k\,\frac{n}{m}\,\frac{\tau''}{F_{V0}} - n\right)l\right] \quad (52')$$

and

$$w = v_1 t_{10}\left[1 - \left(k\,\frac{n}{m}\,\frac{\tau''}{F_{V0}} - n\right) l\right]. \qquad (53')$$

In the case of constant feed force as the authors discussed in the first part of their paper, $f(l) = g(l) = 0$, and hence Eqs. (52) and (53) yield

$$t_1 = t_{10}\left(1 - \frac{lk\tau''}{F_{V0}\tan\beta''}\right) \qquad (52'')$$

and

$$w = v_1 t_{10}\left(1 - \frac{k\tau''}{F_{V0}\tan\beta''}\,l\right), \qquad (53'')$$

which are similar to Eqs. (23) and (24) in the authors' paper.

Eqs. (52) and (53) or (52′) and (53′) are general equations in which the increase in tool forces and the decrease in depth of cut or feed rate due to flank wear are taken into consideration. These equations can be applied to the analysis of the cutting mechanism on a worn cutting tool.

W. A. Mohun[3]

Although the authors do not specifically say so, it is implicit in their paper that the land is assumed to be parallel to the direction of motion of the tool and to the newly formed metal surface; we shall refer to this for convenience as a horizontal land. This is, no doubt, the accepted concept of wear lands in the present state of the art. The authors are correct in showing in Fig. 2(*b*) that friction and its associated normal force develop at the wear land as the land comes into existence and grows, but a little reflection will show that this cannot occur if the land is truly horizontal. Fig. 2(*a*) is a representation of the forces on an ideally sharp tool at the first instant of cutting. Initially, with a sharp tool, the resultant force R' exerted by the tool is balanced entirely by the resultant, R, of the forces exerted by the chip on the cutting face of the tool, and, ultimately, by the similar and equal reaction, R, at the shear plane. The forces exerted by the chip on the tool face are dependent upon the depth of cut, upon the rake angle of the tool, upon the ultimate shear stress of the metal, and upon the coefficient of friction between chip and tool. If by legerdemain we suddenly add a horizontal land to the tool, we change none of these conditions at the chip-tool interface and hence we do not change the resultant force exerted by the chip on the tool. All of the feed force F_V continues to be balanced by the forces exerted by the chip and there is no vertical feed force left over to press the land against the new metal surface—that is, no reaction F_{VW} exists, so there can be no friction.

Now, it is true in practice that friction *does* exist between the wear land and the new metal surface; hence the metal surface must exert a resultant force F_{VW} against the land, but the authors fail to show the origin of this force. The introduction of equation (13) into the derivation is unnecessary in explaining decreased depth of cut, and tends to divert attention from the prime cause of decreasing depth of cut with increasing land area under constant feed force. Equation (13) may be removed from equation (24) by combining the latter with equation (20), to give

$$\dot{V} = vwd_o\left[1 - \frac{F_{VW(T)}}{F_V}\right] \qquad (24')$$

Proceeding now with a derivation analogous to that used by the authors, we obtain

$$F_{VW(T)} = k_3 - k_4\dot{V}_{(T)} \qquad (26')$$

$$k_3 = F_{VW(\infty)}$$

$$k_4 = \frac{F_{VW(\infty)}}{\dot{V}_0} \qquad (28')$$

and

$$\frac{F_{VW(T)}}{F_{VW(\infty)}} = 1 - \frac{\dot{V}}{\dot{V}_0} \qquad (30')$$

The decrease in nondimensionalized stock removal rate in Fig. 4 may, therefore, be related to the nondimensionalized increase in F_{VW} just as readily as to the nondimensionalized increase in land area a_L.

By rearranging equation (30′) we obtain

$$\frac{\dot{V}}{\dot{V}_0} = 1 - \frac{F_{VW(T)}}{F_{VW(\infty)}} = \frac{F_{VW(\infty)} - F_{VW(T)}}{F_{VW(\infty)}} \qquad (35a)$$

which should be substituted for equation (35), which it somewhat resembles, for reasons which will appear below.

The writer will very shortly release for publication a series of papers on "Grinding With Abrasive Disks" in which it is shown that the wear land is not truly horizontal. The tool is worn, forming the land, by a process of attrition which is temperature-dependent. Initially, with a sharp tool, heat is released along the shear plane and along the chip-tool interface so that temperature is highest at the front face of the tool, and, after a land develops, temperature falls as one proceeds along the land away from the cutting edge. Friction between the land and the new metal surface mitigates this temperature gradient somewhat, but the rate of attritious wear decreases as one passes from the hot tip of the tool toward the cooler trailing edge of the wear land. Hence the land is not horizontal, but slopes downward toward the trailing edge—this slope the writer has called "attritious camber." Because the land is not horizontal, the trailing edge must elastically depress the new metal surface as the land passes over it. The elastic reaction of the metal surface is the source of the force F_{VW}. It is dependent in magnitude not only upon the area of the land, but also upon the magnitude of the camber. The impending papers will show that the camber need only be of the order of magnitude of one minute of arc to account for the effects observed in grinding with abrasive disks under constant feed force.

Following equation (30′) the authors' word equation may be rephrased

$$\frac{\text{Elastic reaction at time } T}{\text{Final elastic reaction}} = 1 - \frac{\text{Stock removal rate at time } T}{\text{Initial stock removal rate}}$$

and this form is preferable because it is the increase in elastic reaction rather than in the land area which is the direct cause of the diminution in stock removal rate. Because the decrease in stock removal rate and the increase in friction have a common cause, namely, increase in the elastic reaction F_{VW}, there is, of course, a correlation between them, as the authors have shown. The increase in F_{VW} is, in turn, a result of the increase in the land area, a_L, but not in the simple manner which the authors have assumed, since the angle of the attritious camber converts the relationship from one in simple friction to one of applied elasticity which is too complex to deal with here.

Equations (32) to (35) are in error. The unit pressure P on the land is F_{VW}/a_L, not F_V/a_L; and since F_{VW} is not constant (it is zero initially, rising to F_V at infinite time), an operation with F_{VW} such as that used to obtain equation (32) is ruled out. Equation (35) should be replaced by equation (35*a*). There is, therefore, no basis for the statement that a minimum pressure is required for cutting to occur. This is only true in practice because initially the sharp edge of the tool is not a theoretical knife edge,

[3] Industrial Consultant, Toronto, Ontario, Canada; formerly, Director of Research, General Abrasive Company, Inc., Niagara Falls, N. Y.

but has some width corresponding, in effect, to an initial land area.

The authors' model assumes that the pressure distribution across the face of the land is uniform. Because of the attritious camber the actual pressure distribution is not only nonuniform, it is nonlinear. The impending papers by the writer will show that the pressure distribution is roughly cubic. The authors have provided a useful service in attempting to combine Shaw and Finnie's concept of the friction mechanism with the forces on the wear land. As they have pointed out, the real contact area increases with the normal force—hence it is not constant across the land because of the attritious camber. The writer has provided the authors with copies of his impending papers. A re-examination of equation (37) in the light of the much more complex but more realistic situation created by the attritious camber would be very useful, but is certainly too big a task to be attempted in the closure to this paper.

The model presented by the authors is inadequate only in that the wear land is horizontal. We are concerned here with a distinction somewhat like the old question of the chicken and the egg: Which comes first, the friction force or the normal force? Unlike the egg, there is a definite answer: The attritious camber comes first, causing a normal elastic reaction F_{VW} which is directly responsible for the diminution in depth of cut and in rate of stock removal. The growth of attritious camber includes a growth in land area a_L, but no longer horizontal. The growth in friction force follows from the growth in a_L and in F_{VW} so that the authors are correct in showing that the growth in land area is associated with a growth in friction force and that these are associated with a decrease in stock removal rate—provided that the implication is removed that the friction process is the *cause* of the decrease in depth of cut and in stock removal rate. Apart from the unfortunate error in equation (32) to the end of that section, the authors' equations are a useful representation of the growth of the friction force (a topic which the writer had not so fully developed in his impending papers). As previously mentioned with reference to equation (37), a further refinement of the friction equations is potentially possible by recognizing that the pressure distribution is actually nonuniform, but the writer has not investigated the implications of this refinement. Although their model is inadequate in the respect previously mentioned, it is a marked improvement over previous models, and the authors are to be commended for having made a significant advance in the understanding of the consequences of tool wear in metal cutting and grinding.

Authors' Closure

The authors express thanks to Mr. Hitomi and Mr. Mohun for their interest and for the additional light shed by their discussions on the nature of the forces on a worn cutting tool.

In summary, it should be noted that our development is essentially a formal exercise in which logical consistency is the point of principal concern. Though by making certain assumptions we reach certain conclusions, it is axiomatic that the role of conclusions and assumptions can be reversed in whole or in part. Thus, it is altogether fitting that Mr. Hitomi and Mr. Mohun reach similar conclusions by different routes or by different choices of assumptions.

The principal interest of Mr. Hitomi's approach resides in the fact that it reveals the necessity for distinguishing between constant feed and constant depth of cut. In one, the depth of cut must be adjusted by the amount of the tool wear, whereas in the other no such adjustment is involved. It is interesting that Mr. Hitomi's approach leads to the same result as our equations (23) and (24) for the case of constant feed force. However, the generality claimed for his equations (52) and (53) or (52′) and (53′) is not entirely evident. For example, in equations (52′) and (53′) it is assumed that $r = 1$, where r is the ratio between the first and nth cuts. Such an assumption is tantamount to the assumption of constant cutting rate, so that (52′) and (53′) appear trivial.

A point of correction should be noted in the part of Mr. Hitomi's argument immediately following equation (48). The shear stress and normal stress as defined by Finnie and Shaw are applicable not to the apparent contact area but to the real contact area. Therefore, Mr. Hitomi's development should incorporate an argument of the type presented in our equations (14) through (17). This part of the argument was not included in our paper at the time it was before Mr. Hitomi for discussion, but its inclusion in no way invalidates his approach.

Mr. Mohun's observation that it is the increase in elastic reaction that is the direct cause of diminution of stock removal rate is, of course, well taken. Clearly the force F_{VW} implies an elastic reaction, but the evidence does not seem conclusive that for such a reaction to occur the wear land must exhibit a camber of the type noted. A plane surface slid under pressure against a piece of rubber will cause the rubber to deform elastically and exert a reaction against the rubbing surface. Within certain limits, the rubber will exert a reaction against the rubbing surface regardless of whether the two surfaces are parallel or whether one is tilted in either a positive or negative sense with respect to the other. Conceivably a similar process might occur in metal cutting, the extent of the reaction depending on the geometry of the wear land and the elastic limit of the material being cut. It is of interest to note that in Kobayashi and Thomsen's [5] experimental results, the effect of the wear land was felt even for several degrees of flank clearance angle.

Mr. Mohun's objection to equations (32) and (35) is a matter of definition. Our definition is consistent with the definition of unit pressure as used in classical Hertzian analysis of penetration. For us, unit pressure is defined as the force per unit area of wear land, though it is well recognized that this average pressure is not the actual stress on the wear land, because the stress on the wear land is partially relieved by chip flow. In the limit, however, it is evident that the unit pressure defined as F_{VW}/a_L approaches F_V/a_L and the distinction is unessential. Actually, of course, a discontinuity is involved. At a value of F_V/a_L infinitesimally larger than the critical value, the actual pressure on the wear land is F_{VW}/a_L, whereas for values of F_V/a_L infinitesimally smaller than the critical value the actual pressure on the wear land is F_V/a_L. Except for approaching the discontinuity from the opposite side, the approach is similar to the Hertzian analysis of a spherical indenter penetrating a plane. As the load on the indenter is increased, the area of contact increases until some critical pressure is reached at which the plane undergoes plastic flow. After flow has occurred, however, the pressure at the interface can no longer be computed as load divided by contact area.

In conclusion, it is evident that much additional work remains to be done to clarify the actual physical process attending the cutting action of a worn cutting tool. Our paper is presented in the hope that it may provide a formal framework for more detailed analysis.

E. G. THOMSEN
Professor of Metal Processing, University of California, Berkeley, Calif. Mem. ASME

S. KOBAYASHI
Lecturer in Mechanical Engineering, University of California, Berkeley, Calif.

M. C. SHAW
Professor of Mechanical Engineering, Massachusetts Institute of Technology, Cambridge, Mass. Mem. ASME

Some Controlled Metal-Cutting Studies With Resulfurized Steels

Cutting tests, including controlled tool-chip contact area and controlled artificial flank wear-land studies, were made with five resulfurized steels having nearly identical strength properties. It was found that the dynamic shear stress was 62,700 psi and appeared to be identical for all steels at the two cutting speeds of 356 and 936 fpm with sulfur contents of the alloys ranging from 0.11 to 0.37 per cent. For the low sulfur steel ($S = 0.033$ per cent), the dynamic shear stress was found to be 72,000 psi. A comparison of the effective stresses obtained from compression tests with those from metal cutting tests showed good correlation at equal strains.

The controlled tool-chip contact area and the controlled wear-land studies at feeds of approximately 0.005 ipr and cutting speeds of 318 to 356 fpm appear to indicate that sublayer plastic flow at the tool chip and tool work interfaces was essentially absent.

Introduction

In a recent article Shaw, Smith, and Cook [1][1] reported a study of tool wear and tool life of a series of five steels of varying controlled sulfur content with nearly identical mechanical properties. The authors showed that under certain combinations of speeds and feeds manganese sulfide in the steel may not always have beneficial effects. They found in particular, that for certain cutting speeds the wear in the vicinity of a feed of 0.005 ipr was unusually high.

The University of California co-operated with the Massachusetts Institute of Technology in running a series of independent tests on these same materials in order to complete the picture of the effect of sulfur in steels on the tool forces and friction under various controlled cutting conditions. This work was sponsored by the Machinability Section of the Rock Island Arsenal and the complete data are included in a report to the Arsenal [2].

Experimental Procedure

Materials. The steels used in this investigation were made from the same heat in a small open-hearth furnace at the Gary Works of the United States Steel Corporation. Each steel was provided with a different sulfur content by sulfur additions to the ingot during pouring of the mold. The chemical analyses of the billets from which the tubular specimens were made are shown in Table 1.

The true stress-true strain properties of these materials, shown in Fig. 1, were obtained from static compression tests, now considered a standard test at the U.C. laboratories. The test specimens consist of short, solid cylinders with a slenderness ratio of about unity, which in the present case were machined from the tube wall with axial orientation. The test specimens were provided with shallow spiral grooves at their flat ends in order to act as lubricant reservoirs. This method of testing was first described by Loizou and Sims [3]. The actual test then consists of compressing the cylinder in a frictionless die set between parallel, flat, and lapped hardened steel anvils. The height of the cylinder at any given instant as a function of load is obtained from a dial indicator which records the spacing of the anvils. The test is interrupted at frequency intervals by release of the load and measuring and relubrication of the cylinder. This procedure has the effect of minimizing bulging and often eliminating it altogether. The test is continued generally until the height of the cylinder has been reduced to one half of its original height, which corresponds to a true strain of approximately $\bar{\epsilon} = \ln h_0/h = \ln 2 \simeq 0.7$. The data are corrected for springback by plotting the load as a function of height and then drawing a continuous curve through the experimental points. Superimposing the actual measured instantaneous heights of the specimen after release of the load on this same graph and drawing a parallel curve to the first one automatically provides a load-versus-height curve in which the small elastic strains have been deleted. The true stress can then be calculated from the ratio of load over actual area. This requires the assumption of a constant volume type of deformation so that the instantaneous cross section of the specimen can be calculated from the initial dimensions and the instantaneous height of the specimen. A typical load-height curve is shown in Fig. 2. It is to be noted that the four steels, SS2 to SS5, give almost identical stress-strain curves, while steel SS1 has a curve

[1] Numbers in brackets designate References at end of paper.

Contributed by the Production Engineering Division and presented at the Winter Annual Meeting, New York, N. Y., November 27–December 2, 1960, of The American Society of Mechanical Engineers. Manuscript received at ASME Headquarters, July 28, 1960. Paper No. 60—WA-115.

Table 1 Composition and properties of special resulfurized steels (SS steels)

Hot rolled—sulfur added in ladle

Steel	C	Mn	P	S	Si	N	Upper[a] yield, psi	Lower[a] yield, psi	Tensile[a] strength, psi	Elongation[a] in 2 in., per cent	Reduction[a] in area, per cent	Rockwell[a] B
SS1	0.08	0.99	0.08	0.033	0.03	0.002	36,700	32,600	55,700	41.0	71.8	56.6
SS2	0.08	0.99	0.09	0.11	0.12	0.003	36,500	32,900	54,700	40.5	68.1	59.3
SS3	0.08	0.99	0.09	0.18	0.18	0.002	34,600	32,000	54,500	38.5	66.4	56.5
SS4	0.07	0.99	0.09	0.26	0.25	0.002	31,900	29,500	53,300	38.5	65.1	56.2
SS5	0.09	1.04	0.09	0.37	0.40	0.002	33,400	29,800	54,700	34.0	57.4	58.4

[a] Tensile data obtained by United States Steel Corporation at Monroeville using standard 0.505-in-diameter tension test bars.

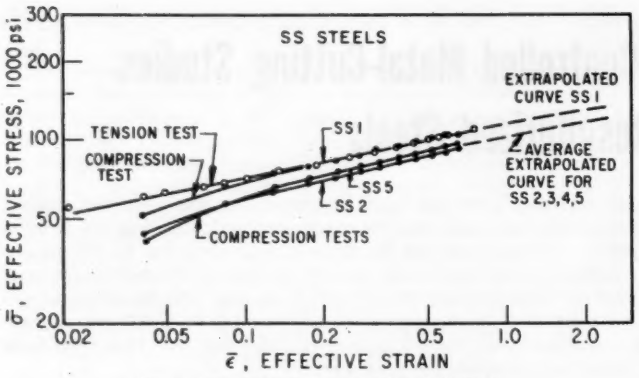

Fig. 1 True stress-strain properties of SS steels

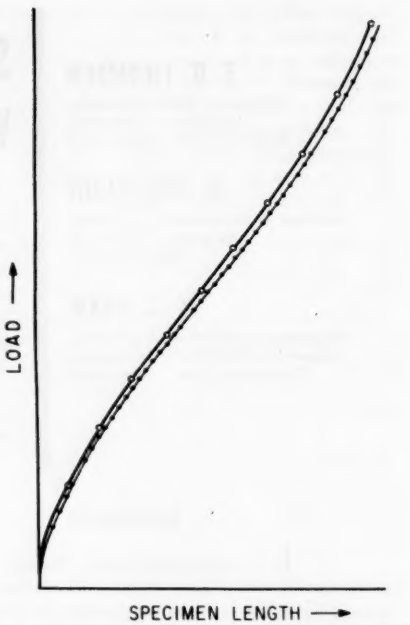

Fig. 2 Typical load-height curve in compression test

of its own. In order to check the possibility of perhaps getting incorrect data due to end friction during compression testing, micro tensile tests were also run for steel SS1 and the well-known Bridgman correction was applied after necking. It is seen that the curves are nearly identical except at the beginning of the test when the strains are small. It should be remarked that the lubricant for the compression tests was molybdenum disulfide and all tests are average results of at least two individual test runs.

Test Equipment, Cutting Tools, and Specimens. The cutting tests were of short duration, usually approximately 10 revolutions of the workpiece, and consisted of end cutting in an engine lathe of tubular specimens shown in Table 2. The lathe was an American Pace Makers lathe and was equipped with a two-component force dynamometer as well as temperature measuring equipment. The details of the equipment and preparation of tools have been reported in several papers [4, 5, 6, 7] and the temperature measurements have been described in a companion paper [8]. The $^3/_8 \times {}^1/_4 \times 1^1/_2$ in. long K5H steel cutting grade cemented carbide tools were from the same batch and were refinished after each test in order to assure a sharp tool with known geometry. The tool forces were recorded on a dual channel Sanborn recorder, while the temperatures were recorded on a polaroid film taken from the voltage trace on the viewing screen of a dual channel oscilloscope. These voltages were converted with the aid of calibration curves to the following temperatures, namely:

Table 2 Tubular test specimens of resulfurized steels

Condition Material	(hot rolled)	Outside diameter, in.	Wall thickness, in.	Original bar stock diameter
SS1	As received	1.800	0.202	$4^1/_2$ inch
SS2	As received	1.989	0.200	$4^1/_2$ inch
SS3	As received	1.989	0.200	$4^1/_2$ inch
SS4	As received	1.989	0.200	$4^1/_2$ inch
SS5	As received	1.990	0.199	$4^1/_2$ inch

(*a*) T_{TW} is the average tool-chip contact temperature produced by the thermoelectric effect of the tool-chip thermocouple; in the case of the flank friction studies, the thermocouple is formed between the chip, flank, and tool, which are in contact simultaneously.

(*b*) T_0 is the instantaneous initial temperature due to the thermoelectric effect between a 57 per cent Cu and 43 per cent Ni (Advance, Ceroc insulated) alloy thermocouple wire and the workpiece in which it is embedded.

(*c*) T_s is an average shear plane temperature measured just prior to the time that the thermocouple wire of (*b*) is cut off by the tool.

(*d*) T_f is the temperature at the trailing edge of the flank, also obtained by the embedded thermocouple of (*b*).

Calibration and interpretation of results have been discussed elsewhere and the reader is referred to the article cited previously [8].

Test Conditions

The tests consisted of three types, namely:

(*a*) regular tests; no attempt was made here to confine or limit chip or workpiece contact with the tool.

(*b*) controlled tool-chip contact tests; the contact area on the face of the tool was artificially controlled.

(*c*) controlled flank contact length (artificial wear-land) tests; the flank of the tool had a flat ground on it which was set to a 0 or -1 deg (negative) clearance angle.

This latter angle was chosen to insure enforced contact. The conditions for these three tests are outlined in Table 3.

Results and Discussion

(a) Regular Test Series. The cutting forces for steels SS1 and SS5 using rake angles of 20 and 0 deg for two speeds ranging from 318–356 fpm and 836–936 fpm for the regular tests are given in Figs. 3 to 6 inclusive. The curves for the alloys SS2, SS3, and SS 4 are similar, but have not been shown in order to conserve space. It is seen from these curves that the forces rise nearly

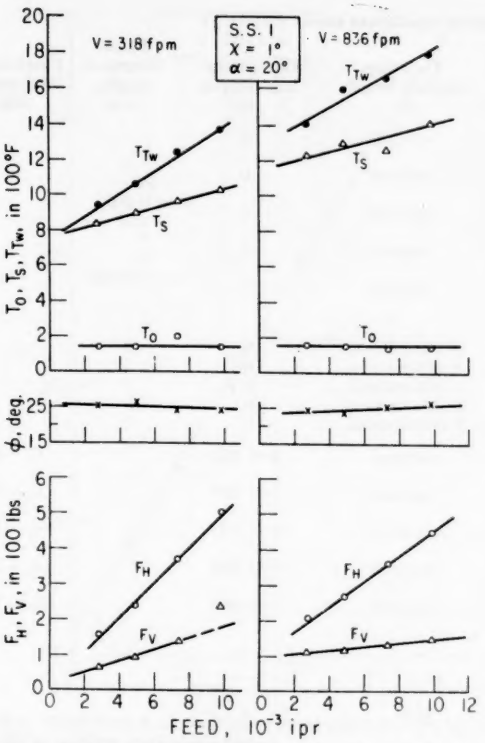

Fig. 3 Regular cutting tests for steel SS1 with α = 20 deg

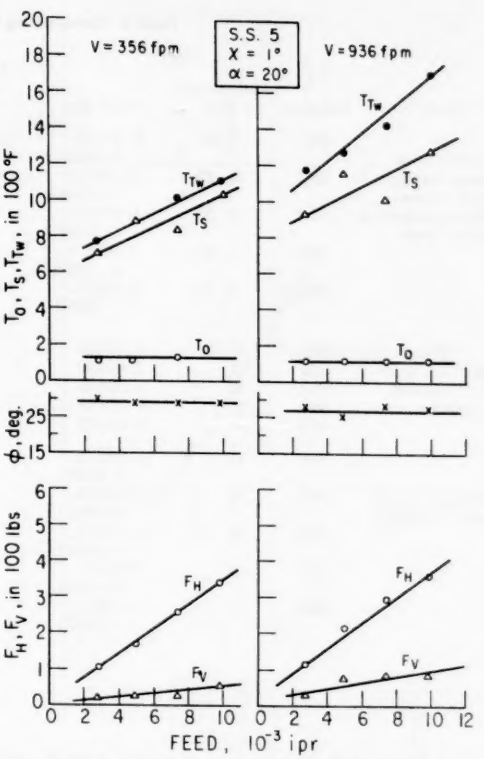

Fig. 4 Regular cutting tests for steel SS5 with α = 20 deg

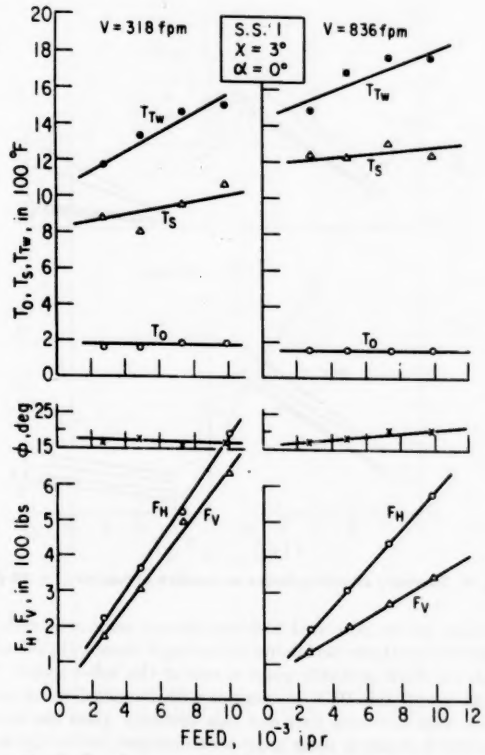

Fig. 5 Regular cutting tests for steel SS1 with α = 0 deg

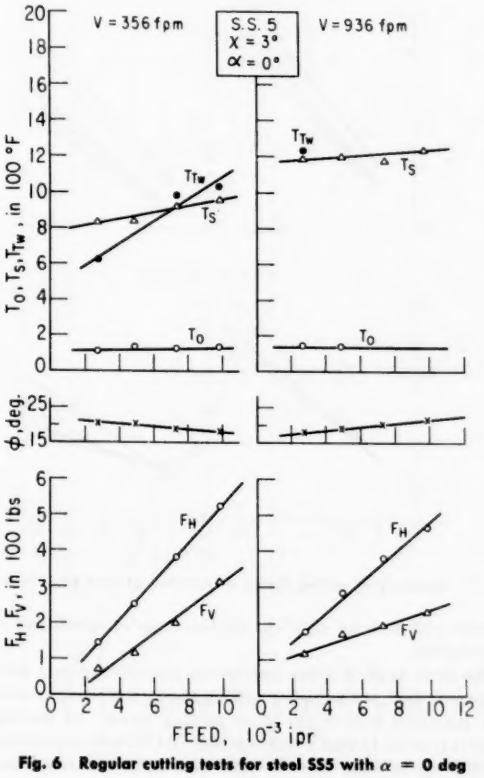

Fig. 6 Regular cutting tests for steel SS5 with α = 0 deg

Table 3 Metal-cutting test conditions for resulfurized steels

Study	Material	Rake angle, deg	Feed ipm	Cutting speed, fpm	Tool-chip contact length, in.	Flank-wear-land length, in.	Flank clearance angle, deg	Flank-wear land angle, deg
(a) Correlation of shear strength with stress-strain properties Regular tests	SS1	0, 20	0.00275–0.00981	318,836	natural	0	1 for α = 0 deg and 3 for α = 20 deg	
	SS2	0, 20	0.00275–0.00981	356,936	natural	0		
	SS3	0, 20	0.00275–0.00981	356,936	natural	0		
	SS4	0, 20	0.00275–0.00981	356,936	natural	0		
	SS5	0, 20	0.00275–0.00981	356,936	natural	0		
(b) Controlled cool-chip contact length	SS1	0	0.00489	318	0.004-natural	0	3	
	SS2	0	0.00489	356	0.004-natural	0	3	
	SS3	0	0.00489	356	0.004-natural	0	3	
	SS4	0	0.00489	356	0.004-natural	0	3	
	SS5	0	0.00489	356	0.004-natural	0	3	
(c) Controlled flank contact length	SS1	0	0.00275, 0.00981	318	natural	0–0.030		0, −1
	SS2	0	0.00275, 0.00981	356	natural	0–0.030		0, −1
	SS3	0	0.00275, 0.00981	536	natural	0–0.030		0, −1
	SS4	0	0.00275, 0.00981	356	natural	0–0.030		0, −1
	SS5	0	0.00275, 0.00981	356	natural	0–0.030		0, −1

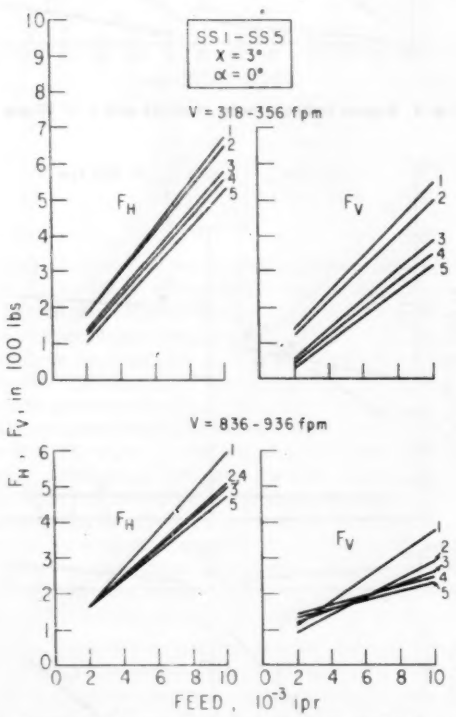

Fig. 7 Summary of cutting forces as function of feed at α = 0 deg

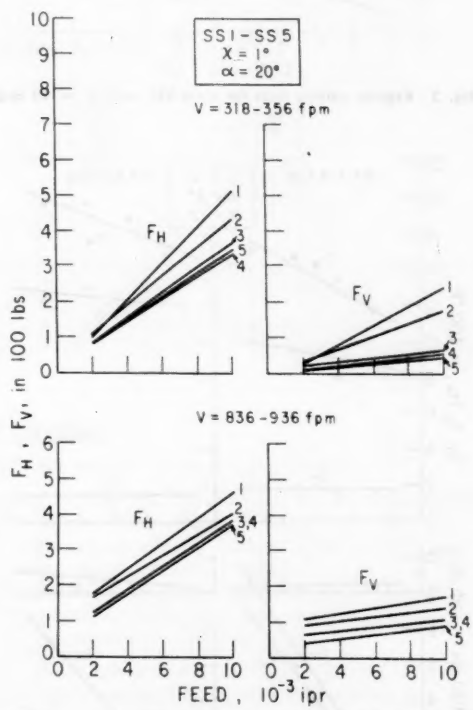

Fig. 8 Summary of cutting forces as function of feed at α = 20 deg

linearly with feed for all alloys for the range of speeds and feeds investigated.

The shear angle ϕ either increases or remains constant with an increase in feed at the higher cutting speed, but tends to *decrease* with increased feed at the lower cutting speed. At the higher speed it is unlikely that a built-up edge (BUE) will be present and the increase in shear angle ϕ with feed, sometimes observed, is probably due to decreased tool-face friction associated with the higher temperatures pertaining at the larger feeds. On the other hand, the BUE probably plays a role at the lower speed. We should expect this BUE to increase with increased speed or increase with increased feed and this probably gives rise to the observed decrease in shear angle with increased feed at the lower cutting speed.

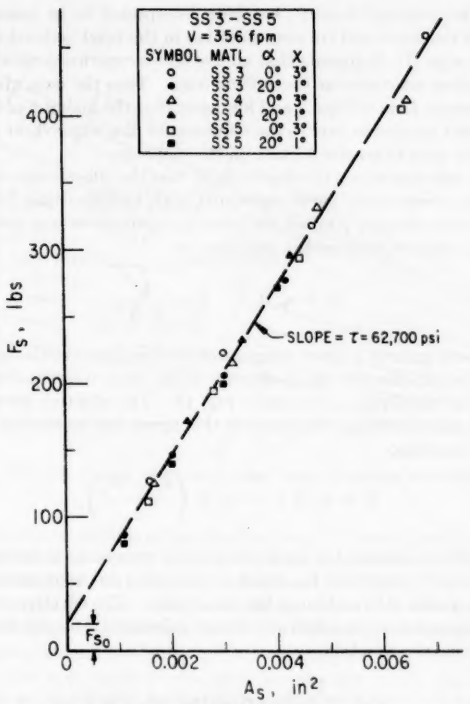

Fig. 9(a) Shear force F_s as function of shear plane area A_s for steels SS3–SS5 at a cutting speed of 356 fpm

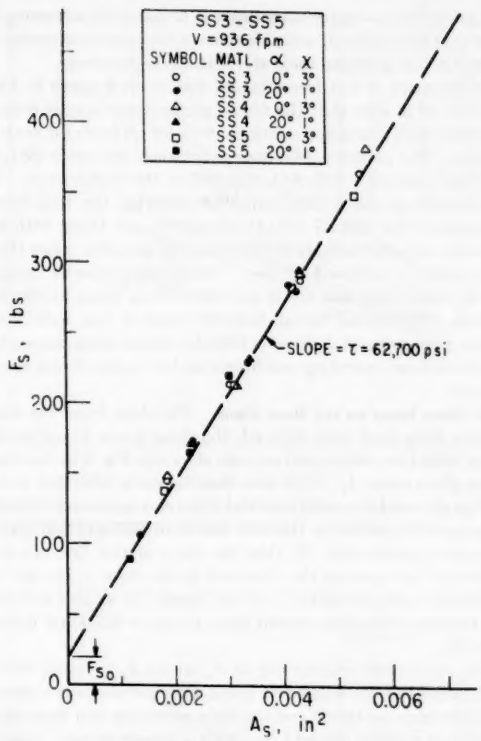

Fig. 9(b) Shear force F_s as function of shear plane area A_s for steels SS3–SS5 at a cutting speed of 936 fpm

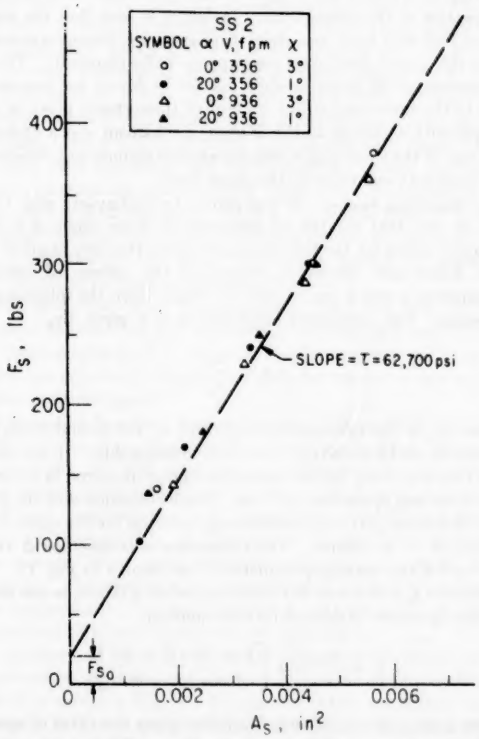

Fig. 9(c) Shear force F_s as a function of shear plane area A_s for steel SS2

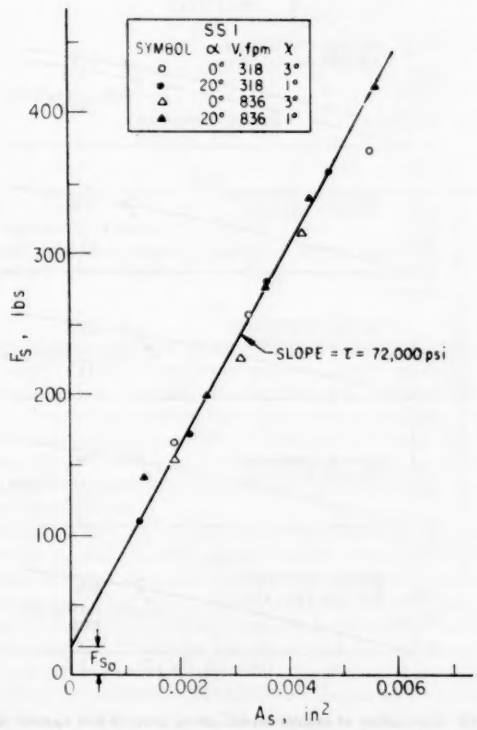

Fig. 9(d) Shear force F_s as function of shear plane area A_s for steel SS1

Generally the temperatures appear to rise with increasing feed, as would be expected, and this reflects the increased energy that is required to machine these steels at the higher feeds.

A summary of the forces for all five steels is given in Figs. 7 and 8. It is seen that the forces at the lower speeds definitely decrease with increasing sulfur content for all feeds for both rake angles. The greatest difference is between the steels SS1, SS2, and the remainder SS3, SS4, and SS5 at the higher feeds. Thus the benefit of the sulfur content in lowering the tool forces is appreciable for SS3 (S = 0.18 per cent) over those with lower content, but additional benefit appears to diminish when the sulfur content is increased further. At the higher speeds, the forces for all conditions and steels are lower than those at the lower speeds. The curves for all but SS1 tend to fuse into a single curve, indicating that there is little to choose from among these steels at these operating conditions as far as tool forces are concerned.

(b) Shear Stress on the Shear Plane. The data from the regular cutting tests have been reduced, the shear forces F_s on the shear plane have been calculated and are shown in Fig. 9 as function of shear plane areas A_s. It is seen that for steels SS3, SS4, and SS5 of Figs. 9(a and b), a single straight line can be drawn through all experimental points for the two speeds of 356 and 936 fpm. It was shown previously [5] that the slope of this line can be interpreted to represent the dynamic shear stress τ_s on the shear plane and is unaffected by cutting speed. A similar conclusion can be drawn from the present data, i.e., τ_s = 62700 psi for steels SS3–SS5.

The shear force relationship of F_s versus A_s for steels SS1 and SS2, shown in Figs. 9(c and d), is not quite so conclusive, since the data are more scattered and the data points for SS1 have shifted to give an average straight line with a steeper slope. Inasmuch as the intercept from F_s has been interpreted to be associated with the stress and friction condition in the neighborhood of the tool edge [7], it appears that all five alloys experience essentially identical resistance at the cutting edge. Thus the data given in summary form in Figs. 7 and 8 suggest that the higher tool forces for SS1 are due in part to the requirement of a larger shear stress and in part to greater friction on the tool face.

It also was shown previously [5, 6] that the effective stress of a static stress-strain curve correlated with metal-cutting data at the same effective strain if the following equivalence was accepted from the distortion energy criterion, i.e.,

$$\bar{\sigma} = \sqrt{3}\,\tau_s, \quad \bar{\epsilon} = \frac{\gamma_s}{\sqrt{3}}. \tag{1}$$

Consequently a direct comparison between metal-cutting data and static effective stress-effective strain data was possible. A similar correlation is shown in Fig. 10. The effective stress for each metal-cutting data point of this figure was calculated from the equation,

$$\bar{\sigma} = \sqrt{3}\,\tau_s = \sqrt{3}\left(\frac{F_s - F_{s0}}{A_s}\right), \tag{2}$$

in order to permit the application of an approximate correction for the intercept force F_{s0}, which is considered not to be associated with plastic deformation on the shear plane. The effective strains for the metal-cutting data points were calculated in the usual manner from the equation,

$$\bar{\epsilon} = \frac{1}{\sqrt{3}}\,[\cot\phi + \tan\,(\phi - \alpha)], \tag{3}$$

where ϕ is the shear angle and α is the rake angle. It is seen that the correlation is good in that the effective stresses of the metal-cutting data points are in approximate agreement with the static properties at the same strain. In fact it is seen that the several steels SS2–SS5 have lost their distinguishing characteristics and that the plastic flow properties appear to be identical. Thus an improvement in machinability (as far as forces are concerned) due to the increasing sulfur content of these steels, must be associated with a change in the friction mechanism and a change in the size of the shear angle, but apparently cannot be a function of the plasticity condition in the shear zone.

(c) Machining Factors. It was shown by Kobayashi and Thomsen [9, 10] that for the co-ordinates of shear angle ϕ and the quantity given by the friction angle minus the rake angle $\beta - \alpha$ (the Ernst and Merchant variables) the curves of constant parameters η and ξ can be plotted, which have the following significance: The parameter effectiveness η is given by,

$$\eta = \frac{w_m}{w_a} \tag{4}$$

where w_m is the minimum energy and w_a the actual energy required for an identical ($\beta - \alpha$) angle relationship. It was shown also that η is unity for the minimum energy required in an actual metal-cutting operation, $w_a = w_m$, which coincides with the Ernst and Merchant [11] minimum energy solution for the same β and α (i.e., $\beta - \alpha$) values. The theoretical relationships ϕ versus $\beta - \alpha$ for the various parameters η are shown in Fig. 11. The parameter ξ, which is called the machinability factor, is also shown on this figure and is defined by the equation,

$$\xi = \frac{\tau_s}{s} = \eta\left[\frac{1 - \sin\,(\beta - \alpha)}{2\cos\,(\beta - \alpha)}\right], \tag{5}$$

where ξ for a given cutting condition gives the ratio of specific shear energy τ_s to specific cutting energy s. Thus the parameter

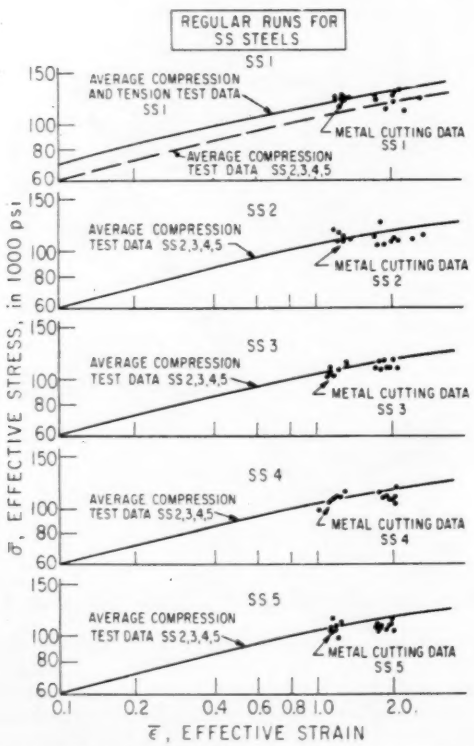

Fig. 10 Correlation of regular metal-cutting data of five special sulfurized steels with static stress-strain properties

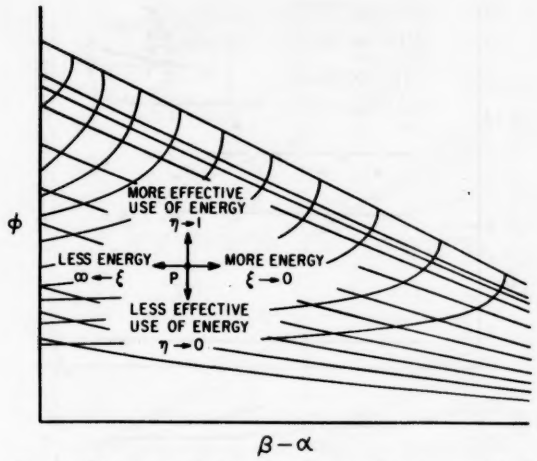

Fig. 11 The energy chart as a road map of cutting conditions

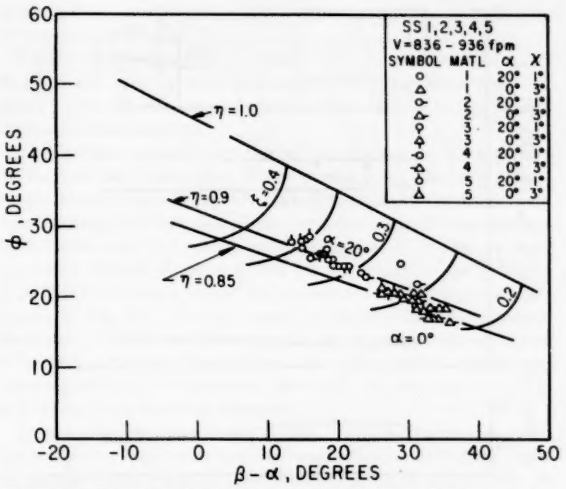

Fig. 12(a) The cutting data of steels SS1 to SS5 for regular tests at V = 836 and 936 fpm plotted on the ϕ versus $\beta - \alpha$ energy chart

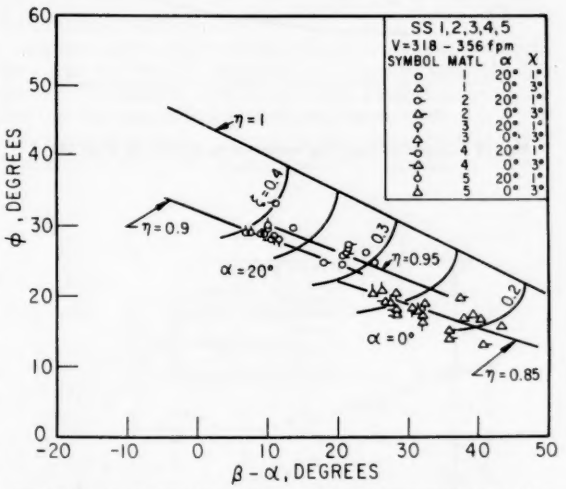

Fig. 12(b) The cutting data of steels SS1 to SS5 for regular tests at V = 318 and 356 fpm plotted on the ϕ versus $\beta - \alpha$ energy chart

ξ gives the magnitude of the specific energy of cutting relative to a given dynamic shear stress and η is a parameter which indicates how effectively this energy is used to produce the cut. A schematic representation of a metal-cutting state is shown also in Fig. 11 as an equilibrium state P, and the changes in energy for changing cutting conditions are indicated by arrows. It is thus clear that a ϕ versus $\beta - \alpha$ plot, like the one of Fig. 11, is in reality an energy plot, and might be called a road map of energy states. It will tell what will happen and where one will go as the cutting conditions are altered.

The experimental data of the regular runs are plotted in Fig. 12 on a skeleton energy graph of the type of Fig. 11. For the higher speeds, shown in Fig. 12(a), all data points align themselves along the curves of constant effectiveness $\eta = 0.9$ and 0.85 for the two rake angles $\alpha = 20$ deg and $\alpha = 0$ deg, respectively. It is thus seen that the approach to minimum energy is greater for $\alpha = 20$ deg than for $\alpha = 0$ deg. Furthermore, it is evident that, from an energy point of view, more energy is required to cut at a 0-deg rake angle than would be required for a 20-deg rake angle. It is seen also that increasing the sulfur content in the workpiece tends to increase the machinability factor ξ and consequently reduces the required energy for cutting. A similar trend is in evidence for the data obtained at the lower speeds, as shown in Fig. 12(b), even though the data points show evidently somewhat more scatter than those at the higher speeds.

It is clear from these energy graphs then, that one can discriminate between low and high energy cuts and it is seen further that these graphs tend to show that sulfur is beneficial in metal cutting from an energy standpoint alone for the particular cutting conditions investigated.

(d) Controlled Tool-Chip Contact Studies. The results from the controlled tool-chip contact studies are given in Figs. 13 and 14 for steels SS1 and SS5, respectively. It is seen that the cutting forces take on minimum values at contact lengths of about 0.006 in. These observations are in agreement with those made by Chao and Trigger [12]. It may also be observed that the minimum cutting forces occur simultaneously with maximum shear angles ϕ. The shear plane temperature T_s and the tool-workpiece temperature T_{TW} seem to follow a trend which is not as well defined because of scatter in the data points.

A summary of the effect of sulfur content of the steels on the metal-cutting variables at the approximate optimum length l_f = 0.006 in. is shown in Fig. 15. It is seen that the tool forces for this particular feed decrease continuously with increasing sulfur content but that the shear angles are nearly unaffected. It should be remarked that at another speed and feed a different relationship may apply. The several temperatures appear to follow no definite trend and T_0 varies by nearly 100 deg F as indicated in the figure. It must be assumed that part of this variation is due to the short but variable time for each test and it is suspected that the junctions formed between the workpiece and the Advance wires, which are embedded in it, depend to a considerable extent on the cutting action.

For comparison, Fig. 15 also shows the tool forces and shear angles for natural tool-chip contact lengths. It is seen that increasing the sulfur content is beneficial in reducing the forces and increasing the shear angle, thereby reducing the difference between the values obtained with restricted and natural tool-chip contact lengths. It may be also noted that the tool forces for SS5 with natural contact lengths are lower than those for SS1 and SS2 with restricted tool-chip contact lengths under optimum conditions. Consequently, sulfur contents of 0.26 and 0.37 per cent appear to be as effective in reducing tool forces for these

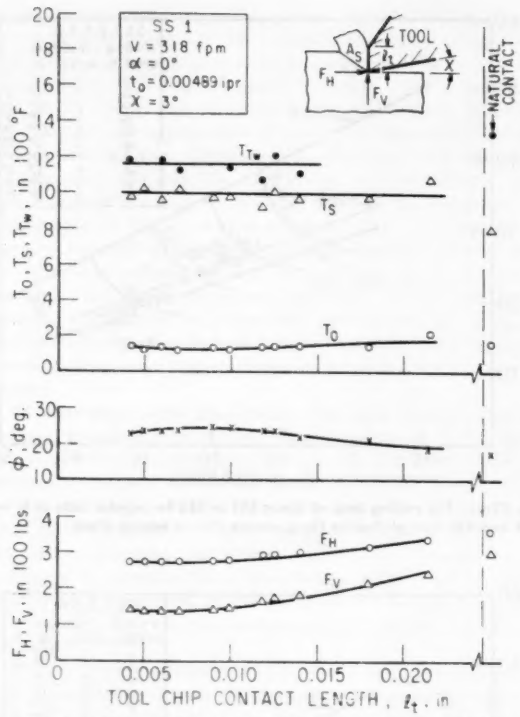

Fig. 13 Controlled tool-chip contact-area studies for steel SS1

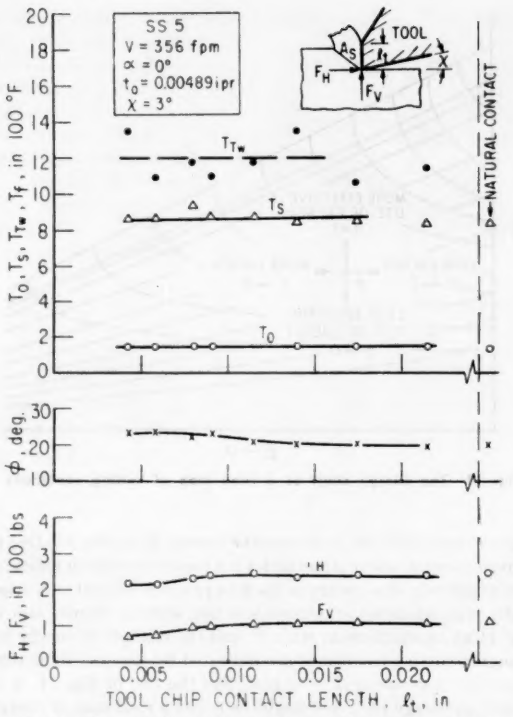

Fig. 14 Controlled tool-chip contact-area studies for steel SS5

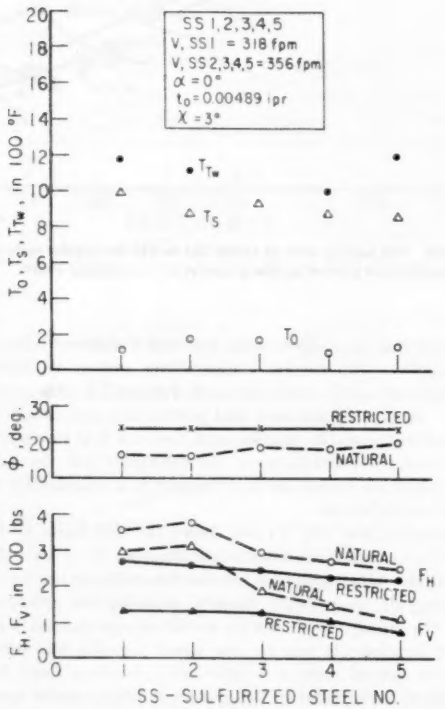

Fig. 15 Summary of performance of the SS steels at optimum condition for controlled tool-chip contact areas

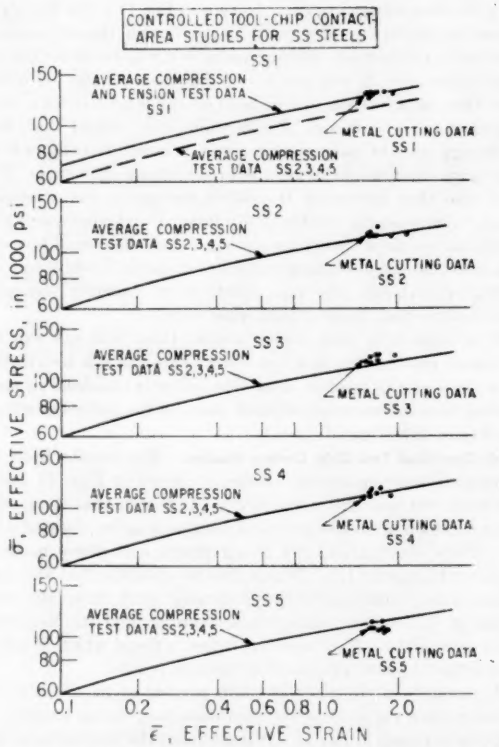
CONTROLLED TOOL-CHIP CONTACT AREA STUDIES FOR SS STEELS
SS 1
AVERAGE COMPRESSION AND TENSION TEST DATA SS1
METAL CUTTING DATA SS1
AVERAGE COMPRESSION TEST DATA SS2,3,4,5
SS 2
AVERAGE COMPRESSION TEST DATA SS2,3,4,5
METAL CUTTING DATA SS2
SS 3
AVERAGE COMPRESSION TEST DATA SS2,3,4,5
METAL CUTTING DATA SS3
SS 4
AVERAGE COMPRESSION TEST DATA SS2,3,4,5
METAL CUTTING DATA SS4
SS 5
AVERAGE COMPRESSION TEST DATA SS2,3,4,5
METAL CUTTING DATA SS5
$\bar{\sigma}$, EFFECTIVE STRESS, in 1000 psi
$\bar{\epsilon}$, EFFECTIVE STRAIN

Fig. 16 Correlation of metal-cutting data obtained with controlled tool-chip contact-areas of the five SS steels with static stress-strain properties

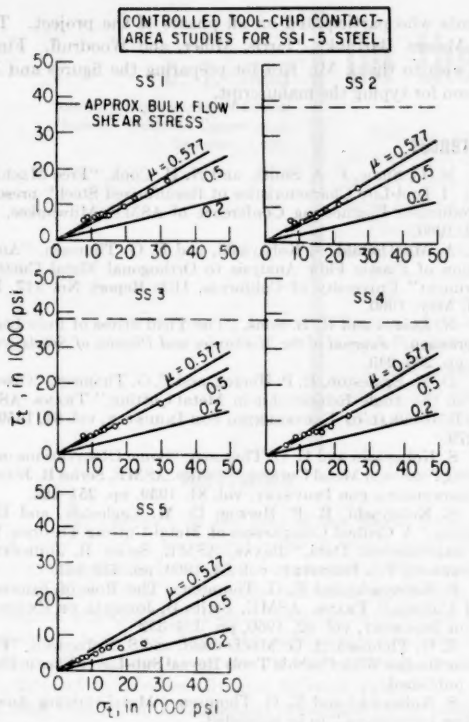

Fig. 17 Friction stresses on the tool face for the SS steels with controlled tool-chip contact-areas

particular test conditions as is the optimum tool contact length for nonsulfurized steels.

The effective stress-effective strain data for all restricted tool-chip contact tests are compared with the average static effective stress versus effective strain curve in Fig. 16. It is seen again that correlation is good.

The frictional stress τ_t and the normal stress σ_t on the tool face for the restricted tool-chip contact studies have also been calculated and are shown in Fig. 17. It is seen that the shearing stress τ_t is less than the bulk flow shear stress calculated for an equivalent British steel [8], which was approximately 38,000 psi and requires a normal stress of 58,000 psi for sublayer flow to start. This bulk flow shear stress is also shown as a dotted curve on the graphs of Fig. 17. It thus is seen that the condition for sublayer flow is not fulfilled and friction must be primarily a consequence of breaking and ploughing of junctions. The precise mechanism, however, cannot be determined since only the nominal stress distribution on the tool face is known.

(e) Controlled Flank-Wear-Land Studies. Representative results of the controlled flank-wear-land studies for the five sulfurized steels at the two feeds of 0.00275 and 0.00981 ipr are given in Figs. 18 and 19. The cutting forces for clearance angles of −1 deg (negative) rise linearly with increasing length of wear land for all steels except for SS4 and SS5. For these latter steels the tendency for a break in the force curves appears to be present, indicating incipient sublayer flow.

The test results obtained with 0-deg clearance angles seem to show that the frictional effects for all steels were essentially absent but the tests are inconclusive. This seems to point up the fact that tool alignment for this type of test at a 0-deg angle is of paramount importance. For a fuller discussion of sublayer flow in friction processes the reader is referred to reference [8], but

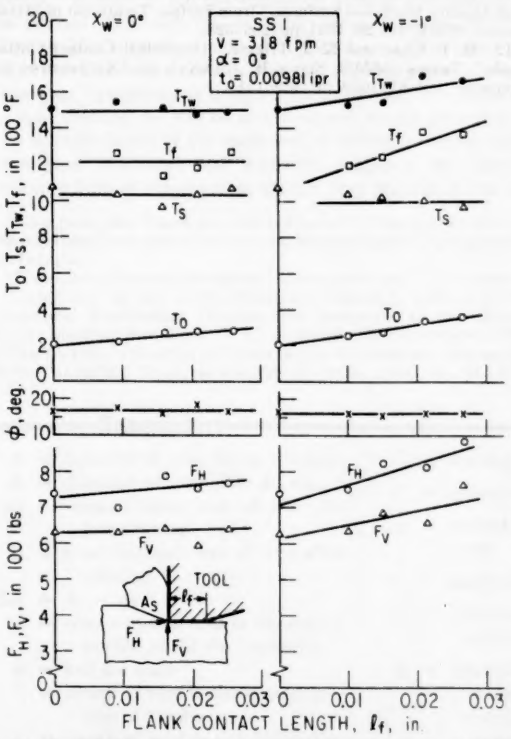

Fig. 18 Controlled flank wear-land studies with steel SS1 at t_0 = 0.00981 ipr

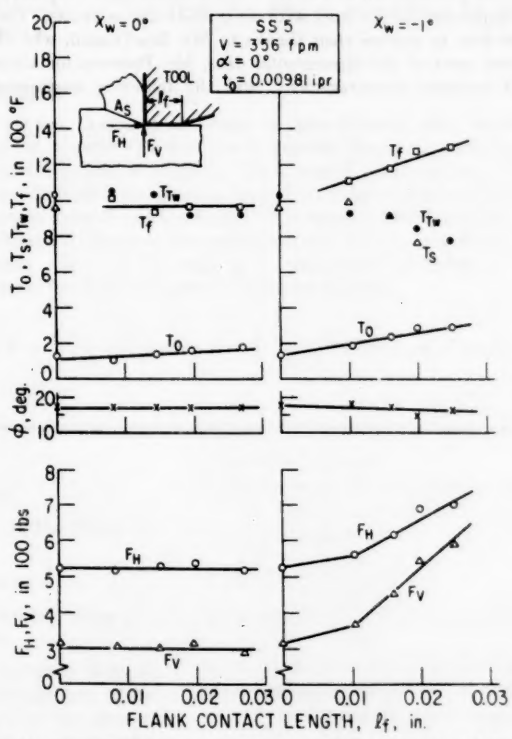

Fig. 19 Controlled flank wear-land studies with steel SS5 at t_0 = 0.00981 ipr

from the controlled flank-wear-land studies under discussion here, sublayer plastic flow was essentially absent.

Conclusions

1 The dynamic shear stress, for natural and controlled tool-chip contact studies, remained essentially constant for the test conditions employed.

2 Correlation of the dynamic shear stresses in terms of effective stresses for the condition of (1) with flow stresses from tension or compression tests evaluated at the same effective strains was good.

3 The effect of increasing sulfur content (up to $S = 0.37$ per cent) in reducing tool forces appears to be as effective for the particular feed and speed used as is reducing the tool-chip contact surface to its optimum value for a nonsulfurized steel of similar mechanical properties.

4 Manganese sulfide content up to 0.37 per cent does not appear to affect significantly the plastic flow properties of these steels.

5 The controlled contact area studies indicated that sublayer plastic flow in the chip near the tool-chip interface and in the work-piece in the vicinity of the wear-land interface appeared to be absent.

6 The experimental data, when plotted on an energy chart having the co-ordinates of ϕ and $\beta - \alpha$, showed that such a graph permits identification of superior machinability in terms of forces.

Acknowledgments

The authors wish to express their appreciation to the Machinability Section of the Rock Island Arsenal for providing the funds for the investigation and to the United States Steel Corporation for supplying the bar stock with controlled sulfur contents. They also wish to express their thanks to Mr. MacDonald, who obtained most of the experimental data, Mr. Petersen for advice and constant encouragement, and the following engineering students who participated on all phases of the project. These are: Messrs. Bartakke, Harris, Miller, and Woodruff. Finally, they wish to thank Mr. Kot for preparing the figures and Mrs. Johnson for typing the manuscript.

References

1 M. C. Shaw, P. A. Smith, and N. H. Cook, "Free Machining Steel: I Tool-Life Characteristics of Resulfurized Steel," presented to Production Engineering Conference of ASME, Milwaukee, May 17–19, 1960.

2 A. MacDonald, S. Kobayashi, and E. G. Thomsen, "An Application of Plastic Flow Analysis to Orthogonal Metal Cutting—Experiment" University of California, IER Report No. 117, Issue No. 4, May, 1960.

3 N. Loizou and R. B. Sims, "The Yield Stress of Pure Lead in Compression," *Journal of the Mechanics and Physics of Solids*, vol. 1, 1953, pp. 234–243.

4 D. M. Eggleston, R. P. Herzog, and E. G. Thomsen, "Observations on the Angle Relationship in Metal Cutting," TRANS. ASME, Series B, JOURNAL OF ENGINEERING FOR INDUSTRY, vol. 81, 1959, pp. 263–279.

5 S. Kobayashi and E. G. Thomsen, "Some Observations on the Shearing Process in Metal Cutting," TRANS. ASME, Series B, JOURNAL OF ENGINEERING FOR INDUSTRY, vol. 81, 1959, pp. 251–262.

6 S. Kobayashi, R. P. Herzog, D. M. Eggleston, and E. G. Thomsen, "A Critical Comparison of Metal-Cutting Theories With New Experimental Data," TRANS. ASME, Series B, JOURNAL OF ENGINEERING FOR INDUSTRY, vol. 82, 1960, pp. 333–347.

7 S. Kobayashi and E. G. Thomsen, "The Role of Friction in Metal Cutting," TRANS. ASME, Series B, JOURNAL OF ENGINEERING FOR INDUSTRY, vol. 82, 1960, pp. 324–332.

8 E. G. Thomsen, A. G. MacDonald, and S. Kobayashi, "Flank Friction Studies With Carbide Tools Reveal Sub-Layer Plastic Flow," to be published.

9 S. Kobayashi and E. G. Thomsen, "Metal-Cutting Analysis II—New Parameters," to be published.

10 S. Kobayashi and E. G. Thomsen, "An Application of Plastic Flow Analysis to Orthogonal Metal Cutting," University of California, IER Report Series 117, Issue No. 3, April, 1960.

11 H. Ernst and M. E. Merchant, "Chip Formation, Friction, and High Quality Machined Surfaces," from Surface Treatment of Metals, TRANS. ASME, vol. 29, 1941, pp. 299–328.

12 B. T. Chao and K. J. Trigger, "Controlled Contact Cutting Tools," TRANS. ASME, Series B, JOURNAL OF ENGINEERING FOR INDUSTRY, vol 81, 1959, pp. 139–151.

C. T. YANG
Advisory Engineer, International Business Machines Corporation, San Jose, Calif.

On the Mechanics of Wire Drawing[1]

Split-die technique was adopted to find the coefficient of friction in wire drawing directly from experiment. Simple dynamometers with wire resistance strain gages were used for measuring separating force and drawing force instead of cumbersome equipment used by former researchers. Reasonably good results were obtained.

The effect of the land or parallel portion in the die on the coefficient of friction was indicated in the results. Its importance was emphasized.

A theoretical equation of the drawing stress with the effect of land considered was derived. Using the coefficient of friction obtained by the split-die method, drawing stresses were calculated from the derived equation. A comparison of the theoretical and experimental drawing stresses was made. Results were tabulated and plotted.

It was concluded that including the land in the analysis of wire drawing is important and further research in analyzing the shear deformation must be pursued in order to get a close agreement between theoretical analysis and experimental results.

Introduction

At present, in the field of the plastic forming of metals there is not a theoretical equation which could give an exact prediction of the forming force or pressure. Wire drawing is of no exception. One of the main difficulties involved in wire drawing, for example, is to obtain the coefficient of friction which is generally calculated from the afore-mentioned theoretical equation with known die geometry and drawing conditions. Also, different theories usually give different values.

In 1948, MacLellan [1][2] suggested calculation of the coefficient of friction in wire drawing directly from experiments by means of a split die; the drawing forces on the wire and normal force tending to separate the die-halves during drawing could be measured directly. Though he did not succeed in getting good results by this method, Wistreich [2], in 1955, obtained reasonable data adopting MacLellan's experimental technique. However, the equipment used was quite cumbersome. In this paper a simple strain gage dynamometer designed for measuring two forces on the split drawing die will be described and results presented.

In the calculation of the coefficient of friction using the split-die method MacLellan and Wistreich neglected the parallel portion or land of the die, even though they thought it was important to include. In the present paper, a formula for the calculation of the coefficient of friction including the effect of the land in the die was derived and comparison of the values of coefficients from both calculations, including and neglecting the land, was made. The difference between the coefficients calculated with and without the land was found to be appreciable.

In the theoretical equation of drawing stresses derived by Sachs [3] and others, the land in the die was also neglected. Since most people in this field think that it is important to include the land in the analysis, the author, using Sachs' approach, has derived a theoretical equation which includes the effect of the land. Using this theoretical equation and values of the coefficients of friction obtained from the split-die method, numerical calculations of the drawing stresses were made. The drawing stresses from experiments and from theoretical analysis were plotted for comparison.

[1] This paper was based on work performed by the author when he was Associate Professor of Mechanical Engineering of The University of Michigan.

[2] Numbers in brackets designate References at end of the paper.

Contributed by the Metal Processing Research Activity of the Production Engineering Division and presented at the Winter Annual Meeting, New York, N. Y., November 27–December 2, 1960, of The American Society of Mechanical Engineers. Manuscript received at ASME Headquarters, July 27, 1960. Paper No. 60—WA-114.

Analysis

(A) The Coefficient of Friction in Wire Drawing With Split-Die

In Fig. 1 a wire with diameter d_1 is drawn through a conical split die with a land of length l_2. By means of dynamometers to be described later, the drawing force F_l and the separating force or normal force F_r are measured. It is assumed that the mean coefficient of friction in the conical part and that in the land are the same. The half die angle is ϕ. Summation of forces in the transverse direction gives the following equation:

$$F_r\pi = \left(\frac{A_1 - A_2}{\sin\phi}\right) p\cos\phi - \left(\frac{A_1 - A_2}{\sin\phi}\right)\mu p\sin\phi + \pi d_2 l_2 p \tag{1}$$

Nomenclature

d_1 = diameter of wire before drawing
d_2 = diameter of wire after drawing
A_1 = cross-sectional area of wire before drawing
A_2 = cross-sectional area of wire after drawing
$\Delta A = A_1 - A_2$
A = cross-sectional area in the conical portion of the die (variable)
ϕ = half die angle
l_1 = length of wire in the conical portion of the die
l_2 = length of land or parallel portion of the die
F_l = drawing force
F_r = separating force
p = normal pressure on the wire in the die
σ_x = longitudinal stress
dx = infinitesimal distance along the axial direction
ds = infinitesimal inclined distance along the circumference of the conical portion of the die corresponding to horizontal distance dx
r = radial distance
μ = coefficient of friction between the die wall and drawn wire
σ_r = radial stress
$C = \dfrac{1 + \mu\cot\phi}{1 - \mu\tan\phi}$
σ_0 = yield stress at the elastic and plastic boundary
σ_2 = σ_x at exit or the drawing stress
σ_0' = average stress between σ_0 and the flow stress at a flow strain of $\log_e\left(\dfrac{A_1}{A_2}\right)$

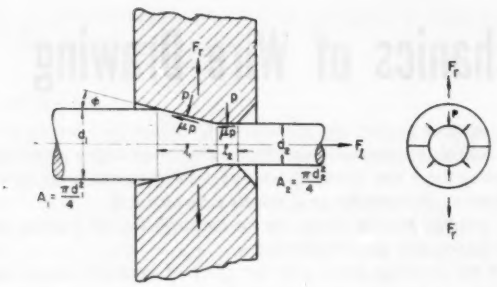

Fig. 1 Sketch of wire drawing showing drawing force F_l and separating force F_r exerted on the split-die

where $$A_1 = \frac{\pi d_1^2}{4} \quad \text{and} \quad A_2 = \frac{\pi d_2^2}{4}$$

In Equation (1) a factor π has to be introduced, because the separating force, F_r, is equal to $1/\pi$ (p, circumferential area of the die). Static equilibrium of longitudinal forces yields:

$$F_l = \left(\frac{A_1 - A_2}{\sin \phi}\right) p \sin \phi + \left(\frac{A_1 - A_2}{\sin \phi}\right) \mu p \cos \phi + \mu \pi d_2 l_2 p \quad (2)$$

By solving these two simultaneous equations and eliminating the variable p, one gets

$$\mu = \frac{\Delta A \cot \phi + \pi d_2 l_2 - \pi \left(\frac{F_r}{F_l}\right) \Delta A}{\left(\frac{F_r}{F_l}\right) \pi (\Delta A \cot \phi + \pi d_2 l_2) + \Delta A} \quad (3)$$

where

$$\Delta A = A_1 - A_2$$

From Equation (3) the coefficient of friction in a drawing die including the effect of land can be calculated. After μ is computed, the normal pressure p on the die wall can be calculated from Equation (2). In Equation (3), if l_2 is neglected, the following equation will be obtained:

$$\mu = \frac{\cot \phi - \pi \left(\frac{F_r}{F_l}\right)}{1 + \pi \left(\frac{F_r}{F_l}\right) \cot \phi} \quad (4)$$

Equation (4) is the same equation derived by MacLellan in 1948 though in his equation (refer to Reference [1]) the factor π was erroneously missed. Numerical calculations from Equations (3) and (4) of the wire drawing data of aluminum and zinc will be shown later.

(B) Theoretical Equation of Drawing Stresses. In Fig. 2 a wire is shown drawn through a die which has a conical and a parallel portion, where σ_x is the longitudinal stress and p the normal pressure. It is assumed that shear is neglected in the drawn part and drawing is a hot-working process, i.e., the yielding stress σ_0 is constant.

An equilibrium of the longitudinal forces acting on the strip of width dx in the conical portion is now considered. The static equilibrium equation is shown as follows:

$$\frac{\partial}{\partial x}(\sigma_x A)dx - 2\pi r p ds (\sin \phi + \mu \cos \phi) = 0 \quad (5)$$

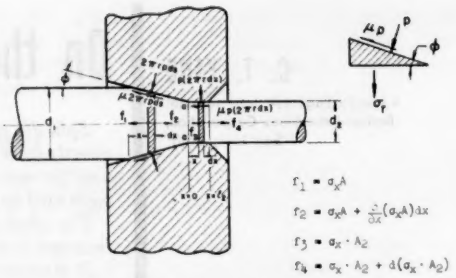

Fig. 2 Sketch of wire drawing showing forces applied to strips of infinitesimal length in conical and parallel portions

where A is the cross-sectional area of wire at the point x and r is the radius of area A; ds is the slant distance of dx.

$$\text{Since} \quad \frac{dx}{ds} = \cos \phi \quad \text{and} \quad ds = \frac{dx}{\cos \phi} \quad (6)$$

Equation (5) becomes:

$$\frac{\partial}{\partial x}(\sigma_x A) = 2\pi r p (\tan \phi + \mu)$$

or

$$d(\sigma_x A) = 2\pi r p (\tan \phi + \mu) dx \quad (7)$$

$$\text{Since} \quad A = \pi r^2, \quad \text{one gets} \quad dx = \frac{dA}{2\pi r \tan \phi} \quad (8)$$

By substituting Equation (8) into Equation (7), it yields,

$$d(\sigma_x A) = p(1 + \mu \cot \phi) dA \quad (9)$$

To express p in terms of σ_r, the radial stress, one considers an equilibrium of the transverse forces on a wedge in Fig. 2 and the following equation is obtained:

$$\sigma_r = p(\mu \sin \phi - \cos \phi) \frac{ds}{dx}$$

or

$$\sigma_r = p(\mu \tan \phi - 1) \quad (10)$$

Substituting Equation (10) into Equation (9) it yields,

$$d(\sigma_x A) = -C \sigma_r dA \quad (11)$$

where

$$C = \frac{1 + \mu \cot \phi}{1 - \mu \tan \phi} \quad (12)$$

To find a relation between σ_x and σ_r a yielding criterion should be used. For problems symmetrical with respect to the longitudinal axis, the Von Mises and Tresca criteria of yielding give the same result, which is stated as follows:

$$\sigma_x + \sigma_r = \sigma_0 \quad (13)$$

where σ_x is tensile and σ_r is compressive. From Equations (11) and (13) one has:

$$\frac{d\sigma_x}{\sigma_x(1 - C) + C\sigma_0} + \frac{dA}{A} = 0 \quad (14)$$

Integrating Equation (14) and eliminating the integrating constant by applying the following boundary conditions:

$$\text{at} \quad A = A_1 \quad \text{(die entry)}, \quad \sigma_x = 0 \quad (15)$$

the following equation will be obtained:

$$\sigma_x = \frac{C}{1-C}\sigma_0\left[\left(\frac{A_1}{A}\right)^{1-C} - 1\right] \tag{16}$$

At the entrance of the parallel zone, point a, where A is A_2, the drawing stress will be

$$(\sigma_x)_a = \frac{C}{1-C}\sigma_0\left[\left(\frac{A_1}{A_2}\right)^{1-C} - 1\right] \tag{17}$$

where A_2 is the cross-sectional area of the parallel zone.

Now the equilibrium of the longitudinal forces in the parallel zone is to be considered. It is assumed that p and μ are the same in the two zones. Summation of the longitudinal forces on the strip dx in the parallel zone yields:

$$\frac{d_2}{4}\,d\sigma_x - \mu p dx = 0 \tag{18}$$

By applying a similar yielding criterion as in Equation (13); that is,

$$\sigma_x + p = \sigma_0 \tag{19}$$

and eliminating p in Equations (18) and (19), one obtains

$$\frac{d\sigma_x}{\sigma_x - \sigma_0} = -\left(\frac{4\mu}{d_2}\right)dx \tag{20}$$

Integrating Equation (20) results:

$$\log_e(\sigma_x - \sigma_0) = -\left(\frac{4\mu}{d_2}\right)x + \text{constant} \tag{21}$$

Now the boundary condition in the land gives,

$$\text{at } x = 0, \quad \sigma_x = (\sigma_x)_a \tag{22}$$

Substituting Equation (22) into Equation (21) yields:

$$\log_e[(\sigma_x)_a - \sigma_0] = \text{constant} \tag{23}$$

Eliminating the integration constant between Equations (21) and (23) and rearranging, the following equation results:

$$\sigma_x = \{(\sigma_x)_a - \sigma_0\}\, e^{-\frac{4\mu}{d_2}x} + \sigma_0 \tag{24}$$

At the exit of the die, $x = l_2$ in Equation (24), the drawing stress is:

$$\sigma_2 = \left\{\sigma_0\left(\frac{C}{1-C}\right)\left[\left(\frac{A_1}{A_2}\right)^{1-C} - 1\right] - \sigma_0\right\} e^{-\frac{4\mu}{d_2}l_2} + \sigma_0 \tag{25}$$

If l_2 is zero, Equation (25) becomes Equation (17) which is very close to the Sachs' equations.

The strain-hardening effect in wire drawing can be taken care of in Equation (25) by adopting a suitable σ_0. It is suggested by the author to take the mean value of the initial yield stress and the flow stress at the drawing strain of $\log_e A_1/A_2$.

Numerical calculations of the drawing stresses with and without the parallel zone in the die were made according to Equations (25) and (17). Numerical results were also plotted.

Experiments and Results

A horizontal broach machine was used for the wire drawing experiment; the ram functions as a draw-head. The setup is schematically shown in Fig. 3.

Two wire resistance strain gage dynamometers were designed and made to measure the drawing force and separating force individually on the two-half die. The drawing force dynamometer is a simple pull-bar type as shown in Fig. 3 and the separating force dynamometer is schematically shown in Figs. 3 and 4. The die was made of high-speed steel and the die plate of 11ST4 aluminum alloy. In the curved opening of the die plate in Fig. 4 a thin ring of aluminum alloy was inserted on which four vertical strain gages (A19) were attached, which measured the separating force.

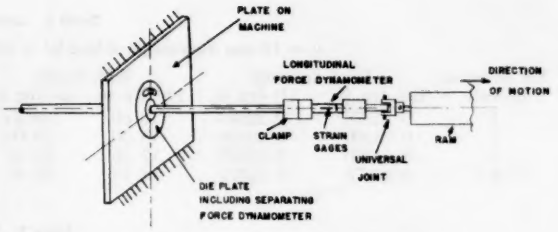

Fig. 3 Setup of wire-drawing experiment

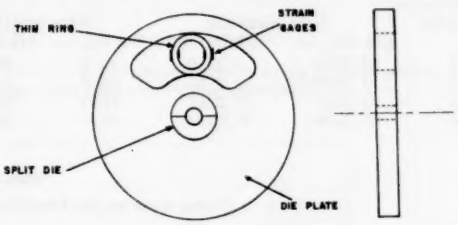

Fig. 4 Dynamometer to measure separating force

The profile of the split die is shown in Fig. 5 with a land of 0.014 in. and a half die angle of 10 deg 6 min. The die was tightly fit onto the die plate which was bolted onto a vertical plate on the machine.

Pure aluminum and zinc wires of 1/4 in. in diameter in annealed condition were tested. Reductions of cross-sectional areas of about 5, 10, 15, and 20 per cent were tested. For the first three reductions 1/4-in. diameter wires were drawn preliminarily into about 0.243, 0.234, and 0.230 in. diameters, respectively, with three different dies (nonsplitting) and annealed afterward. Then they were ready for the test in the split die. This will ensure the same die geometry in all the drawings.

During the tests white lead mixed with machine oil was used as a lubricant, which was found best for aluminum and zinc drawing. Calibration of the dynamometers was done on a thirty-ton Baldwin tensile testing machine. A typical shape of the two forces measured on a Sanborn recorder is shown in Fig. 6. During drawing, metal squeezed out into the gap of the split die to form fins on two sides of the drawn wire. But the height of the fins was measured to be less than 0.0005 in. and the width of the fin at its root less than 0.0008 in. It is believed that the split die opened in the tests at a much smaller gap than in Wistreich's test.

The data of drawing aluminum wire are shown in Table 1 and

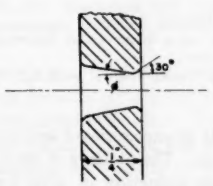

Fig. 5 Profile of the drawing die

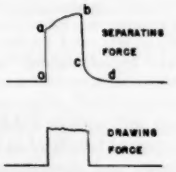

Fig. 6 Typical force curves recorded on Sanborn recorder

Table 1 Aluminum drawing

ϕ = 10 deg 6 min length of land (l_2) = 0.014 in.; lubricant = white lead + machine oil

No. of series of tests	Wire diameter Bef drg, in.	Wire diameter Aft drg, in.	Wire length Bef drg, in.	Wire length Aft drg, in.	Speed of drg, in/sec	Reduction in area	Forces Drg F_1, lb	Forces Sep F_r, lb	Ratio of F_r/F_1
1	0.22976	0.22503	19.60	20.33	12/4.5	0.0407	96.7	115.3	1.192
2	0.23500	0.22528	18.50	20.08	12/5.2	0.0811	128.3	156.0	1.215
3	0.24300	0.22525	17.26	20.25	12/5.8	0.1406	165.0	221.0	1.340
4	0.24978	0.22507	18.70	20.86	12/5.9	0.1882	181.7	263.3	1.448

Table 2 Zinc drawing

ϕ = 10 deg 6 min length of land (l_2) = 0.014 in.; lubricant = white lead + machine oil

No. of series of tests	Wire diameter Bef drg, in.	Wire diameter Aft drg, in.	Wire length Bef drg, in.	Wire length Aft drg, in.	Speed of drg, in/sec.	Reduction in area	Forces Drg F_1, lb	Forces Sep F_r, lb	Ratio of F_r/F_1
1	0.2295	0.2250	19.6	20.3	12/5.4	0.0398	135	213	1.578
2	0.2340	0.2245	18.5	19.9	12/6.1	0.0792	227	312	1.373
3	0.2430	0.2240	17.5	20.3	12/6.5	0.1497	327	431	1.315
4	0.2500	0.2240	16.6	20.4	12/6.6	0.1972	395	496	1.260

Table 3 Aluminum drawing

ϕ = 10 deg 6 min length of land (l_2) = 0.014 in.; lubricant = white lead + machine oil

No. of series of tests	$\frac{A_1}{A_2}$	Red. of area	Drg stress expl, psi	μ With l_2	μ Without l_2	p With l_2, psi	p Without l_2, psi	μp With l_2, psi	μp Without l_2, psi
1	1.043	0.0407	2430	0.1754	0.0844	18,950	28,750	3322	5040
2	1.089	0.0811	3219	0.1422	0.0796	16,570	20,250	2358	2885
3	1.165	0.1406	4140	0.0943	0.0567	15,110	16,550	1424	1560
4	1.231	0.1882	4570	0.0679	0.0402	12,170	12,740	827	865

No. of series of tests	$\frac{\sigma_2}{\sigma_0}$ without l_2	σ_2[a] without l_2, psi	$\frac{\sigma_2}{\sigma_0'}$ with l_2	σ_0'[b], psi	σ_2 with l_2, psi	$\frac{\sigma_2}{\sigma_0}$ without l_2 (Sachs)	σ_2[a] without l_2 (Sachs), psi
1	0.0847	364	0.123	7750	953	0.0818	352
2	0.1518	648	0.181	8560	1550	0.1475	634
3	0.2280	980	0.245	8950	2190	0.2242	966
4	0.2790	1200	0.290	9350	2710	0.2760	1187

[a] Assume no work-hardening; σ_0 = 4300 psi.

[b] Consider work-hardening; taking σ_0' as a mean value between 4300 psi and the flow stress at a strain of $\log_e A_1/A_2$, i.e., 11,200, 12,800, 13,700, and 14,400 psi, respectively.

NOTE: In calculating "σ_2/σ_0 without l_2," and "σ_2/σ_0' with l_2," "μ with l_2" has been used.

Table 4 Zinc drawing

ϕ = 10 deg 6 min length of land (l_2) = 0.014 in.; lubricant = white lead + machine oil

No. of series of tests	$\frac{A_1}{A_2}$	Red. of area	Drg stress expl, psi	μ With l_2	μ Without l_2	p With l_2, psi	p Without l_2, psi	μp With l_2, psi	μp Without l_2, psi
1	1.041	0.0398	3400	0.1140	0.0247	36,000	51,400	4110	5860
2	1.086	0.0792	5730	0.1110	0.0515	34,400	41,200	3810	4575
3	1.177	0.1497	8290	0.0965	0.0613	28,070	30,450	2710	2940
4	1.245	0.1972	10000	0.0976	0.0720	24,780	26,370	2415	2574

No. of series of tests	$\frac{\sigma_2}{\sigma_0}$ without l_2	σ_2[a] without l_2, psi	$\frac{\sigma_2}{\sigma_0'}$ with l_2	σ_0'[b], psi	σ_2 with l_2, psi	$\frac{\sigma_2}{\sigma_0}$ without l_2 (Sachs)	σ_2[a] without l_2 (Sachs), psi
1	0.0664	325	0.094	8,730	820	0.0654	298
2	0.1609	733	0.185	10,080	1865	0.1308	595
3	0.2430	1109	0.263	11,680	3070	0.2400	1093
4	0.3238	1474	0.342	12,430	4270	0.3200	1458

[a] Neglecting work-hardening; σ_0 = 4560 psi.

[b] Consider work-hardening, taking σ_0' as a mean value between 4560 psi and the flow stresses at strain of $\log_e A_1/A_2$, i.e., 12,900, 15,600, 18,800, and 20,300 psi, respectively.

NOTE: In calculating "σ_2/σ_0 without l_2," and "σ_2/σ_0' with l_2," "μ with l_2" has been used.

those of zinc wire in Table 2. The data in each series of testi are an average of results of at least three tests. The plotting of drawing forces and separating forces versus reduction of area for aluminum and zinc is shown in Fig. 7.

From the data in Table 1 numerical calculations were made, and results were listed in Table 3. The yield strength σ_0 of aluminum used in the calculation was taken from a tensile test curve shown in Fig. 8. The tensile testing was done on a Riehle tensile testing machine. In Fig. 8, part (*a*), is a true stress-true strain curve showing the work-hardening of the specimen and

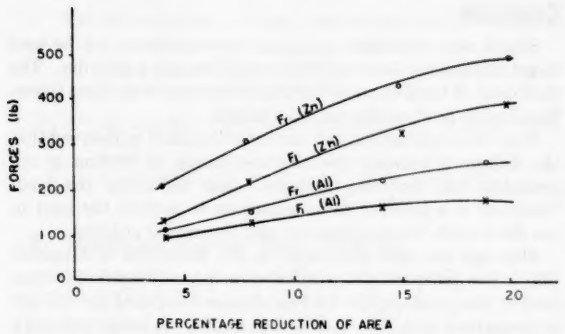

Fig. 7 Experimental drawing forces F_f and separating forces F_r plotted versus percentage reduction of area for pure aluminum and zinc

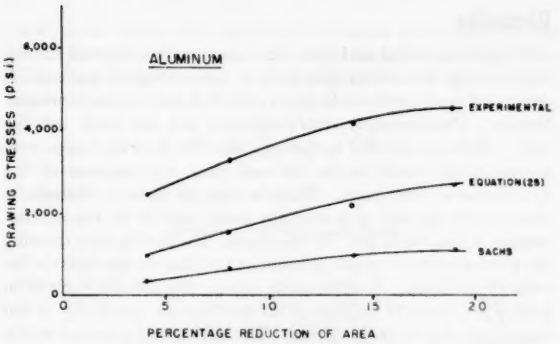

Fig. 9 Theoretical and experimental drawing stresses plotted versus percentage reduction of area for aluminum (250)

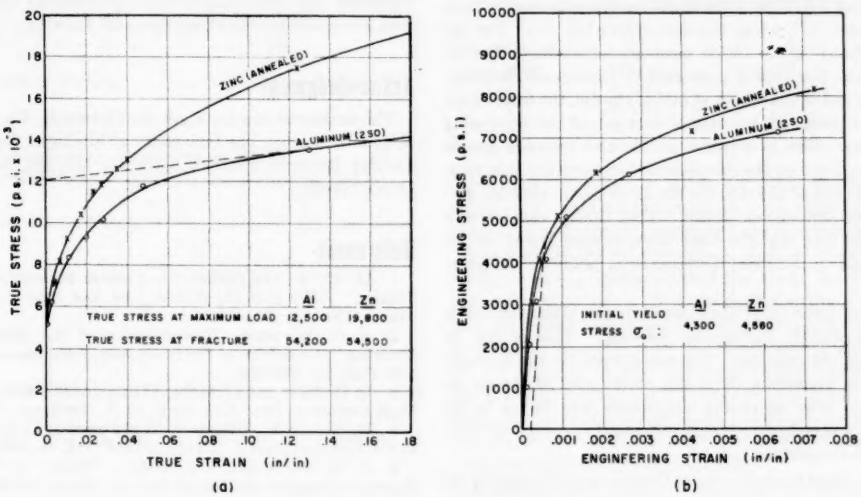

Fig. 8 Stress-strain curves for pure aluminum and zinc

part (*b*) is an engineering stress-engineering strain curve showing the yielding strengths obtained by a 0.2 per cent offset method. In Table 3, μ, with and without l_2, was calculated according to Equations (3) and (4), respectively. Using the calculated values of μ, normal pressure p was also computed from Equation (1). To compute the drawing stresses σ_2, values of "μ with l_2" has been used. "σ_2/σ_0 without l_2" was calculated from Equation (17), σ_0 being 4300 psi. In calculating "σ_2/σ_0' with l_2," Equation (25) was used. To calculate the drawing stress, "σ_2 with l_2," σ_0' was taken as a mean value of the initial yield strength 4300 psi and a flow stress at a strain of $\log_e A_1/A_2$. For example, for a reduction of area of 0.0407, $\log_e A_1/A_2 = \log_e 1.043 = 0.04$. The flow stress at a true strain of 0.04 was found to be 11,200 psi, in Fig. 8, part (*a*). Therefore, $\sigma_0' = {}^1/_2(4300 + 11{,}200) = 7750$ psi. In such a way the strain-hardening effect could be included in the drawing stress equation.

Since the Sachs' equation has been considered as a fairly good theoretical equation to calculate the drawing stresses, it was also used to calculate these stresses. The Sachs' equation is listed as follows:

$$\frac{\sigma_2}{\sigma_0} = \frac{1+B}{B}\left[1 - \left(\frac{A_1}{A_2}\right)^{-B}\right] \tag{26}$$

where $B = \mu/\tan\phi$, and σ_0 is the yield strength without strain-hardening. The results of the numerical calculations of the coefficients of friction, normal pressure p, shear stress μp, and drawing stresses for aluminum from different theoretical equations were listed in Table 3. The drawing stresses in Table 3 were also plotted as shown in Fig. 9. Similarly, experimental data for zinc drawing were tabulated in Table 2 and results of numerical calculations were listed in Table 4. The drawing stresses in Table 4 were plotted as shown in Fig. 10.

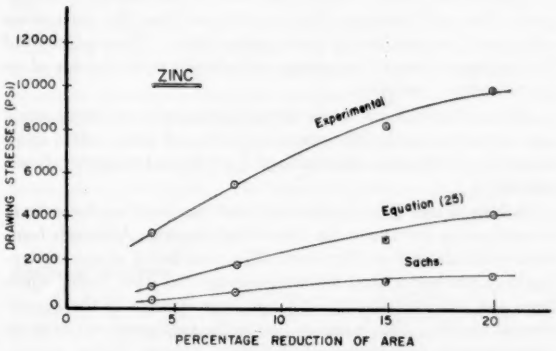

Fig. 10 Theoretical and experimental drawing stresses plotted versus percentage reduction of area for pure zinc (annealed)

Discussion

To get the radial and drawing forces on the drawing die experimentally the author first tried to adopt Majors' method [4] using a whole die with strain gages attached on the outside circumference. Unfortunately, this technique did not work out too well. This may be due to the fact that the drawing forces were comparatively small on the die and thus the response of the dynamometer was poor. Then a ring of barium titanate, a piezoelectric crystal, was specially made and fit to the circumference of the whole die. It was hoped that during wire drawing the piezo-electricity would give enough output on the recorder for accurate analysis. Unfortunately again, this did not succeed in getting good results because of the troublesome instability of the transducer due to creep effects. The author last resorted to the split-die technique and reasonably good results were obtained.

Remarks should be made concerning the shape of the recorded curves of the separating force and the drawing force in Fig. 6. In the top curve of Fig. 6 the force increases instantaneously from point "o" to point "a", when the wire enters the die. The increase of force from "a" to "b" is most probably due to the expansion of the wire due to heat generated by friction and forming. At point "b" the end of the wire is at exit of the die, the force drops suddenly, but at point "c" the rate of decrease of the separating force slows down. This is because the die also expands due to heat and exerts a force on the die plate and thus on the thin ring. When the wire is out of the die, the die cools down, shrinks, and the exerted force diminishes slowly. This theory can be substantiated by the fact that the force increase from point "a" to point "b" is equal to the force decrease from point "c" to point "d."

On the drawing force curve the force increases instantaneously and then drops slightly during the drawing. This is due to the opening up of the split-die. The gap opened by the split-die was estimated by measuring the width at the root of the fin on the drawn wire. The maximum magnitude was found to be 0.0008 in. which was considered relatively small as compared with that in Wistreich's experiment.

It can be seen that the coefficient of friction depends mainly on the ratio of the separating force to the drawing force, if the die geometry and drawing conditions are kept the same.

From Table 3 and Table 4 it can be seen that the difference between the coefficients of friction obtained from the calculation with land l_2 and without l_2 is very appreciable. The coefficient of friction has a trend of decreasing with respect to an increase of reduction ratio (per cent).

Also in Tables 3 and 4, the normal pressure p and shear stress μp decrease with the increase of reduction of area. At a small reduction of area the effect of land l_2 seems to be comparatively small.

In Figs. 9 and 10 it is observed that the drawing force from experiment is far above the theoretical curves. Although force values calculated from Equation (25), considering strain-hardening in σ_0, are better than the values computed from Sachs' equation, the former data are still not close enough to the experimental results. This is mainly due to the negligence of the shear deformation in the theoretical analysis.

The theoretical equation derived by Davis and Dokos [5] was used to check two sets of data on aluminum drawing. The force magnitude from their equation seems unreasonably higher than the experimental. Hu's equation [6] was also used for checking the same two sets of drawing stresses. For low reduction in area the drawing stress falls below the curve plotted from Sachs' equation, but for the high reduction the drawing stress is close to the curve plotted from Equation (25) in Fig. 9. The numerical calculations of the afore-mentioned equations are shown in the Appendix.

Conclusion

Simple wire resistance strain gage dynamometers can be used to get the drawing force and separating force on a split die. The coefficient of friction can be calculated directly from these forces. Reasonably good results can be obtained.

From the experimental and calculated results it is observed that the difference between the two coefficients of friction is appreciable, one including and the other neglecting the land. Therefore it is believed to be important to include the land in the die in both the experimental and theoretical analysis.

Although the land is included in the derivation of Equation (25) in this paper and also in calculating the coefficients of friction used in this equation, the drawing stresses computed are still low in comparison with the experimental results. It seems that work due to shear deformation, generally neglected, must be included in the theoretical equation. Further study in this respect must be pursued. However, the shape of the theoretical curve from Equation (25) and that of the experimental curve agree fairly well, especially for the aluminum wire drawing.

Acknowledgment

The author wishes to thank the Horace H. Rackham School of Graduate Studies, The University of Michigan, for its grant under Faculty Research Fund, Project No. 1157ER, in support of the present study.

References

1 G. D. S. MacLellan, "A Critical Survey of Wire-Drawing Theory," *Journal of the British Iron and Steel Institute*, vol. 158, March, 1948, pp. 347–356.

2 J. G. Wistreich, "Investigation of the Mechanics of Wire Drawing," *Proceedings of The Institution of Mechanical Engineers*, vol. 169, 1955, pp. 654–665.

3 O. Hoffman and G. Sachs, "Theory of Plasticity," McGraw-Hill Book Company, Inc., New York, N. Y., 1953, pp. 176–180.

4 H. Majors, Jr., "Studies in Cold Drawing, Part 3, Determination of Friction Coefficient," TRANS. ASME, vol. 78, 1956, pp. 79–87.

5 E. A. Davis and S. J. Dokos, "Theory of Wire Drawing," *Journal of Applied Mechanics*, vol. 11, TRANS. ASME, vol. 66, 1944, pp. 193–198.

6 L. W. Hu, "Analysis of Die Profiles in Wire Drawing," *Journal of The Franklin Institute*, April, 1957, pp. 317–329.

APPENDIX

(A) Theoretical Drawing Stress From Davis and Dokos

$$\sigma_1 = \left[1 + \frac{\tan\phi}{\mu}\right]\left\{6\Omega \log_e \frac{d_1}{d_2} - \left(3\Omega\frac{\tan\phi}{\mu} - \sigma_0'\right)\cdot\left[1 - \left(\frac{d_2}{d_1}\right)^{\frac{2\mu}{\tan\phi}}\right]\right\} + \sigma_0\left(\frac{d_2}{d_1}\right)^{\frac{2\mu}{\tan\phi}}$$

where

σ_1 = drawing stress, psi
μ = coefficient of friction
ϕ = half die angle
Ω = strain-hardening coefficient in shear
= 4320 psi for aluminum (2SO)
σ_0 = initial yield stress (stress at the boundary between the elastic and plastic ranges) = 4300 psi for aluminum (2SO)
σ_0' = idealized yield stress
= 12,000 psi for aluminum (2SO)

1 For the reduction of cross-sectional area of 4.07 per cent,

$$\mu = 0.1754, \quad \frac{d_1}{d_2} = \frac{0.22976}{0.22503}, \quad \sigma_1 = 4842 \text{ psi}$$

2 For the reduction of cross-sectional area of 18.82 per cent,

$$\mu = 0.0679, \quad \frac{d_1}{d_2} = \frac{0.24978}{0.22507}, \quad \sigma_1 = 7400 \text{ psi}$$

(B) Theoretical Drawing Stress From Hu

$$\frac{\sigma_1}{\sigma_0} = \left(\frac{B}{A}\right)\left[1 + 2\left(\frac{k}{\sigma_0}\right)\frac{1}{A}\right]\left[1 - \left(\frac{r_2}{r_1}\right)^{-A}\right] - 2\left(\frac{B}{A}\right)\left(\frac{k}{\sigma_0}\right)\log_e\left(\frac{r_2}{r_1}\right)$$

where

$$A = \frac{2\mu(1+\alpha^2)}{\mu - \alpha}, \quad B = \frac{2\alpha(1+\mu\alpha)}{\mu - \alpha}$$

μ = coefficient of friction

$\alpha = \dfrac{1}{\tan\phi} = \cot\phi = \cot 10 \text{ deg } 6 \text{ min} = 5.6144$

k = coefficient of strain-hardening = 12,000 psi

σ_0 = initial yield stress = 4300 psi for aluminum (2S0)

1 For the reduction of cross-sectional area of 4.07 per cent,

$$\mu = 0.1754, \quad A = -2.10, \quad B = -4.10, \quad \frac{r_2}{r_1} = 0.980$$

$$\frac{\sigma_1}{\sigma_0} = 0.0433$$

2 For the reduction of cross-sectional area of 18.82 per cent

$$\mu = 0.0943, \quad A = -0.796, \quad B = -2.80, \quad \frac{r_2}{r_1} = 0.902$$

$$\frac{\sigma_1}{\sigma_0} = 0.305$$

DISCUSSION

John L. Alden[3]

What does this study contribute to the drawing of wire in commercial practice?

Why was not copper selected instead of zinc, a material drawn only in very small quantities?

Why was steel used as the die material when it is not used in commercial practice?

What is the expected influence on drawing force of commercial speeds (1000 to 10,000 fpm), solid dies, the usual die profiles, and the customary lubricants as contrasted with the text conditions?

Richard L. Kegg[4] and Serope Kalpakcioglu[5]

The author's consideration of land friction in the development of his wire drawing theory is a step forward in the knowledge of the wire drawing process. This should approximate the actual case more closely than past work even though shear deformations are neglected.

We would like to point out that the author's use of a linear strain-hardening relationship has resulted in poorer agreement between his theory and experimental results than would be the case if the actual true stress-true strain curve were used. If the average stress σ_0' is taken from the actual true stress-true strain curve

$$\sigma_0' = \frac{1}{\epsilon_{max}}\int_0^{\epsilon_{max}} \sigma d\epsilon$$

Tables 3 and 4 are altered as follows:

Table 3 Aluminum drawing

No. of series of tests	$\frac{\sigma_2}{\sigma_0'}$ with l_2	σ_0', psi	σ_2 with l_2, psi
1	0.123	9,300	1140
2	0.181	10,500	1900
3	0.245	11,500	2820
4	0.290	12,300	3570

Table 4 Zinc drawing

No. of series of tests	$\frac{\sigma_2}{\sigma_0'}$ with l_2	σ_0', psi	σ_2 with l_2, psi
1	0.296	10,300	3050
2	0.355	12,500	4440
3	0.406	15,000	6090
4	0.470	16,000	7530

When this revised draw stress is plotted in Figs. 9 and 10 the curves of Equation (25) are quite a bit higher and closer to the curve of experimentally measured drawing stresses.

For high strain rate processes, such as metal cutting, Kobayashi, et al. [7] have suggested the use of the flow stress at the final value of strain as the average flow stress. This would result in even better agreement between the author's theory and experiment. However, since the strain rate in the present process (of the order of 10 sec^{-1}) is between the strain rate in conventional tensile testing and the strain rate in metal cutting, it would seem that more would have to be known about the behavior of the materials used as a function of strain rate before this argument could be applied to the present case.

It seems that the author's discussion of Fig. 6 needs some clarification. If all of the work of deformation were converted to heat and distributed uniformly through the wire a temperature rise of the order of 15 deg F would result. The thermal expansion of the wire resulting from this temperature rise would be quite small and would hardly account for the increase in separating force shown in Fig. 6. It is more likely that the author's explanation concerning the force decrease from "*c*" to "*d*" is also applicable to the increase from "*a*" to "*b*." That is, the accumulation of heat in the die may cause a temperature rise of considerably more than 15 deg F and result in a thermal gradient between die and die plate. This thermal gradient could then cause a compressive force on the dynamometer ring and appear as an increasing separating force.

Additional Reference

7 S. Kobayashi, R. P. Herzog, D. M. Eggleston, and E. G. Thomsen, "A Critical Comparison of Metal-Cutting Theories With New Experimental Data," JOURNAL OF ENGINEERING FOR INDUSTRY TRANS. ASME, Series 3, vol. 82, 1960, p. 333.

Erich G. Thomsen[6] and Shiro Kobayashi[7]

The author is to be congratulated for his excellent paper presented here. The experimental data and the demonstration of the importance of the land in wire drawing are of particular interest.

Comparison of equation (25) with Sachs' analysis given in the final results (Figs. 9 and 10) certainly shows the importance of the

[3] Management Consultant, Tucson, Ariz. Mem. ASME.

[4] Senior Research Engineer, The Cincinnati Milling Machine Company, Cincinnati, Ohio. Assoc. Mem. ASME.

[5] Research Supervisor, The Cincinnati Milling Machine Company.

[6] Professor of Metal Processing, University of California, Berkeley, Calif. Mem. ASME.

[7] Lecturer in Industrial Engineering, University of California.

role that the land plays in the mechanics of wire drawing. However, it is still uncertain whether the deviation of equation (25) from the experimental data is due to the shear deformation neglected in equation (25) or due to the more complex phenomenon of friction.

The stress analysis for the conical part which results in equation (25) is almost the same as that derived by Sachs, except that the yield condition is given by equation (13). It is evident at once, therefore, that the redundant work due to shearing cannot be negligible unless the drawing conditions are those for small die angles and large reductions. In order to bring the effect of shear deformation into the analysis of wire drawing, let us apply the slip-line solution obtained for sheet drawing to wire drawing. This can be done by merely replacing $t'/2k$ (Hill's notation,[8] t' = mean drawing stress, k = maximum shear stress) and reduction of thickness in sheet drawing by $(\sigma_x)_a/\sigma_0'$ (author's notation) and reduction of area in wire drawing, respectively. Friction may be included in sheet drawing by letting

$$\frac{t'}{2k} \cong \frac{t}{2k}\,(1 + \mu \cot \phi)$$

and correspondingly in wire drawing by letting

$$\frac{(\sigma_x)_a}{\sigma_0'} \rightharpoonup \frac{(\sigma_x)_a^*}{\sigma_0'}\,(1 + \mu \cot \phi)$$

The quantities t and $(\sigma_x)_a^*$ are drawing stresses for frictionless dies in sheet and wire drawing, respectively, and Hill[8] has made them available in the form of $t/2k$ as functions of sheet reduction for given die angles. It may be noted that by applying slip line solutions one can, at least for the conical part, eliminate the contradiction in assumptions required for obtaining equation (4) (p is constant over the die surface) and for deriving equation (25) (p varies along the die surface).

Using the slip line solution for the conical part and assuming the same stress analysis as that of the author for the land part of the die, the drawing stress is given by

$$\sigma_2 = \sigma_0' \left\{ \frac{(\sigma_x)_a^*}{\sigma_0'}\,(1 + \mu \cot \phi) - 1 \right\} e^{\frac{-4\mu}{d_2} \cdot l_2} + \sigma_0' \quad (26)$$

for a work-hardening material.

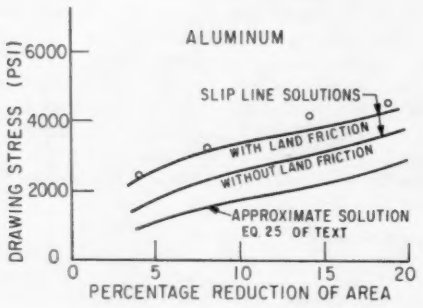

Fig. 11

Fig. 11 shows theoretical drawing stresses obtained by use of equation (26) as solid curves and the aluminum experimental data by open circles. The two curves based on slip-line solutions were obtained by using appropriate coefficients of friction, i.e, using the experimental value of μ (without l_2) when the land was absent and the experimental values of μ (with l_2) when the land was present. It should be mentioned that in these latter calculations a mean flow stress, σ_m, was used instead of σ_0' of the author since σ_m seems to be a more realistic flow stress.

It is seen in the figure that the agreement between theory and experiment is now remarkably good when the effect of the land is taken into consideration.

[8] R. Hill, "The Mathematical Theory of Plasticity," Clarendon Press, Oxford, England, 1950, p. 167.

Author's Closure

The author wishes to thank Messrs. Alden, Kegg, Kalpakcioglu, and Professors Thomsen and Kobayashi for their kind discussion.

For practical interest, this paper shows that in estimating the drawing load the die land friction should be included. This is one step further toward a close answer for drawing load estimation.

Zinc was selected for drawing material because it is different from aluminum in structure; while both Al and Cu are FCC, Zn is HCP.

H.S.S. was used for die material mainly because it was available then in our laboratory. Since the die life is not important in the tests and steel dies gave most of the information the author expected, more expensive die materials were not used.

The influence of drawing speeds on drawing forces is different with different metals. A stress strain-rate curve will give a general indication in this regard. In our drawing tests, speed was very low because of limited capacity of the machine used (an old horizontal broach machine). Concerning the effect of die profiles on drawing forces, it is suggested to refer to Reference [6] in the present paper. Lubricants usually act differently for different wire and die materials. Mr. Alden is advised to refer to "Lubrication in Wire Drawing," by J. G. Wistreich, Conference on Lubrication and Wear, The Institution of Mechanical Engineers, October, 1957.

The author agrees completely with Messrs. Kegg and Kalpakcioglu's suggestion in using the area under the $\bar{\sigma}$-$\bar{\epsilon}$ curve to get a better average flow stress.

The author still believes that the rise in separating force from a to b in Fig. 6 is due to the temperature rise during drawing. The temperature calculated from the plastic working is the average temperature. The temperature on the surface of the wire at the instant of drawing could be much higher than 15 deg F above room temperature. The author experienced the fact that the wire right after drawing was so hot that he could not touch it. Putting thermocouples in the die was tried, but it was difficult to get them close to the die surface.

It is most unlikely that one can apply the same explanation for force drop from c to d to force rise from a to b in Fig. 6 because aluminum die plate will expand more and faster than H.S.S. die.

The author appreciates the suggestion of Professors Thomsen and Kobayashi in combining the author's and Hill's equation as shown in Equation (26). However, he is a little dubious concerning whether these two equations could be combined, since the author used "strip analysis" and Hill used slip-line method. The basic assumptions of these two methods are very different. Thus, it remains yet to be seen if Equation (26) yields good results to all metals in drawing load estimation.

KATSUNDO HITOMI[1]
Assistant Professor,
Department of Mechanical Engineering,
Kyoto University, Kyoto, Japan

Fundamental Machinability Research in Japan

This manuscript presents a brief description of fundamental research in Japan in the field of machinability.

I Introduction

MACHINABILITY research in Japan has been affected by development of metal-cutting theory and manufacturing technique in foreign countries, especially, the United States and Germany.

Research work in this area started about thirty years ago when Professor Okoshi [1],[2] Tokyo University, presented the first report on fundamental study on cutting action and type of chip. Since then much fundamental and also practical work has been done to develop Japanese manufacturing processes. Reports have been presented in the fields of mechanics of orthogonal cutting and three-dimensional cutting, cutting temperature, tool life test, wear process of carbide and ceramic tools, surface roughness, chip control, cutting fluid, chatter, hot machining, cold machining, drilling, milling, and others. In addition to regular cutting operations, fine finishing techniques such as grinding, polishing, lapping, superfinishing, ultrasonic machining, electrodischarge machining, etc., have been investigated and developed.

Among these subjects, in this paper the author will discuss topics such as fundamental analyses of mechanics of orthogonal cutting, cutting temperature, tool wear process, development of ceramic tooling, chatter, surface roughness, and two special topics investigated and developed recently in Japan.

II Fundamental Analysis of the Mechanics of Metal Cutting

Fundamental research on the cutting mechanism has been continued since Okoshi's first study [1]. It has been influenced by similar research in other countries, especially, studies by Ernst, Merchant, Schmidt, Shaw, Trigger, Kronenberg, Hucks, Opitz, and others.

The following is a brief statement regarding main concepts on the mechanics of orthogonal cutting developed in Japan.

(a) Indentation Action of a Cutting Tool. Masuko [2] analyzed the cutting mechanism from the viewpoint of a new concept of indentation force produced on the round cutting edge by elastic deformation of the tip of the tool. He considered both deformation force on chip R' and indentation force at a cutting edge R'' as shown in Fig. 1. The resultant force R is the so-called cutting force.

The indentation force R'' is produced owing to the dullness of the cutting edge and also due to the elastic deformation of the cutting tool, and its theoretical equation was deduced.

$$R'' = \frac{1}{\delta + \sin\delta} \frac{\sin\delta}{1 - \sin\frac{\delta}{2}} \frac{q^2}{E} C,$$

where

δ = lip angle of cutting tool
q = distribution load on tip of tool
E = elastic coefficient of cutting tool
C = constant

This force was divided into two parts—the component of central direction of the lip angle R_1'' and the perpendicular component R_2''. Theoretical equations for both components were deduced.

Masuko applied these equations to the experimental data for aluminum alloy and carbon steel, and explained the paradox in metal-cutting theory such as size effect, increase of friction angle with an increase in rake angle or depth of cut, extremely large shearing stress on shear plane at small depth of cut compared with static material test, and so on.

(b) Analysis of Friction Process and Shear Angle. Sata and Mizuno [3] investigated the friction process on the tool face when a continuous chip is produced in dry cutting, and then deduced equations for friction angle and shear angle.

They considered the cutting model as shown in Fig. 2, and noted two regions of plastic deformation; that is, the shear plane OA and the tool-chip interface OB. From equilibrium of forces acting on the shear plane and the tool-chip interface, the line connecting the shear point A and the chip separating point B is parallel to the resultant cutting force R. The equation of ratio

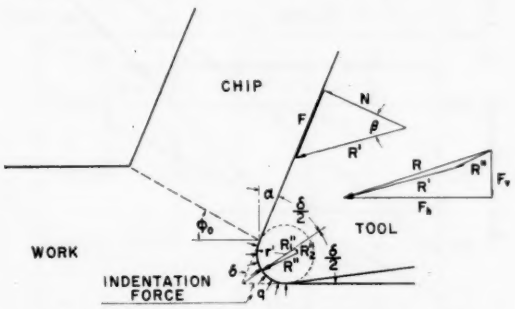

Fig. 1 Cutting mechanism with the indentation force

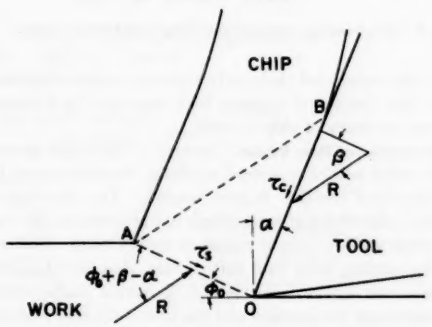

Fig. 2 Cutting model for analysis of friction process and shear angle

[1] When the paper was presented, Department of Industrial Engineering, The Pennsylvania State University, University Park, Pa.

[2] Numbers in brackets designate References at end of paper.

Contributed by the Production Engineering Division and presented at the Winter Annual Meeting, New York, N. Y., November 27–December 2, 1960, of THE AMERICAN SOCIETY OF MECHANICAL ENGINEERS. Manuscript received at ASME Headquarters, July 26, 1960. Paper No. 60—WA-78.

between shearing stresses on the tool-chip interface and the shear plane was deduced from the geometrical relationship:

$$\frac{\tau_c}{\tau_s} = \frac{\sin 2\beta}{\sin 2(\phi_0 + \beta - \alpha)},$$

where ϕ_0 is shear angle, α is rake angle, and β is friction angle. Cutting tests with carbon steel showed

$$\frac{\tau_c}{\tau_s} = 1.$$

This relation was also confirmed by experimental results of other investigators. It is concluded that the shearing stress on the tool-chip interface is equal to that on the shear plane, hence to that in the yield state.

Using the boundary condition that the stresses on the free surfaces of work and chip are zero, and with a help of experimental results, they deduced the equation for friction angle on the tool face.

$$\beta = 37.5° + \frac{\alpha}{2}$$

From the foregoing equations, the shear angle was expressed as follows:

$$\phi_0 = \alpha \qquad \text{for} \quad \alpha \geqslant 15°$$
$$\phi_0 = 15° \qquad \text{for} \quad \alpha \leqslant 15°.$$

They confirmed that these relations are in good agreement with various cutting data, as shown in Fig. 3.

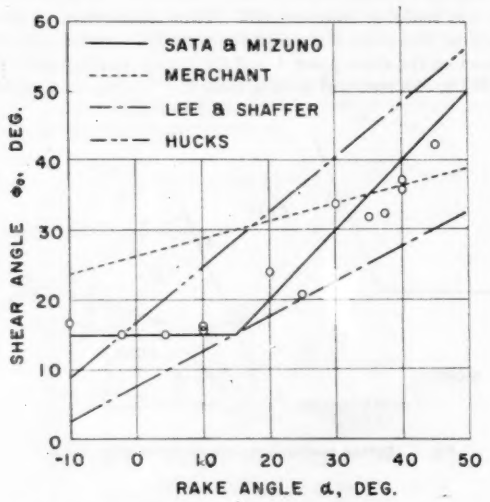

Fig. 3 Relationship between rake angle and shear angle

They also concluded that perfect contact occurs between chip and tool face due to the extreme high stress on the interface and the strong tendency of chip to weld.

(c) The Concept of Flow Region. Instead of the single shear plane concept, which contains several conflicts, Okushima and Hitomi [4, 5] developed the flow region concept. The flow region is a transitional deformation zone which exists between the rigid region of work and the plastic region of steady chip. It was ascertained, by cutting tests with soft metals, that the shear process takes place over a wide area instead of along a single plane.

They analyzed the location and the size of the flow region when a continuous chip is produced. Assuming that the starting

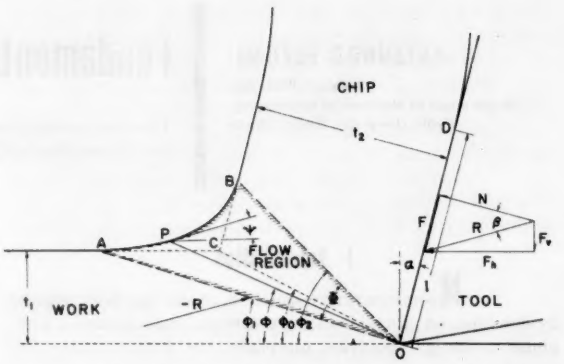

Fig. 4 Cutting mechanism with the flow region

boundary line OA and the ending boundary line OB of the flow region are straight (in reality slightly convex downward and upward, respectively), and considering the yield condition inside the flow region and chip, theoretical equations for angles of boundary lines of the flow region were deduced (see Fig. 4).

$$\phi_1 = \frac{K_1}{2} - \frac{\beta}{2} + \frac{\alpha}{2}$$

$$\phi_2 = \frac{K_2}{2} - \frac{\beta}{2} + \alpha$$

$$K_1 = \sin^{-1}\left\{\frac{2}{k_1}\sin\beta + \sin(\beta - \alpha)\right\}$$

$$K_2 = \cos^{-1}\left(\frac{2}{k_2}\sin\beta - \cos\beta\right)$$

$$k_1 = \frac{l}{t_1}, \quad k_2 = \frac{l}{t_2},$$

where α is rake angle, β is friction angle, l is chip contact length, t_1 is depth of cut, and t_2 is chip thickness. The sector angle or size of the flow region is

$$\Phi = \phi_2 - \phi_1 = \frac{\alpha}{2} - \frac{K_1}{2} + \frac{K_2}{2}.$$

The shearing strain inside the flow region was expressed as follows:

$$\gamma = \cot\phi - \cot(\phi + \psi),$$

where ϕ is inclination angle of an arbitrary radial plane OP, and ψ is angle between the machined surface and the tangent of the free surface of the flow region at an arbitrary point P. In a particular case, the shearing strains on the starting and ending boundary lines are

$$\gamma_1 = 0, \qquad \gamma_2 = \cot\phi_2 + \tan(\phi_2 - \alpha).$$

The foregoing theory was applied to the cutting results for lead and brass. An example is shown in Fig. 5. In this figure, the conventional shear angle ϕ_0 and shear strain γ_0 based upon the cutting mechanism of a single shear plane are also shown. The inclination angle of starting boundary line of the flow region ϕ_1 is smaller and that of ending boundary line ϕ_2 is larger than the conventional shear angle ϕ_0; in other words, the sector angle of the flow region Φ has always some positive value. This verifies the rationality of the flow region concept. Fig. 6 shows an example of the schematic cutting model based upon this concept. The strain in chip γ_2 is much smaller than the conventional shear

strain γ_0. Thus the cutting mechanism with the flow region seems to be more reasonable than the conventional cutting mechanism with a single shear plane not only from the standpoint of smooth movement of a metal particle but from the viewpoint of strain and strain rate.

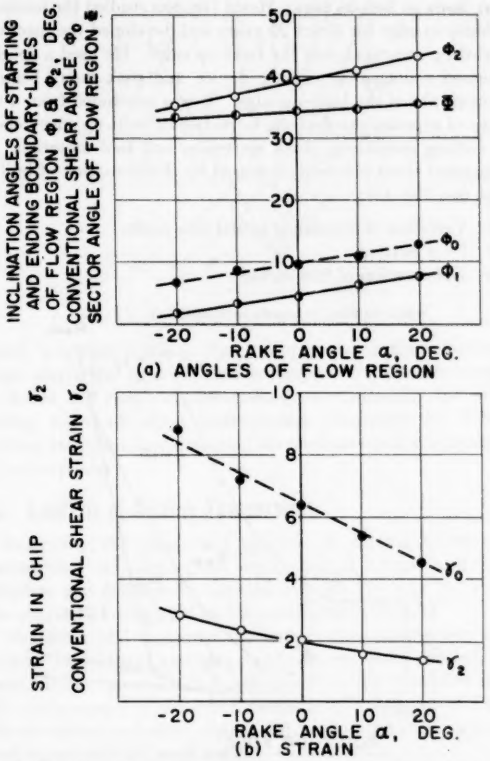
INCLINATION ANGLES OF STARTING AND ENDING BOUNDARY-LINES OF FLOW REGION Φ1 & Φ2, DEG.
CONVENTIONAL SHEAR ANGLE Φ0
SECTOR ANGLE OF FLOW REGION
RAKE ANGLE α, DEG.
(a) ANGLES OF FLOW REGION
STRAIN IN CHIP
CONVENTIONAL SHEAR STRAIN
RAKE ANGLE α, DEG.
(b) STRAIN

Fig. 5 Experimental results for analysis of orthogonal cutting; work material, lead; tool material, high-speed steel; width of cut, 11.0 mm; depth of cut, 0.10 mm; cutting speed, 5.2 m/min; dry

The grid deformation was analyzed, considering the flow region. The result is shown in Fig. 7. Smooth distortion of grid during cutting is seen.

Okushima and Hitomi also applied the concept of flow region to an analysis of the mechanism of discontinuous chip formation, and obtained the theoretical equations for angles of starting and ending (fracture) lines. Comparing the theory with cutting test of carbon steel, both were in good agreement.

They [6] also proved the existence of the flow region by investigating the secondary flow in chip, and found that the size of the flow region decreases with an increase in cutting speed.

Nakayama [7] considered the similar deformation zone, taking photographs of cutting process.

(d) The Concept of Chip Contact Area on Tool Face. Takeyama and Usui [8] discovered the importance of the tool-chip contact area. In their experiment, they used a special cutting tool which varied contact area artificially as shown in Fig. 8. It was found out that

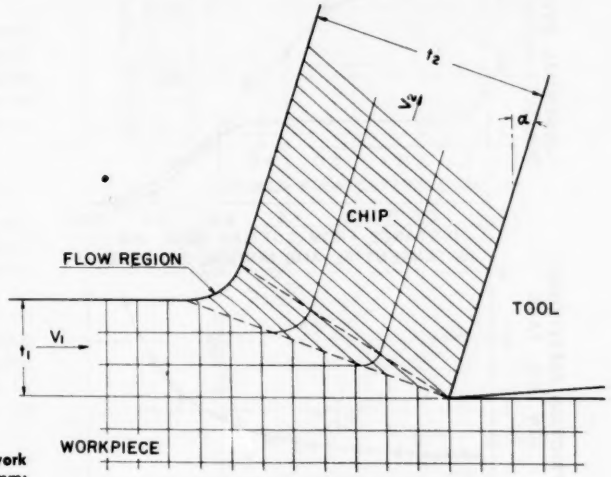

Fig. 7 Grid deformation in metal cutting

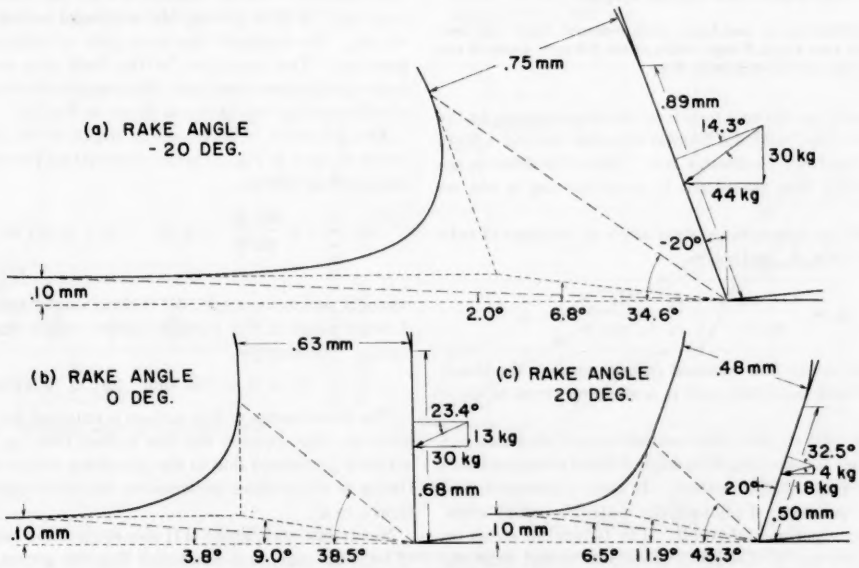

Fig. 6 Schematic cutting model with the flow region drawn from Fig. 5

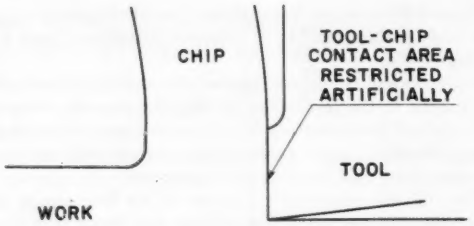

Fig. 8 Cutting tool with artificially varied tool-chip contact area

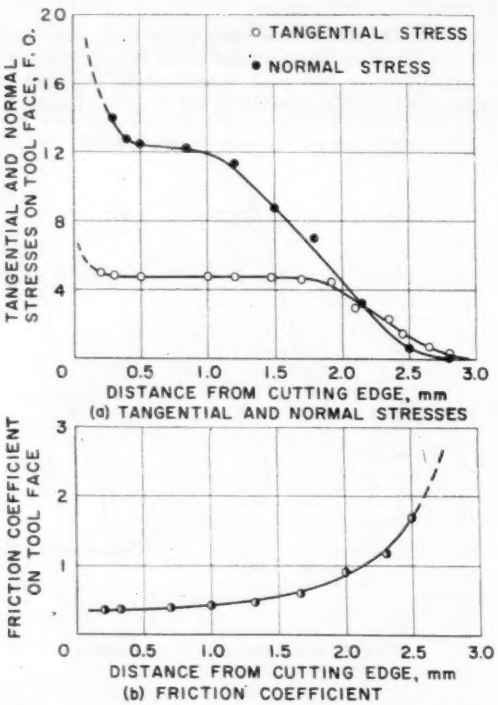
TANGENTIAL AND NORMAL STRESSES ON TOOL FACE, F. O.
TANGENTIAL STRESS
NORMAL STRESS
DISTANCE FROM CUTTING EDGE, mm
(a) TANGENTIAL AND NORMAL STRESSES
FRICTION COEFFICIENT ON TOOL FACE
DISTANCE FROM CUTTING EDGE, mm
(b) FRICTION COEFFICIENT

Fig. 9 Stress distribution on tool face; work material, lead; tool material, epoxy resin; rake angle, 7 deg; width of cut, 5.0 mm; depth of cut, 0.87 mm; cutting speed, 0.018 m/min; dry

the frictional force on the tool face is in direct proportion to the tool-chip contact area, and the friction in metal cutting follows Amontons' law and not Coulomb's law. Hence the friction coefficient which has been considered in metal cutting is not reliable.

They deduced the equation for shear angle ϕ_0 in terms of rake angle α, contact area A_0, and others.

$$\phi_0 = \frac{1 - \sin\alpha}{\cos\alpha} + \frac{k_0}{\tau_0}\frac{A_0}{A_0' \cos\alpha},$$

where A_0' is area in cut, k_0 is constant (nearly equal to the shearing strength of work material), and τ_0 is shearing stress in shear plane.

In connection with the tool-chip contact area, Takeyama and Usui [9] succeeded in measuring the tangential and normal stresses on tool face by photoelastic method. In their experiment lead was cut with a tool made of photoelastic material—epoxy resin. Fig. 9 shows the experimental result. The tangential stress on tool face was observed to distribute uniformly except near the separating point of chip where rapid decrease was seen. On the other hand, the normal stress on tool face had the maximum value at the cutting edge and decreased gradually along the tool-chip interface. From these data the friction coefficient at various points on tool face was calculated. It was not uniform. This also verifies their concept of tool-chip contact area.

(e) Study on Built-Up Edge. Hoshi [10] has studied the formation of built-up edge for about 20 years and developed the mechanics of cutting accompanying the built-up edge. He used a specially designed sudden-stop cutting device and took many beautiful photographs of the built-up edge. It was concluded from a wide range of experiments that the formation of built-up edge depends on cutting conditions, work materials, and tool materials. He recognized three phenomena caused by the formation of built-up edge (see Fig. 10):

1 Variation or increase in actual rake angle.
2 Over cutting.
3 Deformation of free surface.

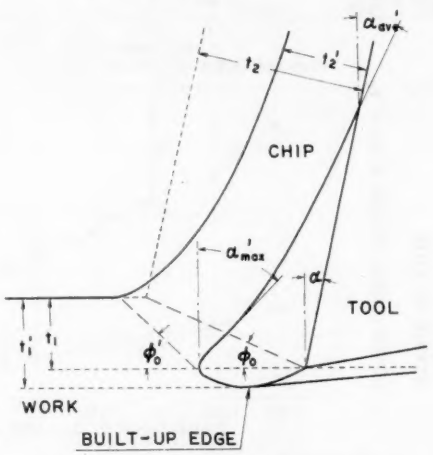

Fig. 10 Cutting model with built-up edge

Generally the actual rake angle increases when the built-up edge develops. Hoshi concluded that the average actual rake angle α_{ave}' is 30 to 35 deg, the maximum actual rake angle α_{max}' 45 deg. He assumed the back side of built-up edge was a parabola. The equations for the back side and flank side of built-up edge were deduced. As a result, the fundamental shape of built-up edge was drawn as shown in Fig. 11.

The difference between actual depth of cut t_1' and apparent depth of cut t_1 in Fig. 10 is the over cutting phenomenon. It was expressed as follows:

$$t_1' - t_1 = C' t_1 \frac{\sin\phi_0'}{\sin\beta'}\{\cos(\beta' - \phi_0') + \cot\phi_0' \sin(\beta' - \phi_0') - \operatorname{cosec}\phi_0'\},$$

where β' is friction angle, ϕ_0' is shear angle, and C' is constant. A single prime in this equation means values when built-up edge exists. For example,

$$t_1' - t_1 = 0.07 \text{ mm} \quad \text{for} \quad t_1 = 0.2 \text{ mm}.$$

The deformation of free surface is enlarged by the existence of built-up edge, because the free surface rises up before shearing action is performed due to the ploughing action of built-up edge. Owing to this surface deformation the thickness of chip changes from t_2 to t_2'.

Nakayama and Iguchi [11] also studied the cause of formation of built-up edge, and concluded that the generation of built-up edge is related to the cutting temperature and not to the cutting

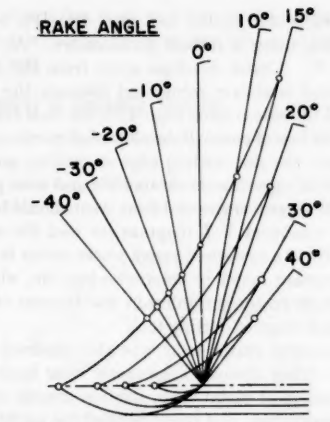

Fig. 11 Fundamental shape of built-up edge

speed, and that built-up edge disappears over the temperature range above the recrystallization temperature of work material.

Okoshi and Sata [12] determined experimentally the critical cutting speed at which built-up edge disappears for different cutting conditions and discussed the formation and disappearance of built-up edge.

III Analysis of Cutting Temperature

Regarding the theoretical analysis of cutting temperature, Yamamoto [13] pointed out weaknesses of Trigger and Chao's solution, and developed a new theory. He [14] also has studied the effect of cutting fluid on the cutting temperature.

Okushima [15] measured the temperature distribution in the vicinity of the tip of a cutting tool by thermo-color method, using a specially designed divisible orthogonal cutting tool shown in Fig. 12. An example of the experimental results is shown in Fig. 13. He also calculated rates of heat diffusing to the chip region, the tool region, and the work region.

IV Tool Life Test and Wear Process

Regarding wear process of the cutting tool, tool life test, testing method, etc., many reports have been presented by Okoshi, Sata, Takeyama, Kogure, Okushima, Okusa, Irie, and others.

Okushima [16] studied the fundamental wear process of high-speed steel tools. In order to observe wear aspect of the cutting tool easily and in detail, he used a divisible orthogonal cutting tool shown in Fig. 12, and cut tubular specimen of carbon steel dry on a lathe. It was found that the length of flank wear V_B and the width of crater K do not always increase continuously, but stepwise; in other words, either V_B or K increases while the other remains constant. Sometimes both progress at the same time. This is shown in Fig. 14. However, plotting the relationship between wear area S and cutting time T or cutting length L, it was noticed to be in almost direct proportion.

Next, Okushima and Okusa [17] widely studied the wear proc-

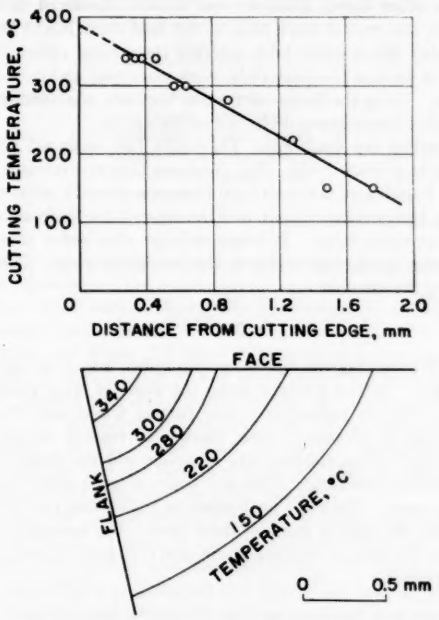

Fig. 13 Temperature distribution in cutting tool; work material, 0.24% carbon steel; tool material, high-speed steel; rake angle, 0 deg; relief angle, 12 deg; width of cut, 3.0 mm; depth of cut, 0.022 mm; cutting speed, 26.0 m/min; dry

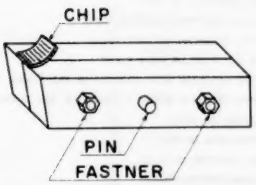

Fig. 12 Divisible orthogonal cutting tool

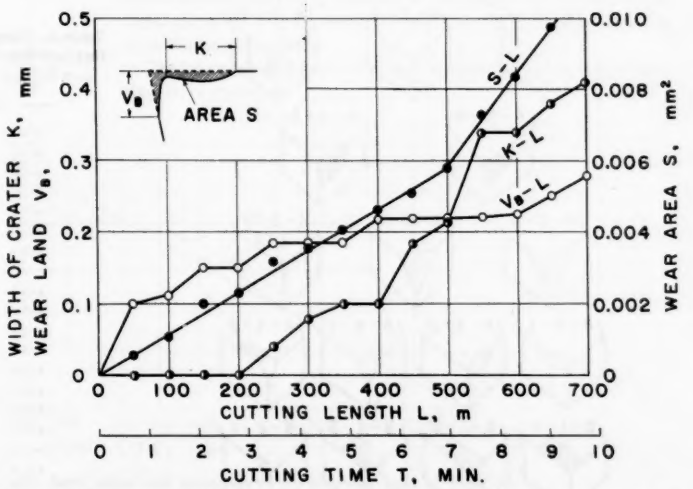

Fig. 14 Wear process of high-speed steel tool; work material, 0.24% carbon steel; rake angle, 0 deg; relief angle, 12 deg; width of cut, 3.0 mm; feed (depth of cut), 0.024 mm/rev; cutting speed, 72.0 m/min; dry

ess of carbide tools and classified the fundamental failure of carbide as shown in Fig. 15 and Table 1. From this wide range of experiments, the process of flank wear was also investigated. It was concluded that the critical flank wear for carbide tooling should not be fixed as Boston determined, but depends on the work material, tool material, and cutting conditions. The reason for this is as follows: The final stage at which carbide tools must be reground is not determined solely by the flank wear. It is sometimes affected by the crater wear. Even if flank wear is small, carbide tools sometimes reach the final stage due to a large amount of crater on the face or chipping on the cutting edge. In this case, the critical flank wear should be taken as a small value. On the other hand, if crater wear is not considered to be important, the critical flank wear at the final stage might be large. Thus they developed a table showing the critical values of flank wear for various tool materials, work materials, and cutting conditions. Using the foregoing results, they are establishing a test method to determine carbide tool performance.

Regarding the flank wear, Takeyama [18] analyzed the wear process of carbide tools. Fig. 16 shows the experimental result. It was found that the wear land increases directly with cutting time on bilogarithmic paper, and the slope of the increase is small in the primary stage. It becomes large after some amount of flank wear is reached. This is the secondary stage. The wear land V_B is expressed

$$V_B = cT^m V^n,$$

where T is cutting time, V is cutting speed, and c, m, and n are constants. In the primary stage the slope of wear progress is almost constant regardless of the cutting speed, and the wear occurs due to abrasion. After flank wear reaches some critical value, the cutting temperature increases and the slope of wear progress becomes large. This secondary stage is affected by the cutting speed. The more heat-sensitive the cutting tool material, the lower the critical value of flank wear. For example, 0.25 to 0.30 mm for cast iron cutting grade, and 0.40 to 0.45 mm for steel cutting grade.

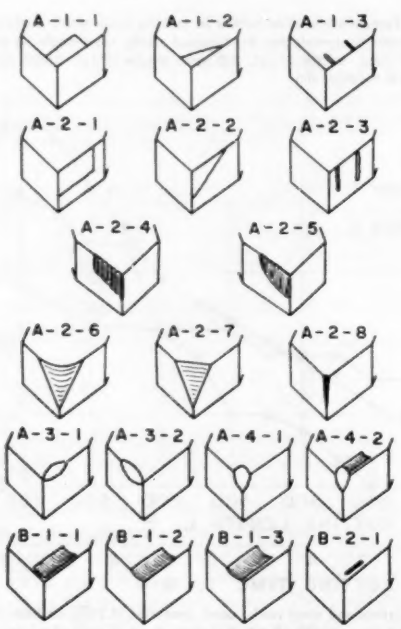

Fig. 15 Fundamental failure in carbide tooling

Regarding the crater on the tool face, Irie [19] observed its process in detail, using a surface profilometer. An example is shown in Fig. 17. Crater develops apart from the side cutting edge Some land is always recognized between the border line of crater A and the side cutting edge until the final failure occurs. The other border line of crater B develops and grows apart farther and farther from the side cutting edge as cutting proceeds.

From a series of experiments on tool life and wear process, Irie recommended that both crater and flank wear should be combined to establish a combined V-T diagram for tool life standard as shown in Fig. 18. In low-speed range where crater is small flank wear is an important factor to determine tool life, while in high-speed range where crater is significant the amount of crater determines the final stage of cutting tool.

The importance of crater wear was also reported by Okoshi and Sata [20]. They discussed the crater wear from the standpoint of mechanism of metal wear, friction process on tool face and cutting temperature, and recommended the use of heat-sensitive tool materials and the selection of proper cutting conditions in order to resist cratering.

Recently Sata and Nakajima [21] have started to use radioactive cutting tools in tool life tests. They tested carbon steel and

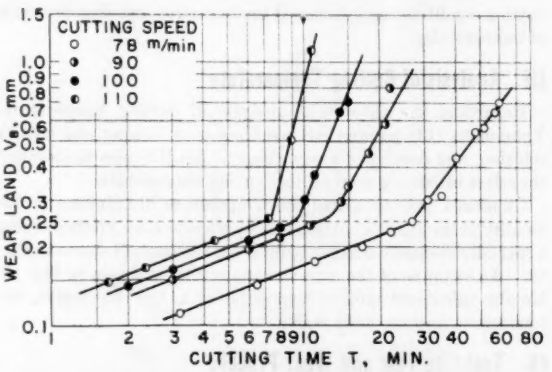

Fig. 16 Process of flank wear of carbide tool; work material, cast iron FC 27; tool material, carbide G1 (cast iron cutting grade); tool geometry, 0, 6, 6, 6, 15, 15, 0.2 mm; depth of cut, 2.0 mm; feed, 0.17 mm/rev; dry

Table 1 Fundamental failure of carbide tools in three-dimensional cutting (see Fig. 15)

TYPE	EXPLANATION
A-1-1	RECTANGULAR TYPE CHIPPING ON FACE
A-1-2	TRIANGULAR TYPE CHIPPING ON FACE
A-1-3	ABNORMAL TYPE CHIPPING ON FACE
A-2-1	RECTANGULAR TYPE CHIPPING ON SIDE FLANK
A-2-2	TRIANGULAR TYPE CHIPPING ON SIDE FLANK
A-2-3	ABNORMAL TYPE CHIPPING ON SIDE FLANK
A-2-4	TRIANGULAR TYPE CHIPPING WITH GROOVES ON END FLANK
A-2-5	TRIANGULAR TYPE CHIPPING WITHOUT GROOVE ON END FLANK
A-2-6	ARC TYPE CHIPPING ON NOSE
A-2-7	LINEAR TYPE CHIPPING ON NOSE
A-2-8	ABNORMAL TYPE CHIPPING ON NOSE
A-3-1	CHIPPING ON SIDE CUTTING EDGE
A-3-2	CHIPPING ON END CUTTING EDGE
A-4-1	INITIAL FAILURE
A-4-2	FINAL FAILURE
B-1-1	CRATERING WITH LANDS ALONG SIDE AND END CUTTING EDGES
B-1-2	CRATERING WITHOUT LAND ALONG SIDE AND END CUTTING EDGES
B-1-3	CRATERING WITH LAND ALONG SIDE CUTTING EDGE AND WITHOUT LAND ALONG END CUTTING EDGE
B-2-1	WEAR DUE TO SEPARATION OF SHEAR

several kinds of stainless steel, and introduced empirical formulas indicating the relationship between tool life and cutting speed by the short-run test.

V Development of Ceramic Tooling

One of the recent topics in the metal-cutting area in Japan is ceramic tooling.

The first cutting test with a ceramic cutting tool was made by Tamaru and Shiraishi [22] about four years ago. They used an imported English-made ceramic, "Sintox," and compared its cutting performance with that of carbide tool from the standpoint of tool life and wear process when cutting tool steel, stainless steel, and plastics.

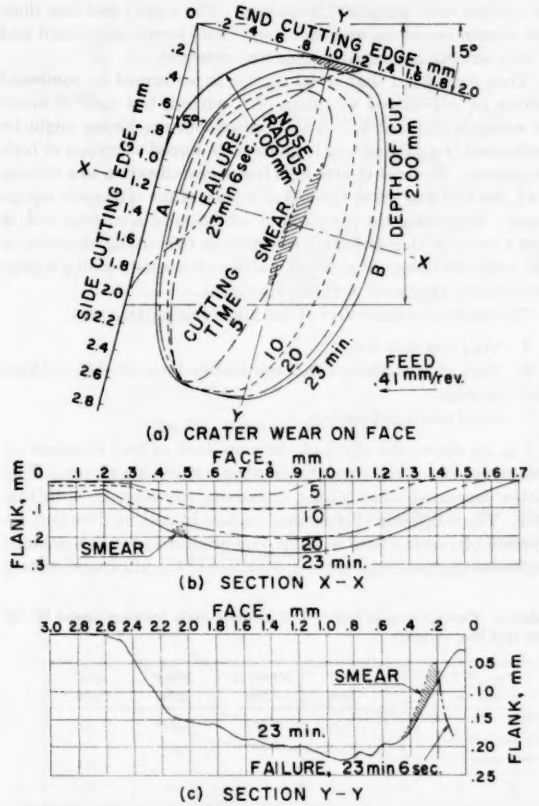

Fig. 17 Development of crater wear of carbide tool; work material, carbon tool steel SK 7(0.58% C); tool material, carbide S1(steel cutting grade); tool geometry, 4, 6, 6, 6, 15, 15, 1.0 mm; depth of cut, 2.0 mm; feed, 0.41 mm/rev; cutting speed, 200.0 m/min; dry

In recent years a manufacturing technique for ceramic in Japan has been developed based on the experience of manufacture of carbide. At present several companies produce ceramic tools commercially (see Table 2), and some industries are using them on a limited basis. Since ceramic tools are more brittle than carbide tools, the manufacturers are attempting to increase the ductility of ceramic tools.

Table 2 Manufacturers of ceramic cutting tools in Japan

TRADE MARK	COMPANY	PERIOD
TUNGALOX	TOSHIBA TUNGALOY COMPANY	1958
N. T. K.	NIPPON TOKUSHU TOGYO COMPANY	1958
KEMICALOX	NIPPON CHEMICAL CERAMIC COMPANY	1958
ALOX	SUMITOMO ELECTRIC INDUSTRIES, LTD.	1959
DIALOX	MITSUBISHI METAL MINING COMPANY	1959
----	HITACHI, LTD.	----

Regarding fundamental research on ceramic tooling, investigators have investigated the cutting performance of ceramic tools in comparison with carbide tools for the purpose of developing better ceramic tool material.

Okushima and Fujii [23] have studied ceramic tooling in a wide range of experiments. They investigated the relationship between physical properties and tool life, and determined the optimum tool geometry and cutting conditions when cutting carbon steel. It was found that the higher the transverse rupture strength and the specific gravity and the finer the grain size of ceramic material, the better the tool life.

Regarding the type of failure in ceramic tooling, they reported that it is similar to that in carbide tooling. However, since ceramic is more brittle and has less affinity for welding than carbide, cracking or chipping on the nose or the cutting edge of ceramic tool was more common, and no cratering was observed on the face as is often observed for carbide tool. The typical shape of failure of ceramic tool at the nose is shown in Fig. 19. The marked peculiarity in ceramic tooling is that even when some amount of flank wear has been reached or some damage has occurred on the nose it is possible to continue cutting and sometimes get a fairly good machined surface. It is impossible to do so in the case of carbide.

The following optimum cutting conditions for machining carbon steel were reported:

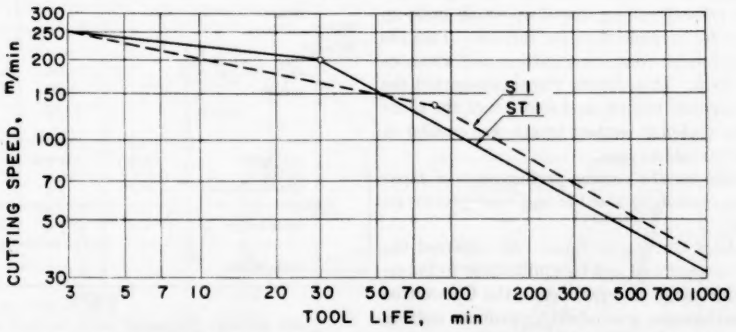

Fig. 18 V-T diagram combined with flank wear and crater; tool life criterion, land of flank wear 0.3 mm or depth of crater 0.1 mm; work material, carbon tool steel SK 7(0.58% C); tool material, carbides S1(WC-TiC-Co) and ST1(WC-TiC-TaC-Co); tool geometry, 4, 6, 6, 6, 15, 15, 1.0 mm; depth of cut, 2.0 mm; feed, 0.41 mm/rev; dry

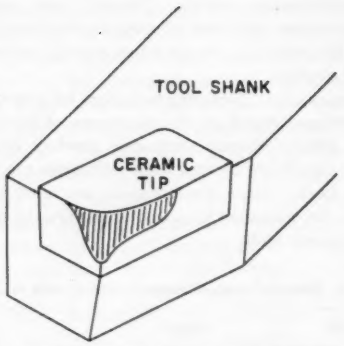

Fig. 19 Typical failure of ceramic tool

Feed	about 0.1 mm/rev.
Depth of cut	no effect
Back rake angle	−5 to −10 deg
Side rake angle	small positive value
Relief angle	5 deg
Nose radius	less than 1.0 mm

It was checked to see if the double rake angle tool was effective. It was effective. The best conditions were

Primary rake angle	0 deg
Secondary rake angle	5 deg
Width of land	the same as feed rate

Okushima and Fujii [24] always observed the bright machined surface when turning with a ceramic tool, more beautiful than that with a carbide tool, and tried to explain this phenomenon according to the oxide film generated on the machined surface after cut.

They [25] also investigated the welding property between carbide and ceramic materials and work materials at high temperature. The experiment was carried out statically in a furnace. It was observed that ceramic and work materials welded together, and the critical temperature for welding depended on the chemical compositions of ceramic and work materials. The interface strength between ceramic and metal was weaker than that between carbide and metal. It was explained from this that formations of crater and built-up edge are much less for ceramic tool than for carbide tool.

Okoshi and Sata [26] compared the grinding properties of carbide and ceramic tools, and recommended the use of a diamond wheel of very fine grain size for ceramic tool. They observed that the built-up edge appears in the case of ceramic tooling at low cutting speed, but the critical cutting speed at which built-up edge disappears is lower for ceramic than for carbide. Tool life test was also run for alloy steel, comparing cutting performances of ceramic and carbide tools. In addition, they investigated the cutting mechanism for ceramic tooling, and found that the shear angle was larger and the tool-chip contact length was smaller in ceramic tooling than in carbide tooling.

Takeyama [27] investigated the cutting performance of Japanese-made ceramic tools, examining tool life and wear process on cast iron and alloy steel.

The Committee of Metal Cutting in Japan [28] reported the cutting performance of ceramic tool and its application to industry. As a result of a wide range of experiments, the Committee discussed the cutting mechanism, grindability, optimum cutting conditions, and tool geometry. In addition, tool life for Japanese-made ceramic was compared with that for foreign-made ceramics. Work materials used were cast iron, meehanite iron, carbon steel, and alloy steel. The results are shown in Table 3. American and Russian-made ceramics are quite good, because they have more background in research and application than other countries. German-made ceramic is also found to be fairly good. Regarding Japanese-made ceramic, some are very good, in some cases better than foreign-made ceramics, but some are not good.

VI Special Topics

(a) Ultrasonic Cutting Method. Masuko and Kumabe [29] invented the ultrasonic cutting technique, which uses a tool forced to vibrate with ultrasonic frequency. The experiment was done for aluminum, brass, and cast iron. Tool forces were small and a very smooth machined surface was obtained.

They considered that metal cutting is performed by combined effects of self-excited vibration of a cutting tool and of notch or wedge of the tool tip. Therefore smooth machining might be performed if a cutting tool is given some forced vibration of high frequency. In order to give high frequency vibration to a cutting tool, the tool was set at the end of a horn of the ultrasonic equipment. Regarding the direction of vibration of a cutting tool, it was found out that the same direction as the cutting direction is the most effective. Fig. 20 shows the ultrasonic turning equipment which they used in their experiment.

The marked peculiarities of the ultrasonic cutting are:

1 Very low tool force.

2 Thin chip thickness and continuous type of chip without built-up edge.

3 Good machined surface.

Fig. 21 shows the effect of the amplitude of tool vibration on tool forces and surface roughness when cutting aluminum. Tool forces decreased when giving ultrasonic vibration to a cutting tool. The roughness of machined surface in cutting direction decreased. In cases where built-up edge produces a rough machined surface in regular cutting, the application of the ultrasonic cutting

Table 3 Comparison of tool life of ceramic tools (cutting speed for 60 min tool life, m/min)

WORK MATERIAL / MADE IN		CAST IRON	MEEHANITE IRON	CARBON STEEL	ALLOY STEEL
JAPAN	A	○ 251	○ 260	○ 212	○ 320
	B	○ 321	○ 295	○ 120	○ 431
	C				× 395
	D	161		140	
U. S. A.	A				× 342
	B				○ 385
U. S. S. R.			○ 220	○ 92[a]	○ 401
ENGLAND				140[a]	
WEST GERMANY	A_1				○ 373
	A_2		× 240		
	B_1		○ 300		
	B_2		※ 200	88[b]	
TOOL LIFE CRITERION (FLANK WEAR, mm)		AVERAGE 0.2	MAXIMUM 0.4	AVERAGE 0.3	MAXIMUM 0.3
DEPTH OF CUT, mm		1.5	1.0	1.5	2.0
FEED, mm/rev.		0.2			
TOOL GEOMETRY		(-5, -7, 5, 7, 15, 15, 0.8mm) except a (0, 10, 6, 8, 45, 45, 0.5mm) b (-6, -6, 6, 6, 30, 30, ---)			

NOTE: ○ STABLE WEAR PROGRESS
× UNSTABLE CHIPPING

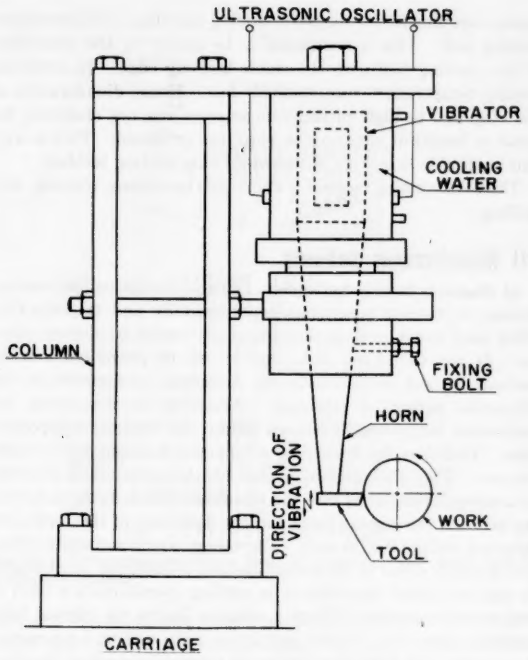

Fig. 20 Ultrasonic cutting device

method produces a smooth surface. The reason for this is that a built-up edge is not produced in this forced vibration cutting.

The cutting ratio was very large as shown in Table 4, for example, in the case of aluminum, approximately 1 in comparison with 0.2 to 0.5 in the regular cutting method. Therefore the shear angle is very large, and the chip produced is thin.

The similar experimental results were obtained for brass and cast iron.

Regarding the type of chip, all chips observed in their experiments were the continuous type without built-up edge even at cutting conditions where the discontinuous chip was produced in regular cutting. The continuous chip was obtained in the case of cast iron at amplitude over 6μ.

This ultrasonic cutting method was found effective at any cutting speed.

(b) Silver-White Chip Cutting Method. Hoshi [10] invented the silver-white chip cutting method or briefly SWC cutting method as a result of his long time investigation of built-up edge [see Section II(e)]. In this method the built-up edge is used to cut the work material. This is accomplished by continuously generating a built-up edge on the carbide cutting tool. By this cutting method cutting resistance and cutting temperature become low even at heavy cutting conditions in comparison with regular cutting. As a result tool life increases, and the machined surface increases in smoothness.

The SWC cutting method contains three important factors.

1 The process to form the stable built-up edge on a flat land at a cutting edge.

2 The process to induce the built-up edge to flow continuously along the side cutting edge.

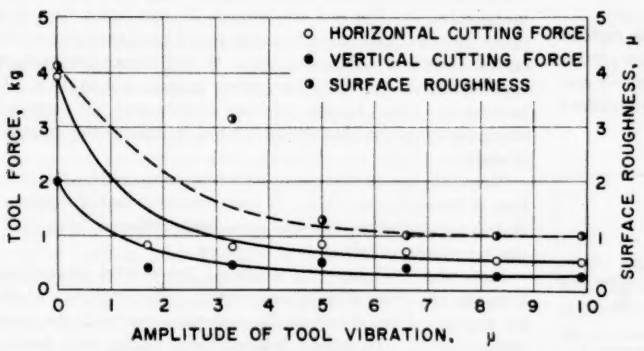

Fig. 21 Effect of amplitude of tool vibration on tool force and surface roughness; work material, aluminum; rake angle, 22 deg; width of cut, 1.5 mm; depth of cut, 0.05 mm; cutting speed, 0.2 m/min.; dry

Table 4 Effect of amplitude of tool vibration on cutting ratio and shear angle; work material, aluminum; rake angle, 22 deg; width of cut, 1.5 mm; depth of cut, 0.05 mm; cutting speed, 0.2 m/min; dry

AMPLITUDE μ	CUTTING RATIO	SHEAR ANGLE DEG.
0.0	0.2	1 2
1.7	1.3	6 5
3.3	1.3	6 5
5.0	0.8	4 8
6.6	1.3	6 5
8.3	1.0	5 8
9.9	1.3	5 8

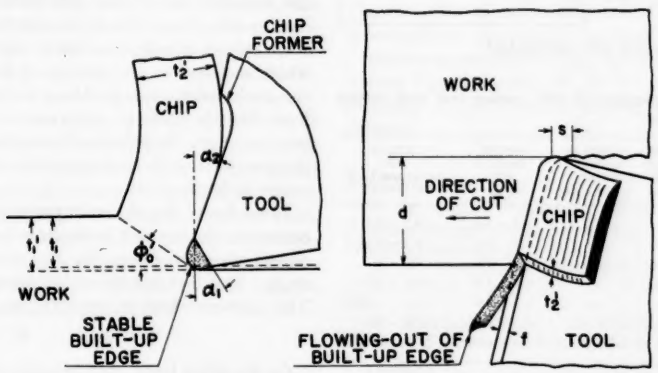

Fig. 22 Mechanism of SWC cutting

3 The process to control chip flow.

Fig. 22 shows these three processes.

The built-up edge which is generated on a flat land at the cutting edge acts as an actual cutting edge. Over cutting ($t_1' - t_1$) always occurs. Regular chip flows out along the tool face and is bent by the action of chip former. The built-up edge which acts as an actual cutting edge flows out along the side cutting edge continuously. The smooth and continuous flowing-out of the built-up edge is obtained by choosing appropriate values of side cutting edge angle and nose radius. This phenomenon of flowing-out of built-up edge is a special peculiarity of SWC cutting.

Fig. 23 shows a typical shape of the SWC cutting tool. The tool has double rake angles—primary rake angle α_1 and secondary rake angle α_2. Typical values for these angles are

$$\alpha_1 = -30 \text{ deg}, \qquad \alpha_2 = 15 \sim 30 \text{ deg}.$$

The tool has third rake angle α_3 in order to control chip flow. Regarding the width of flat land,

$$f = \left(\frac{1}{2} \sim \frac{3}{4}\right) s$$

is very effective in practical use, where s is feed rate. Nose radius is related to the flowing-out phenomenon of built-up edge. A typical value is

$$r = 1.0 \sim 1.5 \text{ mm}.$$

The tool has the secondary cutting edge u in order to induce built-up edge to flow out easily and also to hold the tool tip strong. Its optimum length is about half of the depth of cut. Table 5 shows representative dimensions of SWC cutting tool and cutting conditions when machining low carbon steel.

Tool material used for SWC cutting is double or triple carbide.

By SWC cutting with the tool mentioned above, the cutting resistance was about 15 per cent less and the tool life 20 per cent longer than with the standard cutting tool. Both crater and flank wears were smaller for the SWC cutting tool than for the standard cutting tool. This is considered to be caused by the protection of the cutting tool with the stable built-up edge. In addition, cutting temperature was relatively low. Hence discoloration of the chip due to high cutting temperature was not observed, instead a beautiful silver-white chip was produced. This is why this cutting is called the silver-white chip cutting method.

The SWC cutting method is applicable to turning, planing, and milling.

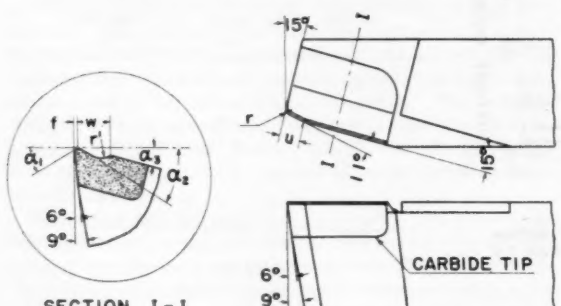

Fig. 23 Typical SWC cutting tool

Table 5 Representative dimensions of SWC cutting tool and cutting conditions for low carbon steel

TOOL SIZE No.	WIDTH OF FLAT LAND f, mm	WIDTH OF CHIP FORMER w, mm	RADIUS OF CHIP FORMER r', mm	LENGTH OF SECONDARY CUTTING EDGE u, mm	OPTIMUM DEPTH OF CUT d, mm	OPTIMUM FEED RATE s, mm/rev.
1	0.1	2.0	0.5	0.0	1.0 - 3.0	0.2 - 0.4
2	0.2	2.5	1.0	1.0	2.0 - 5.0	0.3 - 0.5
3	0.3	4.0	1.5	2.0	3.0 - 6.0	0.4 - 0.7
4	0.4	6.0	2.0	3.0	5.0 - 8.0	0.5 - 0.9
5	0.5	8.0	4.5	4.0	5.5 - 9.0	0.7 - 1.2
6	0.6	9.0	5.0	5.5	6.5 - 10.0	0.8 - 1.4
7	0.7	10.0	5.5	6.0	7.0 - 15.0	1.0 - 1.5

NOTE: OPTIMUM CUTTING SPEED 70 - 120 m/min.
DRY CUTTING.

VII Miscellaneous Subjects

(a) Chatter in Cutting Operations. Doi and coworkers [30] studied chatter in cutting operations experimentally and theoretically. They used specially designed optical equipment to observe chatter. It was found out that chatter can be prevented if some method is used to eliminate the horizontal component in the ellipsoidal pattern of vibration. Whenever chatter occurs, the horizontal component increases before the vertical component does. Therefore the horizontal component is considered to cause chatter. They also considered that chatter perpetuates if vibration energy is absorbed into the vibration system owing to a time lag between the cutting force and the deflection of the workpiece (about 0.0005 to 0.0010 sec). The energy which maintains vibration is nearly equal to the energy loss due to damping in vibration. It was concluded that chatter in cutting operations is a kind of self-excited vibration. Once workpiece begins to vibrate horizontally, area of cut varies, and hence main cutting force varies. As a result, the workpiece begins to vibrate in vertical direction with the same frequency, and so does the cutting edge. Therefore the cutting tool vibrates in an ellipsoidal pattern.

The chatter mark which appears in cutting operations was also investigated by Doi and coworkers. It was found that if the phase lag of undulation between the present and previous cuttings on the machined surface was about 60 deg the maximum energy was induced to the vibration system to maintain chatter. The undulation caused by the previous cutting was not necessarily the main factor for chatter, but helped to enlarge the amplitude of chatter.

They [31] also investigated the vibration caused by the formation of discontinuous chip. It was concluded that the character of this type of vibration was completely different from that of chatter which is a self-excited vibration.

Kato and Goshima [32] analyzed the chatter phenomenon from the viewpoint of nonlinear system. The frequency of chatter was calculated theoretically and compared with the experimental results. Equations deduced theoretically were found to explain the relationship among the frequency of chatter, natural frequency, and cutting conditions.

(b) Roughness of the Machined Surface. Okushima and coworkers [33, 34] investigated the occurrence of surface roughness in the cutting direction. Two kinds of surface roughness were observed when mild steel was cut; namely, the tear type surface roughness, which is caused by the remains of sloughing-off built-up edge on the machined surface, and the grain type surface roughness, which looks like the grain of wood and occurs without accompanying built-up edge. Both kinds of roughness decrease with an increase in rake angle, with an increase in cutting speed, and with a decrease in depth of cut.

It was found that the tear type surface roughness, which usually occurs in the low and medium cutting speed range, can be removed when using a cutting tool having a land of negative relief angle. This tool and its cutting mechanism are shown in Fig. 24. The optimum shape is, for example,

$$h = 5\mu, \qquad \theta = -3 \text{ deg}.$$

On the other hand, they investigated the effect of roughness of the cutting edge on the surface roughness. The surface roughness

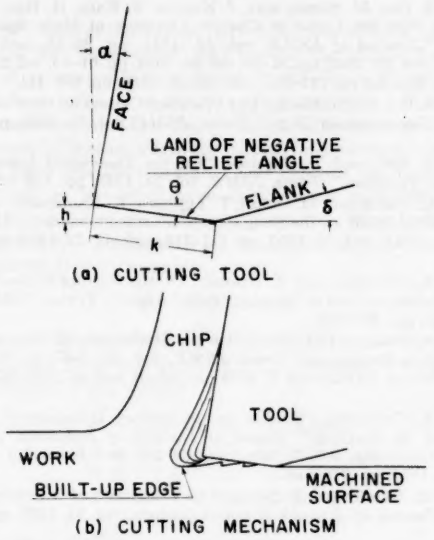

Fig. 24 Cutting tool having a land of negative relief angle and its cutting mechanism

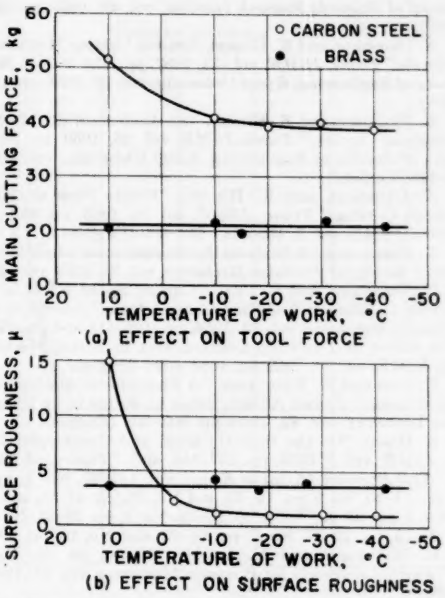

Fig. 25 Effect of sub-zero cutting on tool force and surface roughness; work material, 0.2% carbon steel and brass; rake angle, 18 deg; width of cut, 2.0 mm; depth of cut, 0.1 mm; cutting speed, 2.4 m/min; coolant, 1 l/min of alcohol cooled by liquid nitrogen

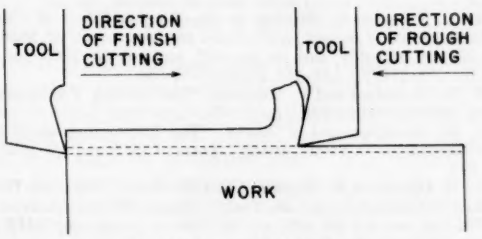

Fig. 26 Reversal finish cutting

was not affected by the roughness of cutting edge of a tool provided that it is within a certain limit.

They also determined the effect of relief angle of a conventional cutting tool on surface roughness. The optimum value was 6 to 8 deg.

Iwaki and Mori [35] considered that the roughness of the machined surface in orthogonal cutting is a replica of the roughness of the cutting edge and discussed the relationship between them. They classified the types of surface roughness into two: An abnormal roughness caused by the built-up edge, and an autogenerating roughness caused by the property of work material.

Takenaka [36] investigated surface roughness in three-dimensional cutting for various work materials and cutting conditions, and discussed the effect of built-up edge on the roughness of the machined surface.

Okoshi and Sata [37] investigated the generation and sloughing-off of built-up edge in three-dimensional cutting and discussed its effect on the roughness of the machined surface.

Masuko and Kumabe [38] determined how to obtain a fine surface especially at low cutting speeds. Sub-zero cutting, reversal finish cutting, and ultrasonic cutting were recommended.

In sub-zero cutting they poured 1 l/min of alcohol cooled by liquid nitrogen on the work material. Experimental results for carbon steel and brass are shown in Fig. 25. In the case of carbon steel which produces a built-up edge at low cutting speed, the sub-zero cutting method was effective in reducing surface roughness as well as tool force. But it was not effective for brass. It was concluded that work materials which have sub-zero brittleness produce a smooth surface when using this cutting method.

Reversal finish cutting is a method in which finish cutting is performed in the opposite direction from that of rough cutting as shown in Fig. 26. With this cutting method residual strain caused on the machined surface by rough cutting is removed, and hence the machined surface is improved. The depth of cut in finish cutting is an important factor. Based on their experiments a cutting depth of 0.03 to 0.05 mm was recommended for carbon steel.

Regarding ultrasonic cutting, it is effective in reducing the surface roughness as mentioned in Section VI(a).

Acknowledgment

The author wishes to express his appreciation to the authors whose articles are cited in this manuscript. Appreciation should also be expressed to Prof. K. Okushima, Kyoto University, for providing many technical papers on machinability research done in Japan.

Originally this manuscript was prepared for and presented at the Machinability Seminar, June 5–10, 1960, at the Pennsylvania State University. The author would like to thank Dr. A. O. Schmidt, Kearney and Trecker Corporation, and Prof. G. L. Thuering, The Pennsylvania State University, for providing an opportunity to present this manuscript at the Seminar.

Further appreciation should be expressed to Dr. L. P. Tarasov, Norton Company, and Mr. R. O. Lane, Macklin Company, for providing an opportunity to present this manuscript at the ASME Meeting.

References[3]

1 M. Okoshi, "Research on the Cutting Force," *Scientific Papers of Institute of Physical and Chemical Research*, vol. 14, 1930, pp. 193–225 (English).

2 M. Masuko, "Fundamental Research on Metal Cutting," *Trans. JSME*, vol. 19, 1953, pp. 32–39, and vol. 22, 1956, pp. 371–377.

3 T. Sata and M. Mizuno, "Friction Process on Cutting Tool and Cutting Mechanism," *Trans. JSME*, vol. 21, 1955, pp. 416–423,

[3] Articles are written in Japanese except ones which are noted as (English).

or *Journal of Scientific Research Institute*, vol. 49, 1955, pp. 163–174 (English).

4 K. Okushima and K. Hitomi, "On the Cutting Mechanism for Soft Metals," *Trans. JSME*, vol. 23, 1957, pp. 674–680, or *Memoirs of Faculty of Engineering, Kyoto University*, vol. 19, 1957, pp. 135–166 (English).

5 K. Okushima and K. Hitomi, "An Analysis of the Mechanism of Orthogonal Cutting," *Trans. JSME*, vol. 25, 1959, pp. 54–60, or *Memoirs of Faculty of Engineering, Kyoto University*, vol. 20, 1958, pp. 95–116 (English).

6 K. Okushima and K. Hitomi, "Plastic Flow of Metal in Orthogonal Cutting," *Trans. JSME*, vol. 26, 1960, pp. 423–429, or *Bulletin of JSME*, vol. 3, 1960, pp. 556–560 (English).

7 K. Nakayama, "A Study on the Mechanism of Metal Cutting," *Journal of Society for Precision Mechanics*, vol. 23, 1957, pp. 528–532.

8 H. Takeyama and E. Usui, "Cutting Speed Effect in Metal Machining . . . Effect of Tool-Chip Contact Area," *Journal of Society for Precision Mechanics*, vol. 22, 1956, pp. 108–113 and pp. 224–228, or "The Effect of Tool-Chip Contact Area in Metal Machining," TRANS. ASME, vol. 80, 1958, pp. 1089–1096 (English).

9 E. Usui and H. Takeyama, "A Photoelastic Analysis of Machining Stresses," TRANS. ASME, Series C, JOURNAL OF ENGINEERING FOR INDUSTRY, vol. 82, 1960, pp. 303–308 (English).

10 K. Hoshi, "On the Built-Up Edge and Counterplot for It," *Trans. JSME*, vol. 5, 1939, pp. 137–148, and "Theory of Built-Up Edge," *Tool Engineer* (*Kikai to Kogu*), vol. 1, 1957, No. 7, pp. 5–9, No. 8, pp. 11–20, No. 9, pp. 15–20, and No. 10, pp. 47–58, and vol. 2, 1958, No. 1, pp. 25–32, No. 2, pp. 25–32, No. 3, pp. 26–33, No. 4, pp. 41–50, No. 5, pp. 29–37, No. 7, pp. 69–73, and No. 10, pp. 59–66.

11 K. Nakayama and K. Iguchi, "Studies on the Built-Up Edge," *Journal of Society for Precision Mechanics*, vol. 22, 1956, pp. 104–108.

12 M. Okoshi and T. Sata, "Formation and Disappearance of Built-Up Edge in Machining," *Journal of Scientific Research Institute*, vol. 33, 1957, pp. 155–164.

13 A. Yamamoto, "The Effect of Heat Generated in Metal Cutting," *Journal of Society for Precision Mechanics*, vol. 20, 1954, pp. 19–24.

14 A. Yamamoto, "Studies on the Cooling Effect of Cutting Fluid," *Journal of Society for Precision Mechanics*, vol. 22, 1956, pp. 273–277, pp. 350–354, and pp. 423–427, and vol. 23, 1957, pp. 136–140, pp. 273–277, pp. 454–459, and pp. 576–580.

15 K. Okushima and R. Shimoda, "The Cutting Temperature," *Trans. JSME*, vol. 23, 1957, pp. 73–77.

16 K. Okushima and N. Asaka, "The Failure Process of High Speed Steel Tools in Steel Cutting," *Trans. JSME*, vol. 23, 1957, pp. 680–683.

17 K. Okushima, S. Nagatomi, and K. Okusa, "Study on Testing Method of Cemented Carbide Tool," *Trans. JSME*, vol. 21, 1955, pp. 738–744, and vol. 23, 1957, pp. 347–359, or *Bulletin of JSME*, vol. 1, 1958, pp. 79–85 (English).

18 H. Takeyama, T. Murai, and E. Usui, "Study on High Speed Machining . . . Analysis of Carbide Tool Wear," *Journal of Mechanical Laboratory*, vol. 10, 1956, pp. 23–34.

19 T. Irie, "Wear of Carbide Tool in Steel Cutting," *Journal of JSME*, vol. 58, 1955, pp. 600–604.

20 M. Okoshi and T. Sata, "Crater Wear of Carbide Cutting Tools," *Trans. JSME*, vol. 25, 1959, pp. 988–995.

21 T. Sata and K. Nakajima, "Machinability Tests of Steels by Means of Radioactive Carbide Tools," *Journal of Society for Precision Mechanics*, vol. 25, 1959, pp. 312–319.

22 S. Tamaru and K. Shiraishi, "The Cutting Performance of Ceramic Tool," *Mechanical Engineering* (*Kikai Gijutsu*), vol. 4, 1956, no. 7, pp. 65–88.

23 K. Okushima and Y. Fujii, "The Cutting Performance of Ceramic Tool in Steel Cutting," *Trans. JSME*, vol. 24, 1958, pp. 681–686, or *Bulletin of JSME*, vol. 2, 1959, pp. 217–223 (English).

24 K. Okushima and Y. Fujii, "The Machined Surface With Ceramic Cutting Tool," *Trans. JSME*, vol. 26, 1960, pp. 1223–1231.

25 K. Okushima and Y. Fujii, "Physical Properties of Ceramic Tool Material," *Trans. JSME*, vol. 26, 1960, pp. 418–423, or *Bulletin of JSME*, vol. 3, 1960, pp. 560–565 (English).

26 M. Okoshi and T. Sata, "On Ceramic Cutting Tools," *Trans. JSME*, vol. 23, 1957, pp. 691–696.

27 H. Takeyama, "Machining Performance of Home-Made Ceramic Tool and Analysis of Its Wear Process," *Journal of Society for Precision Mechanics*, vol. 23, 1957, pp. 581–585, and vol. 24, 1958, pp. 173–177.

28 "Report of the Special Committee on Cutting," *Journal of Society for Precision Mechanics*, vol. 25, 1959, pp. 465–493.

29 M. Masuko and J. Kumabe, "Study on the Ultrasonic Cutting," *Trans. JSME*, vol. 24, 1958, pp. 109–114, and *Journal of Society for Precision Mechanics*, vol. 24, 1958, pp. 56–60.

30 S. Doi, M. Shimoyama, J. Kuroda, S. Kato, H. Ban, and T. Owada, "On the Cause of Chatter Vibration of Main Spindle of Lathe," *Journal of JSME*, vol. 54, 1951, pp. 39–43, and *Trans. JSME*, vol. 19, 1953, pp. 34–39, vol. 20, 1954, pp. 61–65, vol. 21, 1955, pp. 110–114 and pp. 727–731, and vol. 22, 1956, pp. 408–411.

31 S. Doi and H. Mori, "The Vibration Caused by the Formation of the Discontinuous Chip," *Trans. JSME*, vol. 25, 1959, pp. 963–971.

32 S. Kato and T. Goshima, "On the Theoretical Research of Chatter Vibration," *Trans. JSME*, vol. 24, 1958, pp. 115–124.

33 K. Okushima, M. Omori, T. Fujihara, K. Kameyama, and M. Tanaka, "A Study on the Roughness of Machined Surface of Metals," *Trans. JSME*, vol. 21, 1955, pp. 711–715, and vol. 22, 1956, pp. 704–709.

34 K. Okushima and K. Hitomi, "On the Cutting by the Special Tool Having a Land of Negative Relief Angle," *Trans. JSME*, vol. 23, 1957, pp. 684–690.

35 A. Iwaki and M. Mori, "On the Mechanism of Generation of the Surface Roughness," *Trans. JSME*, vol. 23, 1957, pp. 360–376, or *Bulletin of JSME*, vol. 1, 1958, pp. 86–94 and pp. 329–337 (English).

36 N. Takenaka, "Studies on the Surface Roughess of Metals Finished by Cutting," *Report of Institute of Industrial Science, Tokyo University*, vol. 1, 1951, pp. 169–206, and *Journal of JSME*, vol. 54, 1951, pp. 210–216.

37 M. Okoshi and T. Sata, "The Roughness of Machined Surface," *Journal of Scientific Research Institute*, vol. 33, 1957, pp. 295–309.

38 M. Masuko and J. Kumabe, "A Few New Methods of Metal Cutting to Get a Fine Surface at Low Speed," *Journal of JSME*, vol. 62, 1959, pp. 98–104, or *Bulletin of JSME*, vol. 2, 1959, pp. 487–494 (English).

DISCUSSION

James M. Galimberti[4]

The author is to be congratulated on an excellent description and evaluation of the fundamental research being done in Japan in the field of machinability and metal-cutting research.

There are, however, a few points that require clarification relative to several theories in this area in the U. S.

1 Since the shear strain at point B in Fig. 4 is considerably less than γ_0 at point C and γ_1 at point A is zero, it would have been well to show γ_1 to γ_2 as a function of ϕ. Also, would γ at point C necessarily reach a peak at ϕ_0?

2 Is it implied in Fig. 11 that the general shape of the built-up edge remains the same from -40 to $+15$ deg but then changes between $+15$ and $+40$ deg?

3 Is the α_{ave}' of 30–35 deg and the α_{max}' of 45 deg as completely unrelated to the tool α as is implied? If so, this is in disagreement with Fig. 11.

4 The plot of surface finish in Fig. 21 of finish improving as a function of amplitude is in almost complete contradiction to practice where every effort is made to eliminate chatter and vibration. Also, what frequencies were used?

5 In the reversal finishing cut of Fig. 26, have the authors used this technique in grinding to reduce residual grinding strains of thin stock?

M. Kronenberg[5]

It is interesting to note that one of the Japanese scientists (Masuko) quoted by the author considers the increase in the friction angle with increasing rake angle of the tool as a "paradox in metal cutting theory." He overlooks apparently the fact that the term "friction angle" is a misnomer in the case of metal cutting, as has been discussed in the ASME TRANS. some time ago.[6] The coefficient of friction, is a term which should be re-

[4] Project Engineer, Kennametal, Inc., Latrobe, Pa.

[5] Consulting Engineer, Professor Emeritus, Cincinnati, Ohio. Mem. ASME.

[6] "Apparent Coefficient of Friction," TRANS. ASME, vol. 76, 1954, pp. 228–29.

placed by "ratio of the friction force to the normal force"; it may change in the "paradoxical" way because the friction force remains often constant with a change in the rake angle, while the normal force increases as the rake angle decreases. In this respect, therefore, metal-cutting friction is different from conventional cases of friction where the friction force changes while the normal force remains constant. This explains the "paradox."

Formulas to this effect have already been published in the Japanese translation of a book on metal-cutting science published by this writer.[7] The formula for the friction angle presented in the paper by Hitomi, namely:

$$\beta = 37.5° + 0.5\alpha \quad (1)$$

does, in my opinion, not apply to all conditions and materials, as shown in Fig. 27 of this discussion. The following formulas have been derived by this writer:[7]

$$\beta = 33° + 0.73\alpha \quad \text{(Cast iron)} \quad (2)$$
$$\beta = 31° + 0.67\alpha \quad \text{(Steel)} \quad (3)$$
$$\beta = 27° + 0.52\alpha \quad \text{(Bronze)} \quad (4)$$
$$\beta = 32° + 0.15\alpha \quad \text{(Copper)} \quad (5)$$

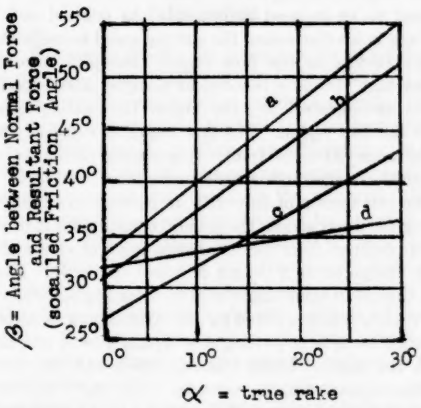

Fig. 27 Relationship between the so-called friction angle and the true angle of the tool*

a = Cast iron; $\beta = 0.73\alpha + 33°$ (average)
b = Steel; $\beta = 0.67\alpha + 31°$ (average)
c = Bronze; $\beta = 0.52\alpha + 27°$
d = Copper: $\beta = 0.15\alpha + 32°$

* Reproduced from Kronenberg, "Grundzuege der Zerspanungslehre" (Principles of Metal Cutting Science), Springer Verlag, Berlin, Heidelberg, Germany, second edition, 1954, p. 15.

It would be important to learn why a sudden break in the shear angle-true rake relationship should occur at 15 deg; the reason is not explained in the paper. I agree, however, with the statement on page 534 of the paper to the effect, that "the friction coefficient which has been considered in metal cutting is not reliable." Various theories have been developed during the past ten years with regard to the shear plane or shear region and the ideas presented by the authors (Okushima and Hitomi) of a wide flow region deserve further consideration. The authors do not explain in sufficient detail the method they have used for measuring the final shear angle and their tests were apparently run at extremely low cutting speeds of only 15.5 ft/min. It would also be desirable to learn what equation applies to the case of the shear strain at initial shear angle.

The equation given for the final shear strain corresponds exactly to the conventional formula and can be represented by a diagram,

[7] M. Kronenberg, "Principles of Metal Cutting Science," translated into Japanese by H. Kabaike, 293 pages, Tokyo, Japan, 1938, pp. 122–124.

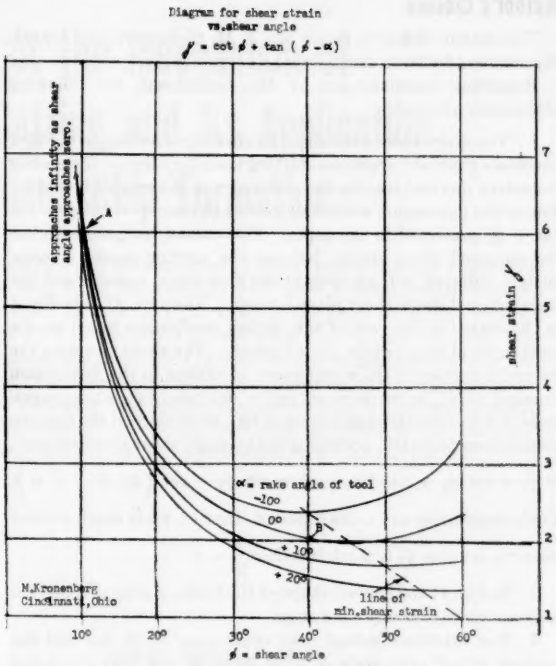

Fig. 28 Diagram for shear strain versus shear angle $\gamma = \cot\phi + \tan(\phi - \alpha)$

Fig. 28, from which the shear strain can be readily determined for a given shear angle and rake angle. In Fig. 5 of the author's paper an initial shear angle of 10 deg is shown for the case of zero rake (it is termed inclination angle) increasing to 40 deg as the final shear angle (or inclination angle). Fig. 28 shown here shows that under such circumstances the shear strain drops (in agreement with the author's statement) from 6.0 to 2.0 (points A and B on Fig. 28).

The investigations carried out by Masuko and Kumabe, using ultrasonic cutting techniques, lead to conclusions similar to those obtained in tests with ultrahigh cutting speeds which we have carried out in consultation with the Lockheed Aircraft Corp.[8] In these tests where cutting speeds up to 115,000 ft/min were employed by firing a workpiece past a cutting tool and removing a substantial chip, it was found on the basis of high-speed photography of the escaping chip, that the shear angle can be greater than 45 deg, which has hitherto been considered the maximum but never attained until recently.[9] According to Table 4 of the paper presented by Hitomi, shear angles up to 65 deg were obtained which correspond to our own data where a maximum of 61.9 deg was found. Shear angles greater than 45 deg lead to the conclusion that the chip is thinner than the thickness of the metal removed, quite contrary to all past experience. A great number of puzzling problems arise in this regard, too numerous to be discussed here.

The authors do not give information as to the frequency of vibration, rendering it impossible to determine the actual cutting speed, which, in my opinion must have been rather high in view of the large shear angles. The angles also indicate that the chip is moving at a higher velocity than the cutting speed of work and tool before chip formation. We certainly are facing here a new frontier and challenge in metal-cutting science.

[8] De Groat and Ashburn, "Ultra High Speed Machining," *American Machinist*, 22 February, 1960, pp. 111–126.

[9] See also discussion by this writer of paper No. 60—WA-80 presented before ASME Annual Meeting, 1960, by F. L. Bagley.

Author's Closure

The author wishes to thank Mr. J. M. Galimberti and Dr. M. Kronenberg for their discussions.

Regarding questions put by Mr. Galimberti, the following statements are made.

1 The magnitude of the shear strain in the flow region in Fig. 4 ncreases gradually from the starting boundary line to the ending boundary line and reaches the maximum at the ending boundary line of the flow region according to the equation $\gamma = \cot\phi - \cot(\phi + \psi)$ presented in the paper. This cannot compare with the conventional shear strain, because the cutting model is completely different in both cases of the flow region concept and the conventional single shear plane concept. The area ACB in Fig. 4 is eliminated in the case of the cutting mechanism based on the conventional single shear plane concept. The shear strain on the extended surface of OC is expressed, according to the flow region concept, as $\gamma_{oe} = \cot\phi_0 - \cot(\phi_0 + \psi_0)$, where ψ_0 is the magnitude of ψ at the extended surface of OC, while that on the conventional shear plane OC, according to the single shear plane concept, is $\gamma_0 = \cot\phi_0 + \tan(\phi_0 - \alpha) = \cot\phi_0 - \cot\left(\phi_0 + \frac{\pi}{2} - \alpha\right)$. Both magnitudes are quite different, that is, γ_{oe} is much smaller than γ_0, because ψ_0 is much less than $\frac{\pi}{2} - \alpha$.

2 In Fig. 11 the general shape of the built-up edge remains the same or similar for any rake angle.

3 The maximum actual rake angle α_{max}' of 45 deg and the average actual rake angle α_{ave}' of 30 to 35 deg were concluded from the experimental results by Hoshi and not from the theoretical point of view. These values change slightly with the tool rake angle α. However, α_{max}' of 45 deg can be satisfied at the tip of built-up edge for any tool rake angle as shown in Fig. 11. α_{ave}' of 30 to 35 deg is satisfied for small tool rake angle, though this is not true for large positive or negative tool rake angle.

4 The frequency used in the ultrasonic cutting method by Masuko and Kumabe was quite high, 10,000 to 50,000 cycles (18,400 cycles for Fig. 21), and is much larger than that in the usual chatter which produces rough machined surface and is troublesome in the practical machining. But high frequency and small amplitude used in the ultrasonic cutting method are effective in improving the surface finish as mentioned in the paper.

5 The reversal finish cutting has been applied by Masuko and Kumabe to the so-called machining techniques such as planning, turning, boring, hobbing, gear shaping, sawing, and so on. This is effective in order to reduce residual strain of thick stock. This finishing technique may be applied to grinding which removes very thin stock, though this has not been done yet.

The author agrees with the statement by Dr. Kronenberg on the term "friction angle." This term should be reconsidered, because it is liable to be misunderstood. The true meaning of this angle is the directional angle of the resultant cutting force in regard to the tool face. But, so far as the term friction force is used in metal-cutting theory, the paradox pointed out by Masuko is true. Moreover, it is difficult to imagine that the friction force is greater than the normal force as is often observed in metal cutting.

The formula, $\beta = 37.5° + \frac{\alpha}{2}$, presented by Sata and Mizuno was deduced theoretically, based upon some assumptions. This may cause the contradiction with the data obtained by Dr. Kronenberg. The reason why a sudden break in the relationship between shear angle and rake angle (Fig. 3) occurs at a rake angle of 15 deg is explained by considering two types of cutting model of continuous chip formation from theoretical and experimental investigations, namely, (i) $\angle AOB = 90°$ for $\beta \geq 45°$ or $\alpha \geq 15°$ and (ii) $OA = OB$ for $\beta \leq 45°$ or $\alpha \leq 15°$, using the above formula. This finally leads to two expressions for shear angle presented in the paper (for a detailed explanation, refer to Reference [3]).

A plastic deformation zone named the flow region should be considered between the rigid region of work and the plastic region of steady chip in order to eliminate several conflicts in the conventional single shear plane concept, such as an abrupt change of movement of a metal particle, an infinite acceleration which a metal particle receives, extremely large strain and strain rate, etc. Okushima and Hitomi calculated the inclination angles of the starting and ending boundary lines of the flow region from the equations presented in the paper by the cutting data or measured them with photomicrographs of metal-cutting process obtained by sudden stop of cutting, and compared both results. Both were ascertained to be in good agreement. As pointed out by Dr. Kronenberg in his discussion, the cutting speed is one of the most important factors in the flow region concept. According to Okushima and Hitomi's theoretical analysis and experimental results on carbon steel [6], the higher the cutting speed, the narrower the flow region. The flow region is extremely large in low speed range (30 to 300 fpm). It is considered that this region might vanish in superhigh speeds (more than 2000 fpm). This means the localization of flow with an increase in cutting speed. Regarding the shear strain, the general equation for it in the flow region was deduced from the theoretical point of view and is presented in the paper as $\gamma = \cot\phi - \cot(\phi + \psi)$. The shear strain at the initial shear angle or at the starting boundary line of the flow region, which is asked by Dr. Kronenberg, is deduced by this equation as $\gamma_1 = 0$, putting $\phi = \phi_1$ and $\psi = 0$, as is also presented in the paper. Using this expression and the expression for the final shear strain, $\gamma_2 = \cot\phi_2 + \tan(\phi_2 - \alpha)$, the stress and strain relationship in metal cutting can be well explained (see Reference [5]).

The ultrasonic cutting technique invented by Masuko and Kumabe is a very interesting machining method and leads to the conclusion similar to that obtained in the investigation on ultrahigh speed machining carried out by Dr. Kronenberg in regard to large cutting ratio (nearly equal to one). However, this result was obtained even in very low cutting speed in the case of the ultrasonic cutting method. As the author answered the fourth question of Mr. Galimberti, the frequency of tool vibration in Masuko and Kumabe's experiment was 18,400 cycles. Supposing that the amplitude of tool vibration in this case as 10μ, the actual cutting speed is the sum of the speed associated with tool vibration (38.0 fpm) and the apparent cutting speed (0.7 fpm), namely, 38.7 fpm. This is still low speed, compared with ultrahigh speed discussed by Dr. Kronenberg. Therefore, it is considered that a large cutting ratio is a special peculiarity obtained by the ultrasonic cutting method vibrating a tool with a high frequency.

KEIJI OKUSHIMA
Professor. Mem. ASME

KATSUNDO HITOMI[1]
Assistant Professor. Mem. ASME

Department of Mechanical Engineering,
Kyoto University, Kyoto, Japan

An Analysis of the Mechanism of Orthogonal Cutting and Its Application to Discontinuous Chip Formation

Instead of the conventional theory of the mechanics of metal cutting based on a process of shear confined to a single shear plane, the concept of flow region, a fairly large transitional deformation zone which exists between the rigid region of work and the plastic region of steady chip, was developed. The mechanics of orthogonal cutting was analyzed, theoretical equations for angles of boundary lines of the flow region and for strain in chip were deduced in the case of simple continuous chip formation and confirmed in cutting tests on lead. The concept of flow region was also applied to discontinuous chip formation, and theoretical expressions for angles of boundary lines of the flow region were ascertained to be in agreement with the experimental result for carbon steel.

Introduction

Recently theoretical studies on metal cutting have been well developed; especially regarding the most fundamental analysis of the mechanics of orthogonal cutting producing a continuous or discontinuous chip. Various theories have been presented; e.g., Piispanen [1, 2],[2] Ernst and Merchant [3, 4], Lee and Shaffer [5], and Hill [6], assuming a perfectly plastic solid, strain-hardening or inhomogeneity of the material. In most analyses, however, it has also been assumed for the sake of simplicity that the chip formation is a process of shear (without fracture for continuous chip and with fracture for discontinuous chip) confined to a single plane extending from the tip of cutting tool to the sharp intersection of the free surfaces of workpiece and chip, i.e., the shear plane as shown in Fig. 1. Such cutting mechanism, based on simple shear along a single shear plane, contains the following conflicts:

(*a*) A moving metal particle must attain an infinite acceleration when it passes across the shear plane, changing its position from the work region to the chip region.

(*b*) An infinite stress gradient exists on the shear plane.

(*c*) The rate of strain is extremely large compared with that in static material tests.

(*d*) Extremely large strain is produced abruptly on the shear plane, and the relationship between stress and strain in cutting does not agree with that in static material tests.

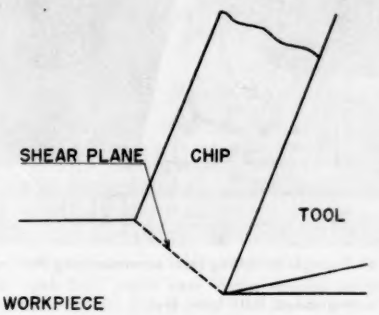

Fig. 1 Cutting process with single shear plane

In order to eliminate these conflicts in the conventional cutting theory based upon the shear process along the single plane, it is evident that the existence of a fairly large transitional zone *AOB*, as shown in Fig. 2, for plastic deformation of metal should be taken into consideration between the rigid region of work and the plastic region of steady chip. Through this deformation zone the shear stress, the plastic strain, and the velocity of a moving metal particle change gradually and continuously. The free surface has no sharp intersection as in the conventional single shear plane theory, but is a smooth curve from the free surface of work to the back side of steady chip. In the present paper this deformation zone will be called the "flow region." The authors [7] already pointed out the existence of the flow region experimentally in cutting tests with soft metals such as lead and Lipowitz alloy [Bi 50.0%, Pb 26.7%, Sn 13.3%, and Cd 10.0%], observing the

[1] At the time the paper was presented, Department of Industrial Engineering, The Pennsylvania State University, University Park, Pa.

[2] Numbers in brackets designate References at end of paper.

Contributed by the Metal Processing Research Activity of the Production Engineering Division and presented at the Winter Annual Meeting, New York, N. Y., November 27–December 2, 1960, of The American Society of Mechanical Engineers. Manuscript received at ASME Headquarters, July 27, 1960. Paper No. 60—WA-79.

Nomenclature

= width of cut
f = ratio of size of flow region relative to chip thickness = s/t_2
F_h = horizontal or principal cutting force
F_v = vertical or thrust cutting force
k = constant showing degree of strain-hardening of material
k_1 = ratio between chip contact length and depth of cut = l/t_1
k_2 = ratio between chip contact length and chip thickness = l/t_2
K_1 = angle relative to angle of starting boundary line of flow region
K_2 = angle relative to angle of end boundary line of flow region
l = chip contact length on tool face
m = constant showing degree of strain-hardening of material
r = cutting ratio = t_1/t_2
R = resultant cutting force
s = size of flow region
t_1 = depth of cut
t_2 = thickness of chip
x = distance from arbitrary point on free surface of flow region to the horizontal line through cutting edge
α = rake angle

(Continued on next page)

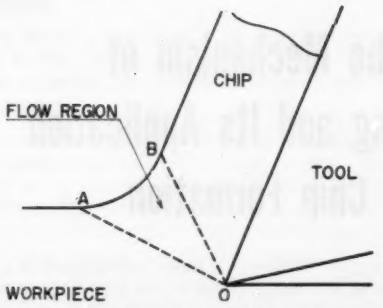

Fig. 2 Cutting process with flow region

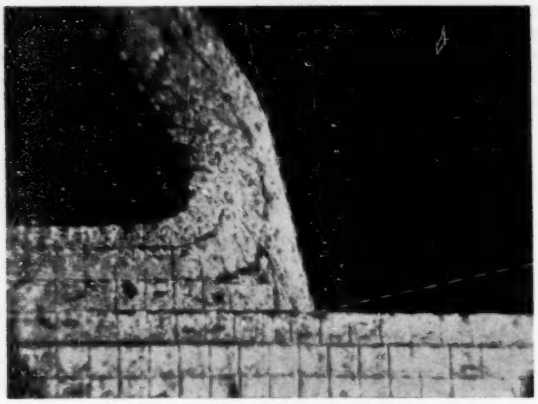

Fig. 3 Example of cutting state accompanying flow region (Work material, Lipowitz alloy; rake angle, −15 deg; depth of cut 0.025 in.; cutting speed, 0.01 fpm; dry)

cutting mechanism with a microscope. An example is shown in Fig. 3, in which it is evident that the shear process took place over a large area instead of along a single plane.

A similar deformation zone has been taken into consideration quite recently by Nakayama [8], Kececioglu [9], and Christopherson, Oxley, and Palmer [10].

The flow region is different from the preflow region, which according to Finnie and Shaw [11] is located in the vicinity of the free surface of the workpiece ahead of the shear plane.

The concept of flow region can also be applied to the discontinuous chip formation, which removes the conventional conflict that fracture occurs abruptly on the particular single shear plane and is associated with extremely large strain. In Fig. 2, the plastic deformation begins to occur at the starting boundary line of the flow region OA, the plastic strain increases gradually as the cut progresses, and the shear stress increases due to strain-hardening. Finally, the stress reaches the shearing limit at the end boundary line OB, fracture occurs, and a fragment of discontinuous chip is produced. The continuous chip will be produced if the shear stress or strain does not reach the breaking limit at the end boundary line of the flow region.

The present paper deals with the theoretical analysis of the mechanics of orthogonal cutting based on the flow region concept. In the case of the continuous chip without built-up edge, expressions for angles between the starting and end boundary lines and the cutting direction, and for strain in chip were deduced theoretically using the assumption of a perfectly plastic material, and the expressions were confirmed in cutting tests on lead. In addition, the flow region concept was applied to the discontinuous chip formation, and theoretical expressions for angles of the boundary lines were ascertained to be in agreement with the experimental result for carbon steel. Regarding the cutting tests, orthogonal cutting was performed dry on a shaper.

Analysis of the Mechanism of Orthogonal Cutting Based on the Flow Region Concept[3]

In this section the cutting mechanism producing a continuous chip without built-up edge will be analyzed according to the concept of flow region.

Assuming that the work material is a perfectly plastic solid and that the elastic strain is negligible in comparison with the plastic strain as is often considered in metal cutting, the shear stress-strain relation (τ-γ diagram) is shown in Fig. 4. In this figure τ_0 is the yield shear stress, i.e., the shear-flow stress. It might be also assumed for the sake of simplicity that the starting (work side) and end (chip side) boundary lines of the flow region are straight lines as shown in Fig. 5, though they are in reality slightly convex downward and upward, respectively. The transitional flow of metal transforming from the region of work to the region of steady chip occurs in the flow region AOB, and the stress in this area must be in the yield state. Hence, on both boundary lines,

$$\tau_{OA} = \tau_{OB} = \tau_0. \tag{1}$$

When a cut having a width b and a depth t_1 is made by an orthogonal cutting tool with a rake angle α, thickness of chip and resultant cutting force are denoted by t_2 and R, respectively. Assuming that the shear stresses on both boundary lines distribute uniformly, the following expressions are obtainable:

$$\tau_{OA} = \frac{R \sin \phi_1 \cos (\phi_1 - \alpha + \beta)}{bt_1} \tag{2}$$

and

$$\tau_{OB} = \frac{R \cos (\phi_2 - \alpha) \cos (\phi_2 - \alpha + \beta)}{bt_2}, \tag{3}$$

[3] For a detailed discussion on this and next sections, see Reference [12].

Nomenclature

β = friction angle on tool-chip interface
γ = shear strain
γ_0 = conventional shear strain based on cutting process of single shear plane
γ_1 = shear strain on starting boundary line of flow region
γ_2 = shear strain on end boundary line of flow region, or strain in chip
ϵ = angle between perpendicular line to tool face and grid line in steady chip which was formerly perpendicular to uncut surface
τ = shear stress
τ_0 = yield shear stress, or shear-flow stress
ϕ = inclination angle of arbitrary radial plane in flow region
ϕ_0 = conventional shear angle based on cutting process of single shear plane
ϕ_1 = inclination angle of starting boundary line of flow region
ϕ_2 = inclination angle of end boundary line of flow region
Φ = sector angle of flow region
ψ = angle of tangent to free surface of flow region with machined surface
ψ_2 = angle of tangent to free surface at end point of flow region with machined surface

where β is the mean friction angle on the tool-chip interface, and ϕ_1 and ϕ_2 are the inclination angles of starting and end boundary lines of the flow region, respectively.

According to recent reports by Finnie and Shaw [13] and Sata and Mizuno [14], the average tangential stress along the tool-chip interface OD is in the yield state; that is,

$$\tau_{OD} = \frac{R \sin \beta}{bl} = \tau_0, \tag{4}$$

where l is the contact length of chip on the tool face.

The inclination angles of starting and end boundary lines of the flow region ϕ_1 and ϕ_2 are expressed explicitly from Equations (1) to (4).

$$\phi_1 = \frac{K_1}{2} - \frac{\beta}{2} + \frac{\alpha}{2} \tag{5}$$

$$\phi_2 = \frac{K_2}{2} - \frac{\beta}{2} + \alpha \tag{6}$$

$$K_1 = \sin^{-1}\left\{\frac{2}{k_1} \sin \beta + \sin (\beta - \alpha)\right\} \tag{7}$$

$$K_2 = \cos^{-1}\left(\frac{2}{k_2} \sin \beta - \cos \beta\right) \tag{8}$$

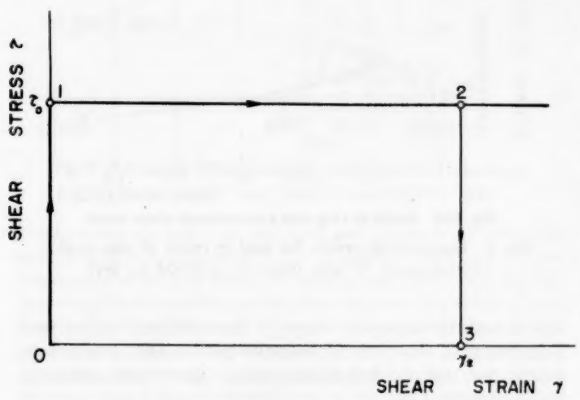

Fig. 4 Shear stress-strain diagram for perfectly rigid-plastic material

$$k_1 = \frac{l}{t_1} \tag{9}$$

$$k_2 = \frac{l}{t_2} \tag{10}$$

The sector angle of the flow region is obtained as the difference between both angles; that is, from Equations (5) and (6)

$$\Phi = \phi_2 - \phi_1 = \frac{\alpha}{2} - \frac{K_1}{2} + \frac{K_2}{2}. \tag{11}$$

Meyer and Archibald [15, 16] and Creveling, Jordan, and Thomsen [17] obtained

$$k_1 \approx 2 \quad \text{and} \quad k_2 \approx 1, \tag{12}$$

respectively, as cutting results for steel. Substituting Equation (12) into Equations (7) and (8),

$$K_1 = \sin^{-1}\{\sin \beta + \sin (\beta - \alpha)\} \tag{7'}$$

$$K_2 = \cos^{-1}(2 \sin \beta - \cos \beta) \tag{8'}$$

It is well known that the mean friction angle on the tool face β, which is seen in the foregoing equations, can be calculated from the following expression:

$$\tan \beta = \frac{F_v + F_h \tan \alpha}{F_h - F_v \tan \alpha}, \tag{13}$$

where F_h is the horizontal or principal cutting force and F_v is the vertical or thrust cutting force.

Next, in order to obtain the plastic shear strain in the flow region, let us determine the shear strain on an arbitrary radial plane OP which extends from the tip of the cutting tool to the free surface in the flow region, denoting its inclination angle to the cutting direction by ϕ. If the metal did not undergo plastic deformation, a metal particle on the free surface of the uncut material would proceed toward X. In reality, however, it moves toward P as a result of plastic deformation, and has the motion component toward $A'P$-direction (this is the tangent to the free surface of the flow region at an arbitrary point P, and makes angle ψ with the machined surface). Hence, the shear strain which metal receives until a metal particle reaches the radial plane OP is given by $\frac{A''P}{A'Q}$, where A' and A'' are intersections between the original horizontal free surface of work X and the tan-

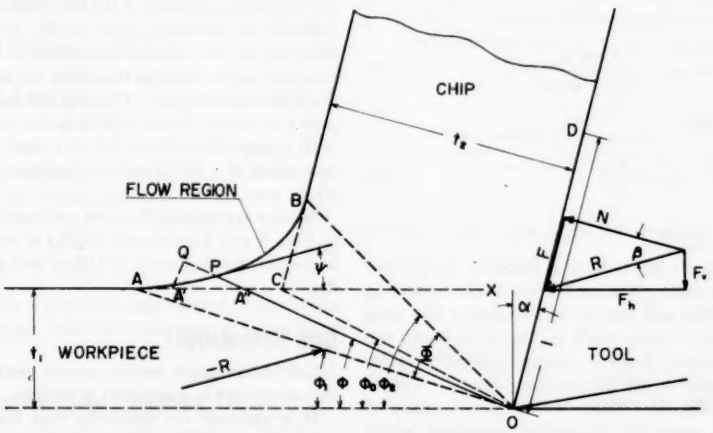

Fig. 5 Analysis of cutting mechanism based on flow region concept

gent at P, and the radial plane OP, respectively, and Q is a point at which a perpendicular line from A' to a radial plane OP intersects it. This amount of shear strain is expressed with angles ϕ and ψ as follows:

$$\gamma = \cot \phi - \cot (\phi + \psi). \tag{14}$$

In particular, the shear strains on the starting and end boundary lines of the flow region are

$$\gamma_1 = 0, \tag{15}$$

and

$$\gamma_2 = \cot \phi_2 + \tan (\phi_2 - \alpha), \tag{16}$$

respectively. It follows from this that, instead of an abrupt large shear strain which occurs on a single shear plane in the conventional theory, the shear strain is zero on the starting boundary line of the flow region, and increases gradually until it reaches maximum at the end boundary line of the flow region. Then the metal flows out into the chip region in a state of permanent plastic strain γ_2, which is given by Equation (16). The variation of the shear strain is shown in Fig. 4 as 0, 1, 2, and 3 which correspond, respectively, to the work region, the starting boundary line, the end boundary line, and the chip region.

Cutting Test With Lead

Since lead is ductile and does not strain-harden at room temperature because of its low recrystallization temperature, it always produces a continuous type of chip without built-up edge. Hence, it is an appropriate material to demonstrate the theoretical analysis of the cutting mechanism developed under the assumption of a perfectly plastic solid as described in the previous section.

Orthogonal cutting was performed dry with a lead specimen having a width of cut of 0.433 in. in a shaper under various cutting conditions.

The material was cut with sharp-edged orthogonal high-speed steel cutting tools of various rake angles (−20 to 20 deg) at a constant cutting speed of 17 fpm and a constant depth of cut of 0.004 in. Cutting resistance R, namely, horizontal component F_h and vertical component F_v were recorded on oscillograph paper by a strain gage type tool dynamometer, and chip thickness t_2 and chip contact length l were measured after cutting. Using these data, the inclination angles of starting and end boundary lines ϕ_1 and ϕ_2, the sector angle of the flow region Φ, the angle of friction β, and the strain in chip γ_2 were calculated from Equations (5) to (11), (13), and (16), and are shown in Fig. 6 in terms of rake angle. In this figure the conventional shear angle ϕ_0 and shear strain γ_0, calculated from the following expressions based on the cutting mechanism of a single shear plane, are also shown:

$$\phi_0 = \tan^{-1} \frac{r \cos \alpha}{1 - r \sin \alpha}, \tag{17}$$

where r is the cutting ratio,

$$r = \frac{t_1}{t_2}, \tag{18}$$

and

$$\gamma_0 = \cot \phi_0 + \tan (\phi_0 - \alpha). \tag{19}$$

Referring to Fig. 6(*a*), all angles have a tendency to increase with an increase in rake angle. The inclination angle of starting boundary line ϕ_1 is smaller and that of end boundary line ϕ_2 is larger than the conventional shear angle ϕ_0; in other words, the sector angle of the flow region Φ always has some positive value. This proves the rationality of the flow region concept. This is shown schematically in Fig. 7. While the calculated values of the conventional shear angle by theoretical equations which have been presented by many investigators are not in complete

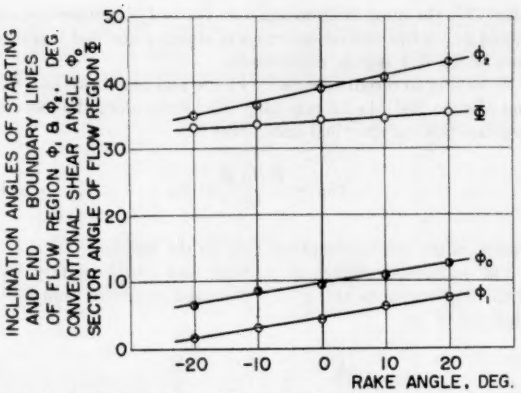

Fig. 6(*a*) Inclination angles of starting and end boundary lines, sector angle of flow region, and conventional shear angle

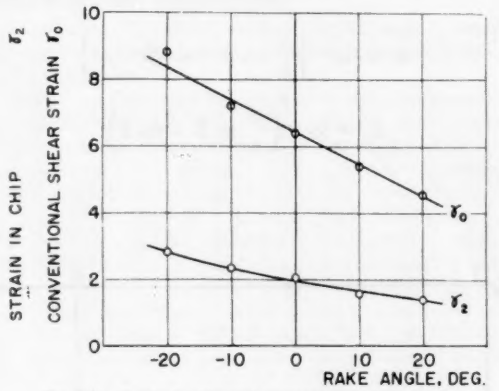

Fig. 6(*b*) Strain in chip and conventional shear strain

Fig. 6 Experimental results for lead in terms of rake angle (Cutting speed, 17 fpm; depth of cut, 0.004 in.; dry)

accord with the observed values or the calculated values from Equation (17), especially for negative rake angles, it is a noteworthy fact that the flow region concept shows quite rationally the machining state.

From Fig. 6(*b*) strain in chip and the conventional shear strain decrease with an increase in rake angle, and strain in chip based on the cutting mechanism of the flow region concept is much smaller than the conventional shear strain. It appears from this result that the rate of strain is also smaller for the cutting state based on the flow region concept than that for the cutting state based on the single slip concept. Thus the cutting model with a flow region seems to be more reasonable than the conventional cutting model with a single shear plane not only from the standpoint of smooth movement of a metal particle but from a viewpoint of strain and strain rate.

Similar experimental results and schematic drawings are shown in Figs. 8 and 9 for several depths of cut (0.0008 to 0.020 in.) at a constant cutting speed of 17 fpm and a constant rake angle of 0 deg.

Grid Deformation[4]

Grid deformation for the cutting mechanism based on the flow region concept is considered as follows.

It is assumed for simplicity that the steady chip slides uni-

[4] For detailed discussion on this subject, see Reference [7].

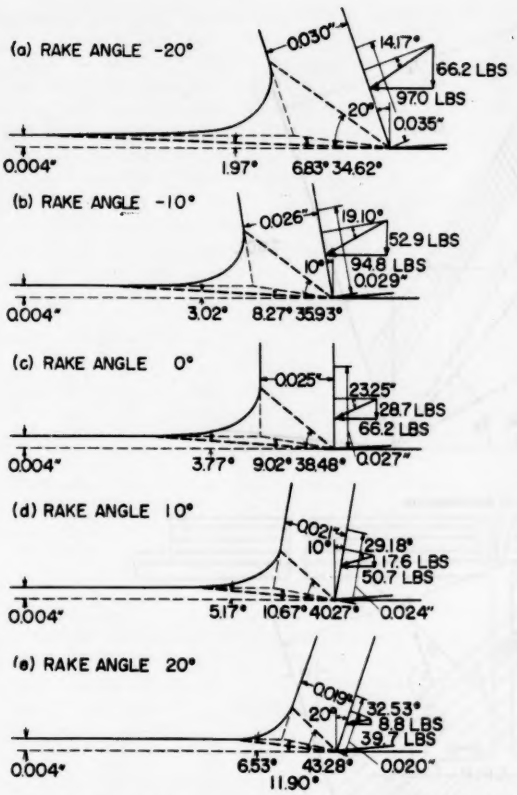

Fig. 7 Schematic cutting model for lead in terms of rake angle (Cutting speed, 17 fpm; depth of cut, 0.004 in.; dry)

formly along the tool face, and that grid deformation under the machined surface is neglected. Let us consider a case in which the free surface of the flow region is a circular arc, as shown in Fig. 10. Denoting the intersection of the free surfaces of work and steady chip by C, $AC = BC \equiv s$. The grid which was a rectangle perpendicular to the cutting direction before cut is deformed to a parallelogram after cut. Taking account of nonchange in density of metal during plastic deformation, ϵ, the angle between a perpendicular line to the tool face and a grid line in the steady chip which was formerly perpendicular to the uncut surface, can be derived.

$$\tan \epsilon = \tan (\phi_2 - \alpha) + r^2 \cot \phi_1 - f(r + 1)$$
$$- 2f^2 \left[1 - \left(\frac{\pi}{4} - \frac{\alpha}{2} \right) \cot \left(\frac{\pi}{4} - \frac{\alpha}{2} \right) \right] \cot \left(\frac{\pi}{4} - \frac{\alpha}{2} \right), \quad (20)$$

where f is a dimensionless quantity, that is, a ratio of the size of the flow region relative to chip thickness.

$$= \frac{s}{t_2} \quad (21)$$

Fig. 11 shows an example of grid deformation in cutting process accompanying a flow region. Smooth distortion of grid during cutting is seen.

An Analysis of Discontinuous Chip Formation

The mechanism of discontinuous chip formation has been analyzed by Piispanen [2], Field and Merchant [18], Cook,

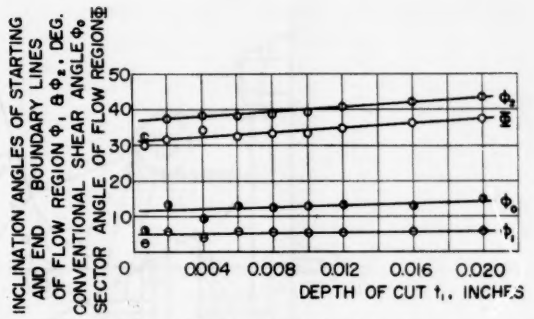

Fig. 8(a) Inclination angles of starting and end boundary lines, sector angle of flow region, and conventional shear angle

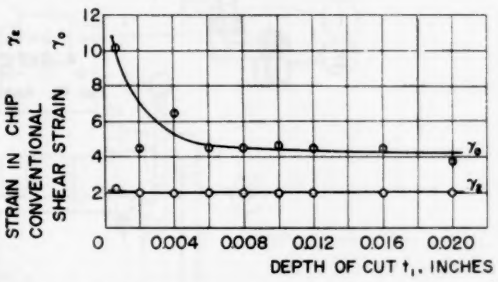

Fig. 8(b) Strain in chip and conventional shear strain

Fig. 8 Experimental results for lead in terms of depth of cut (Cutting speed, 17 fpm; rake angle, 0 deg; dry)

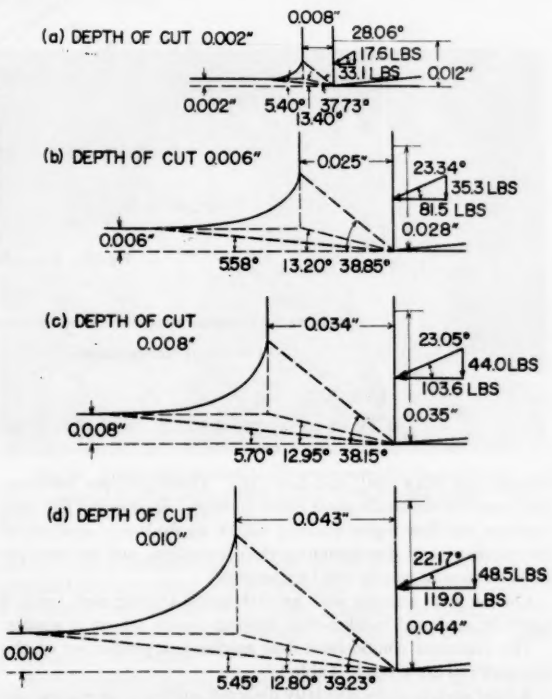

Fig. 9 Schematic cutting model for lead in terms of depth of cut (Cutting speed, 17 fpm; rake angle, 0 deg; dry)

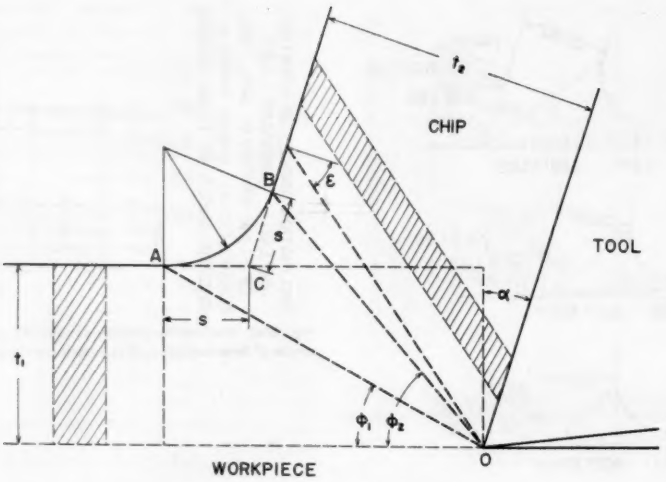

Fig. 10 Analysis of grid deformation

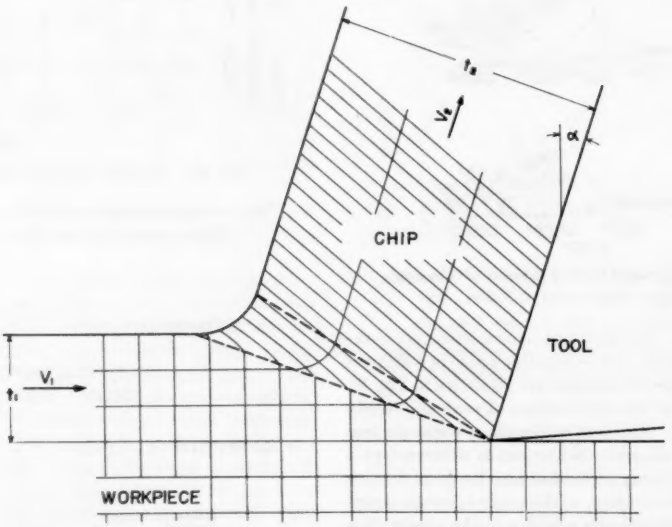

Fig. 11 Example of grid deformation

Table 1 Chemical composition and mechanical properties of work material (carbon steel)

Chemical composition (%)								Hardness Rockwell	Ultimate strength	Percentage elongation
C	Mn	Si	Cu	Cr	S	P	Fe	B scale	(psi)	(%)
0.44	0.65	0.33	0.17	0.10	0.024	0.017	Remain	89	91,000	25

Finnie, and Shaw [19], and Lee [20]. These analyses, however, are based on the single shear plane concept. In this and the next sections, the flow region concept will be applied to an analysis of the mechanics of discontinuous chip formation, and an example of experimental results will be discussed.

Carbon steel was cut with an orthogonal cutting tool, using a specially designed sudden-stop cutting device set on a shaper.

The chemical composition and mechanical properties of the test material are given in Table 1.

A brief sketch of the specially designed sudden-stop cutting device is shown in Fig. 12. The instant the cutting tool ① cuts the workpiece ② for some fixed cutting length, the trip block ③ touches the lever ④, which releases the clamp ⑤ that supports the workpiece ②. Cutting stops and the workpiece ② proceeds in the cutting direction together with the cutting tool ①. The cutting tool ① is set on the tool dynamometer ⑥, which is fixed on the ram ⑦ of a shaper, and the cutting resistance, i.e., horizontal and vertical components are recorded during cutting. The whole equipment except the cutting tool ①, the tool dynamometer ⑥, and the trip block ③ is set on the table ⑧ of the shaper. It was determined from the experiments that stopping time of cutting by this test equipment was about 0.0013 sec, which seems to be sufficiently short to be used for sudden-stop cutting tests.

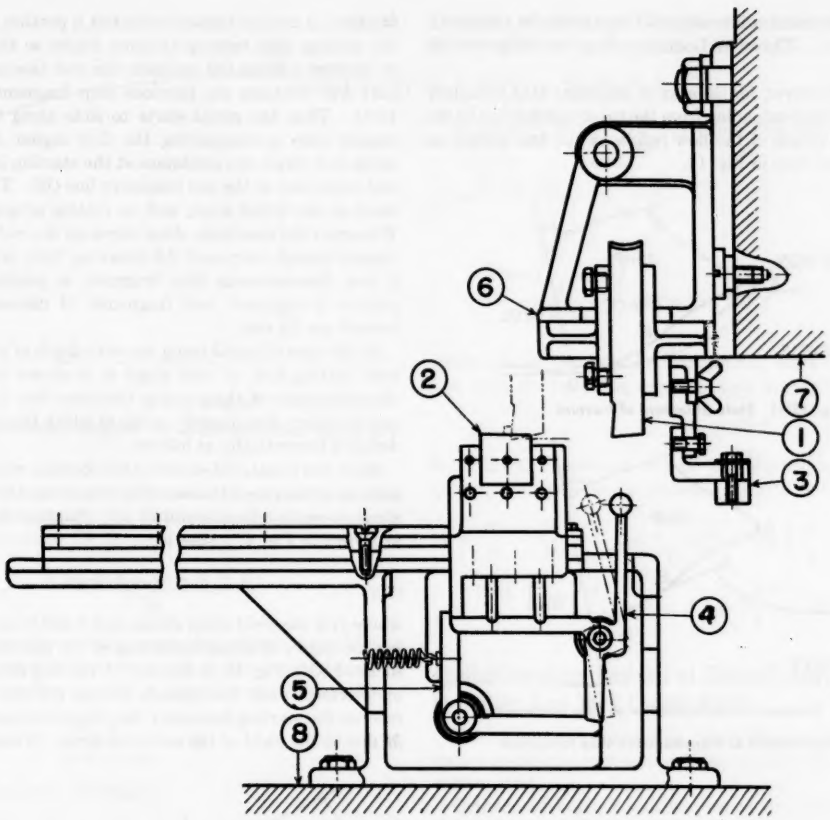

Fig. 12 Sketch of sudden-stop cutting device

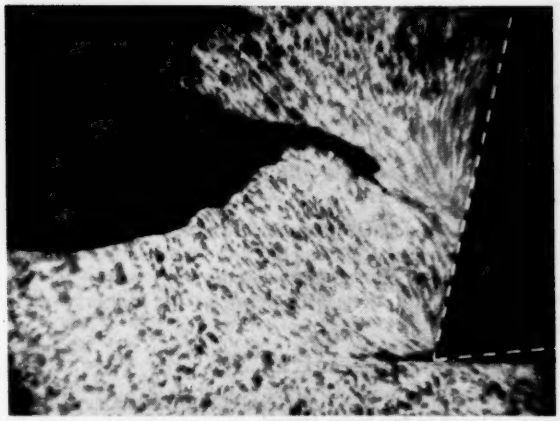

Fig. 13 Typical photograph of discontinuous chip formation (1) (Work material, carbon steel; cutting speed, 17 fpm; rake angle, 12 deg; depth of cut, 0.015 in.; dry)

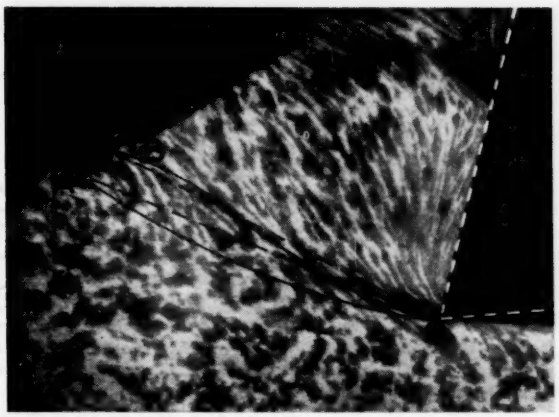

Fig. 14 Typical photograph of discontinuous chip formation (2) (Work material, carbon steel; cutting speed, 17 fpm; rake angle, 12 deg; depth of cut, 0.010 in.; dry)

Cutting carbon steel for various depths of cut at 17 fpm cutting speed with orthogonal high-speed steel cutting tool with 12 deg rake angle, a discontinuous type of chip was produced for depths of cut over 0.004 in. A typical example of discontinuous chip formation is shown in Fig. 13. Fig. 14 shows a state at which a fragment of discontinuous chip is about to occur. A trace of the crack line is shown by the solid line marked OB. Plastic flow has already occurred ahead of this line, and so a flow region is recognized. The starting boundary line of the flow region, which is obtained by observing the deformation of the crystal lattice, is shown by the solid line OA. Thus, generally speaking, boundary lines of the flow region are not straight, but curved. This is explained as follows.

Since boundary lines are slip planes, they intersect the free surfaces of work or chip at 45 deg. They also must cross the face of the cutting tool at its tip by at least 90 deg according to Hill's

theorem on the maximum intensity of singularities in a material in yield state [21]. Therefore boundary lines are obliged to be curved.

It is assumed, however, for the sake of simplicity that boundary lines are straight lines extending from the tip of cutting tool to the starting and end points of the flow region on the free surface as shown with dashed lines in Fig. 14.

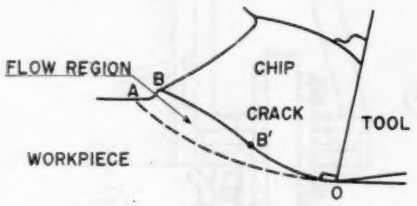

Fig. 15(a) State at instant of fracture

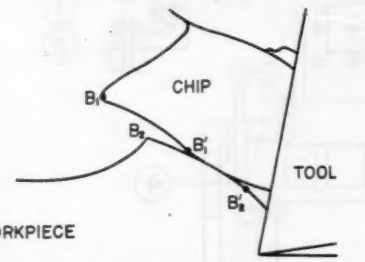

Fig. 15(b) Process during formation of chip fragment

Fig. 15 Explanation of discontinuous chip formation

fracture, is not cut immediately, but a portion of workpiece near the cutting edge rises up to some degree so that some part OB' of fracture surface OB contacts the tool face and the remaining part BB' contacts the previous chip fragment as shown in Fig. 15(b). Then the metal starts to slide along the tool face as a regular chip accompanying the flow region AOB. The shear stress and strain are minimum at the starting boundary line OA, and maximum at the end boundary line OB. The cutting force is small at the initial stage, and, as cutting progresses, it increases. Whenever the maximum shear stress on the end boundary line increases enough to exceed the breaking limit, fracture occurs and a new discontinuous chip fragment is produced. The above process is repeated, and fragments of discontinuous chip are formed one by one.

In the case of metal being cut with depth of cut t_1 by an orthogonal cutting tool of rake angle α as shown in Fig. 16, the inclination angle of the starting boundary line ϕ_1 and that of the end boundary line (namely, a line at which fracture occurs) ϕ_2 are deduced theoretically as follows.

Since work material should strain-harden when fracture occurs such as in the discontinuous chip formation, the relation between shear stress and shear strain or τ-γ diagram might be assumed as shown in Fig. 17; that is,

$$\tau = \tau_0 + k\gamma^m, \tag{22}$$

where τ_0 is the yield shear stress, and k and m are constants showing the degree of strain-hardening of the material. Fig. 17 is associated with Fig. 16 as follows. A moving metal particle in the undeformed work corresponds to the position O, and when it reaches the starting boundary line, it corresponds to the position M due to the yield of the metal in shear. When a metal particle

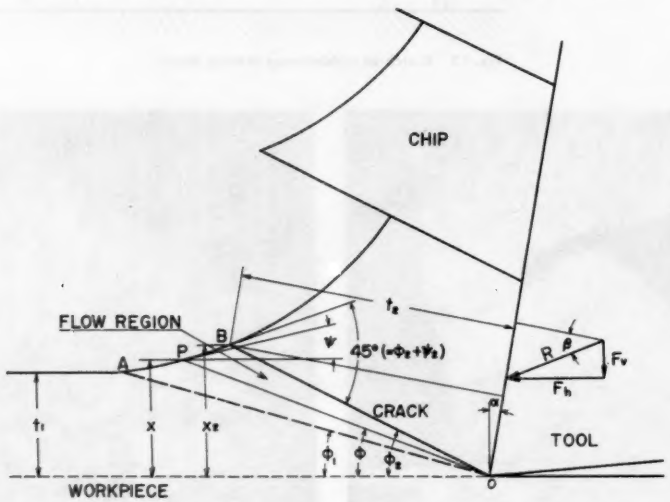

Fig. 16 Analysis of discontinuous chip formation based on flow region concept

Fig. 15(a) shows the instant when fracture occurs on the end boundary line of the flow region. Once fracture has occurred, a fragment of discontinuous chip flows out along the tool face without any restriction. The instant fracture occurs, the shear stress decreases below the breaking limit, and a new chip is ready to be formed. This behavior and cutting process are almost the same as continuous chip formation except that fracture occurs when the shear stress on the end boundary line reaches the breaking limit again as cutting proceeds. At the very initial stage the workpiece, which has an inclined free surface at OB due to previous passes into the flow region, it changes its location from the position M to the position N continuously along the curve until it reaches the breaking point N. The breaking point N corresponds to the end boundary line, i.e., the fracture line, at which fracture occurs periodically, and a discontinuous chip is produced. Therefore the average shear stress must reach its maximum value at the end boundary line of the flow region. Denoting the distance from an arbitrary point P on the free surface of the flow region to the horizontal line through the cutting edge by x, and the maximum cutting force with which fracture is about to occur by R for

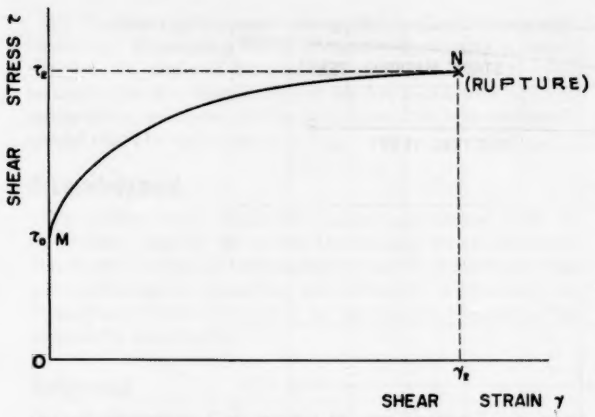

Fig. 17 Shear stress-strain diagram for strain-hardening rigid-plastic material

width of cut b, and assuming that the shear stress distributes uniformly on the radial plane in the flow region, the shear stress on an arbitrary radial plane OP is expressed as

$$\tau = \frac{R \sin \phi \cos (\phi - \alpha + \beta)}{bx}. \tag{23}$$

This reaches the maximum value when the inclination angle of an arbitrary radial plane ϕ becomes equal to the inclination angle of the end boundary line ϕ_2; that is, from the condition that

$$\left(\frac{d\tau}{d\phi}\right)_{\phi=\phi_2} = 0, \tag{24}$$

the following equation is obtained.

$$\left(\frac{dx}{xd\phi}\right)_{\phi=\phi_2} = \cot \phi_2 - \tan (\phi_2 - \alpha + \beta) \tag{25}$$

On the other hand, geometrically

$$\frac{dx}{xd\phi} = \cot \phi - \cot (\phi + \psi). \tag{26}$$

Hence, for $\phi = \phi_2$

$$\left(\frac{dx}{xd\phi}\right)_{\phi=\phi_2} = \cot \phi_2 - \cot (\phi_2 + \psi_2), \tag{27}$$

where ψ_2 is the value of ψ at the end boundary line. Since the end boundary line of the flow region in the case of the discontinuous chip formation is a slip plane with fracture, it makes an angle of 45 deg against the free surface. Therefore,

$$\phi_2 + \psi_2 = \frac{\pi}{4}. \tag{28}$$

From Equations (25), (27), and (28),

$$\phi_2 = \frac{\pi}{4} + \alpha - \beta. \tag{29}$$

This is the equation showing the condition at which fracture occurs if a discontinuous chip is produced.

The inclination angle of the starting boundary line ϕ_1 in this case is obtained as follows: Since the shear stress is τ_0, and x is equal to depth of cut t_1 and ϕ to ϕ_1 on the starting boundary line, from Equation (23)

$$\tau_0 = \frac{R \sin \phi_1 \cos (\phi_1 - \alpha + \beta)}{bt_1}. \tag{30}$$

The shear strain γ_2 and the shear stress τ_2 on the end boundary line are obtained by Equations (14)[5] and (23).

$$\gamma_2 = \cot \phi_2 - \cot (\phi_2 + \psi_2)$$
$$= \cot \left(\frac{\pi}{4} + \alpha - \beta\right) - 1 \text{ [from Eqs. (28) and (29)]}, \tag{31}$$

$$\tau_2 = \frac{R \cos (\phi_2 - \alpha) \cos (\phi_2 - \alpha + \beta)}{bt_2}$$
$$= \frac{R \cos \left(\frac{\pi}{4} - \beta\right)}{\sqrt{2}\, bt_2} \text{ [from Eq. (29)]}, \tag{32}$$

where t_2 is the theoretical maximum chip thickness. From Equation (22), the following relation exists among τ_0, τ_2, and γ_2.

$$\tau_2 = \tau_0 + k\gamma_2^m \tag{33}$$

Substituting Equations (30) to (32) into Equation (33), the required expression for the inclination angle ϕ_1 can be obtained.

$$\phi_1 = \frac{\alpha}{2} - \frac{\beta}{2} + \frac{1}{2} \sin^{-1} \left[\sqrt{2}\, r \cos \left(\frac{\pi}{4} - \beta\right) - \frac{2bkt_1}{R} \left\{ \cot \left(\frac{\pi}{4} + \alpha - \beta\right) - 1 \right\}^m + \sin (\beta - \alpha) \right] \tag{34}$$

Application of an Analysis of Discontinuous Chip Formation to Cutting Test With Carbon Steel

The theoretical analysis of discontinuous chip formation discussed in the previous section was applied to the cutting test with carbon steel.

Orthogonal cutting was performed dry for carbon steel (see Table 1), using the specially designed sudden-stop device set on a shaper. The cutting conditions were:

Rake angle	α = 12.0 deg
Width of cut	b = 0.057 in.
Depth of cut	t_1 = 0.010 in.
Cutting speed	V_1 = 17 fpm

A discontinuous type of chip obtained is shown in Fig. 14, and this is the state at which fracture is about to occur. The following quantities were measured:

Thickness of chip	t_2 = 0.027 in.
Horizontal cutting force	F_h = 223 lb
Vertical cutting force	F_v = 75 lb
Inclination angle of the starting boundary line of the flow region	ϕ_1 = 19.0 deg
Inclination angle of the end boundary line of the flow region	ϕ_2 = 27.0 deg

The mean friction angle on the tool-chip interface is calculated from Equation (13).

$$\beta = \tan^{-1} \frac{75 + 223 \tan 12.0°}{223 - 75 \tan 12.0°} = 30.6°$$

From Equation (29) the theoretical value for the inclination angle of the end boundary line (i.e., fracture line) is calculated.

$$\phi_2 = 45° + 12.0° - 30.6° = 26.4°$$

[5] Regarding the shear strain in the flow region in the case of discontinuous chip formation, it is expressed in Equation (14) as in the case of simple continuous chip formation discussed in the previous section.

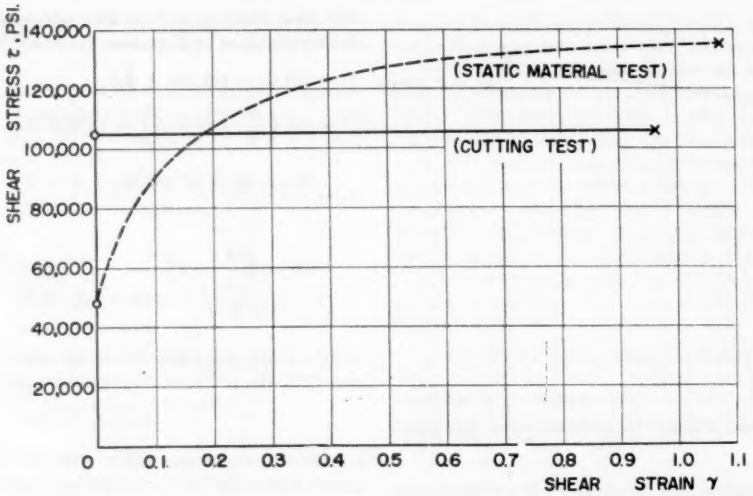

Fig. 18 Comparison of shear stress-strain diagrams for carbon steel in cutting test and static material test

This is seen to be in agreement with the observed value (27.0 deg).

The inclination angle of the starting boundary line ϕ_1 can be calculated from Equation (34), but constants k and m in the equation are unknown in the present stage. The shear stress-strain diagram obtained by the conventional static material test cannot be used in this case because of the large strain rate and the heat generated in metal cutting. Therefore it is necessary to determine the shear stress-strain diagram for metal cutting using the observed values in the cutting test.

Substituting the observed values into Equation (30), the shear stress on the starting boundary line is obtained

$$\tau_0 = \frac{\sqrt{223^2 + 75^2}\sin 19.0^\circ \cos(19.0^\circ - 12.0^\circ + 30.6^\circ)}{0.057 \times 0.010}$$

$$= 104{,}000 \text{ psi.}$$

The shear stress (i.e., breaking stress) and shear strain on the end boundary line (i.e., fracture line) are calculated from Equations (31) and (32).

$$\tau_2 = \frac{\sqrt{223^2 + 75^2}\cos(27.0^\circ - 12.0^\circ)\cos(27.0^\circ - 12.0^\circ + 30.6^\circ)}{0.057 \times 0.027}$$

$$= 104{,}000 \text{ psi}$$

$$\gamma_2 = \cot 27.0^\circ - 1 = 0.96$$

Using thus obtained values ($\tau = \tau_0$ for $\gamma = 0$ and $\tau = \tau_2$ for $\gamma = \gamma_2$), the shear stress-strain diagram for carbon steel in the cutting test can be drawn as shown in a solid line in Fig. 18, where the yield point and the breaking point are connected with an approximately straight line. In this figure the stress-strain diagram for the same material in a static material test is drawn in a dashed line, which was obtained from the experimental result of the relation between twisting moment and specific twisting angle by Ludwik's method [22]. Comparing both diagrams, the yield shear stress is larger, the degree of strain-hardening or the slope of the diagram in plastic region is smaller, and the ductility is less in the case of a cutting test than in the case of a static material test. These are obvious from consideration of large strain rate and heat generated in metal cutting. Equations of these two diagrams are expressed as follows:

$$\tau = 49{,}000 + 88{,}000\gamma^{0.235}$$

for static material test,

$$\tau = 104{,}000 + 208\gamma$$

for cutting test,

where τ is in psi.

Using constant values k and m in metal cutting, that is, $k = 208$ and $m = 1$, the inclination angle of the starting boundary line is calculated from Equation (34).

$$\phi_1 = \frac{12.0^\circ}{2} - \frac{30.6^\circ}{2} + \frac{1}{2}\sin^{-1}\left[\sqrt{2}\,\frac{0.010}{0.027}\cos(45^\circ - 30.6^\circ) - \frac{2 \times 0.057 \times 208 \times 0.010}{\sqrt{223^2 + 75^2}}\{\cot(45^\circ + 12.0^\circ - 30.6^\circ) - 1\} + \sin(30.6^\circ - 12.0^\circ)\right]$$

$$= 19.4^\circ$$

This shows remarkable agreement with the observed value (19.0 deg).

Conclusions

Instead of the conventional theory of the mechanics of metal cutting based on the single shear plane, the concept of the transitional deformation zone, i.e., the flow region, which exists between the rigid region of work and the plastic region of steady chip, was developed. The mechanics of orthogonal cutting was analyzed in the case of a simple continuous chip, and the concept was also applied to the discontinuous chip formation. The foregoing analysis and experimental results lead to the following conclusions.

(1) The expressions for angles of the boundary lines of the flow region were deduced theoretically in the case of the simple continuous chip under the assumption of a perfectly plastic solid and confirmed in cutting tests with lead.

(2) Conflicts in the cutting mechanism based on the single shear plane, such as an abrupt change of movement of a metal particle, an infinite acceleration which a metal particle receives, extremely large strain and strain rate, etc., can be removed by the flow region concept.

(3) The flow region concept was applied to discontinuous chip formation. Considering the strain-hardening property of metal, equations for angles of the starting boundary line and the end boundary line (i.e., fracture line) of the flow region were deduced theoretically, and determined to be in agreement with the experimental result for carbon steel.

Acknowledgment

The authors would like to express their appreciation to Dr. A. O. Schmidt, Kearney & Trecker Corporation, for providing the opportunity to present this manuscript and for his valuable suggestions during its preparation; and to Prof. G. L. Thuering, The Pennsylvania State University, for his help in translating this manuscript into English.

References

1 V. Piispanen, "Lastunmuodostumisen Theoriaa," *Teknillinen Aikakauslehti*, vol. 27, 1937, pp. 315–322.

2 V. Piispanen, "Theory of Formation of Metal Chips," *Journal of Applied Physics*, vol. 19, 1948, pp. 876–881.

3 H. Ernst and M. E. Merchant, "Chip Formation, Friction and High Quality Machined Surfaces," Surface Treatment of Metals, ASM, 1941, pp. 299–378.

4 M. E. Merchant, "Mechanics of the Metal Cutting Process. I. Orthogonal Cutting and a Type 2 Chip; II. Plasticity Conditions in Orthogonal Cutting," *Journal of Applied Physics*, vol. 16, 1945, pp. 267–275 and pp. 318–324.

5 E. H. Lee and B. W. Shaffer, "The Theory of Plasticity Applied to a Problem of Machining," *Journal of Applied Mechanics*, vol. 18, TRANS. ASME, vol. 72, 1951, pp. 405–413.

6 R. Hill, "The Mechanics of Machining: A New Approach," *Journal of the Mechanics and Physics of Solids*, vol. 3, 1954, pp. 47–53.

7 K. Okushima and K. Hitomi, "On the Cutting Mechanism for Soft Metals," *Memoirs of the Faculty of Engineering, Kyoto University, Japan*, vol. 19, 1957, pp. 135–166; *Trans. Japan Society of Mechanical Engineers*, vol. 23, no. 134, 1957, pp. 674–680.

8 K. Nakayama, "A Study on the Mechanism of Metal Cutting," *Journal of the Society for Precision Mechanics of Japan*, vol. 23, 1957, pp. 528–532.

9 D. Kececioglu, "Shear-Strain Rate in Metal Cutting and Its Effect on Shear-Flow Stress," TRANS. ASME, vol. 80, 1958, pp. 158–168.

10 D. G. Christopherson, P. L. B. Oxley, and W. B. Palmer, "Orthogonal Cutting of a Work-Hardening Material: Theoretical and Experimental Investigation," *Engineering*, vol. 186, no. 4820, July 25, 1958, pp. 113–116.

11 I. Finnie and M. C. Shaw, "The Shear Stress in Metal Cutting," TRANS. ASME, vol. 77, 1955, pp. 115–123.

12 K. Okushima and K. Hitomi, "An Analysis of the Mechanism of Orthogonal Cutting," *Memoirs of the Faculty of Engineering, Kyoto University, Japan*, vol. 20, 1958, pp. 95–116; *Trans. Japan Society of Mechanical Engineers*, vol. 25, no. 150, 1959, pp. 54–60.

13 I. Finnie and M. C. Shaw, "The Friction Process in Metal Cutting," TRANS. ASME, vol. 78, 1956, pp. 1649–1657.

14 T. Sata and M. Mizuno, "Friction Process on Cutting Tool and Cutting Mechanism," *Journal of the Scientific Research Institute, Japan*, vol. 49, 1955, pp. 163–174; *Trans. Japan Society of Mechanical Engineers*, vol. 21, no. 106, 1955, pp. 416–423.

15 A. W. Meyer and F. R. Archibald, "Carbide Milling of Steel," *Mechanical Engineering*, vol. 67, 1945, pp. 659–667.

16 F. R. Archibald, "Analysis of the Stresses in a Cutting Edge," TRANS. ASME, vol. 78, 1956, pp. 1149–1154.

17 J. H. Creveling, T. F. Jordan, and E. G. Thomsen, "Some Studies of Angle Relationships in Metal Cutting," TRANS. ASME, vol. 79, 1957, pp. 127–138.

18 M. Field and M. E. Merchant, "Mechanics of Formation of the Discontinuous Chip in Metal Cutting," TRANS. ASME, vol. 71, 1949, pp. 421–430.

19 N. H. Cook, I. Finnie, and M. C. Shaw, "Discontinuous Chip Formation," TRANS. ASME, vol. 76, 1954, pp. 153–162.

20 E. H. Lee, "A Plastic-Flow Problem Arising in the Theory of Discontinuous Machining," TRANS. ASME, vol. 76, 1954, pp. 189–194.

21 R. Hill, "On the Limits Set by Plastic Yielding to the Intensity of Singularities of Stress," *Journal of the Mechanics and Physics of Solids*, vol. 2, 1954, pp. 278–285.

22 A. Nadai, "Theory of Flow and Fracture of Solids," Engineering Societies Monographs, vol. 1, McGraw-Hill Book Company, Inc., New York, N. Y., 1950, p. 349.

DISCUSSION

S. Kobayashi[6] and E. G. Thomsen[7]

The authors have presented an interesting analysis of the mechanics of metal cutting by assuming an extended shear zone. While it is true that shearing takes place over a narrow region, there is no experimental nor theoretical evidence to confirm the authors' contention that at conventional speeds, under the absence of a built-up edge, the shear zone reaches the proportions proposed by the authors.

The conflicts mentioned by the authors do not in reality appear to be sufficient to disregard the older and simpler theories unless in effect it can be demonstrated that the proposed zone really exists at higher cutting speeds than those employed by the authors and with other metals. If it is assumed that the shear zone is not a plane but a narrow region, then the authors' conflicts (*a*) and (*b*) disappear since infinite accelerations and infinite stress gradients need not be postulated. As to conflict (*c*), it is undoubtedly true that the strains in metal cutting are higher than those achievable from a tension test, but high strains under compressive types of loading in forming operations are quite common and may be of the same order of magnitude as those in metal cutting. Conflict (*d*) is nonexisting since a number of investigators, including the present discussers, have written a number of papers in which they demonstrated the existence of a constant dynamic shear stress in metal cutting and reported excellent correlation on the basis of effective stress—effective strain relationships between metal cutting and tension test data.

The authors refer to a perfectly plastic solid, but in their analysis violate the condition for equilibrium which inevitably leads to the type of slip-line fields proposed by Lee and Shaffer [5]. It does not appear to be possible to construct a slip-line field satisfying equilibrium and continuity for the sector postulated by the authors where each one of the radial lines is at the same time one of maximum shear.

The authors in their analysis evidently assume that shear straining is accompanied by rotation of the maximum shear direction as the element moves through the shear zone. It is not clear just how such a state of strain can exist in the element with their proposed state of stress. Furthermore, the total shear strain of the metal in the chip should be determined by considering the summation of the increments of shear strain. It can be shown then that the true total shear strain would be given by,

$$\gamma = \cot \phi_1 + \tan (\phi_2 - \alpha),$$

instead of equation (16). In this case the foregoing shear strain is greater than that obtainable with a single shear plane, a result unfortunately not anticipated by the authors. It should be mentioned too, that the shear strain calculated by the authors could not be correlated with the data of a tension test, since the stress or strain path was not determined. Consequently, the effective strain cannot be calculated in this manner.

Authors' Closure

The authors appreciate the discussion by Dr. Kobayashi and Professor Thomsen.

There might be some difficulty in the authors' new concept of the flow region from the standpoint of the present plasticity theory. However, the authors consider that this idea eliminates some conflicts of the conventional mechanics of orthogonal cutting as mentioned in the Introduction. The discussers' consideration of a narrow shear zone is not sufficient, because this zone is not actually evaluated in the theoretical analysis

[6] Lecturer in Industrial Engineering, University of California, Berkeley, Calif.

[7] Professor of Metal Processing, University of California, Berkeley, Calif. Mem. ASME.

and formulas are not deduced for it. In fact, the conventional analysis itself cannot eliminate conflicts (*a*), (*b*), and (*c*) mentioned in the Introduction in so far as this narrow zone is assumed as a single shear plane. Regarding conflict (*d*), if a single shear plane concept is assumed, it is impossible to draw the stress-strain diagram or the path of stress and strain in metal cutting such as, for example, Fig. 4, Fig. 17, or Fig. 18, which correlates to the cutting model; that is, the metal particle moves along the stress-strain diagram similar to that in static material test.

The authors suggest a wide flow region between the rigid region of work and the plastic region of steady chip. However, the word "wide" is used in this paper, meaning "regional," compared with "single" in the conventional theory. Sometimes the flow region is narrow. In reality, the wideness of this flow region depends upon cutting conditions. The most important factor is found to be the cutting speed. According to the authors' theoretical analysis and experimental results of carbon steel on the secondary plastic flow in the chip [23],[8] the higher the cutting speed, the narrower the flow region. The flow region is extremely large in low speed range (30 to 300 fpm). It is considered that this region might vanish in super-high speeds (more than 2000 fpm). This localization of flow with an increase in cutting speed appears to be consistent with the localization of shear in static material tests by Zener and Hollomon [24]. Even in super-high speeds it is important to consider a very narrow flow region in order to eliminate the conventional conflicts in metal cutting.

There are several other experimental and theoretical evidences to confirm the authors' concept. The regional deformation can be clearly observed in photographs of Figs. 3 and 14 for both formations of continuous and discontinuous types of chip. It is impossible to explain the difference of both formations with a single shear plane theory. The discussers point out that Lee and Shaffer's slip-line field can not be drawn when a flow region is considered. However, this slip-line field appears not to be applied to a metal-cutting model without modification, because this does not explain anything about fracture such as in the case of discontinuous chip formation.

Another theoretical evidence of the existence of the flow region refers to the explanation of the phenomenon of chip curl [25].

As pointed out by the discussers, the rotation of the shear direction is not explained well in the present paper. But the important matter is that the plastic flow occurs in some regional deformation zone ahead of the tool tip. The plastic flow of combined shear and compression might occur inside this region. The authors assumed, in the present paper, only the shear process along the radial plane in the flow region. Although one singular point of the sharp intersection between the free surfaces of work and chip was eliminated with the present flow region concept, another singular point of the cutting edge has not been eliminated yet. Further consideration is necessary on this point. Moreover, boundary lines of the flow region are not straight but curved as mentioned in the present paper. This suggests that the deformation process in the flow region is not simple. Therefore, the strain in chip should be re-evaluated. Assuming the boundary lines of the flow region as straight lines, the strain in chip is simply expressed as equation (16), using a general equation (14) of the strain in the flow region, contrary to the equation suggested by the discussers. It seems to be difficult to deduce a formula of strain in chip by considering the summation of the increments of shear strain since the shape of the free surface or the relation between angles ϕ and ψ is not known. Differing from the discussers' opinion, the shear stress and strain calculated by the authors are reasonable and the path of shear stress and strain is well shown in Fig. 18. The difference between stress-strain diagrams in cutting test and static material test is explained by the large strain rate and the heat generated in cutting.

[8] Numbers in brackets from 23 to 25 designate References at end of closure.

Additional References

23 K. Okushima and K. Hitomi, "Plastic Flow of Metal in Orthogonal Cutting," *Trans., Japan Society of Mechanical Engineers*, vol. 26, no. 163, 1960, pp. 423–429; *Bulletin of Japan Society of Mechanical Engineers*, vol. 3, no. 12, 1960, pp. 556–560.

24 C. Zener and J. H. Hollomon, "Effect of Strain Rate Upon Plastic Flow of Steel," *Journal of Applied Physics*, vol. 15, 1944, pp. 22–32.

25 K. Okushima and K. Hitomi, "The Mechanism of Chip Curl in Orthogonal Cutting," *Journal of the Society for Precision Mechanics of Japan*, vol. 25, no. 193, 1959, pp. 320–327.

New Development in the Theory of the Metal-Cutting Process

Part II The Theory of Chip Formation

P. ALBRECHT
Research Associate, Physical Research Department, The Cincinnati Milling Machine Company, Cincinnati, Ohio

Introduction of the concept of ploughing into the metal-cutting process lead to the abandoning of the assumption of collinearity of the resultant force on tool face and on the shear plane. With this understanding the tool face force is found to produce a bending effect causing bending stresses in the shear zone. Study of the chip formation mechanism when varying cutting speed showed that increased bending action reduces the shear angle and vice versa. A set-up for the development of an analytical model of the chip formation process based on the combined effect of shear and bending stresses in the shear zone has been given.

Application of the gained insight to the design of the cutting tool for maximum tool life by controlling of the chip-tool contact was suggested. Brief introduction to the study of cyclic events in chip formation and their relation to the tool life is presented.

Introduction

CONSIDERABLE effort has been expended in the past on developing the theory of chip formation. For purposes of this presentation of new developments in this field it is not necessary to review even briefly all the approaches taken by the investigators in this field. Instead literature on the subject is cited in the bibliography at the end of the paper. The number of approaches used indicates that the task was not an easy one and in each subsequent attempt the approach was changed somewhat by each investigator in the hope of obtaining better agreement of theory with experiment.

Research in the past has been essentially a search for the most essential factors in the problem. Results presented in this paper are another step in this direction aimed at bridging the gap which still exists between theory and experiment in the theory of chip formation. The approach used is to consider the effect of "ploughing" on chip formation and to offer additional observations which serve as a broader basis for the derivation of the new analytical model of the chip formation process. In an earlier paper by the author [1][1] the mechanism of "ploughing" was first introduced into the mechanism of the metal-cutting process. The ploughing has been recognized as a process of plastic deformation of the metal taking place due to the presence of the sharpness rounding on the cutting edge. Because the ploughing is a process different from the shearing of the metal in the shear zone it should be treated separately in the analysis of the cutting process. The separation of the force required for performing of ploughing, termed the ploughing force, lead to a better understanding of the metal-cutting mechanism, explaining some of its well-known paradoxes.

Contributed by the Metal Processing Research Activity of the Production Engineering Division and presented at the Winter Annual Meeting, New York, N. Y., November 27–December 2, 1960, of THE AMERICAN SOCIETY OF MECHANICAL ENGINEERS. Manuscript received at ASME Headquarters, July 25, 1960. Paper No. 60—WA 63.

Observational Part of Chip Formation Theory

An over-all impression of previous work on chip formation theory indicates that the observational part which usually preceeds the derivation of the analytical model of the event was left essentially unchanged in each case.

The observational part of the studies of chip formation resulted in an idealized picture, as shown in Fig. 1 (for orthogonal cutting). The diagram, Fig. 1, indicates that the tool removes the stock (of thickness t_1) by shearing it ahead of the tool in a zone which is quite thin compared to its length, and which can

[1] Numbers in brackets designate Biblography at end of paper.

Nomenclature

Variables of Tool Shape (for the orthogonal cutting process with built-up edge)

- α = rake angle
- a_b = rake angle of the natural built-up edge
- a_{ba} = rake angle of the artificial built-up edge
- $\pm\beta$ = tool face clearance angle, positive or negative
- f = width of tool face for a tool with tool face clearance
- r = sharpness radius, which gives the magnitude of sharpness rounding of the cutting edge
- r_e = effective sharpness radius, which accounts for the change of sharpness rounding due to the presence of the built-up edge
- e = elevation of the built-up edge over the tool face

Dimensions of Cut

- t_1 = thickness of uncut chip
- t_2 = thickness of chip after its separation from the work
- w = width of cut in orthogonal cutting

Tool Forces

- R = resultant tool force (or briefly tool force)
- F_c = cutting force (component of R in direction of tool motion)
- F_t = thrust force (component of R perpendicular to the direction of tool motion)
- P = main ploughing force or chip ploughing force at the extreme cutting edge
- P_e = component of the ploughing force polygon which takes part in shearing
- Q = tool face force
- Q_{cr} = tool face force for a tool with a restricted chip tool contact area
- Q_{ci} = tool face force for a tool with an extended chip tool contact

(Continued on next page)

usually be very well represented by the shear plane AB. The position of the shear plane is customarily defined by means of the so-called shear angle ϕ, which is the angle between the shear plane and the direction of tool motion. After being sheared the metal becomes a chip which slides first along the tool face, following its shape (straight portion of the chip in Fig. 1), and then, beyond a certain point O on the tool face, curls away from that tool face, maintaining its natural curvature. Because the curvature of the chip is due to the plastic deformation of the metal and, as noted previously, this plastic deformation usually is confined to a thin shear zone, it was concluded that the chip must be born curled at the shear zone. Then, because of contact with the tool face, it flattens out elastically over some length before it leaves the tool face and returns to its original curvature. To this picture, gained by visual observation, was added a force system which consists of a resultant force R on the tool face and a resultant force S on the shear plane. Both forces were assumed to be collinear, and in order to satisfy the requirement of static equilibrium they must be equal in magnitude and oppose each other in direction (Fig. 1).

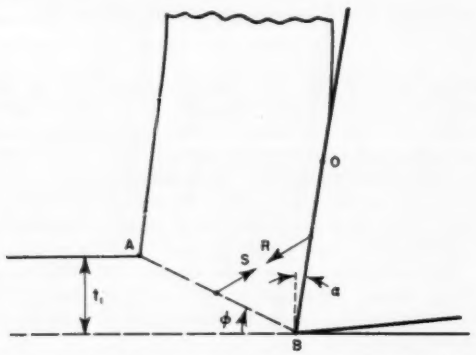

Fig. 1 Configuration of the metal cutting mechanism used in development of chip formation theory by the previous investigators

The described picture was used by investigators of the chip formation process almost without exception. In some investigations a few changes were made when studying the plastic deformation in the shear zone or when taking into account the presence of a built-up edge. The latter change was considered only as a change of the tool face shape.

Present Approach

As mentioned in the introductory section, the approach taken in the present work has two main points. First, it considers the consequences of identifying the ploughing process as a separate process in metal cutting and, secondly, it undertakes improvement of the idealized picture of the metal-cutting process (described in the previous section) in order to obtain a better base for the derivation of the analytical model.

In the following section both points will be discussed in relation to the conventional picture of the chip formation process. As the ploughing process is introduced and the new observational data added, an improved picture will result which will be used in the derivation of the improved analytical model.

Improved Picture of the Chip Formation Process

Let us now consider the changes which the indicated approach will bring into the conventional picture of the chip formation process. All these changes can conveniently be introduced step by step, illustrating each of them by a separate picture.

Changes Caused by the Ploughing Process. By introduction of the ploughing process the force system will be changed to the picture shown in Fig. 2. Here, after resolving the resultant force R into two forces P and Q, two force systems are obtained in terms of action on the part of the tool and reaction on the part of work-

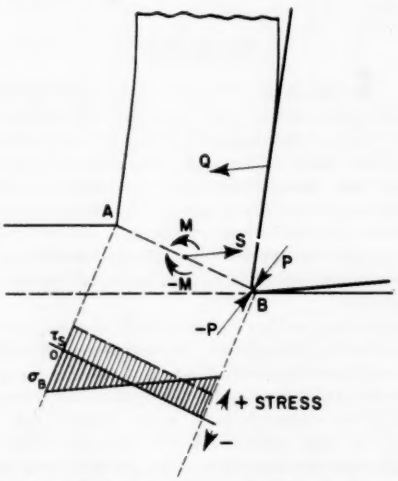

Fig. 2 New force distribution of the metal-cutting mechanism, showing that after separation of the ploughing force P from the cutting forces the remaining force Q on tool face can hardly be assumed to be collinear with the force S on the shear plane. Consequently the bending effect of the force Q causes a bending stress at the shear zone.

Nomenclature

S = total force on the shear plane

S_s = component of S in the direction of shearing at the shear plane

B = force on the face of a natural built-up edge

B_a = force on the face of an artificial built-up edge

Variables of the Bending Effect

$M = Qz$ = bending moment at the shear plane from the force Q

z = shortest distance between the force Q and middle of the shear plane

x = distance of the point of application of force Q from the cutting edge

Ratios of the Cutting Process

$r_t = \frac{t_1}{t_2}$ chip thickness ratio or cutting ratio

$\lambda = \frac{\tau}{t_1}$ or $\frac{\tau_a}{t_1}$ = ploughing ratio, for the cutting process without or with the built-up edge

$\zeta = \frac{z}{t_1}$ = bending ratio

$\xi = \frac{x}{t_1}$ = relative distance of the point of application of force Q from the cutting edge

$q = \frac{Q}{wt_1}$ = specific tool face force

Shear Plane Position

ϕ = shear angle

Workpiece Material Properties

Y = yield stress of the workpiece material in uniaxial tension or compression

Coefficients of Friction and Friction Angles

$\mu_Q = \tan \tau_Q$ = coefficient of friction on chip-tool interface

τ_Q = friction angle corresponding to the coefficient of friction μ_Q

τ_r = friction angle on the sharpness rounding of a tool with a built-up edge

piece. Force P, acting directly on a portion of the workpiece and part of the chip adjacent to it, is balanced out by the force $-P$. In order to maintain the equilibrium between the tool and workpiece, the remaining force Q must also be balanced out by reaction on the part of the workpiece, so the forces Q and S must be equal and parallel and oppose each other in direction. It can be noted that by subtracting the ploughing force P the remaining force Q on the tool face changed its direction significantly from that of the resultant force R of Fig. 1. This fact and the study of pictures of the cutting process reconstructed to scale indicate that the forces Q and S can not generally be collinear. Thus the assumption of the past about the force on the tool face and on the shear plane being collinear will be dropped in favor of the more general case indicated above. This is the most significant change in the force diagram for development of a chip formation theory which takes into account the ploughing process. If the forces Q and S are not considered to be collinear there must be a bending moment M in the shear plane. This fact will be considered in more detail in the following sections.

Significance of the Bending Moment. As soon as it has been established that forces Q and S are generally not collinear in a cutting process, and hence there is a bending moment acting upon the shear plane, an essential question arises: Is this bending moment significant to the chip formation process or not? In order to be able to answer the question a suitable criterion is needed. As a criterion for this purpose the stress induced in the shear plane by the bending moment is used. The compressive bending stress σ at point A due to this bending moment can be compared with the stress caused by another type of load on the shear plane, namely, with the shear stress τ. Then, if the ratio σ/τ is found to be large the bending load may be considered to play a significant role in chip formation and vice versa.

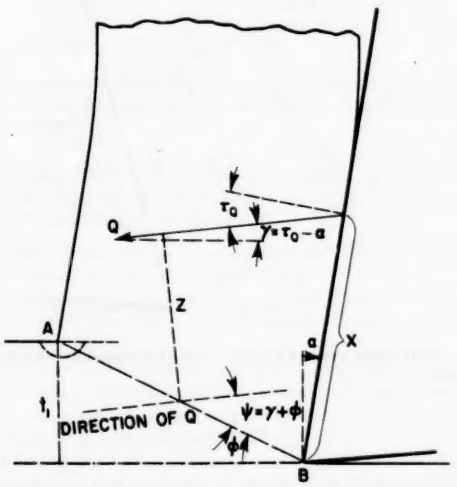

Fig. 3 Dimensions of the cutting mechanism used for derivation of the analytical expression of bending stresses at the shear zone and other relations

Values can be computed for the stresses σ and τ to determine the above ratio for a representative case. The average shear stress in the shear plane can be computed by using the familiar equation (1) which can be derived from Fig. 3:

$$\tau = \frac{Q}{w_1 t_1} \sin \phi \cos (\gamma + \phi) \tag{1}$$

The equation for the bending stress at point A of the shear plane can also be derived from Fig. 3 as follows:

Bending moment at the shear plane:

$$M = Qz \tag{2}$$

Distance of the middle point of the shear plane from the force Q:

$$z = x \cos \tau_Q - \frac{t_1}{2} \frac{\sin (\gamma + \phi)}{\sin \phi}$$

or:

$$z = \frac{t_1}{2} \left[2 \cos \tau_Q \frac{x}{t_1} - \frac{\sin (\gamma + \phi)}{\sin \phi} \right] \tag{3}$$

Compressive stress at the point A of the shear plane due to the bending moment M:

$$\sigma = \frac{M}{D} \quad \text{where} \quad D = \frac{w t_1^2}{6 \sin^2 \phi}$$

and:

$$\sigma = \frac{Q}{w t_1} 3 \sin \phi \left[2 \cos \tau_Q \frac{x}{t_1} \sin \phi - \sin (\gamma + \phi) \right] \tag{4}$$

The expression for the ratio of bending to shear stresses at the point A of shear plane would be:

$$\frac{\sigma}{\tau} = 3 \frac{2 \cos \tau_Q \frac{x}{t_1} \sin \phi - \sin (\gamma + \phi)}{\cos (\gamma + \phi)} \tag{5}$$

Data for the calculation of this ratio can be drawn from a representative case. For this purpose the picture of the cutting process was reconstructed to scale, Fig. 4. All the necessary quantities to calculate the stress ratio from equation (5) can be taken directly from Fig. 4. It has been calculated from the data of Fig. 4 that the compressive stresses due to bending at point A of the shear plane are about 5 times greater than the average shear stress at the shear plane. Such a high ratio indicates that the stresses due to the bending moment at the shear plane are large and hence should be considered in the theory of chip formation. This will be the most significant change resulting from the introduction of the ploughing process.

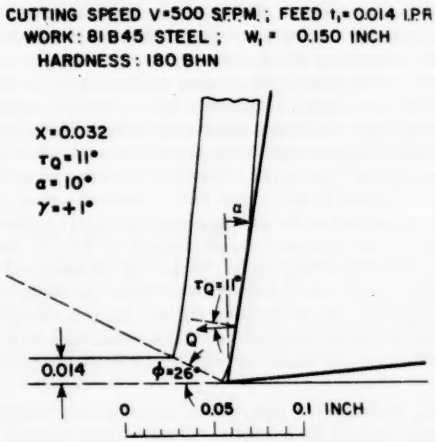

Fig. 4 Cutting mechanism when machining steel reconstructed in scale

At this point it would be appropriate to introduce the new observational findings needed to complete the picture which will permit the derivation of analytical expressions of the new chip formation theory.

Nature of the Chip-Tool Contact. Determination of the contact

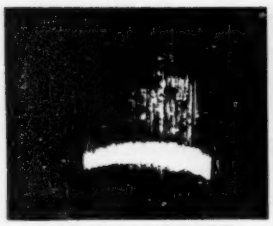

500 S.F.P.M. 0.014 I.P.R.
A

Fig. 5(A) Photograph of the plan view of the chip tool contact area showing varying degrees of contact at different regions

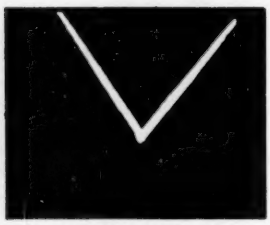

500 S.F.P.M. 0.014 I.P.R.
B

Fig. 5(B) Optical cross section of the cutting edge (the same tool as in "A") showing presence of a small built-up edge at high cutting speed when machining steel

stress on the chip-tool interface is an important problem in the study of the chip formation process.

The observation of the chip-tool contact area gave an interesting clue to the nature of these contact stresses. In Fig. 5, photograph A shows such a contact area which consists of several regions which are differently shaded. Let us consider now the significance of these portions of the chip-tool contact area. Starting from the top, a rather large rounded portion of the area over which the chip passes may be seen. In this region the chip is no longer in intimate, but rather, very intermittent contact with the tool. Proceeding in this same area toward the cutting edge, the dark area is encountered where the chip has already left the tool face but still slides in the very vicinity of it. Proceeding further in the same direction a sharp boundary between this darker region and a white slightly bent strip is reached. This white strip is the region of intense chip tool contact where the stresses are high, and if summed up over the white area would yield practically the whole chip-tool contact force Q. The bent shape of the white strip is caused by the end effect of the chip width. For a smaller ratio of uncut chip thickness t_1 to the width of chip, the bent area appears straight with only a small curvature at its ends. It can be noted that this area of high contact stresses ends a considerable distance in from the cutting edge. It is seen to end, as it began, with a sharp boundary. This leads to the conclusion that the chip starts to leave the tool surface on both sides of the white strip and that a region of low contact stress occurs again on the side nearer the cutting edge, with shading similar to that on the other side of the white strip. This region of low contact stresses can, under certain circumstances, where conditions are such that a very pronounced built-up edge exists, become an area where contact between chip and tool can be occasionally broken. In such a case the contact stress in this region may occasionally drop to zero. Finally, one arrives at the cutting edge where a tiny built-up edge is present as can be seen from photograph B, Fig. 5. Here the contact stresses are high again. Metal will be separated at the very point of the small built-up edge where no contaminating films are present as yet—friction stress is high, reaching almost the value of the shearing stress. These conditions may be responsible to a great extent for the development of the built-up edge.

Having examined the plan view of the chip-tool contact area, a sectional view can be reconstructed from this discussion. Such reconstruction is represented by the sketch, Fig. 6. In Fig. 7 it is shown that the chip does not straighten out under the action of chip-tool contact stresses. The chip-tool contact stresses rather change the original chip curvature, decreasing it in a certain part of the chip and increasing it in another.

The resultant radius of curvature R_r of the chip loaded by the chip-tool contact stresses would be given by the equation (6):

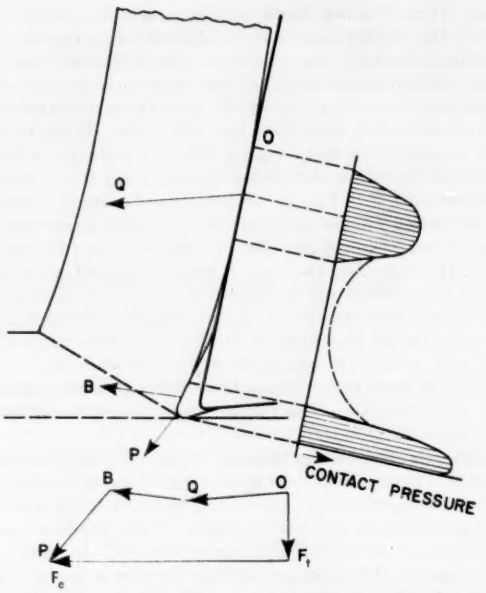

Fig. 6 Sketch showing the nature of chip tool contact as derived from studies such as represented in Figs. 4 and 5. The shaded area represents the region where the chip tool conctact pressures are not appreciable.

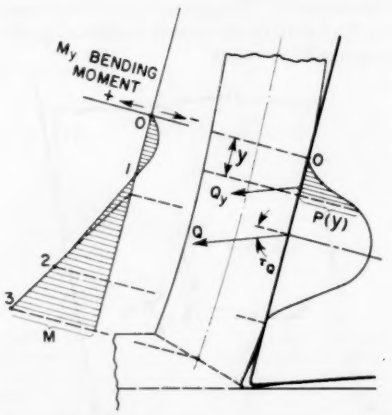

Fig. 7 Study of the effect of chip-tool contact stresses upon the curvature of the chip

$$\frac{1}{R_r} = \frac{1}{R_c} + \frac{M_y}{EI} \tag{6}$$

where

R_c = original radius of curvature of the chip

$I = \dfrac{wt_2^3}{12}$ = moment of inertia of the chip cross section

E = modulus of elasticity of chip material

and where M_y, the bending moment acting on the chip cross section at a distance y from point 0, is given by the differential equation:

$$\frac{d^2M_y}{dy^2} = p - \frac{t_2\mu_Q}{2}\frac{dp}{dy} \tag{7}$$

where $p = p(y)$ is the normal component of the chip-tool contact stress. As is indicated in Fig. 7, the bending moment M_y has

negative values (a positive moment increases the original curvature of the chip and negative decreases it) in the region between points 0 and 1 and thus straightens out the original chip curvature somewhat. On the other hand, between points 1 and 3 the bending moment M_y is positive and here the original curvature of the chip is increased by the chip-tool contact stresses.

The point of separation of the chip from the workpiece is slightly elevated from the plane of the tool face due to the presence of a small built-up edge. This allows the chip to remain curled. In fact the elevation necessary for the chip to remain curled is very small as can be easily calculated using Fig. 8. For example, a chip with a radius of curvature of 2 inches has to be elevated from the tool only 0.00025 in. in order to preserve its curvature in the case where its point of contact with the tool is a distance of 0.030 in. from the cutting edge. Similarly, the elevation required would be only 0.0001 in. if the distance of contact with the tool face from the cutting edge were 0.020 in.

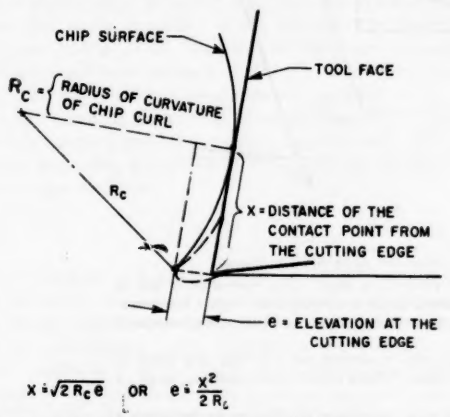
CHIP SURFACE
TOOL FACE
R_c = RADIUS OF CURVATURE OF CHIP CURL
R_c
X = DISTANCE OF THE CONTACT POINT FROM THE CUTTING EDGE
e = ELEVATION AT THE CUTTING EDGE
$X \doteq \sqrt{2R_c e}$ OR $e \doteq \frac{X^2}{2R_c}$

Fig. 8 Approximate relationship between the elevation of the point of separation of the chip from the work and chip-tool contact distance from the cutting edge

There are a number of factors which support strongly the nature of the chip-tool contact indicated in Fig. 6. The most significant of them are enumerated below:

1 Study of the chip-tool contact area as it was just discussed on the basis of the photographs of Fig. 5.

2 Further observations of the chip-tool contact relationship at a low cutting speed (20–40 sfpm) when this is more pronounced and easier to observe.

3 The fact that the crater on the tool face begins to develop some distance in from the cutting edge indicates that there is on the tool face a region of relatively low contact stresses, immediately behind the cutting edge.

4 Further, the experience that lubricating fluids have an effect on friction in a cutting process suggests that there should be a region of less intimate contact between the chip and tool where the fluid would have a chance to penetrate in order to be able to lubricate the chip-tool interface.

5 The study of the temperature distribution along the tool face made by Chao and Trigger [11] indicates also that the maximum temperatures occur in a region of chip-tool contact which is located some distance from the cutting edge.

This agrees with the character of the chip-tool contact shown in Fig. 6.

Effect of Bending Upon the Shear Angle

The effect of the bending moment of force Q upon the shear angle has been observed in turning over a range of cutting speeds and for a constant t_1. This study was accompanied by the reconstruction of, from such photographs as shown in Fig. 5, the configuration of the cutting mechanism to scale; such as seen in Fig. 4. The main features observed in such reconstructed pictures were condensed into the form of four sketches A, B, C, and D of Fig. 9, arranged in sequence of increasing cutting speed. As will be seen from the discussion of these results, the bending effect of the force Q changes during such experiments in a natural manner. These variations can be correlated to the variation of shear angle. Thus the effect of the bending moment of force Q upon the magnitude of the shear angle can be observed experimentally.

In the region of low cutting speeds the built-up edge is very pronounced; the elevation of the point of separation of the metal above the plane of the tool face is high. The subsequent ploughing effect of the large built-up edge greatly increases the curvature of the chip. The situation shown in Fig. 9(A) may arise as an extreme case. In this figure the chip does not touch the tool face at all, hence force Q is zero and the chip formation will be effected by force B on the built-up edge. Vector B passes very near the middle of the shear zone thus having practically no bending effect, and the shear angle, governed here mainly by the maximum shear stress, should be high. This was actually observed to be so in Fig. 10, as indicated by the relatively high value of cutting ratio r_t at the low cutting speed of about 20 sfpm. As speeds increase the size of the built-up edge reduces and the chip curl starts to contact the tool face as is shown in Fig. 9(B). After the contact takes place force Q assumes a certain magnitude and because the vector Q is at some distance z from the middle of the shear plane it creates a bending stress on the shear plane. This bending action of force Q will be accompanied by the decrease of the cutting ratio and thus the decrease of shear angle, apparent from the experimental results of Fig. 10. Here it can be observed directly how an increase of the bending action of the force Q reduces the shear angle.

Let us consider now what would happen to the situation illustrated in Fig. 9(B) when the cutting speed would be further increased. The built-up edge will reduce in size and that would cause the chip-tool contact to become heavier increasing force Q. Simultaneously the point of application of force Q would move toward the cutting edge thus decreasing the distance z between the vector Q and the mid-point of the shear plane. These two effects of decrease of the built-up edge with increasing cutting speed are illustrated qualitatively in Fig. 11. The product of these two quantities Q and z, i.e., the bending moment, $M = Qz$, would have a maximum as shown by the curve M in the same figure. It can be seen in the experimental plot Fig. 10 that the minimum value of cutting ratio (that means of the shear angle) corresponds to the maximum value of the bending moment M in Fig. 11.

On the Shear Angle Relationship

Initially it would be well to look at the shear angle relationship derived on the basis of assumption that the position of the shear plane will be defined by the requirements of maximum shear stress. Two solutions of this type will be considered here, the Lee and Shaffer [13] solution, Equation (8), and Merchant's first [2] solution, Equation (9):

$$\phi = 45° - (\tau - \alpha) \tag{8}$$

$$\phi = 45° - \frac{1}{2}(\tau - \alpha) \tag{9}$$

Upon recognition of the ploughing in metal cutting as a separate process, both shear angle relationships can be derived again very similarly to the way in which their authors had derived them originally. The only difference would be that instead of the force

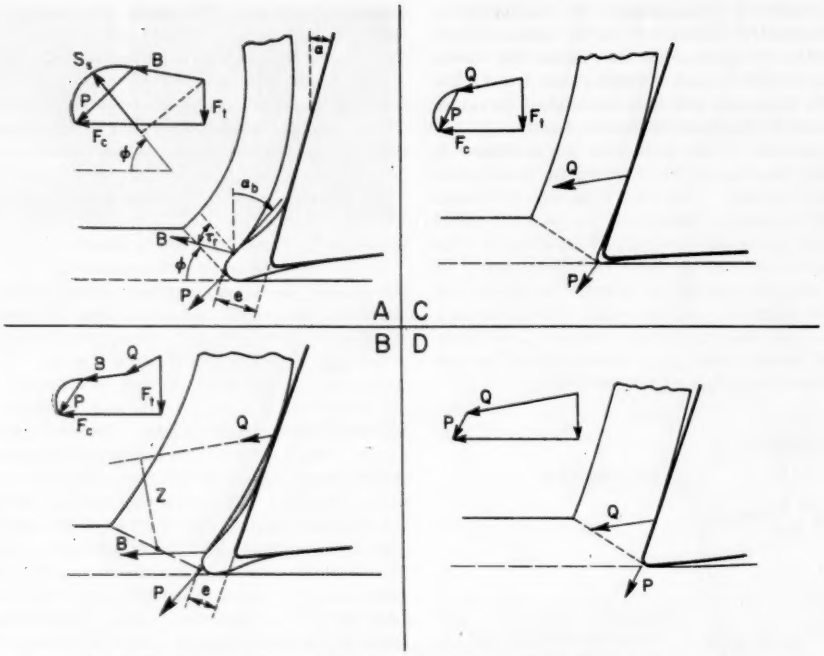

Fig. 9 Experimental study of the effect of bending moment upon the shear angle

(A) Extreme case when the chip does not contact the tool face, force Q is zero. Chip formation is due to the maximum shear stress from load B on the built-up edge and shear angle is consequently high. The bending effect of force Q is negligible. Such a situation might arise at low cutting speeds and with a work material giving a large built-up edge.

(B) With increased cutting speed elevation e reduces the chip starts to contact the tool face and force Q exerting bending stresses in the shear zone decreases the shear angle. Rake angle of the built-up edge α_b decreases.

(C) Further increase of the cutting speed causes the force Q to increase, decreasing simultaneously the distance of its point of application from the cutting edge. Built-up edge is very much reduced and force B loses its significance.

(D) At high cutting speeds bending effect of the force Q is reduced because its point of application has moved toward the cutting edge reducing the distance z. Shear angle is further increased because of the reduced bending effect.

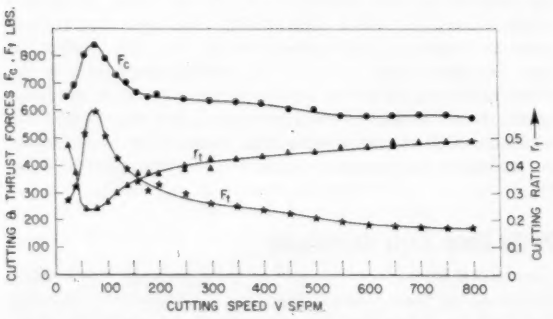

Fig. 10 Experimental result showing the variation of cutting ratio and similarity of shear angle with increasing cutting speed. Mechanism causing the variations illustrated by Figs. 9 and 11.

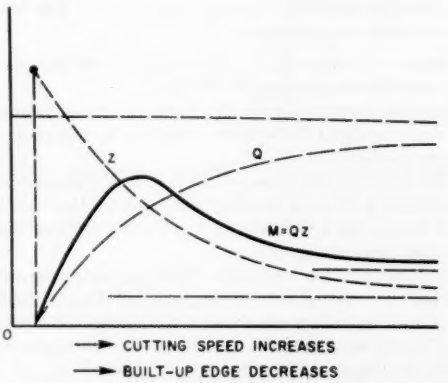

Fig. 11 Minimum cutting ratio and shear angle in Fig. 10 occurs at the cutting speed where the bending effect of force Q is a maximum. This maximum occurs because of decreasing character of the distance z and increasing of the force Q with increasing cutting speed.

R on the tool face there would be the force Q, the friction angle τ_Q of which does not depend on α or ϕ. Thus because of consideration of ploughing as a separate process in metal cutting the relationships (8) and (9) would not change their form except for the friction angle τ which becomes τ_Q:

$$\phi = 45° - (\tau_Q - \alpha) \tag{10}$$

$$\phi = 45° - 1/2\,(\tau_Q - \alpha) \tag{11}$$

Here the Merchant's variable $\tau_Q - \alpha$ may be used again for the plotting of the graphs of equations and of experimental points. This variable may be denoted by γ for the sake of brevity:

$$\tau_Q - \alpha = \gamma \tag{12}$$

Upon introduction of notation (12) the shear angle relationships (10) and (11) will take the form:

$$\phi = 45° - \gamma \tag{13}$$

$$\phi = 45° - \frac{1}{2}\gamma \tag{14}$$

It should be noted here that the angle γ determines the inclination of the force Q acting on tool face in relation to the surface of the workpiece.

The relation (13) (Lee and Shaffer) says simply that the shear plane is inclined to the direction of the resultant force on tool face at an angle of 45 degrees, Fig. 12(A). This would correspond to the situation when a specimen, shown in the upper part of Fig. 12(A), would yield at an angle of 45 degrees to the direction of the load Q which acts parallel to the boundary surface of the specimen. However, comparing the foregoing situation of an actually compressed specimen with the configuration encountered in a cutting process it can be noted that the direction of compressive load (force Q on the tool face) does not generally coincide with the direction of the surface of the specimen (that is with the direction of the work surface). In such a case when the direction of load is not parallel to the boundary of the specimen, as shown in the upper part of Fig. 12(B), the plane of maximum average shear stress would not be at an angle of 45 deg with the direction of the load. The angle which it would assume, denoted by ψ, can be found by expressing the average shear stress generally as a function of the angle ψ and then equating the first derivative of this function (regarding ψ) to zero. The angle ψ can be obtained for this more general case:

$$\psi = 45° + \frac{1}{2}\gamma \tag{15}$$

Thus the angle of inclination of the plane of maximum average shear stress with respect to the direction of load becomes greater than 45 deg because of the difference between the direction of the load and the direction of the boundary of the specimen. Denoting the angle between the plane of maximum shear stress and direction of the boundary of the specimen by ϕ and noting that $\psi = \gamma + \phi$ we obtain expression for ϕ from the Eq. (15):

$$\phi = 45° - \frac{1}{2}\gamma$$

This expression is, of course, the Merchant's first solution, Eq. (14). Now it can be seen that the Lee and Shaffer solution, Eq. (13), merely says that the plane of the maximum shear stress is at 45 deg to the direction of the load at the tool face regardless of the orientation of machined surface to this load. Merchant's first solution, as it is here demonstrated, accounts for the difference in direction of the machined surface and the force acting on tool face, thus determining more accurately the position of the plane of maximum shear stress for the conditions encountered generally in a metal-cutting process. For this reason Merchant's first solution will be used in this work for determining the direction of the plane of maximum shear stress.

As is well known, from experience in destructive testing of materials, the direction of maximum shear stress determines the way the metal starts to yield with a good degree of approximation. Why is it then that in metal cutting the direction of the shear plane diverges from the direction of maximum shear stress as it is known from other experience. The answer to that question would be the fact that the metal in a cutting process is stressed in a more complicated way than the metal of a specimen in destructive testing. As was shown here by a representative case, the force on tool face can cause bending stresses which may be several times higher than the shearing stress caused by the same force. Thus when determining the position of the shear plane it seems to be necessary to take into account both shearing and bending stresses on the shear plane. As may be seen in Fig. 2 the maximum compressive stress due to bending occurs at the small region on the work surface designated by A. It can be also seen,

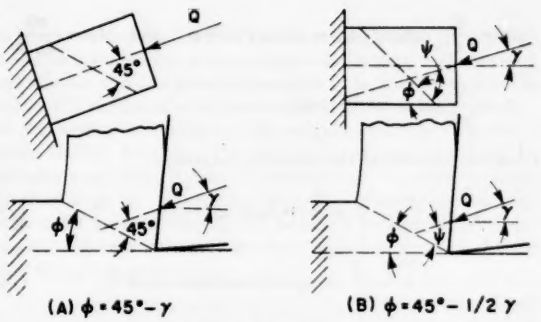

Fig. 12 Sketches A and B illustrate the reason for the difference in Lee and Shaffer's solution and Merchant's first solution which are both based on the assumption of yielding in the direction of maximum shear stress. The reason for difference lies in the fact that Merchant's first solution takes into account the difference in direction of the tool face force and machined surface while Lee and Shaffer's solution does not.

from the same figure, that the location of the region A on the work surface would determine the magnitude of the shear angle. Because the small region A, Fig. 2, at the work surface is brought to the plastic state by the two different stresses, one shearing stress and another compressive stress from the bending moment, the "intensity of stress" should be considered at the region A in order to obtain the combined effect of both stresses. Locating then, the position of the region A for maximum intensity of stress the shear angle would be determined and a shear angle relationship based on the combined effect of both considered stresses would be obtained.

Generally, if the state of stress in a material is described by the stress tensor:

$$S_{ij} = \begin{bmatrix} s_{11} & s_{12} & s_{13} \\ s_{21} & s_{22} & s_{23} \\ s_{31} & s_{32} & s_{33} \end{bmatrix},$$

the intensity of stress s based on the von Mises yield criterion would be given by the expression:

$$2s^2 = (s_{11} - s_{22})^2 + (s_{22} - s_{33})^2 + (s_{33} - s_{11})^2 + 6(s_{23}^2 + s_{31}^2 + s_{12}^2)$$

Considering the state of plane stress with two stresses one compressive σ due to the bending effect of force Q (in the region A of the shear plane) and another stress τ due to the shearing component of the force Q, the following simplified state of stress will result:

$$S_{ij} = \begin{bmatrix} \sigma & \tau & 0 \\ \tau & 0 & 0 \\ 0 & 0 & 0 \end{bmatrix}$$

and the expression for intensity of stress reduces to:

$$s^2 = \sigma^2 + 3\tau^2 \tag{16}$$

Determining now the σ and τ from the configuration of the cutting mechanism given in Fig. 3 the following expressions may be obtained:

For the bending stress σ:

$$\sigma = \frac{M}{D} \quad \text{where} \quad M = Qz \quad \text{and} \quad D = \frac{wt_1^2}{6 \sin^2 \phi}$$

$$\sigma = 6 \frac{Q}{wt_1} \frac{z}{t_1} \sin^2 \phi$$

and the shear stress τ:

$$\tau = \frac{Q_s}{A_s} \quad \text{where} \quad Q_s = Q \cos(\gamma + \phi) \quad \text{and} \quad A_s = \frac{wt_1}{\sin \phi}$$

$$\tau = \frac{Q}{wt_1} \sin \phi \cos(\gamma + \phi)$$

Upon introduction of the following notations:

$$\zeta = \frac{z}{t_1} = \text{bending ratio} \tag{17}$$

$$q = \frac{Q}{wt_1} = \text{specific tool face force} \tag{18}$$

$$\psi = \gamma + \phi = \text{angle between the force } Q \text{ and shear plane} \tag{19}$$

the expressions for σ and τ take the form:

$$\sigma = 6q\zeta \sin^2 \phi \tag{20}$$

$$\tau = q \sin \phi \cos \psi \tag{21}$$

Inserting expressions (20) and (21) into the expression for the intensity of stress (16), the intensity of stress s as a function of q, ζ, γ, and ϕ is obtained:

$$s^2 = 3q^2(12\zeta^2 \sin^4 \phi + \sin^2 \phi \cos^2 \psi) \tag{22}$$

or

$$s = s(q, \zeta, \gamma, \phi) \tag{23}$$

From the function expression (22) it can be seen that the intensity of stress s in the region A depends on the magnitude of the load which is expressed by the variables q and ζ and on the way in which the load is applied, given by the angle γ, and finally on the location of the region A on the work surface given by the angle ϕ. The region on the work surface where the intensity of stress s will be the greatest starts to yield first. In order to find at which point this would occur for a given load the partial derivative of the intensity of stress s with respect to the variable ϕ, which locates the point A on work surface, should be set to zero. This condition gives the equation determining ϕ (the shear angle relationship) which would locate the region of maximum stress intensity near the work surface. Let us carry out the indicated procedure for the case where there will be no bending action in the cutting process, i.e., where ζ will be zero in expression (22), and it reduces to:

$$s = \sqrt{3} q \sin \phi \cos \psi \tag{24}$$

Intensity of stress s in expression (24) depends on q, γ, and ϕ but it can be represented by a surface in three dimensions as shown in Fig. 13 because for the variables γ and ϕ only one axis is required. Expression (24) can be written in the form:

$$s = \frac{\sqrt{3}}{2} q[\sin(\gamma + 2\phi) - \sin \gamma] \tag{25}$$

Expression (25) as well as Fig. 13 shows that the intensity of stress s is proportional to the specific force q, but with increasing ϕ the intensity of stress would first increase and then decrease because of the sinusoidal function in expression (25). This shows that the function expression (25) would have a maximum with relation to ϕ. The location of this maximum can be found by equating the partial derivative of intensity of stress with respect to ϕ to zero:

$$\frac{\partial s}{\partial \phi} = \frac{\sqrt{3}}{2} q \frac{\partial}{\partial \phi} [\sin(\gamma + 2\phi) - \sin \gamma] = 0$$

This leads to the equation:

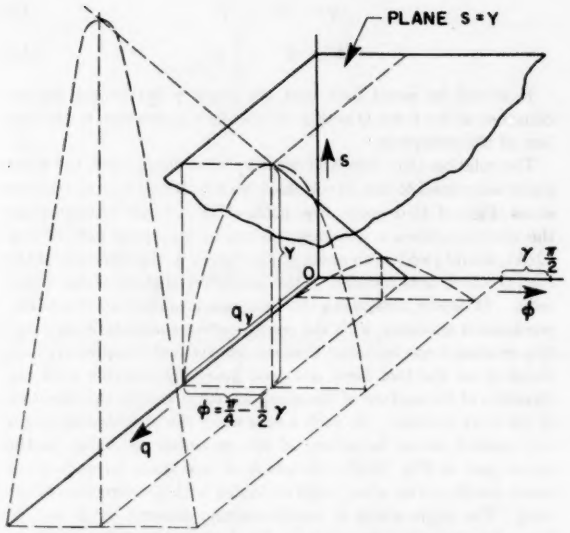

Fig. 13 Representation of intensity of stress s expression (25) by means of a surface in three dimensions. The shear angle relationship is given by the position of the partial maximum of such a surface.

$$\cos(\gamma + 2\phi) = 0$$

and to the Merchant's first solution:

$$\phi = \frac{\pi}{4} - \frac{1}{2}\gamma,$$

as could be expected, because if ζ is set to zero only shearing stresses would remain in expression (22).

Now we may return to expression (22) where the intensity of stress depends on bending stress as well as on shearing stress.

After writing expression (22) in the form:

$$s^2 = 3q^2(12\zeta^2 \sin^4 \phi + \frac{1}{4}[\sin(\gamma + 2\phi) - \sin \gamma]^2) \tag{26}$$

It can be seen here that the surface expressed by function s (25) shown in Fig. 13 is geometrically added to another surface σ (20) which depends on the bending ratio ζ. The bending ratio ζ is a function of the angle ϕ. This function, as yet undefined, should have decreasing character with increasing ϕ, as can be easily seen from physical consideration. For very low values of ϕ and a thick chip the point of application of the force Q moves out far from the cutting edge and ζ is likely to take high values. As the angle ϕ increases ζ would decrease as the chip thickness reduces. Thus the surface σ would be similar in character to the surface of Fig. 13, because both surfaces are given by the product of two functions of ϕ, one of decreasing and another of increasing character. Thus the surface which would result from geometric addition of both considered surfaces would again have a character similar to the surface of Fig. 13 but with the position of partial maximum displaced in a way which would depend on the form of the function $\zeta = \zeta(\phi)$. The location of the partial maximum in Fig. 13 determines the shear angle relationship for maximum shearing stress, and the displaced partial maximum of the combined surface (26) would determine the shear angle relationship based on shear and bending stresses in the shear plane. Thus it can be seen that the development of such a shear angle relationship would depend on the definition of function $\zeta = \zeta(\phi)$. The bending ratio ζ depends also on the cutting speed v, as is qualitatively indicated in Fig. 11, by decreasing curve z with increasing cutting speed. Furthermore ζ also depends on the uncut chip thickness t_1,

therefore $\zeta = \zeta(\phi, v, t_1)$. Through this function the cutting conditions v and t_1 would define the position of the partial maximum of function (26) thus entering into the shear angle relationship:

$$\phi = \phi(\gamma, v, t_1) \tag{27}$$

Let us now look at the shear angle relationship determined experimentally and shown in Fig. 14. Here in the customary plot ϕ versus γ a family of experimentally determined well-defined curves is presented. This family of experimental curves replaces the flock of points which it has been customary to present when studying the shear angle relationship. The results plotted in Fig. 14 show that the experimental shear angle relationship has a shape of a well-defined curve thus indicating that a uniqueness of solution exists regarding the shear angle in metal cutting. As can be seen in Fig. 14 the position of the experimental shear angle relationship depends on the uncut chip thickness t_1, so that the dependence of ϕ on t_1 indicated in relation (27) is already experimentally verified. Experimental verification of the dependence of shear angle ϕ on the cutting speed v is given in the plot r_t versus v of Fig. 10. Correspondingly the effect of cutting speed upon the family of curves in Fig. 14 would be such that for a higher speed than that of Fig. 14 all curves would shift up in the diagram toward the straight line representing the Merchant's first solution. When reducing the cutting speed the family of curves in Fig. 14 would assume a lower position on the diagram.

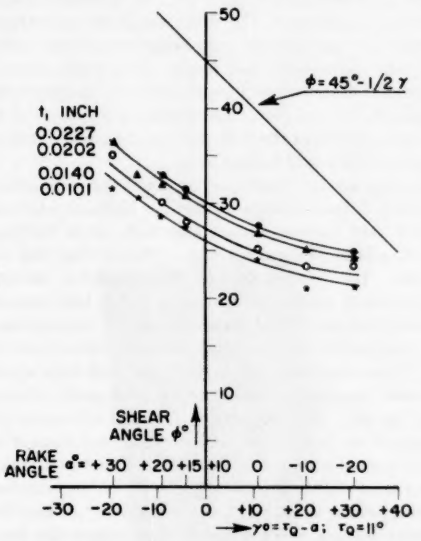

Fig. 14 Experimental shear angle relationship in form of curves. Position of a curve can be seen to depend on the uncut chip thickness t_1. Position of the family of curves is dependent upon the cutting speed. Straight line curve of Merchant's first solution, for the case when the bending effect would be zero, is shown on the diagram.

Reduction of the cutting speed would lower the position of the curves in Fig. 14 until the cutting speed corresponding to the lowest value of cutting ratio (indicative of shear angle) in Fig. 10 is reached. Reduction of the cutting speed beyond this value would shift the curves in Fig. 14 upward again. This situation can be illustrated by a family of surfaces in the three-dimensional space. Plotting the angle ϕ on the vertical axes versus γ and v on two horizontal co-ordinate axes for the different fixed values of t_1 a three-dimensional representation of the shear angle relationship $\phi = \phi[\gamma(\alpha, \tau_Q), v, t_1]$ can be obtained. The diagrams such as shown in Fig. 14 for different fixed cutting speeds would represent the cross sections of the above surfaces representing the shear angle relationship in three dimensions. Finally, considering the variables which would affect the shear angle and thus which should be included into a shear angle relationship, it can be seen that another variable is needed in order to be able to express the ability of a particular workpiece material to form a built-up edge. On this ability would depend the magnitude of the elevation e shown in Figs. 8 and 9. The elevation e affects in its turn the distances x and z and the bending moment $M = Qz$ which affects the shear angle ϕ. Expressing the ability of workpiece material to form the built-up edge by the variable ϵ (related to the elevation e) it can be written that the shear angle ϕ depends on 5 variables α, τ_Q, v, t_1, and ϵ:

$$\phi = \phi[\gamma(\alpha, \tau_Q), v, t_1, \epsilon] \tag{28}$$

This means that for each work material with a different ability to form the built-up edge a different three-dimensional shear angle relationship (as described above) would be necessary.

If now the results of experimental measurement of ϕ, which will depend on all independent variables in expression (28), will be plotted in a diagram with only two independent variables, a flock of points will be obtained as was usually the case in an experimental plot of ϕ versus γ. Such flocks of experimental points may even cause the impression that the uniqueness of solution for the position of the shear plane does not exist. It may even lead to the idea that there could be a region of possible solution for the shear angle which would depend on the initial conditions. But the well-defined experimental curves of Fig. 14 indicate that there is uniqueness of solution for a cutting process, and that only the number of variables entering into such a solution would be much greater than the two which were usually taken into account when developing a shear angle relationship.

Control of the Chip-Tool Contact Area

Consider first the effect of artificial restriction of chip-tool contact area upon the chip formation mechanism. It can be easily seen that restriction of the chip-tool contact moves the point of application of the force Q toward the cutting edge thus reducing the bending effect of this force at the shear plane which, in turn, leads to an increased shear angle. In fact the increase of shear angle has been observed in experiments conducted with a restricted chip-tool contact. This situation is illustrated in Fig. 15(A), here the force Q reduces because of the reduced shear plane area. Thus it can be seen in which simple way the effect of restricted chip-tool contact area upon the tool forces can be explained as soon as the effect of the bending moment of force Q upon the shear angle is considered.

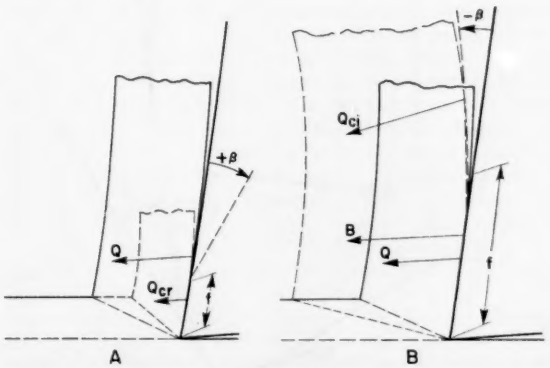

Fig. 15 Making use of the positive or negative tool face clearance β a restricted or extended chip tool contact may be obtained as it is shown under A or B, respectively. In the case of reduced chip tool contact the bending effect is reduced and shear angle increased. The opposite is true for an increased chip-tool contact.

Consider further the controlling of the chip-tool contact area in a more general way. We know already that the chip-tool contact area can be restricted to some extent by making use of the tool face clearance angle β, Fig. 15(A). Let us inquire now about the other side of the range of controlled chip-tool contact area, that is, about the artificially extended chip-tool contact area. How can the artificial extension of the chip-tool contact area be achieved? From Fig. 15(B) it can be seen that artificial extension of the chip-tool contact can be achieved by making use of the negative tool face clearance. If the angle β would be given negative values in connection with a suitable tool face length f, an increased chip-tool contact will be obtained. The extension of the chip-tool contact will increase the bending moment action and thus decrease the shear angle and, in turn, increase the tool forces. This situation is illustrated in Fig. 15(B) where it can be seen that we would have two tool face forces, one on the old tool face portion f and one on the new tool face created by the surface due to the negative clearance angle $-\beta$. The negative tool face angle $-\beta$ if sufficiently increased would lead to the well-known chip breaking action. It can be seen now that, generally, the controlled chip-tool contact area includes the artificially reduced as well as artificially increased regions. The artificial reduction or increase of the chip-tool contact reduces or increases the bending effects in the cutting mechanism and thus controls the shear angle and the tool forces.

Artificial Built-Up Edge

If the artificial extension of the chip-tool contact described in the last section and illustrated in the Fig. 15(B) would be compared with the situation which exists at the low cutting speeds, Fig. 9(B), a great likeness can be noticed. That means that the cutting mechanism with a natural built-up edge presents a very similar situation to that obtained by the artificially extended chip-tool contact. This leads to the possibility of designing a tool with an artificial built-up edge shown in Fig. 16. In this figure the small remaining portion of the original tool face can be considered as a face of an artificial built-up edge and the new surface obtained by the negative tool face clearance can be considered as a tool face of a tool with an artificial built-up edge. The force on the artificial built-up edge may be denoted by B_a and the corresponding rake angle by α_{ba} as shown in Fig. 16.

The natural sharpness radius of the artificial built-up edge can be increased if desired for experimentation in order to obtain more likeness with a natural built-up edge. Such tool design may be used for the study of the built-up edge effects because it has a "controlled built-up edge," size of which can be changed at will independently of the cutting conditions and of the ability of the work material to form a built-up edge. The experimentation with artificial built-up edge may have the purpose of controlling the chip-tool contact for improved tool wear and a better tool life as it is discussed in the next section.

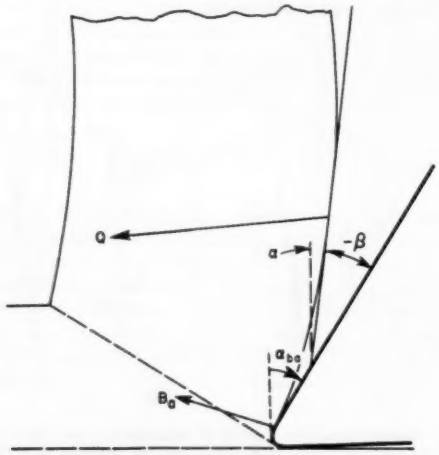

Fig. 16 Similarity of the situations shown in Figs. 9(B) and 15(B) leads to the design of a tool with the equivalent of an "artificial" built-up edge as shown in this figure

On the Design of the Cutting Tool for Maximum Tool Life

Insight gained into factors affecting chip formation can provide a possible means of controlling tool wear and thus serve as a basis for designing a tool for maximum tool life.

The nature of chip-tool contact is an important factor in chip formation and one of the most significant factors determining the progress of wear on the tool face. Through what has been learned here, there would appear to be a possibility to optimize tool cratering and thus increase tool life. It may be of advantage to either reduce or extend the area of natural chip-tool contact depending on the properties of the work material. Different work materials have different ability to form a built-up edge. Steel, for instance, generally forms a built-up edge and because of the resultant elevation e, Fig. 8, would provide a considerable length of chip tool contact with a considerable bending effect reducing the shear angle and imposing greater cutting forces. In this case a reduction of chip-tool contact area brought about by introducing a positive tool face clearance as in Fig. 15(A) reduces the bending effect (because distance z, Fig. 9(B), would be reduced) with the consequent increase in shear angle which would lead in turn to a thinner chip and reduced tool forces. It is known from experience that the described technique generally improves the wear conditions on the tool face. The resulting reduction of the load would be greater than the reduction of the contact area, so that load to area ratio would be improved.

Contrary to steel, for instance, titanium and some other metals exhibit very little tendency to form a built-up edge and thus promote a very narrow contact area with small bending effect; the result, a large shear angle with a thinner chip and moderate tool forces. The disadvantage of this situation is the extremely narrow chip-tool contact area, causing a high heat concentration of the small volume of tool material near the cutting edge. This can be aggravated by the poor thermal conductivity of such metals. Excessive temperature combined with high specific load on the small area causes rapid tool wear and early collapse of the cutting edge [6]. In such a case it is suggested that a technique be employed to extend the natural chip-tool contact area by means of negative tool face clearance as shown in Fig. 15(B) By doing so an additional bending effect would be introduced into the cutting process as the result of the negative tool face clearance. This added bending effect would tend to reduce the shear angle and increase the chip thickness thus extending the chip-tool contact area. This should be a desired effect because it would move the area of cratering to a position more remote from the dangerous vicinity of the cutting edge. Heat generation would be spread over a wider area providing better means for heat dissipation. This in turn should result in lower tool-chip interface temperatures and reduced rate of tool wear. In spite of the fact that tool forces would increase due to decreased shear angle the load to area ratio may improve because of the greater increase in contact area as compared to the increase in load, for a selected value of negative tool face clearance. In such a way the tool life might be increased for metals which because of the lack of built-up edge possess a very narrow chip-tool contact area. A tool with a negative tool face clearance, Fig. 15(B), may be looked upon as a tool with an artificial built-up edge, Fig. 16. It can be seen that some effects of the built-up edge may be used for controlling of chip-tool contact and improvement of the wear conditions on the tool face.

Summarizing it can be said that the improved tool wear conditions may be obtained through control of chip-tool contact. Such an optimum chip-tool contact can be greater or smaller than that naturally occurring for a particular material. Which way the correction of contact area should be made depends on the characteristic of the material with respect to built-up edge formation. Control in either sense can be achieved by means of the techniques given above.

Introduction to the Cyclic Chip Formation

Apart from the well-known types of tool wear there is another one less known which occurs in the form of small cracks along the wear land on the flank of the tool. As was observed by the author such cracks develop slowly and resemble fatigue cracks in their behavior. Observation also showed that there was a periodic force variation accompanying the development of these cracks. This periodic force variation was caused by the cyclic chip formation which also was observed and studied by the author. The study of the mechanism of cyclic chip formation was conducted with the aim of developing an appropriate means of its control reducing or eliminating the development of fatigue cracks and thus improving tool life. Some results of the author's study which is presently in progress will be presented here as a brief introduction to the mechanics of cyclic chip formation. Basically cyclic chip formation involves periodic variation of shear angle. The shear angle fluctuates between two values and due to that the chip thickness varies in cycles producing the shape of teeth on the back of the chip as shown in Fig. 17. The shape of the tooth indicates a relaxation type of event because it has two states at a certain instant, i.e., a discontinuity, which can be seen in Fig. 17 where the drop from the greatest to the lowest thickness of the chip occurs. Physically this would happen in a very short period of time during which the chip formation changes from the highest to the lowest value of shear angle. The metal does not escape appreciably along the tool face at this stage and compressive stresses which are bound to build up because of continuing motion of the tool would cause the barreling effect as can be seen on the front portion of the tooth in Fig. 17. Following the event further it can be seen that the tool face force finally builds up so much that it shears the metal along the lower position of the shear plane. Thus the "back" of the tooth starts to form by moving out of the workpiece in the direction of shear plane, Fig. 17. Simultaneously the direction of the shear plane changes as the shear angle increases and the back of the tooth becomes the envelope curve of the instantaneous positions of the shear plane during a cycle. The increasing shear angle finally reaches the upper limit where the chip formation again practically stops and the front of the consecutive tooth will be barreled by compression. Further the cycle repeats itself producing another tooth as described above.

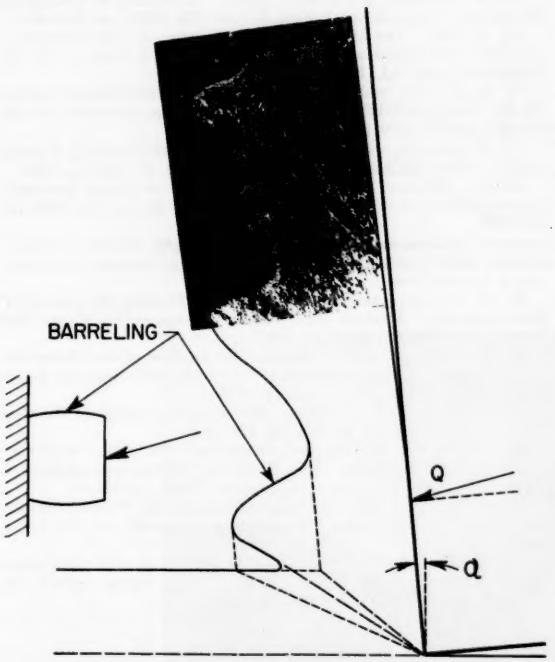

Fig. 17 Cyclic chip formation occurs due to the fluctuation of the shear angle between two values causing the chip thickness to vary during the cycle thus forming a "tooth" on the back of the chip

Development of the analytical model of cyclic chip formation showed that the peak to valley distance of a "tooth" should be proportional to the uncut chip thickness t_1. This was confirmed by experiments with a good degree of approximation. Further the prediction equation for the frequency of cyclic chip formation gave a linear dependence between frequency and cutting speed. The slope of the obtained straight line was found to be inversely proportional to t_1. It has been also found that for a certain combination of cutting speed and uncut chip thickness the cyclic chip formation does not occur. This defines two regions in the diagram of cutting conditions (t_1 versus v) separated by a boundary curve. The boundary curve was found to depend on the hardness of the workpiece and on the tool geometry. Summarizing briefly, it can be said that cyclic chip formation has been found to depend on the cutting conditions, and further on the tool geometry and on the hardness of work material. On the other hand, changing of the dynamic properties of the cutting system did not affect appreciably cyclic events in chip formation. In the further study of the cyclic chip formation the author intends the assessment of the causes of instability leading to the cyclic events as a final stage of this investigation.

Summary of Results

The present paper is a continuation of Part I, Bibliography [1], of the author's recent paper on the ploughing process in metal cutting. However, in some parts the present paper is a further development of Part I. It was realized that also the presented results are in turn capable of further development and ways for the further research have been indicated. The introduction of the concept of ploughing and study of the reconstruction in scale configuration of the cutting mechanism lead to the conclusion that the resultant force on the tool face cannot generally be assumed to be collinear with the resultant force on the shear plane. Consequently the tool face force would exert bending stresses over the shear plane. These bending stresses were found to exceed several times the average shear stress, from the calculation of a representative case. The significant level of bending stress at the shear plane indicated that bending load should have a substantial effect on the position of shear plane, i.e., on the magnitude of the shear angle. Results of an experiment in turning indicated that an increase of the bending moment reduces the shear angle and vice versa. In cases when the bending moment is negligibly small the chip formation is governed mainly by the maximum shear stress. Maximum shear gives higher values of the shear angle and presence of the bending stresses reduces the shear angle. Bending effect was found to be small at very low and at high cutting speeds, having a maximum at a certain moderate cutting speed as it can be seen in Figs. 10 and 11. These studies lead to the conclusion that a shear angle relationship should be based on the combined effect of shear and bending stresses. For this purpose both known solutions based on the direction of maximum shear, the

Merchant's first solution and the Lee and Shaffer's solution were examined. The difference of solutions, which were derived on the same basic assumption, was found to be due to the fact that Merchant's first solution accounts for the inclination of the force on tool face to the workpiece surface and the Lee and Shaffer's result does not. Because, generally, in metal cutting the tool face force is inclined to the work surface, the Merchant's first solution is in a better agreement with existing condition. For this reason Merchant's first solution was incorporated into the present combined shear-stress bending-stress approach. The set-up for the development of the analytical model of the chip formation has been presented. The ways in which the cutting speed and uncut chip thickness would enter into the shear angle relationship were indicated. An experimental shear angle relationship has been presented in the form of a family of well-defined curves instead of the flock of points usually presented on such occasions. This result, Fig. 14, proves experimentally that the uncut chip thickness should enter into the shear angle relationship. It can be also seen from the plot, Fig. 10, that there is experimental evidence for the cutting speed to be included in the shear angle relationship. Further the ability of work material to form a built-up edge is a factor affecting the shear angle. Generally it was concluded that there is uniqueness of solution for a cutting process, so that there is no region of permissible values of shear angle which would depend on the randomness of initial conditions. Well-defined shape of the curves, Fig. 14, supported by a good repeatability of such measurements provides experimental proof for this conclusion.

The study of the effect of chip-tool contact stresses upon the initial curvature of the chip lead to the conclusion that the chip does not straighten out under the action of contact stresses. The contact stresses were found to reduce the initial curvature of the chip only in a small portion of chip at the "end" of the chip-tool contact area. On all the remaining length of the chip up to the shear zone the curvature of the chip would increase due to chip-tool contact stresses.

As a counterpart to the well-known technique of restriction of the natural chip-tool contact area a technique for the extension of the chip-tool contact has been found. In this way a complete range of controlled chip-tool contact area was obtained with a reduced contact regarding the natural on one side and increased chip-tool contact on the other.

The application of techniques for controlling of chip-tool contact to the design of a tool for maximum tool life has been indicated. The possibility of increasing of the narrow chip-tool contact for the work materials which do not form a built-up edge, as titanium and others, has been shown. The ways of controlling crater wear by means of controlled chip tool contact for work materials of different properties were pointed out.

Acknowledgments

The author wishes to acknowledge here that the knowledge of metal cutting which emanated from these Laboratories contributed considerably to the research presented here. Especially the theory by Dr. M. E. Merchant, Director of Physical Research, presented in his paper "Mechanics of the Metal Cutting Process," as well as the work of many investigators included in the literature, inspired the author to further study of the subject on the basis of the progress previously achieved.

The author is also very much indebted to Mr. E. J. Krabacher, Senior Research Supervisor, who contributed greatly in the preparation of this paper.

Appreciation should be expressed to the Laboratories' technical personnel whose skill was essential in performing the experimental work.

Bibliography

1 P. Albrecht, "New Developments of the Theory of the Metal-Cutting Process, Part I, The Ploughing Process in Metal Cutting," TRANS. ASME, Series B, JOURNAL OF ENGINEERING FOR INDUSTRY, vol. 82, 1960, pp. 348–358.

2 M. E. Merchant, "Mechanics of the Metal Cutting Process," *Journal of Applied Physics*, vol. 16, 1945, pp. 267–275.

3 Hans Ernst, "Physics of Metal Cutting," Machining of Metals, American Society for Metals, 1938, pp. 1–34.

4 Hans Ernst and M. E. Merchant, "Chip Formation, Friction and Finish," *Trans. ASM*, vol. 29, 1941, pp. 299–378.

5 M. Field and M. E. Merchant, "Mechanics of Formation of the Discontinuous Chip in Metal Cutting," TRANS. ASME, vol. 75, 1949, pp. 421–430.

6 M. E. Merchant, E. J. Krabacher, H. W. Young, and J. H. Miller, "Titanium Is Unorthodox When Machined. . .," *American Machinist*, July 5, 1954, pp. 118–121.

7 M. C. Shaw, N. H. Cook, and I. Finnie, "The Shear-Angle Relationship in Metal Cutting," TRANS. ASME, vol. 75, 1953, pp. 273–288.

8 M. C. Shaw and P. A. Smith, "Methods of Applying Cutting Fluids," ASTE Research Fund, Research Report no. 3, March 20, 1956.

9 M. C. Shaw and W. Holken, "Über Selbsterregte Schwingungen bei der Spanender Bearbeitung," *Industrie-Anzeiger*, Nr. 63, Aug. 6, 1957, pp. 35–40.

10 B. T. Chao and K. J. Trigger, "Cutting Temperatures and Metal-Cutting Phenomena," TRANS. ASME, vol. 73, 1951, p. 777.

11 B. T. Chao and K. J. Trigger, "Temperature Distribution at the Tool-Chip Interface in Metal Cutting," TRANS. ASME, vol. 77, 1955, pp 1107–1121.

12 J. T. Lapsley, Jr., R. C. Grassi, and E. G. Thomsen, "Correlation of Plastic Deformation During Metal Cutting With Tensile Properties of the Work Material," TRANS. ASME, vol. 72, 1950, pp. 979–983.

13 E. H. Lee and B. W. Shaffer, "The Theory of Plasticity Applied to a Problem of Machining," *Journal of Applied Mechanics*, vol. 22, TRANS. ASME, vol. 73, 1951, pp. 405–413.

14 W. B. Palmer and P. L. B. Oxley, "Mechanics of Orthogonal Machining," *Proceedings, I.Mech.E.*, vol. 173, 1959, pp. 623–654.

15 R. Hill, "The Mechanics of Machining: A New Approach," *Journal of Mechanics and Physics of Solids*, vol. 8, 1954, pp. 47–53, Pergamon Press Ltd., London, England.

16 B. T. Chao and K. J. Trigger, "Controlled Contact Cutting Tools," TRANS. ASME, Series B, JOURNAL OF ENGINEERING FOR INDUSTRY, vol. 81, 1959, pp. 139–151.

17 H. Takeyama and E. Usui, "The Effect of Tool-Chip Contact Area in Metal Machining," TRANS. ASME, vol. 80, 1958, p. 1089.

18 M. Masuko, "Fundamental Research on Metal Cutting," *Trans. JSME*, vol. 19, 1953, pp. 32–39, and vol. 22, no. 118, 1956, pp. 371–377.

19 K. Nakayama, "Studies on the Mechanism of Metal Cutting," *Bulletin of the Faculty of Engineering*, Yokohama National University, vol. 8, March, 1959.

20 K. Okushima and K. Hitomi, "On the Cutting Mechanism for Soft Materials," *Memoirs of the Faculty of Engineering*, Kyoto University, vol. XIX, no. II, April, 1957.

21 K. Okushima and K. Hitomi, "An Analysis of the Mechanism of Orthogonal Cutting," *Memoirs of the Faculty of Engineering*, Kyoto University, vol. XX, no. 2, January, 1958.

22 G. Rohlke, "Zur Mechanik des Zerspanvorganges," *Werkstatt und Betrieb*, vol. 91, no. 8, 1958, pp. 473–483.

23 G. Weber, "Beitrag zur Analyse des Standzeitverhaltens," Fortsehritliche Fertigung und Moderne Werkzengmaschinen, 7. Aachener Werkzengmachinen-Kolloquium, 1954, pp. 80–90.

24 H. Philipp, "Über die Spanbildung und die Werkstuckoberflache beim Walzenfrasen," *Werkstatt und Betrieb*, vol. 92, no. 7, 1959.

25 E. K. Henriksen, "Stress Distribution in the Continuous Chip—A Solution of the Paradox of Chip Curl," TRANS. ASME, vol. 73, 1951, pp. 461–464 with Discussion.

DISCUSSION

W. B. Rice[2]

The author is to be congratulated, in general, for a significant contribution to the literature of metal cutting; and, in particular, for the emphasis he places on the fundamental task of improving the idealized picture of the cutting process.

Recently reported experimental investigations carried out at Queen's University[3] contribute to the improvement of the idealized picture and to the author's thesis; thus they are being presented here.

Cyclic Chip Formation. Results obtained at Queen's support the author's contention that under many conditions chip formation is a cyclic phenomenon. This is illustrated in Fig. 18 of the discussion. A plausible explanation is:

(1) The material is compressed ahead of the tool, bulging upward, as shown at the left of the figure, until rupture occurs.

(2) Rupture occurs when the slip-line field has the appropriate configuration. That is, it occurs when (*a*) the direction of the maximum shearing *stress*, (*b*) the direction of the minimum area subjected to shearing stress, and (*c*) the direction of the minimum shearing *strength* are optimum. This statement will be recognized as a disguised version of the minimum energy principle. As the author has stated, metal in a cutting process is stressed in a more complicated way than the metal of a specimen in destructive testing.

(3) As the segment is being displaced along the rupture surface, the formation of the next segment begins.

(4) Subsequently, the newly formed segment, and the rest of the chip, consisting of previously formed segments, are forced

[2] Associate Professor in Mechanical Engineering, Queen's University, Kingston, Ontario, Canada.

[3] W. B. Rice, "The Formation of Continuous Chips in Metal Cutting," Engineering Institute of Canada, 1960. Annual General Meeting, Paper No. 22.

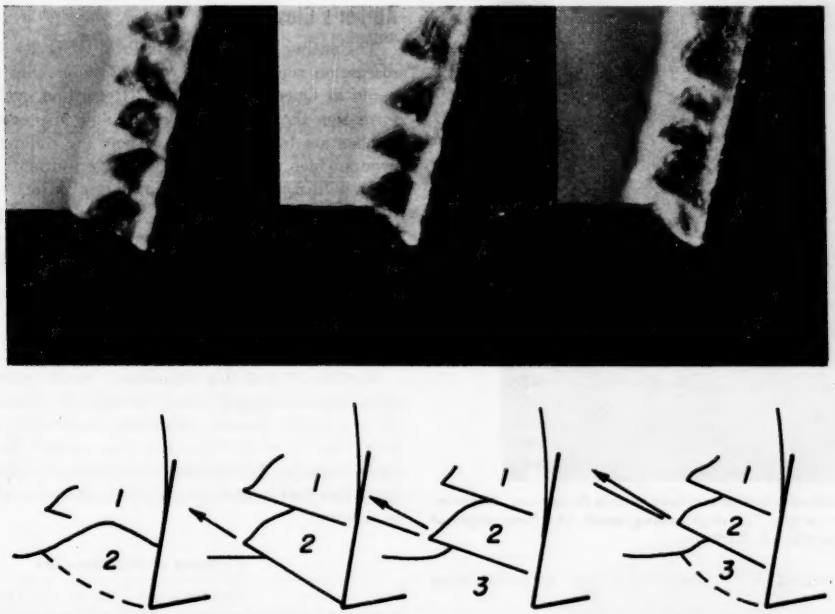

Fig. 18 Illustration of cyclic nature of continuous chip formation. Material, 26S aluminum; rake angle, 14½ deg; cutting speed, 228 fpm; feed, 0.018 in. per rev; chip width, 0.125 in.

Fig. 19 Cyclic and noncyclic chip formation

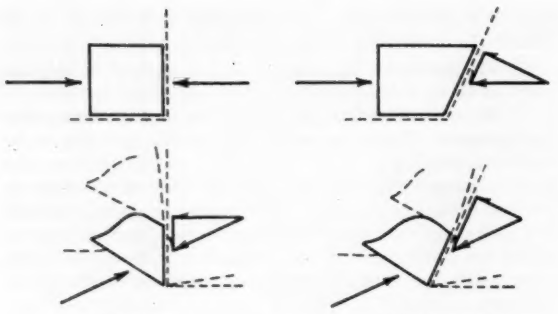

Fig. 20 Illustration of effect of rake angle upon frictional force

Fig. 21 Effect of artificially limited tool face on chip formation. Material, 265 aluminum; rake angle, $7^1/_2$ deg; cutting speed, 211 fpm; depth of cut, 0.017 in; tool-face length, 0.021 in.

upward by the bulging of the material of the segment being formed.

The author has pointed out that for a certain combination of cutting and speed and uncut chip thickness the cyclic chip formation does not occur. As shown in Fig. 19 of the discussion, an increase in the rake angle causes a departure from cyclic chip formation, which may be explained as follows. The upper part of Fig. 20 of the discussion illustrates the fact that the frictional force necessary to prevent a wedge from moving up an inclined surface increases as the incline decreases (that is, as α increases). At the same time the normal force between the wedge and the inclined surface decreases, and consequently the friction decreases, and eventually the wedge will slip. The lower part of Fig. 20 illustrates comparable conditions in chip formation. In the case of the small rake angle and limited movement up the tool face, the slip-line field, and hence the deformation, is radically different from that associated with the large rake angle and easy sliding. Thus the chips are quite different.

Chip Curl. The mechanism of chip formation just described provides an explanation of why, as the author states, the chip is "born curled." From Fig. 18 it is evident that the plastic deformation of the segment being formed rotates the previous segment counterclockwise, thus imparting curvature to the chip.

Chip-Tool Contact. The photograph of the plan view of the chip-tool contact area, Fig. 5(A) of the paper, indicates that maximum rubbing between the chip and the tool occurs at a considerable distance from the cutting edge. This is consistent with the experience at Queen's, and may be explained by the mechanism of chip formation illustrated in Fig. 18 of the discussion as follows:

(1) Just prior to rupture there appears to be no *sliding* of the segment being formed relative to the tool face. The friction in the region of the tool tip is *static*. However, the segment which has just been completed *does* slide along the tool face at a considerable distance from the cutting edge.

(2) At rupture sliding occurs generally.

Thus most of the sliding, and hence most of the wear, occurs at a considerable distance from the cutting edge.

When the tool face is limited to the depth of cut, or smaller, as shown in Fig. 21 of the discussion, the bulging of the segment being formed rotates the previous segment clockwise, and the chip is opposite to that encountered with the full-faced tool.

Author's Closure

The author wishes to thank Prof. W. B. Rice for an interesting discussion concerning the discontinuous chip formation studies made at Queen's University. Regarding cyclic events in chip formation there is more material now in preparation for further publication by the author. There are different types of cyclic events which may be observed in chip formation; one is usually termed "discontinuous chip formation" which is always cyclic in its nature because of the rupture which occurs periodically in the shear zone, yielding a segmented chip. Professor Rice illustrates and describes this type of chip formation in Fig. 18 of his discussion. Discontinuous chip formation was also studied and very well described by M. Field and M. E. Merchant in their paper "Mechanics of Formation of the Discontinuous Chip," Reference [5] of the bibliography in the paper.

Another type of chip formation, "continuous chip formation," when no periodic ruptures of the chip take place, may or may not be of a cyclic nature, depending on several conditions. This later type of chip formation was mainly the subject of the author's study. The whole classification of different types of chip formation may be conveniently summarized in the form of a table as follows:

Types of chip formation

	Continuous	Discontinuous
Steady state	*Continuous chip formation* No ruptures occur in the shear zone; the chip is essentially of a constant thickness. Type 2 and 3 chip according to Ernst and Merchant specification.	
Cyclic	*Cyclic chip formation* Continuous chip without periodic ruptures in the shear zone. Cyclic variations of the chip thickness occur due to fluctuations of shear angle.	*Discontinuous chip formation* Segmental chip caused by periodic ruptures in the shear zone. Type 1 chip according to Ernst and Merchant specification.

In the table the commonly used terms are in *italics* and a brief description of the particular types of chip formation is given.

The note of Professor Rice on chip curling concerns again the discontinuous chip of a segmental nature. The author's efforts were to describe the nature of curling of a continuous chip. One

of the reasons for curling of a continuous chip has been pointed out by the author, Reference [1] of the paper's bibliography. There, the ploughing effect was found to press additional metal into the chip surface, thus expanding one side of the chip and contributing to its curling. Another event which would contribute to chip curling has been indicated in the present paper. It has been shown that the normal stress along the shear zone from the cutting edge to the work surface (line AB in Fig. 2 of the paper) is not constant. Compressive stress normal to AB is higher in the vicinity of A than it is in the vicinity of B. This means that the metal which is in the plastic state in the shear zone will be more deformed under the compressive stress in the region of A and this will cause the chip to curl in the way it does. Another effect of the stress normal to the shear zone would be the widening of the chip which was usually neglected in the past because in most cases it is small. Actually if we consider only the shear component τ_s of the stress in the shear zone, as in the case in Merchant's first solution, the state of stress in the shear zone will be described by the tensor S_{ij};

$$S_{ij} = \begin{bmatrix} 0 & \tau_s & 0 \\ \tau_s & 0 & 0 \\ 0 & 0 & 0 \end{bmatrix} = \text{stress tensor of Merchant's first solution.}$$

The tensor of stress deviation S'_{ij} would in this case be the same as stress tensor S_{ij} because all normal stresses (in the main diagonal) are zero. Because $s_{11} = s_{22} = s_{33} = 0$ there will be no chip widening, $w_1 = w_2$, and no chip curling in this solution.

In view of the fact that in a metal cutting process all six components of the symmetric stress tensor S_{ij} are generally other than zero, the author's suggestion in this paper is to take into account at least one of the normal stress components in addition to the shear stress component considered before. In this case the stress tensor would have two components; one the shear stress τ and the second the stress σ normal to the shear zone.

$$S_{ij} = \begin{bmatrix} \sigma & \tau & 0 \\ \tau & 0 & 0 \\ 0 & 0 & 0 \end{bmatrix} = \text{stress tensor suggested by the author in the paper.}$$

The tensor of stress deviation S'_{ij} which indicates the nature of plastic deformation which would take place will have the form:

$$S'_{ij} = \begin{bmatrix} \frac{2\sigma}{3} & \tau & 0 \\ \tau & -\frac{\sigma}{3} & 0 \\ 0 & 0 & -\frac{\sigma}{3} \end{bmatrix}$$

The presence of the normal stresses indicates that widening of the chip would take place and the variation of $2\sigma/3$ along the shear plane, in the direction from the cutting edge to the work surface, would contribute to the curling of the chip. These two additional effects are included in the state of stress suggested by the author. The main effect of the introduction of σ, that is, its effect upon the shear angle, has been discussed in the paper.

Another variant of the state of stress in the shear zone in a metal cutting process was suggested by D. C. Drucker in his paper "An Analysis of the Mechanics of Metal Cutting" (*Journal of Applied Physics*, November, 1949). The state of stress suggested by Drucker is shearing plus hydrostatic pressure. The stress tensor corresponding to such a state of stress will be:

$$S_{ij} = \begin{bmatrix} \sigma_n & \tau & 0 \\ \tau & \sigma_n & 0 \\ 0 & 0 & \sigma_n \end{bmatrix} = \text{state of stress considered by Drucker.}$$

The tensor of stress deviation S'_{ij} in this case will be identical with the stress deviation of Merchant's first solution. That means that only plastic deformation due to shear will occur and no plastic deformation due to normal stresses will take place. Consequently the components σ_n would have no effect upon the shear angle, widening of the chip, or curling of the chip.

A general question about the number of stress components of the complete stress tensor:

$$S_{ij} = \begin{bmatrix} s_{11} & s_{12} & s_{13} \\ s_{21} & s_{22} & s_{23} \\ s_{31} & s_{32} & s_{33} \end{bmatrix}; \quad s_{12} = s_{21};\ s_{13} = s_{31};\ s_{23} = s_{32};$$

which should be considered to obtain good agreement between theory and observation depends on a number of conditions. For instance the properties of the metal cut would be one of the major factors. Just to give an example, let us compare the cross sections of chips obtained by machining two steels of different mechanical properties shown in Fig. 22 of this closure. Chip cross section (*a*) is of an extremely ductile steel; it shows a great variation in thickness after separation from the workpiece. In this case stress components s_{23} and s_{32} produce an appreciable plastic deformation in the chip and thus cannot be disregarded. Chip cross section (*b*) of the same Fig. 22 shows a chip of a different kind of steel; its thickness remains essentially constant across the width of the chip. This indicates that the same stress components s_{23} and s_{32} cause very little plastic deformation in this material and therefore can be safely neglected in describing the state of stress of this particular chip formation process.

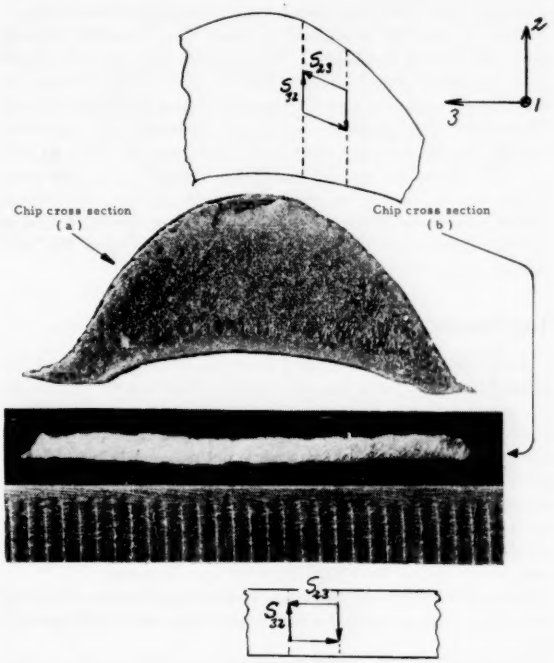

Fig. 22

H. TAKEYAMA
Research Engineer, Government Mechanical Laboratory, Tokyo, Japan

Performances of Carbide Tools in Machining 18-8 Stainless Steel

The austenitic 18-8 stainless steel is one of the most troublesome materials to be machined because of the tendencies of work-hardening, high temperature, and adhesion. The ultimate object of the experiment is to establish the machining standard of the austenitic stainless steel with carbide tools based upon tool life. Generally speaking, tool life in a modern machining practice should be specified not only by the flank wear, but by the crater. This paper describes the process of obtaining the optimum cutting conditions for turning the stainless steel from the viewpoint of tool life, and discusses how the tool life is governed by flank wear and crater depending upon the cutting conditions.

Introduction

THIS REPORT is only the introduction of the project to establish the machining standards for various important metals specified by the Japanese Standard. The major items of the test are selection of carbide grade, tool shape, speeds, and feeds for turning the 18-8 stainless steel, and close investigation of the tool life from the viewpoint of both flank wear and crater.

According to the test result, grade MB2 (triple carbide No. 2) and MC1 (universal use No. 1) are best for turning the 18-8 stainless steel. These notations of carbide grades are based upon a new classification system of carbide grades which has been introduced by the author so that machining data may be universal or interchangeable.

For rough turning of the 18-8 stainless steel, the side rake angle should be 0 to 5 deg, and for finishing it should be 10 to 15 deg.

Whether tool life is reached by flank wear or crater depends upon the cutting conditions. Namely, in a light cut at a higher speed the tool failure is reached usually by the crater, whereas in a heavy cut at a lower speed the tool is destined by the flank wear. Therefore it is necessary to obtain and investigate the composite tool-life curves for both flank wear and crater in order to find out the reasonable cutting conditions. Based upon the composite tool-life curves, the optimum speeds and feeds for turning the 18-8 stainless steel have been tabulated for various values of tool-life criteria for both flank wear and crater with the best carbide grade MB2.

Test Procedure

Each test item is conducted from the viewpoint of tool life specified by both flank wear and crater. The tool-life criteria for the judgment of tool failure are 0.024 in. in maximum width of wear land and 0.0020 in. in maximum depth of crater in most tests. The shape of the flank wear is not necessarily rectangular, but the wear is mostly excessive at the nose in turning the 18-8 stainless steel. The maximum wear land which is progressive to be fatal is measured with a tool-maker's microscope. As to the crater, the sectional profile is traced by the stylus linked with the magnifying optical lever (500 times) of a profilometer.

In the new classification system of carbide grades introduced by the author, sintered carbides are classified into two major groups,

Contributed by the Metal Processing Research Activity of the Production Engineering Division and presented at the Winter Annual Meeting, New York, N. Y., November 27–December 2, 1960, of THE AMERICAN SOCIETY OF MECHANICAL ENGINEERS. Manuscript received at ASME Headquarters, February 1, 1960. Paper No. 60—WA-1.

Table 1 Classification of sintered carbides

Straight tungsten carbide (P)

Machining tool (A)		Anti-abrasion tool (B)	Mining tool (C)
General notation	Grade	General notation	General notation
PAn	PAO3 PAO2 PAO1 PA1 PA2 PA3	PBn	PCn

Multicarbide (M)

Double carbide (A)		Triple carbide (B)		Universal use (C)		Automatic machine use (D)
General notation	Grade	General notation	Grade	General notation	Grade	General notation
MAn	MAO2 MAO1 MA1 MA2 MA3	MBn	MBO2 MBO1 MB1 MB2 MB3	MCn	MC1 MC2	MDn

i.e., straight or plain tungsten carbides (P) and multicarbides (M), each group being subdivided into several groups as shown in Table 1.

The detailed test conditions are as follows

Test lathe:	six feet lathe of Heinemann type
Tool size:	$^3/_4$ in. × $^3/_4$ in.
Carbide grade:	PAO1, PA1, MA1, MA2, MBO1, MB1, MB2, MB3, MC1, MC2
Tool shape:	0, var., 6, 6, 15, 15, 1/50
Depth of cut:	0.080 in.
Feed:	0.0067, 0.0100, 0.0134 ipr
Material cut:	18-8 stainless steel (corresponding to AISI 304); 0.06%C, 18.95%Cr, 9.02%Ni, 0.67% Si, 1.21%Mn, 0.033%P, 0.005%S; tensile strength 78,600 psi; 137 Bhn
Size of material:	6 in. diam × 25 in.

Test Results

Selection of Carbide Grade. The best carbide grade for turning the 18-8 stainless steel has been selected from typical commercial grades, PAO1, PA1, MA1, MA2, MBO1, MB1, MB2, MB3, MC1, and MC2, from the standpoint of both flank wear and crater tool life. The test is conducted for two different feeds,

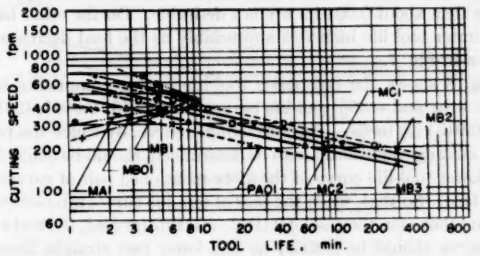

Fig. 1 Tool-life curves of flank wear for various grades of carbides. Material cut, 18-8 stainless steel; tool shape (0, 10, 6, 6, 15, 15, 1/50); depth of cut, 0.080 in.; feed, 0.0134 ipr; tool-life criterion, 0.024 in. width; cutting fluid, dry.

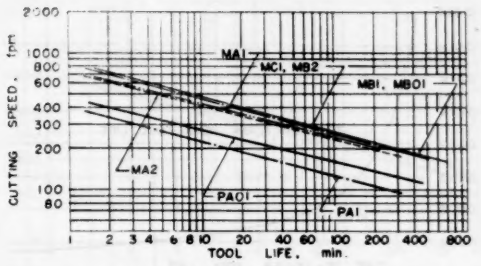

Fig. 2 Tool-life curves of crater for various grades of carbides. Cutting conditions same as in Fig. 1 except tool-life criterion, 0.0020 in. depth.

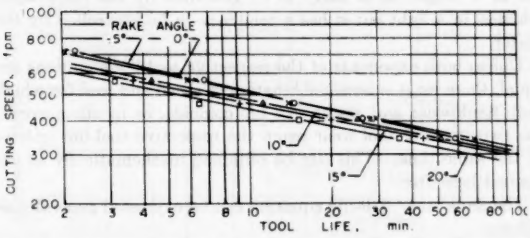

Fig. 3 Tool-life curves of flank wear for varying side rake angles. Cutting conditions same as in Fig. 1 except tool, triple carbide No. 2; tool shape (0, var., 6, 6, 15, 15, 1/50); feed, 0.0100 in.; tool-life criterion, 0.019 in. width.

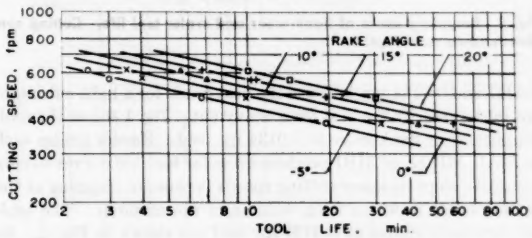

Fig. 4 Tool-life curves of crater for varying side rake angles. Cutting conditions same as in Fig. 3 except tool-life criterion, 0.0020 in. depth.

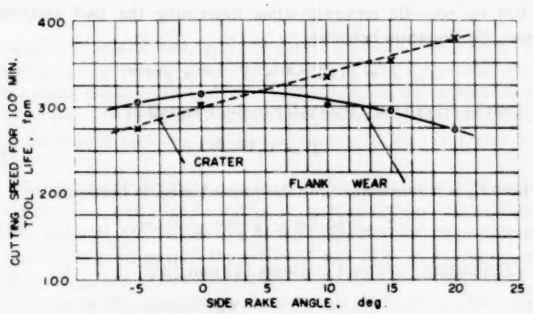

Fig. 5 Relationship between side rake angle and cutting speed for 100 minute tool life. Cutting conditions same as in Figs. 3, 4.

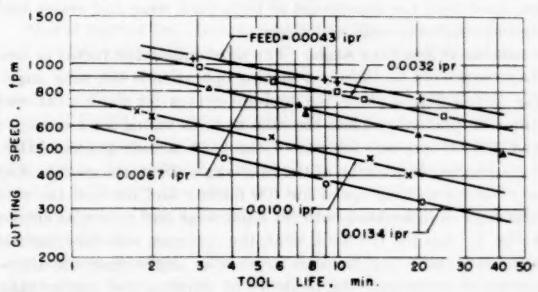

Fig. 6 Tool-life curves of flank wear for varying feeds. Cutting conditions same as in Fig. 1 except tool, triple carbide No. 2; feed, variable.

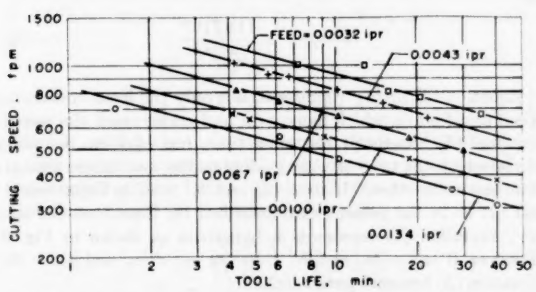

Fig. 7 Tool-life curves of crater for varying feeds. Cutting conditions same as in Fig. 2 except tool, triple carbide No. 2; feed, variable.

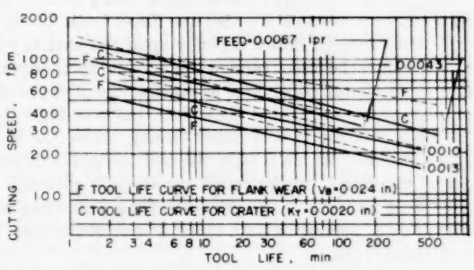

Fig. 8 Composite tool-life curves for various feeds. Cutting conditions same as in Figs. 6, 7.

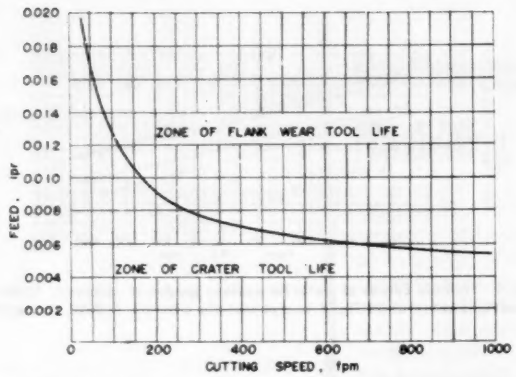

Fig. 9 Boundary curve of flank-wear and crater tool life. Cutting conditions same as in Figs. 6, 7.

0.0067 and 0.0134 ipr, because the best grade for a light cut might not be necessarily the best for a heavy cut. Fig. 1 shows the tool-life curves for flank wear at 0.0134 ipr feed. Harder grades such as MA1, MBO1, or MB1 produce irregular tool-life curves having a positive slope at lower cutting speeds because of chipping at the cutting edges resulting from welding of the material. The tool-life curves for crater at 0.0134 ipr feed are shown in Fig. 2. As seen in the data, straight tungsten carbides such as PAO1 and PA1 have been proved to be unapplicable for the material because of their excessive craterings. Thus MB2 and MC1 can be recommended as the most reliable grades for turning the stainless steel from the standpoint of both flank wear and crater tool life in a relatively wide feed range.

Selection of Side Rake Angle. The most important factor in tool shape to govern tool life in a turning operation is side rake angle. Fig. 3 and Fig. 4 show the tool-life curves for flank wear and crater, respectively, when the rake angle is varied for a constant feed, 0.0100 ipr, and for one of the best carbide grades, MB2. For a clearer observation of the rake-angle effect, the relationship between the cutting speed for 100 minute tool life and the side rake angle is illustrated both for flank wear and crater, as shown in Fig. 5. Against the flank wear, the optimum side rake angle is between 0 and 5 deg, because larger rake angles than the aforementioned value have the tendency of chipping and smaller rake angles result in a great heat generation or an excessive flank wear. As to cratering, the larger the rake angle, the longer the tool life, but it is recommended to be 10 to 15 deg taking the fear of chipping into consideration. Therefore, the best rake angle for the actual operations should be determined taking account of the cutting conditions, because whether the direct cause of the tool failure is flank wear or crater depends upon the cutting conditions. Namely, if the direct cause of the tool failure is crater, the side rake angle should be as large as possible the strength of the cutting edge allows and, if it is flank wear, the rake angle should be 0 to 5 deg. In the case of finish turning, where the cutting speed for a definite tool life is high, the tool failure is likely to be reached by the crater, but for rough turning it is governed generally by the flank wear. The critical cutting conditions where the tool failure is reached by both types of wear at the same time will be discussed later.

Feeds and Speeds. Generally speaking, tool life increases as the feed decreases. However, the flank-wear tool life in machining the 18-8 stainless steel decreases at the feeds smaller than approximately 0.004 ipr as seen in Fig. 6. The reasons for this seem to be size effect, relative dullness of the cutting edge in relation to the feed used, work-hardened layer of the material and lack of positive feeding inherent in smaller feeds which accelerates work-hardening. Therefore, as far as the tool life is concerned, smaller feeds than about 0.004 ipr are not desirable. On the other hand, the crater tool life increases appreciably as the feed decreases as shown in Fig. 7.

Fig. 8 shows the composite tool-life curves comprising both flank wear and crater tool-life curves for 0.0043, 0.0067, 0.0100, and 0.0134 ipr feeds. The real tool-life curve, by which the practical cutting conditions are to be determined, should be defined by the lower tool-life curve of the afore-mentioned pair of curves for each feed. So that, when the pair of tool-life curves intersect with one another as in the case of 0.0043 or 0.0067 ipr feed, the real tool-life curve should be defined by the lower two straight lines as shown by the solid lines in Fig. 8. As seen in Fig. 8, at larger feeds, where the cutting speed for a definite tool life is low, the flank wear tool-life curve is situated lower than the crater tool-life curve within 300 minute tool life at least. In other words, the tool life in a rough cut is likely to be governed by the flank wear, whereas in a light cut it has a tendency to be controlled by the crater.

Unless both exponents of the respective tool-life equations are equal, there must exist a combination of speed and feed for which both flank-wear and crater tool life coincide, or in other words, the two types of tool wear reach the respective tool-life criteria at the same time. This can be obtained mathematically as explained hereafter.

The flank wear tool-life equation can be expressed generally as follows

$$T = C_1 V^{a_1} f^{b_1} \tag{1}$$

where T is the tool life (min), V the cutting speed (fpm), f the feed (ipr), and C_1 a constant. For the carbide grade MB2 and 0.024 in. tool-life criterion when machining the 18-8 stainless steel, the equation becomes

$$T = (11.7)^{4.76} \times V^{-4.76} \times f^{-4.38} \tag{1}'$$

On the other hand, the crater tool-life equation is

$$T = C_2 V^{a_2} f^{b_2} \tag{2}$$

where C_2 is a constant. For the present case, it becomes

$$T = (89)^{3.86} \times V^{-3.86} \times f^{-1.92} \tag{2}'$$

Eliminating T from Equations (1) and (2),

$$V^{a_1 - a_2} f^{b_1 - b_2} = \frac{C_2}{C_1} \tag{3}$$

or

$$V^{0.90} f^{2.36} = \frac{(11.7)^{4.76}}{(89)^{3.86}} \tag{3}'$$

Equation (3) or (3)′ represents, not only the locus concerning speed and feed on which flank wear and crater reach the respective tool-life criteria at the same time, but also the boundary across which the type of wear leading to the tool failure changes from one to the other. If $|a_1| > |a_2|$ and $|b_1| > |b_2|$ in Equations (1) and (2) as in the present case described by Equations (1)′ and (2)′, Equation (3) represents a hyperbola as shown in Fig. 9. However, if $|a_1| > |a_2|$ and $|b_1| < |b_2|$, or $|a_1| < |a_2|$ and $|b_1| > |b_2|$, Equation (3) becomes parabolic.

Now let us explain the present case, where $|a_1| > |a_2|$ and $|b_1| > |b_2|$, or Equation (3) is hyperbolic. As seen in Fig. 8, the flank wear governs the tool life on the left-hand side of the intersecting point of both tool-life curves for a definite feed, or on the side of higher cutting speeds with regard to the intersecting point, because on this side the flank wear tool-life curve is always lower than the crater tool-life curve. That is to say, referring to Figs. 8 and 9, the side of higher cutting speeds at a definite feed, or the

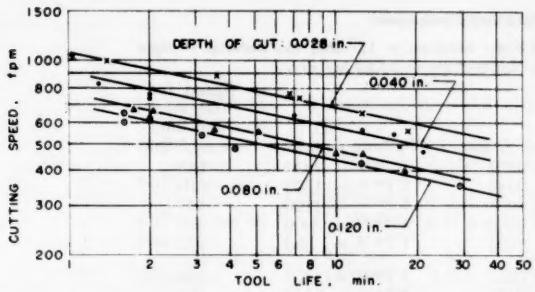

Fig. 10 Tool-life curves of flank wear for varying depths of cut. Cutting conditions same as in Fig. 6 except depth of cut, variable.

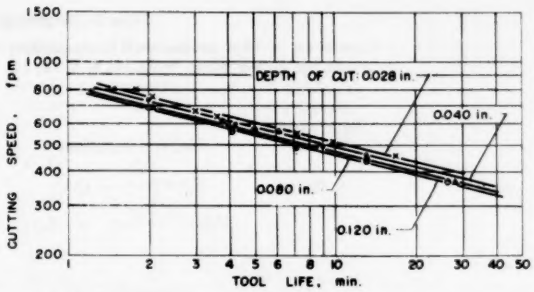

Fig. 11 Tool-life curves of crater for varying depths of cut. Cutting conditions same as in Fig. 7 except depth of cut, variable, tool life criterion, 0.0015 in.

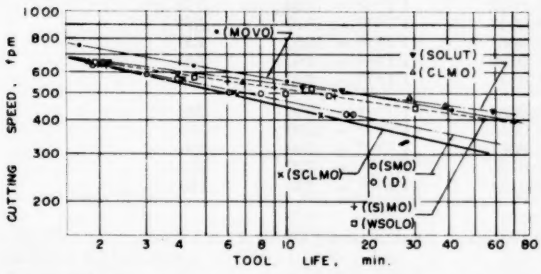

Fig. 12 Tool-life curves of flank wear for various cutting fluids. Cutting conditions same as in Fig. 1 except tool, triple carbide No. 2; feed, 0.0100 ipr.

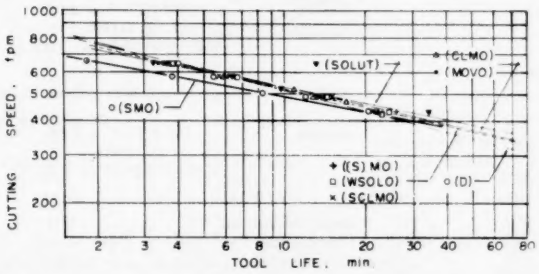

Fig. 13 Tool-life curves of crater for various cutting fluids. Cutting conditions same as in Fig. 2 except tool, triple carbide No. 2; feed, 0.0100 ipr.

right-hand side of the hyperbolic curve, the flank wear governs the tool life, whereas on the left-hand side of the hyperbolic curve the crater controls the tool life. In other words, the upper or right-hand side of the hyperbola in Fig. 9 corresponds to the domain of flank-wear tool life, and the other side to that of crater tool life.

It does solely depend upon the relative magnitude between the exponents a_1 and a_2 or b_1 and b_2, or practically upon material cut, tool material, etc., which side of the hyperbola corresponds to the type of wear to govern the ultimate tool life. If $|a_1| < |a_2|$ and $|b_1| < |b_2|$, the relative situations of the two domains should be opposite to the foregoing case, although the locus is still hyperbolic.

If the flank-wear tool life is conformed to the crater tool life for a definite tool-regrinding time, then the most efficient production will be expected. In this case, the relationships become as follows

$$V_g^{a_1} f_g^{b_1} C_1 = T_g \tag{4}$$

$$V_g^{a_2} f_g^{b_2} C_2 = T_g \tag{5}$$

where V_g and f_g are the cutting speed (fpm) and the feed (ipr) for the afore-mentioned special condition, respectively, and T_g the tool-regrinding time (min). V_g and f_g can be calculated from Equations (4) and (5) as follows

$$V_g = \left\{ \frac{\left(\frac{T_g}{C_1}\right)^{1/b_1}}{\left(\frac{T_g}{C_2}\right)^{1/b_2}} \right\}^{\frac{1}{\frac{a_1}{b_1} - \frac{a_2}{b_2}}} \tag{6}$$

$$f_g = \left\{ \frac{\left(\frac{T_g}{C_1}\right)^{1/a_1}}{\left(\frac{T_g}{C_2}\right)^{1/a_2}} \right\}^{\frac{1}{\frac{b_1}{a_1} - \frac{b_2}{a_2}}} \tag{7}$$

Effect of Depth of Cut. In many materials the effect of depth of cut on tool life, especially on crater tool life, is very slight when carbide tools are used. For example, according to the author's test, in the case of Ni-Cr-Mo alloy steel or high temperature alloy G18B (JESOP) the effect of depth of cut can be neglected practically in a relatively wide range of depth of cut. However, it is not true in the case of the 18-8 stainless steel as shown in Figs. 10 and 11, although the effect is naturally smaller compared with that of speed or feed as indicated by the general tool-life equations described later.

Machining Standard. The general tool-life equations for flank wear and crater can be obtained approximately as follows, respectively

$$V d^{0.31} f^{0.90} T^{0.21} = 5.3, \qquad f \geqq 0.004 \tag{8}$$

$$V d^{0.07} f^{0.80} T^{0.26} = 75 \tag{9}$$

where the tip material is triple carbide No. 2 (MB2), the tool shape 0, 10, 6, 6, 15, 15, 1/50, the tool-life criteria 0.024 in. and 0.002 in. for flank wear and crater, respectively, the cutting fluid dry, T the tool life (min), V the cutting speed (fpm), f the feed (ipr), and d the depth of cut (in.).

Since the tool failure of a carbide tool is usually defined by the time until the tool wear reaches a predetermined value or a tool-life criterion, the speed for definite tool life, feed, and depth of cut should vary depending upon the tool-life criterion. Therefore the machining standard for carbide tools becomes much more complicated than that for high-speed steel tools. Tables 2 and 3 are the machining standards of the 18-8 stainless steel for various tool-life criteria of both flank wear and crater, where the cutting speeds are specified for 100 minute tool life. In selecting the cutting speed for a definite feed and a predetermined tool-life criterion by using Tables 2 and 3, the lower cutting speed of the two for flank wear and crater should be adopted for the practical purpose.

As to the side rake angle again, if the type of wear corresponding to the afore-mentioned lower speed in Tables 2 and 3 is flank

Table 2 Machining standard data (flank wear)

Material cut = 18-8 stainless steel (corresponding to AISI 304); hardness = 137 Bhn; tool material = triple carbide No. 2; tool shape = (0, 10, 6, 6, 15, 15, 1/50); depth of cut = 0.080 in.; dry.

Tool-life criterion (flank wear), V_B, in.	General equation	Feed, f, ipr	Tool-life equation	Speed for 100 min tool life, ${}_FV_{100}{}^*$,[b] fpm
0.032	$Vf^{0.88}T^{0.19} = 13.0$	0.0032	$VT^{0.19} = 1330$	555
	$f \geqq 0.004$	0.0043	$VT^{0.19} = 1570$	650
	$(Vd^{0.31}f^{0.88}T^{0.19} = 5.9)$	0.0067	$VT^{0.19} = 1120$	445
		0.0100	$VT^{0.19} = 800$	330
		0.0134	$VT^{0.19} = 590$	225
0.028	$Vf^{0.90}T^{0.21} = 12.1$	0.0032	$VT^{0.21} = 1370$	520
	$f \geqq 0.004$	0.0043	$VT^{0.21} = 1540$	585
	$(Vd^{0.31}f^{0.90}T^{0.21} = 5.5)$	0.0067	$VT^{0.21} = 1110$	440
		0.0100	$VT^{0.21} = 790$	300
		0.0134	$VT^{0.21} = 580$	220
0.024	$Vf^{0.90}T^{0.21} = 11.7$	0.0032	$VT^{0.19} = 1220$	510
	$f \geqq 0.004$	0.0043	$VT^{0.20} = 1310$	550
	$(Vd^{0.31}f^{0.90}T^{0.21} = 5.3)$	0.0067	$VT^{0.20} = 1050$	420
		0.0100	$VT^{0.21} = 760$	290
		0.0134	$VT^{0.22} = 600$	215
0.019	$Vf^{0.88}T^{0.19} = 11.0$	0.0032	$VT^{0.19} = 1250$	500
	$f \geqq 0.004$	0.0043	$VT^{0.19} = 1270$	510
	$(Vd^{0.31}f^{0.88}T^{0.19} = 5.0)$	0.0067	$VT^{0.19} = 940$	390
		0.0100	$VT^{0.19} = 710$	255
		0.0134	$VT^{0.20} = 530$	210

[a] Depth of cut, in.

[b] Cutting speed for 0.080 in. depth of cut. The cutting speed for an arbitrary depth of cut ${}_FV_{100}$ is calculated by the equation ${}_FV_{100} = 0.455d^{-0.31}{}_FV_{100}{}^*$.

Table 3 Machining standard data (crater)

Cutting conditions same as in Table 2

Tool-life criterion (crater), K_T, in.	General equation	Feed, f, ipr	Tool-life equation	Speed for 100 min tool life, ${}_cV_{100}{}^*$,[b] fpm
0.0040	$Vf^{0.49}T^{0.25} = 117$	0.0032	$VT^{0.25} = 1900$	615
	$(Vd^{0.07}f^{0.49}T^{0.25} = 98)$	0.0043	$VT^{0.25} = 1670$	545
		0.0067	$VT^{0.26} = 1410$	445
		0.0100	$VT^{0.23} = 1080$	370
		0.0134	$VT^{0.24} = 895$	300
0.0032	$Vf^{0.50}T^{0.25} = 105$	0.0032	$VT^{0.25} = 1770$	590
	$(Vd^{0.07}f^{0.50}T^{0.25} = 88)$	0.0043	$VT^{0.25} = 1550$	510
		0.0067	$VT^{0.25} = 1320$	420
		0.0100	$VT^{0.24} = 1030$	380
		0.0134	$VT^{0.24} = 860$	289
0.0024	$Vf^{0.50}T^{0.25} = 98$	0.0032	$VT^{0.25} = 1670$	540
	$(Vd^{0.07}f^{0.50}T^{0.25} = 82)$	0.0043	$VT^{0.25} = 1510$	475
		0.0067	$VT^{0.26} = 1250$	385
		0.0100	$VT^{0.24} = 960$	320
		0.0134	$VT^{0.24} = 820$	270
0.0020	$Vf^{0.50}T^{0.26} = 89$	0.0032	$VT^{0.26} = 1660$	500
	$(Vd^{0.07}f^{0.50}T^{0.26} = 75)$	0.0043	$VT^{0.27} = 1510$	430
		0.0067	$VT^{0.25} = 1210$	360
		0.0100	$VT^{0.25} = 960$	300
		0.0134	$VT^{0.25} = 810$	250

[a] Depth of cut, in.

[b] Cutting speed for 0.080 in. depth of cut. The cutting speed for an arbitrary depth of cut ${}_cV_{100}$ is calculated by the equation ${}_cV_{100} = 0.838d^{-0.07}{}_cV_{100}{}^*$.

Table 4 Specifications of cutting fluids used

Cutting fluid	Notation	Specific weight, 68 F/43 F	Viscosity, R50	Coefficient of boundary friction	Four Ball pressure, psi	Remarks
Dry	(D)	...	...	...	...	...
Sulfurized oil (active)	([S]MO)	0.910	69.9	0.13	157	...
Sulfurized oil (inactive)	(SMO)	0.908	78.0	0.14	114	...
Chlorinated oil	(Cl MO)	0.938	71.0	0.13	285	...
Sulfo-chlorinated oil	(S Cl MO)	0.908	68.0	0.14	171	...
Mixed oil	(MOVO)	0.902	72.0	0.13	100	Mineral oil, rape oil, others
Soluble oil (1:20)	(W Sol O)	...	...	...	...	Amino-derivative, E. P. agent, organic salt, activation agent, others
Chemical solution (1:20)	(Solut)	...	...	...	...	Na NO_2, others

Table 5 Evaluating data of cutting fluids in turning 18-8 stainless steel

Cutting conditions same as in Fig. 12

Cutting fluid	Tool-life equation for flank wear (V_B = 0.024 in.)	Speed for 100 min tool life		Tool-life equation for crater (K_T = 0.0020 in.)	Speed for 100 min tool life	
		Fpm	Per cent		Fpm	Per cent
Dry	$VT^{0.19} = 725$	295	100	$VT^{0.26} = 920$	289	100
Sulfurized oil (active)	$VT^{0.15} = 722$	360	122	$VT^{0.21} = 860$	325	112
Sulfurized oil (inactive)	$VT^{0.19} = 715$	302	102	$VT^{0.18} = 722$	312	108
Chlorinated oil	$VT^{0.13} = 720$	394	133	$VT^{0.22} = 866$	321	111
Sulfo-chlorinated oil	$VT^{0.22} = 752$	256	87	$VT^{0.22} = 870$	321	111
Mixed oil	$VT^{0.18} = 788$	360	122	$VT^{0.22} = 880$	312	108
Soluble oil (1:20)	$VT^{0.15} = 709$	358	121	$VT^{0.23} = 886$	315	109
Chemical solution (1:20)	$VT^{0.13} = 712$	390	132	$VT^{0.20} = 856$	341	118

wear, the side rake angle should be 0 to 5 deg, but if it is crater, then the side rake angle should be 10 to 15 deg.

Effect of Cutting Fluids. Much information has been set forth hitherto about the effect of cutting fluid upon the tool lives of carbide tools at relatively high cutting speeds. Generally speaking, cutting fluids are much less effective for carbide tools than for high-speed steel tools which are more heat-sensitive and to be used at much lower cutting speeds. According to the test result, however, the cutting speed for 100 minute tool life can be increased about 33 per cent when machining the 18-8 stainless steel with a carbide tool.

In the present test the 18-8 stainless steel is machined with eight typical cutting fluids including dry cut as shown in Table 4. The neat cutting oils in Table 4 are prepared so that the physical properties except Four Ball pressure may be constant as far as possible and the inherent characteristic of each cutting oil resulted by the components can be clearly detected in the machining test. Figs. 12 and 13 show the tool-life curves for flank wear and crater, respectively, when the 18-8 stainless steel is machined in the streams (1 gal/min) of the cutting fluids listed in Table 4. The tool-life equations and the cutting speeds for 100 minute tool life are listed in Table 5. The carbide grade is MB2(triple carbide No. 2), the tool shape 0, 10, 6, 6, 15, 15, 1/50, the depth of cut 0.080 in., the feed 0.010 ipr, and the tool-life criteria 0.024 in. width and 0.0020 in. depth for flank wear and crater, respectively. The test result has clarified that the effect of cutting fluid on tool life or machining efficiency is unexpectedly substantial in machining the 18-8 stainless steel with carbide tools if a correct cutting fluid is applied, so that the adequate application of cutting fluid is very beneficial practically even in machining operations with carbide tools. Such marked speed increase up to 33.4 per cent for 100 minute tool life of flank wear may be due to the poor machinability of the 18-8 stainless steel which is characterized by high cutting temperature, work adhesion, and work-hardening.

The most effective cutting fluid for turning the 18-8 stainless steel with the carbide tools is chlorinated oil or chemical solution from the viewpoint of flank-wear tool life as seen in Table 5. The film of $Fe Cl_3$ near the cutting edge which will be formed during machining when applying chlorinated oil can be expected to be an excellent lubricant or separator at the flank where the frictional condition or the temperature is not so severe as to lose its lubricating ability. This is associated with the higher Four Ball pressure as shown in Table 4. One thing with chlorinated oil, however, is that some antismoke device is necessary because of its offensive smoke during machining. On the other hand, chemical solution is free from such trouble. However, the reason why chemical solution is effective as the cutting fluid is not known by the author.

What is worthy of attention is that the effect of most cutting fluids is much more substantial for the flank-wear tool life than for the crater as seen in the data. As a matter of fact, the cutting force is supported mostly on the rake face, so that the stresses on the flank will be much lower than those on the rake face as already pointed out in the reported photoelastic analysis of the stresses on tool faces by the author and the co-worker.[1] Also from the viewpoint of temperature distribution, it has been reported by H. Opitz[2] that the maximum temperature in a tool is found a little behind the cutting edge on the rake face. Summarizing the foregoing facts, it will be concluded that the frictional condition on the flank is not so severe as that on the rake face both in stress and temperature, that is to say, the friction on the flank is nearer to routine sliding friction, where a cutting fluid is more likely to penetrate and lubricate effectively. This is con-

[1] E. Usui and H. Takeyama, "Photoelastic Analysis of Machining Stresses," *Journal of The Government Mechanical Laboratory*, vol. 12, no. 4, 1958, p. 125.

[2] H. Opitz, "Temperature Field of a Turning Tool and the Reactions in the Zone of Contact," *Microtecnic*, vol. 8, 1954, p. 183.

sidered to be the reason why most cutting fluids are more effective for the flank-wear tool life.

As widely known, major functions of a cutting fluid are lubrication and cooling. However, it seems that the latter function plays only a minor role compared with the former according to the experimental result in Fig. 12, because one of the best cutting fluids, chlorinated oil, has much poorer cooling ability than water soluble oil (1:20) which has been verified to be much poorer as the cutting fluid in the tool-life test. Since flank wear is considered to be less temperature-dependent than crater or rather to be of abrasion, the foregoing description will be reasonable.

Another important function of a cutting fluid is to make the slope of the tool-life curve of flank wear shallow as seen in Fig. 12. This is very important from a practical point of view, because such a trend apparently makes the tool life at commercial cutting speeds considerably longer. The physical meaning seems to be that a cutting fluid is more effective at lower cutting speeds as the coolant or the lubricant.

Sulfo-chlorinated oil is detrimental to the flank-wear tool life in turning the 18-8 stainless steel. It is clearly observed that the tool point is chemically attacked and eroded seriously under the severe condition of machining. Therefore, the chemical activity of E. P. agents in a cutting fluid should be adequate depending upon the cutting condition or the material cut.

Conclusions

(1) From the viewpoint of tool life, cutting conditions should be determined taking account of both flank wear and crater in rather high speed machining.

(2) On the basis of the principle (1), the machining standard for turning the 18-8 stainless steel has been established.

(3) The best carbide grade for turning the 18-8 stainless steel is triple carbide No. 2 (MB2) or universal use No. 1 (MC1).

(4) The side rake angle for turning the 18-8 stainless steel should be 0 to 5 deg, if the tool failure is reached by the flank wear, whereas, if by crater, the side rake angle should be 10 to 15 deg.

(5) In turning the 18-8 stainless steel the feed should not be smaller than 0.004 ipr from the viewpoint of tool life.

(6) The locus of critical speeds and feeds which separates the domains of flank-wear and crater tool life has been obtained experimentally and theoretically. The relative position of each domain across the locus is determined by the relative magnitude of the exponents of the pair of tool-life equations.

(7) The general tool-life equations and the machining standard for turning the 18-8 stainless steel have been obtained for flank wear and crater. The practical conditions should be selected on the basis of the lower limit considering both types of tool wear.

The methodological principle treated in this paper will hold for turning any other material with carbide tools.

(8) The effect of cutting fluid upon tool life in turning the 18-8 stainless steel is marked. The cutting speed for 100 minute tool life (flank wear) can be increased up to about 33 per cent.

(9) The best cutting fluid for turning the 18-8 stainless steel with carbide tools is chlorinated oil or chemical solution.

(10) The effect of most cutting fluids is much more substantial for the flank-wear tool life than for the crater.

(11) By applying cutting fluids the tool-life curves for flank wear become shallow. This trend makes the tool life at commercial cutting speeds much longer.

(12) The chemical activity of a cutting fluid should be adequate, otherwise the cutting edge will be chemically eroded.

(13) Lubricity seems to be a much more important function for the cutting fluid in turning the 18-8 stainless steel than cooling ability.

DISCUSSION

Orlan W. Boston[3]

This paper describing the methods and procedure of obtaining optimum cutting conditions for turning 18-8 stainless steel, based on the life of sintered carbide tools, is well planned and executed. The use of both flank wear and crater is unique. The writer tried to co-ordinate results of these two methods of failure when using high-speed steel tools on structural steels a number of years ago, without success, as the crater, if formed, assumed widely varied shapes.

It appears that the use of a particular class of carbide, as determined by Mr. Takeyama, is necessary when turning 18-8 stainless steel. For this carbide tool the best side rake was determined. The side cutting edge angle is of equal importance, but this was not varied. Except for this omission, and a variation of relief which may affect results slightly, the author has determined experimentally the influences of all other important variables, including cutting fluids.

The cutting-speed tool-life relationship for both flank wear and cratering appear to be adequate for the basis of his conclusions. Equating the two cutting-speed equations for the one hundred-minute tool life is appropriate to determine the boundary line represented by Fig. 9, across which the type of wear leading to tool failure changes from one to the other.

Mr. Takeyama's conclusions are set forth completely and clearly. We will look forward to further reports of his work in which similar data for other materials machined will be presented. He has established himself as a reliable researcher, since his graduate studies at the University of Michigan a decade ago, and is to be highly commended for this work.

Author's Closure

The author wishes to express his gratitude to the discusser for giving helpful suggestions and for realizing what the author intended in the methodological pursuit.

Since the same type of work for various materials is still being continued by the author, he will add the variable of side cutting edge angle as the discusser pointed out. The author does not consider his approach for establishing the machining standards ideal, of course, so that he is entirely open to accept the further instructions or criticisms.

---

[3] Ann Arbor, Mich. Fellow ASME.

Milling Forces Measured With a Planetary-Gear Torquemeter[1]

J. R. ROUBIK
Senior Research Engineer,
Kearney & Trecker Corporation,
Milwaukee, Wis. Assoc. Mem. ASME

Cutting-force data, obtained with a torquemeter of planetary-gear design in carbide milling tests on SAE-1018 cold-rolled steel at feeds from 0.002 to 0.030 in. per tooth, cutting speeds from 87 to 957 fpm, and depths of cut from 0.100 to 0.300 in. with a tool geometry of −7°, 0°, 3°, 5°, 0°, 15°, 1/64" × 45°, are presented. The influences of variations in cutting speed, feed per tooth, and depth of cut on tangential cutting force are depicted graphically. Cutting-force values for other workpiece materials are also included.

With these data a comparative method of experimentally verifying the computed high efficiency of the torquemeter itself is derived and applied.

A method of obtaining highly accurate determinations of milling machine efficiency under actual oscillatory cutting loads is described with an example.

Actual and theoretical traces of the variation of tangential cutting force with both single and multiple-toothed face milling cutters are illustrated for comparison.

Introduction

Because of its relative simplicity, turning is generally resorted to for cutting-force measurements with dynamometers. If due consideration is given to the similarities and differences between turning and milling, data obtained in turning tests may, for approximations, be applied to milling situations. In order to obtain more direct information on the behavior of milling forces, a planetary-gear dynamometer was designed and built [1],[2] Fig. 1.

Several objectives, which have been accomplished in initial cutting tests with this instrument and are reported here, were as follows:

1 Determination of the influence of cutting speed, feed, and depth of cut on tangential cutting force in milling SAE-1018 cold-rolled steel with carbide.

2 Use of these data to verify experimentally by a comparative method the estimated high efficiency of the torquemeter.

3 Measure milling machine efficiency under actual cutting loads.

4 Determine the variation in cutting force during the cutting sweep of a single milling tooth.

5 Determine the variation in cutting force during a cut with a multiple-toothed cutter.

The extensive testing to meet these objectives also served to prove that the torquemeter performed satisfactorily.

Additional test results on machine efficiency and cutting-force requirements of uranium, a tungsten alloy, and an aluminum alloy are also reported.

Equipment and Procedure

In addition to the torquemeter and related components, a strain-gage load cell to sense the torquemeter-reaction-lever force, a strain-gage input box, a universal amplifier, a direct-writing oscillograph, and a storage-type oscilloscope to record force behavior were utilized. Additional equipment included a 20-hp calibrated motor driving the milling-machine spindle, a recording polyphase wattmeter, and various mechanical and electrical tachometers. The force-measuring system was periodically calibrated with dead weights or an accurate spring balance.

A Kearney & Trecker 50-hp CSM horizontal milling machine with a separate feed motor and the 20-hp calibrated motor in place of the standard 50-hp spindle motor was used in all of the initial cutting tests.

In all basic cutting-force tests, only single-toothed cutters were used for simplicity. These were obtained by setting one blade of a multiple-toothed cutter to a sufficiently greater cutting radius than the remaining blades. To test for torquemeter rotational-speed influence on cutting-force measurement, three sizes of cutters, each operating at approximately the same cutting speed but at different angular velocities, were utilized. These cutters were standard Kearney & Trecker CSM right-hand face mills in nominal 8-in. (10 teeth), 10-in. (12 teeth), 12-in-diam (14 teeth) sizes with C-5 grade carbide blades all having the following tool signature: −7, 0 deg × 0.210 in. on +15, 3, 5, 0, 15, 1/64 in. × 45 deg. Actually, the single-toothed versions had effective cutting diameters of 8.250, 10.250, and 12.312 in. For the torquemeter efficiency tests, an 8.188-in-diam, 10-toothed face mill of the same kind and with a similar tool geometry was selected. Conditions and materials used in additional tests are mentioned in conjunction with the results of those tests.

Two 4 × 4 × 12-in. pieces of SAE-1018 cold-rolled steel, cut from the same bar, were used in all the initial milling tests. Chemical analysis in percentages was: 0.15 C; 0.7 Mn; 0.035 S; 0.013 Ph; and remainder, Fe. Hardness was 138–143 Bhn. The workpiece was held in a special fixture, Fig. 1. Material consumption was minimal since the two pieces were only partially used up during the course of all the initial cutting tests, encompassing more than 250 test conditions with an average of 10 to 15 chips formed under each condition.

Basic cutting-force tests were conducted dry at cutting speeds of approximately 87, 156, 288, 522, and 957 fpm, feeds per tooth of approximately 0.002, 0.005, 0.010, 0.020, and 0.030 in., and depths of cut of 0.100, 0.200, and 0.300 in. The foregoing test conditions were duplicated with nominal 8, 10, and 12-in-diam face mills. These conditions were considered sufficient in range and number to provide data from which the influence of speed,

---

[1] This paper is based on a thesis submitted in partial fulfillment of the requirements for the degree of Master of Science (Mechanical Engineering) at the University of Wisconsin, 1959.

[2] Numbers in brackets designate References at end of paper.

Contributed by the Metal Processing Research Activity of the Production Engineering Division and presented at the Winter Annual Meeting, New York, N. Y., November 27–December 2, 1960, of The American Society of Mechanical Engineers. Manuscript received at ASME Headquarters, February 3, 1960. Paper No. 60—WA-3.

feed, and depth on cutting force could be established. Usually eight or more force pulses were recorded in each test. These cuts were taken with the horizontal planes through the center of the cutter and the center of the workpiece, in the direction of table feed, coinciding Data were gathered with single-toothed cutters since such force pulses lend themselves to a more simple analysis than those obtained with multiple-toothed cutters [2, 3] in which more than one tooth is in the cut at all times. Cutting force, energy, power, and speed values are readily derived [1] from oscillograms of the torquemeter-lever-reaction force.

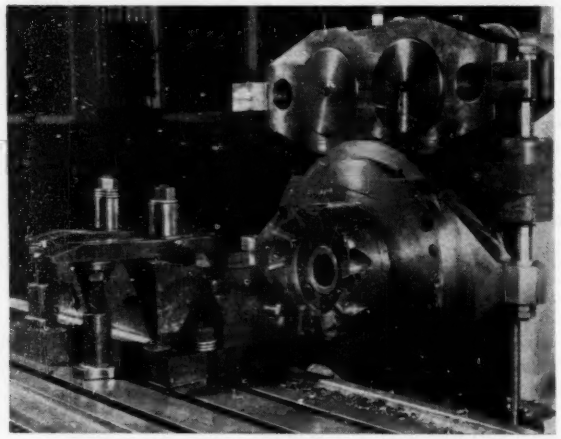

Fig. 1 Cutting test setup with milling torquemeter

Torquemeter is mounted on spindle nose of horizontal milling machine. Visible part of torquemeter constitutes lever arm attached to sun gear in planetary-gear train. Strain-gage load cell, right, is rigidly attached to reaction member on machine overarms and holds lever arm fixed. Cell is in tension for cut with 8-in-diam, right-hand face mill shown.

One method of measuring the efficiency of the milling torquemeter involves the comparison of wattmeter measurements of cuts having the same theoretical power demand taken with and without the torquemeter. Since the spindle speed of the torquemeter is always 0.6 that of the machine, identical cuts with the same cutter cannot be taken, and a problem arises in establishing conditions for cuts of equivalent power requirement. If comparative cuts are taken with the same machine-spindle speed in each case, the efficiency of the machine-spindle drive can be presumed constant. The basic cutting-force data gathered with the torquemeter, assuming errors due to the estimated small losses in the torquemeter are negligible, can be used to establish different cutting conditions requiring equal power. If comparative cuts are then taken and the power values are in close agreement, within the limits of experimental error, then it must be presumed that the torquemeter losses actually are small and that they can be neglected without introducing significant errors.

Over-all machine efficiency is determined by taking simultaneous cutting-force and electrical power-input measurements during cuts with multiple-tooth cutters. Output or cutting power can be derived from the cutting-force record and input power to the machine drive can be determined with a calibrated motor. To expedite machine-efficiency measurements, the output of the load cell or input to the universal amplifier can be integrated by an appropriate integrating resistance-capacitance network to obtain a recorded average cutting force rather than a sawtooth or irregular force trace which requires several time-consuming planimeter measurements of the area under the trace to obtain an accurate value of the average cutting force.

Test Results

Basic Data. A typical oscillogram for a single-tooth milling test, Test No. 2-141, is shown in Fig. 2 and the derived data are listed in Table 1 along with values for other similar test cuts. More

Table 1 Milling torquemeter data (obtained from force oscillograms)

Workpiece Mat'l: SAE-1018 CRS ; 4 - in. width; 12- in. length; 138-143 BHN. Date 1958
Machine: 50- hp K&T CSM horizontal milling machine. Setup: Cutter & Work CENTERED
Cutter: 10.250- in.- diam. RIGHT hand FACE- milling cutter. No. of teeth cutting - 1
Rake: 0° A 0.200" ON +15° radial, -7° axial. Corner angle: 15° WITH 45° x 0.020" CHP.

Test No.	Depth In.	Machine Dial Rpm	Cutter Act. Rpm	Feed, Ipm Dial	Feed, Ipm Actual	R, Lbs. Min.-Max.	R, Lbs. Ave.	U_c, Energy- $\frac{in.lb}{in.^3}$	$\frac{hp/in^3}{min.}$	F_t, lbs Ave.	Speed, Fpm	Feed, Ipt
2-130	0.200	320	194.8	1/32	0.467	(10) 30-38	33.3	406,000	1.03	194.9	522.1	.00240
131				1/16	0.958	(15) 54-62	58.4	398,600	0.88	393.0		.00492
132				1/8	1.899	(9) 93-100	96.3	287,100	0.73	563.7		.00975
133				3/4	3.850	(9) 160-170	163.3	263,100	0.61	956.0		.01966
134				5/16	5.389	(11) 202-217	210.6	222,900	0.56	1232.9		.02766
2-140	0.200	177	107.6	1/32	0.467	(9) 52-63	55.6	375,000	0.96	325.6	288.6	.00434
141				1/16	0.958	(8) 96-106	102.1	338,800	0.86	597.8	289.0	.00870
142				1/4	2.290	(8) 182-195	187.4	257,700	0.65	1097.1		.02129
143				3/8	3.191	(9) 230-250	243.3	240,100	0.61	1424.3		.02966
2-130	0.200	96	58.5	3/8	0.388	(7) 77-95	84.3	372,100	0.94	493.4	156.8	.00663
131				1/16	0.558	(8) 97-114	105.4	323,400	0.82	617.0		.00954
132				1/8	1.141	(4) 165-185	175.0	262,700	0.66	1024.5		.01950
133				1/2	1.596	(6) 220-246	245.0	262,900	0.66	1034.2		.02728

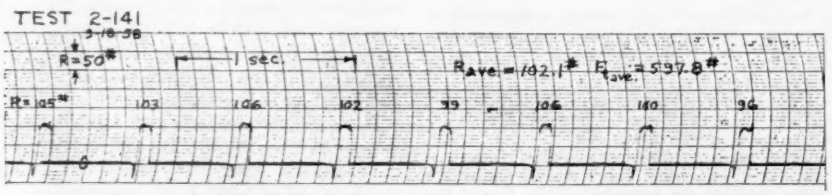

Fig. 2 Typical oscillogram of tangential cutting force with single-toothed face mill

Trace is for test 2-141, listed in Table 1, and constitutes raw data from which one datum point is obtained for curves such as depicted in Figs. 3 and 4. Note resemblance of force pulses to central section of theoretical pulse shown in Fig. 13.

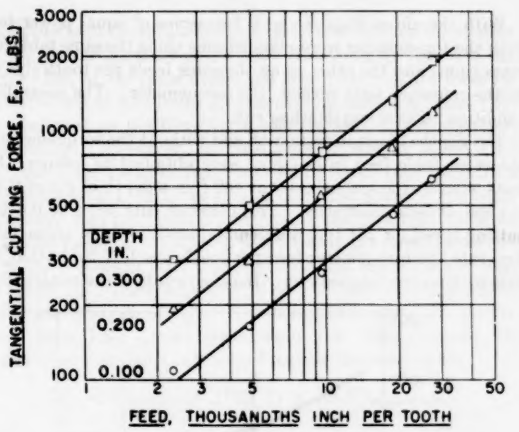

a) 8.250-in-diam face mill at 517 fpm

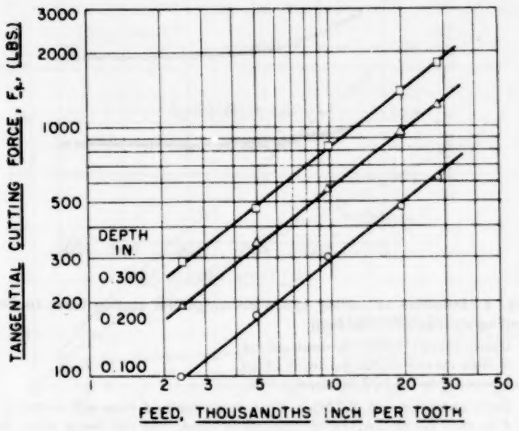

(b) 10.250-in-diam face mill at 522 fpm

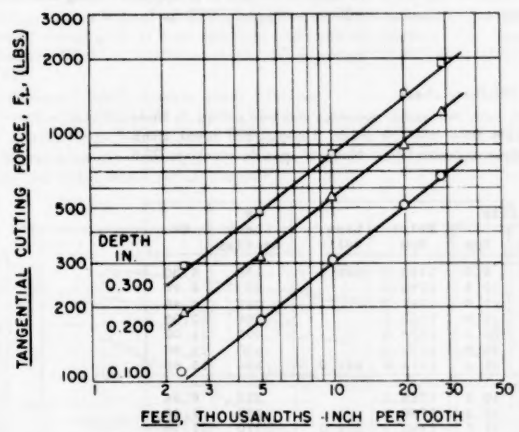

(c) 12.312-in-diam face mill at 517 fpm

Fig. 3 Tangential cutting force versus feed per tooth at 520 fpm with various sizes of face mills

All cutters were right hand and single toothed and were centered with the 4-in. width of cut in SAE-1018 cold-rolled steel at depths of cut of 0.100, 0.200, and 0.300 in. Tool signature: −7°, 0°, 3°, 5°, 0°, 15°, 1/64" × 45°.

Although cutter angular velocities varied from 240 to 160 rpm, the curves are practically identical showing no influence of rotational speed in this range on force measurements taken with the torquemeter

than 200 such tests involving more than 2000 force pulses were evaluated to obtain the information depicted in Figs. 3, 4, 5, 8, 9, 13, and 15.

In comparing graphs *a*, *b*, and *c* in Fig. 3, obtained at approximately 522 fpm cutting speed, but at different angular velocities with 8-in., 10-in., and 12-in-diam face mills, it can be seen that the curves are practically identical. Thus, no influence of torquemeter output speed, from 160 to 240 rpm, could be detected. Tangential cutting force was increased with an increase in either the feed per tooth or the depth of cut, but in less than a direct proportion.

A summary of all the data for the combination of workpiece material, tool material, and tool geometry tested is presented in Fig. 4. Each curve can be represented by an equation of the type

$$F_t = K_f f^{0.766}$$

where K_f = a constant dependent on depth of cut and cutting speed.

Variation of tangential cutting force with change in cutting speeds at 0.010-ipt feed and depths of 0.100, 0.200, and 0.300 in. is illustrated in Fig. 5. As cutting speed was increased from 85 to 520 fpm, cutting force was decreased approximately 20 per cent but remained constant as the speed was further increased to 950 fpm.

The broken line in Fig. 5 represents data [5] obtained with a lathe dynamometer in orthogonal turning of a tube of AISI-1015 steel at 0.010-ipr feed and 0.100-in. width of chip with a 0-deg-rake carbide tool. The cutting conditions were similar to those in milling except that a 15-deg corner angle, a −7-deg axial-rake angle, a secondary or end-cutting edge, and a 140-Bhn steel were used in milling, while in orthogonal turning, the comparable angles were both 0 deg, no secondary or end-cutting edge was operative, and a 120-Bhn steel was used. In the light of these differences, each of which would account for slightly higher forces in the milling tests, the milling data compare very favorably with the turning data in both magnitude and behavior.

Additional basic cutting force and energy data [7] obtained with the torquemeter for a powder-metallurgy tungsten-nickel-

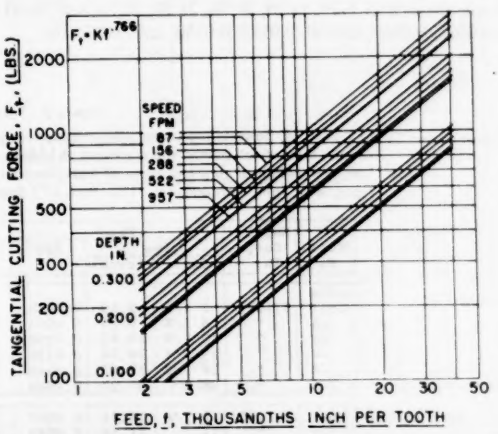

Fig. 4 Influence of feed per tooth on tangential cutting force in milling at different speeds and depths of cut

Summary of data obtained in milling 4-in-wide SAE-1018 cold-rolled steel (140 Bhn) with carbide (C-5), single-toothed, right-hand, 8, 10, and 12-in-diam face mills centered in the cut at speeds of 87, 156, 288, 522, and 957 fpm; depths of cut of 0.100, 0.200, and 0.300 in.; and feeds per tooth of approximately 0.002, 0.005, 0.010, 0.020, and 0.030 in. All cuts were dry. Data points are not shown to avoid crowding, but each line was obtained from approximately 15 data points, 5 for each of the three cutter sizes. Distribution of data points along each line is similar to that in Fig. 3. Tool signature: −7°, 0°, 3°, 5°, 0°, 15°, 1/64" × 45°.

copper alloy, natural uranium, and an aluminum alloy are presented in Figs. 6 and 7. The significant change in slope in these curves is characteristic of the particular double radial-rake-angle [6] geometry used in these tests. The point at which this change in slope occurs is associated with the ratio between the uncut chip thickness and the width of the primary-radial-rake land which, together with the peripheral relief surface, forms the cutting edge.

Torquemeter Efficiency. The influences of depth of cut and relative feed per tooth on relative cutting force in milling over the range of conditions tested have been derived from Fig. 4 and are presented in Figs. 8 and 9. Relative cutting force F was affected by depth of cut d as follows:

$$F = (10\,d)^{0.940}$$

or

$$d = 0.1\,F^{1.064}$$

Force was not directly proportional to depth [8] because of the influence of the chamfer at the nose of the tool and the secondary or end-cutting edge which produces the finished surface in face milling. If the relative cutting force at 470 fpm cutting speed is expressed in terms of feed per tooth f or uncut chip thickness t as

$$F = f^{0.706} = t^{0.706}$$

then, at 280 fpm it is

$$F = 1.065\,f^{0.706}$$

These particular expressions were chosen to facilitate setting up cutting conditions which require the same power with and without the torquemeter in comparative torquemeter tests.

In torquemeter efficiency tests, Table 2, the same machine-spindle speed of 216 rpm was used to eliminate changes in machine efficiency. The same cutter was used in all tests, each of which required a fraction of a minute, only long enough to obtain a constant wattmeter trace. Reference tests without the torquemeter were carried out at 469 fpm, and 0.100-in. depth of cut at feeds of 5.39, 11.29, 23.25, 27.27, 32.75, and 46.30 ipm or 0.0025, 0.0052, 0.0106, 0.0125, 0.0150, and 0.0211 ipt.

With the aid of Figs. 8 and 9 two series of equal power tests with the torquemeter were planned, one using the same table feed rates (ipm) and the other using the same feeds per tooth (ipt) as in the reference tests without the torquemeter. The controlling condition utilized was depth of cut.

The depths of cut in tests with and without the torquemeter at the same table feed rates (ipm) were obtained as follows. For tests without the torquemeter at 469 fpm a depth of cut of 0.100 in. was chosen arbitrarily. Torquemeter cuts were at 0.6 this cutting speed, or 281 fpm and, consequently, at any given table feed rate the torquemeter feed per tooth was 1.67 times that for cuts without the torquemeter. In other words, if the relative feed

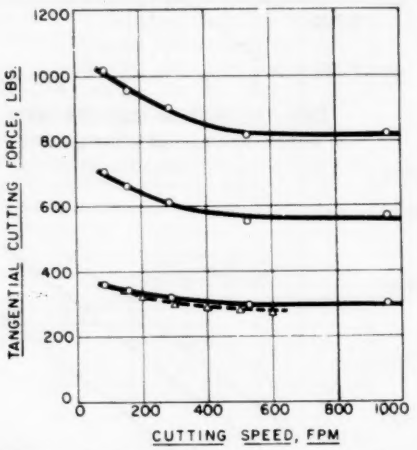

Fig. 5 Influence of cutting speed on tangential cutting force in face-milling steel at 0.010-ipt feed

Upper curve—0.300 in. depth of cut
Middle curve—0.200 in. depth of cut
Lower curve—0.100 in. depth of cut

Data obtained with 8.250-in-diam single-toothed face mill centered in a 4-in-wide cut on SAE-1018 cold-rolled steel. All cuts were dry. Tool signature: $-7°, 0°, 3°, 5°, 0°, 15°, 1/64'' \times 45°$.

Dashed line [5] is for AISI-1015 steel in orthogonal turning with a 0°-rake carbide tool at 0.100-in. width and 0.010-ipr feed, dry.

Table 2 Torquemeter efficiency check

T3 and T4, torquemeter cuts; M4, machine cuts. All tests with the same sequence number set up to have equal theoretical power requirements. 8.188-in. diam, rh CSM face mill (10 teeth, 0 deg radial rake), climb cut; 4-in. width of cut; top edge of workpiece on cutter horizontal center line. Nominal speeds: machine, 216 rpm, 469 fpm; torquemeter, 130 rpm, 279 fpm.

Test No.	Depth Cut, In.	Feed, Ipm		Ipt	Motor Slip		Motor Rpm	Line Volts	Kw Chart Reading	Kw
		Dial	Actual		Rev./Sec	Rpm				
Idle					13/120	6.5	1793.5	238.5	.150	4.50
T3-1	0.1014	3 1/8	3.19	0.0024	5/28.7	10.5	1789.5		.232	6.96
-2	"	6 3/8	6.63	0.0051	3/14.1	12.8	1787.2		.282	8.46
-3	"	13 1/8	13.67	0.0104	2/7.1	16.9	1783.1		.366	10.98
-4	"	15 3/4	16.36	0.0125	1.5/5.0	18.0	1782.0		.400	12.00
-5	"	18 1/2	19.63	0.0149	3/8.9	20.2	1779.8		.430	12.90
-6	"	26	27.27	0.0208	3/7.1	25.4	1774.6	240.0	.530	15.90
T4-1	0.1063	5 1/4	5.39	0.0041	4/22.3	10.8	1789.2		.228	6.84
-2	"	11	11.29	0.0086	3/13.7	13.1	1786.9		.282	8.46
-3	"	22	23.25	0.0177	1.5/5.1	17.7	1782.3	239.0	.370	11.10
-4	"	26	27.27	0.0208	2/6.1	19.7	1780.3	239.0	.400	12.00
-5	"	31	32.75	0.0249	1.5/4.1	22.0	1778.0	239.5	.440	13.20
-6	"	44	46.30	0.0352	1/2.3	26.1	1773.9	239.0	.540	16.20
Idle					6.5/60	6.5	1793.5	238.5	.150	4.50
Idle					10/91.3	6.6	1793.4	238.5	.150	4.50
M4-1	0.100	5 1/4	5.39	0.0025	2/11.3	10.6	1789.4	237.5	.228	6.84
-2	"	11	11.29	0.0052	2/9.4	12.8	1787.2	237.5	.280	8.40
-3	"	22	23.25	0.0106	1.5/5.3	17.3	1783.7	237.5	.368	11.04
-4	"	26	27.27	0.0125	1.5/4.8	18.8	1781.2	238.5	.400	12.00
-5	"	31	32.75	0.0150	1.5/4.5	20.0	1780.0	238.5	.432	12.96
-6	"	44	46.30	0.0211	4/8.9	27.0	1773.0	237.5	.534	16.02
Idle					10/92.2	6.5	1793.5	238.0	.150	4.50

for a cut without the torquemeter is taken as 1.00, then the relative feed for the torquemeter cut is 1.67. Referring to Fig. 9, it can be seen that, at the same depth and speed, the relative force for a relative feed of 1.67 (with torquemeter) is only 1.481, not 1.67, times as great as the force for a relative feed of 1.00 (without torquemeter). However, the torquemeter cutting speed (281 fpm) was lower than the machine cutting speed (469 fpm), thus involving a force 1.065 times greater than that which would occur at the same feed per tooth, cutting speed, and depth in a cut without the torquemeter. Thus, the tool forces in the torquemeter cut, due to differences in both feed per tooth and cutting speed were 1.577, not 1.67, times the values in cuts without the torquemeter at the same depth of cut. If cutting force with the torquemeter were 1.67 times larger than the force without the torquemeter then both cuts would require the same power.

$$(F_t \times V)_{\text{machine}} = (1.67\ F_t \times 0.6\ V)_{\text{torquemeter}}$$

where

V = cutting speed, fpm, in machine cuts without the torquemeter

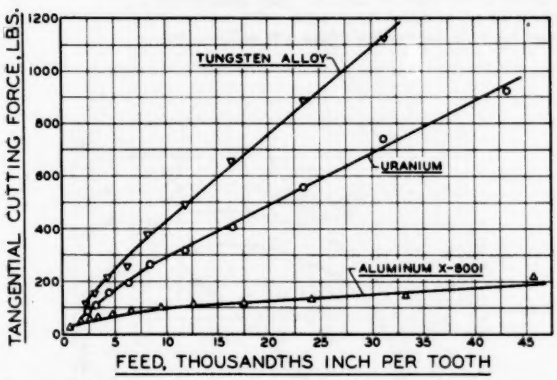

Fig. 6 Tangential cutting force versus feed per tooth in face milling various metals

All cuts were dry at 0.100-in. depth of cut with 8.4-in-diam, single toothed, carbide (C-2) face mills centered with the width of cut. Tool signature: 0°, 0° × 0.060″ on +30°, 8°, 8°, 0° × 0.030″, 15°, 0.015″ × 45°.

Aluminum X-8001; 1.88 in. wide; 570 fpm.
Uranium (natural); 1.44 in. wide; 230 fpm.
Tungsten alloy; 1.20 in. wide; 230 fpm.

The tungsten alloy (Mallory 1000) is an alloy of 90 per cent tungsten, 6 per cent nickel, and 4 per cent copper.

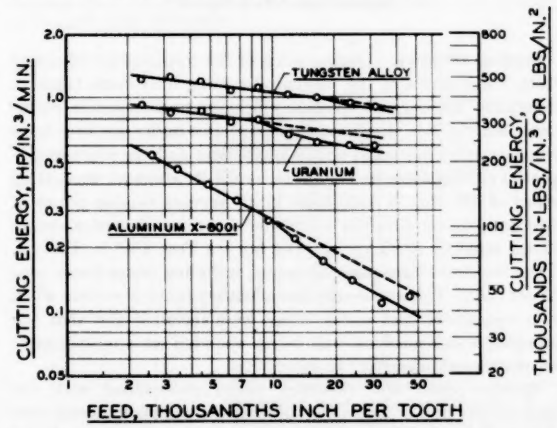

Fig. 7 Cutting-energy requirements in face milling various metals
Curves derived from data in Fig. 6

F_t = cutting force, lb in machine cuts without the torquemeter

It was necessary, therefore, to increase cutting force in cuts with the torquemeter from 1.577 to 1.67 times the force in cuts without the torquemeter. That is, cutting force with the torquemeter must be increased 1.67/1.577 or 1.059 times by an increase in depth of cut. Referring to Fig. 8,

$$d = 0.1\ F^{1.064} = 0.1(1.059)^{1.064} = 0.1063 \text{ in.}$$

Therefore, in comparative tests in which the same machine speed (216 rpm), cutter, width of cut, entry condition, and table feed rates (ipm) are used, if cuts without the torquemeter are made at 0.100 in. depth of cut, cuts with the torquemeter must be made at 0.1063 in. depth to require equivalent power.

By a similar procedure it was found that, in tests in which the same machine speed (216 rpm), cutter, width of cut, entry condition, and feeds per tooth (ipt) are used, if cuts without the torquemeter are made at 0.100 in. depth of cut, cuts with the torquemeter must be made at 0.1614 in. depth of cut to require equivalent power.

Since the machine used in these tests had a separate feed-drive motor, changes in feed power at different feed rates do not influence the power measured at the spindle motor. At lower machine speeds, the foregoing depth-of-cut relations would be

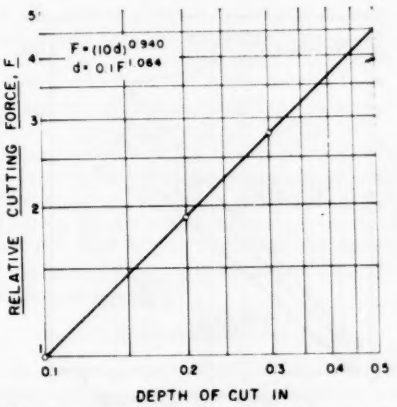

Fig. 8 Relative tangential cutting force versus depth of cut in carbide face milling SAE-1018 steel
Derived from data in Fig. 4

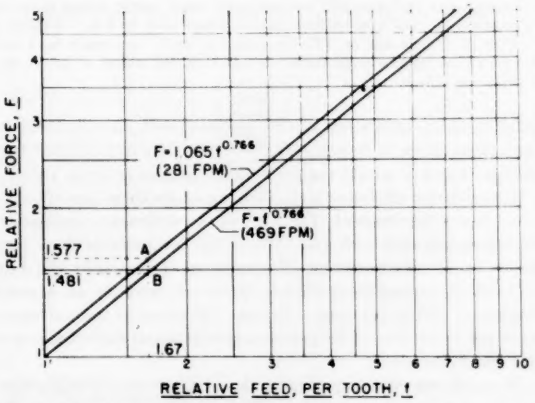

Fig. 9 Relative tangential cutting force versus feed per tooth in carbide face milling SAE-1018 steel at 280 and 470 fpm
Derived from data in Fig. 4

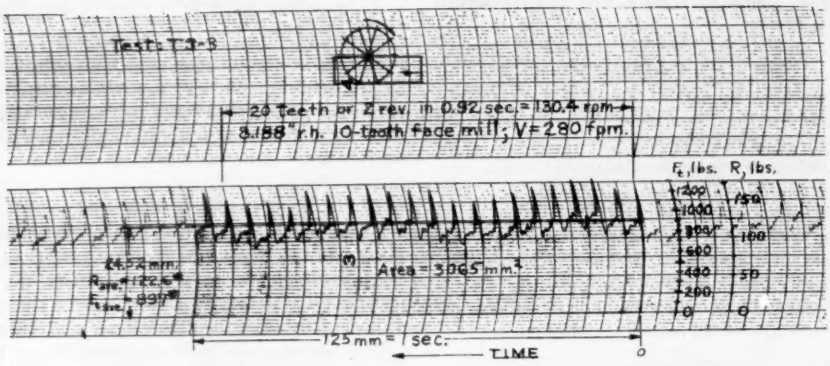

Fig. 10 Oscillogram of tangential cutting force with multi-toothed face mill in torquemeter efficiency test

Taken with an 8.188-in-diam, 10-toothed, right-hand face mill at 280 fpm, 0.0105 ipt, and 0.161 in. depth of cut on a 4-in-wide block of SAE-1018 steel as sketched, see Test T3-3 in Table 2. Tool signature: −7°, 0°, 3°, 5°, 0°, 15°, 1/64" × 45°.

Mean tangential force, 897 lb; average maximum force, 1187 lb; average minimum force, 746 lb. Metal-removal rate of 8.8 cu in/min required average power at the cutter of 7.61 hp (from oscillogram). A simultaneous wattmeter recording indicated a steady 10.98 kw or 14.64 hp input to the motor resulting in an over-all efficiency under these conditions of 52 per cent for a 50-hp machine driven with a 20-hp calibrated motor.

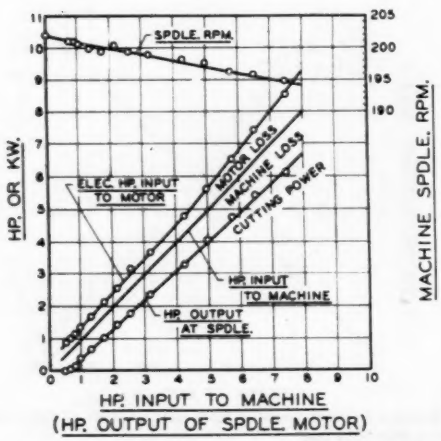

Fig. 11 Sample power data for milling-machine spindle transmission driven by 5-hp motor

Torquemeter and electrical measurements taken under cutting loads at approximately 200 rpm machine spindle speed with an 8-in., 16-toothed carbide (C-2) face mill on 192-Bhn cast iron at 17 ipm table feed and depths of cut ranging from 0.003 to 0.200 in. for widths of cut of approximately $3^1/_2$ in.

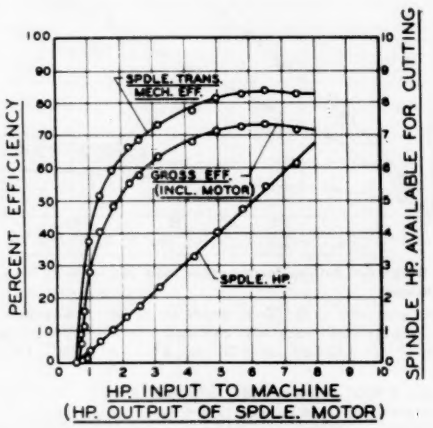

Fig. 12 Sample efficiency curves for milling-machine spindle transmission driven by 5-hp motor

Derived from data in Fig. 11

valid for SAE-1018 steel, but at higher speeds, the tendency of the cutting force to become constant (compare 522 and 957 fpm in Figs. 4 and 5) would require some alteration of these values.

Torquemeter efficiency tests were run under these conditions of equal power requirement, Table 2, and the wattmeter readings for corresponding cuts with and without the torquemeter were very nearly equal. Torquemeter efficiencies, as indicated by the data in Table 2, ranged from 99.3 to 101.8 per cent for an over-all average of 100.09 per cent. Average efficiency in tests at equal feeds per tooth was 99 88 per cent and at equal table feed rates was 100.29 per cent.

Of course, an efficiency of more than 100 per cent is impossible, but it must be concluded from these results that losses in the torquemeter were less than 1 per cent and can be neglected for practical purposes.

Machine Efficiency. During some of the torquemeter efficiency tests, oscillograms of the tangential cutting force were taken to determine the over-all machine efficiency under specific conditions, see Fig. 10. In this instance, the area under the force trace was measured five times with a planimeter and the average tangential cutting force was found to be 897 lb which at the cutting speed of 280 fpm is equivalent to an average cutting power of 7.61 hp. A simultaneous wattmeter recording showed a steady motor input of 10.98 kw or 14.64 hp, see Test T3-3 in Table 2. Thus the over-all machine efficiency, including motor losses, was 52 per cent. This apparently low efficiency is not abnormal when it is considered that motor losses were included and that the nominal 50-hp machine was being operated at approximately $^1/_4$ of its rated capacity.

Spindle power and efficiency values determined with the torquemeter and accurate electrical measurements in actual cuts on a horizontal milling machine, the spindle transmission being driven by a 5-hp motor, are illustrated in Figs. 11 and 12.

Single-Tooth Force Pulse. If the uncut chip thickness t at the milling-cutter center line (in the direction of feed) which is equal to the feed advance per tooth f (modified for corner angles other than 0 deg) is assigned a relative value of unity, then, as a first approximation generally involving only a small error, the uncut chip thickness at any point in the arc of travel of the cutting edge through the workpiece is

$$t = f \cos \theta$$

where θ = angular displacement of cutting edge measured from the cutter center line which is in the direction of feed

As indicated by the test data, the relative cutting force F depends on the relative feed per tooth or chip thickness as follows:

$$F = f^{0.786}$$

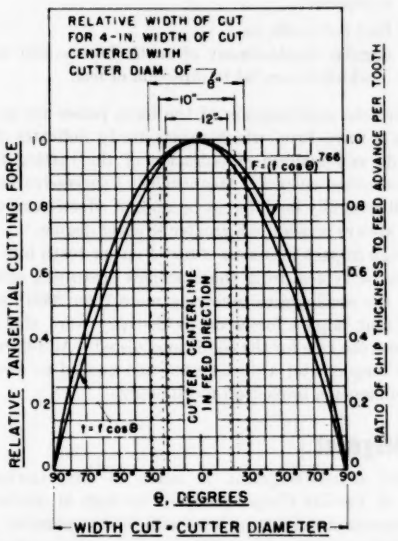

Fig. 13 Variation in uncut chip thickness and tangential cutting force in 180-deg milling arc of a single tooth

Curve $t = f \cos \theta$, represents ratio of chip thickness to feed advance per tooth at various positions of the tooth (0 deg corner angle) in its cutting arc. If force were directly proportional to feed, this curve would also represent the variation in force.

Curve $F = (f \cos \theta)^{0.786}$ represents the cutting-force pulse of a single milling tooth through a cutting arc of 180 deg and was determined with the aid of the first formula above and the relation expressed in Fig. 9. The dashed lines indicate the relative portions of this pulse which would be obtained with 8, 10, and 12-in-diam cutters centered with a 4-in. width of cut as used in many of the tests.

The relative cutting force F has a value of unity when milling a chip having a relative thickness of unity.

Thus, the relative cutting force acting on the cutting edge at any instant during its arc of travel through the workpiece is very nearly

$$F = (f \cos \theta)^{0.786}$$

This relation is depicted in Fig. 13 for a milling tooth sweeping through a cutting arc of 180 deg (width of cut equal to cutter diameter). Depending on the position of the cutter with respect to the width of cut, the general shape of a normal cutting-force pulse, except for initial impact, should closely resemble an appropriate sector of the curve shown. Comparison of the proper central sectors in Fig. 13 with actual force traces in Figs. 2 and 14 shows good agreement.

Oscillations superposed on the basic force-pulse form are caused partly by the gearing, as is the case with any sensitive tool dynamometer on a gear-driven machine tool, and partly by the basic process of chip formation [4], the two causes probably being closely interrelated.

Multiple-Tooth Force Pulses. The pulsations of cutting force acting on a multiple-toothed milling cutter can be obtained by appropriate superposition of the force pulses of individual teeth [2, 3]. Construction of the cutting-force curve in this manner is illustrated in Fig. 15, for the particular conditions of torquemeter test T3-3, see Fig. 10 and Table 2. It should be noted that the force curve, Fig. 15 was constructed assuming no cutter runout and proceeds in time from left to right while the actual recorded force trace, Fig. 10, involves cutter runout and proceeds from right to left.

When unity is the value assigned to the maximum cutting force for a single-tooth pulse, the maximum, average, and minimum relative cutting-force values in Fig. 15 are, respectively, 2.27, 1.71, and 1.30. From Fig. 4, the maximum cutting force on a single tooth for Test M4-3, see Table 2, is approximately 310 lb. For Test T3-3, see Fig. 10 and Table 2, which requires very nearly the same power, $F_t V_t = F_m V_m$, as Test M4-3 the maximum cutting force on a single tooth is in inverse proportion to the cutting speeds in these tests and

$$F = 310(469/279) = 520 \text{ lb}$$

With a relative cutting force of 1.00 being equivalent to 520 lb, the maximum, average, and minimum cutting-force values indicated theoretically by Fig. 15 for Fig. 10 are 1180, 889, and 676 lb, respectively. These values compare to actual average measured force values in Fig. 10 of 1187, 897, and 746 lb, respectively. With the exception of the difference in minimum force values, which can be explained by consideration of the burr formed on

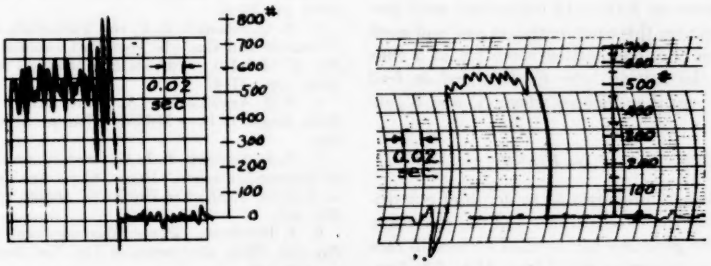

Fig. 14 Tangential cutting-force pulse at 189 fpm and 0.0095 ipt

Left: Oscilloscope flat-response trace (Memoscope)

Right: Oscillograph trace (nearly flat response up to 100 cps).

Recordings were made simultaneously in milling SAE-1018 cold-rolled steel, dry, with 12.312-in-diam, rh, single-toothed carbide (C-5) face mill. Cutter was centered with 4 in. width of cut at 0.150 in. depth of cut. Tool signature: $-7°, -11° \times 0.210''$ on $+14°, 3°, 5°, 0, 15°, 1/32'' \times 45°$.

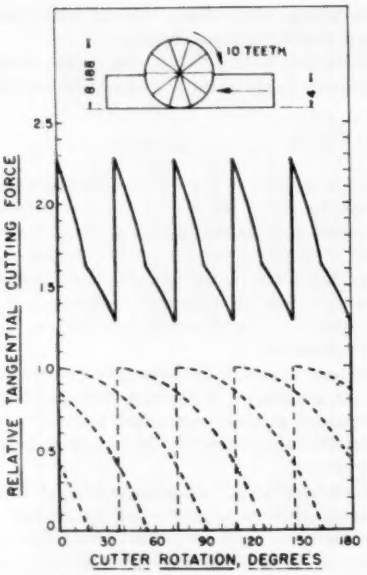

Fig. 15 Constructed tangential cutting-force curve for condition shown in milling with a multiple-toothed face mill

Dashed lines represent cutting-force pulses of individual teeth, see right half of pulse in Fig. 13. Solid line, obtained by superposition of individual pulse values, represents force fluctuation for situation depicted. Relative tangential cutting forces are: 2.27, maximum; 1.71, average; and 1.30, minimum on the basis of a relative cutting-force value of 1.00 assigned to the maximum force for a single tooth. Cutter runout was assumed to be zero. Compare with actual trace in Fig. 10.

exit of the tool from the cut, there is exceptional agreement in shape and magnitude between the actual and theoretical force traces shown in Figs. 10 and 15.

Conclusions

By virtue of the data presented here, the planetary-gear torquemeter has been proved to be a useful and reliable instrument for measuring tangential cutting force in milling. Comparative experimental efficiency tests at 216 rpm input speed confirmed that operating losses in the torquemeter under cutting loads were less than 1 per cent and can be neglected for practical purposes. Tangential cutting forces in milling, as well as the manner of force variation during the cutting sweeps of one or more milling teeth were accurately determined over a broad range of conditions. With accurate electrical power-input measurements, the efficiencies of a milling machine under various actual cutting conditions have also been determined.

The carbide milling tests on SAE-1018 cold-rolled steel provided basic machining data for this combination of tool and work material indicating, when only one cutting condition at a time was varied, that tangential cutting force F_t depended on feed per tooth f and depth of cut d as follows, where K_f and K_d are constants:

$$F_t = K_f f^{0.708} \quad \text{and} \quad F_t = K_d d^{0.940}$$

Cutting force was not directly proportional to depth of cut primarily because of the small tool-nose chamfer and the secondary or face-cutting edge which produces the finished surface in face milling. With an increase in cutting speed from 85 to 520 fpm, cutting force decreased about 20 per cent, but remained constant from 520 to 960 fpm. Neglecting impact forces in milling, cutting force for equivalent cutting conditions appears to be the same in milling as in turning. This point could be established more clearly by turning a workpiece mounted on the torquemeter.

Oscillations superposed on the basic force-pulse form are caused partly by the gearing, as is the case with any sensitive tool dynamometer on a gear-driven machine tool, and partly by the basic process of chip formation, the two causes probably being closely interrelated.

The tangential cutting force F_t on a single milling tooth may be expressed with little error as

$$F_t = K(f \cos \theta)^{0.786}$$

where

K = a constant
f = feed per tooth, in.
θ = angular displacement of tooth from cutter center line which is parallel to direction of feed

Appropriate superposition of the force pulses for single teeth provides a wave form which satisfactorily indicates the actual magnitude and manner of pulsation of the cutting force with multiple-toothed cutters. Magnitudes of successive force pulsations will generally be different because of effective cutter runout which is always present to a greater or lesser degree.

Although impact forces on entry of cutter teeth into the work appear to be typical from the examples presented, observations of all of the oscillograms involving more than 2000 force pulses indicate that impact forces on tooth entry were the exception rather than the rule for the conditions tested. Additional studies with the torquemeter are suggested and needed to evaluate the factors influencing impact on tooth entry.

Acknowledgment

Grateful acknowledgment is made to Mr. Gerhard Hug, Kearney & Trecker Corporation, for his help in conducting the various experimental cutting tests with the torquemeter.

References

1 J. R. Roubik, "A Milling Torquemeter of Planetary-Gear Design," TRANS. ASME, Series B, JOURNAL OF ENGINEERING FOR INDUSTRY, vol. 83, 1961, pp. 155–162.

2 R. Weilenmann, "Beitrag zur Berechnung des Leistungsbedarfs beim Fräsen," *Werkstatt und Betrieb*, vol. 90, May, 1957, pp. 296–298.

3 H. Opitz, "Influence of Vibrations on Tool Life and Surface Condition in Milling Operation," *Microtecnic*, vol. 12, April, 1958, pp. 72–87.

4 H. Opitz and J. Kob, "Cutting Forces and Temperatures When Milling With Carbide Cutters," *The Tool Engineer*, vol. 30, Jan., 1953, pp. 35–41.

5 A. O. Schmidt, B. F. von Turkovich, J. R. Roubik, and I. Ham, "Ceramic and Carbide Tool Performance—Part II," ASME Paper No. 57—SA-101; *Current Engineering Practice (India)*, vol. 2, Oct., 1959, pp. 37–43.

6 J. B. Armitage and A. O. Schmidt, "An Investigation of Radial Rake Angles in Face Milling," TRANS. ASME, vol. 66, 1944, pp. 633–643.

7 A. O. Schmidt, B. L. Richardson, and J. R. Roubik, "Machining of Reactor Materials," Paper, Space Age Tooling Seminar, University of Arizona, 1959; *The Engineers' Digest*, vol. 20, Dec., 1959, pp. 497–502, 521.

8 I. Bendixen, "Power Measurements in Milling," ASTE Paper No. 194, 1959; abstracted in *The Tool Engineer*, vol. 42, April, 1959, pp. 102–106.

CONTENTS

(*Continued*)

545 **An Analysis of the Mechanism of Orthogonal Cutting and Its Application to Discontinuous Chip Formation** (60—WA-79)
Keiji Okushima and Katsundo Hitomi

557 **New Development in the Theory of the Metal-Cutting Process, Part II—The Theory of Chip Formation** (60—WA-63)
P. Albrecht

572 **Performances of Carbide Tools in Machining 18-8 Stainless Steel** (60—WA-1)
H. Takeyama

579 **Milling Forces Measured With a Planetary-Gear Torquemeter** (60—WA-3)
J. R. Roubik

Journal of ENGINEERING FOR INDUSTRY

Information for Authors

• Manuscripts should be submitted in final form to the Editor. Each manuscript must be accompanied by a statement that it has not been published elsewhere nor has it been submitted for publication elsewhere. A paper which would occupy more than 8 pages of the Journal may be returned to the author for abridgment.

• The author should state his business connection, the title of his position, and his mailing address. A short abstract (50 to 100 words) should be included on the first page immediately preceding the introductory paragraph of the paper.

Three copies of the manuscript are required. One of these must be a carefully prepared printer's copy, typed in double spacing, on one side of the page only, with wide margins, on $8^1/_2$ by 11-in. opaque white paper. Mimeographed manuscripts, if prepared with exceptional care, can be accepted provided they are completely edited.

• As far as possible, all mathematical expressions should be typewritten. Greek letters and other symbols not available on the typewriter should be carefully inserted in ink. Care should be taken to distinguish between capital and lowercase letter, between zero (0) and the letter (*O*), between the numeral (1) and the letter (*l*), etc. A letter representing a vector cannot be printed with an arrow above or below it. The letter should be underscored with a single wavy line, wherever it appears in the text, to designate boldface type.

• A list of symbols carefully marked for the use of the editor (thus: κ, Greek l.c. kappa), if it has not been included in the body of the paper, should accompany the manuscript on a separate page.

• Before preparing a manuscript the author should study printed articles in the Journal, with special attention to the form and style of mathematical expressions, tables, footnotes, references, and abstract. Numbers that identify mathematical expressions should be enclosed in parentheses. Numbers that identify references at the end of the paper should be enclosed in brackets. Care should be taken to arrange all tables and mathematical expressions in such a way that they will fit into a single column when set in type. Equations that might extend beyond the width of one column (fractions that should not be broken or long expressions enclosed in parentheses) should be rephrased to go on two or more lines within column width. Fractional powers are preferred to root signs and should always be used in more elaborate formulas. The solidus should be used instead of the horizontal line for fractions wherever possible.

• A normal paper should not exceed 8 pages in the Journal. It is about 8000 words or 20 double-spaced typewritten pages exclusive of drawings. A Technical Brief should not exceed 750 words or about one page in the Journal inclusive of drawings.

• Originals and two copies of figures must accompany the manuscript. Line drawings should not be larger than $8^1/_2 \times 11$ in. and should be planned for reduction to column width. Lettering should be large enough to be clearly legible when the illustration is reduced. The originals of line drawings must be in India ink on white or pale blue tracing paper or tracing cloth. Photographs of equipment or test specimens must be glossy prints and should be used sparingly. Captions for figures should be typed double-spaced and included as the last page of the manuscript. The figure number and author's name should be written in the margin or on the back of each illustration.

• Titles of papers should be brief.

• Authors can obtain copies of the ASME Manual MS-4, "An ASME Paper," from the Editor and are urged to do so before drafting their papers in final form.

• Papers published in Journals of the Transactions of the ASME must be presented at a Meeting, either in person or by title.

• An author is entitled to 25 preprints free of charge (in the case of two authors, 15 each; three or more authors, 10 each). Larger quantities of preprints or reprints can be ordered from Editorial Department, The American Society of Mechanical Engineers, 345 East 47th Street, New York 17, N. Y. Quotations will be sent on request.

Please address all communications to:

Editor, ASME,

United Engineering Center

345 East 47th Street,

New York 17, N. Y.

ASME Publications Committee